INVESTIGATING SENSITIVITY IMPROVEMENT METHODS FOR QUADRUPOLAR NUCLEI IN SOLID-STATE NUCLEAR MAGNETIC RESONANCE

Henri Colaux

A Thesis Submitted for the Degree of PhD
at the
University of St Andrews

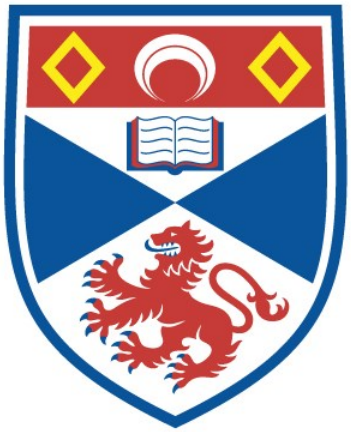

2016

Investigating sensitivity improvement methods for quadrupolar nuclei in solid-state nuclear magnetic resonance

Henri Colaux

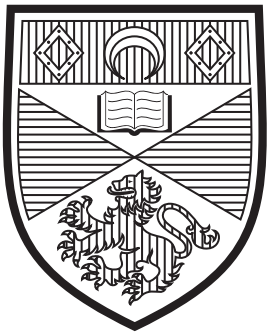

University of
St Andrews

This thesis is submitted in partial fulfilment for
the degree of PhD at the University of St Andrews

August 2016

Declaration

1. Candidate's declarations:

I, Henri Colaux, hereby certify that this thesis, which is approximately 77,000 words in length, has been written by me, and that it is the record of work carried out by me, or principally by myself in collaboration with others as acknowledged, and that it has not been submitted in any previous application for a higher degree.

I was admitted as a research student in September 2012 and as a candidate for the degree of PhD in September 2013 ; the higher study for which this is a record was carried out in the University of St Andrews between 2012 and 2016.

Date 30th August 2016 signature of candidate .....

2. Supervisor's declaration:

I hereby certify that the candidate has fulfilled the conditions of the Resolution and Regulations appropriate for the degree of PhD in the University of St Andrews and that the candidate is qualified to submit this thesis in application for that degree.

Date ..... signature of supervisor .....

3. Permission for publication:

In submitting this thesis to the University of St Andrews I understand that I am giving permission for it to be made available for use in accordance with the regulations of the University Library for the time being in force, subject to any copyright vested in the work not being affected thereby. I also understand that the title and the abstract will be published, and that a copy of the work may be made and supplied to any bona fide library or research worker, that my thesis will be electronically accessible for personal or research use unless exempt by award of an embargo as requested below, and that the library has the right to migrate my thesis into new electronic forms as required to ensure continued access to the thesis. I have obtained any third-party copyright permissions that may be required in order to allow such access and migration, or have requested the appropriate embargo below.

The following is an agreed request by candidate and supervisor regarding the publication of this thesis:

No embargo on print copy nor electronic copy.

Date 30th August 2016 signature of candidate .....

..... signature of supervisor .....

Abstract

The study of quadrupolar nuclei using NMR spectroscopy in the solid state significantly increased in popularity from the end of the 20th century, with the introduction of specific methods to acquire spectra free from the effects of the quadrupolar interaction, that results in broadened lineshapes that cannot be completely removed by spinning the sample at the magic angle (MAS), unlike most of the other interactions present in the solid state. The first technique which allows, without any specific hardware, the removal of this broadening has been the *Multiple-Quantum* MQMAS experiment. The method quickly gained a popularity within the NMR community, with numerous successful applications published. However, the multiple-quantum filtration step in this experiment relies on severely limits sensitivity, restricting application to the most sensitive nuclei.

Extending the applicability of MQMAS to less receptive nuclei requires the use of signal improvement techniques. There are multiple examples of such approaches in the literature, but most of these require additional optimisation that may be time-consuming, or simply impossible, on less receptive nuclei. This work introduces a novel signal improvement technique for MQMAS, called FAM-N. Its optimisation is solely based on density matrix simulations using SIMPSON, implying no additional experimental optimisation is required, while improving the signal in MQMAS spectra by equivalent or higher amounts than other common methods. In order to prove the applicability of this method on virtually any system, FAM-N has been investigated by simulation, and tested experimentally using a number of model samples, as well as samples known to be challenging to study by NMR.

This work also explores other aspects of NMR spectroscopy on quadrupolar nuclei. Adiabatic inversion of the satellite populations can be performed to improve the central transition signal in static or MAS spectra. A range of methods has been tested and compared, with particular attention given to hyperbolic secant-shaped pulses, for which

its performance have been described. Finally, cross-polarisation from a spin $I = 1/2$ nucleus to a quadrupolar nucleus has been investigated. After reviewing the theory for the static case, simulations have been performed under MAS in order to identify the conditions for efficient magnetisation transfer, with applications in spectral editing or for the combination with MQMAS.

Acknowledgements - Remerciements

« Lorsqu'on emploie trop de temps à voyager, on devient enfin étranger en son pays. »

"When too much time is occupied in travelling, we become strangers to our native country."

René Descartes, Le discours de la méthode
(*Discourse on the Method*)

English

This is with these words that René Descartes, long before our time, expressed the benefits of travelling, of change of sceneries and of cultural boundaries in the development of his thinking method, based on doubt and critical mind, looked back as the "Cartesian thinking", which, as originally reported, allows to "organize one's thoughts" and to "seek truth in the sciences" and that became the act that initiated modern science. Three rewarding years in Scotland allow me to wholeheartedly confirm this statement.

As complicated may the organisation of data into a credible argumentation be,

Français

C'est en ces mots que René Descartes, bien avant notre époque, énonçait les bienfaits du voyage, du dépaysement et des barrières culturelles dans l'exercice de sa méthode de pensée, basée sur le doute et l'esprit critique, qui passa à la postérité sous le nom de « pensée cartésienne », permettant d'« organiser sa pensée » et « chercher la vérité dans les sciences » et qui constitua l'acte fondateur de la science moderne. Trois enrichissantes années en Écosse me permettent de confirmer sans réserve cette affirmation.

Aussi compliqué qu'il soit d'organiser ses données en une argumentation crédible,

it is even more difficult to express one's feeling for a, yet essential, acknowledgement section. Even though I usually do not express myself in these terms, people that are very dear to me are numerous, and way too numerous for me to be sure not to forget any of them. But I could not bring myself, first, to omit the rationalists, the humanists, the Lumières and all the great thinkers and philosophers, such as Descartes, whose influence was a determining factor in my decision to pursue a scientific carrier, and neither can I omit those eccentric but hilarious science teachers and who were able to pass on their passion, without whom I would not be here writing this -especially at the moment to put into practice their teaching, and to organise my own thoughts in order to suggest new advances in science.

il l'est bien plus de transcrire toutes ses sentiments pour une, pourtant indispensable, section de remerciement. Et bien que je n'ai pas l'habitude de l'exprimer en ces termes, les personnes qui comptent pour moi sont très nombreuses, bien trop nombreuses pour avoir la certitude de n'en omettre aucune. Mais je ne pouvais me résoudre, pour commencer, à omettre de mentionner les rationalistes, les humanistes, les Lumières, et tous les grands penseurs et philosophes qui, à l'instar de Descartes, m'ont fortement inspiré par leurs écrits à poursuivre dans cette voie. Ni à omettre tous ces professeurs de sciences, excentriques mais délirants et qui ont su transmettre le goût et la passion de leur matière, et sans qui je ne serais probablement pas en train d'écrire ses lignes -surtout au moment de, moi-même, mettre leurs enseignements en pratique, et d'organiser ma propre pensée afin de proposer de nouvelles avancés dans les sciences.

Paying honour to whom honour is due, my first acknowledgment goes to my PhD supervisor, Prof. Sharon Ashbrook, for her help, guidance, time and advices that permitted my project to reach an end, as well as, nonetheless, for finding the courage to read throughout my dissertation. I would also like to express my gratitude to those who first introduced me to the world of NMR, and convinced me to carry on. Starting with my former project

À tout seigneur tout honneur, mes premiers remerciements vont à ma directrice de thèse, Sharon Ashbrook, pour son aide précieuse, son temps et ses conseils qui ont permis l'aboutissement de mon projet de thèse. Ainsi que, mine de rien, d'avoir eu la patience de relire complètement mon manuscrit. Il me faut ensuite remercier les personnes qui, les premiers, m'ont introduit dans le monde de la RMN et m'ont donné envie d'y continuer. À

supervisors, Dr. Fabien Ferrage, for his introduction to the solution state NMR of proteins, Dr. Piotr Tekely, for the one to the solid state, as well as Prof. Geoffrey Bodenhausen and the members of the NMR methodology group of the École Normale Supérieure, and Prof. Gareth Morris and the NMR methodology group of Manchester university for their welcome, their advices and for giving me the opportunity to further enhance my knowledge with diffusion NMR. I finally wish to thank Dr. Daniel Dawson and Dr. Nasima Kanwal, with whom I have worked closely on various parts on this work, as well as Dr. Dinu Iuga and Dr. Julien Trébosc for their help in the experiments carried out at the UK 850 MHz solid-state NMR facility in Warwick and at the 800 MHz spectrometer of the university of Lille, respectively.

Now, I wish to thank those who made an considerable contribution in the shadows to the writing of my thesis thanks to an essential moral support, even though not acknowledged as such. The list is also long and I apologise in advance to those who will read without finding their name.

Starting with my family, who did not hesitate to take upon themselves to pay throughout my long and expensive studentship. My unique little brother has always been, against all odds, my best moral support.

commencer par mes anciens directeurs de stages, Fabien Ferrage, pour m'avoir initié à la RMN des protéines en solution, et Piotr Tekely, pour la phase solide, ainsi que Goeffrey Bodenhausen et tous les membres du groupe de méthodologie RMN de l'École Normale Supérieure, et Gareth Morris et tout le groupe de méthodologie RMN de l'université de Manchester pour leur accueil chaleureux, leurs conseils et pour m'avoir permis d'agrémenter mes connaissances avec la RMN de diffusion. Je voudrais finalement remercier Daniel Dawson et Nasima Kanwal, avec qui j'ai collaboré étroitement à l'élaboration de diverses parties de ce travail, ainsi qu'à Dinu Iuga et Julien Trébosc pour l'aide qu'ils m'ont apporté pour les expériences effectuées, respectivement, au 850 MHz de l'université de Warwick et au 600 MHz de l'université de Lille.

Je voudrais maintenant remercier toutes ces personnes qui, dans l'ombre, ont plus que contribué à la rédaction de mon mémoire au moyen d'un indispensable soutien moral, bien qu'il ne soit pas pas reconnu comme tel. Là aussi, la liste est longue et je prie de m'excuser chacune des personnes qui liront ceci mais ne s'y trouveront pas.

À commencer par ma famille qui, pendant tout ma longue et très onéreuse scolarité, n'ont pas hésité à mettre la main à la pâte et financer mes études jusqu'à son terme. Mon unique petit frère, Pierre,

Even though she is no longer able to express it, my mother, who knows the role she played in my life. My father, who lives his life in an admirable way. My grand parents, for being … my grand parents. My uncle and my aunts, and my two cousins for … well, nothing in particular, but I am happy they are here. Finally, those I barely have known, such as my late grandfather, deceased before he got the occasion to rap on my knuckles for all of the mistakes that my dissertation probably contains.

Following all my friends, especially those I knew for a long time and those, for some of them, I was not given the opportunity to meet in a long time, Brice, Boris, Guillaume, Rémi, Romain … my former colleagues and friends from the École Normale Supérieure, in particular Adrien, Mélanie and Simon and their more than questionable (but efficient) sense of humour; and some of my classmates who, I am sure, will recognize themselves if they read this text. Without exception, all my friends from the FFJE* and my acquaintances in Japan, thinking of the good time we spent together. Amongst them, it is impossible not to mention Hikaru and her never-ending good mood.

At the same time I would like to greet all

qui, contre vents et marées, a été et ce depuis longtemps mon meilleur soutien moral. Ma mère qui, si elle n'est plus en mesure de l'exprimer, sait quel rôle elle a joué dans ma vie. Mon père, qui a su faire sa vie de manière admirable. Mes grand-parents, pour être … mes grand-parents. Mon oncle et ma tante, ainsi que mes deux cousines pour … rien en particulier, mais heureux qu'elle soit là. Enfin, tous ceux que je n'ai que peu connu, dont feu mon autre grand père, décédé trop tôt pour avoir l'occasion de me taper sur les doigts pour les fautes que contient très probablement ce manuscrit.

Tous mes amis ensuite, en particulier ceux de longue date et ceux que je n'ai pas eu l'occasion de revoir depuis longtemps pour certains, dont Brice, Boris, Guillaume, Rémi, Romain … Mes ancien collègues et amis de l'École Normale Supérieure, notamment Adrien, Mélanie et Simon et leur humour on ne peut plus douteux mais efficace ; et aussi plusieurs autres de mes camarades de promotion qui, j'en suis sûr, se reconnaîtront s'ils lisent ceci. Sans exception, tous mes amis du FFJE*, et toutes mes connaissances au Japon, en souvenir de tous les excellents moments que nous avons passé ensemble. Parmi eux, il m'est impossible de ne pas mentionner Hikaru et son éternelle bonne humeur.

Je salue chaleureusement au passage tous les collègues de St Andrews ; ceux de

Forum Franco-Japonais des Étudiants

my colleagues from St Andrews ; those of Japan society, Marc, Tomochika, and Aki-sensei for his outstanding classes. And finally, obviously, all the group members. I don't think it is helpful to recall the name of every single person of them as I meet them almost every day at the time I am writing this, but instead that we had great laughs about more or less serious and more or less mature topics, that we enjoyed together some of the (few) activities of St Andrews, that we all experienced the joys and sadness of being a PhD student (or a post-doc), as we attempted to see through the mysteries and the endless whims of NMR, for which we sacrificed a good deal of our lives and of our sanity. Finally, I want everyone to remember the sense of solidarity and mutual aid I took advantage of when I was writing my thesis by "forcing" them to read parts of it.

2016, the year when I will most certainly become a Doctor of Philosophy, begins with the persistent memories of the Paris attacks, while an outbreak, which seems to be inexorable, of new forms of fanaticism is taking place across the planet. In a time of great technological progress suggesting the possibility of a smarter future, there is a stunning stagnation of economical, political and social theories, a worsening of the environmental problems and a rise of poverty throughout the

la Japan Society, Marc, Tomochika, et Aki-sensei pour ses cours exceptionnels. Et enfin, bien entendu et à plus d'un titre, tous mes membres du groupe. Il ne me semble pas utile de rappeler le nom chacun d'entre eux que je croise presque tous les jours au moment où j'écris ceci, mais plutôt que nous avons bien ri sur des sujets plus ou moins sérieux et plus ou moins matures, que nous avons profité ensemble des joies et tristesses que procure la vie de thésard (ou de post-doc), des (quelques) activités que propose St Andrews, des mystères insondables et des caprices à répétition de la RMN, pour laquelle nous avons sacrifié une bonne partie de nos vies, et de notre santé mentale. Enfin, ce que je voudrais que l'on retienne est cet esprit de solidarité et d'entraide, dont j'ai bien tiré profit pendant la rédaction en « forçant » la plupart d'entre eux à relire des parties de cette thèse.

2016, qui sera probablement l'année qui fera de moi un docteur en sciences naturelles, commence avec le souvenir toujours tenace des attentats de Paris, sous fond d'une montée qui semble inexorable de nouvelles formes de fanatisme idéologique à divers endroits du monde. Alors que de grands progrès technologiques laissent présager les possibilités d'un futur plus intelligent, on assiste à une surprenante stagnation des théories économiques, politiques et sociales, à l'aggra-

world.

Although being worried about the future of the world we live in, doing a doctorate taught me that a mountain of problems to be solved is not some sort of unchangeable mystical entity. One can climb a mountain, little by little, with one problem at a time and taken in sequence. This is but a matter of time, patience, method and good willing. As I think, naively but honestly, this world to be constituted of too many good-willing people for any desperate-looking situation to be so. Therefore, I would like to dedicate my work to those values in which I believe in and to the people who mean a lot to me, and to History for the lessons it grants us about the future, as all this keeps me moving forward. The new technologies will push further and further the possibilities of mankind to communicate, to expand their horizons and to confront their ideas and solutions; solutions that, pulled together, whatever their scope and scale, will constitute The solution to the addressed issues. As the myth of the end of History dies away for good, it is more than ever time not to surrender to defeatism, and to unite all forces for the constitution of this ensemble.

vation des problèmes environnementaux et à la paupérisation de toute une partie de la population mondiale.

Bien que je sois inquiet pour l'avenir du monde dans lequel nous vivons, faire un doctorat m'a appris qu'une montagnes de problème à résoudre n'est pas une sorte d'entité mystique immuable et infranchissable. Une montagne se franchit, petit à petit, un problème à la fois pris dans l'ordre. Tout n'est qu'affaire de temps, de patience, de méthode et de bonne volonté. Car je pense, naïvement mais honnêtement, ce monde constitué de bien trop de gens de bonne volonté pour qu'aucune situation désespérée ne le soit vraiment. Je voudrais donc dédier mes travaux à ces valeurs auquelles je crois et à ceux qui comptent pour moi, et à l'histoire et à ce qu'elle nous apporte comme leçons pour l'avenir, car c'est tout ceci qui me pousse à aller de l'avant. Les nouvelles technologies permettront de plus en plus aux hommes de communiquer, d'étendre leurs horizons et de confronter leurs idées et leurs solutions ; solutions qui, mises bout à bout, quelque soit leur ampleur et envergure, deviendront un ensemble qui constituera La réponse aux problèmes soulevés. Alors que se brise pour de bon le mythe de la fin de l'histoire, il est plus que jamais nécessaire de ne pas céder au défaitisme, et de réunir toutes ces bonnes volontés à la construction de cet ensemble.

As I live in uncertainty and I do not know what tomorrow will be made of, I have chosen scientific research as it appears as the best way for me to leave something constructive to the world, by enabling even just a little more the expansion of the human knowledge. Keeping this in mind, I present the outcome of three and a half years of research, hoping that these will be useful in a way or another and that it will find its place in the construction of that ensemble.

Vivant dans l'expectative et ne sachant pas de quoi demain sera fait, j'ai trouvé en la recherche scientifique ce qui me semble être le meilleur moyen pour moi de laisser quelque chose de constructif au monde, en permettant d'étendre ne serait-ce qu'un peu l'étendue des connaissances humaines. C'est donc dans cet esprit que je présente l'aboutissement de trois années et demi de recherche, en espérant qu'elles puissent être d'une manière ou d'une autre mises à profit et qu'elles trouveront leur place dans la construction de cet ensemble.

« Science sans conscience n'est que ruine de l'âme. »

"Science without conscience is but the ruin of the soul."

François Rabelais, Pantagruel

”Every portrait that is painted with feeling is a portrait of the artist, not of the sitter. The sitter is merely the accident, the occasion. It is not he who is revealed by the painter; it is rather the painter who, on the coloured canvas, reveals himself.”

Basil Hallward in Oscar Wilde, The picture of Dorian Gray

Table of contents

General introduction

Work concerned with sensitivity improvement in NMR[1] spectroscopy [1–3] often starts by quoting this famous saying:

> "There are currently three problems with NMR spectroscopy: Sensitivity, sensitivity and sensitivity"
>
> Attributed to Robert G. Griffin

This stresses the fact that sensitivity is, and still remains, the number one issue in NMR spectroscopy, as demonstrated by the countless techniques primarily aimed at improving the sensitivity of specific NMR methods. CPMG[2],[4, 5] CP[3],[6, 7] or the recent developments in DNP[4] [8, 9] are examples of the multiple answers proposed to address this issue.

Concerning the different materials synthesized and studied in the field of material science (MOFs, ceramics, zeolites, minerals, catalysts, ...), many contain inorganic transition metals. As Figure 1 reveals, most of those elements have at least one NMR-active isotope, making NMR a very suitable technique for the investigation on those materials. Figure 1 also shows that most of the transition metals do not possess a spin $I = 1/2$, *e.g.*, have more than two energy levels. A total of 69% of all NMR-active isotopes in the periodic table possess half-integer spin above $1/2$, and 6% an integer spin. NMR of those nuclei presents further difficulties than when studying $I = 1/2$ nuclei. Nuclei with spins $I > 1/2$ are subject to quadrupolar interaction in the solid state,[5] which significantly broaden resonances, and this anisotropy cannot be completely removed by conventional signal-narrowing techniques such as MAS[6].[10] Furthermore, many of these

[1] NMR: *Nuclear Magnetic Resonance*
[2] CPMG: *Carr-Purcell-Meiboom-Gill*
[3] CP: *Cross Polarisation*
[4] DNP: *Dynamic Nuclear Polarisation*
[5] Hence also refereed to as "quadrupolar nuclei"
[6] MAS: *Magic-Angle Spinning*

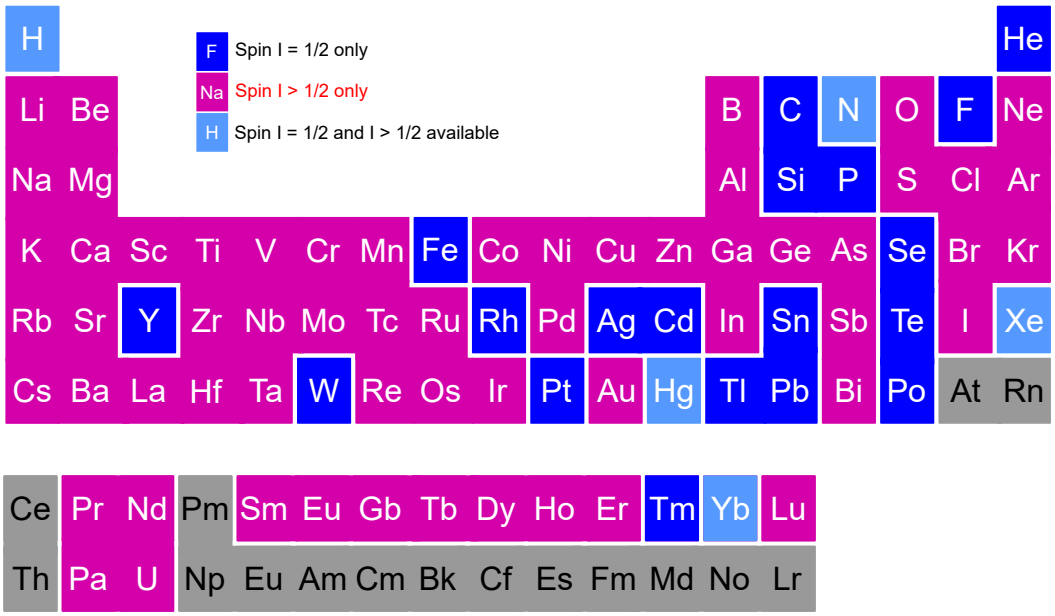

Figure 1: *Periodic table of the elements, coloured according to the spin I available for the elements.*

nuclei possess other unfavourable properties, complicating their investigation even further. While some common quadrupolar nuclei possess a gyromagnetic ratio comparable to that of ^{13}C (such as ^{23}Na, ^{27}Al, ^{45}Sc, ^{87}Rb, ^{93}Nb ...), many other important nuclei exhibit a low gyromagnetic ratio (low-γ), implying broader lineshapes and lower signal-to-noise per unit of time than their high-γ counterparts. Furthermore, many of them also have a low natural abundance, decreasing further the signal-to-noise per unit of time unless the material is isotopically enriched. Finally, it is common that many samples contain only a small fraction, or even traces, of a certain inorganic element, decreasing further the sensitivity of NMR experiments.

This work investigates methods for improving NMR sensitivity, with a particular focus on quadrupolar nuclei. Part I introduces all the theoretical aspects relevant to this work. Chapter 1 introduces the basic theory behind NMR spectroscopy, both from a semi-classical mechanical and a quantum-mechanical point of view, as well as some additional technical aspects. Chapter 2 introduces the different interactions taking place in the solid state, including the quadrupolar interaction, an essential aspect of this work. Narrowing the lineshapes of the NMR spectra of quadrupolar nuclei to retain just their isotropic components requires specific techniques, which are introduced in Chapter 3 along with the common techniques used in this work. Among the existing techniques, the MQMAS[7] experiment [11, 12] was the first method published to resolve

[7] MQMAS: *Multiple-Quantum Magic-Angle Spinning*

this issue without the need for dedicated and delicate to engineer hardware.[13, 14] On the downside, the MQMAS experiment suffers from an inherently low sensitivity due to the MQF[8] step it employs, adding to the difficulty of NMR on quadrupolar nuclei described previously. A few years later, the STMAS[9] technique was introduced,[15] which relies only on single-quantum transitions. It fulfils the same function and results very similar spectra as MQMAS, but without the sensitivity issues. Its usage has remained somewhat limited due to strict requirements for the magic angle calibration and the spinning speed stability.

Part II focuses on methods for sensitivity improvement in the MQMAS experiment. After an illustration of the low sensitivity of the MQMAS experiment, sensitivity enhancement methods published in the literature are presented in Chapter 4: SPAM[10],[16] FAM[11],[17, 18] and DFS[12].[19] The mechanisms of saturation or inversion of the satellite transitions, by which FAM and DFS produce signal improvement in MQMAS, is also discussed.[20] Other approaches used in MQMAS, including FASTER[13] [21] and RIACT[14] [22] are also presented. Finally, FAM-N[15], the main contribution of this work to the issue, will be introduced in this chapter.[23] FAM-N is a composite pulse based on the FAM approach, derived from simulations performed using the density-matrix propagation package SIMPSON[16].[24] Chapter 5 is dedicated to a theoretical investigation of the performances of FAM-N under various conditions, illustrated by experiments conducted on several model samples and on nuclei with various spin quantum numbers. The performance of FAM-N is also compared to the methods introduced in Chapter 4 using model samples. Chapter 6 focuses on the experimental verification of the efficiency of FAM-N in the general case. FAM-N is applied under various conditions in order to prove the wide applicability of the method under various conditions, *i.e.*, samples with different quadrupolar interactions, different sensitivity and different dilution. Some samples which are known from literature to be challenging to investigate using the MQMAS experiment will also studied. Chapter 6 also reports investigations conducted on miscellaneous aspects of FAM-N pulses, comprising preliminary elements for the extension of the method to 5QMAS[17], and discussions on problems reported in previous

[8] MQF: *Multiple-Quantum Filtration*
[9] STMAS: *Satellite-Transition Magic-Angle Spinning*
[10] SPAM: *Soft Pulse Adding Mixing.*
[11] FAM: *Fast-Amplitude Modulation*
[12] DFS: *Double Frequency Sweep*
[13] FASTER: *FAst Spinning gives Transfer Enhancement at Rotary resonance*
[14] RIACT: *Rotor-Induced Adiabatic Coherence Transfer*
[15] FAM-N: *Fast-Amplitude Modulation* with *N* pulses
[16] SIMPSON: *SIMulation Package for SOlid-state Nmr*
[17] 5QMAS: *Quintuple-Quantum Magic-Angle Spinning*

sections.

Part III presents the investigations conducted on other aspects of NMR of quadrupolar nuclei. Some pulses, such as the HS[18] pulse,[25, 26] but also the RAPT[19] [27] and DFS pulses, can efficiently increase the signal of conventional MAS spectra by a maximum factor of $2I$ (I being the spin quantum number) by means of an adiabatic inversion of the satellite transitions. The performance of the HS pulse under fast MAS is reported in Chapter 7, and compared to DFS, RAPT and one other method designed for the same purpose, termed COMPACT[20].[28] The implementation of HS into RIACT, introduced in Chapter 4, will also be assessed. Chapter 8 explores some aspects of CP from a spin $I = 1/2$ nucleus to a quadrupolar nucleus. While the role of CP in experiments involving spins $I = 1/2$ is signal enhancement, CP to a quadrupolar nucleus is primarily aimed at investigating connectivity. This experiment has been theoretically described for the static case.[29, 30] CP simulations under static and MAS conditions have been performed, and are reported, compared and discussed in Chapter 8. The purpose of the investigation is to gain insight into Hartmann-Hahn conditions when a quadrupolar nucleus is involved and to find suitable conditions to record CP spectra with a good sensitivity, of for CP combined with MQMAS.

The UK 850 MHz solid-state NMR Facility used in this research was funded by EPSRC and BBSRC (contract reference PR140003), as well as the University of Warwick including via part funding through Birmingham Science City Advanced Materials Projects 1 and 2 supported by Advantage West Midlands (AWM) and the European Regional Development Fund (ERDF). Financial support from the TGIR-RMN-THC Fr3050 CNRS for conducting the research is gratefully acknowledged.

[18] HS: *Hyperbolic Secant*
[19] RAPT: *Rotor-Assisted Population Transfer*
[20] COMPACT: *COMposite Pulses Adapted for Central Transitions*

Part I

The theory and applications of NMR

« La notion de passoire est indépendante de la notion de trou, et réciproquement.»

”The notion of a colander is independent of the notion of a hole, and reciprocally.”

Rouxel, Les Shadoks

mocking the non-intuitive principles of quantum mechanics.

Chapter 1

General NMR theory

Introduction

NMR[1] spectroscopy is a powerful technique for investigating the chemical, structural and physical properties of matter. This technique exploits the magnetization that results from the inherent spin a nucleus possesses, and its interaction with a magnetic field, from which useful information can be extracted.

First observed by Rabi *et al.* [1] and developed by physicists Bloch and Purcell,[2, 3] jointly awarded with the Nobel Prize in 1952,[31, 32] the NMR phenomenon met with little interest in the physics community as, unfortunately, the signal observed depended on the chemical environment of the nucleus and was therefore considered unattractive to probe physical quantities. However, the chemistry community realised the significant potential of this technique for obtaining information on the chemical structure of molecules. Previously limited by the field strength of simple electromagnets, the method gained considerable interest with the development of superconducting coils during the 1970s, enabling much higher magnetic fields to be achieved. Nowadays, NMR spectroscopy is widely and routinely used in the fields of physics, biology and chemistry for the study of molecules, materials, and proteins, and in medical imaging through MRI[2].

Although there were some early applications of NMR to the study of solids, the technique became more generally applicable much later, with considerable development

[1] NMR: *Nuclear Magnetic Resonance*
[2] MRI: (nuclear) *Magnetic Resonance Imaging*

from the 1980s onwards. Solid-state NMR is technically more difficult to implement than liquid-state or solution-state NMR, and the spectra obtained usually more challenging to interpret. Recent improvements in both hardware and software have enabled spectra with good sensitivity and resolution to be obtained for a range of nuclei, with applications across chemistry, biology and materials science.

NMR can be either described using a semi-classical- or a quantum-mechanical approach. A full quantum-mechanical treatment is necessary in order to fully describe all the physics behind the NMR phenomenon, but classical mechanics can be used to describe many of the main properties in a more instinctive way. More detailed information can be found in [33–46].

1.1 Semi-classical mechanics approach

1.1.1 The magnetic moment

The nucleus of atom can be described simplistically as a positively-charged sphere with an inherent gyration, resulting in a spin angular momentum. The amplitude of this angular momentum cannot decrease, and requires energies on the order of magnitude of γ-rays to be increased (technique called Mössbauer spectroscopy [47, 48]). In the context of NMR experiments, only the orientation of the angular momentum can be changed. According to Maxwell's Laws,[49] a moving charge - and thus a rotating charge - creates a magnetic field throughout the surrounding space.

It is customary, as well as convenient, to describe the magnetic field using a dipolar magnetic moment, expressed as a vector quantity $\vec{\mu}$, created at the barycentre of the charge distribution as shown in Figure 1.1. For one single charged particle, it is defined as

$$\vec{\mu} = {}^{1}\!/_{2}.q\vec{r} \wedge \vec{v} \tag{1.1.1}$$

where

- q is the charge of the particle,
- $\vec{r}$ is a position vector pointing to a specific volume element from the origin,
- $\vec{v}$ is the velocity of the particle,
- $\wedge$ denotes the vector product.

For any random charge distribution, the charge q in the previous expression can be replaced by $\rho(\vec{r})$, denoting the charge density pointed by $\vec{r}$ from the origin (thus expressed as a charge per unit volume), and the velocity $\vec{v}$ by $\vec{v}(\vec{r})$, denoting the velocity of the charge located at $\vec{r}$, giving the general expression

$$\vec{\mu} = \frac{1}{2} \iiint_V \rho(\vec{r}).\vec{r} \wedge \vec{v}(\vec{r}).dV \quad , \tag{1.1.2}$$

where dV is a volume element. The integral is performed over all the volume in the surrounding space. The magnetic field $\vec{B}$ created at $\vec{r}$ from the origin, from a magnetic moment $\vec{\mu}$, is expressed by

$$\vec{B}(\vec{r}) = \frac{\mu_0}{4\pi} \vec{\nabla} \wedge \left[\vec{\mu} \wedge \frac{\vec{r}}{\|\vec{r}\|^3} \right] \quad , \tag{1.1.3}$$

where μ_0 is the vacuum permeability constant, and $\vec{\nabla}\wedge$ is the curl operator. For example, applying Equation (1.1.2) on a charged sphere, with total charge q equally distributed within its volume, of radius R and with a rotation vector $\vec{\Omega}$ gives

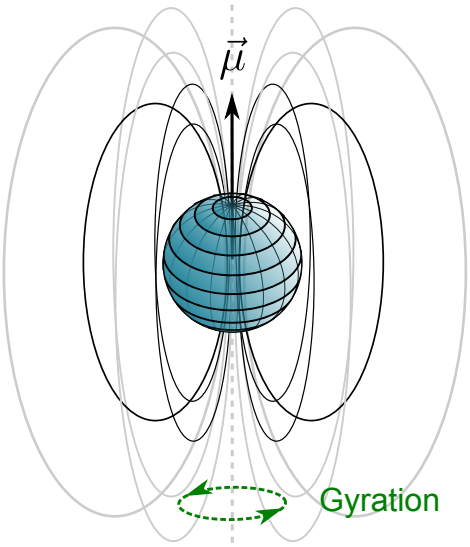

Figure 1.1: *Schematic of a rotating nucleus and its dipolar moment, $\vec{\mu}$, and corresponding lines of magnetic field, as pictured in semi-classical mechanics.*

$$\vec{\mu} = {}^2\!/_9 . q R^2 \vec{\Omega} \quad , \tag{1.1.4}$$

thus, establishing the collinear relationship of the magnetic moment and the rotation vector. The relationship between the magnetic moment $\vec{\mu}$ and the angular momentum $\vec{L}$ can also be easily established. Recalling the definition of an angular momentum for a single particle

$$\begin{aligned} \vec{L} &= \vec{r} \wedge \vec{p} \\ &= m\vec{r} \wedge \vec{v} \quad , \end{aligned} \tag{1.1.5}$$

where $\vec{p}$ is the momentum of the considered particle and m is its mass. It is thus straightforward to see from Equations (1.1.1) and (1.1.5) that a fundamental property of the magnetic dipolar moment is that is is proportional, and thus collinear, to the angular momentum. Equation (1.1.5) can be rearranged to give

$$\vec{\mu} = \underbrace{\frac{q}{2m}}_{=\gamma} \vec{L} \quad . \tag{1.1.6}$$

The quantity γ, defined in a general manner as the ratio of $\|\vec{\mu}\|$ and $\|\vec{L}\|$, is called the gyromagnetic ratio. Although the definition of γ from Equation (1.1.6) is true for classical systems, it differs for elementary particles, such as atomic nuclei and electrons. The value of γ for each nuclei is known from experimental measurements and tabulated (Harris *et al.* [50, 51] and Appendix C.2).

1.1.2 Precession and Larmor frequency

It can be established externally applied magnetic fields interact with magnetic moments. When submitted to a static magnetic field, $\vec{B}_0$, the following quantities arise: a force $\vec{F}$, a torque $\vec{\tau}$ and an interaction energy E_m, given by [52]

$$\begin{cases} \vec{F} = (\vec{\mu}.\vec{\nabla}).\vec{B}_0 & \text{(1.1.7a)} \\ \vec{\tau} = \vec{\mu} \wedge \vec{B}_0 & \text{(1.1.7b)} \\ E_m = -\vec{\mu}.\vec{B}_0 \quad , & \text{(1.1.7c)} \end{cases}$$

where $\vec{\nabla}.$ is the divergence operator. It can be established immediately from Equation (1.1.7a) that a force is created only if there is a magnetic field gradient. The static magnetic fields used in NMR are overall homogeneous, and the nuclear magnetism is small compared to electronic magnetism ensuring the force has a negligible impact. However, the interaction energy and angular momenta are of key importance to explain the magnetic resonance phenomenon.

From the torque derived in Equation (1.1.7b), it can be deduced that a magnetic field affects the spin properties of a nucleus. To describe the evolution of $\vec{\mu}$ under the effect of a magnetic field $\vec{B}_0$, it is first necessary to define a frame, customarily chosen to be a direct orthonormal Cartesian frame fixed relative to the laboratory, termed the laboratory frame and here denoted Σ_{lab}. This frame can be described by an origin point 0, placed in the center of the system, and by three unit vectors $(\vec{u}_x, \vec{u}_y, \vec{u}_z)$, where $\vec{u}_z$ is set collinear to $\vec{B}_0$. The plane $(O, \vec{u}_x, \vec{u}_y)$, perpendicular to $\vec{B}_0$, is referred to as the transverse plane. It is convenient to define the transverse plane as a complex frame, where $\vec{u}_x$ relates to $\vec{u}_y$ according to

$$\vec{u}_y = i\vec{u}_x \quad , \tag{1.1.8}$$

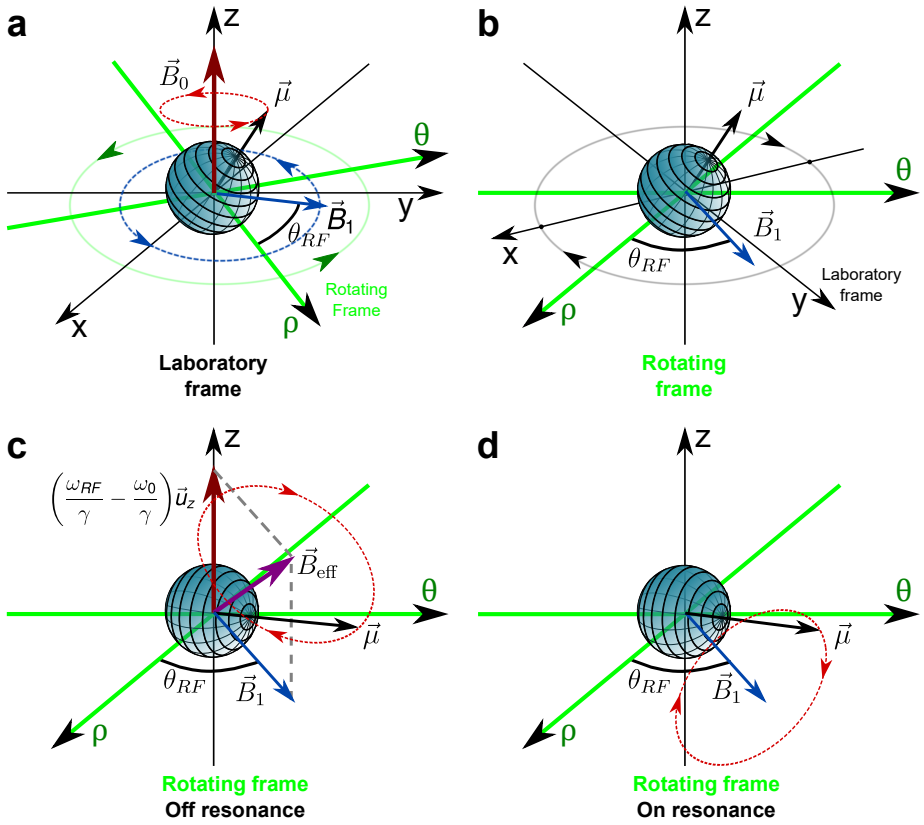

Figure 1.2: *Schematic representations of **(a)**: the laboratory frame Σ_{lab} and how it relates to the rotating frame Σ_{rot}, and **(b)**: Σ_{lab} seen from Σ_{rot}. Representation of the motion of the magnetisation vector $\vec{\mu}$ in **(c)**: the rotating frame Σ_{rot} with an RF field off resonance ($\omega_{\text{RF}} \neq \omega_0$), and in **(d)**: the rotating frame Σ_{rot} with an RF field on resonance ($\omega_{\text{RF}} = \omega_0$).*

where i is the imaginary unit. The position and orientation of any magnetisation vector $\vec{\mu}(t_0)$ is expressed in Σ_{lab} as

$$\vec{\mu}(t_0) = \mu(t_0)\exp(i\theta_0)(\sin\phi_0.\vec{u}_x + \cos\phi_0.\vec{u}_z) \quad , \tag{1.1.9}$$

where $\mu = \|\vec{\mu}\|$ is the norm of the vector and the two angles θ_0 and ϕ_0 are respectively the latitudinal and longitudinal angles defining the orientation of μ in Σ_{lab}. The component of the magnetisation along $(O, \vec{u}_z)$ is called longitudinal magnetisation, and the component of the magnetisation in the transverse plane is called transverse magnetisation.

The evolution of the magnetisation is given by the AMT[3] expressed in Σ_{lab}

$$\left(\frac{d\vec{L}}{dt}\right)_{\Sigma_{\text{lab}}} = \sum(\vec{\tau})_{\Sigma_{\text{lab}}} \quad , \tag{1.1.10}$$

where $\sum(\vec{\tau})_{\Sigma_{\text{lab}}}$ are the sum of the force moments expressed in Σ_{lab}. Expressed in terms

[3] AMT: *Angular Momentum Theorem*

of the magnetic moment $\vec{\mu}$ using Equation (1.1.6), Equation (1.1.10) gives

$$\left(\frac{d\vec{\mu}(t)}{dt}\right)_{\Sigma_{\text{lab}}} = \gamma\vec{\mu}(t) \wedge \vec{B}_0 \quad . \tag{1.1.11}$$

Redefining Equation (1.1.11) in Σ_{lab}, using $\vec{\mu}(t_0)$ expressed in Equation (1.1.9) as the initial condition, results in

$$\vec{\mu}(t)_{\Sigma_{\text{lab}}} = \mu(t_0)\exp(i(\theta_0 - \gamma B_0 t))\sin\phi_0.\vec{u}_x + \mu(t_0)\exp(i\theta_0)\cos\phi_0.\vec{u}_z \quad . \tag{1.1.12}$$

The magnetisation vector accomplishes a precession motion around the magnetic field in Σ_{lab} at an angular frequency

$$\omega_0 = -\gamma B_0 \quad , \tag{1.1.13}$$

where ω_0 is called the Larmor frequency,[4] while the magnetisation along $\vec{u}_z$ does not evolve. The relative sign in Equation (1.1.13) reflects the fact that the precession motion goes clockwise around $\vec{u}_z$. The Larmor frequency is the quantity of interest to be measured in every NMR experiment. This defines the resonance frequency for the system, and is at the root of the so-called nuclear magnetic resonance phenomenon.

1.1.3 Nutation and RF frequency

It can be deduced from the expression of the interaction energy in Equation (1.1.7c), that the energy is a minimum when $\vec{\mu}$ is aligned with $\vec{B}_0$. To modify the initial precession angle θ_0, it is possible to apply an oscillating magnetic field $\vec{B}_1$, termed the RF[5] field, in the transverse plane that can be expressed

$$\vec{B}_1(t) = B_1\exp(i(\omega_{\text{RF}}t + \theta_{\text{RF}})).\vec{u}_x \quad , \tag{1.1.14}$$

where ω_{RF} is the oscillation frequency of the field, and θ_{RF} the phase of the RF field. Under the application of an RF field, the AMT expressed in Equations (1.1.10) and (1.1.11) gives

$$\left(\frac{d\vec{\mu}(t)}{dt}\right)_{\Sigma_{\text{lab}}} = \gamma\vec{\mu}(t) \wedge (\vec{B}_0 + \vec{B}_1) \quad . \tag{1.1.15}$$

Owing to the oscillating nature of $\vec{B}_1$, it is convenient to express the magnetic field in another direct orthonormal frame that rotates at the same frequency as $\vec{B}_1$ with a

[4] Denoted ν_0 ($= -\gamma B_0/2\pi$) when expressed in cycles per second (Hz) rather than in radians per second.
[5] RF: *Radio-Frequency*

given phase. This frame is called the rotating frame, denoted Σ_{rot}, and is defined by $(0, \vec{u}_\rho, \vec{u}_\theta, \vec{u}_z)$, which are related to Σ_{lab} through

$$\Sigma_{\text{rot}} \begin{cases} \vec{u}_\rho = \exp(i\omega_{\text{RF}}t).\vec{u}_x & \text{(1.1.16a)} \\ \vec{u}_\theta = \exp(i\omega_{\text{RF}}t).\vec{u}_y = \exp(i(\omega_{\text{RF}}t + \pi/2)).\vec{u}_x \quad , & \text{(1.1.16b)} \end{cases}$$

with $\vec{u}_z$ being the same vector in both Σ_{lab} and Σ_{rot}. Graphical representations of Σ_{lab} and Σ_{rot} are shown in Figures 1.2a and 1.2b. The AMT in Equation (1.1.15) can be translated from Σ_{lab} to Σ_{rot} (see Appendix B.2, Equation (B.2.1)) using

$$\begin{aligned} (\vec{\mu})_{\Sigma_{\text{lab}}} &= \exp\left(i(+\omega_{\text{RF}}t + \theta_{\text{RF}})\right) . \exp\left(i(-\omega_{\text{RF}}t + \theta_{\text{RF}})\right) . (\vec{\mu})_{\Sigma_{\text{lab}}} \\ &= \exp\left(i(+\omega_{\text{RF}}t + \theta_{\text{RF}})\right) . (\vec{\mu})_{\Sigma_{\text{rot}}} \quad . \end{aligned} \tag{1.1.17}$$

In Σ_{rot}, $\vec{B}_1$ does not move and has a fixed direction in the transverse plane, defined by

$$\vec{B}_1 = B_1 \exp(i\theta_{\text{RF}}).\vec{u}_\rho \quad . \tag{1.1.18}$$

Combining Equations (1.1.15) and (1.1.17) leads to the following expression of the AMT in Σ_{rot}

$$\left(\frac{d\vec{\mu}(t)}{dt}\right)_{\Sigma_{\text{rot}}} = \gamma \left(\vec{\mu}(t)\right)_{\Sigma_{\text{rot}}} \wedge \left[\left(\frac{\omega_{\text{RF}}}{\gamma} - \frac{\omega_0}{\gamma}\right).\vec{u}_z + B_1 \exp(i\theta_{\text{RF}}).\vec{u}_\rho\right] \quad . \tag{1.1.19}$$

Equation (1.1.19) can be interpreted as $\vec{\mu}(t)$ rotating in Σ_{rot} clockwise around an effective magnetic field $\vec{B}_{\text{eff}}$ illustrated in Figure 1.2c. This effective magnetic field can be defined as[6]

$$\vec{B}_{\text{eff}} = \left(\frac{\omega_{\text{RF}}}{\gamma} - \frac{\omega_0}{\gamma}\right).\vec{u}_z + B_1 \exp(i\theta_{\text{RF}}).\vec{u}_\rho \quad . \tag{1.1.20}$$

The quantity

$$\Delta\omega_0 = \omega_0 - \omega_{\text{RF}} \tag{1.1.21}$$

is referred to as the frequency offset,[7] as it expresses the difference between the Larmor frequency and the RF field frequency. It can be shown from Equation (1.1.19) that if the RF field is on resonance, *i.e.*, $\omega_{\text{RF}} = \omega_0$ or $\Delta\omega_0 = 0$, $\vec{B}_0$ vanishes in Σ_{rot} and $\vec{\mu}$ precesses only around the static $\vec{B}_1$ as illustrated in Figure 1.2d. If the RF field is off resonance, *e.g.*, $\omega_{\text{RF}} \neq \omega_0$ or $\Delta\omega_0 \neq 0$, $\vec{\mu}$ precesses around the effective magnetic field $\vec{B}_{\text{eff}}$ defined in

[6] In the literature, for example in Tannús and Garwood,[53] and in Appendix F, $\vec{B}_{\text{eff}}$ is defined as the opposite as in Equation (1.1.20), and the magnetisation described as rotating counter-clockwise around this magnetic field.

[7] Or $\Delta\nu_0$ when expressed in Hz.

Equation (1.1.20) as illustrated in Figure 1.2c. This case is also useful to describe cases when several signal components with slightly different Larmor frequencies are present in the sample (see Section 2.2.1). Off-resonance effects are also essential to describe adiabatic passages (see Appendix F). If the RF field is on resonance, Equation (1.1.19) simplifies to

$$\left(\frac{d\vec{\mu}(t)}{dt}\right)_{\Sigma_{\text{rot}}} = \gamma\,(\vec{\mu}(t))_{\Sigma_{\text{rot}}} \wedge (B_1.\vec{u}_\rho) \quad . \tag{1.1.22}$$

Solving Equation (1.1.22) with the initial magnetisation $\vec{\mu}(t=0) = \mu_0.\exp(i\theta_0).\vec{u}_z$, *e.g.* $\vec{\mu}$ initially aligned with $\vec{B}_0$, it can be obtained that

$$(\vec{\mu}(t))_{\Sigma_{\text{rot}}} = \mu(t_0)\exp(i\theta_0)\,(\cos(\gamma B_1 t)\vec{u}_z - \sin(\gamma B_1 t).\vec{u}_\rho)) \quad . \tag{1.1.23}$$

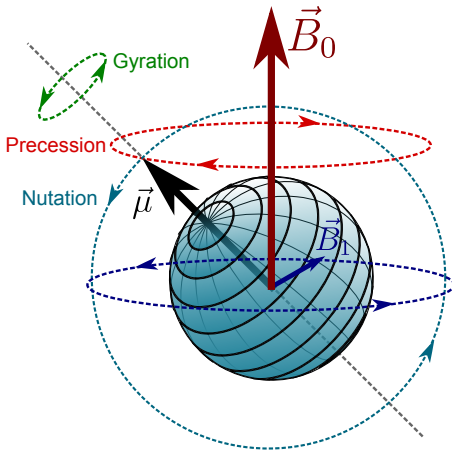

Figure 1.3: *Schematic of the three rotation motions of the magnetic moment vector $\vec{\mu}$ in Σ_{lab}.*

In Σ_{rot}, when the RF field is on resonance, the magnetisation performs a rotation around the vector $B_1\exp(i\phi).\vec{u}_\rho$ at the frequency

$$\omega_1 = -\gamma B_1 \quad . \tag{1.1.24}$$

The quantity ω_1 is referred to as the RF field strength.[8] The rotation of $\vec{\mu}$ in Σ_{lab} around $\vec{B}_1$ is termed a nutation, and occurs clockwise around $\vec{u}_\rho$. The motion of the magnetic moment submitted to an RF field in Σ_{lab} can be described as the superposition of the gyration described in Section 1.1, a precession at ω_0, and a nutation at ω_1, as shown in Figure 1.3.

It is straightforward from Equation (1.1.23) to show that the application of an RF field on resonance has the effect of changing the precession angle (ϕ_0 in Equation (1.1.9)). Once the magnetisation is away from its equilibrium position along $\vec{B}_0$, the precession motion can be observed and the precession at the Larmor frequency can be recorded.

[8] Denoted ν_1 when expressed in Hz.

1.2 Quantum-mechanical approach

In the last section, the effect of the magnetic fields $\vec{B}_0$ and $\vec{B}_1$ has on nuclear magnetic moments $\vec{\mu}$ has been described using semi-classical mechanics arguments. According to the theory of quantum decoherence,[54] a system behaving according to the laws of quantum mechanics should act on average the same way a classical system does. Therefore, the classical approach for NMR detailed in the previous section gives a quantitative outline of the phenomenon. However, a classical approach does not cover all the possibilities, such as multiple-quantum coherence, at the heart of many successful and highly useful experiments. To understand all the possibilities offered by NMR spectroscopy, a quantum-mechanical formalism must be introduced.

1.2.1 The quantum formalism

According to the hypothesis formulated by De Broglie in 1924,[55] for a quantum particle, the notion of trajectory must be substituted by the concept of a wavefunction $\Phi(\vec{r},t)$ describing a probability of finding the particle at a point of space pointed by $\vec{r}$. All the properties of a particle, or of an ensemble of particles, can be derived from the total wavefunction. The operation of measuring any physical quantity can be represented by the action of an operator, denoted $\hat{A}$.[9] Physical quantities for quantum particles have a limited, quantified number of possible values, which do not correspond to the classical minima, but are stable.[10] The result of the application of $\hat{A}$ on Φ belongs to an assemble of values, denoted $\{a\}$, called eigenvalues. Each eigenvalue has an associated eigenvector, $\Phi_a(\vec{r})$. The interpretation of $\Phi_a(\vec{r})$ is, if $\Phi(\vec{r},t_0)=\Phi_a(\vec{r})$, where t_0 is the moment of the measurement, the value given by the measure would be a with a 100% probability. This is mathematically expressed by

$$\hat{A}\Phi_a(\vec{r}) = a\Phi_a(\vec{r}) \quad . \tag{1.2.1}$$

In the formalism introduced by Schrödinger, the state of a system can equally be described by a state vector $|\Phi\rangle\,(t)$, expressed in the space of quantum states, this space being described by a basis composed of a De Broglie wavefunctions $\Phi(\vec{r}_i,t)$.

In the quantum formalism, the angular momentum and magnetic momentum introduced

[9] Such operators are marked with a hat ˆ.

[10] An example of this being the assumption made in Section 1.1.1, stating that a nucleus has a inherent spinning and emits radiation (see Figure 1.1).

previously are related to an operator denoted as

$$\vec{L} \leftrightarrow \hat{I} \tag{1.2.2a}$$

$$\vec{\mu} \leftrightarrow \hat{\mu} \quad , \tag{1.2.2b}$$

with $\hat{\mu}$ and $\hat{I}$ corresponding to the magnetic moment operator and angular momentum operator, respectively. As in Equation (1.1.6), these quantities are related by the gyromagnetic ratio γ according to[11]

$$\hat{\mu} = \gamma \hat{I} \quad . \tag{1.2.3}$$

The angular momentum operator is described in the Cartesian frame by its three components

$$\hat{I} = \hat{I}_x + \hat{I}_y + \hat{I}_z \quad . \tag{1.2.4}$$

We define the commutator between two operators $\hat{A}$ and $\hat{B}$

$$\left[\hat{A}, \hat{B}\right] = \hat{A}.\hat{B} - \hat{B}.\hat{A} \quad . \tag{1.2.5}$$

It can be established that the squared magnitude of the angular momentum $\hat{I}^2$ commutes with any of the components of $\hat{I}$, *e.g.*,

$$\left[\hat{I}^2, \hat{I}_x\right] = \left[\hat{I}^2, \hat{I}_y\right] = \left[\hat{I}^2, \hat{I}_z\right] = 0 \quad . \tag{1.2.6}$$

Choosing the component of $\hat{I}$ along z, the ensemble $\{\hat{I}^2, \hat{I}_z\}$ constitutes a CSCO[12], and therefore can be described by the same eigenvectors and their eigenvalues can be measured simultaneously.[37] Moreover, the operators $\hat{I}^2$ and $\hat{I}_z$ (as well as all the other components of $\hat{I}$, $\hat{\mu}$ and $\hat{\mu}^2$) are observables. At a basic level, an observable is Hermitian, *i.e.*, its matrix representation is equal to its transposed conjugate matrix $\hat{A}^{\dagger *}$. Observables have two properties: their eigenvalues are real, and the eigenvectors associated with two different eigenvalues are orthogonal. The eigenvalues of $\hat{I}^2$ and $\hat{I}_z$ are characterised by two quantum numbers. These quantum numbers are respectively referred to as the spin quantum number I, and the magnetic quantum number[13] m_I. The spin quantum number I, which is an intrinsic property of each nucleus, determined as shown in Table 1.1 by the parity of the number of protons and neutrons.[56] The

[11] It is also possible to define $\hat{\mu} = \gamma\hbar\hat{I}$ such that $\hat{I}$ is dimensionless.
[12] CSCO: *Complete Set of Commuting Observables*
[13] or azimuthal quantum number.

Number of protons	Number of neutrons	Nuclear spin I
even	even	0
even	odd	$1/2, 3/2, 5/2, \ldots$
odd	even	$1/2, 3/2, 5/2, \ldots$
odd	odd	$1, 2, 3, \ldots$

Table 1.1: *Possible spin quantum numbers, I, a nuclei can possess depending upon the number of protons and neutrons.[56]*

magnetic quantum number, m_I, describes each of the $2I + 1$ magnetic state a nucleus can adopt. This number can take one of the values

$$m_I = I, I-1, I-2, \ldots, -I+1, -I \quad . \tag{1.2.7}$$

Following Dirac's notation,[57] an eigenvector (*ket*) is noted

$$|I, m_I\rangle \quad , \tag{1.2.8}$$

and it transposed conjugate (*bra*) is noted as

$$\langle I, m_I| = |I, m_I\rangle^{*\dagger} \quad . \tag{1.2.9}$$

As $|I, m_I\rangle$ are the eigenvectors of $\{\hat{I}^2, \hat{I}_z\}$, it follows that

$$\begin{cases} \hat{I}^2 |I, m_I\rangle = \hbar^2 I(I+1) |I, m_I\rangle & \text{(1.2.10a)} \\ \hat{I}_z |I, m_I\rangle = \hbar m_I |I, m_I\rangle \quad , & \text{(1.2.10b)} \end{cases}$$

where $\hbar$ is the reduced Planck's constant.[14] The eigenvectors $|I, m_I\rangle$ is a basis of the Hilbert space of the quantum states, with an associated scalar product denoted

$$\langle \Phi_1 | \Phi_2 \rangle \quad , \tag{1.2.11}$$

between any two vectors $|\Phi_1\rangle$ and $|\Phi_2\rangle$.[37] Defining the expectation values of any given operator $\hat{A}$ as

$$\langle \hat{A} \rangle = \frac{\langle I, m_I | \hat{A} | I, m_I \rangle}{\langle I, m_I | I, m_I \rangle} \tag{1.2.12}$$

[14] $\hbar = h/2\pi$, where h is Planck's constant

the expectation values for $\hat{I}^2$ and $\hat{I}_z$ are given by

$$\begin{cases} \langle \hat{I}^2 \rangle = \hbar^2 I(I+1) & \text{(1.2.13a)} \\ \langle \hat{I}_z \rangle = \hbar m_I \quad . & \text{(1.2.13b)} \end{cases}$$

Therefore, any total wavefunction $|\Phi\rangle(t)$ can be expressed at a time t as a linear combination of the eigenvectors $|I, m_I\rangle$ according to

$$|\Phi\rangle(t) = \sum_{i=-m_I}^{i=m_I} C_i(t) |I, m_I\rangle \quad , \tag{1.2.14}$$

where $\{C_i\}_{i \in \mathbb{N}^\star}$ are complex coefficients. As $|I, m_I\rangle$ are the eigenvectors of observables, they are orthogonal, *e.g.*,

$$\langle I, m_{I1} | I, m_{I2} \rangle = 0 \text{ if } m_{I1} \neq m_{I2} \quad . \tag{1.2.15}$$

Pauli's matrices [58] σ_x, σ_y and σ_z (see Appendix B.1) are the matrix representation of $\hat{I}_x$, $\hat{I}_y$ and $\hat{I}_z$ multiplied by $\hbar/2$.[37, 59] Even though these operators commute with $\hat{I}^2$ as shown Equation (1.2.6), the components of $\hat{I}$ (Equation (1.2.4)) do not commute with each other. For example, the commutator between $\hat{I}_x$ and $\hat{I}_y$ is

$$\left[\hat{I}_x, \hat{I}_y\right] = i\hbar \hat{I}_z \quad . \tag{1.2.16}$$

Commutation relations involving all the elements of $\hat{I}$ can be re-established using the property the property $[\hat{A}, \hat{B}] = -[\hat{B}, \hat{A}]$ and circular permutation of the operators (*e.g.*, $[\hat{I}_x, \hat{I}_y] = [\hat{I}_y, \hat{I}_z]$ ...). Since the frame in which $\hat{I}_x$, $\hat{I}_y$ and $\hat{I}_z$ are represented is purely arbitrary, they necessarily have the same eigenvalues as $\hat{I}_z$ (Equation (1.2.10b)). However, since from Equation (1.2.16) they do not constitute a CSCO, $\hat{I}_x$, $\hat{I}_y$, $\hat{I}_z$ and $\hat{I}^2$ cannot be represented in a unique basis of eigenvectors. Instead, their eigenvectors can be expressed in terms of those of $\hat{I}_z$. In the case of a spin $I = 1/2$, those eigenvectors are

$$\begin{cases} |1/2, \pm 1/2\rangle_x = \dfrac{1}{\sqrt{2}}(|1/2, 1/2\rangle \pm |1/2, -1/2\rangle) & \text{(1.2.17a)} \\ |1/2, \pm 1/2\rangle_y = \dfrac{1}{\sqrt{2}}(|1/2, 1/2\rangle \pm i\,|1/2, -1/2\rangle) \quad . & \text{(1.2.17b)} \end{cases}$$

We now can define $|1/2, \pm 1/2\rangle_x$ and $|1/2, \pm 1/2\rangle_y$ the eigenvectors of $\hat{I}_x$ and $\hat{I}_y$. From this,

it can be established that

$$\hat{I}_x \left|1/2, 1/2\right\rangle) = \frac{\hbar}{2} \left|1/2, -1/2\right\rangle) \tag{1.2.18a}$$

$$\hat{I}_x \left|1/2, -1/2\right\rangle) = \frac{\hbar}{2} \left|1/2, 1/2\right\rangle) \tag{1.2.18b}$$

$$\hat{I}_y \left|1/2, 1/2\right\rangle) = i\frac{\hbar}{2} \left|1/2, -1/2\right\rangle) \tag{1.2.18c}$$

$$\hat{I}_y \left|1/2, -1/2\right\rangle) = -i\frac{\hbar}{2} \left|1/2, 1/2\right\rangle) \quad . \tag{1.2.18d}$$

The creation operator $\hat{I}_+$, and the annihilation operator $\hat{I}_-$, are two useful operators regularly used in quantum mechanical problems. They are defined, respectively, as

$$\hat{I}_+ = \hat{I}_x + i\hat{I}_y \tag{1.2.19a}$$

$$\hat{I}_- = \hat{I}_x - i\hat{I}_y \quad . \tag{1.2.19b}$$

Even though those two operators do not constitute a CSCO, they possess interesting properties, such as

$$\hat{I}_+ \left|1/2, 1/2\right\rangle) = 0 \tag{1.2.20a}$$

$$\hat{I}_- \left|1/2, -1/2\right\rangle) = 0 \tag{1.2.20b}$$

$$\hat{I}_+ \left|1/2, -1/2\right\rangle) = \hbar \left|1/2, 1/2\right\rangle) \tag{1.2.20c}$$

$$\hat{I}_- \left|1/2, 1/2\right\rangle) = \hbar \left|1/2, -1/2\right\rangle) \quad . \tag{1.2.20d}$$

1.2.2 The density matrix formalism

Let us now consider a more complex system, for example, a multi-spin system. A basis of unit eigenvectors describing the entire system can be formed from the so-called tensor product "$\otimes$" of all the eigenvectors of each of the k systems according to [37]

$$\left|u_i\right\rangle = \left|I_1, m_{I_{1i}}\right\rangle \otimes \left|I_2, m_{I_{2i}}\right\rangle \otimes \ldots \otimes \left|I_k, m_{I_{ki}}\right\rangle \quad , \tag{1.2.21}$$

with $k \in \mathbb{N}$ and $i \in [1, I_1 \times I_2 \times \ldots \times I_k]$. To be perfectly rigorous, an real spin system would be composed of an ensemble of these spin states, but for which some quantities, such as temperature, are only known statistically, and this may not apply to any particular element of this ensemble. This can be taken into account by expressing the total state

vector $|\Phi\rangle(t)$ as having a probability p_1 to be in the state ϕ_1, p_2 to be in the state ϕ_2, *etc.*, giving

$$|\Phi\rangle_k(t) = \sum_{m=1}^{m=k} p_m |\Phi\rangle_m(t) \text{ with } \sum_{m=1}^{m=k} p_m = 1 \quad . \tag{1.2.22}$$

The notion of a statistical mixture of quantum states must not be confused with the decomposition of a total state vector into the basis set of eigenvectors presented in Equation (1.2.14), as each element $|\Phi\rangle_k(t)$ describing the quantum state at a time t can be decomposed into

$$|\Phi\rangle_n(t) = \sum_{i=1}^{i=n} C_i(t) |u_i\rangle \quad . \tag{1.2.23}$$

Combining Equation (1.2.23) with Equation (1.2.22) gives the total quantum state expressed

$$|\Phi\rangle(t) = \sum_{m=1}^{m=k} p_m \sum_{i=1}^{i=n} C_{i,m}(t) |u_{i,m}\rangle \quad , \tag{1.2.24}$$

where $\{|u_{i,j}\rangle\}$ describes the basis set of the n vectors describing the space of quantum states for the state vector $|\Phi\rangle_j(t)$. For simplicity, we take $\{|u_i\rangle\}_{i\in[1,n]}$ to be orthonormal and $|\Phi\rangle(t)$ normalised, *e.g.*, the coefficients $C_i(t)$ in Equation (1.2.24) satisfy the equation

$$\sum_{i=1}^{i=n} C_i^*(t) C_i(t) = 1 \quad . \tag{1.2.25}$$

The expectation value for an operator $\hat{A}(t)$ (see Equation (1.2.12)) is

$$\langle \hat{A} \rangle(t) = \frac{\langle \Phi | \hat{A}(t) | \Phi \rangle}{\langle \Phi | \Phi \rangle} = \sum_{\substack{i=1 \\ j=1}}^{\substack{i=n \\ j=n}} \sum_{m=1}^{m=k} p_m . C_{i,m}^*(t) C_{j,m}(t) . \langle u_{i,m} | \hat{A} | u_{j,m} \rangle \quad . \tag{1.2.26}$$

It is important to consider the case of a pure state, where the total function of the ensemble of the spin-systems is perfectly known, so all p_k but one are zero. In this case, Equation (1.2.12) simplifies to

$$\langle \hat{A}(t) \rangle = \sum_{\substack{i=1 \\ j=1}}^{\substack{i=n \\ j=n}} C_i^*(t) C_j(t) \langle u_i | \hat{A} | u_j \rangle \quad . \tag{1.2.27}$$

It can be noted that the quantity

$$\rho_{ij}(t) = C_i^*(t) C_j(t) \quad , \tag{1.2.28}$$

that appears in Equation (1.2.27), is the i, j element of the matrix defined

$$\hat{\rho} = |\Phi\rangle \langle\Phi| \quad . \tag{1.2.29}$$

The resulting matrix $\hat{\rho}$ is known as the density operator of the state $|\Phi\rangle$,[34] and its matrix representation is referred to as the density matrix

$$\hat{\rho}(t) = \begin{array}{c} \\ |u_1\rangle \\ |u_2\rangle \\ \vdots \\ |u_i\rangle \\ \vdots \\ |u_n\rangle \end{array} \begin{array}{c} \begin{array}{cccccc} |u_1\rangle & |u_2\rangle & \dots & |u_j\rangle & \dots & |u_n\rangle \end{array} \\ \begin{bmatrix} \rho_{11}(t) & \rho_{12}(t) & \dots & \rho_{1j}(t) & \dots & \rho_{1n}(t) \\ \rho_{21}(t) & \rho_{22}(t) & \dots & \rho_{2j}(t) & \dots & \rho_{2n}(t) \\ \vdots & \vdots & \ddots & \vdots & & \vdots \\ \rho_{i1}(t) & \rho_{i2}(t) & \dots & \rho_{ij}(t) & \dots & \rho_{in}(t) \\ \vdots & \vdots & & \vdots & \ddots & \vdots \\ \rho_{n1}(t) & \rho_{22}(t) & \dots & \rho_{nj}(t) & \dots & \rho_{nn}(t) \end{bmatrix}_n \end{array} \quad . \tag{1.2.30}$$

In the case of a statistic mixture of states, ρ_{ij} in Equation (1.2.28) becomes

$$\rho_{ij}(t) = \sum_{m=1}^{m=k} p_m . C_i^*(t) C_j(t) \quad . \tag{1.2.31}$$

The ensemble of the eigenvectors $|u_i\rangle \langle u_j|_{\{i,j\} \in [1,n]^2}$ defines a Liouville space, which is the product of two Hilbert spaces. In the pure-state case, the density matrix has the following useful properties

$$\begin{cases} \rho^{*\dagger}(t) = \rho(t) & \text{(1.2.32a)} \\ \text{Tr}\left[\rho^2(t)\right] = 1 \quad . & \text{(1.2.32b)} \end{cases}$$

where Tr[ ] denotes the trace of a matrix. The expectation value of an operator $\hat{A}$ in Equations (1.2.26) and (1.2.27) can be written as a function of the density operator as

$$\langle \hat{A} \rangle = \text{Tr}[\hat{\rho}\hat{A}] = \text{Tr}[\hat{A}\hat{\rho}] \quad , \tag{1.2.33}$$

Likewise, the value of the element i, j of the density matrix ρ is returned by the operator

$$\rho_{ij} = \text{Tr}[\hat{\rho}\hat{O}_{j,i}] \quad , \tag{1.2.34}$$

where $\hat{O}_{j,i}$ is a matrix of same dimension as $\hat{\rho}$, whose elements are all 0 apart from the element j, i, which is 1. It can be noticed that the index orders of the desired density matrix element ρ_{ij} are inverted compared to that of $\hat{O}_{j,i}$ in Equation (1.2.34).

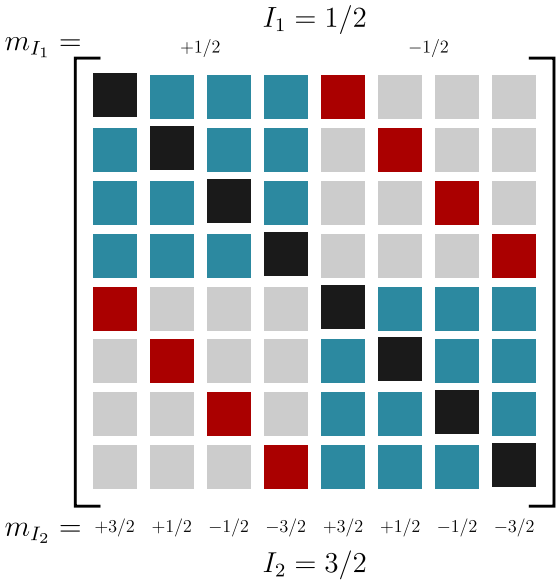

Figure 1.4: *Schematic of a density matrix for two spins $I_1 = 1/2$ and $I_2 = 3/2$ nuclei, described my the magnetic quantum numbers m_{I_1} and m_{I_2}, respectively. Black elements correspond to populations, red elements to coherences between the states of I_2, blue elements to coherences between the states of I_1, and light gray elements to coherences between I_1 and I_2.*

Equation (1.2.33) illustrates the ability of the density matrix to describe all properties related to an operator $\hat{A}$ in a single matrix, eliminating to need to calculate these properties for each individual spin. The matrix coherence also provide a convenient way to express any constructive/destructive interference between the different states. Expressing C_i using the form

$$C_i = \| C_i \| \exp(i\theta_i) \quad , \tag{1.2.35}$$

with $\| C_i \|$ and θ_i being the modulus and the phase of C_i, respectively, the matrix density elements are

$$\rho_{ij}(t) = \begin{cases} \| C_i \| . \| C_j \| & \text{if } i = j \quad \text{(1.2.36a)} \\ \| C_i \| . \| C_j \| \exp(i(\theta_i - \theta_j)) & \text{else} \quad \text{(1.2.36b)} \end{cases}$$

The quantum states $\Phi(t)$ and $\exp(i\theta).\Phi(t)$, $\theta \in \mathbb{R}$, correspond to the same quantum states. At thermal equilibrium, the phase of all elements in a same quantum state is randomly distributed, resulting in the term $\exp(i(\theta_i - \theta_j))$ in Equation (1.2.36b) averaging to zero, so all non-diagonal elements are zero. If $\exp(i(\theta_i - \theta_j)) \neq 0$, we define that there is a coherence between the states i and j. The coherence order, p, is defined as the difference between the two magnetic quantum numbers associated with the spins i and j

$$p_{ij} = m_{I_i} - m_{I_j} \quad . \tag{1.2.37}$$

A schematic density matrix is shown Figure 1.4. For $k \in [1, n]$, the different elements of the matrix density are termed as followed

- $\rho_{k,k}$ (*e.g.*, the diagonal elements) correspond to populations of the quantum states,
- $\rho_{k,k\pm1}$ matrix elements correspond to 1Q[15] coherence,
- $\rho_{k,k\pm2}$ matrix elements correspond to 2Q[16] coherence,
- $\rho_{k,k\pm3}$ matrix elements correspond to 3Q[17] coherence,
- etc ...

The sign of the coherence also has an importance, as described for example in Section 3.1.1 and Appendix D. Multiple-quantum coherence is only possible for either a spin $I > 1/2$, or for an ensemble of spins $I \geq 1/2$, as shown in Figure 1.4.

1.2.3 Evolution of the quantum states in a magnetic field

To determine the time evolution of the system state vector, the quantum-mechanical formalism uses the Hamiltonian operator. Initially introduced as a reformulation of classical mechanics,[60] the Hamiltonian is an operator describing the total energy of a system, and can often be related to the classical expression of mechanical energy.

As a first step, the evolution with time of a total state vector $|\Phi\rangle(t)$ is calculated using Schrödinger equations.[61, 62] If the Hamiltonian for a given system is time independent, for example to describe the interaction between nuclear magnetic spins and an external magnetic field (see Section 1.1.1), energy states can be determined by finding the eigenvalues and eigenvectors of the TISE[18]

$$\hat{H}\,|\Phi\rangle = E\,|\Phi\rangle \quad , \tag{1.2.38}$$

where E is the associated energy (eigenvalue of $\hat{H}$) of the system. In this case, the energy levels are sometimes described as "stationary", as they correspond to stable energy levels of the system. Alternatively, for time-dependent problems, such as the interaction of an RF field on nuclear spins (see Section 1.1.3), the TDSE[19] must be solved. The TDSE is expressed as

[15] 1Q: *Single-Quantum* (transition)
[16] 2Q: *Double-Quantum* (transition)
[17] 3Q: *Triple-Quantum* (transition)
[18] TISE: *Time-Independent Schrödinger Equation*
[19] TDSE: *Time-Dependent Schrödinger Equation*

$$i\hbar\frac{d\left|\Phi\right\rangle}{dt}(t)=\hat{H}\left|\Phi\right\rangle(t)\quad . \tag{1.2.39}$$

If a quantum state at t = t_0 is $\left|\Phi\right\rangle(t_0)$, the TISE can be expressed in a form involving an operator called the evolution operator denoted $\hat{U}$. The evolution of the quantum state between times t and t_0 is given by

$$\left|\Phi\right\rangle(t)=\hat{U}(t-t_0)\left|\Phi\right\rangle(t_0)\quad . \tag{1.2.40}$$

For the particular case when the Hamiltonian is time-independent, the propagator can be expressed as

$$\hat{U}(t-t_0)=\exp\left(-\frac{i}{\hbar}\hat{H}\times(t-t_0)\right)\quad . \tag{1.2.41}$$

If the Hamiltonian is time-dependent, and if and only if it commutes with itself at any time,[20] Equation (1.2.41) must be written

$$\hat{U}(t-t_0)=\exp\left(-\frac{i}{\hbar}\int_{t_0}^{t}\hat{H}(\tau)d\tau\right)\quad . \tag{1.2.43}$$

Concerning the time evolution of the density matrix discussed in Section 1.2.2, it can be shown using the TDSE and its complex conjugate that

$$i\hbar\frac{d\hat{\rho}(t)}{dt}=\left[\hat{H},\hat{\rho}(t)\right]\quad . \tag{1.2.44}$$

This is termed the called the LVNE[21]. Its general solution can be expressed in terms of propagators $\hat{U}$ defined such that

$$\hat{\rho}(t)=\hat{U}(t)\hat{\rho}(t_0)\hat{U}^{-1}(t)\quad . \tag{1.2.45}$$

The treatment of the interaction between a magnetic moment and a static magnetic field along an arbitrary (Oz) axis, already discussed using the semi-classical mechanics formalism in Section 1.1.2,[67] is executed in quantum mechanic using the Hamiltonian associated with the interaction energy expressed in Equation (1.1.7c)

[20] The Baker–Campbell–Hausdorff formula [63–66] shows that the product of the exponential of two operators $\hat{A}$ and $\hat{B}$ is given by

$$\exp\hat{A}.\exp\hat{B}=\exp\left(\hat{A}+\hat{B}+\frac{1}{2}\left[\hat{A},\hat{B}\right]+\frac{1}{12}\left(\left[\hat{A},\left[\hat{A},\hat{B}\right]\right]+\left[\hat{B},\left[\hat{B},\hat{A}\right]\right]\right)+\dots\right)\quad , \tag{1.2.42}$$

hence $\forall\{t_1,t_2\}$, $\left[\hat{H}(t_1),\hat{H}(t_2)\right]=0$ is a necessary condition for $\exp\hat{H}(t_1).\exp\hat{H}(t_2)=\exp\left(\hat{H}(t_1)+\hat{H}(t_2)\right)$, and therefore for Equation (1.2.43) to be valid. See also the Magnus extension in Section 2.1.2 for further details.

[21] LVNE: *Liouville-Von Neumann Equation*

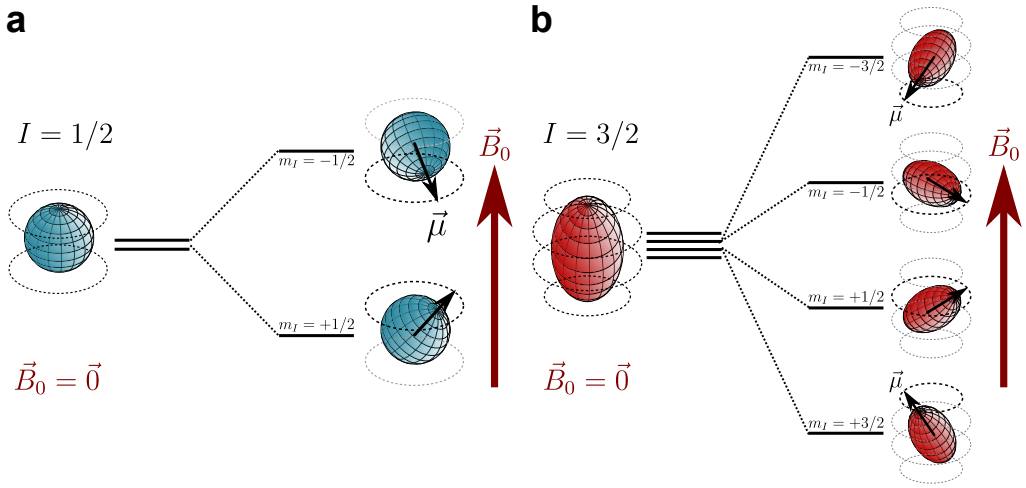

Figure 1.5: *Splitting of the different energy levels in Σ_{lab} for **(a)**: a spin $I = 1/2$ and **(b)**: a spin $I = 3/2$.*

$$\hat{H}_z = -\gamma \hat{I}.\hat{1}_3.\hat{B}_0 \quad , \tag{1.2.46}$$

where $\hat{1}_3$ is the order-three identity matrix, and $\hat{B}_0$ is the magnetic field vector in quantum mechanics written

$$\hat{B}_0 = \begin{bmatrix} 0 \\ 0 \\ B_0 \end{bmatrix} \quad . \tag{1.2.47}$$

Simplifying Equation (1.2.46) results in

$$\hat{H}_z = \underbrace{-\gamma B_0}_{=\omega_0} \hat{I}_z \quad . \tag{1.2.48}$$

The Larmor frequency, ω_0, already established in Equation (1.1.13), now appears in the expression of the Hamiltonian. As established in Section 1.2.1, $\hat{I}_z$ has eigenvalues $2I + 1$ eigenvalues described by $m_I = -I, -I + 1, \ldots, I - 1, I$, and eigenvectors denoted $|I, m_I\rangle$. It is then straightforward that the time-independant Schrödinger equation (Equation (1.2.38)) gives

$$\hat{H}_z |I, m_I\rangle = \hbar\omega_0 m_I |I, m_I\rangle \quad . \tag{1.2.49}$$

This last equations shows that the presence of the magnetic field results in the removal of the degeneracy between the $2I + 1$ energy levels. Each energy level now has an energy $E_{m_I} = m_I \hbar\omega_0$, and the energy difference between two successive energy levels is $\Delta E_{m,m+1} = \hbar\omega_0$ in Σ_{lab}, as illustrated in Figure 1.5. This splitting is also known as the nuclear Zeeman effect.[68]

To determine the evolution of the state vector under these conditions, we apply the TDSE in Equation (1.2.39) to a vector of the state space $|\Phi\rangle(t)$. For simplicity, the system is restricted from now on to the case of $I = 1/2$ and $m_I \in [-1/2, 1/2]$. In this case, the state vector can be written using the general form

$$|\Phi\rangle(t) = C_{+1/2}(t)\,|1/2, 1/2\rangle + C_{-1/2}(t)\,|1/2, -1/2\rangle \quad . \tag{1.2.50}$$

As the two states $|\Phi\rangle(t)$ and $\exp(i\theta)\,|\Phi\rangle(t)$, where $\theta \in \mathbb{R}$ is an arbitrary phase, describe the same quantum states, $|\Phi\rangle$ can be multiplied by an arbitrary phase $\exp(i\theta_0)$. Taking the normalised state vector $|\Phi\rangle(t)$, there is a unique angle ϕ such that the two coefficients of the two eigenvector $|I, m_I\rangle$ can be expressed

$$|\Phi\rangle(t=0) = \cos\phi_0.\exp(i\theta_0)\,|1/2, 1/2\rangle + \sin\phi_0.\exp(i\theta_0)\,|1/2, -1/2\rangle \quad , \tag{1.2.51}$$

as $\cos^2\phi_0 + \sin^2\phi_0 = 1$. Applying the time-dependent Schrödinger equation, we obtain

$$\begin{aligned} |\Phi\rangle(t) = \cos\phi_0.\exp\left(i(\theta_0 - \frac{1}{2}\omega_0 t)\right)|1/2, 1/2\rangle \\ + \sin\phi_0.\exp\left(i(\theta_0 + \frac{1}{2}\omega_0 t)\right)|1/2, -1/2\rangle \quad . \end{aligned} \tag{1.2.52}$$

Using Equation (1.2.52), the expected value of the observables $\hat{I}_z$ and $\hat{I}_+$ can be shown to be

$$\begin{cases} \langle \hat{I}_z \rangle = \dfrac{\hbar}{2}\cos(\phi_0) & \text{(1.2.53a)} \\ \langle \hat{I}_+ \rangle(t) = \dfrac{\hbar}{2}\sin(\phi_0).\exp(i(\theta_0 + \omega_0 t)) \quad . & \text{(1.2.53b)} \end{cases}$$

It can be shown that Equations (1.2.53a) and (1.2.53b) give an identical conclusion to that given in Equation (1.1.12)). The expectation value of the component of $\hat{I}$ along z (termed the longitudinal axis in Section 1.1.2) does not vary over time, while the component in the plane x, y (called the transverse plane in Section 1.1.2)) evolves undertaking a precession motion at a rate ω_0.

As introduced in Section 1.1.3, modifying the initial precession angle can be achieved by the application of a RF field applied at a frequency near the Larmor frequency. The Zeeman Hamiltonian can then be added to a RF field Hamiltonian $\hat{H}_{\text{RF}}$, giving the total Hamiltonian

$$\hat{H} = \hat{H}_z + \hat{H}_{\text{RF}} \quad , \tag{1.2.54}$$

with

$$\hat{H}_{\text{RF}} = -\gamma \hat{I}.\hat{1}_3.\hat{B}_1 \quad , \tag{1.2.55}$$

the RF field vector $\hat{B}_1$ being expressed as

$$\hat{B}_1 = \begin{bmatrix} B_1 \cos\left(\omega_{\text{RF}} t + \theta_{\text{RF}}\right) \\ B_1 \sin\left(\omega_{\text{RF}} t + \theta_{\text{RF}}\right) \\ 0 \end{bmatrix} \quad . \tag{1.2.56}$$

Simplifying Equation (1.2.55) gives

$$\hat{H}_{\text{RF}}(t) = \omega_1 \left(\hat{I}_x \cos(\omega_{\text{RF}} t + \theta_{\text{RF}}) + \hat{I}_y \sin(\omega_{\text{RF}} t + \theta_{\text{RF}}) \right) \quad , \tag{1.2.57}$$

with ω_1 defined in Equation (1.1.24). The same approach as in Section 1.1.3 is undertaken: the system is expressed in a frame Σ_{rot} rotating at the frequency of the RF field. This is achieved by defining a rotating state vector $|\Phi\rangle_\rho (t)$ such as

$$|\Phi\rangle (t) = \exp\left(-\frac{i}{\hbar} \omega_{\text{RF}} t \hat{I}_z \right) . \exp\left(+\frac{i}{\hbar} \omega_{\text{RF}} t \hat{I}_z \right) |\Phi\rangle (t) \tag{1.2.58a}$$

$$= \exp\left(-\frac{i}{\hbar} \omega_{\text{RF}} t \hat{I}_z \right) |\Phi\rangle_\rho (t) \quad . \tag{1.2.58b}$$

Rewriting the TDSE for $|\Phi\rangle_\rho (t)$, we obtain

$$i\hbar \frac{d|\Phi\rangle_\rho}{dt}(t) = (\hat{H}_\rho - \omega_{\text{RF}} \hat{I}_z) |\Phi\rangle_\rho (t) \quad . \tag{1.2.59}$$

where

$$\hat{H}_\rho = \exp\left(-\frac{i}{\hbar} \omega_{\text{RF}} t \hat{I}_z \right) \hat{H}(t) \left(+\frac{i}{\hbar} \omega_{\text{RF}} t \hat{I}_z \right) \tag{1.2.60}$$

is now the rotated Hamiltonian expressed in Equation (1.2.54) (see Appendix B.2, Equation (B.2.7) for details about rotations of operators). In Equation (1.2.59), we have the quantum-mechanics analogue of the effective magnetic field $\vec{B}_{\text{eff}}$, expressed in Equation (1.1.20). After expansion, we obtain that

$$\hat{H}_\rho(t) = (\omega_0 - \omega_{\text{RF}}) \hat{I}_z + \omega_1 (\hat{I}_x \cos(\theta_{\text{RF}}) + \hat{I}_y \sin(\theta_{\text{RF}})) \quad . \tag{1.2.61}$$

The frequency offset $\Delta\omega_0 = \omega_0 - \omega_{\text{RF}}$, already defined in Equation (1.1.21), is featured in Equation (1.2.61). Resolving Equation (1.2.59) using $\hat{H}_\rho$, choosing the RF field to be on resonance (*e.g.*, $\Delta\omega_0 = 0$), and substituting the initial state vector defined in

Equation (1.2.49), we obtain values for the coefficients of

$$C_{+1/2}(t) = \exp(i\theta_0)\left(\cos(\phi_0)\cos\left(\frac{\omega_{\mathrm{RF}}t}{2}\right) + i\sin(\phi_0).\sin\left(\frac{\omega_{\mathrm{RF}}t}{2}\right)\right) \tag{1.2.62a}$$

$$C_{-1/2}(t) = \exp(i\theta_0)\left(\sin(\phi_0)\cos\left(\frac{\omega_{\mathrm{RF}}t}{2}\right) + i\cos(\phi_0).\sin\left(\frac{\omega_{\mathrm{RF}}t}{2}\right)\right) \quad . \tag{1.2.62b}$$

The expectation values of $\hat{I}_z$ and $\hat{I}_+$ expressed in the rotating frame are

$$\begin{cases} \langle\hat{I}_z\rangle_{\Sigma_{\mathrm{rot}}}(t) = \dfrac{\hbar}{2}\cos(\phi_0 + \omega_1 t) & \text{(1.2.63a)} \\ \langle\hat{I}_+\rangle_{\Sigma_{\mathrm{rot}}}(t) = \dfrac{\hbar}{2}\sin(\phi_0 + \omega_1 t).\exp(i(\theta_0 + \theta_{\mathrm{RF}})) \quad . & \text{(1.2.63b)} \end{cases}$$

As in Equation (1.1.23), it has been re-established that under an RF field on resonance with the Larmor frequency of a given element, the magnetisation nutates and is moved away from its equilibrium position, permitting the Larmor frequency to be recorded.

1.3 Some practical elements

1.3.1 Bulk magnetization

The interaction energy term in Equation (1.1.7c) shown the effect of a magnetic field on the energy of a nuclear spin. This causes a coherent alignment of magnetic moments along the axis of the static magnetic field as shown in Figure 1.6. From the contribution of each individual magnetization vector, a global, macroscopic magnetization can be determined

$$\vec{M} = \frac{1}{V}\sum_N \vec{\mu} \quad \left(\langle\hat{M}\rangle = \frac{1}{V}\sum_N\langle\hat{\mu}\rangle\right) \quad , \tag{1.3.1}$$

where N is the number of nuclei and V the volume enclosing the nuclei. As stated initially in Section 1.1, the norm of the individual magnetisation vectors $\vec{\mu}$ remains unchanged by NMR experiments, unlike the norm of the bulk magnetisation vector $\vec{M}$ that will vary depending on the relative alignment of the individual magnetisation vectors $\vec{\mu}$ from which it is composed. $\vec{M}$ can be described as being the result of a "coherent" alignment of the $\vec{\mu}$. All the equations established in Chapter 1, particularly Equations (1.1.12) and (1.1.23) can correct either expressed in terms of $\vec{\mu}(t)$ or $\vec{M}(t)$, but only $\vec{M}$ is observable and recordable.

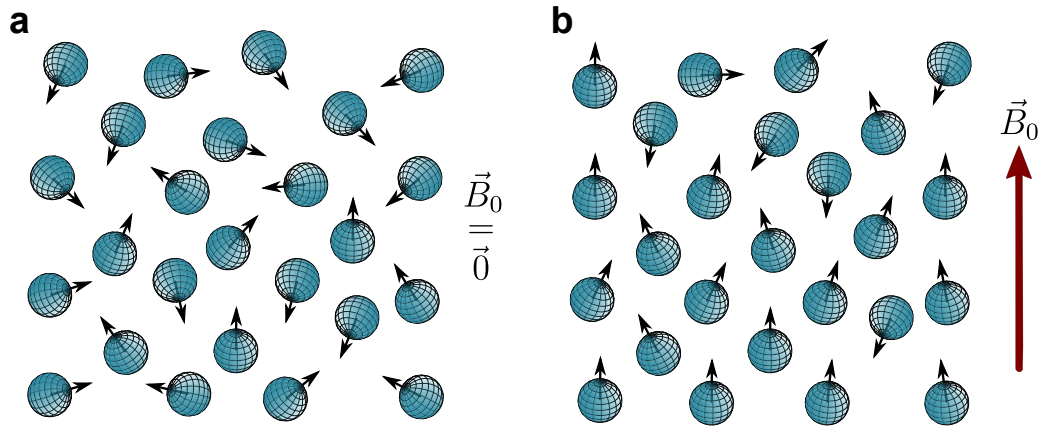

Figure 1.6: *Illustration of the orientation of the magnetic dipolar moments **(a)**: in the absence of any external magnetic field and **(b)**: in the presence of an external magnetic field $\vec{B}_0$.*

It is convenient to separate $\vec{M}(t)$ into one component in the transverse plane M_T, and one component along the longitudinal axis M_L

$$\vec{M}(t) = M_T(t)\exp(i\phi_0).\vec{u}_x + M_L(t).\vec{u}_z \quad . \tag{1.3.2}$$

The global magnetization at thermal equilibrium $\vec{M}_{\text{eq}}$ can be determined from statistical mechanics as

$$\vec{M}_{\text{eq}} = \frac{1}{V}.\frac{\sum_N \vec{\mu}.\exp\left(-\frac{E_m}{k_B T}\right)}{\sum_N \exp\left(-\frac{E_m}{k_B T}\right)} \quad , \tag{1.3.3}$$

where N is the total number of nuclei, T is the temperature, k_B is Boltzmann's constant, and the interaction energy E_m has a discrete number of possible values as determined in Equation (1.3.5). It is straightforward that no coherent orientation of the vectors $\vec{\mu}$ would exist at thermal equilibrium if no magnetic field is applied along a given direction; thus the resultant magnetisation along this direction is $\vec{0}$. Combining Equations (1.2.3) and (1.2.13b) with Equation (1.3.3), it can be shown that $\vec{M}_{\text{eq}}$ is expressed for any spin I as [69]

$$\vec{M}_{\text{eq}} = \gamma\hbar\frac{N}{V}\left[\left(I+\frac{1}{2}\right)\coth\left(\left(I+\frac{1}{2}\right)\frac{\gamma\hbar B_0}{k_B T}\right) - \frac{1}{2}\coth\left(\frac{1}{2}.\frac{\gamma\hbar B_0}{k_B T}\right)\right].\vec{u}_z \tag{1.3.4}$$

or, for the important case when $I = 1/2$,

$$\vec{M}_{\text{eq}} = \frac{N}{V}.\frac{\hbar\gamma}{2}\tanh\left(\frac{1}{2}.\frac{\hbar\gamma B_0}{k_B T}\right)\vec{u}_z \quad , \tag{1.3.5}$$

termed the Brillouin function.The interaction energy can also be used to determine the

population of each spin system. Assuming the spin population can be described using Boltzmann distribution, for a spin $I = 1/2$ nucleus, this is given by

$$\frac{N_{-1/2}}{N_{+1/2}} = \exp\left(-\frac{\gamma\hbar B_0}{k_B T}\right) \quad . \tag{1.3.6}$$

To establish an order of magnitude for the population difference, a favourable case is considered. For ^{1}H in a static magnetic field B_0 = 14.1 T (ν_0 = 600.0 MHz) at a temperature T = 300 K, the ratio between the two populations is

$$N_{-1/2} : N_{+1/2} \leftrightarrow 100000 : 100006 \quad . \tag{1.3.7}$$

The value for the ratio of the energy of the Zeeman interaction energy over thermal energy is

$$\frac{\gamma\hbar B_0}{k_B T} = 5.96 \times 10^{-4} \quad . \tag{1.3.8}$$

As a result, even though one of the most favourable possible cases has been considered, the ratio is still extremely low. Thus, a reasonable approximation is to assume that the magnetisation is always in the high-temperature/low gyromagnetic ratio regime, *e.g.*,

$$\frac{\gamma\hbar B_0}{k_B T} \ll 1 \quad . \tag{1.3.9}$$

Under this approximation, $\vec{M}_{\text{eq}}$ at thermal equilibrium for any spin I can be written

$$\vec{M}_{\text{eq}} = \frac{N}{V}\frac{\gamma^2\hbar^2}{3k_B T} I(I+1).\vec{B}_0 \quad , \tag{1.3.10}$$

which corresponds to the classical expression of Curie magnetism.[70] When magnetisation is perturbed from its equilibrium value as defined Equation (1.3.10), it returns to its equilibrium position after a certain period of time. There are two relaxation processes that are common to all NMR experiments that enables this.[22]

Spin-lattice relaxation or T₁ relaxation

Spin-lattice relaxation is a process by which the magnetization, initially perturbed from equilibrium, returns to the thermal equilibrium. The magnetisation recovers progressively its equilibrium value $\vec{M}_{\text{eq}}$, along the static magnetic field axis, in a process taking place in a typical time T_1. This relaxation process only affects the magnetization along

[22] Additional relaxation mechanisms can take place during some experiments or for some spin systems. An example is the spin-lattice relaxation taking place in the transverse plane during cross polarisation experiments, characterised by $T_{1\rho}$ and described in Section 3.1.3.

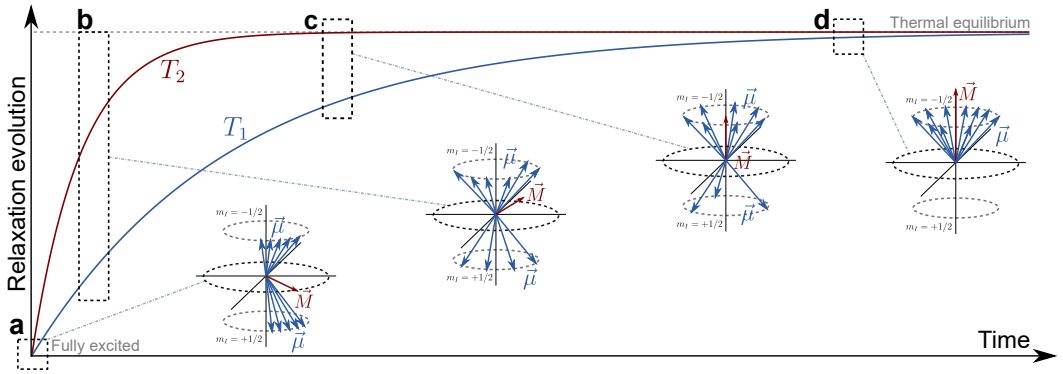

Figure 1.7: *Illustration of the effects of spin-lattice and spin-spin relaxation processes on a spin $I = 1/2$ nucleus with an initial bulk magnetisation $\vec{M}$ in the transverse plane. The evolution of these relaxation processes are illustrated by plotting $1 - \exp(-t/T_{1,2})$ in blue and red for T_1 and T_2 respectively. $\vec{\mu}$ and $\vec{M}$ are represented at several steps of the relaxation.* ***(a)****: $\vec{\mu}$ vectors are fully coherent and the resultant $\vec{M}$ only has components in the transverse plane.* ***(b)****: $\vec{\mu}$ vectors have lost most of their coherence and spin-lattice relaxation starts to occur. $\vec{M}$ has components in the transverse plane that are reduced compared to* ***(a)****, and a component of $\vec{M}$ along the axis of the static magnetic field axis starts to appear.* ***(c)****: $\vec{\mu}$ vectors have lost all of their coherence, $\vec{M}$ has only a component along the static magnetic field, reduced compared to that at thermal equilibrium.* ***(d)****: Magnetisation has almost reach thermal equilibrium, and $\vec{\mu}$ vectors recovered their coherent alignment along the z-axis.*

the axis of the magnetic field axis, and not that in the transverse place. The process can be described as a torque $\vec{\tau}_1$

$$\vec{\tau}_{T_1} = \frac{1}{T_1}\left(\vec{M}_{\text{eq}} - \vec{M}_L\right) \quad . \tag{1.3.11}$$

Spin-spin relaxation or T₂ relaxation

Spin-spin relaxation is a process that causes the loss of magnetisation in the transverse plane, which is described by the time constant T_2. This process corresponds to the loss of coherence between the different individual magnetic moments, whose sum in the transverse becomes smaller and smaller with time. This is due to local variations of the static magnetic field and to internal interactions discussed in Chapter 2. This relaxation process takes place in the transverse plane. It can be described by adding to the AMT the torque $\vec{\tau}_{T_2}$ expressed

$$\vec{\tau}_{T_2} = \frac{\vec{M}_T}{T_2} \quad . \tag{1.3.12}$$

Bloch equations

The combined effect of spin-lattice and spin-spin relaxation processes are shown in Figure 1.7. This figure also illustrates the fact that the norm of $\vec{M}$ changes during relaxation while the norm of the individual $\vec{\mu}$ vectors are not affected. The AMT expressed in Equation (1.1.12) can be rewritten in terms of bulk magnetisation $\vec{M}$, taking into account both relaxation mechanisms

$$\left(\frac{d\vec{M}(t)}{dt}\right)_{\Sigma_{\text{lab}}} = \gamma\vec{M}(t) \wedge \vec{B}_0 + \frac{1}{T_1}\left(\vec{M}_{\text{eq}} - \vec{M}_L(t)\right) - \frac{\vec{M}_T(t)}{T_2} \quad . \tag{1.3.13}$$

Solving Equation (1.3.13) in Σ_{lab} results in

$$\begin{cases} M_T(t) = M_T(t_0)\exp(i(\phi_0 - \omega_0 t))\exp\left(-\dfrac{t}{T_2}\right) & \text{(1.3.14a)} \\ M_L(t) = M_L(t_0)\exp\left(i\phi_0 - \dfrac{t}{T_1}\right) + M_{\text{eq}}\left(1 - \exp\left(\dfrac{1}{T_1}\right)\right) \quad . & \text{(1.3.14b)} \end{cases}$$

Equations (1.3.14a) and (1.3.14b) are best known as the Bloch equations,[2] describing the magnetic resonance phenomenon from a semi-classical point of view, *i.e.*, a macroscopic picture, rather than dealing with individual spins. These equations are not used in NMR simulation programs,[71] but they provide an easy and straightforward way to visualise magnetisation and its evolution as a vector, often termed the "vector model".[23]

1.3.2 NMR hardware set-up

In modern NMR spectrometers, the static magnetic field is produced by a superconducting coil[24] submerged in a tank filled with liquid helium, surrounded by another tank filled with liquid nitrogen to limit the fusion of the liquid helium, as illustrated in Figure 1.8a.

The RF pulse is produced with a coil L included in a RLC[25] passband circuit (Figure 1.8b), whose resonance frequency corresponds to the RF frequency ω_{RF}.[74, 75] As all nuclei have different gyromagnetic ratios, the passband circuit will have the effect of selecting a limited range of frequencies and thus only the nucleus of interest. This can be achieved by adjusting the variable capacitances of the capacitors C_M and C_T

[23] Adiabatic pulses are described in Appendix F using the vector model.

[24] There are alternative experimental set-ups, for example electromagnets (often for relaxometry), permanent magnets [72] or electromagnet placed inside a superconducting coil to reach very high fields.[73]

[25] RLC: Resistor (R), inductor (L), capacitor (C)

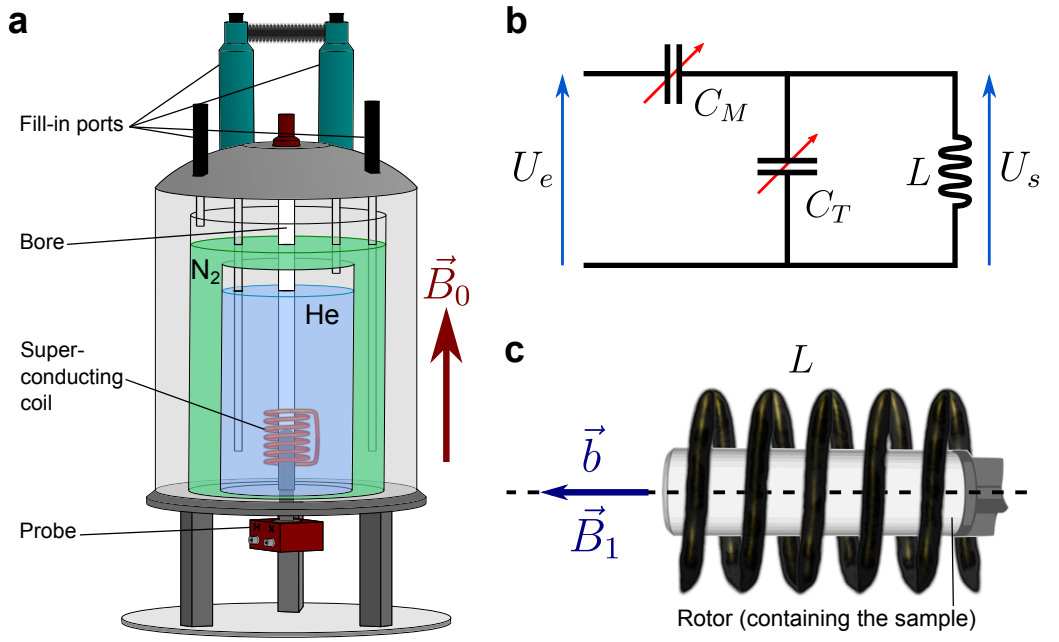

Figure 1.8: ***(a)****: Schematic of a modern NMR spectrometer equipped with a superconducting coil that created the static field* $\vec{B}_0$. ***(b)****: Equivalent circuit diagram of a simple probe, with* C_M *and* C_T *being the matching and tuning capacitors, respectively, and* L *is the RF/recording coil.* ***(c)****: Schematic representation of the rotor containing the sample inside the coil* L *pictured in* ***(b)****, showing the direction of the RF field* $\vec{B}_1$ *and the unit magnetic field* $\vec{b}$.

illustrated Figure 1.8b. The probed can be qualified as ”tuned” for a given nucleus if the following three conditions are fulfilled:

- The resonance frequency must be at (or close to) the Larmor frequency of the desired nucleus with an applied static magnetic B_0.
- The total impedance must be as near as possible to 50 Ω to limit dissipated or reflected power.
- The quality factor must be high in order to select only the Larmor frequency of the nucleus of interest.

The electronics in Figure 1.8b are incorporated into a probe, placed at the center of the superconducting coil (Figure 1.8a). According to Faraday’s law of induction, the voltage observed at the terminals of the RF coil $U_s(t)$ (equivalently called the ”NMR signal”) generated by the bulk magnetisation $\vec{M}$ of the nuclei placed in the RF coil (Figure 1.8c), can be expressed as being in the following form

$$U_s(t) = -\frac{\partial \Phi_B}{\partial t} = \frac{\partial}{\partial t} \int \vec{b}(\vec{r}).\vec{M}(\vec{r},t).dr \quad . \tag{1.3.15}$$

where Φ_B is the magnetic flux through the recording coil. As the observed signal de-

pends on the characteristics of the RF coil, such as position, structure, gain, *etc.*, $\vec{b}(\vec{r})$ is defined as the magnetic field produced at a point at $\vec{r}$ from the origin by a unit current, as illustrated in Figure 1.8c, so Equation (1.3.15) is always valid, and illustrates the electromagnetic reciprocity, *i.e.*, that the coil can be exploited both to produce the RF fiend and to record the NMR signal. As an illustration, $\vec{b}$ would be in the center of a "long" coil composed of N loops of radius R,

$$\vec{b} = \frac{\mu_0 N I_0}{2R} \vec{u}_b \quad , \tag{1.3.16}$$

where I_0 corresponds to a unit electric current of 1 A and $\vec{u}_b$ is a unit vector along the axis of symmetry of the coil. It can directly be deduced by combining Equations (1.1.13) and (1.3.15) that the NMR signal oscillates at the Larmor frequency, *e.g*,

$$U_s(t) \propto \frac{d \parallel \vec{M_T}(t) \parallel}{dt} \propto \frac{d}{dt} \parallel e^{i\omega_0 t} \parallel \quad . \tag{1.3.17}$$

From Equations (1.3.10) and (1.3.15), it can be shown that the amplitude of the NMR signal is proportional to

$$U_s \propto \frac{\gamma^3 B_0^2}{T} \quad . \tag{1.3.18}$$

In solid-state NMR, the sample is generally packed in a rotor as illustrated Figure 1.8c, so it can be rotated (see Section 2.2.3). The RF field $\vec{B}_1$ as shown on Figure 1.8c goes along the axis of the coil, which at first sight does not seems consistent with previously written Equations (1.1.14) and (1.2.57), describing the RF magnetic field $\vec{B}_1$ as describing a circle. However, the oscillating magnetic field B_1 produced along an axis can be expressed as the sum of two oscillating components at ω_{RF} and $-\omega_{\text{RF}}$ such that

$$B_1 . \exp(i\theta_{\text{RF}}) \cos(\omega_{\text{RF}} t) = \frac{1}{2} B_1 . \exp(i\theta_{\text{RF}}) \left(\exp(+i\omega_{\text{RF}} t) + \exp(-i\omega_{\text{RF}} t)\right) \quad . \tag{1.3.19}$$

If $+\omega_{\text{RF}}$ approaches the Larmor frequency, then $-\omega_{\text{RF}}$ component is far off resonance and has no effect on the nuclear spins, therefore can be omitted. With only the $+\omega_{\text{RF}}$ component, we find an expression for $\vec{B}_1$ similar to that given in Equation (1.1.14).

A NMR spectrum spectrum is usual presented processing with FT[26] (see Appendix G) of the raw NMR signal, or FID[27].[76] In general, relaxation processes are sufficiently long to be ignored during pulses.[28] Since $\vec{B}_1$ and $\vec{b}$ are perpendicular with respect to $\vec{B}_0$, the

[26] FT: *Fourier Transform*

[27] FID: *Free Induction Decay*

[28] This may no be applicable if long pulses are applied (see examples in Section 3.1.3 and Appendix F), or if long relaxation periods are necessary.

signal is maximum when $\vec{M}$ is moved perpendicular to $\vec{B}_0$, *i.e.*, in the transverse plane. This is accomplished when the bulk magnetisation $\vec{M}$ is moved by an angle of 90° from its equilibrium value, *e.g*, when $\vec{B}_1$ is applied for a duration τ_p for which the quantity

$$\beta = \omega_1 \tau_p \quad , \tag{1.3.20}$$

denoted the flip angle, is equal to $\pi/2$. Acquiring a basic NMR spectrum consists of applying a 90° pulse, to record the FID, and to apply a FT. When a system is perturbed from equilibrium, the system is submitted to the Zeeman interaction and returns to equilibrium by a photon-driven process. The photon having an angular momentum $I = 1$, the rule of spin conservation imposes that a transition can take place only between adjacent energy levels, *i.e.*, that satisfy the selection rule

$$\Delta m_I = \pm 1 \quad . \tag{1.3.21}$$

This results in only $p = \pm 1$ coherences (1Q) being directly observable in NMR experiments. By convention, only the coherence order $p = -1$ is observed, which consists in the detection of $\langle \hat{I}_+ \rangle$ (see Equation (3.1.9) for the implication of this for the NMR signal).

Chapter 2

Interactions in NMR

Introduction

Chapter 1 described the principles at the root of the NMR phenomenon and NMR spectroscopy. The interactions described in the previous chapter, the static magnetic field and the application of RF pulses, are controlled by the user and, as such, are called external interactions. These interactions provide only a small amount of information of chemical interest. This chapter describes internal interactions that affect the spins, *i.e.*, those inherent to the system, which are of actual interest for chemical problems.

A significant number of samples of interest need to be studied in the solid state rather than in solution or the liquid state. Such samples include minerals, catalysts, microporous frameworks, ceramics, and some proteins, for which data may be of scientific relevance only if experiments are performed on the samples in the physical state of interest. However, NMR spectroscopy of solids differs in many aspects from that in solution. The near-absence of molecular motion within the solid state causes interactions that are not observable in liquid-state NMR spectra to become important. Despite the additional amount of information that these interactions may provide, they often cause severe broadening of the spectral lineshapes, thus affecting the ease with which any information can be extracted. Throughout the development of solid-state NMR, methods have been proposed to counteract the line broadening occurring in solid-state NMR spectra, which are now routinely implemented in modern spectrometers.

This chapter uses informations obtained from [33, 34, 36, 37, 49, 56, 77–85].

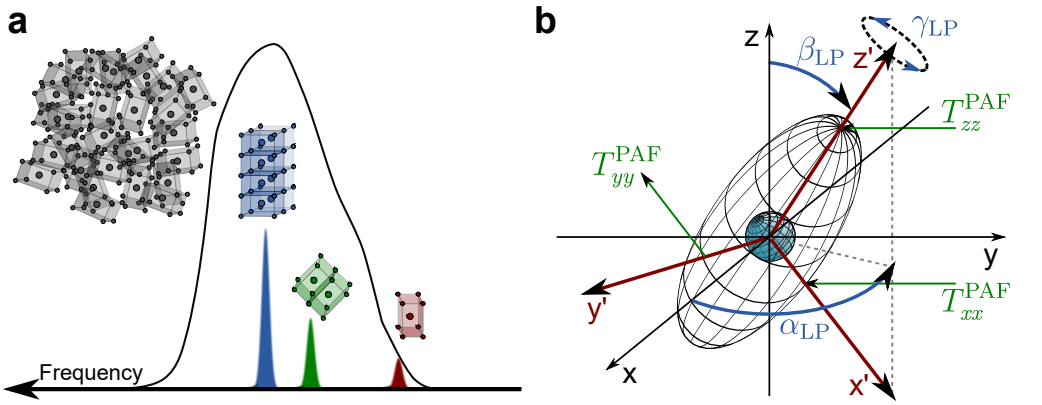

Figure 2.1: ***(a)****: Schematic NMR spectrum for a powdered sample of a disordered material, composed of the contributions from several crystallite orientations.* ***(b)****: Illustration of an interaction tensor represented by an ellipsoid, labelled with axes defining the laboratory frame* Σ_{lab}*, depicted in black, and the PAF, depicted in red.*

2.1 Theoretical background

2.1.1 General interaction Hamiltonian

All of the principles introduced in Chapter 1 are valid for either solution-state or solid-state NMR spectroscopy, but, to take into consideration the existence of other interactions in the solid state, additional terms must be included in a total interaction Hamiltonian for a given system, that now takes the form

$$\hat{H} = \underbrace{\hat{H}_Z + \hat{H}_{\mathrm{RF}}}_{\text{External Interactions}} + \underbrace{\sum \hat{H}_{\mathrm{int}}}_{\text{Internal Interactions}} \quad . \tag{2.1.1}$$

In contrast to external interactions, $\sum \hat{H}_{\mathrm{int}}$ contains all interactions taking place in the sample, between the observed nucleus and other nuclei, the electrons, electrons in bonds, or with local electric and magnetic fields. These interactions are usually smaller than the external interactions described previously (see Table 2.1), but are key to provide structural information about the sample.

A typical interaction Hamiltonian for a spin $\hat{I}$ can be written using the form [77, 83, 85]

$$\hat{H}_{\mathrm{int}} = C_{IJ}.\omega_{IJ}.\hat{I}.\overleftrightarrow{T}.\hat{J} \quad , \tag{2.1.2}$$

where

- ω_{IJ} is the characteristic frequency of the interaction (see Table 2.1),
- $\hat{I}$ is the angular momentum operator associated with the spin I,

- $\overleftrightarrow{T}$ is the interaction tensor,
- $\hat{J}$ is either the angular momentum operator $\hat{I}$, the that of a different spin $\hat{S}$, or a magnetic field vector,
- C_{IJ} is a constant to ensure consistent units, related to $\hbar$ or γ.

The Hamiltonians expressing the interaction between a nucleus and a magnetic field introduced previously (Section 1.2.3, Equations (1.2.46) and (1.2.57)) possess this form with $\overleftrightarrow{T} = \hat{1}_3$. More generally, the interaction tensor is a second-rank matrix of the form

$$\overleftrightarrow{T} = \begin{bmatrix} T_{xx} & T_{xy} & T_{xz} \\ T_{yx} & T_{yy} & T_{yz} \\ T_{zx} & T_{zy} & T_{zz} \end{bmatrix} \quad . \tag{2.1.3}$$

Any tensor can be decomposed into the sum of three tensors: an isotropic tensor, $\overleftrightarrow{T}_{\text{iso}}$, a traceless symmetrical tensor, $\overleftrightarrow{T}_{\text{sym}}$, and a traceless antisymmetrical tensor, $\overleftrightarrow{T}_{\text{anti}}$, such that

$$\overleftrightarrow{T} = \overleftrightarrow{T}_{\text{iso}} + \overleftrightarrow{T}_{\text{sym}} + \overleftrightarrow{T}_{\text{anti}} \quad , \tag{2.1.4}$$

where

$$\overleftrightarrow{T}_{\text{iso}} = \frac{1}{3}.\text{Tr}[\overleftrightarrow{T}].\hat{1}_3 \tag{2.1.5a}$$

$$\overleftrightarrow{T}_{\text{sym}} = \frac{1}{2}\left(\overleftrightarrow{T} + \overleftrightarrow{T}^{\dagger}\right) - \overleftrightarrow{T}_{\text{iso}} \tag{2.1.5b}$$

$$\overleftrightarrow{T}_{\text{anti}} = \frac{1}{2}\left(\overleftrightarrow{T} - \overleftrightarrow{T}^{\dagger}\right) \quad . \tag{2.1.5c}$$

$\overleftrightarrow{T}_{\text{iso}}$ describes the isotropic part of the interaction, *i.e.*, whose effect do not depend on the orientation of the crystallite or molecule. In solution, the rapid and random reorientation of the spins averages most interaction tensors are often reduced to this isotropic part. However, in a typical sample in the solid state, the random orientation of each individual crystallite, and the presence of anisotropic interactions causes line broadening. This results from the fact that the peak for each crystallite appears at a different frequency, as illustrated in Figure 2.1a. Mathematically speaking, if $\overleftrightarrow{T}$ is not proportional to $\hat{1}_3$, *i.e.*, if $\overleftrightarrow{T} \neq \overleftrightarrow{T}_{\text{iso}}$, then the interaction has an anisotropic component. This anisotropy is characterised by the elements of the matrix $\overleftrightarrow{T} - \overleftrightarrow{T}_{\text{iso}} = \overleftrightarrow{T}_{\text{sym}} + \overleftrightarrow{T}_{anti}$.

The antisymmetrical tensor $\overleftrightarrow{T}_{\text{anti}}$ is rarely considered in practice,[86] as it describes weaker effects than the symmetrical tensor which are only described by second-order developments or above (see Section 2.1.2 for further details). However, it can be

calculated or measured experimentally in some cases.[87–89] The most important effects of an interaction can be derived from the symmetric part of the tensor, which means that only $\overleftrightarrow{T} = \overleftrightarrow{T}_{\text{iso}} + \overleftrightarrow{T}_{\text{sym}}$ is considered in this approximation.

The interaction tensor $\overleftrightarrow{T}$ is described in Σ_{lab}, where it contains non-diagonal elements if the general case, and, thus, is not convenient to manipulate. An appropriate transformation is to express the interaction tensor in a basis such that $\overleftrightarrow{T}$ is diagonal, through the diagonalisation of $\overleftrightarrow{T}$. The resulting eigenvectors describe a basis in which the effects of an interaction occur only along the axis of this frame, as illustrated in Figure 2.1b. Such a basis is known as the PAF[1].[2] In the PAF, the tensor $\overleftrightarrow{T}$ simplifies to

$$\overleftrightarrow{T}^{\text{PAF}} = \begin{bmatrix} T_{xx}^{\text{PAF}} & 0 & 0 \\ 0 & T_{yy}^{\text{PAF}} & 0 \\ 0 & 0 & T_{zz}^{\text{PAF}} \end{bmatrix} \quad , \tag{2.1.6}$$

where T_{xx}^{PAF}, T_{yy}^{PAF} and T_{zz}^{PAF} are the eigenvalues, also known as the principal components, of the tensor. Eigenvalues correspond to noticeable features on NMR spectra, but it is more convenient to define the three important quantities

$$\begin{cases} T_{\text{iso}} = \dfrac{1}{3}(T_{xx}^{\text{PAF}} + T_{yy}^{\text{PAF}} + T_{zz}^{\text{PAF}}) & \text{(2.1.7a)} \\ \Delta_T = T_{zz}^{\text{PAF}} - T_{\text{iso}} & \text{(2.1.7b)} \\ \eta_T = \dfrac{T_{yy}^{\text{PAF}} - T_{xx}^{\text{PAF}}}{\Delta_T} \quad , & \text{(2.1.7c)} \end{cases}$$

where

- T_{iso} is the isotropic part of the interaction,
- Δ_T is the magnitude of the anisotropic part of the interaction,
- η_T is the asymmetry parameter, describing the shape of the anisotropy,

as they are easier both to interpret and to extract for NMR powder lineshapes. Quantities are given here according to the Haeberlen-Mehring-Spiess convention,[90–92] in which the principal components T_{zz}^{PAF}, T_{xx}^{PAF} and T_{yy}^{PAF} are sorted according to their separation from the isotropic value T_{iso}, *i.e.*,

$$|T_{zz}^{\text{PAF}} - T_{\text{iso}}| \geq |T_{xx}^{\text{PAF}} - T_{\text{iso}}| \geq |T_{yy}^{\text{PAF}} - T_{\text{iso}}| \quad . \tag{2.1.8}$$

The rotation transformation between Σ_{lab} and the PAF (or any frame) can be described by the action of three successive rotations, each defined by one of the three angles α,

[1] PAF: *Principal Axis Frame*

[2] The PAF is also often referred to as the PAS (*Principal Axis System*)

Interaction	Typical order of magnitude
Zeeman	10 MHz to 1 GHz
Shielding	0.1 kHz to 100 kHz
Scalar coupling	1 Hz to 1 kHz
Paramagnetic	0.1 kHz to 100 kHz
Knight shift	1 kHz to 1 MHz
Dipolar coupling	1 kHz to 100 kHz
Quadrupolar coupling	0.1 MHz to 100 MHz

Table 2.1: *Table summarizing the typical characteristic frequencies of the main interactions in NMR.*

β and γ, termed Euler angles, detailed in Appendix B.3 and shown in Figure 2.1b. The components of the tensor in the Σ_{lab} can be established from the tensor in the PAF by applying the rotation operator $\hat{R}$ defined in Appendix B.3, Equation (B.3.1), giving

$$\overleftrightarrow{T} = \hat{R}(\alpha_{\text{PL}}, \beta_{\text{PL}}, \gamma_{\text{PL}}).\overleftrightarrow{T}^{\text{PAF}}.\hat{R}(\alpha_{\text{PL}}, \beta_{\text{PL}}, \gamma_{\text{PL}}) \quad , \tag{2.1.9}$$

where the Euler angles α_{LP}, β_{LP} and γ_{LP} defines the three rotations between Σ_{lab} and the PAF.[3]

There has been much successful work carried out using a Hamiltonian expressed in Cartesian coordinates,[93, 94] with the evolution of the spin observables $\hat{I}$ being both convenient and permitting easy for visualisation. Nevertheless, for the case when several interactions must be taken into account, multiple successive rotations between Σ_{lab} and each PAF of the respective interactions are necessary and the interaction Hamiltonian in Equation (2.1.2) is better expressed as a sum of irreducible spherical tensors

$$\hat{H}_{\text{int}} = \omega_{IJ} \sum_{l=0}^{l=2} C_{IJ}^{(l)} \sum_{m=-l}^{m=+l} (-1)^m A_{l,m} T_{l,-m} \quad . \tag{2.1.10}$$

$A_{l,m}$ and $T_{l,-m}$ are irreducible spherical tensors,[95] interpreted respectively as the spatial part and the nuclear spin part of the Hamiltonian $\hat{H}_I$. Using this description, $\hat{H}_I$ acquire interesting rotation properties. Upon the application of the rotation operator

[3]The subscript PL standing for *PAF to Laboratory* (PAF to Σ_{lab}). The Euler angles defining the opposite rotation would be subscripted $\alpha_{\text{LP}} = -\alpha_{\text{PL}}$.

(Appendix B.2) from Σ_{lab} to the PAF, $A_{l,m}$ (or $T_{l,-m}$) become

$$A^P_{l,m'} = \hat{R}(\alpha_{\text{LP}}, \beta_{\text{LP}}, \gamma_{\text{LP}}).A^L_{l,m'} \tag{2.1.11a}$$

$$= \sum_{m'=-m}^{m'=+m} D^l_{m',m}(\alpha_{\text{LP}}, \beta_{\text{LP}}, \gamma_{\text{LP}}).A^L_{l,m'} \quad , \tag{2.1.11b}$$

where $A^L_{l,m'}$ and $A^P_{l,m'}$ are respectively the $A_{l,m'}$ matrices expressed in Σ_{lab} and in the PAF, and $D_{m',m}$ are called the Wigner rotation matrices,[96] and are characterised by an rank l and an order m. D-matrices are related to the spherical harmonics, and also exhibit interesting rotation properties and ease of visualisation.[97] D-matrices can be rewritten for any Euler-angle under the form [98]

$$D^l_{m,l}(\alpha, \beta, \gamma) = \exp(-im'\alpha).d^{(l)}_{m,m'}(\beta).\exp(-im\gamma) \quad , \tag{2.1.12}$$

where $d^{(l)}_{m,m'}(\beta)$ are referred to as reduced Wigner rotation matrices, or d-matrices, and are only a function of the β-Euler angle.[4] The form of the d-matrices are given for example in [99], Chapter 1 of Wasylishen *et al.* [100] or Appendix B.4. The particular case where $m = m' = 0$, $d^{(l)}_{0,0}$, prove important elements for the description of internal interactions in NMR. They relate to Legendre's polynomial [101] according to

$$d^{(l)}_{0,0}(\beta) = P^{(l)}_L(cos\beta) \quad . \tag{2.1.13}$$

The zero-, second- and fourth-order Legendre polynomials are given

$$\begin{cases} P^{(0)}_L(\cos\beta) = 1 & \text{(2.1.14a)} \\ P^{(2)}_L(\cos\beta) = \frac{1}{2}\left(3\cos^2\beta - 1\right) & \text{(2.1.14b)} \\ P^{(4)}_L(\cos\beta) = \frac{1}{8}\left(35\cos^4\beta - 30\cos^2\beta + 3\right) & \text{(2.1.14c)} \end{cases}$$

$P^{(0)}_L$ is a constant and has no dependence upon β, and thus represents the isotropic part of the interaction. $P^{(2)}_L$ has a unique solution

$$\beta^{(2)}_m = \cos^{-1}\left(\frac{1}{\sqrt{3}}\right) \simeq 54.74° \quad . \tag{2.1.15}$$

called the magic angle. $P^{(4)}_L$ has two solutions

[4] In this context, β is often denoted θ in the literature.[34]

$$\begin{cases} \beta_{m1}^{(4)} \simeq 30.56° & \text{(2.1.16a)} \\ \beta_{m2}^{(4)} \simeq 70.12° \quad , & \text{(2.1.16b)} \end{cases}$$

2.1.2 Simplifying interaction Hamiltonians

Most internal interaction Hamiltonians, when written using the form given in Equation (2.1.2), contain tensors and different spin vectors, and can be conceptually and computationally very challenging for large systems. Using appropriate approximation methods, Hamiltonians be can rewritten into much simpler forms, often without any loss in accuracy. In NMR, the three most common methods to approximate interaction Hamiltonians are average Hamiltonian theory, perturbation theory, or secular averaging.[34, 77, 81, 102] This section outlines the basic principles behind these methods.

Average Hamiltonian theory

It has been introduced in Section 1.2.3 that the evolution of a quantum state can be described by the action of a propagator $\hat{U}(t)$ (Equations (1.2.40) and (1.2.45)) on the initial quantum state.[34, 102] It is often the case when, during an NMR experiment, the Hamiltonian describing a system changes successively at times denoted $t_0, t_1, t_2, \ldots, t_n$. In this case, the propagator has the following complicated form

$$\begin{aligned} \hat{U}(t) &= \exp\Big(-i\hat{H}_n(t_n - t_{n-1})\Big).\exp\Big(-i\hat{H}_{n-1}(t_{n-1} - t_{n-2})\Big) \ \ldots \ \exp\Big(-i\hat{H}_1(t_1 - t_0)\Big) \\ &= \prod_{k=n}^{k=1} \exp\Big(-i\hat{H}_k(t_k - t_{k-1})\Big) \quad , \end{aligned} \tag{2.1.17}$$

where all the $\{\hat{H}_k\}_{k\in\mathbb{N}}$ are time independent. Equation (2.1.17) can be seen as a discrete case of Equation (1.2.43). Equation (2.1.17) can be simplified using the method of the mathematician Wilhelm Magnus to approximate the solutions of linear differential equations for an operator (in our case $\hat{H}$). The differential equation to be solved is either the TDSE or the LVNE. From the Magnus expansion,[102] an average Hamiltonian $\bar{H}$ can be established

$$\bar{H} = \bar{H}^{(0)} + \bar{H}^{(1)} + \ldots \quad , \tag{2.1.18}$$

where

$$\bar{H}^{(0)}(t) = \frac{1}{t}\int_{t_0}^{t} dt_1 . \hat{H}(t_1) \tag{2.1.19a}$$

$$\bar{H}^{(1)}(t) = -\frac{i}{2t}\int_{t_0}^{t} dt_1 \int_{t_0}^{t_1} dt_2 \Big[\hat{H}(t_1), \hat{H}(t_2)\Big] \tag{2.1.19b}$$

$$\dots$$

Confusingly, $\bar{H}^{(0)}$ is termed the first-order average Hamiltonian is written and $\bar{H}^{(1)}$ the second-order averaged Hamiltonian. It is obvious from Equation (2.1.19b) that second-order does not need to be considered if $\hat{H}(t_1)$ and $\hat{H}(t_2)$ commute for all t_1 and t_2. The propagator takes the simpler form

$$\hat{U}(t) = \exp\big(-i\bar{H}t\big) \quad . \tag{2.1.20}$$

The precision of the average Hamiltonian $\bar{H}$ depends on the choice of the t. If the Hamiltonian is periodic, which is often the case in solid-state NMR, t can be set to this period, *i.e.*,

$$t = t_n - t_0 \quad . \tag{2.1.21}$$

The Hamiltonian $\hat{H}$ can also be split between multiple small time intervals during which the average Hamiltonian can be considered constant, typically over a period of the fastest oscillating component (usually ν_0 or ν_1). In either case, the average Hamiltonian cannot be used to predict the system evolution within the chosen time interval.

Perturbation theory

A perturbation development can be applied whenever the total Hamiltonian has the form [81, 82, 103]

$$\hat{H} = \hat{H}_0 + \hat{W} \quad , \tag{2.1.22}$$

with $\hat{H}_0$ being the "large" Hamiltonian (the non-perturbed Hamiltonian) whose solutions are perfectly known, and $\hat{W}$ being a "small" but complex Hamiltonian (the (time-independent) perturbation). The effect of $\hat{W}$ can be seen as a "perturbation" of the Hamiltonian is small,[5] The eigenvalues associated with the Hamiltonian would be

[5] *e.g.*, according to Cohen-Tannoudji *et al.*,[81] if the non-diagonal matrix elements of $\hat{W}$ are small compared to the difference between all the eigenvalues of $\hat{H}_0$.

those of $\hat{H}_0$ plus a small correction arising from the perturbation $\hat{W}$. The total energy is written

$$E = E_0 + E_1 + E_2 + \dots \quad , \tag{2.1.23}$$

with E_0 being the non-perturbed energy, *i.e.*, the eigenvalue of $\hat{H}_0$, E_1 the first-order correction to the energy, E_2 the second-order correction, *etc.* Calling $|\phi_k\rangle$ any normalised eigenvector of $\hat{H}_0$, the first- and second-order energy corrections to E_0 are

$$E_1 = \langle \phi_k | \hat{W} | \phi_k \rangle \quad , \tag{2.1.24}$$

interpreted as the average value of the perturbation Hamiltonian in the non-perturbed state $|\phi_k\rangle$, and

$$E_2 = \sum_{k \neq l} \frac{\langle \phi_k | \hat{W} | \phi_l \rangle}{E_k - E_l} \quad . \tag{2.1.25}$$

It is not necessary to consider the effect of higher order perturbation for this work. For the description of interactions in NMR spectroscopy, $\hat{H}_0$ often corresponds to the Zeeman interaction Hamiltonian, almost always predominant relative to the other interactions (see Table 2.1), while internal interactions are treated as a perturbation $\hat{W}$ of the Zeeman interaction.

Secular approximation

In NMR, only phenomena whose frequencies are near to ω_0 are observed while others are filtered out as described in Section 1.3.2. Components of a perturbation Hamiltonian, or any of the terms obtained using one of the two previously-introduced methods, can be neglected if they describe an oscillation of the quantum states far from ω_0, *e.g.*, for example, the term in $\exp(-i\omega_{\mathrm{RF}}t)$ in Equation (1.3.19)).[81]

Mathematically speaking, terms creating an effect far from ω_0 can be visualised as terms being time-dependant when written in Σ_{rot}, at a rate ω_0. Upon the application of the rotation operator describing the transformation from Σ_{lab} to Σ_{rot}

$$\hat{R}_z(\omega_0 t) = \exp\left(\frac{i}{\hbar}\omega_0 t \hat{I}_z\right) \quad , \tag{2.1.26}$$

a rotated interaction Hamiltonian $\hat{W}$ can be separated into time-dependent and time-independent components such as

$$\hat{R}_z^{-1}(\omega_0 t).\hat{W}_I.\hat{R}_z(\omega_0 t) = \underbrace{\hat{R}_z^{-1}(\omega_0 t).\hat{W}_{NS}.\hat{R}_z(\omega_0 t)}_{\text{Time-dependent}} + \underbrace{\hat{W}_S}_{\text{Time-independent}} . \tag{2.1.27}$$

These two components are: a term $\hat{W}_S$ unaffected by $\hat{R}_z(\omega_0 t)$,[6] and a term affected by $\hat{R}_z(\omega_0 t)$, now time dependent in this frame. $\hat{W}_S$ is said to be the "secular" component of the perturbation, and $\hat{W}_{NS}$ is the non-secular component. Secular components have the effect of producing an oscillation of the quantum states at a frequency near or at ω_0, whereas non-secular components create fast oscillations, with little or no effects when observing at ω_0.

To a first approximation, non-secular terms can simply be discarded from the perturbation Hamiltonian. In summary, the "secular approximation" refers to the approach that consists of keeping nothing but the secular part of $\hat{W}$.[7] The approximation made using this approach can then be refined by secular averaging. That is, developing $\hat{W}_{NS}$ into secular Hamiltonians of increasing orders.

2.2 Common interactions

A non-exhaustive list of interactions that can occur in solid-state NMR are given in Table 2.1. This section describes all the most common interactions. Firstly, presented below are some common interactions that are of lesser importance or that occur only in cases not covered in this work.

J-coupling (or scalar coupling)

J-coupling arises from the interaction between NMR-active nuclei, mediated by the electrons in chemical bonds. This interaction exists only for nuclei in atoms joined by chemical bonds. Despite its key importance in solution-state NMR, it is of lesser importance in the solid state as the characteristic frequency is usually much smaller than other interactions (see table Table 2.1), and is therefore often rarely resolved in solid-state spectra. The Hamiltonian for J-coupling interaction is [56, 104]

$$\hat{H}_J = 2\pi \hat{I}.\overleftrightarrow{J}_{IS}.\hat{S} \tag{2.2.1}$$

where $\overleftrightarrow{J}_{IS}$ is the J-coupling tensor between two nuclei.

[6] *e.g.*, $\hat{H}_S$ commutes with $\hat{I}_z$ and $\hat{H}_z$.

[7] Or the secular part of any term obtained from average Hamiltonian theory or perturbation theory.

Paramagnetic Interaction

As the electron is a spin $S = 1/2$ particle, it can also interact with the observed nuclei.[105] However, as electrons in many samples are in closed-shell configurations, paired in the same orbital with an another electron of opposite magnetic spin, the resulting spin is zero and, therefore, no interaction is observed. Paramagnetic interactions occur when there are unpaired electrons within the sample - these may be introduced intentionally for some experiments requiring unpaired electrons or to improve relaxation properties.

2.2.1 Chemical shielding interaction and anisotropy

As originally observed, the Zeeman effect corresponds to the splitting of atomic emission/absorption bands when a magnetic field is applied to the sample.[68, 69] This effect is of the same nature, but is different to the nuclear Zeeman effect observed in NMR spectroscopy. However, this highlights the impact a magnetic field has on the electrons in the surrounding orbitals. Such electrons, as charged particles with a non-linear motion, generate a magnetic field, which tends to oppose the applied static magnetic field $\vec{B}_0$ and, thus, affecting the magnetic field experienced at the nucleus and the observed Larmor frequency. This phenomenon is called the shielding interaction.[106] Its effect is usually referred to as the CS[8], as the electron distribution is affected by the chemical environment, which results in a shift of the observed Larmor frequency. This effect alone is sufficient to deduce considerable information about the environment of the investigated nucleus.[40, 107, 108]

Furthermore, the amplitude of shielding of the nucleus by electrons is also affected by the relative orientation of the magnetic field to the molecular orbitals, from which an anisotropy arises. This effect is known as the CSA[9]. Owing to the rapid rotational motion molecules have in the liquid state, only the isotropic part of the shielding interaction is usually visible, except for very large molecules such as proteins. In solution state, the local magnetic field $\vec{B}_{\text{Loc}}$, corresponding to the magnetic field at the nucleus, can be expressed as

$$\vec{B}_{\text{Loc}} = \vec{B}_0(1 - \sigma_{\text{iso}}) \quad , \tag{2.2.2}$$

[8] CS: *Chemical Shift*
[9] CSA: *Chemical Shift Anisotropy*

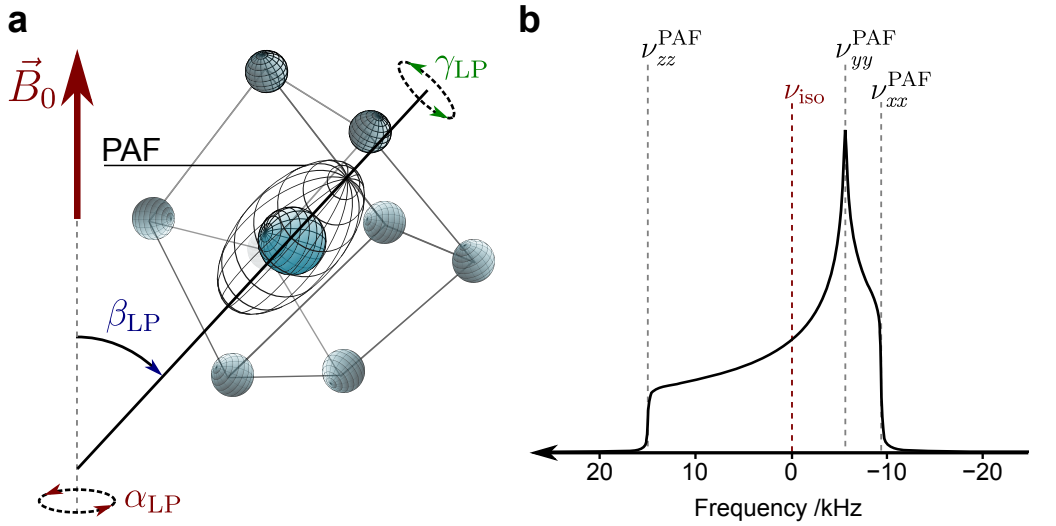

Figure 2.2: ***(a)****: Schematic representation of the relative orientation of the PAF relative to* $\vec{B}_0$*, represented inside a unit cell to illustrate the chemical environment, described by the rotation of the three Euler angles* α_{LP}*,* β_{LP} *and* γ_{LP}*.* ***(b)****: Positions of the principal components* $\sigma_{xx}^{\mathrm{PAF}}$*,* $\sigma_{yy}^{\mathrm{PAF}}$ *and* $\sigma_{zz}^{\mathrm{PAF}}$ *on a simulated lineshape for a powder sample of a spin* $I = 1/2$ *nucleus submitted to CSA according to the Haeberlen-Mehring-Spiess convention (see Equation* (2.1.8)*). Spectrum simulated using 75024 orientations for* ^{15}N *with* B_0 *= 14.1 T (*ν_0 *= 60.8 MHz),* σ_{iso} *= 0,* $\nu_0 \times \Delta_{\mathrm{CSA}}$ *= 15 kHz and* η_{CSA} *= 0.25.*

where σ_{iso} the isotropic shielding parameter, usually very small compared to 1, *i.e.*, $\vec{B}_{\mathrm{Loc}}$ is essentially identical to B_0. In the solid state, the chemical shielding Hamiltonian is, for a spin I, is expressed using the tensorial form given in Equation (2.1.2)

$$\hat{H}_{\mathrm{CS}} = \gamma \hat{I}.\overleftrightarrow{\sigma}.\hat{B}_0 \quad , \tag{2.2.3}$$

where $\overleftrightarrow{\sigma}$ is the chemical shielding tensor and is given by

$$\overleftrightarrow{\sigma} = \begin{bmatrix} \sigma_{xx} & \sigma_{xy} & \sigma_{xz} \\ \sigma_{yx} & \sigma_{yy} & \sigma_{yz} \\ \sigma_{zx} & \sigma_{zy} & \sigma_{zz} \end{bmatrix} \quad . \tag{2.2.4}$$

As stated previously, the tensor is diagonal in the PAF, where it is given by

$$\overleftrightarrow{\sigma}^{\mathrm{PAF}} = \begin{bmatrix} \sigma_{xx}^{\mathrm{PAF}} & 0 & 0 \\ 0 & \sigma_{yy}^{\mathrm{PAF}} & 0 \\ 0 & 0 & \sigma_{zz}^{\mathrm{PAF}} \end{bmatrix} \quad . \tag{2.2.5}$$

The three principal components are used to define the isotropic component σ_{iso}, the anisotropic part Δ_{CSA}, and the asymmetry parameter η_{CSA}, of the chemical shielding interaction (see Equation (2.1.7)). A simplified Hamiltonian of $\hat{H}_{\mathrm{CS}}$ in Equation (2.2.3) can be obtained from average Hamiltonian theory.[34, 83] Truncated to the first order, the Hamiltonian becomes

$$\bar{H}^{(0)}_{\text{CSA}} = -\gamma B_0 \hat{I}_z \sigma_{zz} \quad , \tag{2.2.6}$$

where σ_{zz} is related to the principal components by [77]

$$\sigma_{zz} = \sigma_{\text{iso}} + \frac{1}{2}\Delta_{\text{CSA}}\left[\left(3\cos^2\beta_{\text{PL}} - 1\right) + \eta_{\text{CSA}}\sin^2\alpha_{\text{PL}}\cos 2\beta_{\text{PL}}\right] \quad . \tag{2.2.7}$$

If $\eta_{\text{CSA}} = 0$, the second-order Legendre polynomial $P_L^{(2)}$ (see Equation (2.1.14)) appears in Equation (2.2.7). Applying the TISE on $|I, m_I\rangle$ with $\bar{H}^{(0)}_{\text{CSA}}$ as the Hamiltonian gives

$$\bar{H}^{(0)}_{\text{CSA}} |I, m_I\rangle = m_I \omega_0 \sigma_{zz} |I, m_I\rangle \quad , \tag{2.2.8}$$

which gives a modified and orientation-dependant frequency

$$\begin{aligned} \frac{\omega_{\text{CSA}} - \omega_0}{\omega_0} &= 1 - \sigma_{\text{iso}} \\ &\quad - \frac{1}{2}\Delta_{\text{CSA}}\left[\left(3\cos^2\beta_{\text{PL}} - 1\right) + \eta_{\text{CSA}}\sin^2\alpha_{\text{PL}}\cos 2\beta_{\text{PL}}\right] \quad . \end{aligned} \tag{2.2.9}$$

An implication of Equation (2.2.9) is that, both the isotropic and anisotropic components of the CSA increases proportionally with the field. As a result, the chemical shift is normally quoted in ppm[10] of the Larmor frequency and denote δ_{CS} according to the definition

$$\delta_{\text{CS}} = 10^6 \frac{\omega_0 - \omega_{\text{ref}}}{\omega_{\text{ref}}} \quad , \tag{2.2.10}$$

where ω_{ref} is a reference frequency, obtained from the Larmor frequency of a reference compound for the nucleus and magnetic field of investigation. This quantity is almost exclusively used in the literature instead of the Larmor frequency, as it allows direct comparison of the chemical shifts of a same species recorded on different magnetic fields.

Another implication of Equation (2.2.9) is that the principle components can be easily identified on powder spectra as shown in Figure 2.2, in which distinctive features of the lineshape permits the identification of the frequencies

$$\begin{cases} \nu^{\text{PAF}}_{xx} = \nu_0 . \sigma^{\text{PAF}}_{xx} & \text{(2.2.11a)} \\ \nu^{\text{PAF}}_{yy} = \nu_0 . \sigma^{\text{PAF}}_{yy} & \text{(2.2.11b)} \\ \nu^{\text{PAF}}_{zz} = \nu_0 . \sigma^{\text{PAF}}_{zz} \quad , & \text{(2.2.11c)} \end{cases}$$

and of ν_{CS}, given by

[10] ppm: *part(s) per million*

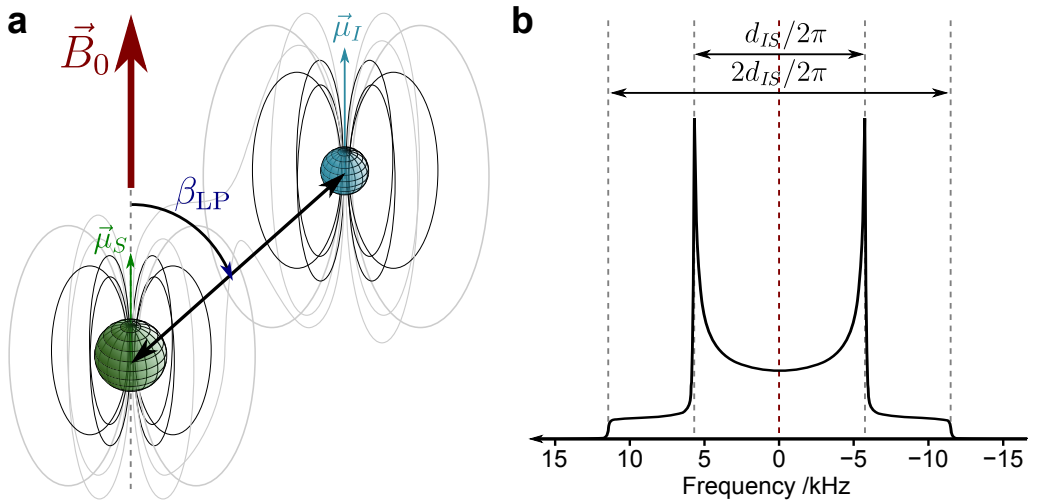

Figure 2.3: ***(a)****: Schematic representation of the dipolar interaction between two spins I and S, with an orientation of the internuclear vector defined by the Euler angles β_{LP} .* ***(b)****: Relation of d_{IS} to a simulated powder lineshape for a spin $I = 1/2$ nucleus submitted to an heteronuclear dipolar coupling. This type of lineshape is often referred to as a Pake doublet.[109] It should be noted that, for an homonuclear dipolar coupling, the total linewidth would be $3d_{IS}/2\pi$. Spectrum simulated using 75024 orientations for ^{15}N with B_0 = 14.1 T (ν_0 = 600.0 MHz for ^{1}H and ν_0 = 60.8 MHz for ^{15}N), for a ^{1}H-^{15}N dipolar interaction of characteristic frequency $d_{\mathrm{IS}}/2\pi$ = 11.47 kHz*

$$\nu_{\mathrm{CS}} = \nu_0(1 - \sigma_{\mathrm{iso}}) \quad . \tag{2.2.12}$$

This last quantity, when quoted in ppm following Equation (2.2.10), is referred to as the isotropic chemical shit, δ_{CS}.

2.2.2 Dipolar interaction

One of the most common sources of broadening in solid-state NMR stems from the interaction between magnetically-active nuclei, through the magnetic fields produced by their respective magnetic moments. The interaction energy between a magnetic field and a magnetic moment was given in Equation (1.1.7c), and combined with the magnetic field produced by a magnetic moment in Equation (1.1.3) gives the classical dipole-dipole interaction energy [49]

$$E_{D_{IS}} = \left(\frac{\mu_0}{4\pi}\right)\frac{1}{r_{IS}^3}\left(\vec{\mu}_I.\vec{\mu}_S - 3.\frac{(\vec{\mu}_I.\vec{r_{IS}}).(\vec{\mu}_I.\vec{r_{IS}})}{r_{IS}^2}\right) \quad , \tag{2.2.13}$$

with I and S referring to two separate nuclei, and $\vec{r}_{IS}$ being the internuclear vector between them. From Equation (2.2.13), it can be observed that this interaction is both distant and orientation dependant. The quantum-mechanical equivalent of this relation

can be obtained by substituting vectors by their equivalent operators. The interaction Hamiltonian between a spin I and a spin S is therefore expressed as [34, 56]

$$\hat{H}_{D_{IS}} = -\left(\frac{\mu_0}{4\pi}\right)\frac{\gamma_I\gamma_S}{\hat{r_{IS}}^3}\left(\hat{I}.\hat{S} - 3.\frac{(\hat{I}.\hat{r}_{IS}).(\hat{S}.\hat{r}_{IS})}{\hat{r}_{IS}^2}\right) \quad , \tag{2.2.14}$$

with $\hat{I}$ and $\hat{S}$ being the angular moment operators associates to I and S. The characteristic frequency for the interaction is thus

$$d_{IS} = -\hbar\left(\frac{\mu_0}{4\pi}\right)\frac{\gamma_I\gamma_S}{r_{IS}^3} \quad . \tag{2.2.15}$$

Table 2.1 shows that dipolar interaction is typically of much lower magnitude than Zeeman interaction, so perturbation theory and secular approximation are justified. Equation (2.2.14) can be written in the same form as Equation (2.1.2)

$$\hat{H}_{D_{IS}} = -\frac{2}{\hbar}\hat{I}.\overleftrightarrow{D}_{IS}.\hat{S} \quad , \tag{2.2.16}$$

where the tensor $\overleftrightarrow{D}$ in the PAF becomes

$$\overleftrightarrow{D}_{IS}^{\text{PAF}} = \begin{bmatrix} -d_{IS}/2 & 0 & 0 \\ 0 & -d_{IS}/2 & 0 \\ 0 & 0 & d_{IS} \end{bmatrix} \quad . \tag{2.2.17}$$

It can be noted that the associated interaction tensor is traceless and two terms are identical, so the dipolar interaction is fully characterised with only the span of the dipolar interaction d_{IS}. An extensive development and rearrangement of Equation (2.2.14) returns an expression for the dipolar Hamiltonian that can conveniently be expressed with terms denoted A to F, referred to as the dipolar alphabet, such that

$$\hat{H}_{D_{IS}} = \frac{d_{IS}}{\hbar}\left(A + B + C + D + E + F\right) \quad , \tag{2.2.18}$$

with A and B being expressed as[11]

$$A = \hat{I}_z\hat{S}_z\left(3\cos^2\beta_{PL} - 1\right) \tag{2.2.19a}$$

$$B = -\frac{1}{4}\left(\hat{I}_+\hat{S}_- + \hat{I}_-\hat{S}_+\right)\left(3\cos^2\beta_{PL} - 1\right) \quad . \tag{2.2.19b}$$

The non-secular terms C to F, omitted here, are tabulated in the literature.[34, 77] While the term A is, in all cases, secular, two cases must be distinguished for B:

1 Spin I and S are the same nuclei. In this case, B is secular and the secular Hamiltonian is

[11] As $\overleftrightarrow{D}_{IS}$ in Equation (2.2.17) only depends on d_{IS}, only the Euler angle β_{LP} is needed to fully describe dipolar interaction in any frame.

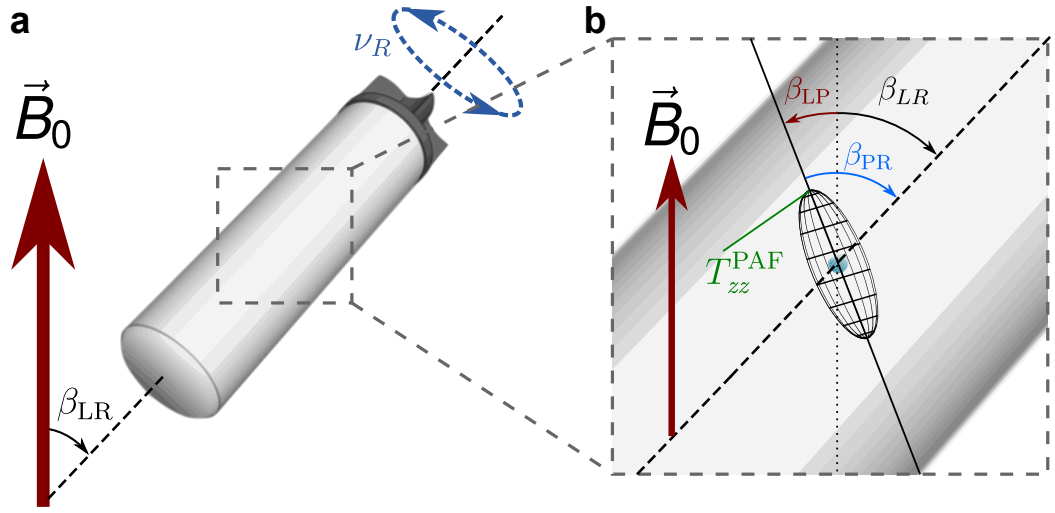

Figure 2.4: ***(a)****: Schematic picture of a rotor spinning in a static magnetic field at an angle β_{LR} at a rate ν_R.* ***(b)****: Schematic of an interaction tensor from a nucleus inside the rotor, showing the angles between Σ_{lab} and the rotor frame β_{LR}, Σ_{lab} and the z-axis of the PAF, β_{LP}, and the z-axis of the PAF to the rotor frame ,β_{PR}.*

$$\hat{H}_{D_{IS}}^{\mathrm{Homo}} = \frac{d_{IS}}{\hbar} P_L^{(2)}(\cos\beta_{\mathrm{LP}}) \left[3\hat{I}_z\hat{S}_z - \hat{I}.\hat{S}\right] \quad , \tag{2.2.20}$$

termed the homonuclear dipolar Hamiltonian. The term $(\hat{I}_+\hat{S}_- + \hat{I}_-\hat{S}_+)$, which comprises the creation (Equation (1.2.19a)) and annihilation (Equation (1.2.19b)) operators, is termed "flip-flop" term, as the magnetisation on one nucleus is increased while the other is lowered.

2 Spin I and S are not the nuclei. B is not secular, leaving only A as the only secular part of the heteronuclear dipolar Hamiltonian now given by

$$\hat{H}_{D_{IS}}^{\mathrm{Hetero}} = \frac{d_{IS}}{\hbar} P_L^{(2)}(\cos\beta_{\mathrm{LP}}).2\hat{I}_z\hat{S}_z \quad . \tag{2.2.21}$$

The presence of B is responsible for varying the total linewidth of the powder lineshape from $2d_{IS}$ in the heteronuclear case, as illustrated in Figure 2.3, to $3d_{IS}$ in the homonuclear case.

2.2.3 Magic-Angle Spinning (MAS)

The possible superposition of several of the interactions described previously may cause a significant line broadening of the signal (as shown in Figure 2.1a), thus increasing the need for efficient line narrowing methods in solid-state NMR. The method that certainly

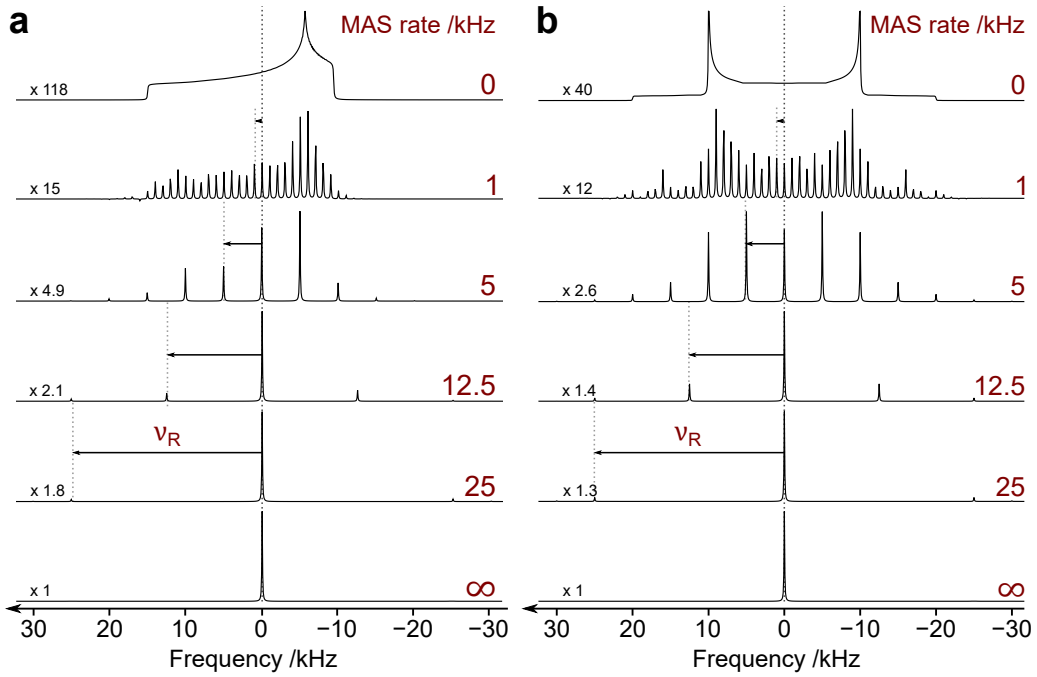

Figure 2.5: *Simulated ^{15}N NMR spectra at B_0 = 14.1 T (ν_0 = 600 MHz for ^1H and ν_0 = 60.8 MHz for ^{15}N) for a sample subject to a **(a)**: CSA interaction, and **(b)**: dipolar interaction, spinning at different MAS rates ν_R. All specta simulated have been simulated using the same conditions interaction strengths as Figure 2.2 for **(a)** and Figure 2.3 for **(b)**.*

has the greatest impact in the field is MAS[12], schematically illustrated in Figure 2.4. Introduced by Andrew,[10] it has been shown to produce a significant line narrowing effect on the spectrum. The principle of the technique is to rotate the sample around an axis inclined at an angle β_{LR} to the static magnetic field as shown in Figure 2.4a.[13]

The approximated Hamiltonian for the CSA in Equation (2.2.7) and the dipolar interaction in Equations (2.2.20) and (2.2.21) both exhibits the term $P_L^{(2)}(\cos\beta_{\text{PL}})$. During the spinning as previously described, in the PAF of an interaction, $\hat{B}_0$ would appear to be changing orientation with time giving

$$\hat{B}_0^{\text{PAF}} = \begin{bmatrix} \sin\beta_{\text{LR}}.\cos(\omega_R t + \gamma_{\text{LR}}) \\ \sin\beta_{\text{LR}}.\sin(\omega_R t + \gamma_{\text{LR}}) \\ \cos\beta_{\text{LR}} \end{bmatrix} , \tag{2.2.22}$$

where ω_R is the spinning rate.[14] To describe this effect, a Hamiltonian or operator initially expressed in the PAF is rotated first to the rotor frame (Transformation expressed

[12] MAS: *Magic-Angle Spinning*
[13] The subscript LR meaning *Laboratory to Rotor frame*, with $\beta_{\text{LR}} = -\beta_{\text{RL}}$.
[14] Or ν_R when expressed in Hz.

by the Euler angles α_{PR},β_{PR} and γ_{PR})[15] before a final rotation to Σ_{lab}. This transformation can be expressed using Wigner D-matrices,[16] such that

$$D^{(l)}_{0,n}(\alpha_{\mathrm{PL}},\beta_{\mathrm{PL}},\gamma_{\mathrm{PL}}) = \sum_{m=-l}^{m=+l} D^{(l)}_{0,m}(0,\beta_{\mathrm{RL}},-\omega_R t+\gamma_{\mathrm{RL}}).D^{(l)}_{0,m}(\alpha_{\mathrm{PR}},\beta_{\mathrm{PR}},\gamma_{\mathrm{PR}}) \quad . \tag{2.2.23}$$

From Equation (2.2.23), it can be established that, over one or more rotor periods (τ_R), the time-average of $P_L^{(2)}$ is

$$\left\langle 3.\cos^2(\beta_{\mathrm{PR}})-1\right\rangle_{\tau_R} = \frac{1}{2}(3.\cos^2\beta_{\mathrm{LR}}-1).(3.\cos^2\beta_{\mathrm{LP}}-1) \quad , \tag{2.2.24}$$

which vanishes when $\beta_{\mathrm{LR}} = \beta_m^{(2)}$. Spinning at an axis inclined at $\beta^{(2)}{}_m$ can remove the broadening of the signal arising from many internal interactions, providing the sample can be rotated sufficiently rapidly, as illustrated on Figure 2.5. If it is not the case, spinning side bands are observed.[110, 111] Nowadays routinely implemented for commercial spectrometers, MAS is generally able to remove completely the CSA contribution for most cases,[17] and significantly reduces interactions of higher characteristic frequencies such as heteronuclear dipolar coupling.

Practically, the sample is packed onto a rotor with small fins (Figure 2.4a). This is suspended and rotated using a compressed air system. Several rotor sizes are available, thus resulting in a range of possible spinning frequencies (see Table C.1 in Appendix C.1). Probes suited to every rotor size are available, and the exact angle of rotation relative to the magnetic field may be adjusted. The smaller the rotor diameter, the greatest line narrowing effect, at the expense, however, of the sensitivity owing to the reduced sample volume. Furthermore, heating due to friction at very fast rotation rates may affect the integrity of fragile samples such as proteins, and so a compromise between spin rate, narrowing of the signal (*i.e.*, resolution) and signal (*i.e.*, sensitivity) is required.

2.3 Quadrupolar interaction

Despite the much greater number of NMR studies conducted on spin $I = 1/2$ nuclei, 75 % of the elements in the periodic table have spin quantum numbers $I > 1/2$. Some

[15] The subscript PR meaning *PAF to Rotor frame*, with $\beta_{\mathrm{PR}} = -\beta_{\mathrm{RP}}$.

[16] A third Euler angle would be redundant to describe a sample spinning around one axis, that can be described either using α_{LR} or γ_{LR}.

[17] This excludes several heavy nuclei which usually experience strong CSA owing to relativistic effects, such as $^{113/115}$Cd, ^{119}Sn, or ^{207}Pb.[106, 112]

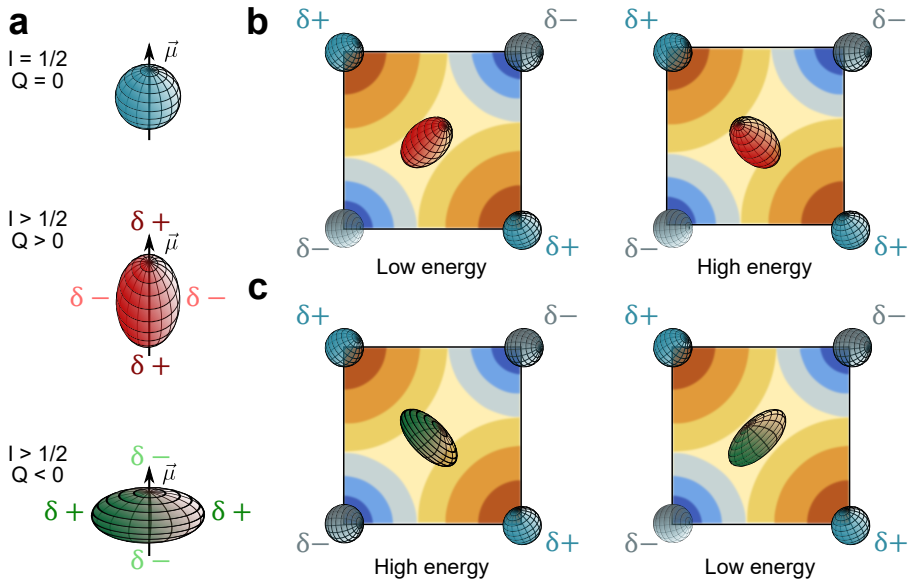

Figure 2.6: ***(a)****: Schematic representation of the quadrupolar moment of a spin $I = 1/2$ nucleus and two spins $I > 1/2$ nuclei for which $Q > 0$ and $Q < 0$, relative to their magnetic moment vectors $\vec{\mu}$.* ***(b,c)****: Schematic of the high and low orientations for a quadrupolar nucleus in a unit cell for* ***(b)****: $Q > 0$ and* ***(c)****: $Q < 0$*

of these (^{23}Na, ^{27}Al, ^{17}O, ^{39}K, ^{25}Mg, ...) are key components of many materials of scientific interest. This paucity stems from the additional energy levels compared to spin $I = 1/2$. In solution, and with the absence of other interactions, all observable NMR transitions are of the same energy (see Figure 1.5b) and, therefore, their signals in an NMR spectrum overlap.

In the solid state, while the internal interaction discussed in the previous section (CSA, dipolar coupling, J-coupling, ...) will also affect the NMR spectra for nuclei with spins $I > 1/2$, the main reason for the deficit of popularity of these nuclei is the so-called "quadrupolar interaction". This interaction, specific to spins with $I > 1/2$, creates a new source of broadening that often dominates that from other internal interactions. In Section 1.1.1, a nucleus has been described as an uniformly charged sphere, but this model does not hold for quadrupolar nuclei. Any random charge distribution can be developed as a sum of electrostatic multipoles.[49] Taking the origin at the barycentre of the electrical charges, the classical interaction energy between a nuclear multipole and any given electric potential ϕ is given by

$$E_M = q\phi(\vec{r}=\vec{0}) \qquad \text{Monopole term} \qquad (2.3.1a)$$

$$- \sum_{k=x,y,z} p_k . \frac{\partial \phi}{\partial k}(\vec{r}=\vec{0}) \qquad \text{Dipole term} \qquad (2.3.1b)$$

$$- \frac{eQ}{6} \sum_{k=x,y,z} \sum_{l=x,y,z} \frac{\partial^2 \phi}{\partial k \partial l}(\vec{r}=\vec{0}) \qquad \text{Quadrupole term} \qquad (2.3.1c)$$

$$+ \ \ldots \ ,$$

where e is the elementary charge, q is the total charge of the charge distribution, p_k is the electric dipolar moment along the k direction and Q is its electric quadrupolar moment[18] of the nucleus. Nuclei are fixed during NMR experiments so the monopole term in Equation (2.3.1a) is constant, and the dipolar term does not exist for atomic nuclei as the charge distribution can be visualised as an ellipsoid.[100] Hence, what remains is the quadrupolar term. The quadrupolar momentum Q can be interpreted as a parameter describing the shape of the ellipsoid of nuclear charge distribution with, by convention, $Q > 0$ if the ellipsoid is prolate and $Q < 0$ if it is oblate, as illustrated in Figure 2.6a.

The quadrupolar interaction (Equation (2.3.1c)) originates from the interaction between the EFG[19] generated by charged atoms in the surrounding of the nucleus of interest, and the nuclei quadrupolar momentum that all spin $I > 1/2$ possesses.[113] The EFG is represented by a second-rank tensor $\overleftrightarrow{V}$, whose element are from

$$V_{kl} = \frac{\partial^2 \phi}{\partial r_k \partial r_l}(\vec{r}=\vec{0}) \quad . \qquad (2.3.2)$$

The effect of the quadrupolar interaction can be described in a simplistic manner as in Figures 2.6b and 2.6c. The nucleus is stabilised when the plus and minus charges of the quadrupole are respectively near the minus and plus charges of the EFG, and destabilised if it is not. The orientation of the nuclei are inverted between the cases $Q > 0$ (Figure 2.6a) and $Q < 0$ (Figure 2.6b). The existence of this interaction in NMR was originally reported by Pound.[114] It is anisotropic as it depends on the orientation of the the electric field gradient in the PAF. This section introduces some theoretical elements explaining the specificities of the quadrupolar interaction.

[18] here given in m^2.
[19] EFG: *Electric Field Gradient*

2.3.1 General considerations

As for the other interactions, the quadrupolar interaction Hamiltonian $\hat{H}_Q$, which is an interaction between the quadrupolar moment Q of the nucleus and the EFG, can be written in Σ_{lab} using the form given in Equation (2.1.2) [34, 40, 115–117]

$$\hat{H}_Q = \frac{eQ}{2I(2I-1)\hbar^2} \hat{I}.\overleftrightarrow{V}.\hat{I} \quad . \tag{2.3.3}$$

This Hamiltonian can be rewritten as a function of the Cartesian components of the spin observables $\hat{I}$ and of the EFG tensor $\overleftrightarrow{V}$, such that [38, 117]

$$\hat{H}_Q = \frac{eQ}{6I(2I-1)\hbar^2} \sum_{\substack{k=x,y,z \\ l=x,y,z}} \left(\frac{3}{2} V_{kl} (\hat{I}_k \hat{I}_l + \hat{I}_l \hat{I}_k) - \delta_{kl} \hat{I}^2 \right) \quad , \tag{2.3.4}$$

where V_{kl} are the elements of $\overleftrightarrow{V}$ from Equation (2.3.2) (expressed, for example, in [100]), and δ_{kl} is Kronecker's delta,[20] defined

$$\delta_{kl} = \begin{cases} 1 & \text{if } k = l \quad , \\ 0 & \text{if } l \neq l \quad . \end{cases} \tag{2.3.5}$$

In the PAF of the quadrupolar interaction, $\overleftrightarrow{V}$ is diagonal, and the three diagonal V_{zz}, V_{yy} and V_{xx} are sorted using the convention

$$|V_{zz}| \geq |V_{yy}| \geq |V_{xx}| \quad . \tag{2.3.6}$$

The principal field gradient can be defined as

$$q = \frac{V_{zz}}{e} \quad , \tag{2.3.7}$$

and the asymmetry parameter is given by

$$\eta_Q = \frac{V_{xx} - V_{yy}}{V_{zz}} \quad . \tag{2.3.8}$$

In addition, the quadrupolar coupling constant can be defined as (given in Hz)

$$C_Q = \frac{e^2 q Q}{h} \quad . \tag{2.3.9}$$

Laplace's theorem [49, 115] states that $\overleftrightarrow{V}$ is traceless, *i.e.*,

$$V_{xx} + V_{yy} + V_{zz} = 0 \quad , \tag{2.3.10}$$

[20] Not to be confused with Dirac's delta in Appendix G.2, Equation (G.2.3)

therefore just the two parameters C_Q and η_Q are sufficient to entirely describe the interaction. In the PAF, the quadrupolar interaction Hamiltonian (Equation (2.3.4)) is written as [38]

$$\hat{H}_Q^{\text{PAF}} = \frac{e^2qQ}{4I(2I-1)\hbar^2}\left[3\hat{I}_z^2 - \hat{I}^2 + \frac{\eta_Q}{2}(\hat{I}_x^2 - \hat{I}_y^2)\right] \quad , \tag{2.3.11}$$

from which we can define the quadrupolar frequency[21,22]

$$\omega_Q = \frac{3e^2qQ}{4I(2I-1)\hbar} \tag{2.3.12a}$$

$$= \frac{3\pi C_Q}{2I(2I-1)} \quad , \tag{2.3.12b}$$

which is spin dependent. In Σ_{lab}, $\hat{H}_Q$ is conveniently expressed as a sum of irreducible spherical tensor operators as described in Equation (2.1.10), giving [34]

$$\hat{H}_Q^{\text{PAF}} = \frac{1}{\hbar}\sum_{m=-2}^{m=2}(-1)^q\hat{T}_{2,m}\Lambda_{2,-m}^{\text{PAF}} \quad , \tag{2.3.13}$$

where $\hat{T}_{2,m}$ are the spherical tensors of rank 2 and order m given by

$$\hat{T}_{2,0} = \frac{1}{\sqrt{6}}\left(3I_z^2 - \hat{I}^2\right) \tag{2.3.14a}$$

$$\hat{T}_{2,\pm1} = \mp\left(\hat{I}_\pm\hat{I}_z + \hat{I}_z\hat{I}_\pm\right) \tag{2.3.14b}$$

$$\hat{T}_{2,\pm2} = \frac{1}{2}\left(\hat{I}_\pm\right)^2 \quad , \tag{2.3.14c}$$

and $\Lambda_{2,m}^{\text{PAF}}$ are the tensors of rank 2 and order m for the quadrupolar coupling expressed in the PAF, written as

$$\Lambda_{2,0}^{\text{PAF}} = \frac{\sqrt{6}}{3}\omega_Q \tag{2.3.15a}$$

$$\Lambda_{2,\pm1}^{\text{PAF}} = 0 \tag{2.3.15b}$$

$$\Lambda_{2,\pm2}^{\text{PAF}} = \frac{\eta_Q\omega_Q}{3} \quad . \tag{2.3.15c}$$

$\hat{H}_Q^{\text{PAF}}$ is then rotated to Σ_{lab} using the rotation operators defined in Appendix B.2 for the three Euler angles $(\alpha_{\text{LP}}, \beta_{\text{LP}}, \gamma_{\text{LP}})$ defining the orientation of the PAF in Σ_{lab} according to

[21] Or $\nu_Q = 3e^2qQ/4I(2I-1)h = 3C_Q/4I(2I-1)$ when expressed in Hz.

[22] ω_Q is in the literature often defined as twice the value given in Equation (2.3.12), *i.e.*, $3e^2qQ/2I(2I-1)\hbar$.

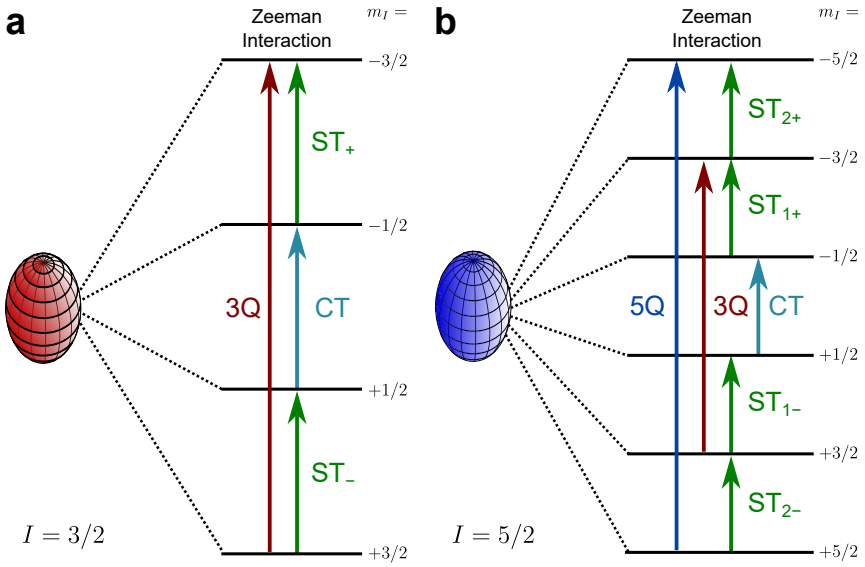

Figure 2.7: *Schematic diagram of the energy levels for **(a)**: a spin $I = 3/2$ and **(b)**: a spin $I = 5/2$ nucleus subject to the Zeeman interaction, with different transitions labelled.*

$$\hat{H}_Q = \hat{R}^{-1}(\alpha_{\text{PL}}, \beta_{\text{PL}}, \gamma_{\text{PL}}).\hat{H}_Q^{\text{PAF}}.\hat{R}(\alpha_{\text{PL}}, \beta_{\text{PL}}, \gamma_{\text{PL}}) \tag{2.3.16a}$$

$$= \frac{1}{\hbar}\sum_{m=-2}^{m=+2}(-1)^m \hat{T}_{2,m}\Lambda_{2,-m} \quad , \tag{2.3.16b}$$

where $\Lambda_{2,m}$ are the quadrupolar coupling tensors expressed in Σ_{lab}, given by

$$\Lambda_{2,m} = \sum_{m'=-2}^{m'=+2} D^{(2)}_{m',m}\left(\alpha_{\text{PL}}, \beta_{\text{PL}}, \gamma_{\text{PL}}\right) \Lambda^{\text{PAF}}_{2,m'} \quad . \tag{2.3.17}$$

2.3.2 Simplifying the quadrupolar Hamiltonian

To simplify the quadrupolar Hamiltonian in Equation (2.3.13), it is possible to apply the secular approximation described in Section 2.1.2, *i.e.*, to suppress all terms that do not commute with the Zeeman Hamiltonian, as these corresponds to the most important effects. The quadrupolar Hamiltonian expressed in irreducible spherical tensors form can be separated into a secular part and a non-secular part (see Section 2.1.2).

First, the quadrupolar interaction affects only nuclei with spin $I > 1/2$, for which additional energy levels are present. The Zeeman energy levels are expressed as (see Equation (1.2.49))

$$E_z(I, m_I) = \langle I, m_I | \hat{H}_z | I, m_I \rangle = \hbar\omega_0 m_I \quad . \tag{2.3.18}$$

The different transitions of interest are shown in Figure 2.7. Special attention is given to the symmetrical CT[23] and 3Q transitions. STs[24] and higher-order symmetrical MQ[25] transitions (*e.g.*, 5Q[26] transition in Figure 2.7b) are also present.

First-order approximation

The first-order truncated Hamiltonian is obtained from Equation (2.3.13), keeping only the secular $q = 0$ terms, giving [118]

$$\hat{H}_Q^{\mathrm{PAF}(1)}/\hbar = \hat{T}_{2,0}\Lambda_{2,0} \quad . \tag{2.3.19}$$

Upon transformation to Σ_{rot} (see Equation (2.3.16)), after expansion and rearrangement,

$$\hat{H}_Q^{(1)} = \frac{1}{\hbar}\left(\hat{I}_z^2 - \frac{\hat{I}^2}{3}\right)\Omega_Q(\alpha_{\mathrm{PL}}, \beta_{\mathrm{PL}}, \eta_Q) \quad , \tag{2.3.20}$$

where Ω_Q is the orientation-dependant quadrupolar frequency, defined as

$$\Omega_Q(\alpha_{\mathrm{PL}}, \beta_{\mathrm{PL}}, \eta_Q) = \frac{1}{2}\omega_Q\left(3\cos^2\beta_{\mathrm{PL}} - 1 + \eta_Q \sin^2\beta_{\mathrm{PL}}\cos 2\alpha_{\mathrm{PL}}\right) \quad . \tag{2.3.21}$$

Clearly, $\hat{H}_Q^{(1)}$ in Equation (2.3.20) commutes with the Zeeman Hamiltonian and hence, is secular. The first-order correction $E_Q^{(1)}$ to the Zeeman energy for the energy level associated with the magnetic quantum number m_I is given by

$$E_Q^{(1)} = \hbar\left(m_I^2 - \frac{I(I+1)}{3}\right)\Omega_Q(\alpha_{\mathrm{LP}}, \beta_{\mathrm{LP}}, \eta_Q) \quad . \tag{2.3.22}$$

The frequency of the transition between energy levels m_{I1} and m_{I2}, where $m_{I2} > m_{I1}$, is given by

$$\omega_Q^{(1)}(m_{I1} \rightarrow m_{I2}) = \left(m_{I2}^2 - m_{I1}^2\right)\Omega_Q \quad . \tag{2.3.23}$$

The effect on the energy levels of a spin $I = 3/2$ nucleus is shown in Figure 2.8, on the left of the cyan dashed line. This shows that $E_Q^{(1)}$ is zero for symmetrical transitions (*e.g.*, between m_{I1} and m_{I2} energy levels where $m_{I1} = -m_{I2}$), as confirmed by Equation (2.3.23). That is, the CT and 3Q transitions for a spin $I = 3/2$ remain unaffected, whereas all STs are subject to a perturbation.

[23] CT: *Central-Transition*
[24] STs: *Satellite-Transitions*
[25] MQ: *Multiple-Quantum* (transition)
[26] 5Q: *Quintuple-Quantum* (transition)

Second-order approximation

Table 2.1 illustrates that quadrupolar interactions can sometimes be of the same order of magnitude as the Zeeman interaction. It has been established that a first-order perturbation is often not sufficiently accurate to describe the effect on the energy levels if the quadrupolar interaction is large. Therefore, a second-order correction term must be added.[33, 119, 120]

The secular part of the Hamiltonian for elements $m \neq 0$ of Equation (2.3.13) can be obtain using the Magnus expansion,[34, 121–125] perturbation theory,[33, 38, 103, 126–128] or secular averaging.[129–132] All of the approaches result in equivalent expressions for the quadrupolar Hamiltonian and of the energy correction after applying the secular approximation.[100, 128, 129, 133] Written in terms of the spherical and quadrupolar coupling tensors, $\hat{T}_{2,m}$ and $\Lambda_{2,m}$, respectively given in Equations (2.3.14) and (2.3.17), the second-order quadrupolar interaction becomes [34]

$$\bar{H}_Q^{(1)} = \hat{H}_Q^{(2)} = -\frac{i\pi}{2\hbar\omega_0} \sum_{m=-2}^{m=+2} \Lambda_{2,-m}\Lambda_{2,m} \left[\hat{T}_{2,m}, \hat{T}_{2,-m}\right] \quad . \tag{2.3.24}$$

In terms of the spin observables $\hat{I}$, the second-order quadrupolar Hamiltonian can be expressed as[27]

$$\begin{aligned} \hbar \times \hat{H}_Q^{(2)} = \frac{3}{24}\frac{\omega_Q^2}{\omega_0}\hat{I}_z \Bigg[& \left(\frac{\hat{I}_z^2}{\hbar^2} - (4I(I+1)+1)\,\hat{1}_N \right) \sin^2 2\beta_{\mathrm{PL}} \\ & - \left(2\frac{\hat{I}_z^2}{\hbar^2} + (1-2I(I+1))\,\hat{1}_N \right) \sin^4 \beta_{\mathrm{PL}} \Bigg] \quad , \end{aligned} \tag{2.3.25}$$

where $\hat{1}_N$ is the order $N = 2I+1$ identity matrix. The following correction energies have been obtained from perturbation theory, quoted with respect to the convention used by Brown and Wimperis.[134] The expression of the second-order correction $E_Q^{(2)}$ can be divided into a spin part and a spatial part following [134, 135]

$$E_Q^{(2)} = \frac{\hbar}{2}.\frac{\omega_Q^2}{\omega_0} \qquad \text{Pre-factor} \tag{2.3.26a}$$

$$\times \Big[A^{(0)}(I, m_I).Q^{(0)}(\eta_Q) \qquad \text{Isotropic term} \tag{2.3.26b}$$

$$+A^{(2)}(I, m_I).Q^{(2)}(\eta_Q, \alpha_{\mathrm{PL}}, \beta_{\mathrm{PL}}, \gamma_{\mathrm{PL}}) \qquad \text{Second-rank term} \tag{2.3.26c}$$

$$+A^{(4)}(I, m_I).Q^{(4)}(\eta_Q, \alpha_{\mathrm{PL}}, \beta_{\mathrm{PL}}, \gamma_{\mathrm{PL}}) \Big] \quad , \qquad \text{Fourth-rank term} \tag{2.3.26d}$$

[27] Here given for η_Q = 0 for simplicity.

with the three spatial functions $Q^{(0)}$, $Q^{(2)}$ and $Q^{(4)}$ being

$$Q^{(0)}(\eta_Q) = \left(1 + \frac{\eta_Q^2}{3}\right) \tag{2.3.27a}$$

$$Q^{(2)}(\alpha_{\mathrm{PL}}, \beta_{\mathrm{PL}}, \gamma_{\mathrm{PL}}, \eta_Q) = \left(1 - \frac{\eta_Q^2}{3}\right) D^{(2)}_{0,0}(\alpha_{\mathrm{PL}}, \beta_{\mathrm{PL}}, \gamma_{\mathrm{PL}}) - \sqrt{\frac{2}{3}}\eta_Q \left(D^{(2)}_{0,2}(\alpha_{\mathrm{PL}}, \beta_{\mathrm{PL}}, \gamma_{\mathrm{PL}}) + D^{(2)}_{0,-2}(\alpha_{\mathrm{PL}}, \beta_{\mathrm{PL}}, \gamma_{\mathrm{PL}})\right) \tag{2.3.27b}$$

$$Q^{(4)}(\alpha_{\mathrm{PL}}, \beta_{\mathrm{PL}}, \gamma_{\mathrm{PL}}, \eta_Q) = \left(1 + \frac{\eta_Q^2}{18}\right) D^{(4)}_{0,0} + \frac{\sqrt{10}}{6}\eta_Q \left(D^{(4)}_{0,2}(\alpha_{\mathrm{PL}}, \beta_{\mathrm{PL}}, \gamma_{\mathrm{PL}}) + D^{(4)}_{0,-2}(\alpha_{\mathrm{PL}}, \beta_{\mathrm{PL}}, \gamma_{\mathrm{PL}})\right) + \frac{35}{18\sqrt{70}}\eta_Q^2 \left(D^{(4)}_{0,4}(\alpha_{\mathrm{PL}}, \beta_{\mathrm{PL}}, \gamma_{\mathrm{PL}}) + D^{(4)}_{0,-4}(\alpha_{\mathrm{PL}}, \beta_{\mathrm{PL}}, \gamma_{\mathrm{PL}})\right) \quad , \tag{2.3.27c}$$

with the Wigner rotation elements given in Equation (2.1.12) and Appendix (B.4). The three spin tensors $A^{(0)}$, $A^{(2)}$ and $A^{(4)}$ are given by [12, 135]

$$A^{(0)}(I, m_I) = -\frac{4}{15} m_I \left(I(I+1) - 3m_I^2\right) \tag{2.3.28a}$$

$$A^{(2)}(I, m_I) = -\frac{2}{21} m_I \left(8I(I+1) - 12m_I^2 - 3\right) \tag{2.3.28b}$$

$$A^{(4)}(I, m_I) = +\frac{2}{35} m_I \left(18I(I+1) - 34m_I^2 - 5\right) \quad . \tag{2.3.28c}$$

It is obvious from Equation (2.3.28) that $A(I, -m_I) = -A(I, m_I)$, meaning that symmetrical transitions such as the CT, 3Q *etc*, on which the first-order quadrupolar interaction had no effect, are now affected by the second-order quadrupolar interaction.

Higher-orders perturbations

The effects of a third-order quadrupolar interaction have been observed for a small number compounds, including ^{27}Al NMR of andalusite (Gan *et al.*,[136] Section 6.1.1 and Appendix C.2). The third-order quadrupolar interaction is of the same nature as the first-order, as it only effects only affects STs,[137] and its effects on conventional spectra are weak.[103]. In the vast majority of cases, third- or higher-order quadrupolar effects are negligible and can simply be ignored.[33, 120, 137]

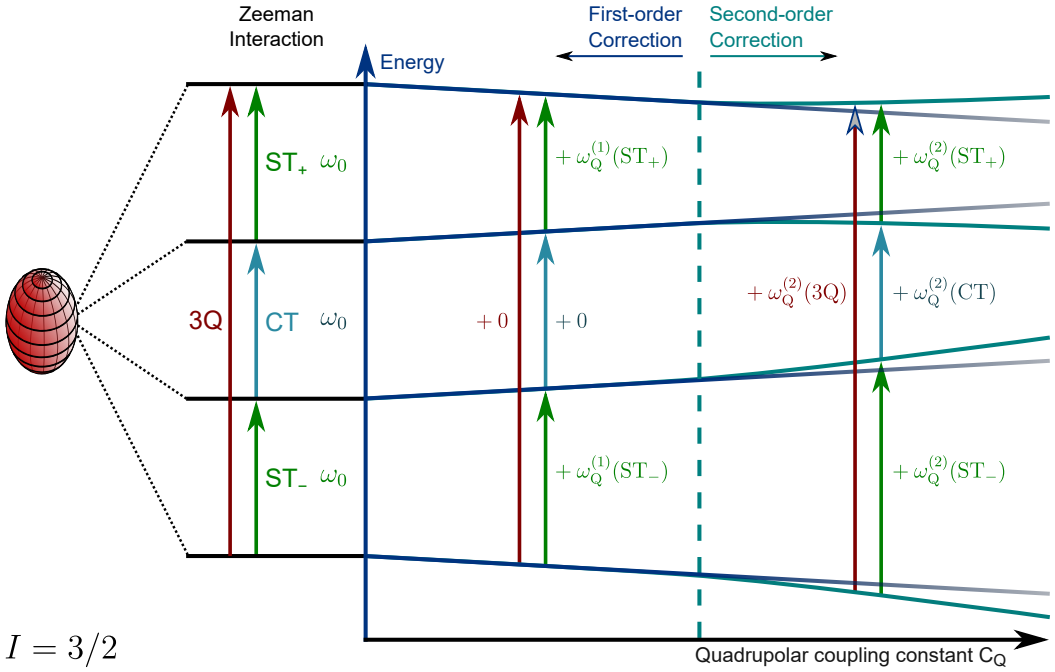

Figure 2.8: *Schematic illustration of the perturbation of the energy levels of a spin $I = 3/2$ nucleus subject to the quadrupolar interaction increasing in intensity from left to right. The dashed cyan line marks the point where second-order quadrupolar interaction become significant compared to a first-order approximation.*

The effect of fast MAS

For the first-order truncated quadrupolar interaction under MAS, the Hamiltonian will be of the same form as in Equation (2.3.20) with Ω_Q now acquiring a time dependence, expressed as[28]

$$\Omega_Q(t) = \frac{\omega_Q}{2}\left(\sin^2(\beta_{\mathrm{PR}})\cos(2\omega_R t + 2\gamma_{\mathrm{PR}}) - \sqrt{2}\sin(2\beta_{\mathrm{PR}})\cos(\omega_R t + \gamma_{\mathrm{PR}})\right) \quad . \tag{2.3.29}$$

As for the other interactions discussed previously, this will be reflected in the MAS spectrum by the signal resulting from the ST exhibiting the form of a spinning sideband manifold (see Figure 2.5), while the CT signal, not affected by $\hat{H}_Q^{(1)}$, remains unchanged.

When fast MAS is employed, the second-order quadrupolar interaction energy correction in Equation (2.3.26) can be obtained using the transformation given in Section 2.2.3, Equation (2.2.23). This results in

[28] Here given for $\eta_Q = 0$.

$$E_Q^{(2)} = \frac{\hbar}{2}.\frac{(\omega_Q)^2}{\omega_0}\Big(A^{(0)}(I,m_I).Q^{(0)}(\eta_Q) + A^{(2)}(I,m_I).d^{(2)}_{0,0}(\beta_{\mathrm{LR}})Q^{(2)}(\beta_{\mathrm{PR}},\gamma_{\mathrm{PR}},\eta_Q) + A^{(4)}(I,m_I).d^{(4)}_{0,0}(\beta_{\mathrm{LR}})Q^{(4)}(\beta_{\mathrm{PR}},\gamma_{\mathrm{PR}},\eta_Q)\Big) \quad , \tag{2.3.30}$$

where the terms $A^{(0)}$, $A^{(2)}$ and $A^{(4)}$ are identical to those in the static case (Equation (2.3.28)), $d^{(2)}_{0,0}$ and $d^{(4)}_{0,0}$ have been defined in Section 2.1.1, Equations (2.1.13) and (2.1.14), and $Q^{(0)}$, $Q^{(2)}$ and $Q^{(4)}$ in Equation (2.3.27) becomes

$$Q^{(0)}(\eta_Q) = \left(1+\frac{\eta_Q^2}{3}\right) \tag{2.3.31a}$$

$$Q^{(2)}(\alpha_{\mathrm{LP}},\beta_{\mathrm{LP}},\gamma_{\mathrm{LP}},\eta_Q) = \left(1-\frac{\eta_Q^2}{3}\right).d^{(2)}_{0,0}(\beta_{\mathrm{PR}}) - \sqrt{\frac{8}{3}}\eta_Q.d^{(2)}_{2,0}(\beta_{\mathrm{PR}}).\cos 2\gamma_{\mathrm{PR}} \tag{2.3.31b}$$

$$Q^{(4)}(\alpha_{\mathrm{LP}},\beta_{\mathrm{LP}},\gamma_{\mathrm{LP}},\eta_Q) = \left(1+\frac{\eta_Q^2}{18}\right).d^{(4)}_{0,0} + \frac{\sqrt{10}}{3}\eta_Q.d^{(4)}_{2,0}(\beta_{\mathrm{PR}}).\cos 2\gamma_{\mathrm{PR}} + \frac{35}{9\sqrt{70}}\eta_Q^2.d^{(4)}_{4,0}(\beta_{\mathrm{PR}}).\cos 4\gamma_{\mathrm{PR}} \quad , \tag{2.3.31c}$$

As introduced in Section (2.1.2), setting β_{PR} to the magic angle $\beta_m^{(2)}$ causes $d^{(2)}_{0,0}$, and thus all the second-rank D-matrices, to vanish in the fast MAS limit (*e.g.* if ν_R is large compared to $\nu_Q^{(2)} = E^{(2)}/h$), resulting in $E^{(2)}$ simplifying to

$$E_Q^{(2)} = \frac{\hbar}{2}\frac{(\omega_Q)^2}{\omega_0}\big(A^{(0)}(I,m_I).Q^{(0)}(\eta_Q) + A^{(4)}(I,m_I).d^{(4)}_{0,0}(\beta_m)Q^{(4)}(\beta_{\mathrm{PR}},\gamma_{\mathrm{PR}},\eta_Q)\big) \quad . \tag{2.3.32}$$

As shown in Equation (2.3.32), the fourth-rank term contains $d^{(4)}_{0,0}$ matrix elements and thus vanishes only for either $\beta^{(4)}_{m1}$ or $\beta^{(4)}_{m2}$ as given in Equations (2.1.16a) and (2.1.16b), but not at the magic angle $\beta_m^{(2)}$. As $E_Q^{(2)}$ in Equation (2.3.32) is orientation dependent, it causes some line broadening that cannot be removed by MAS alone.

2.3.3 The effects of quadrupolar coupling on spectral lineshapes

As with the other interactions described previously, the quadrupolar interaction can be used to obtain structural information about the environment of the nucleus.[138] The description of the lineshape arising from the quadrupolar interaction as a function of

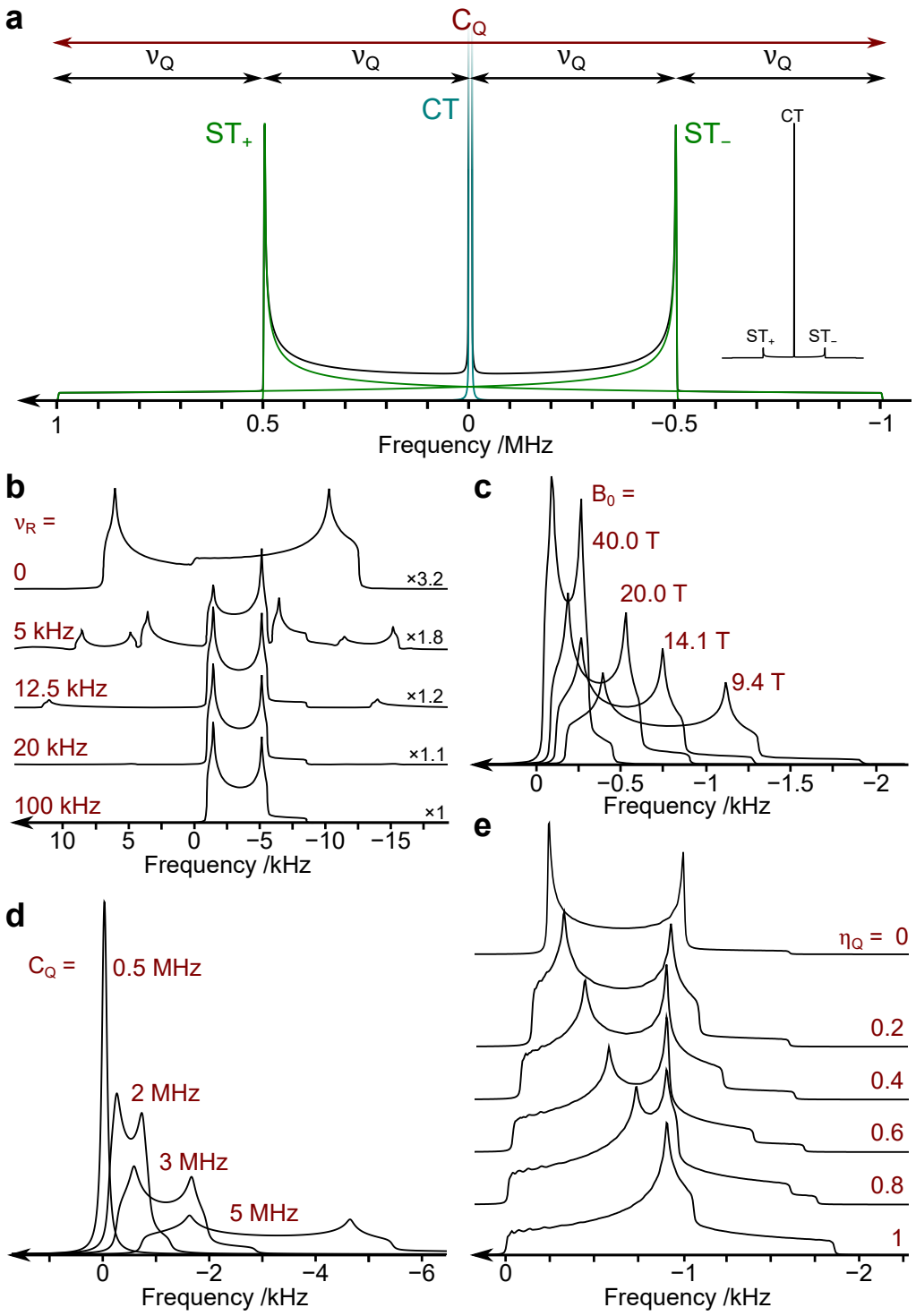

Figure 2.9: ***(a)****: Simulated static powder spectrum of a spin $I = 3/2$ nucleus with C_Q = 2 MHz and η_Q = 0, showing the contributions of the CT (blue lineshape) and STs (green line) to the lineshape, and how C_Q and ν_Q relate to it.* ***(b,c,d,e)****: CT lineshapes for* ***(b)*** *different MAS rates,* ***(c)****: different B_0 fields in the fast MAS limit,* ***(d)****: different C_Q values in the fast MAS limit, and* ***(e)*** *different η_Q values in the fast MAS limit. See the extended caption in Appendix C.3 for further details.*

the experimental parameters and of the so-called quadrupolar parameters C_Q and η_Q has been addressed in the literature.[84, 125, 139, 140]

It can be deduced from Equation (2.3.23) that, for symmetrical transition ($m_{I1} = -m_{I2}$), the first-order quadrupolar energy correction is zero. Therefore, the CT and the symmetrical 3Q, 5Q, or higher-order symmetrical transitions if available, are not affected by the first-order quadrupolar interaction. This enables lineshapes for quadrupolar nuclei with a half-integer spin quantum number to be observable even when very strong quadrupole interaction are present. Indeed, Figure 2.9a illustrates that, while the integrated intensity of a powder spectrum of STs are spread over a wide range of frequencies (green line), with the total width being given by the quadrupolar coupling constant C_Q, the CT (blue line) is much less affected, so the integrated intensity is concentrated in a sharp feature near the central frequency. Experimentally, ST intensities are often below the noise level and often not visible.[141] The shape of the ST lineshape has been described in Equation (2.3.22). It can be noted that, if $\eta_Q = 0$, the STs would exhibit a Pake doublet (see Figure 2.3).

As discussed in Section 2.3.2, MAS is only able to remove interactions described by second-rank tensors, leaving the fourth-rank component (see Equation (2.3.26d)), which have a significant effect on the CT. The expression for the second-order quadrupolar CT lineshape has been established by Narita *et al.* [139] from Equation (2.3.26). This is, reported in Hz, given by

$$\begin{aligned}\nu_{CT}^{(2)} = \frac{\pi}{12}.\frac{\nu_Q^2}{\nu_0}\left(I(I+1)-\frac{3}{4}\right).\big[A(\alpha_{\mathrm{LP}},\eta_Q).\cos^4\beta_{\mathrm{LP}} \\ +B(\alpha_{\mathrm{LP}},\eta_Q).\cos^2\beta_{\mathrm{LP}}+C(\alpha_{\mathrm{LP}},\eta_Q)\big] \quad ,\end{aligned} \tag{2.3.33}$$

where A, B and C are functions of the Euler angles such that

$$A(\alpha_{\mathrm{LP}},\eta_Q) = -\frac{27}{8}-\frac{9}{4}\eta_Q\cos 2\alpha_{\mathrm{PL}}-\frac{3}{8}\eta_Q^2\cos^2 2\alpha_{\mathrm{PL}} \tag{2.3.34a}$$

$$B(\alpha_{\mathrm{LP}},\eta_Q) = -\frac{15}{4}-\frac{1}{2}\eta_Q^2\cos 2\alpha_{\mathrm{PL}}+\frac{3}{4}\eta_Q^2\cos^2 2\alpha_{\mathrm{PL}} \tag{2.3.34b}$$

$$C(\alpha_{\mathrm{LP}},\eta_Q) = -\frac{3}{8}+\frac{1}{3}\eta_Q^2+\frac{1}{4}\eta_Q\cos 2\alpha_{\mathrm{PL}}-\frac{3}{8}\eta_Q^2\cos^2 2\alpha_{\mathrm{PL}} \quad . \tag{2.3.34c}$$

In the fast MAS limits, the three functions in Equation (2.3.34) become [140, 142]

$$A_{\mathrm{MAS}}(\alpha_{\mathrm{LP}}, \eta_Q) = -\frac{21}{16} - \frac{7}{8}\eta_Q \cos 2\alpha_{\mathrm{PR}} - \frac{7}{48}\eta_Q^2 \cos^2 2\alpha_{\mathrm{PR}} \tag{2.3.35a}$$

$$B_{\mathrm{MAS}}(\alpha_{\mathrm{LP}}, \eta_Q) = -\frac{9}{8} + \frac{1}{22}\eta_Q^2 + \eta_Q \cos 2\alpha_{\mathrm{PR}} - \frac{7}{24}\eta_Q^2 \cos^2 2\alpha_{\mathrm{PR}} \tag{2.3.35b}$$

$$C_{\mathrm{MAS}}(\alpha_{\mathrm{LP}}, \eta_Q) = +\frac{15}{16} - \frac{1}{8}\eta_Q \cos 2\alpha_{\mathrm{PR}} - \frac{7}{48}\eta_Q^2 \cos^2 2\alpha_{\mathrm{PR}} \quad . \tag{2.3.35c}$$

As stated in Section 2.3.2 and illustrated in Figure 2.9b, MAS only averages second-rank tensors (Equation (2.3.26c)) and so cannot remove completely the effect of the second-order quadrupolar interaction, resulting in a lineshape width reduced to about a third of the static lineshape,[125, 133, 143] but still broadened under MAS. The notable features of the quadrupolar lineshape in the fast MAS limit are two sharp features corresponding to crystallites where β_{LP} = 0 or 180°, and a shoulder always orientated toward high field. Static quadrupolar lineshapes also possess two or three singularities depending on the value of η_Q.[125] These effects are referred to as the SOQE[29]. Many remarkable features of the second-order quadrupolar lineshape are related to the so-called quadrupolar product, defined as

$$P_Q = C_Q\sqrt{1 + \frac{\eta_Q^2}{3}} \quad . \tag{2.3.36}$$

The pre-factor of the second-order energy correction (Equation (2.3.26a)) indicates that the width of the CT lineshape is inversely proportional to ω_0, as observed in Figure 2.9c), and proportional to ω_Q^2 as observed in Figure 2.9d). This makes it much small than first-order quadrupolar interaction on STs, proportional to ω_Q. Another noticeable effect in Figure 2.9d is that the quadrupolar lineshape shifts toward high field as C_Q gets higher due to Equation (2.3.26b). This effect is know as the QIS[30], and is given by [144]

$$\nu_{\mathrm{QIS}} = -\frac{3}{10}\frac{I(I+1) - 3/4}{(2I(2I-1))^2}.\frac{P_Q^2}{\nu_0} \quad . \tag{2.3.37}$$

Finally, the effect of different values of η_Q is also shown in Figure 2.9e. It can be observed that the sharp features on the quadrupolar lineshape merge and the different crystallite orientations spread across a wider range of frequency. The difference between the minimum and maximum frequencies of a quadrupolar lineshape in the fast MAS limit can be established from Equation (2.3.33) to be [145]

[29] SOQE: *Second-Order Quadrupolar Effects*
[30] QIS: *Quadrupolar Induced Shift*

$$\Delta\nu_Q^{(2)} = \frac{1}{56}\frac{I(I+1) - {}^3\!/_4}{(2I(2I-1))^2}.\frac{C_Q^2}{\nu_0}\left(6+\eta_Q\right)^2 \quad , \tag{2.3.38}$$

thus showing that the total linewidth of the CT is also proportional to C_Q^2. The condition $\nu_R \gg \Delta\nu_Q^{(2)}$ defines what has been previously referred to as the "fast MAS limit".

Chapter 3

NMR techniques

Introduction

All of the simulated spectra shown in Chapter 2 correspond to the idealised case, where the detection operator is simply the start operator evolving under the Zeeman interaction and any other relevant interaction. However, in practice, the necessity to move the magnetisation away from equilibrium by a 90° pulse, before the precession motion and the effect of an interaction can be observed, has been stated in Section 1.3.2. Modern NMR experiments consist of sequences of pulses separated by time intervals, described as ”pulse sequences”. A ideal ”rectangular” pulse corresponds to the RF field B_1 being truncated in time by a step function of fixed duration. This duration have been used to define the flip angle in Equation (1.3.20). Pulses producing a flip angle of 90° or 180° are those most commonly employed. Depending on the arrangement of the pulses and time intervals, a pulse sequence can produce a variety of effects and enable the retrieval, selectively or otherwise, of various pieces of information. The richness and flexibility of pulse sequences is one of the considerable strengths of NMR spectroscopy.

This chapter introduces all the experimental methods relevant to this work. Section 3.1 describes techniques used primarily for spin $I = 1/2$ nuclei but applicable also to quadrupolar nuclei. Section 3.2 introduces theoretical elements specific to quadrupolar nuclei. Finally, Sections 3.3 and 3.4 discusses the specificities of pulse sequences for quadrupolar nuclei and the more complex methods, that are able to remove the effects of the quadrupolar interaction.

This chapter uses information obtained from [33, 34, 41, 42, 56, 84, 115, 146, 147].

3.1 General techniques

This section introduces the most common NMR experiments that produces 1D[1] spectra, widely used and applicable either for nuclei with $I = 1/2$ or $I > 1/2$. Some of these sequences can also be incorporated completely within more complex experiments.

3.1.1 Basic methods

The evolution of magnetisation during a pulse sequence can be modelled by considering the evolution of the density operator $\hat{\rho}$ as a function of time.[41, 148] The density operator can be expressed as a function of the matrix representations of $\hat{I}$ (Appendix B.1), with, at thermal equilibrium and at an initial time t_0,

$$\hat{\rho}(t_0) = \hat{I}_z \quad . \tag{3.1.1}$$

From Equation (1.2.57), the Hamiltonian for the RF interaction is written in the general case in Σ_{rot} as

$$\hat{H}_{RF} = \omega_1(\hat{I}_x . \cos\theta_{RF} + \hat{I}_y . \sin\theta_{RF}) \quad , \tag{3.1.2}$$

with θ_{RF} representing the pulse phase relative to Σ_{rot}, *e.g.*, the direction along which the RF magnetic field is applied. $\theta_{RF} = 0$ corresponds to a pulse applied along the $+x$ axis of Σ_{rot} direction (*e.g.*, $+\rho$ using the convention used in Chapter 1), $\theta_{\text{RF}} = \pi/2$ corresponds to the $+y$ direction in Σ_{rot} (*e.g.*, $+\theta$ using the convention used in Chapter 1), *etc.* The time evolution of the density operator subjected to a time-independent Hamiltonian is given by (Equations (1.2.41) and (1.2.45))

$$\begin{aligned} \hat{\rho}(t) &= U(t).\hat{\rho}(0).U^{-1}(t) \\ &= \exp\left(-\frac{i}{\hbar}\hat{H}t\right).\hat{\rho}(0).\exp\left(+\frac{i}{\hbar}\hat{H}t\right) \quad . \end{aligned} \tag{3.1.3}$$

Applying a pulse for a duration τ_p gives the following

$$\hat{I}_z \xrightarrow{\hat{I}_x} \hat{I}_z \cos(\omega_1\tau_p) - \hat{I}_y \sin(\omega_1\tau_p) \tag{3.1.4a}$$

$$\hat{I}_z \xrightarrow{\hat{I}_y} \hat{I}_z \cos(\omega_1\tau_p) + \hat{I}_x \sin(\omega_1\tau_p) \quad . \tag{3.1.4b}$$

[1] 1D: *One-Dimensional*

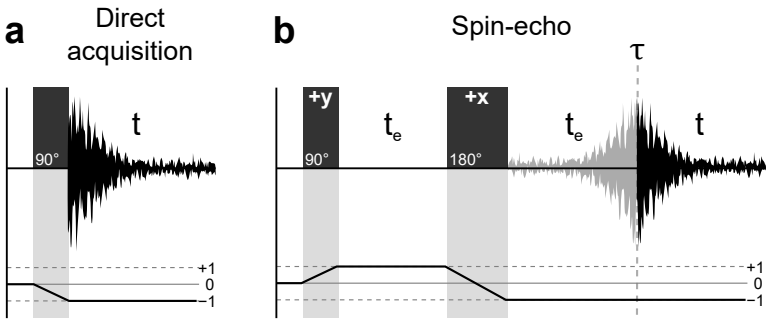

Figure 3.1: *Pulse sequences and CTP for a **(a)**: direct acquisition experiment, and **(b)**: a spin-echo experiment.*

For the particular case of 90° and 180° pulses,

$$\hat{I}_z \xrightarrow{90°_x} -\hat{I}_y \tag{3.1.5a}$$

$$\hat{I}_z \xrightarrow{90°_y} +\hat{I}_x \tag{3.1.5b}$$

$$\hat{I}_z \xrightarrow{180°} -\hat{I}_z \quad . \tag{3.1.5c}$$

Direct acquisition experiments

The simplest NMR experiment consists on a 90° pulse followed by the acquisition of the FID, usually performed under MAS in the solid state. The pulse sequence and its associated CTP[2] is shown schematically in Figure 3.1a (see Appendix D for a more detailed discussion about CTPs). The evolution operator is expressed as

$$\hat{U}(t) = \underbrace{\exp\left(-\frac{i}{\hbar}\omega_0\hat{I}_z t\right)}_{\text{acquisition}} . \underbrace{\exp\left(-\frac{i}{\hbar}.\frac{\pi}{2}\hat{I}_y\right)}_{90° \text{ pulse}} \quad , \tag{3.1.6}$$

taking the pulse applied along the $+y$ direction. Note that the evolution under the Zeeman interaction is omitted during the application of the pulse. The effect of the 90° pulse in Σ_{rot} is

$$\begin{aligned} \exp\left(-\frac{i}{\hbar}.\frac{\pi}{2}\hat{I}_y\right).\hat{\rho}(0).\exp\left(+\frac{i}{\hbar}\frac{\pi}{2}\hat{I}_y\right) &= \exp\left(-\frac{i}{\hbar}\frac{\pi}{2}\hat{I}_y\right).\hat{I}_z.\exp\left(+\frac{i}{\hbar}\frac{\pi}{2}\hat{I}_y\right) \\ &= \hat{I}_x \quad . \end{aligned} \tag{3.1.7}$$

Expressing $\hat{\rho}$ during the acquisition, we can see that

[2] CTP: *Coherence Transfer Pathway*

$$\hat{\rho}(t) = \hat{I}_x . \cos(\omega_0 t) + \hat{I}_y . \sin(\omega_0 t) \quad . \tag{3.1.8}$$

As stated in Section 1.3.2, the coherence order detected is by convention $p = -1$, therefore the (complex) transverse bulk magnetisation acquired in the experiment can be expressed as

$$\left\langle \hat{M}_T \right\rangle (t) = \frac{1}{V} \sum_N \langle \hat{\mu_T} \rangle \qquad \textit{cf.} \text{ Equation (1.3.1)} \tag{3.1.9a}$$

$$= \frac{\gamma}{V} \sum_N \langle \hat{I}_+ \rangle \qquad \textit{cf.} \text{ Equation (1.2.3)} \tag{3.1.9b}$$

$$= \frac{\gamma}{V} \sum_N Tr[\hat{I}_+ \hat{\rho}(t)] \qquad \textit{cf.} \text{ Equation (1.2.33)} \tag{3.1.9c}$$

$$\propto \exp(i\omega_0 t) \quad . \tag{3.1.9d}$$

As previously established in Equation (1.3.15), the signal acquired oscillates at ω_0. In the general case, the signal can be expressed simply as

$$S(t) = S_0 . \exp(i\Delta\omega_0 t + i\phi_0) \quad , \tag{3.1.10}$$

where $\Delta\omega_0$ is the offset defined in Equation (1.1.21), and ϕ_0 is an arbitrary phase.

Spin-echo experiments

The spin-echo (or Hahn-echo) experiment consists of a 90° pulse separated by a time interval t_e from a 90° pulse.[149] This causes the signal to reappear after a time t_e after the application of the 180° pulse, at a time denoted τ in Figure 3.1b (see Appendix G.2). In general, only half of the echo is recorded. This experiment serves several purposes, including

- A precise measurement of the T_2 relaxation time,[3] as the intensity of the echo at τ is mainly unaffected by neither B_0 nor B_1 inhomogeneities.[150]
- Recovery of the part of the signal that would be directly after the 90° pulse in a direct acquisition experiment. Practically, a fixed time (called dead-time) is required for the electric current in the probe coil to relax after the application of a pulse, leaving the probe not able to to acquire accurate data.
- Refocussing of the Zeeman interaction, chemical shift and other interactions.

[3] The relaxation observed in the FID of a direct acquisition experiment is often affected by small relaxation mechanisms such as field inhomogeneities, therefore is faster than the spin-spin relaxation, and is denoted $T_2^\star$.

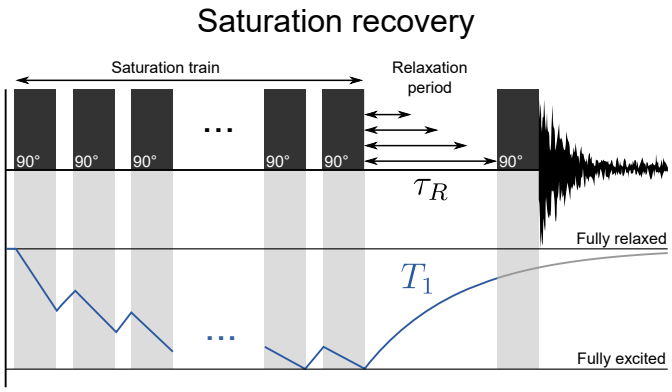

Figure 3.2: *Pulse sequence for a saturation recovery experiment and schematic evolution of the magnetisation along the z direction at several points of the experiment.*

In this experiment, we assume that the system evolves only under the Zeeman interaction during the two echo time intervals in Figure 3.1b. The evolution operator expressed at time τ is given by

$$\hat{U}(\tau) = \underbrace{\exp\left(-\frac{i}{\hbar}\omega_0 \hat{I}_z t_e\right)}_{\text{Second echo period}} . \underbrace{\exp\left(-\frac{i}{\hbar}\pi \hat{I}_x\right)}_{180° \text{ pulse}} . \underbrace{\exp\left(-\frac{i}{\hbar}\omega_0 \hat{I}_z t_e\right)}_{\text{First echo period}} . \underbrace{\exp\left(-\frac{i}{\hbar}\frac{\pi}{2}\hat{I}_y\right)}_{90° \text{ pulse}} \quad . \tag{3.1.11}$$

If we replace one of the period $\exp(-i\omega_0 I_z t_e)$ terms in Equation (3.1.11) by

$$\exp(-i\omega_0 I_z t_e) = \exp(-i\pi I_x)\exp(+i\omega_0 I_z t_e)\exp(+i\pi I_x) \quad , \tag{3.1.12}$$

we obtain

$$\begin{aligned}\hat{U}(\tau) = &\exp\left(-\frac{i}{\hbar}\pi \hat{I}_x\right) \\ &\times \underbrace{\exp\left(+\frac{i}{\hbar}\omega_0 \hat{I}_z t_e\right) . \overbrace{\exp\left(+\frac{i}{\hbar}\pi \hat{I}_x\right) . \exp\left(-\frac{i}{\hbar}\pi \hat{I}_x\right)}^{=1} . \exp\left(-\frac{i}{\hbar}\omega_0 \hat{I}_z t_e\right)}_{=1} \qquad (3.1.13a) \\ &\times \exp\left(-\frac{i}{\hbar}\frac{\pi}{2}\hat{I}_y\right)\end{aligned}$$

$$= \exp\left(-\frac{i}{\hbar}\pi \hat{I}_x\right) . \exp\left(-\frac{i}{\hbar}\frac{\pi}{2}\hat{I}_y\right) \quad . \tag{3.1.13b}$$

Equation (3.1.13b) shows that, at τ, the magnetisation is the same as if no evolution had occurred during $2t_e$. The magnetisation evolves normally during the first echo period,

then evolution is ”reversed” during the second echo period. The spin-echo method can also refocus interactions that commute with $\hat{H}_z$, such as the first-order truncated J-coupling, CSA, and quadrupolar interactions (Equations (2.2.1), (2.2.6) and (2.3.20), respectively).

Saturation-recovery experiments

Along with the inversion-recovery method (not described here), saturation-recovery experiments in Figure 3.2) are one of the classic methods for measuring T_1 relaxation times.[151] The experiment consists of an initial saturation train, ensuring that the bulk magnetisation along the $+z$ axis is constant. After a relaxation time t_R, the magnetisation is moved to the transverse plane to be recorded. As the intensity of the observed signal is directly proportional to $1 - \exp(-t/T_1)$, performing several acquisitions for several time periods enables the determination of T_1 by a least-squares fitting of the peak intensity (or integrated intensity) as a function of the relaxation period.

3.1.2 The CPMG experiment

The CPMG[4] experiment is a very common technique in NMR spectroscopy for obtaining consequent signal improvement at the expense of spectral resolution; or, to quote Dey *et al.*,[152] to ”Trade sensitivity for information”

The acronym CPMG comes from the contraction of the names of Carr and Purcell,[4] whose early experiment was designed to measure diffusion in the liquid state, and Meiboom and Gill,[5] who modified this experiment for T_2 measurements. The CPMG experiment consists of series of a 180° pulses as in Figure 3.3a, refocussing the signal during acquisition. The Fourier transformed spectrum is composed of a series of regularly spaced sharp peaks, or ”spikelets” (Figure 3.3d), whose manifold resembles that of the conventional MAS spectrum (Figure 3.3b). CPMG is most successful on samples with long T_2 relaxation times, as the signal can be refocussed multiple times.[153] CPMG does not necessarily increase the SNR[5], as more noise compared to a simple spin-echo is acquired, but does increase the peak height.

The CPMG experiment has been used to obtain signal enhancement for spin $I = 1/2$ nuclei,[154, 155] for fast measurements of T_2,[5, 156–159] before being applied to quadru-

[4] CPMG: *Carr-Purcell-Meiboom-Gill*
[5] SNR: *Signal-to-Noise Ratio*

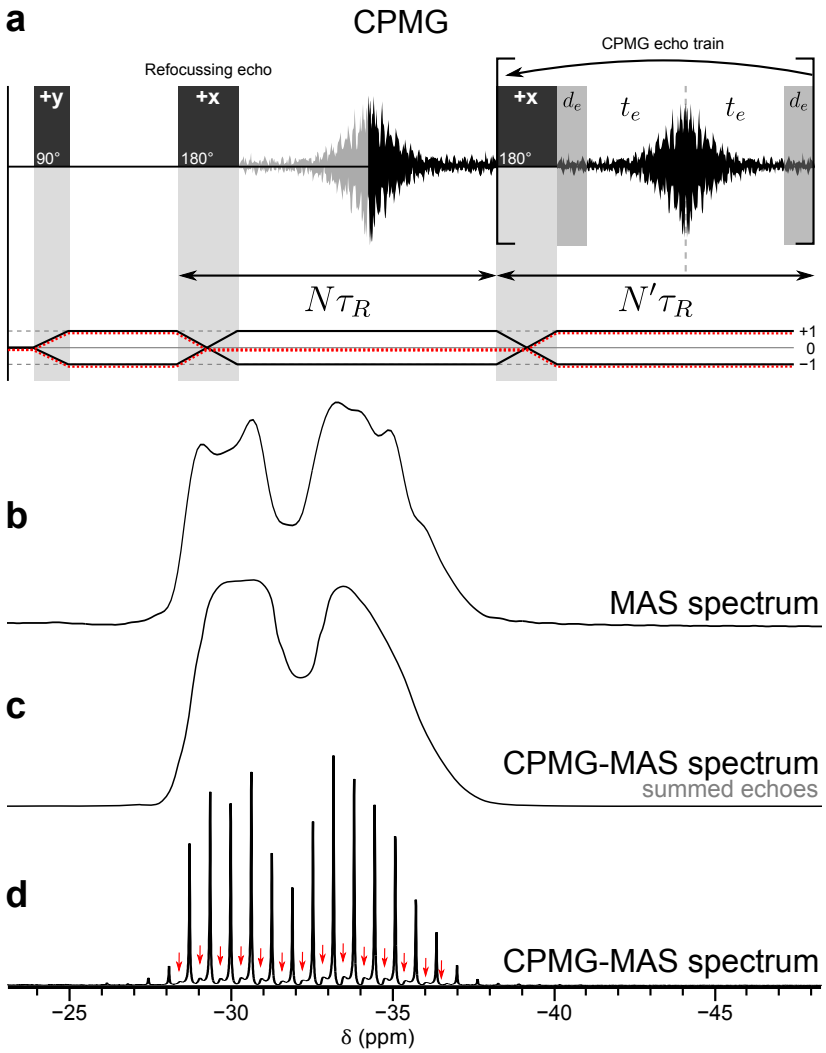

Figure 3.3: ***(a)****: Pulse sequence and CTP (in black) of the CPMG pulse sequence. The dashed red CTP corresponds to that of stimulated echoes.* ***(b,c,d)****: ^{87}Rb MAS spectra of $RbNO_3$ acquired at B_0 = 14.1 T (ν_0 = 196.40 MHz) and ν_R = 12.5 kHz for a total time of 12 min.* ***(b)****: MAS spectrum recorded with 1280 transients.* ***(c)****: CPMG spectrum resulting from the sum of the echoes of spectrum* ***(d)****.* ***(d)****: CPMG spectrum acquired at ν_R = 20 kHz with 640 transients and 62 echoes of duration $N'\tau_R$ = 8.0 ms. The position of stimulated echoes is highlighted by red arrows.*

polar nuclei. CPMG experiments on quadrupolar nuclei are often termed QCPMG[6], although the method is not fundamentally different from the conventional CPMG.[160] It is an ideal method to easily acquire the ST signal, particularly for spins $I = 1$ nuclei such as ^{2}H [161] or ^{14}N,[162] where these are the only feature in the spectrum. CPMG can equally be used to observe the CT signal of quadrupolar nuclei,[163, 164] particularly those with low receptivity or diluted within a given sample such as ^{17}O,[165–167] ^{25}Mg,[168] or ^{39}K,[165] or those with broader CTs, *e.g.*, ^{33}S [169] or ^{35}Cl.[170]

[6]QCPMG: *Quadrupolar Carr-Purcell-Meiboom-Gill*

Under MAS, the CPMG echo period is chosen to be synchronised with the rotor as illustrated Figure 3.3a, with [171]

$$N'\tau_R = t_{180°} + 2t_e + 2d_e \quad , \tag{3.1.14}$$

with t_e being the half echo period, during which the FID is recorded, and d_e the dead time[7] (see spin-echo in Section 3.1.1), during which the FID is not recorded.

The resolution of a CPMG spectrum is determined by the spikelets spacing, $1/2t_e$, and the width of the spikelets relates to T_2. The signal enhancement stems from the intensity of the original signal now being concentrated inside a much lower number of spikelets. Increasing the echo period t_e increases the signal in each spikelet, but reduces the resolution as a result. Although this operation is not always straightforward, there is also the option to add all of the echoes together to form a full-echo, and to recover the original lineshape without loosing the SNR improvement, as shown in Figure 3.3c.[152] However, this requires precise timing of the echo periods and dead times, and the resolution of the processed spectrum remains limited as it is determined by the echo period, in general short.

If the refocussing pulse in Figure 3.3a is not a perfect 180°, or if some of the components of the signal are far from the carrier frequency, a proportion of the signal will pass through population (see Figure 3.3a, dashed red CTP), resulting in so-called simulated echoes. Stimulated echoes appear on a FT spectra as small spikelets, slightly displaced from the spikelets arising from the Hahn-echoes, visible in Figure 3.3d. Stimulated echoes can be reduced by means of phase cycling, z-filtration,[172] and by timing precisely the periods when experiments are performed under MAS.[160] Alternative acquisition methods, such as the PIETA[8] pulse sequence, can also be employed to easily separate the desired signal from the stimulated echoes.

3.1.3 The CP experiment

The CP[9] experiment originates from the work of Hartmann and Hahn, who observed that a dilute spin such as ^{13}C or ^{15}N could be indirectly observed by ^{1}H NMR, through a magnetisation transfer mechanism driven by the ^{1}H-^{13}C or the ^{1}H-^{15}N dipolar interaction, respectively. Subsequently, Pines *et al.* utilised the same phenomenon to transfer

[7] d_e is added before CPMG 180° pulses in the CPMG echo train to preserve the symmetry of the echo during the acquisition window.

[8] PIETA: *Phase Incremented Echo Train Acquisition*

[9] CP: *Cross Polarisation*

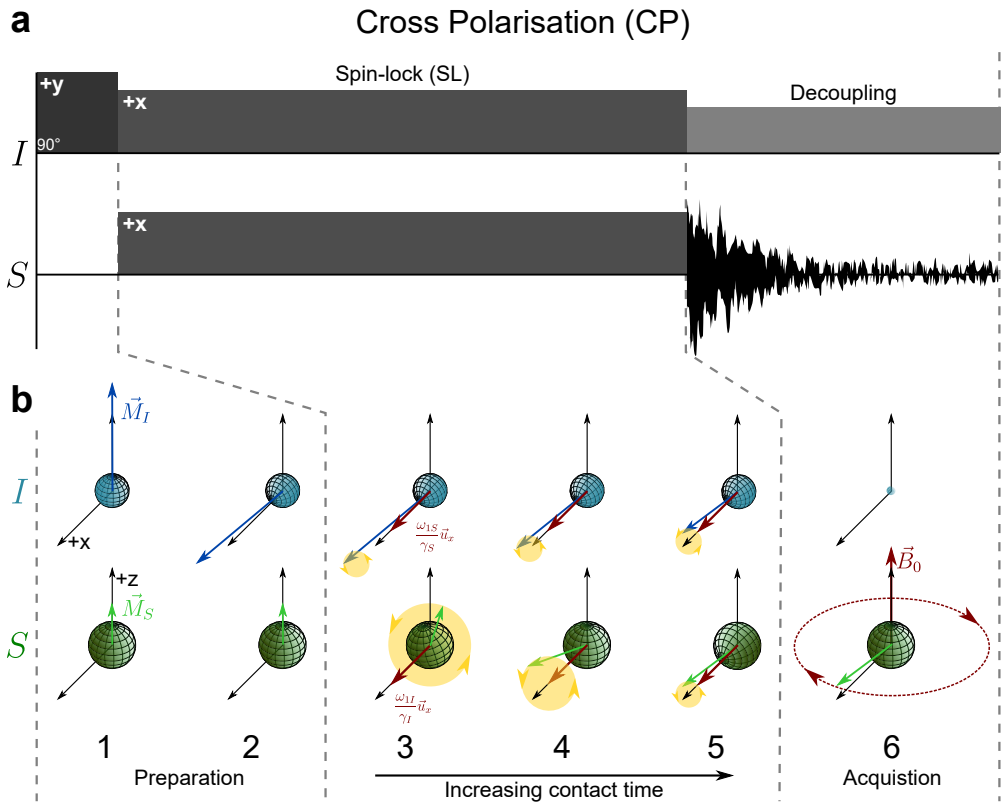

Figure 3.4: ***(a)****: Pulse sequence of a CP between a spin I and a spin S.* ***(b)****: Representation in vector model of the evolution of the magnetisation vectors $\vec{M}_I$ and $\vec{M}_S$, associated with the spins I and S, respectively, at several moments of the pulse sequence, observed in Σ_{rot} except for* ***(6)****.* ***(1)****: Initial state,* ***(2)****: After a 90°_{+x} pulse[10],* ***(3)*** *to* ***(5)****: during contact; and* ***(6)****: during acquisition under I-decoupling. $\vec{M}_I$ and $\vec{M}_S$ are represented nutating around their respective $\vec{B}_1$ by a yellow circle.*

the magnetisation from ^{1}H to ^{13}C, enhancing the NMR signal of ^{13}C.[7] At the present time, CP is commonly used in NMR spectroscopy to obtain signal enhancement for an insensitive nucleus (typically ^{13}C or ^{15}N) when a sensitive nucleus is present (typically ^{1}H or ^{31}P).

The pulse sequence for the CP experiment is shown in Figure 3.4a, with I and S denoting the sensitive and insensitive nuclei, respectively. Figure 3.4b uses the vector model to visualise the effect of the pulse sequence. After an initial 90°_{+y} pulse, the magnetisation of spin I is moved along the $+x$ axis in Σ_{rot}. At this point, an RF pulse along $+x$ is then applied simultaneously to S and I at frequencies ω_{RF_I} and ω_{RF_S}, respectively. This pulse is known as a SL[11] pulse,[173] with the magnetisations "locked" to the direction along which $\vec{B}_1$ is applied the entire time. The duration of the two SL pulses is referred to as

[10] $\vec{M}_I$ is represented slightly off the $+x$ axis so the effect of the SL can be visualised more clearly.
[11] SL: *Spin-Lock*

the contact time, as the SL pulses permit the two nuclei to ”feel” each other. During the contact time, the dipolar interaction tends to align the magnetisation vector $\vec{M}_S$ and $\vec{M}_I$ and to equalise their norms (Figure 3.4b).

Duer [34] described an analytical model for CP, whose main point are presented here and for the simple case of a I-S pair. During the SL, the Hamiltonian is expressed as

$$\hat{H} = \hat{H}_Z + \hat{H}_{\mathrm{RF}}(S) + \hat{H}_{\mathrm{RF}}(I) + \hat{H}_{D_{IS}} \quad , \tag{3.1.15}$$

with $\hat{H}_{d_{IS}}$ expressed in Equation (2.2.21) being the first-order truncated dipolar Hamiltonian. As in Chapter 1.2.3, the system Hamiltonian in Equation (3.1.15) can be expressed in a frame in which its time-dependency is removed. This frame is a rotating frame at the rates ω_{RF_I} and ω_{RF_S}, hence called the double rotating frame $\Sigma_{\mathrm{rot}}^{(\times 2)}$. This is expressed mathematically as (see Equation (1.2.58))

$$|\Phi\rangle = \exp\left(-\frac{i}{\hbar}\omega_{\mathrm{RF}_I} t \hat{I}_z\right) \exp\left(-\frac{i}{\hbar}\omega_{\mathrm{RF}_S} t \hat{S}_z\right) |\Phi\rangle_\rho (t) \quad . \tag{3.1.16}$$

Subsequently, a transformation moves the Hamiltonian into a frame called the toggling frame using the rotation operator given by [34, 174]

$$\hat{R} = \exp\left(-\frac{i}{\hbar}\omega_{1_I} t \hat{I}_y\right) \exp\left(-\frac{i}{\hbar}\omega_{1_S} t \hat{S}_y\right) \quad , \tag{3.1.17}$$

in which the effect of the SL is removed and only the effect of the dipolar Hamiltonian can be seen. This transformation results in an Hamiltonian $\hat{H}^*$ expressed

$$\hbar \times \hat{H}^* = - d_{\mathrm{IS}} \left(\hat{I}_z.\hat{S}_z + \hat{I}_x\hat{S}_x\right) \cos\left(\left(\omega_{1_I} - \omega_{1_S}\right) t\right) \tag{3.1.18a}$$

$$- d_{\mathrm{IS}} \left(\hat{I}_z.\hat{S}_x + \hat{I}_x\hat{S}_z\right) \sin\left(\left(\omega_{1_I} - \omega_{1_S}\right) t\right) \quad . \tag{3.1.18b}$$

If $\omega_{1_I} \neq \omega_{1_S}$, $\hat{H}*$ in Equation (3.1.18) becomes time dependant in the toggling frame, therefore has almost no effect on the system (see the secular approximation in Section 2.1.2). Consequently, the point at which CP is most efficient is when

$$\omega_{1_I} = \omega_{1_S} \quad . \tag{3.1.19}$$

Equation (3.1.19) is called the Hartmann-Hahn condition.[6] It can be shown that if this is fulfilled, the magnetisation of the insensitive nucleus S for a given β_{LP} angle builds-up with time according to the expression [175, 176]

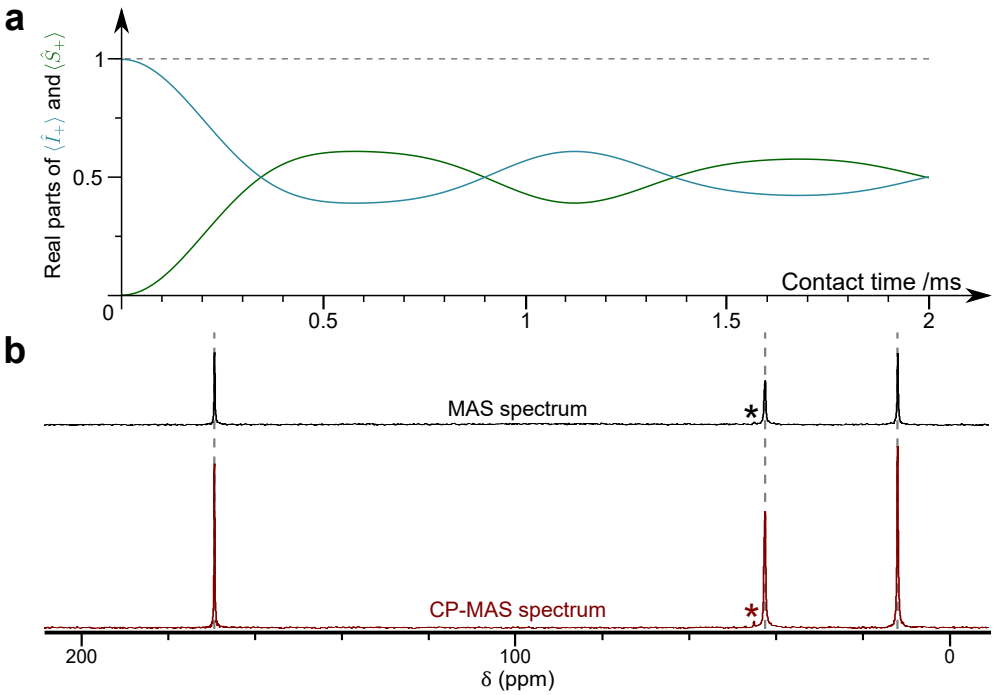

Figure 3.5: ***(a)****: Build-up curves for an isolated ^{1}H-^{15}N pair, plotting the real parts of $\langle \hat{I}_x \rangle$ (blue line, I being ^{1}H) and $\langle \hat{S}_x \rangle$ (green line, S being ^{15}N) as a function of the contact time during SL. Simulated for the static case, with B_0 = 14.1 T (ν_0 = 600.0 MHz for ^{1}H and ν_0 = 60.8 MHz for ^{15}N) and a dipolar coupling constant d_{HN} = 2 kHz, and a ^{15}N CSA with the parameters δ_{CS} = 0, $\nu_0 \times \Delta_{CSA}$ = 2 kHz and η_{CSA} = 0.2.* ***(b)****: Comparison of the signal intensity between two ^{13}C experimental MAS spectrum (black) and a ^{1}H to ^{13}C CP-MAS spectrum (green) of alanine, acquired at B_0 = 14.1 T (ν_0 = 600.0 MHz for ^{1}H and ν_0 = 60.8 MHz for ^{15}N), and a contact time τ_c = 1 ms.*

$$M_S(t) = M_S^{\text{eq}}.\frac{\gamma_I}{\gamma_S}\left(1 - \cos\left(2\pi d_{\text{IS}}.d_{0,0}^{(2)}\left(\beta_{\text{LP}}\right)t\right)\right) \quad , \tag{3.1.20}$$

assuming no relaxation takes place. M_S in Equation (3.1.20) oscillates at d_{IS}, as illustrated in Figure 3.5. Summed over all the crystallites of a powder sample and taking into the effects of other interactions such as CSA, and other sources of local magnetic field variations, M_S progressively attenuates to reach an equilibrium value.[177, 178] While Equation (3.1.20) seems to suggests that the SL can be maintained forever, a spin-lattice relaxation process (see Chapter 1.3.1), characterised by $T_{1\rho}$, takes place in the rotating frame, eventually causing $\vec{M}_S$ and $\vec{M}_I$ to return to their original state.

Under MAS, the condition for most efficient transfer is often given by the modified Hartmann-Hahn condition, given by

$$\omega_{1_I} = \omega_{1_S} + n\omega_r \ , \quad n \in \mathbb{I}^\star \quad , \tag{3.1.21}$$

where $n \in \{-2, -1, +1, +2\}$ under usual conditions. As the Hartmann-Hahn condition is

restricted and RF calibration often somewhat imprecise, in practice, a ramped SL pulse is often used instead.[179] Thanks to the magnetisation transfer *via* dipolar coupling, significant signal improvement can be obtained for the insentive nucleus, as illustrated in Figure 3.5b which shows the comparison between an ^{13}C MAS spectrum and a ^{1}H-^{13}C CPMAS spectrum of alanine.

Another advantage of CP is that it can be repeated every time the sensitive nucleus reaches thermal equilibrium, without waiting for the insensitive nucleus to do so. The absence or near-absence of strong homonuclear coupling between dilute or magnetically weak nuclei often imposes long T_1 relaxation delays (between ten seconds to several minutes), making multiple-dimension correlation experiments or experiments with long phase cycling impractical. On the contrary, ^{1}H or ^{31}P possess a very large gyromagnetic ratios, 100% natural abundance and are typically numerous and close to each other in many samples, permitting the experiments to be repeated faster, thus increasing the acquired signal per unit of time. This results in multiple strong homonuclear dipolar couplings (the order of magnitude being $d_{\mathrm{HH'}}/2\pi \sim 100$ kHz) causing very fast T_1 relaxation. However, CP does not preserve the quantitative signal intensity of the MAS spectrum, as the enhancement depends in practice on the I-spin network around each spin S.

3.2 Concepts in quadrupolar NMR spectroscopy

NMR experiments on quadrupolar nuclei differs in many aspect to those for spins $I = 1/2$. The multiple Zeeman energy levels and the typically strong quadrupolar interaction become of vital importance, compromising the simple vector model description of NMR, with previously non-existent spin dynamics appearing. This section introduces concepts useful for the description of NMR experiments for spins $I > 1/2$ nuclei.

3.2.1 Spin-locking quadrupolar nuclei

The concept of spin-locking magnetisation was introduced in Section 3.1.3 when describing CP for spins $I = S = 1/2$. SL of quadrupolar nuclei has multiple usages, including CP (investigated in details in Chapter 8) and in variations of the MQMAS experiment discussed in Section 4.2. The pulse sequence for a SL experiment on a spin S is shown in Figure 3.6. As for SL for spins $I = 1/2$, transverse magnetisation is

created by an initial pulse followed by a longer pulse phase shifted by 90°, termed a SL pulse, during which the magnetisation is maintained along a fixed direction in Σ_{rot}. One major difference to the $S = 1/2$ case is the possibility to spin-lock MQ-transitions. Theoretical treatments of SL for quadrupolar nuclei have been shown by Vega,[29, 180–184] Ashbrook and Wimperis,[185, 186] and other authors.[187, 188] Most commonly, the first pulse is used to create CT coherence by choosing ν_1 to be of a similar magnitude as the CT linewidth expressed in Equation (2.3.38), thus giving the density matrix of the system as

$$\hat{\rho}(t_0) = \hat{S}_x^{-1/2 \leftrightarrow +1/2} \tag{3.2.1a}$$

$$= \hat{S}_x^{\text{CT}} \quad . \tag{3.2.1b}$$

The initial pulse can also be used to create ST coherences by setting $\omega_1 \geq \omega_Q$ ($\hat{\rho}(t_0) = \hat{S}_x$), or MQ coherences following the method that will be instructed in Section 3.2.2. It should be noted that, in practice, the state created by this first pulse is not necessarily ideal as assumed in Equation (3.2.1). The nutations rates of the different transitions are affected by the orientation of the PAF with respect to Σ_{lab} or Σ_{rot}, thus a mixture of different coherences are typically observed in practice. From this initial state, the density matrix evolves under an Hamiltonian expressed in Σ_{rot} as

$$\hat{H}_\rho = \hat{H}_{\text{RF}} + \hat{H}_Q^{(1)} \tag{3.2.2}$$

with $\hat{H}_{\text{RF}}$ being the RF field Hamiltonian and $\hat{H}_Q^{(1)}$ the first-order truncated quadrupolar Hamiltonian, expressed in Equation (1.2.57) and (2.3.20), respectively. SOQE and frequency offset effects are not considered here, as those effects can often be neglected to describe the SL dynamics on quadrupolar nuclei where $\hat{H}_Q^{(1)}$ is predominant.[185]

Simulated SL intensities, plotting the real parts of $\langle \hat{S}_x^{CT} \rangle$ for C_Q = 1 MHz (Figure 3.6b) and 10 MHz (Figure 3.6c) in the static and MAS cases, show the evolution of magnetisation as a function of the SL pulse duration τ_p. Perfectly locked magnetisation would remain perfectly aligned with the RF field in Σ_{rot}, leaving $\langle \hat{S}_x^{\text{CT}} \rangle$ constant during the SL

Initial dephasing

The first feature that can be observed in Figures 3.6b and 3.6c is a small, sudden drop in the SL efficiency at short τ_p. This effect is difficult to see for static SL intensities, but

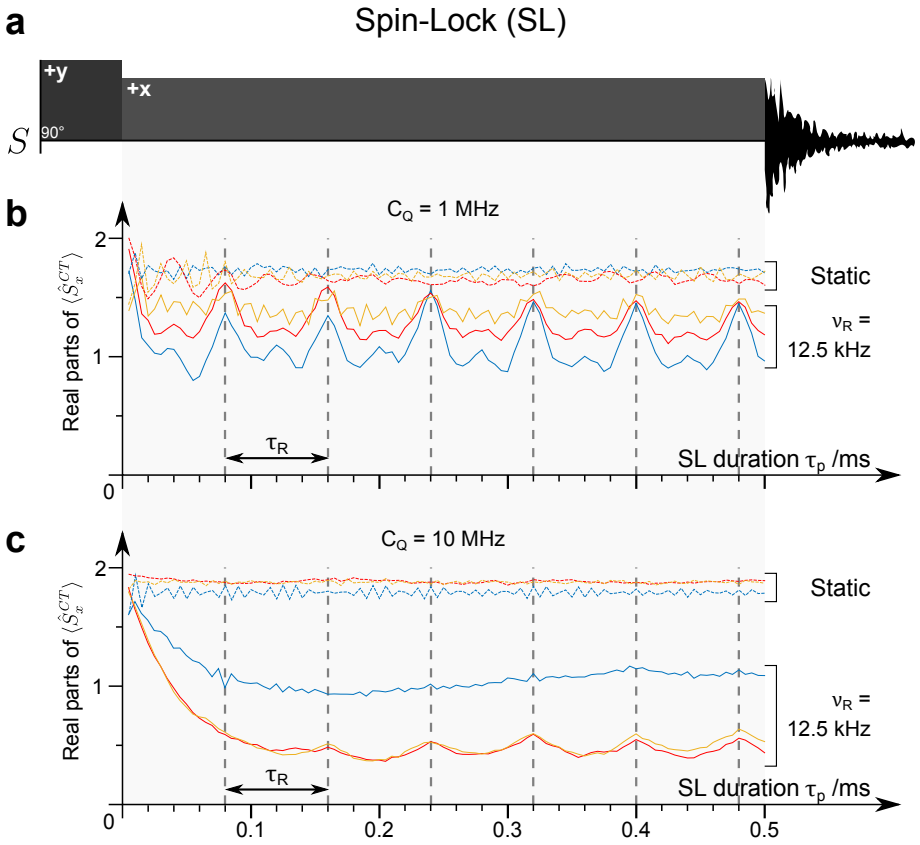

Figure 3.6: ***(a)****: CT-SL pulse sequence.* ***(b,c)****: Evolution of the real part of* $\langle \hat{S}_x^{CT} \rangle$ *as a function of the SL pulse duration* τ_p *for* ν_1 *= 50 kHz (blue lines), 100 kHz (red lines) and 150 kHz (yellow lines),* ν_R *= 0 (dashed lines) and* ν_R *= 12.5 kHz /* τ_R *= 80 µs (solid lines), and* C_Q *=* ***(b)****: 1 MHz and* ***(c)****: 10 MHz.*

is more striking on SL simulations under MAS. Neglecting the effect of MAS initially, this effect can be understand by visualising the density matrix in a frame in which the system Hamiltonian $\hat{H}$ in Equation (3.2.2) is diagonal. Defining V the diagonalisation matrix of $\hat{H}$, it follows that

$$\hat{H}_S^D = V.\hat{H}_S.V^{-1} \quad , \tag{3.2.3}$$

expressed in a frame termed here Σ_V. The Hamiltonian $\hat{H}_S^D$ in Equation (3.2.3) acts on the density matrix expressed in Σ_V, *i.e.*,

$$\hat{\rho}^D(t) = V\hat{\rho}(t)V^{-1} \tag{3.2.4}$$

Recalling that the time-evolution of $\hat{\rho}$ is given by the LVNE (see Equation (1.2.44)),

$$\hat{\rho}(t) = \exp\left(-\frac{i}{\hbar}\hat{H}t\right)\hat{\rho}(t_0)\exp\left(+\frac{i}{\hbar}\hat{H}t\right) \quad , \tag{3.2.5}$$

and combining Equation (3.2.5) and Equation (3.2.4), the time-evolution of $\hat{\rho}^D$ is given by

$$V\hat{\rho}(t)V^{-1} = \exp\left(-\frac{i}{\hbar}\hat{H}^D t\right) V\hat{\rho}(t_0)V^{-1} \exp\left(+\frac{i}{\hbar}\hat{H}t\right) \tag{3.2.6a}$$

$$\Leftrightarrow \rho^D(t) = \exp\left(-\frac{i}{\hbar}\hat{H}^D t\right) \rho^D(t_0) \exp\left(+\frac{i}{\hbar}\hat{H}^D t\right) \quad . \tag{3.2.6b}$$

In the general case, ρ^D is not diagonal. With time-evolution under the diagonal $\hat{H}^D$ in Equation (3.2.6), the off-diagonal elements of ρ^D acquire a time-dependence that, over the different crystallite orientations in a powder, will result in those elements quickly dephasing,[189] leaving only the diagonal elements. As they appear fixed in Σ_V, these elements can stay spin-locked for a long period of time (milli-seconds to seconds), with SL efficiency losses only arising from the spin-lattice relaxation $T_{1\rho}$. This rapid loss of coherence of the off-diagonal matrix elements of ρ^D is at the root of the rapid drop in the SL efficiency observed for SL duration in Figure 3.6.

However, the dephasing described above produces other coherences when observed in Σ_{rot}. Indeed, in Σ_V, the density matrix after a SL time τ_p, $\hat{\rho}^D(\tau_p)$ rapidly becomes diagonal. Performing the reverse transformation by V in Equation (3.2.3) on $\hat{\rho}^D(\tau_p)$ to return to Σ_{rot}, results in a density matrix $\hat{\rho}(\tau_p)$ different from the initial $\hat{\rho}(t_0)$, *e.g.*, where new coherences have appeared.

Evolution of coherences under MAS

In Figures 3.6b and 3.6c, there are two major differences between the behaviour of SL under static and MAS conditions. A more pronounced dephasing can be observed, and the observed $\langle \hat{S}_x^{CT} \rangle$ appears to "peak" every rotor period. These peaks can be understood qualitatively by plotting the eigenstates of $\hat{H}_S^D$ as a function of the rotor angular position γ_{PR}, for a single crystallite. As seen in Section 2.3.2, the quadrupolar frequency acquires a time dependence during MAS as expressed in Equation (2.3.29). This is reflected in the evolution of the eigenstates during the rotor period as shown in Figure 3.7. In the limit $\omega_Q \gg \omega_1$, the eigenstates of $\hat{H}_S^D$ are not the Zeeman eigenstates, but linear combinations of these given by

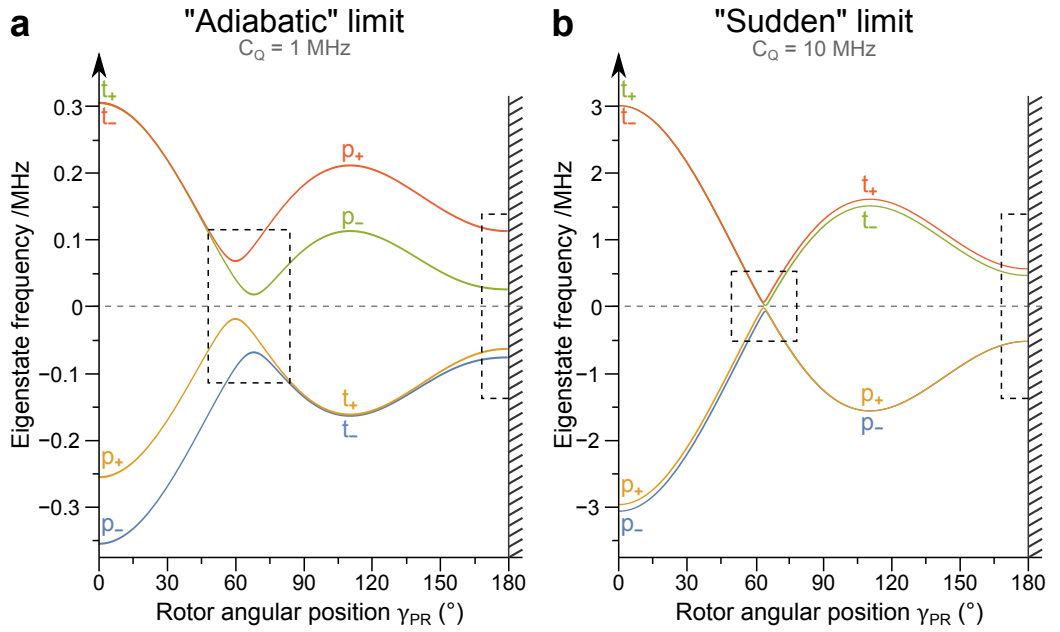

Figure 3.7: *Evolution of the frequencies of the eigenstates, given in Σ_V, of a unique crystallite such that β_{PR} = 90° with ν_1 = 50 kHz, η_Q = 0 and* ***(a)****: C_Q = 1 MHz ($\Omega_Q/2\pi$ = 0.25 MHz)* ***(b)****: C_Q = 10 MHz ($\Omega_Q/2\pi$ = 2.5 MHz). The eigenstates $c_\pm$ and $t_\pm$ are defined in Equation* (3.2.7)*. Both curves are symmetrical compared about 180°. Adiabatic or sudden passages are indicated by dashed boxes.*

$$c_\pm = \frac{1}{\sqrt{2}}\left(|+3/2,+1/2\rangle \pm |+3/2,-1/2\rangle\right) \tag{3.2.7a}$$

$$t_\pm = \frac{1}{\sqrt{2}}\left(|+3/2,+3/2\rangle \pm |+3/2,-3/2\rangle\right) \quad . \tag{3.2.7b}$$

Figures 3.7a and 3.7b presents the evolution of the eigenstates during MAS using identical conditions as in Figures 3.6b and 3.6c, respectively, with $\nu_1 = 50$ kHz. In Figure 3.6b, it can be seen that there are two peaks in $\langle \hat{S}_x^{CT} \rangle$ every rotor period, with an increase in intensity every multiple of the MAS rotor period, and a smaller smaller peak every half of the rotor position. These correspond to the transfers marked in Figure 3.7a by the dashed box for the rotor position being about 60°, and the dashed halfbox for the rotor position being about 180°, respectively. These transfers are termed ”adiabatic”, as the population, for example initially in the states $c_\pm$, are transferred to the states $t_\pm$. The eigenstates in Figure 3.7a seem like they are ”repealing” each other. At the exact moment of the adiabatic passage, the states $c_\pm$ and $t_\pm$ mix to form into a combination of the two states, allowing population exchange. On the other hand, in Figure 3.7b, the two states $c_\pm$ and $t_\pm$ appear to be simply ”crossing” each other. No population is exchanged, defining what is called a ”sudden” passage.[181]

No adiabatic behaviour (*i.e.* no peak) can be observed in Figure 3.7b neither.

As discussed in Appendix F using the vector model, the "level" of adiabaticity of a transfer can be characterised by the so-called adiabaticity factor, established by Vega to be [180, 181]

$$\alpha = \frac{\omega_1^2}{2\omega_Q\omega_R} \tag{3.2.8}$$

The two extreme cases are [181]

- If $\alpha \gg 1$, the MAS induced transfers are adiabatic and eigenstates are exchanged (Figure 3.7a). This is shown by the solid blue curve in Figure 3.6b.
- If $\alpha \ll 1$, the MAS induced transfers are sudden and the eigenstates are not exchange (Figure 3.7b). This is shown by the solid blue curve in Figure 3.6c.

Having either $\alpha \ll 1$ and $\alpha \gg 1$ guarantees that the magnetisation is spin-locked, the case $\alpha \ll 1$ corresponding to a case almost identical to static SL. However, in the intermediate regime, where $\alpha \approx 1$, a significant part of the populations in Σ_V are converted to off-diagonal elements, which will dephase, resulting in a loss of SL efficiency.[186]

3.2.2 Multiple-quantum filtration

MQF[12] is an experiment filtering the FID by an evolution period under a MQ coherence. The pulse sequence and CTP for this experiment are illustrated in Figure 3.8. Comparing the relative strength of the different interactions in Table 2.1, the characteristic strength for RF pulses exceed most internal interactions for spins $I = 1/2$ nuclei, whereas the opposite situation is observed for quadrupolar nuclei. The quadrupolar interaction alters the quantisation axis of the spin states (until now along $\vec{B}_0$) and thus causes the selection rule $\Delta m_I = \pm 1$ (see Equation (1.3.21)) to be relaxed, allowing overtone NMR spectroscopy,[119] and making the excitation and the conversion of MQ coherences being possible using a short pulse.[12, 103] The higher the filtered quantum order is, the lower the efficiency of the excitation. For this reason, 3QF[13] is the most common sort of MQF.

3QF has been theoretically described by Vega and Naor on quadrupolar nuclei using a fictitious spin $I = 1/2$ formalism,[183] in which the different spin observables $\hat{I}$ being separated into one observable $\hat{I}^{i,j}$ for each 1Q coherence of a given system, whose non-zero terms are [38, 182, 190]

[12] MQF: *Multiple-Quantum Filtration*
[13] 3QF: *Triple-Quantum Filtration*

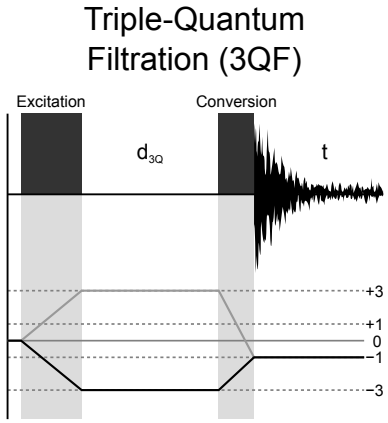

Figure 3.8: *Pulse sequence and CTP for a 3QF experiment.*

$$\begin{cases} \langle i|\, \hat{I}_x^{i,j}\, |j\rangle = \langle j|\, \hat{I}_x^{i,j}\, |i\rangle = \dfrac{\hbar}{2} & \text{(3.2.9a)} \\ \langle i|\, \hat{I}_y^{i,j}\, |j\rangle = -\langle j|\, \hat{I}_y^{i,j}\, |i\rangle = -i\dfrac{\hbar}{2} & \text{(3.2.9b)} \\ \langle i|\, \hat{I}_z^{i,j}\, |j\rangle = -\langle j|\, \hat{I}_z^{i,j}\, |i\rangle = \dfrac{\hbar}{2} & \text{(3.2.9c)} \end{cases} ,$$

where $|i\rangle = |I, I-i+1\rangle$. The spin observables as a function of $\hat{I}^{i,j}$ are expressed for a spin $I = 3/2$ nucleus as

$$\begin{cases} \hat{I}_x = \sqrt{3}\left(\hat{I}_x^{1,2} + \hat{I}_x^{3,4}\right) + 2\hat{I}_x^{2,3} & \text{(3.2.10a)} \\ \hat{I}_y = \sqrt{3}\left(\hat{I}_y^{1,2} + \hat{I}_y^{3,4}\right) + 2\hat{I}_y^{2,3} & \text{(3.2.10b)} \\ \hat{I}_z = 3\hat{I}_z^{1,4} + \hat{I}_z^{2,3} & \text{(3.2.10c)} \end{cases} .$$

Using the spin observables in Equation (3.2.10) to express the Hamiltonian during a pulse applied on resonance along the $+y$ direction in Σ_{rot}, under the Zeeman interaction and first-order quadrupolar interaction, we get

$$\hat{H} = 2\Omega_Q\left(\hat{I}_z^{1,2} - \hat{I}_z^{3,4}\right) + \omega_1\left(\sqrt{3}\hat{I}_y^{1,2} + 2\hat{I}_y^{2,3} + \sqrt{3}\hat{I}_y^{3,4}\right) \quad . \tag{3.2.11}$$

After a unitary transformation $\hat{H}$ is tilted to give $\hat{H}_T$, the "tilted" Hamiltonian, given by

$$\hat{H}_T = \exp\left(-\frac{i}{\hbar}\theta_T \hat{I}_x^{1,2}\right) . \hat{H} . \exp\left(+\frac{i}{\hbar}\theta_T \hat{I}_x^{3,4}\right) \tag{3.2.12a}$$

$$\text{with} \quad \theta_T = \tan^{-1}\left(\frac{\sqrt{3}}{2}\frac{\omega_1}{\Omega_Q}\right) \quad . \tag{3.2.12b}$$

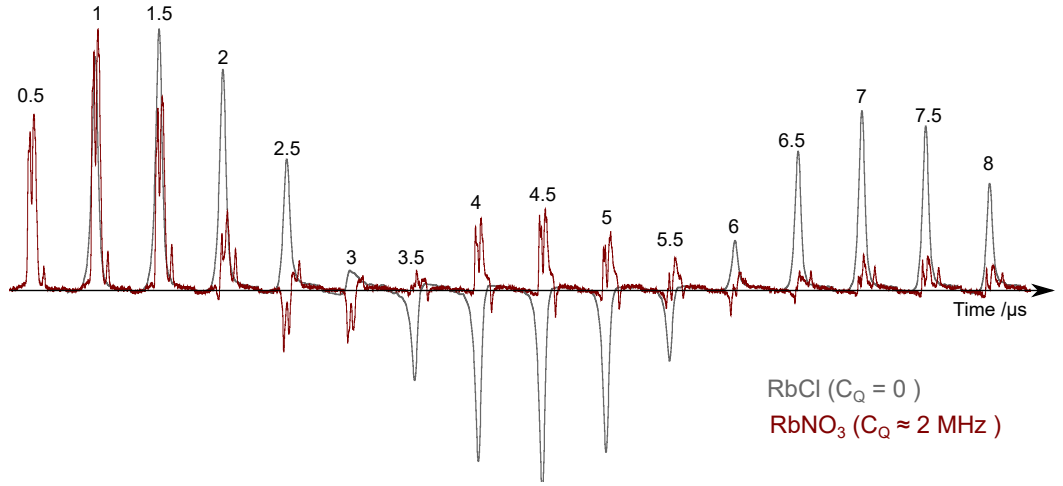

Figure 3.9: *Experimental ^{87}Rb nutation curves as a function of the pulse duration for RbCl (grey line, pseudo spin $I = 1/2$ case, $\nu_{1_{\text{eff}}} = \nu_{1_{\text{inh}}}$ = 155 kHz) and the total lineshape of $RbNO_3$ (red line, general case, $\nu_{1_{\text{eff}}}$ = 220 kHz), performed under the same experimental conditions and RF power, inside the same rotor.*

$\hat{H}_T$ becomes, in the limit $\omega_1 \ll \omega_Q$,

$$\hat{H}_T = 2\Omega_Q \left(\hat{I}_z^{1,2} - \hat{I}_z^{3,4}\right) + \underbrace{2\omega_1 \hat{I}_y^{2,3}}_{\text{1Q term}} + \underbrace{\frac{3}{8}\frac{\omega_1^3}{\Omega_Q^2}\hat{I}_y^{1,4}}_{\text{3Q term}} \quad . \tag{3.2.13}$$

Clearly, the 3Q term of Equation (3.2.13) connects the states $|1\rangle$ and $|4\rangle$ and creates 3Q coherence at an apparent nutation rate of $^3/_8(\omega_1^3/\Omega_Q^2)$. Since 3Q coherence is not directly observable, after 3Q coherence has been created by the excitation pulse, it must be converted to observable 1Q coherence using a "conversion" pulse, as shown in Figure 3.8. As the creation and conversion of 3Q depends on the orientation of the PAF relative to Σ_{lab}, owing to the orientation-dependent term Ω_Q, differences between the efficiency of 3QF for different crystallite orientations are expected, resulting in potential lineshape distortions (see Appendix H). Phase cycling can be used to select only one of the two CTPs of Figure 3.8. For sensitivity reasons, the CTP chosen for MQF is the population $\rightarrow p = -3 \rightarrow p = -1$, as it imposes the conversion to execute a coherence change of $\Delta p = +2$ instead of $\Delta p = -4$. In this case, the signal is expressed

$$S(t) \propto \rho_{1,4}(d_{3Q}).\text{Tr}[\rho(t)\hat{I}_z^{2,3}] \tag{3.2.14a}$$

$$\propto \exp\left(3i\omega_0 d_{3Q}\right).\text{Tr}[\rho(t)\hat{I}_z^{2,3}] \quad , \tag{3.2.14b}$$

for the case of a first-order truncated quadrupolar interaction, where d_{3Q} is the 3Q evolution delay represented in Figure 3.8. A noticeable property is, if $\omega_{\mathrm{Q}} = 0$, $\theta_T = \pi/2$ and the Hamiltonian is identical to the tilted Hamiltonian, with no 3Q term being present in Equation (3.2.13). That is, no 3Q coherence can be created using this approach, and any site not experiencing a quadrupolar interaction will not appear in a 3QF spectrum.

As shown in Equation (3.2.13), the CT term $\hat{I}_z^{2,3}$ causes a nutation at an effective nutation rate $\omega_{1_{\mathrm{eff}}} = 2\omega_1$ on spins $I = 3/2$ nuclei. The RF interaction with a quadrupolar nucleus has been extensively described,[191–197] and shows a complex behaviour in the general case, for which more details can be found in Chapter 8. For the two cases where $\omega_{1_{\mathrm{inh}}} \gg \omega_{\mathrm{Q}}$ and $\omega_{1_{\mathrm{inh}}} \ll \omega_{\mathrm{Q}}$, the nutation rate $\omega_{1_{\mathrm{eff}}}$ is well established.[195] If $\omega_1 \gg \omega_{\mathrm{Q}}$, the RF interaction is dominant and all transitions nutates at

$$\omega_{1_{\mathrm{eff}}} = \omega_{1_{\mathrm{inh}}} = -\gamma B_1 \quad , \tag{3.2.15}$$

where $\omega_{1_{\mathrm{inh}}}$ is the inherent nutation rate. This is called the pseudo-spin $1/2$ case. In the limit $\omega_1 \ll \omega_{\mathrm{Q}}$, the apparent nutation frequency observed for the CT for any spin I can be established to be

$$\omega_{1_{\mathrm{eff}}} = (I + 1/2)\omega_{1_{\mathrm{inh}}} = -(I + 1/2)\gamma B_1 \quad . \tag{3.2.16}$$

For a quadrupolar nucleus, a distinction must be therefore made between $\omega_{1_{\mathrm{eff}}}$ and $\omega_{1_{\mathrm{inh}}}$ (see Figure 3.9).[14] The latter must be calibrated on a sample presenting a near-zero C_Q site, or in the solution state, where quadrupolar interaction has almost no incidence.

3.3 The MQMAS experiment

It has been shown in Section 2.3.3 that, because MAS cannot average the forth-rank second-order quadrupolar tensors (see Equation (2.3.32)), some broadening still remains in MAS spectra of quadrupolar nuclei. Therefore, recording high-resolution, SOQE-free spectra requires specific techniques that are able to completely remove the anisotropic broadening.

From Equation (2.3.26b), it would seems that an obvious solution is to use very strong static magnetic field to reduce the SOQE as illustrated in Figure 2.9c. An example of

[14] Unless otherwise stated, herein a RF field strength simply quoted as ν_1 will refer to the inherent RF field strength, $\nu_{1_{\mathrm{inh}}}$.

the use of an ultra-high field (B_0 = 40 T) magnet to quench the SOQE for ^{27}Al has been published by Gan *et al.*[73] However, besides the rarity of such equipment,

> " [...] most of the residual line width [...] comes from the time fluctuation of the principal field."
>
> Gan *et al.* [73]

thus indicating the limits of the approach. The MQMAS[15] experiment, proposed by Frydman and Harwood,[11, 12] and based on the MQF experiment presented in Section 3.2.2, enables the removal of the quadrupolar interaction. This method has had a tremendous success within the solid-state NMR community, and has become one of the most widely-used techniques for studying quadrupolar nuclei, with countless successful applications reported in the literature.[198–215]

3.3.1 The two-pulse MQMAS experiment

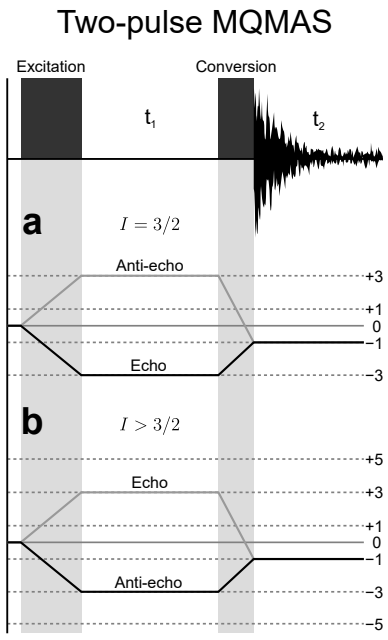

Figure 3.10: *Pulse sequence of a 3QF/MQMAS experiment and CTPs on spins* ***(a)****:* $I = 3/2$ *and* ***(b)****:* $I > 3/2$ *nuclei.*

The simplest MQMAS methods is the MQF experiment presented in Section 3.2.2, Figure 3.10, with a variable d_{3Q} evolution, t_1.[11, 12] This technique results in a 2D[16] spectrum, (see Figure 3.10), whose signal s can be expressed in the general case as [216]

$$s(t_1, t_2) = s_0 . \exp(-i\omega_I t_1) . \exp(-i\omega_D t_2) \quad , \tag{3.3.1}$$

with ω_I and ω_D referring to the frequency recorded in the indirect and direct dimensions, respectively. Theoretical treatment of the MQMAS technique has been widely described in the literature.[11, 12, 134, 217, 218] First and foremost, it is assumed that a spin is submitted only to the Zeeman/Isotropic chemical shielding and to the quadrupolar interaction. Secondly, it is assumed that the system is in the fast MAS limit, meaning

[15] MQMAS: *Multiple-Quantum Magic-Angle Spinning*
[16] 2D: *Two-Dimensional*

I	p	$A^{(0)}(I,p)$	$A^{(2)}(I,p)$	$A^{(4)}(I,p)$
$3/2$	$+1$	$-2/5$	$-8/7$	$54/35$
	$+3$	$6/5$	0	$-6/5$
$5/2$	$+1$	$-16/5$	$-64/21$	$144/35$
	$+3$	$-4/5$	$-40/7$	$228/35$
	$+5$	$20/3$	$40/21$	$-60/7$
$7/2$	$+1$	$-30/15$	$-120/21$	$270/35$
	$+3$	$-54/15$	$-96/7$	$606/35$
	$+5$	$30/15$	$-240/21$	$330/35$
	$+7$	$294/5$	$168/21$	$-966/35$
$9/2$	$+1$	$-48/15$	$-192/21$	$432/35$
	$+3$	$-108/15$	$-168/7$	$1092/35$
	$+5$	$-60/15$	$-600/21$	$1140/35$
	$+7$	$168/15$	$-336/21$	$168/35$
	$+9$	$648/15$	$432/21$	$-2332/35$

Table 3.1: *Zero-, second- and fourth-order spin coefficients of the second-order quadrupolar Hamiltonian as used in Equation (3.3.3), and previously in Equation (2.3.28) expressed as a function of I and $p = 2m_I$.[33, 134, 135, 219]*

that the second-rank component of the second-order quadrupolar interaction vanishes, *e.g.*, the correction to Zeeman energy levels is described by Equation (2.3.32). The frequency of the signal in either the direct or indirect dimension is conveniently separated into an isotropic and an anisotropic contribution

$$\omega_{\text{I/D}} = \omega_{\text{iso}}(I,p) + \omega_{\text{aniso}}(I,p,\beta_{\text{PR}},\gamma_{\text{PR}}) \quad , \tag{3.3.2}$$

where p is the coherence order of the (symmetrical) transition between the two states $|I, m_I = +p/2\rangle \leftrightarrow |I, m_I = -p/2\rangle$. ω_{iso} comprises the isotropic chemical shift and the QIS, and ω_{aniso} the fourth-rank quadrupolar anisotropy term expressed for $\beta_{\text{LR}} = \beta_m^{(2)} \simeq 54.7°$. Those are

$$\omega_{\text{iso}}(I,p) = -p\omega_{\text{CS}} + \frac{\omega_Q^2}{\omega_{\text{CS}}}.A^{(0)}(I,p).Q^{(0)}(\eta_Q) \tag{3.3.3a}$$

$$\omega_{\text{aniso}}(I,p,\beta_{\text{PR}},\gamma_{\text{PR}},\eta_Q) = \frac{\omega_Q^2}{\omega_{\text{CS}}}.A^{(4)}(I,p).Q^{(4)}(\beta_{\text{PR}},\gamma_{\text{PR}},\eta_Q).d_{0,0}(\beta_m) \quad , \tag{3.3.3b}$$

where ω_{CS} is the isotropic chemical shift (see Equation (2.2.12)). The terms $Q^{(0)}$ and $Q^{(4)}$ have been introduced in Section 2.3.2, and the coefficients $A^{(0)}$ and $A^{(4)}$ are given in Table 3.1 as a function of p. This results in a signal expressed

$$
\begin{aligned}
s(t_1,t_2) = s_0.\exp\left(i\omega_{\text{iso}}(MQ)t_1 + i\frac{\omega_Q^2}{\omega_{\text{CS}}}.A^{(4)}(MQ).Q^{(4)}(\beta_{\text{PR}},\gamma_{\text{PR}},\eta_Q).d_{0,0}(\beta_m)t_1\right) \\
\times\exp\left(i\omega_{\text{iso}}(\text{CT})t_2 + i\frac{\omega_Q^2}{\omega_{\text{CS}}}.A^{(4)}(\text{CT}).Q^{(4)}(\beta_{\text{PR}},\gamma_{\text{PR}},\eta_Q).d_{0,0}(\beta_m)t_2\right) \quad .
\end{aligned}
\tag{3.3.4}
$$

with $MQ = \{I, p\}$ and $\text{CT} = \{I, -1\}$. At the point when t_1 and t_2 verify

$$
A^{(4)}(MQ).t_1 + A^{(4)}(CT).t_2 = 0 \quad , \tag{3.3.5}
$$

the two anisotropic part terms are cancelled. As for the spin-echo experiment in Section 3.1.1, the fourth-rank term in the signal in Equation (3.3.4) are refocussed and the signal forms a "quadrupolar" echo. From Equation (3.3.5), it is clear that the t_1 position of the quadrupolar echo changes with the 3Q evolution time. After two successive FT of t_1 and t_2 (see Appendix G.4), this change appears on the acquired MQMAS spectrum as tilted ridges, broadened by the effect of fourth-rank terms in each dimension along a gradient R such that

$$
\omega_I = R(I,p)\omega_D \quad , \tag{3.3.6}
$$

where R is expressed as [217]

$$
R(I,p) = -\frac{A^{(4)}(MQ)}{A^{(4)}(CT)} \tag{3.3.7a}
$$

$$
= p\frac{36I(I+1) - 17p^2 - 10}{36I(I+1) - 27} \quad . \tag{3.3.7b}
$$

The values of R for all I and p are reported in Appendix E.2, Table E.2. Examples of MQMAS spectra exhibiting such tilted ridges can be found in Figures 3.12a, 3.12b and 3.12c. The notation of echo and anti-echo, shown in Figure 3.10, is directly related to the sign of $R(I,p)$, indicating the direction in which the quadrupolar echo is moving in t_1 as t_2 increases. If, for given I and p,

- the position of the quadrupolar echo moves toward high values of t_2 as t_1 increases, *e.g.*, $R(I,p) < 0$, then a given CTP is called an echo pathway.
- the position of the quadrupolar echo moves toward low values of t_2 as t_1 increases, *e.g.*, $R(I,p) > 0$, then a given CTP is called an anti-echo pathway.

Both cases are shown in Figure 3.11. As shown in Table E.2 and illustrated in Figure 3.10, $R(I = 3/2, p = +3)$ is negative so the CTP is termed the echo pathway,

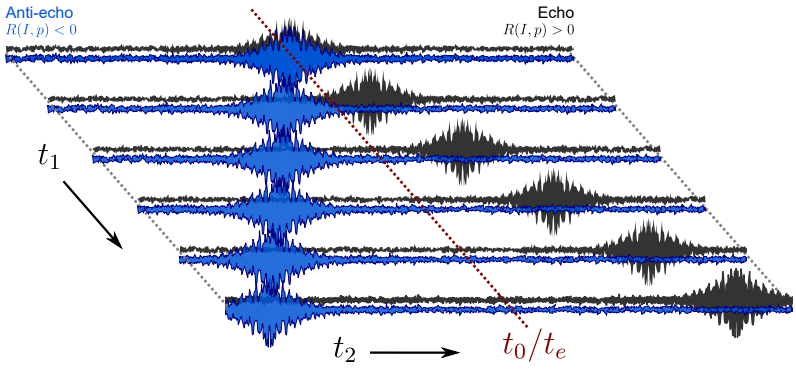

Figure 3.11: *Schematic of the evolution of the center of the quadrupolar echo in a MQMAS spectrum recorded using the echo (black line) and the anti-echo (blue line) CTP, relative to t_0 (start of the acquisition for the two-pulse MQMAS experiment) or t_e (echo period of the shifted-echo MQMAS experiment), as a function of t_1 and t_2.*

while $R(I = 5/2, p = +3)$ is positive and called the anti-echo CTP. For $t_1 = t_0$, where t_0 corresponds to the beginning of the acquisition, the quadrupolar echo occurs at a same position $t_2 = t_0$ using either the echo or the anti-echo CTP. As a result, for a MQF experiment, the CTP chosen is the one that keeps the coherence change to a minimum, as it gives the best signal (see Section 3.2.2). However, as visible in Figure 3.11, for the anti-echo CTP, the quadrupolar echo moves before t_0 disappears outside of the acquisition window as t_1 increases. As a result, two-pulse MQMAS spectra are almost systematically acquired using the echo CTP.

The reason why MQMAS is able to resolve different sites in a sample is, while fourth-order quadrupolar terms give rise to a broadening along $R(I,p)$, the position of the ridges is determined by a combination of ω_0 and ω_{QIS} according to [220]

$$\begin{cases} \omega_I = -p\omega_{\text{CS}} + \omega_{\text{QIS}}(I,p) & \text{(3.3.8a)} \\ \omega_D = \omega_{\text{CS}} + \omega_{\text{QIS}}(I,p) \quad , & \text{(3.3.8b)} \end{cases}$$

where ω_{QIS} is the QIS for the spin I and transition p

$$\omega_{\text{QIS}}(I,p) = \frac{\omega_Q^2}{\omega_0} A^{(0)}(I,p) Q^{(0)}(\eta_Q) \quad , \tag{3.3.9}$$

also reported in Equation (2.3.37). From Equation (3.3.8), it is clear that the ridges lies along a gradient $R(I,p)$ in a MQMAS spectrum. However, it can be deduced from Equation (3.3.8) that the location of the ridges for species with different ω_{CS} and ω_{QIS} values are sorted on the 2D MQMAS spectrum along gradients different from $R(I,p)$, given in Appendix E.2. This results in these ridges appearing at different locations in the

2D MQMAS spectrum, showing that the MQMAS experiment is able to resolve species according to ω_{CS} and ω_{QIS}.

3.3.2 Two common MQMAS techniques

The two-pulse experiments described above has the major limitation that phase-pure 2D lineshapes are not obtained, because of the apparition of "phase twists" on spectra that limit the spectral resolution.[134, 221] Amoureux *et al.* proposed to combine the echo and anti-echo equally, to obtain a signal that is amplitude modulated rather than phase modulated. However, the two coherence pathways with the coherence changes $\Delta p = -4$ and $\Delta p = +2$ can only be combined with equal intensities for all crystallites when $I = 3/2$.[12, 134, 222, 223] The two most common approaches for obtaining purely absorptive lineshapes are described below.

z-filtered MQMAS

The z-filtered MQMAS experiment proposed by Amoureux *et al.* [224] was the first solution proposed to resolve the phase problems for all spins. Instead of combining two CTPs with different coherence changes, this approach combines two symmetrical-pathways with a conversion pulse performing $\Delta p = -3$ and $\Delta p = +3$ transfers, moving the magnetisation back to the $+z$ axis. This last step is termed z-filtration.[172] This is followed by a CT-selective[17] 90° pulse to create $p = -1$ magnetisation. The standard z-filtered MQMAS pulse sequence is shown in Figure 3.13a. The pulse sequence shown in 3.13b is sometimes preferred for compatibility with split-t_1 approaches (see Section (3.3.3)) and most of the signal-improvement techniques introduced in Chapter 4.

Having a symmetrical CTP ensures that the echo and anti-echo signal can be combined equally for all spins.[222, 225] This results in an amplitude modulated signal expressed as

$$\begin{aligned} s(t_1, t_2) = 2s_0 . \cos\left(\left(\omega_{\mathrm{iso}}(MQ) + \omega_{\mathrm{aniso}}(MQ, \beta_{\mathrm{PR}}, \gamma_{\mathrm{PR}}, \eta_Q)\right) t_1\right) \\ \times \exp\left(i \left(\omega_{\mathrm{iso}}(\mathrm{CT}) + \omega_{\mathrm{aniso}}(\mathrm{CT}, \beta_{\mathrm{PR}}, \gamma_{\mathrm{PR}}, \eta_Q)\right) t_2\right) \quad . \end{aligned} \tag{3.3.10}$$

[17] A pulse can be termed "CT selective" if it is applied at the frequency of the CT, and if its effect just exceeds the width of the CT lineshape. In practice, applying a pulse at ν_1^{eff} just above the width of the CT lineshape $\Delta\nu_Q^{(2)}$ in Equation (2.3.38) makes it CT selective.

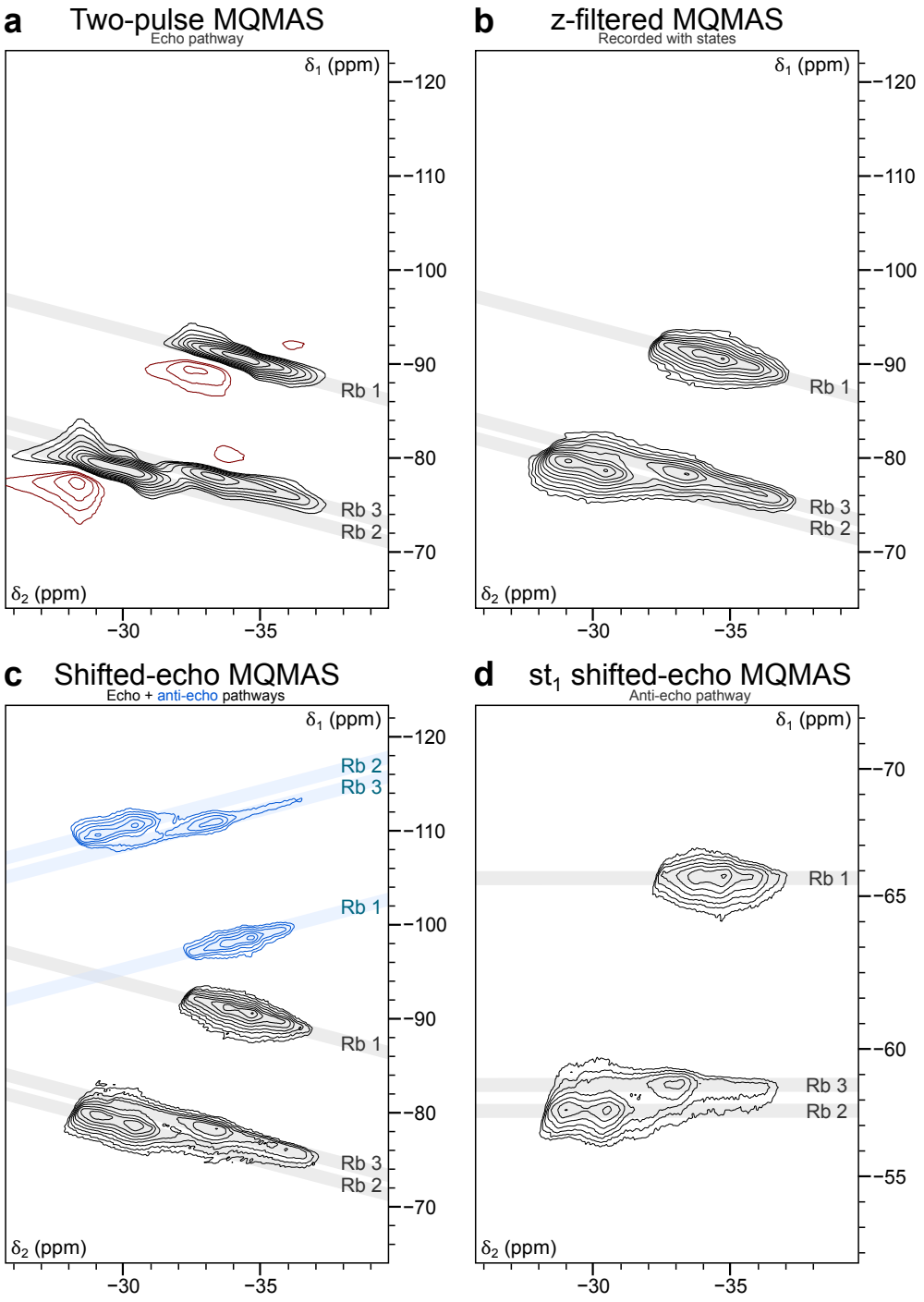

Figure 3.12: *^{87}Rb MQMAS spectra of $RbNO_3$ acquired at B_0 = 14.1 T (ν_0 = 196.4 MHz), ν_1 = 114 kHz and ν_R = 12.5 kHz using different methods.* ***(a)****: MQMAS spectrum recorded with the two-pulse MQMAS pulse sequence using the echo CTP (pulse sequence in Figure 3.10a). The features of a non-purely absorptive lineshape are visible by the negative contour lines in red.* ***(b)****: unsheared z-filtered MQMAS spectrum recorded with States (pulse sequence in Figure 3.13a).* ***(c)****: Overlapping of two shifted-echo MQMAS spectra, recorded using the echo CTP (black) and the anti-echo CTP (blue), respectively (pulse sequence in Figure 3.14a).* ***(d)****: Split-t_1 shifted-echo MQMAS spectrum (pulse sequence in Figure 3.16). See the extended caption in Appendix C.3 for further details.*

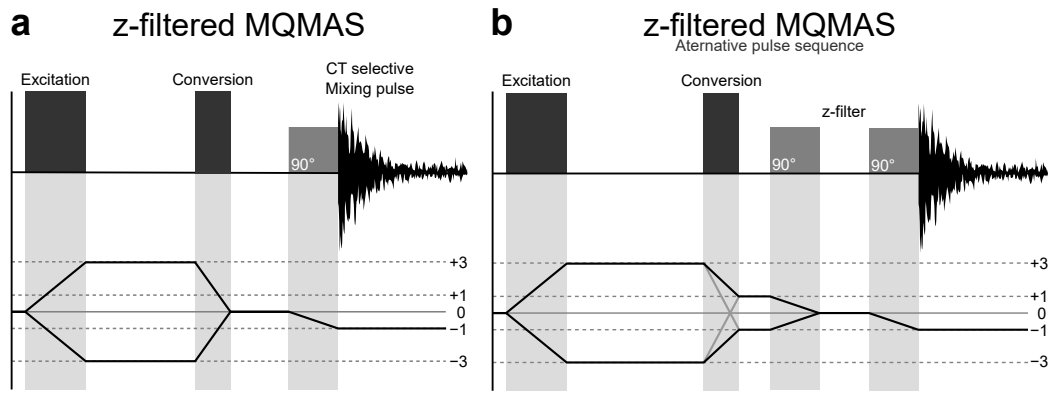

Figure 3.13: *Pulse sequence and CTP for the two common z-filtered MQMAS methods.* ***(a)****: Standard pulse sequence.* ***(b)****: Alternative pulse sequence.*

The cosine component of Equation (3.3.10) results in a 2D FT spectrum that is symmetrical about the center of the indirect dimension (see Appendix G.2), and thus the sign discrimination in this dimension to be lost. To remove this symmetry and recover the sign discrimination, it is necessary to reintroduce the imaginary component in the t_1 dimension. This is made possible by the use of an hypercomplex acquisition method, such as the States-Haberkorn-Ruben method (often simply called *States*),[226] or the TPPI[18] method.[227] For example, States successively records the signal expressed in Equation (3.3.10), then adds 90° to the phase of all the pulses, thus recording the signal

$$\begin{aligned} s(t_1, t_2) = 2j s_0 . \sin\left(\left(\omega_{\text{iso}}(MQ) + \omega_{\text{aniso}}(MQ, \beta_{\text{PR}}, \gamma_{\text{PR}}, \eta_Q)\right) t_2\right) \\ \times \exp\left(i \left(\omega_{\text{iso}}(\text{CT}) + \omega_{\text{aniso}}(\text{CT}, \beta_{\text{PR}}, \gamma_{\text{PR}}, \eta_Q)\right) t_1\right) \quad , \end{aligned} \tag{3.3.11}$$

where j is a quaternion imaginary number.[228, 229] Adding Equation (3.3.10) to Equation (3.3.11) results in the signal that can be expressed in a similar way as in Equation (3.3.4). This hypercomplex signal is processed by hypercomplex FT,[229] differing to the regular complex FT detailed in Appendix G, but results in a pure-absorptive mode lineshape on the 2D when plotting the real part of the signal.[134, 221]

Shifted-echo MQMAS

This second approach for obtaining pure-phase lineshapes was introduced by Massiot *et al.*,[223] based on the shifted-echo approach published by Ernst *et al.* [216] and used by Grandinetti *et al.* [230] to obtain pure-absorptive lineshapes in DAS experiments (see

[18] TPPI: *Time-Proportional Phase Increment*

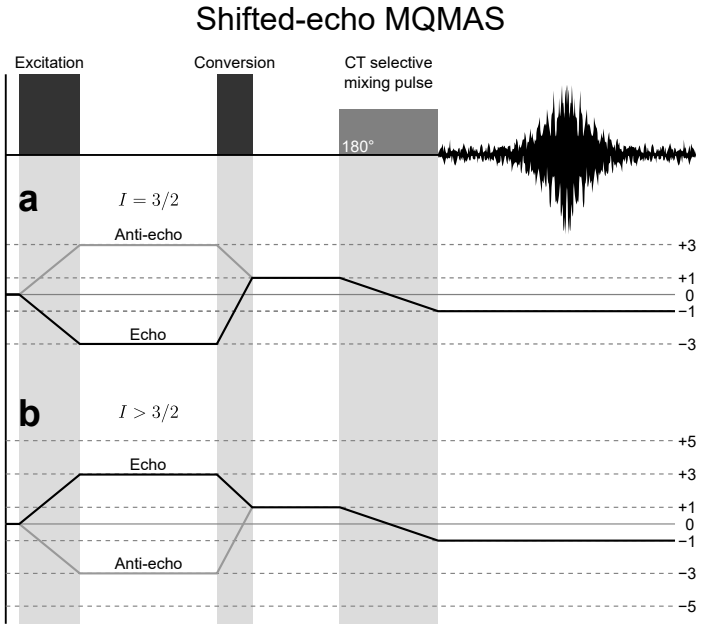

Figure 3.14: *Pulse sequence of the shifted-echo MQMAS experiment and CTPs labelled for **(a)**: spin $I = 3/2$ and **(b)**: spin $I > 3/2$ nuclei.*

Section 3.4.1).

The pulse sequence for this method is reported in Figure 3.14. The shifted-echo selects only of the two CTPs (normally selecting the echo CTP, *i.e.*, the coherence $p = -3$ for spin $I = 3/2$ and $p = +3$ for higher spins as shown in Figure 3.14) with the unwanted CTP being suppressed using phase cycling (see Appendix D),[128] and the signal is recorded after a CT-selective[17] 180° pulse. Instead of removing the phase modulation, the shifted-echo technique acquires the full spin-echo, which has the property that it has only a real part after FT as proven in Appendix G.2, Equation (G.2). This reduces the necessary processing to only a first-order phase correction along the direct dimension, given in Appendix G.2, Equation (G.2.12). This gives a signal expressed as

$$\begin{aligned} s(t_1, t_2) = &\exp\left(\left(\omega_{\text{iso}}(MQ) + \omega_{\text{aniso}}(MQ, \beta_{\text{PR}}, \gamma_{\text{PR}}, \eta_Q)\right) t_1\right) \\ &\times \exp\left(i \left(\omega_{\text{iso}}(\text{CT}) + \omega_{\text{aniso}}(\text{CT}, \beta_{\text{PR}}, \gamma_{\text{PR}}, \eta_Q)\right) (t_2 - t_e)\right) \quad . \end{aligned} \tag{3.3.12}$$

The position of the quadrupolar echo is now shifted by t_e such that

$$A^{(4)}(MQ).t_1 + A^{(4)}(CT).(t_2 - t_e) = 0 \tag{3.3.13a}$$

$$\Leftrightarrow \quad t_2 = t_e + R(I, p) t_1 \quad , \tag{3.3.13b}$$

thus the appellation shifted-echo. Shifted-echo experiments acquired using with the echo and anti-echo CTP are shown in Figure 3.12c,[19] and the position of the full-echo for the echo and anti-echo CTP is shown in Figure 3.11. In practice, MQMAS spectra are often acquired using the echo CTP. Even though the anti-echo CTP allows a minimum coherence change of $\Delta p = -2$ instead of $\Delta p = +4$, in practice, the echo CTP imposes t_e to be taken sufficiently large for the full-echo to be within the acquisition windows for all of the t_1 increments, causing further relaxation and, in the end, a lower signal, as indeed observed in Figure 3.12c.

3.3.3 Methods to rectify the tilting of the MQMAS ridges

As introduced in Section 3.3.2, MQMAS spectra exhibit lineshapes tilted along a gradient defined in Equation (3.3.7) in the 2D spectrum that depends on the spin quantum number and the CTP used, clearly visible in Figures 3.12a, 3.12b and 3.12c.[147] Using one of the following procedures, it is possible to obtain MQMAS spectra that lie along tilted axes,[20] resulting in the ability to obtain projections and extract information from the spectrum with greater ease.

Shearing transformation

The shearing transformation is a post-acquisition processing operation that takes into account the gradient for a given spin/CTP to produce ridges that lie parallel to the δ_2 axis of MQMAS spectra. This is achieved by ”mixing” the coherence in the δ_1 dimension such that

$$\delta_1' = \frac{\delta_1 - R(I,p)\delta_2}{1+ \mid R(I,p) \mid} \quad , \tag{3.3.14}$$

where δ_1 and δ_2 are the chemical shifts for the indirect and direct dimensions of an unsheared MQMAS spectrum, respectively. The shearing process is illustrated in Figure 3.15. This transformation can be visualised as a ”shearing” of the indirect dimension, thus the terminology. It can be noted that this transformation do not alter δ_2. Furthermore, the position of the ridges in the indirect dimension can also be expressed

[19] Sometimes the term ”shifted-anti-echo” is used when the anti-echo CTP is employed.

[20] A sample featuring δ_{iso} or δ_{QIS} distributions would still exhibit tilted lineshapes broadened along others axes.[231, 232]

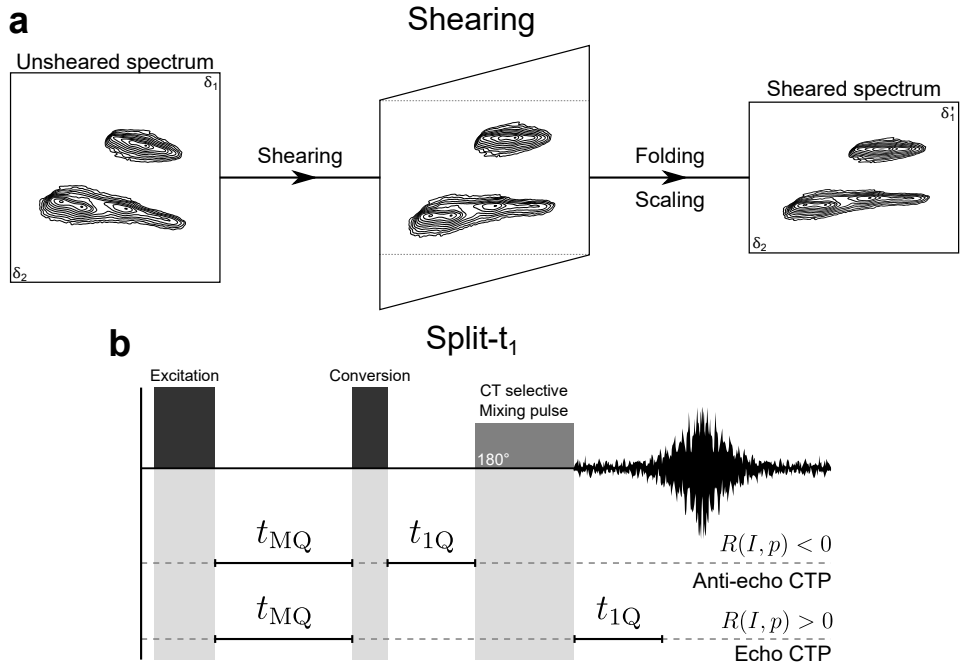

Figure 3.15: ***(a)****: Illustration of the three steps of the shearing transformation of a spectrum.* ***(b)****: Positions of t_{MQ} and t_{1Q} on a shifted echo for the echo and anti-echo CTPs.*

$$\delta_1' = \frac{(\xi(I,p) - R(I,p))\,\delta_{\mathrm{QIS}}(\mathrm{CT}) - (p + R(I,p))\,\delta_{\mathrm{iso}}}{1 + \mid R(I,p) \mid} \quad , \tag{3.3.15}$$

where the quantity

$$\xi(I,p) = \frac{A^{(0)}(\mathrm{MQ})}{A^{(0)}(\mathrm{CT})} \quad , \tag{3.3.16}$$

is known as the scaling factor. ξ can be interpreted as the ”expected” resolution in the sheared indirect dimension, as it is directly linked the apparent shift separation of the ridges. A complete list of the scaling factors $\xi(I,p)$ are given in Appendix E.3, Table E.4. This gives a chemical shift scale defined in the indirect dimension[21] as [212, 220, 236]

$$\Delta\delta_1 = \frac{\Delta\omega_2}{\omega_0} \quad . \tag{3.3.18}$$

[21]There has been debate in the literature concerning how should a ppm be defined in the indirect dimension.[233, 234] Instead of the definition in Equation (3.3.18), corresponding to the definition given in Pike *et al.*,[220] Amoureux and Fernandez use the convention [217, 235]

$$\Delta\delta_1 = \frac{\Delta\omega_2}{\xi(I,p)\omega_0} \quad , \tag{3.3.17}$$

which has the advantage of giving a same value between MQMAS experiments recorded using different coherence order p, but alters the definition of a ppm relative to a Hz in the different dimensions of the same spectrum.

Split-t_1 MQMAS

The split-t_1 approach is a method presented by Brown and Wimperis for MQMAS,[134] which performs the mixing of the 1Q and 3Q signal within the time domain, rather than after the acquisition in the frequency domain. This approach consists of splitting the t_1 evolution into a MQ evolution part t_{MQ} ($p = +M$ or $p = -M$) and a 1Q evolution part $t_{1\mathrm{Q}}$ ($p = +1$ or $p = -1$), as illustrated Figure 3.15 for the shifted-echo experiment. Defining t_1 the following way[22]

$$t_1 = t_{\mathrm{MQ}} + t_{1\mathrm{Q}} \tag{3.3.19a}$$

$$= (1 + \mid R \mid) t_i \quad , \tag{3.3.19b}$$

where t_i is an incremented evolution delay and $1\mathrm{Q} = \{I, +1\}$ or $\{I, -1\}$, it can be deduced that the quadrupolar echo occurs when the condition

$$A^{(4)}(MQ) t_1 + A^{(4)}(1Q) \mid R \mid t_1 + (t_2 - t_e) = 0 \quad , \tag{3.3.20}$$

is fulfilled. $\mid R \mid$ is considered as an absolute value to give a physical meaning to the products $\mid R \mid t_1$ if $R(I, p)$ is negative. Rearrangement gives

$$t_2 = t_e + \underbrace{\left(R - \frac{A^{(4)}(1Q)}{A^{(4)}(CT)} \mid R \mid \right)}_{} t_i \quad . \tag{3.3.21}$$

If the quantity within the brackets in Equation (3.3.21) is zero,

$$t_2 = t_e \quad , \tag{3.3.22}$$

meaning that the quadrupolar echo is now independent of t_1 and always occurs at the same position t_e. Two cases must be distinguished

- If $R(I, p) > 0$ (echo CTP), $A^{(4)}(1Q) = A^{(4)}(CT)$, thus $1\mathrm{Q} = \{I, -1\}$, implying that $t_{1\mathrm{Q}}$ must be placed during a $p = -1$ 1Q evolution period.
- If $R(I, p) < 0$ (anti-echo CTP), $A^{(4)}(1Q) = -A^{(4)}(CT)$, thus $1\mathrm{Q} = \{I, +1\}$, implying that $t_{1\mathrm{Q}}$ must be placed during a $p = +1$ 1Q evolution period.

Both of these cases are shown in Figure 3.15. As the usual CTP chosen for a split-t_1 shifted-echo MQMAS experiment is $p = 0 \rightarrow +3 \rightarrow +1 \rightarrow -1$ to ensure minimum

[22] A equivalent but more practical definition of t_1 is used in Appendix E.4

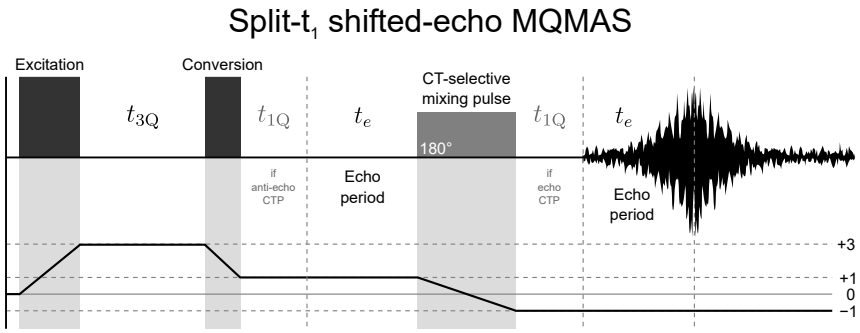

Figure 3.16: *Pulse sequence and CTP for the split-t₁ shifted-echo MQMAS experiment.*

changes in coherence order, the consequence is that the delay t_{1Q} must be placed during the $p = +1$ evolution period if the used MQF is the highest available for the considered spin system (see Figure 3.16). If not, t_{1Q} must be placed during the $p = -1$ evolution delay, *i.e.*, before the acquisition. An example of a ^{87}Rb ($I = 3/2$) shifted-echo split-t₁ spectrum of $RbNO_3$ is shown in Figure 3.12d, and shows three ridges aligned with the δ_2 dimension, and a isotropic spectrum can be easily obtain from a projection.

3.3.4 Methodological considerations and spectral interpretation

The two approaches z-filtered MQMAS and shifted-echo MQMAS both produce MQMAS spectra with pure-absorption mode lineshapes, but the practical differences between these methods have been investigated in the literature.[134, 237, 238] Even though the z-filtered approach combines the contribution of the two CTPs, while the shifted-echo only uses one, paradoxically, it is complicated to establish which of the method is, overall, the most sensitive. On one hand, with the shifted-echo approach, there is no imaginary signal after FT and phasing, and this component contains only noise. The whole echo contains the equivalent of ×2 the signal of a regular FID, for only $\times\sqrt{2}$ more noise, giving a SNR increased by approximately $\times\sqrt{2} \simeq 1.41$.[134, 223] On the other hand, the shifted-echo requires the whole echo to be recorded, requiring a sufficiently long echo period during which the signal may experience T_2 relaxation, decreasing sensitivity. Furthermore, relaxation may cause a distortion on the echo (see Appendix G, Figure G.3), re-introducing an imaginary part and causing some phase problems with the spectral lineshapes.

Sheared and split-t₁ MQMAS spectra should, in principle, be identical (see Appendix E), but the split-t₁ possess several advantages.

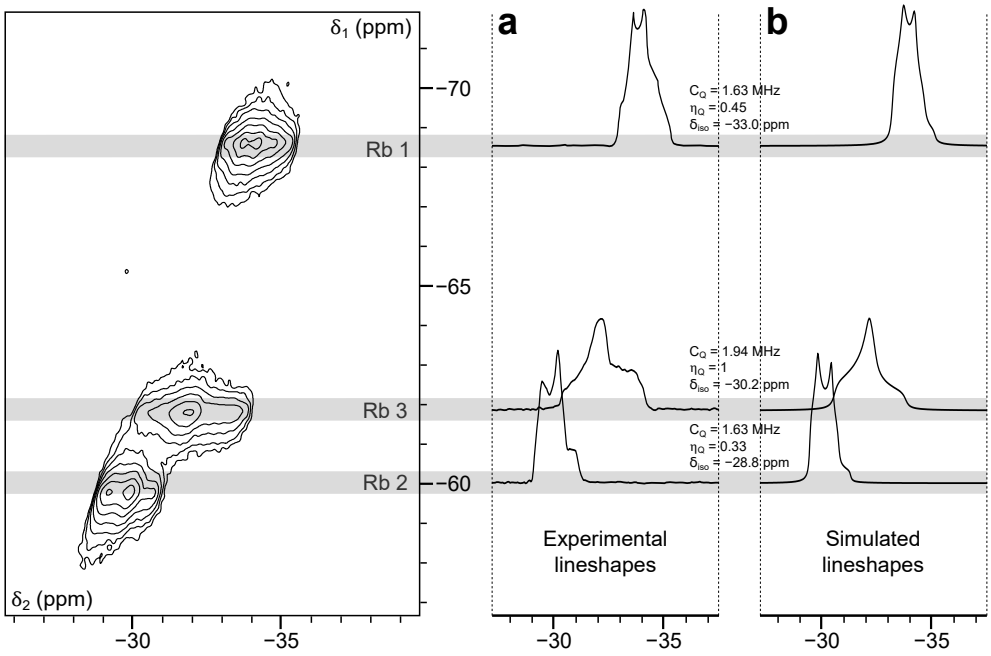

Figure 3.17: ***(a)****: Cross-sections of the individual quadrupolar lineshapes from a ^{87}Rb st₁ shifted-echo MQ-MAS spectrum of $RbNO_3$ recorded at B_0 = 20.0 T (ν_0 = 278.6 kHz).* ***(b)****: Lineshape and corresponding quadrupolar parameters obtained from fitting those extraction with the module SOLA. Literature values are report in Appendix C.2 from Baltisberger* et al. *[239] for comparison. The MQMAS spectrum is reported from Figure 5.11e.*

- As investigated by Brown and Wimperis,[134] shearing a spectrum is not free from artefacts, as it leads to small distortions in the sheared ridges in the anisotropic dimension δ_1, which have been shown to arise solely from the processing method.
- The quadrupolar echo for a non-split-t₁ experiment would result in an echo that appears at a different point in t_2 as t_1 is incremented, requiring the duration of the direct acquisition to be much longer to be recorded for much longer than the visible than for split-t₁ approaches, where the echo appears at a fixed time. In the latter case, the acquisition period can be minimised, limiting the amount of noise processed by the FT and increasing the sensitivity.

In summary, split-t₁ experiments do not intrinsically present any disadvantages compared to a shearing transformation. Setting a shifted-echo experiment to be split-t₁ does not present any difficulty, so is almost systematically applied. Implementing this into z-filtered experiment is not as straightforward as there is not a convenient 1Q evolution period in the pulse sequence apart from acquisition, and the quadrupolar echo occurs just after the final 90° pulse. To introduce a 1Q evolution period, the alternative pulse sequence presented in Figure 3.13b can be employed, but the additional pulse results

in a longer phase cycling and potentially a lower sensitivity. The pulse sequence and CTP for the split-t_1 shifted-echo MQMAS experiment, used throughout this work, is presented in Figure 3.16.

As presented in Section 3.3.2, a sheared or split-t_1 MQMAS spectrum resolves the different components of the signal according to their isotropic shifts and the QIS. An analysis of the MQMAS spectrum gives the following informations:

1. The maximum[23] number of distinct species contained in the sample for the element considered. This can be directly obtained from counting the number of resonances present, either directly on the spectrum or on a projection of the indirect dimension.
2. The quadrupolar product P_Q (Equation (2.3.36)). This quantity is directly related to the QIS shift δ_{QIS}, that can be obtained from the barycentre of the ridges on MQMAS spectra (either sheared or unsheared) as expressed by in Equation (2.3.37), that can be rewritten into a more practical form

$$P_Q = \omega_0 \frac{2I(2I-1)}{3\pi} \sqrt{\delta_Q}.10^{-3} \quad . \tag{3.3.23}$$

   The position of the barycentre of the lineshape in an MQMAS spectra (denoted δ_I and δ_D for the indirect and direct dimension, respectively) provides information on the QIS δ_{QIS}, and the isotropic chemical shift δ_{iso}, as shown in Appendix E.2.
3. If several sites are sufficiently well resolved in an MQMAS spectrum, and appear as well separated ridges, it may then be possible to separate the two quadrupolar parameters C_Q and η_Q by fitting the cross-sections taken parallel to δ_2 of the quadrupolar MAS lineshape as illustrated in Figure 3.17.[240, 241] In order for this fit to be successful, the observed quadrupolar lineshape must not deviate[24] too much from the idealised quadrupolar lineshape.[126, 222] Programs such as DMFit,[242] or the SOLA[25]) module integrated in Topspin,[243] can be used to perform those fittings.

[23] Sometimes, ridges overlap because of very similar δ_{iso} and δ_{QIS}, giving a misleading number of resonances.
[24] As discussed in Section 2.3.3, distortions of the lineshapes can occur on 3QF spectra.
[25] SOLA: *SOlid Lineshape Analyser*

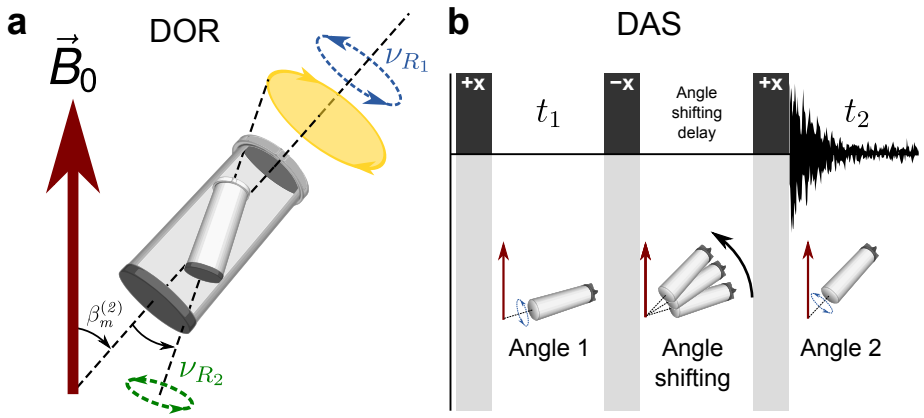

Figure 3.18: ***(a)****: Illustration of a DOR rotor spinning simultaneously around two angles, chosen to remove completely second- and fourth rand second-order quadrupolar broadening.* ***(b)****: Illustration of the DAS pulse sequence with the two evolution period during which the sample spins around two different axes, chosen to ensure the quadrupolar coupling is refocussed.*

3.4 Other high-resolution techniques for quadrupolar nuclei

As briefly discussed in Section 3.2.2, and as will be discussed further in Section 4.1.1, the efficiency of the MQMAS experiment proves to be limited and a user may want to turn to one of the methods described below instead. Generally speaking, all these methods have been reported to offer better sensitivity than MQMAS as they rely on 1Q steps rather than MQF, but with increased technical complexity, and might give lower resolution as MQMAS profits from an MQ dimension with an associated frequency higher than the Larmor frequency.[244]

3.4.1 Double-angle spinning methods

As seen Chapter 2.3.3, MAS is able to suppress the first-order quadrupolar interaction, and second-rank second-order quadrupolar terms, leaving only the anisotropic fourth-rank second-order quadrupolar tensor. This could only be averaged by a spinning at any of two angles $\beta_{m1}^{(4)} = 30.56°$ or $\beta_{m2}^{(4)} = 70.12°$ (see Equation (2.1.16)). Two early approaches to remove both the first- and the second-order anisotropy using multiple-angle spinning are termed DOR[26] and DAS[27]. By spinning at the magic angle $\beta_m^{(2)}$ and $\beta_{m1}^{(4)}$ or $\beta_{m2}^{(4)}$, those methods allows the retrieval of lineshapes reduced to their isotropic

[26] DOR: *DOuble Rotation*
[27] DAS: *Dynamic Angle Spinning*

value, with additional spinning sidebands to be taken into account.[245]

DOR

The DOR [13, 199, 246] approach consists of spinning simultaneously an inner rotor into an outer rotor, the inner rotor being at the magic-angle relative to $\vec{B}_0$ and the outer rotor at one of the angles that removes the fourth-rank second-order quadrupolar broadening (Figure 3.18a). This method has been shown to be efficient, but requires dedicated and expensive probes. Experiments are complicated to set-up and the achievable spinning speeds are limited by the simultaneous double rotation around two axis to just 1 to 8 kHz for the inner rotor, and 1 kHz for the outer rotor. However, DOR is the only technique presented here that allows the acquisition of a spectrum free from SOQE in a 1D approach.

DAS

DAS [14, 230, 239, 247] is a 2D experiment that correlates an evolution period during which the sample is rotated at one angle, followed by a second period with evolution at a second, chosen to refocus the second-rand and fourth-rank second order quadrupolar coupling (Figure 3.18b).[14, 230, 239, 247] Probes for this technique are also expensive and its implementation, with a switch of angle, is technically challenging. Sensitivity is also limited by T_1 relaxation during the angle switch period. The rotation speed is less limited than for the DOR experiment. DAS produces a 2D 1Q-1Q correlation spectrum similar to that of MQMAS, so presents sensitivity advantages but lower resolution than MQMAS have been reported.[248]

3.4.2 The STMAS experiment

The STMAS[28] method is an alternative approach to MQMAS for acquiring isotropic spectra for quadrupolar nuclei. Proposed by Gan,[121] STMAS correlates the STs during an initial evolution period to the CT during acquisition. Like MQMAS, STMAS does not require any specific probe and can be acquired on any standard MAS probe. An STMAS spectra are similar to those from MQMAS, with tilted ridges which, after shearing, result in sites being resolved in δ_1. As the STMAS experiment involves

[28] STMAS: *Satellite-Transition Magic-Angle Spinning*

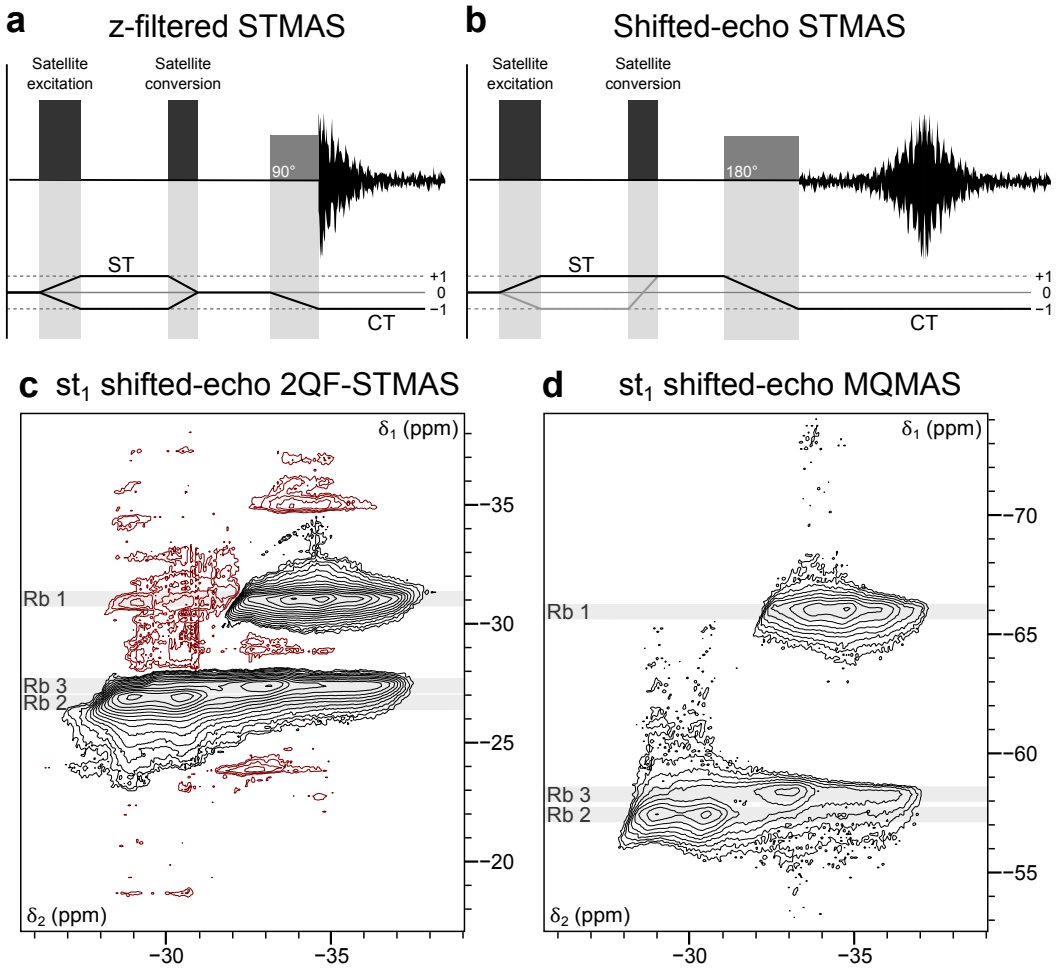

Figure 3.19: *Pulse sequence and CTPs for **(a)**: the z-filter STMAS pulse sequence and **(b)**: the shifted-echo STMAS experiment. **(c,d)**: ^{87}Rb spectra of $RbNO_3$ acquired at B_0 = 14.1 T (ν_0 = 196.4 kHz), ν_1 = 114 kHz and ν_R = 12.5 kHz. **(c)**: st₁-shifted echo MQMAS spectrum reported from Figure 3.12d for comparison. **(d)** split-t₁ shifted-echo 2QF-STMAS spectrum, acquired for ν_1 = 114 kHz. The contour lines have been set to be identical between spectra **(c,d)** to allow direct comparison. See the extended caption in Appendix C.3 for further details.*

only 1Q transitions, the sensitivity for STMAS is typically much higher than those reported for MQMAS, as clearly visible comparing the contour levels of the STMAS and MQMAS spectra reported in Figures 3.19c and 3.19d, respectively.[249–252] Reported improvements can reach an order of magnitude.[253] In this regard, STMAS has a clear advantage over MQMAS since many quadrupolar nuclei have low sensitivity.[254]

As with MQMAS, two approaches to record pure-phase STMAS spectra are available: amplitude-modulated z-filtered (Gan [15] and Figure 3.19), or phase-modulated shifted-echo experiments (Ashbrook and Wimperis [255] or Figure 3.19). Split-t₁ approaches can be incorporated into either of these methods, but is more commonly employed for

the shifted-echo experiment.[218] The STMAS experiment has several disadvantages compared to MQMAS. Separating the STs from the CT is not possible by phase cycling, resulting in CT-CT correlation ridges that are visible on spectra, which can potentially interfere with information-bearing signals. Some approaches are able to reduce or suppress the CT-CT correlation peak, such as the 2QF[29]-STMAS proposed by Kwak and Gan.[256] While this results in losses in sensitivity, it is still higher than MQMAS for the example reported in Figure 3.19c.

Unlike symmetrical MQ transitions, STs are severely affected by the first-order quadrupolar interaction and can exhibit lineshapes over MHz wide (see Section 2.3.3). As a result, in order for an STMAS spectrum to contain high-resolution quadrupolar lineshapes, the magic-angle has to be set with a precision exceeding ±0°3′,[255] and the MAS rate for rotor synchronisation in t_1 has to be very stable, with fluctuations not exceeding more than $\sim$ 1 Hz, otherwise artefacts appear in the spectra.[121, 257] Owing to these technical difficulties, STMAS is less popular than MQMAS. Articles describing methodological developments or applications are mostly from Gan,[15, 256] Taulelle and Amoureux,[248, 249, 251, 258, 259] and Ashbrook and Wimperis.[253, 255, 260–263] Even though STMAS has been reported to be more robust than MQMAS at high MAS rates,[257] technical difficulties in maintaining a very stable spinning rate at fast MAS ($\nu_R > 20$ kHz) limits the applicability of the method.[252, 257]

Generally, the expected resolution on in MQMAS spectrum has been reported to be higher than that of STMAS,[248] although this statement depends on the spin quantum number I, and the coherence order p used for MQMAS, and the ST chosen for STMAS. Scaling factors for MQMAS and STMAS are reported in Appendix E.3, Tables E.4 and E.5, respectively. For example, the expected difference in resolution for 3QMAS[30] and ST$_1$MAS on a spin $I = 3/2$ nucleus are $17/8 \simeq 2.125$ and 1, respectively.

[29] 2QF: *Double-Quantum Filtration*
[30] 3QMAS: *Triple-Quantum Magic-Angle Spinning*

Part II

The FAM-N pulse for sensitivity improvement in MQMAS

« On ne fait jamais attention à ce qui a été fait ; on ne voit que ce qui reste.»

”One never notices what has been done; one only sees what remains.”

Marie Skłodowska-Curie

Chapter 4

Signal improvement methods for MQMAS experiments

Introduction

The MQMAS experiment described in Section 3.3, quickly grew in popularity from the moment it was first introduced. Its ease of implementation and its ability to resolve resonances without the need for dedicated hardware made a huge contribution to the popularisation of NMR studies of quadrupolar nuclei.

As discussed in Section 3.3.1, MQMAS is based on the MQF experiment. Even though the creation and conversion of MQ coherence is enabled by the presence of the quadrupolar interaction, it is clear that the phenomenon remains relatively inefficient as the ”orientation” of the tilted Hamiltonian of Section 3.2.2, that breaks the selection rule shown in Equation (1.3.21), thus allowing multiple-photon processes to take place, essentially remains along $\vec{B}_0$ as the Zeeman interaction remains predominant. It results from this that MQF, and therefore MQMAS, would exhibit a dramatically lower sensitivity than direct acquisition experiments. The sensitivity problems of MQMAS have been widely reported and investigated in the literature,[222, 241, 251, 264, 265] and are an important consideration, as many quadrupolar nuclei have poor, inherent sensitivity. This restricts the applicability of MQMAS to nuclei and samples with inherently higher sensitivity, such ^{23}Na,[198–202, 204, 266–271] or ^{27}Al.[164, 203–207, 209–211, 236, 261, 272] Many other nuclei have much lower sensitivity, although successful MQMAS have been recorded for insensitive or dilute nuclei such as ^{17}O,[166, 208, 212–215,

262, 273–279] for which this issue can be partially overcome with isotopic enrichment. Nevertheless, the insensitivity of MQMAS still remains an important issue, and so STMAS, DOR or DAS may be preferred in some case.

As a result, many techniques have been designed to acquire MQMAS spectra with enhanced sensitivity. Most commonly, higher sensitivity is achieved by improving the efficiency of MQF using more efficient coherence-transfer schemes than a short single pulse. This section describes approaches for signal improvement of MQMAS. Such methods can roughly be divided into three categories:

1 ”General” signal improvement methods, that enables higher sensitivity for NMR regardless of the method use, for example NUS[1],[280–282] acquisition at low temperature and DNP[2],[9] or simply isotopic enrichment if applicable.

2 SL-based methods. As introduced in Section 3.2.1, population and coherences are adiabatically swept during a SL on a quadrupolar nucleus as the rotor spins. This approach can be used to both create and convert MQ coherence, and is discussed in Section 4.2. These methods are often attractive when MQMAS is performed under fast MAS.

3 Finally, approaches exploiting modulated pulses to improve the efficiency of the MQ to 1Q conversion pulse, which, as will be detailed in Section 4.3, is the step that limits sensitivity under standard conditions. Such techniques are generally efficient, versatile, and relatively easy to implement.

4.1 The conventional MQMAS experiment

This section discusses the advantages and disadvantages of the short, hard[3] pulse, abbreviated CW[4], for MQ excitation or conversion pulse applied using the strongest RF field strength ν_1 available experimentally. Two ”general” signal improvement strategies for MQMAS will also be presented.

[1] NUS: *Non-Uniform Sampling*
[2] DNP: *Dynamic Nuclear Polarisation*
[3] *i.e.*, applied at a strong RF field ν_1.
[4] CW: *Continuous-Wave*

4.1.1 Sensitivity of the short pulse 3QF experiment

As stated in Section 3.2.2, MQF must be carried out using at least two pulses, one for the MQ excitation, and one for its conversion into observable magnetisation. The use of numerical simulations is a convenient way to probe the efficiency of the two pulses separately, and under various conditions and constraints. The numerical calculations shown in Figure 4.1 have been performed for 3QF on ^{23}Na ($I = 3/2$), and show the efficiency of short MQ excitation and conversion pulses for different RF field strengths ν_1, quadrupolar constants C_Q, and MAS rates ν_R.

In this section, the case of short RF pulses, centred on the frequency of the CT resonance, for both 3Q excitation and conversion, is considered.[5] As discussed in Section 2.3.2, STs are severely affected by the first-order quadrupolar interaction, and are spread over a large range of frequencies on either side of the CT. Described in a qualitative manner, the strategy of the short pulse is to maximise the range of frequencies affected by the pulse in order to excite the ST resonances. As reported in the literature, it is clear on all plots in Figure 4.1 that the conversion pulse has always approximately a third of the duration of the excitation pulse, for any spin I and coherence p.[222]

RF field strength (ν_1) From Figures 4.1a and 4.1b, it is striking that the efficiency of 3QF is greatly enhanced by using strong RF fields. Both conversion and excitation steps show higher maximum intensities at created shorter pulse durations as ν_1 increases, hence illustrating Vega and Naor's concept.[183] On the other hand, when only a weak RF is available, longer pulses are required for a very limited efficiency.

Quadrupolar coupling constant (C_Q) The impact of varying C_Q on the efficiency of the excitation pulse shown in Figure 4.1c is not as simple to describe, but two regimes are clearly visible. Firstly, as the presence of quadrupolar interaction enables 3QF excitation to be possible with a single pulse, weak or non-existent quadrupolar interactions result in inefficient 3Q excitation. Conversely, when C_Q is large, SOQE become significant and the CT becomes broader while the STs spread over a large range of frequencies. This results in the RF field is too weak to efficiently affect the frequencies of the STs. As a result, there are optimum values for C_Q and ν_1 for which 3Q excitation is most efficient ($C_Q = 0.6$ MHz for $\nu_1 = 100$ kHz on Figure 4.1c) under a particular set of conditions.

[5] Explanation for the behaviour visible in Figure 4.1 for long pulse durations will be given in Section 4.2.

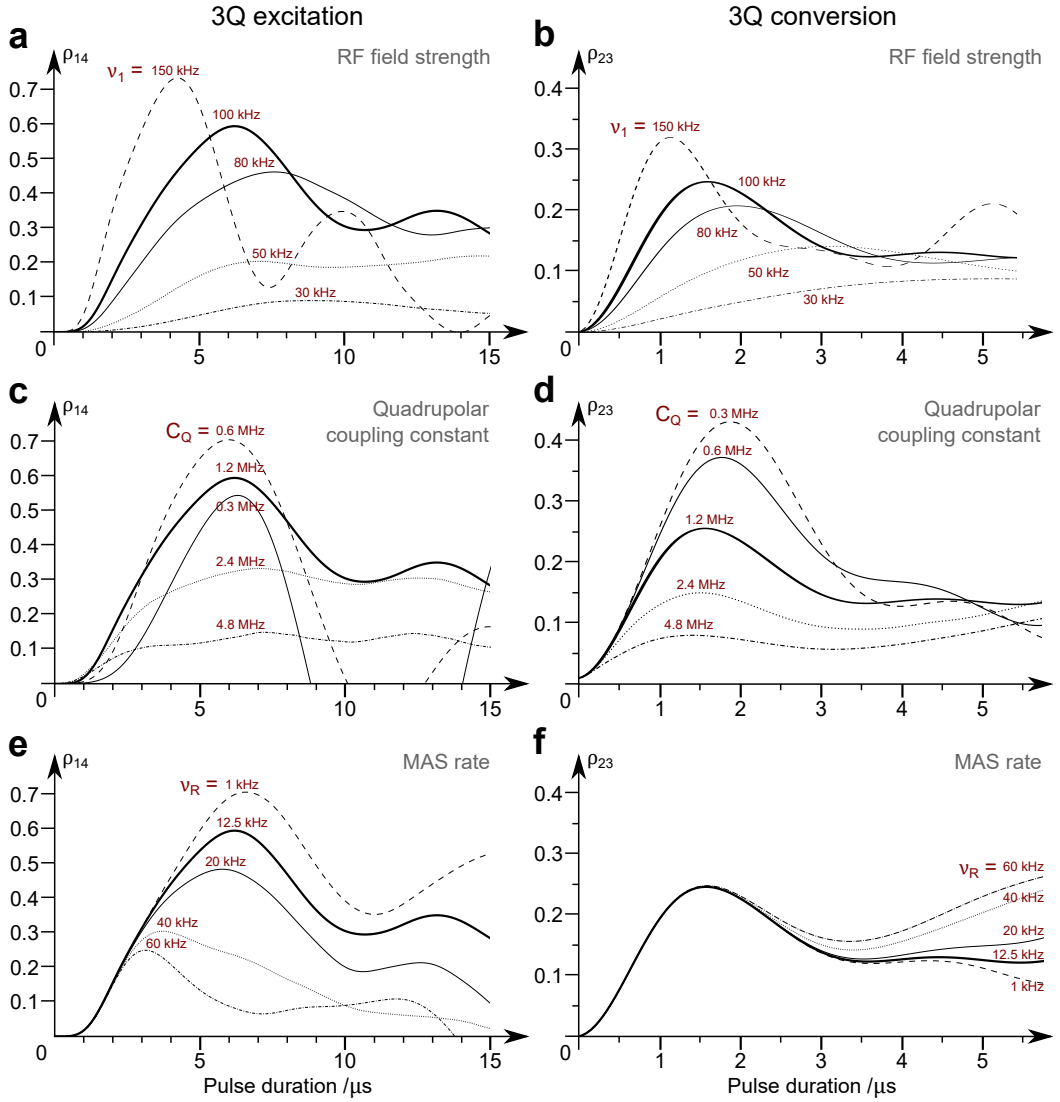

Figure 4.1: *^{23}Na ($I = 3/2$) simulations at B_0 = 14.1 T (ν_0 = 158.7 MHz) showing the effect of **(a,c,e)**: a hard pulse for 3Q excitation by plotting the real part of the density matrix element ρ_{14} starting from population at thermal equilibrium | $\hat{I}_z$, and **(b,d,f)**: a short pulse for 3Q to 1Q conversion by plotting the real part of ρ_{23} ($p = +1$ 1Q CT coherence) when starting from ρ_{14} = 1 (3Q, $p = +3$). **(a,b)**: Simulated for C_Q = 1.2 MHz, ν_R = 12.5 kHz and ν_1 = 150 kHz (dashed line), 100 kHz (solid line), 80 kHz (solid bold line), 50 kHz (dotted line) and 30 kHz (dashed and dotted line). **(c)** and **(d)** Simulated for ν_1 = 100 kHz, ν_R = 12.5 kHz and C_Q = 0.3 MHz (dashed line), 0.6 MHz (solid line), 1.2 MHz (solid bold line), 2.4 MHz (dotted line) and 4.8 MHz (dashed and dotted line). Simulated for ν_1 = 100 kHz, C_Q = 1.2 MHz and ν_R = 1 kHz (dashed line), 12.5 kHz (solid bold line), 20 kHz (solid line), 40 kHz (dotted line), and 60 kHz (dashed and dotted line). The solid bold curve representing 100 kHz, 1.2 MHz and ν_R = 12.5 kHz bold curve are identical in **(a,c,e)**, and in **(b,d,f)**. All simulations were performed for 320 crystallite orientations and 20 γ-angles.*

Unlike the 3Q excitation, the efficiency of the 3Q conversion pulse in Figure 4.1d shows a clear variation: The lower C_Q, the less efficient the 3Q conversion. Finally, this shows that a MQMAS spectrum is not a quantitative technique, as the efficiency of the 3QF step largely depends on C_Q.

MAS rate (ν_R) As discussed in Section 2.2.3, MAS introduces a time dependence into the system Hamiltonian, which may result in unexpected effects for 3Q excitation or conversion. For the case of short pulses, the effect of this time dependency on 3Q conversion and excitation is negligible, as visible in Figures 4.1e and 4.1f, where the efficiencies of neither the 3Q excitation or conversion pulses changes with MAS for pulse durations below 2 µs. However, while the conversion pulse is shorter than 2 µs in Figure 4.1f, and therefore not significantly affected by MAS, the excitation pulse is sufficiently long that effects of MAS rate appear, resulting in a decrease in the amount of 3Q coherence created by 70% between ν_R = 1 and 60 kHz. Furthermore, the duration at which maximum efficiency is obtained changes with the MAS rate. This behaviour is of concern as MQMAS spectra of compounds with significant C_Q values, and therefore, broad CTs, can only be recorded under very fast MAS.[6]

A general conclusion from Figure 4.1 is, under standard experimental conditions,[7] that the conversion step is the major source of sensitivity issues in MQMAS.[283] However, at fast MAS, the efficiency of the excitation become the limiting problem.[264] The overall sensitivity and resolution of a MQMAS spectrum is, in general, increased by setting the MQ evolution period to multiples of the MAS rotor period, enabling spinning sidebands in the indirect dimension to fold on the top of each others.[241, 284, 285]

The sensitivity of 3QF generally remains much lower than STMAS, with signal losses ranging from a factor of 2 to an order of magnitude.[250, 251, 257] Figure 4.1 also illustrates the considerable deterioration in the efficiency of 3QF when only low RF fields are available, as would-be expected for low-γ nuclei, *i.e.*, nuclei with a low gyromagnetic ratio.[8]). Other difficult samples include those where quadrupolar nuclei are at sites of

[6] The optimum MAS rate for maximum MQF efficiency while sufficiently narrowing the CT lineshape can be estimated from Equation (2.3.38).

[7] *e.g.*, for strong RF fields ($\nu_1 \geq 100$ kHz), medium quadrupolar frequency (ν_Q = 0.1 to 1 MHz) and standard MAS rates ($\nu_R \leq 20$ kHz).

[8] There is no objective definition for a low-γ nucleus, but it is often defined (as used for example by MacKen-

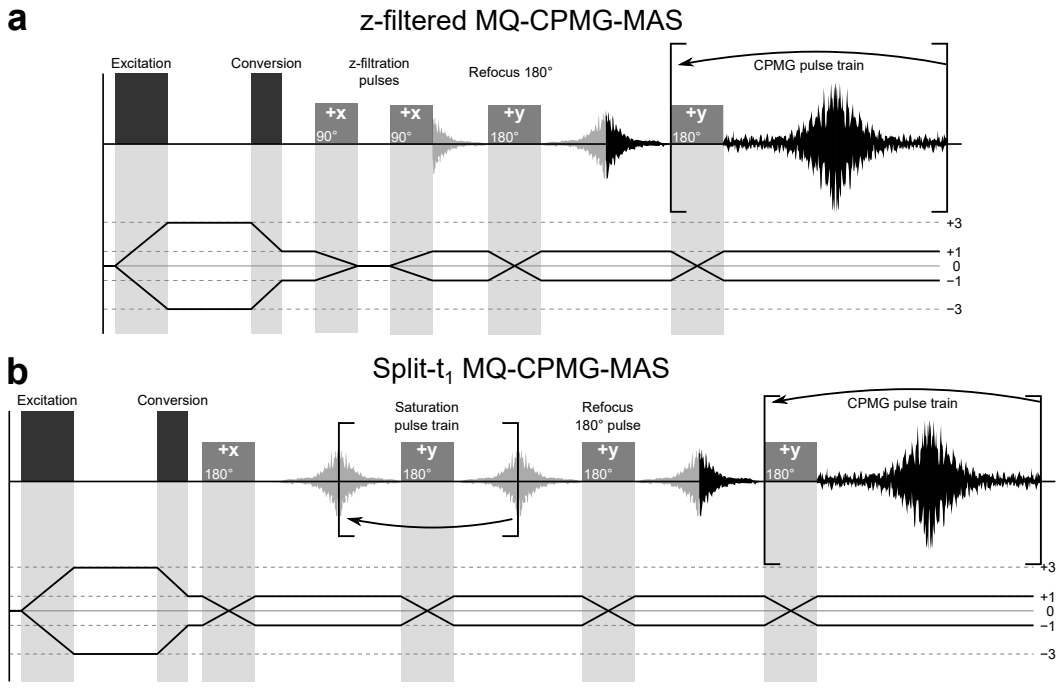

Figure 4.2: *Pulse sequences and CTP of two MQ-CPMG-MAS techniques,* ***(a)****: with z-filter [265] and* ***(b)****: with a 180° pulse saturation train.[164]*

crystallographic asymmetry, imposing large EFG, and hence high C_Q,[33, 231, 286, 287] for which 3QF is less efficient as visible in Figure 4.1. Finally, inherently insensitive nuclei, with low natural abundance, or which exist in diluted amounts in the sample, are also problematic.

4.1.2 The MQ-CPMG-MAS experiment

In the introduction to this chapter, it has been stated that methods exists to improve the overall sensitivity of MQMAS that do not vary the MQF step. Combining MQMAS and CPMG is one of these approaches, with the resolution of MQMAS and the signal intensity improvement of CPMG.

Two MQ-CPMG-MAS pulse sequences proposed in the literature are shown in Figures 4.2a and 4.2b. As the combination of MQMAS and CPMG requires a consideration of the problems each of the two methods, precautions must be taken to obtain spectra with purely-absorptive lineshapes with a limited amount of stimulated echoes. The pulse sequence in Figures 4.2a is perhaps the most common pulse MQ-CPMG-MAS method pre-

zie and Smith [40] as the lowest frequency available for most commercial probes, *e.g.*, that of ^{15}N. That is, $\gamma/2\pi$ = 4.31 MHz.T^{-1}, 40.5 MHz on a B_0 = 9.4 T magnet, or approximately one tenth of the ^{1}H Larmor frequency.

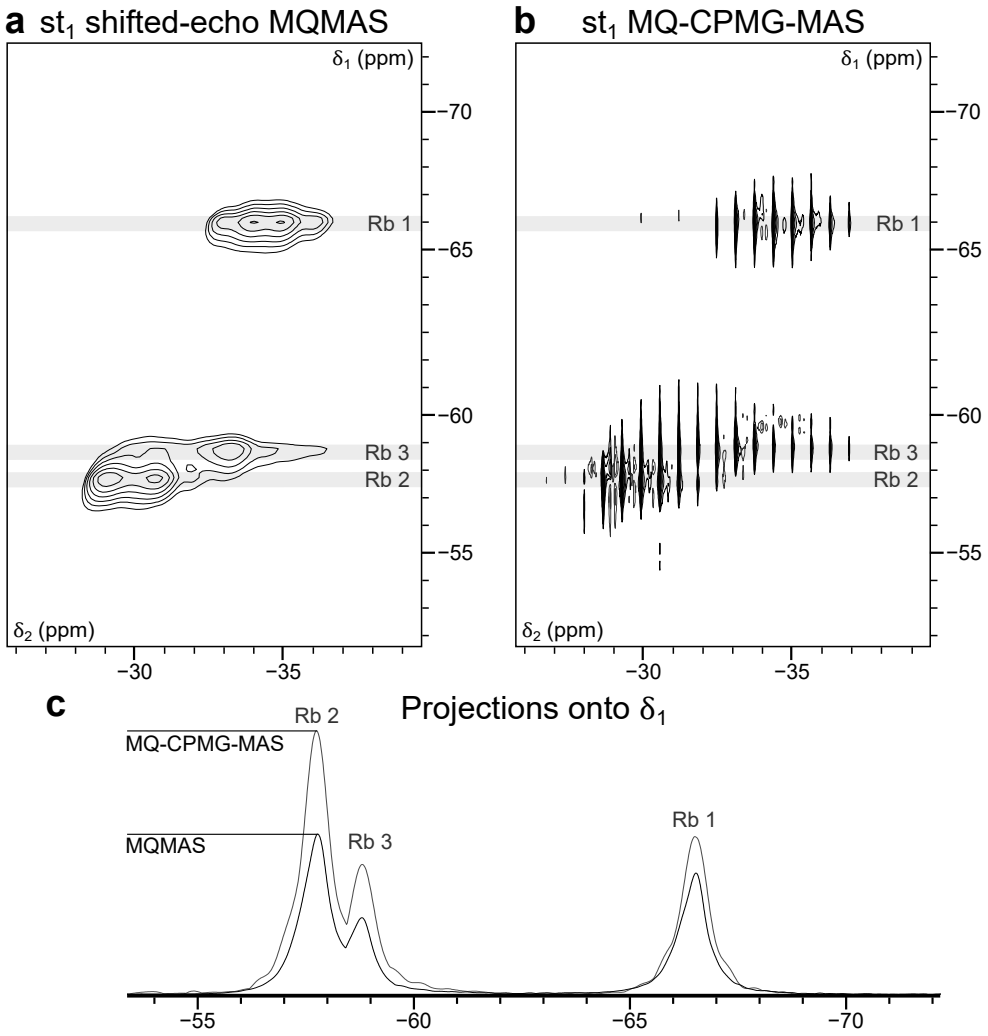

Figure 4.3: *^{87}Rb MQMAS spectra of $RbNO_3$ recorded at B_0 = 14.1 T (ν_0 = 196.40 MHz) and ν_R = 12.5 kHz using **(a)**: the split-₁ shifted-echo pulse sequence (Figure 3.14) and **(b)**: the MQ-CPMG-MAS split-₁ recorded with the pulse sequence (Figure 4.2b). Contour lines in **(a,b)** are identical to allow direct comparison. **(c):** Positive projections of the indirect dimension of **(a,b)**. See the extended caption in Appendix C.3 for further details.*

sented in the literature.[171, 265, 288, 289] It employs a z-filtration step for both these purposes. With this formulation, split-t₁ is only possible for spin $I = 3/2$ nuclei. In the alternative pulse sequence presented in 4.2b, split-t₁ can be implemented for any spin I as it exhibits both $p = +1$ and $p = -1$ 1Q periods (see Figure 3.16). Instead of a z-filtration, this pulse sequence utilises a saturation train of 180° pulses, not phase-cycled relative to each other, to ensure equal the amounts of $p = +1$ and $p = -1$ coherences. 2 or 3 pulses are normally sufficient to ensure this is the case according to Larsen and Farnan.[164] For each of the two pulse sequences, the two coherences are recorded simultaneously, and so sign discrimination must be restored with States [226] or TPPI.[227]

A ^{87}Rb MQ-CPMG-MAS spectrum of ^{87}Rb recorded using the pulse sequence in Figure 4.2b is shown in Figure 4.3b, while Figure 4.3a shows the conventional MQMAS spectrum recorded under identical conditions for comparison. The characteristic spikelet manifold of CPMG spectra (see Section 3.1.2, Figure 3.3b) can be observed in Figure 4.3b. The peak intensity of the spikelets is higher in the MQ-CPMG-MAS spectrum than in the conventional MQMAS spectrum, as visible in Figure 4.2c, although it can be seen that the simulated echoes in the MQ-CPMG-MAS spectrum, as described in Section 3.1.2 for conventional CPMG spectra. As for the regular CPMG experiment, the CPMG echoes can be added to recover the original lineshape. Because CPMG limits the resolution of the lineshapes in the direct dimension, is is usually not possible to separate C_Q from η_Q using lineshape fitting, unless the resolution after summation of the CPMG echoes is sufficient to allow this. However, the information about the number of distinct sites and P_Q are still obtainable from the barycentre of the ridges (see Section 3.3.4 and Appendix E). Larsen and Farnan have argued that their pulse sequence in Figure 4.2b enables the peak intensities in the indirect dimension to be recorded with quantitative intensities.[164]

4.1.3 The SPAM pulse

As shown in 4.1.1, MQ conversion is the limiting step for the sensitivity of MQF experiments under standard conditions,[264] and so many sensitivity improvement strategies have focused on developing more efficient conversion schemes (see Section 4.3). SPAM[9], published by Gan and Kwak,[16] is one of these methods. SPAM is analogue to multiplex phase cycling,[290] where the data corresponding to various CTPs are stored separatly, then added in a constructive way. This last method, however, requires additional data storage space and dedicated acquisition and processing programs. SPAM offers a signal enhancement in MQMAS spectra by enabling multiple CTPs to contribute to the signal.

As illustrated in Figure 4.4a, SPAM is a composite pulse,[291, 292] composed of

- a short, high-power pulse, similar to those described in Section 4.1.1,
- followed by a CT-selective pulse, termed the mixing pulse.

In a MQMAS experiment, the CW conversion pulse is substituted by this pulse scheme. As the elements of SPAM are not phase-cycled relative to one another, all coherence

[9] SPAM: *Soft Pulse Adding Mixing.*

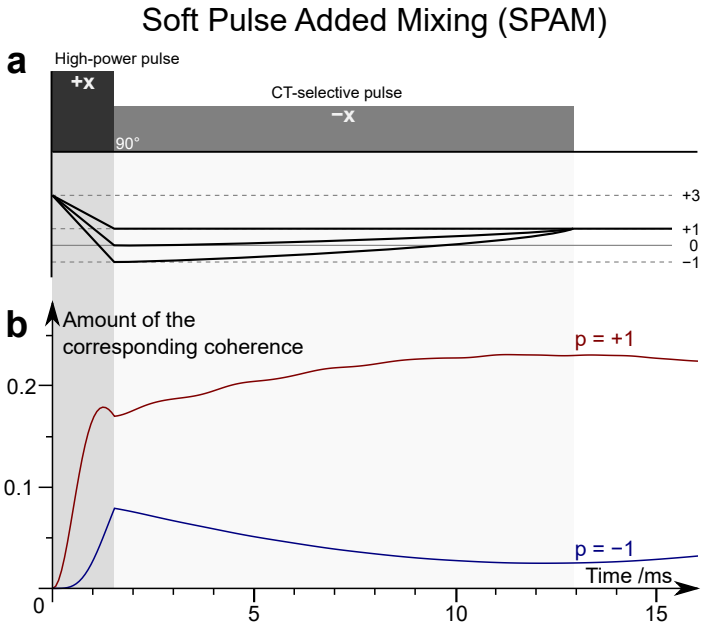

Figure 4.4: ***(a)****: Pulse sequence and CTP of the SPAM conversion pulse for a $p = +3 \rightarrow p = +1$, corresponding to the transfer executed in a split-t_1 shifted-echo experiment (see Figure 3.16).* ***(b)****: Simulation of the evolution of the two CT 1Q coherences $p = +1$ | ρ_{23} (red line) and $p = -1$ | ρ_{32} (blue line) as a function of time during the SPAM pulse in* ***(a)****. Simulated for ^{87}Rb with B_0 = 14.1 T (ν_0 = 196.4 MHz), C_Q = 2 MHz, η_Q = 0, ν_R = 12.5 kHz and ν_1 = 114 kHz for the high-power pulse and 8 kHz for the mixing pulse.*

orders can potentially be created between the two pulses as illustrated in the CTP of Figure 4.4a. The mixing pulse is chosen CT selective, *e.g.*, as discussed in Section 3.3.2, is only effective for the CT. As a result, only the two CT 1Q coherences $p = +1$ and $p = -1$, as well as the population of the CT energy levels, are affected by the mixing pulse, as shown in Figure 4.4. SPAM allows signal enhancement by an optimum mixing of the three pathways into the desired final $p = +1$ (or $p = -1$) coherence. Figure 4.4b shows the evolution of the two CT 1Q coherences as a function of time during the high-power and CT-selective components of the pulse, with an initial $p = +3$ coherence. With the two components of SPAM oppositely phased, the amount of $p = +1$ coherence is clearly enhanced while that of $p = -1$ drops.[10] As investigated by Gan and Kwak, the mixing is most efficient when the mixing pulse provides an effective 90° nutation.[16]

Optimising SPAM requires the experimental optimisation of an effective CT-selective 90° pulse, which is a requirement for both shifted-echo and z-filtered MQMAS experiments for conversion to observable magnetisation. Furthermore, SPAM can be substituted for the conversion pulse in most of the MQMAS methods introduced in

[10] The opposite is observed when the two components of SPAM have the same relative phase.

Section 3.3, as well as in STMAS.[249, 258] In this respect, it is the easiest and most versatile of the improvement methods discussed in this work, as illustrated by the number applications in the literature.[249, 258, 293–296] However, improvements using SPAM have been reported to be, generally speaking, more limited than those offered by modulated pulses (see Section 4.3).[237, 297] Enhancements reported by Gan and Kwak being are 50% for the $p = \pm 3 \rightarrow \mp 1$ transfer, and 30% for the $p = \pm 3 \rightarrow \pm 1$ transfer. The maximum efficiency of the mixing pulse is always when it achieves a nutation of 90°. However, starting from a short pulse optimised for the $p = \pm 3$ to $p = \pm 1$ transfer as in Section 4.1.1, further enhancement can be obtained from experimentally increasing the duration of the high-power pulse, as the optimum pulse durations for $p = \pm 3 \rightarrow p = \pm 1$ and $p = \pm 3 \rightarrow p = \mp 1$ are different.[222] As SPAM mixes $p = +1$ and $p = -1$ coherences, the best high-power pulse for SPAM achieves an effective nutation between the optimum duration for the two transfers. This imposes an extra optimisation step that requires MQF to obtain the maximum improvement.

Owing to its ease of implementation and its similar formulation to modulated pulses, the performances of SPAM will be investigated along with that of modulated pulses in Section 5.3.

4.2 SL-based MQMAS methods

It has been discussed in Section 4.1 and shown in Figure 4.1 that the sensitivity-limiting step of the conventional MQMAS experiment in the fast MAS limit clearly stems from the excitation pulse. It has been discussed in Section 3.2.1 that, during a SL, coherence exchange occurs during sample rotation. This phenomenon can be used to excite and convert MQ coherences, and therefore be exploited to perform MQMAS. In comparison to the MQMAS with single conversion and excitation pulses, these methods can be very attractive in the fast MAS regime. However, many of these methods result in distorted lineshapes.

4.2.1 The RIACT experiment

RIACT[11] is a technique that exploits the adiabatic interconversion of the quantum states $c_{\pm}$ and $t_{\pm}$ during a SL under MAS, as described in Section 3.2.1 to create 3Q coherence

[11] RIACT: *Rotor-Induced Adiabatic Coherence Transfer*

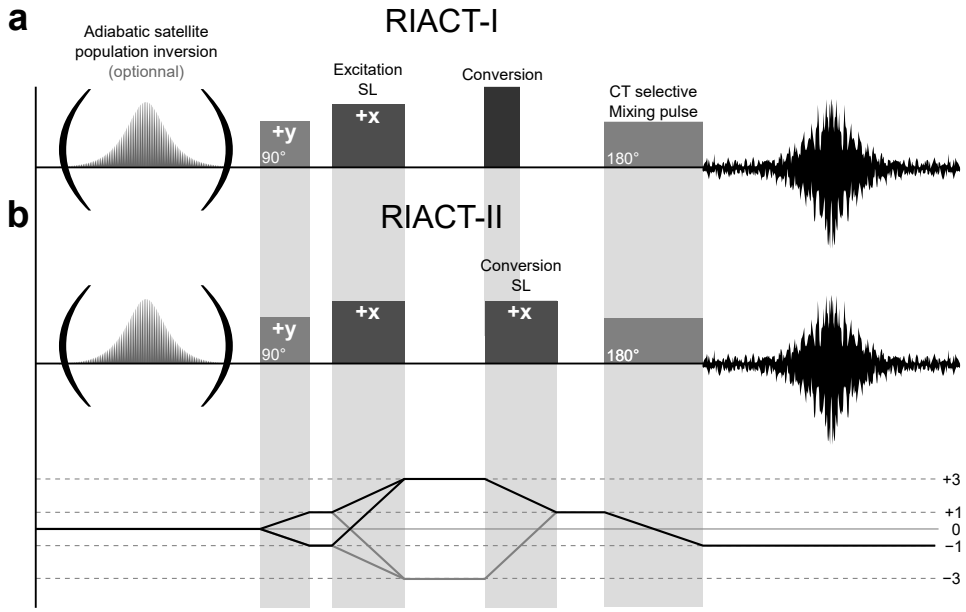

Figure 4.5: *Pulse sequences and CTPs for **(a)**: RIACT-I and **(b)**: RIACT-II.*

from 1Q coherence, or vice versa. The concept of the creation of 3Q coherence by SL was theoretically described by Vega and Naor,[182, 183], and later investigated in more details in a dedicated article.[181] The RIACT experiment was originally published by Wu *et al.*, showing direct proof of 3Q coherence being created in this fashion.[22]

Pulse sequences for the two RIACT experiments are presented in Figure 4.5. A distinction was made between RIACT-I (Figure 4.5a), where only the excitation pulse in composed of a SL while the conversion is carried out by a hard pulse, and RIACT-II (Figure 4.5b) where both excitation and conversions are carried out with SL. The MQ excitation step is composed of the same pulses as the SL experiment shown in Figure 3.6a: an initial CT-selective 90° pulse to move the CT magnetisation into the transverse plane, followed by a SL, maintaining the magnetisation along an axis and allowing population and coherence exchange.

The technique is based on the same phenomenon that enables the populations of the quantum-states $c_{\pm}$ and $t_{\pm}$, eigenstates of the Hamiltonian in Σ_V (see Section 3.2.1), to be interconverted when $\Omega_Q(t)$ changes sign. Recalling the expression for $c_{\pm}$ and $t_{\pm}$ in Σ_V in Equation (3.2.7)

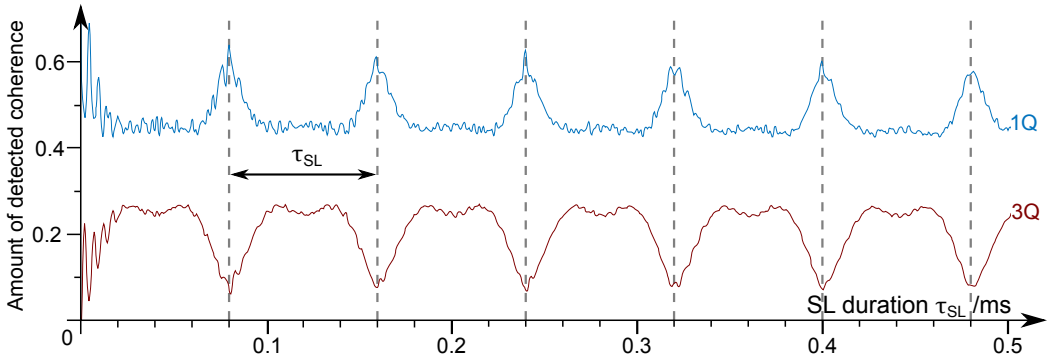

Figure 4.6: *Simulation showing the evolution of 1Q | real part of ρ_{23} (blue line) and 3Q | real part of ρ_{14} (red line) as a function of time during SL, on ^{23}Na ($I = 3/2$) with B_0 = 14.1 T (ν_0 = 158.8 MHz) for ν_1 = 100 kHz, ν_R = 12.5 kHz, C_Q = 1 MHz (ν_Q = 0.25 MHz) and η_Q = 0, for 320 crystallite orientations and 20 γ-angles.*

$$c_{\pm} = \frac{1}{\sqrt{2}}\left(|+3/2,+1/2\rangle \pm |+3/2,-1/2\rangle\right) \tag{4.2.1a}$$

$$t_{\pm} = \frac{1}{\sqrt{2}}\left(|+3/2,+3/2\rangle \pm |+3/2,-3/2\rangle\right) \quad , \tag{4.2.1b}$$

it is clear that they give rise to, respectively, CT 1Q coherences[12] and 3Q coherences. If starting the SL from an initial density matrix $\hat{\rho}(t_0) = \hat{I}_x^{\mathrm{CT}}$, a coherence transfer will occur twice per rotor period following the cycle

$$\hat{I}_x^{\mathrm{CT}} \rightarrow \hat{I}_x^{3\mathrm{Q}} \rightarrow \hat{I}_x^{\mathrm{CT}} \ldots \tag{4.2.2}$$

in the adiabatic regime (see Equation (3.2.8)). This interconversion is illustrated by the simulation shown in Figure 4.6. As established by Wu *et al.* and shown on Figure 4.6, the maximum 3Q coherence creation from initial 1Q coherence, or 1Q created from initial 3Q coherence, is obtained for a SL duration of

$$\tau_P = \frac{\tau_R}{4} \quad . \tag{4.2.3}$$

Therefore, despite the apparent complexity of this method, optimising RIACT is in fact very straightforward as the excitation and conversion SL have a fixed duration of $\tau_R/4$, while the only other requirement is an optimised CT-selective 90° pulse.

As originally reported,[22] RIACT was not meant to improve the sensitivity of MQMAS but to improve the quantitativity of MQMAS for spins $I = 3/2$. The efficiencies of short 3Q excitation and conversion pulses have been shown in Section 4.1.1 to largely depend

[12] Here, ST coherence is not created as the initial 90° pulse is chosen to be CT selective.

on the quadrupolar parameters, resulting in observed intensities in the isotropic dimension of MQMAS spectra that do not reflect the actual proportion of the crystallographic sites. As investigated by Wu *et al.*,[22] the efficiency of SL is less dependent on the quadrupolar parameters than two short pulses, reducing the differences in excitation/-conversion efficiencies between sites with different quadrupolar parameters. The same article reports that RIACT is also able to enhance the sensitivity of MQMAS relative to the short-pulse approach for some C_Q values. However, and unlike the two-pulse method, RIACT can benefit from initial adiabatic inversion of the satellite populations, performed using the adiabatic pulses that will be introduced in Chapter 7.[298–300] For this reason, the use of RIACT as a signal improvement technique for MQMAS will be investigated in Section 7.2.3.

RIACT does present several drawbacks compared to the conventional MQMAS:

- Even though the SL is less influenced by the quadrupolar parameters for spins $I = 3/2$ nuclei, consideration of the efficiency of the SL should be undertaken to ensure that of RIACT.
- For spins $I = 5/2$ nuclei, in the adiabatic regime, only 5Q and 1Q coherences are adiabatically converted,[13] while the central 3Q coherence is only being inverted.[17, 115] By extension, RIACT can only be employed for 3QMAS on spins $I = 3/2$, 5QMAS on spins $I = 5/2$, *etc.* ...
- The SL can only create 1Q coherence, so cannot be used in the standard z-filtered MQMAS experiment in Figure 3.13a, and the alternative pulse sequence in Figure 3.13b is required.
- Another important limitation of the technique is its offset dependence. Significant[14] off-resonance effects cause $c_\pm$ and $t_\pm$ not to be eigenstates of the Hamiltonian, hence reducing the efficiency of the 1Q-3Q interconversion.[22] The eigenstates remain as $c_\pm$ and $t_\pm$ if the frequency difference between t_+ and t_- stays superior than the offset frequency, *e.g.*,

$$\Delta\nu_0 \leq \frac{\nu_1^3}{6C_Q^2}\left(2I(2I+1)\right)^2 \quad . \tag{4.2.4}$$

- Finally, increased lineshape distortions have been reported in RIACT spectra in the literature.[300, 302–304]

[13] Non-adiabatic effects may result in 3Q being created and observed on spins $I = 5/2$, although with a limited sensitivity.[301]

[14] Estimated by Wu *et al.* to a maximum of $\Delta\omega_0$ = ±6 kHz with ν_1 = 80 kHz for ^{23}Na in $NaNO_3$.[22]

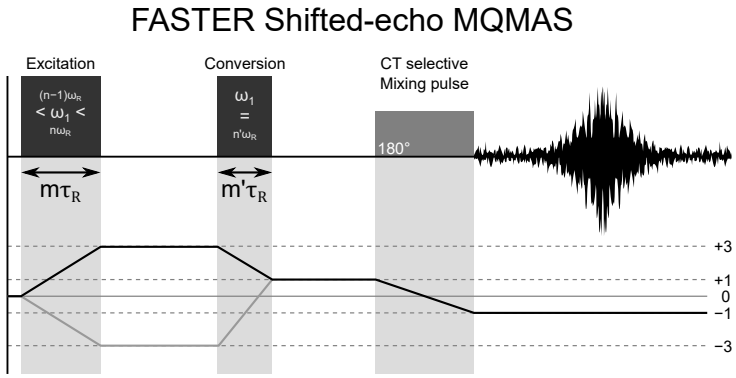

Figure 4.7: *Pulse sequence and CTP of the FASTER shifted-echo MQMAS method, with* $\{n, n', m, m'\} \in \mathbb{N}^{\star 4}$.

4.2.2 The FASTER experiment

FASTER[15] is an alternative approach introduced to obtain MQMAS spectra with improved SNR, particularly at fast MAS or for samples with high C_Q. This approach relies on a resonance effect between the RF field and MAS, first reported by Vosegaard *et al.*,[21] and later described in more detail theoretically.[305, 306]

The pulse sequence for a FASTER shifted-echo MQMAS experiment is shown in Figure 4.7. As with RIACT, FASTER features substitute pulse schemes for both the 3Q excitation and conversion. However, it has been shown in Section 4.1.1 that, while the conversion pulse is the step limiting the sensitivity of the MQF or MQMAS experiment, the limiting step becomes the excitation pulse at fast MAS (see Figure 4.1e). Therefore, the FASTER experiment is particularly interesting for enhancing the efficiency of the 3Q excitation. However, unlike RIACT, this method can be adapted for any transfer, and on any spin.[307] The FASTER pulse sequence is not fundamentally different from the standard shifted-echo MQMAS experiments shown in Figure 3.14, with the main difference being the pulse durations t_p and the applied RF field strengths ν_1, both related to the MAS rate ν_R or the rotor period τ_R by a set of four integer numbers denoted n, n', m and m' as shown in Figure 4.7. As a result of this, optimising FASTER involves finding suitable values for these four numbers, with suitable conditions for a given transfer being referred to as a RR[16] condition.

Finding RR conditions for the $\hat{I}_z \rightarrow p = \pm 3$ transfer can be achieved experimentally or by using numerical simulations, where the amount of 3Q created by a pulse from initial population state is determined for a realistic range of RF field strengths, as a function of

[15] FASTER: *FAst Spinning gives Transfer Enhancement at Rotary resonance*
[16] RR: *Rotary Resonance*

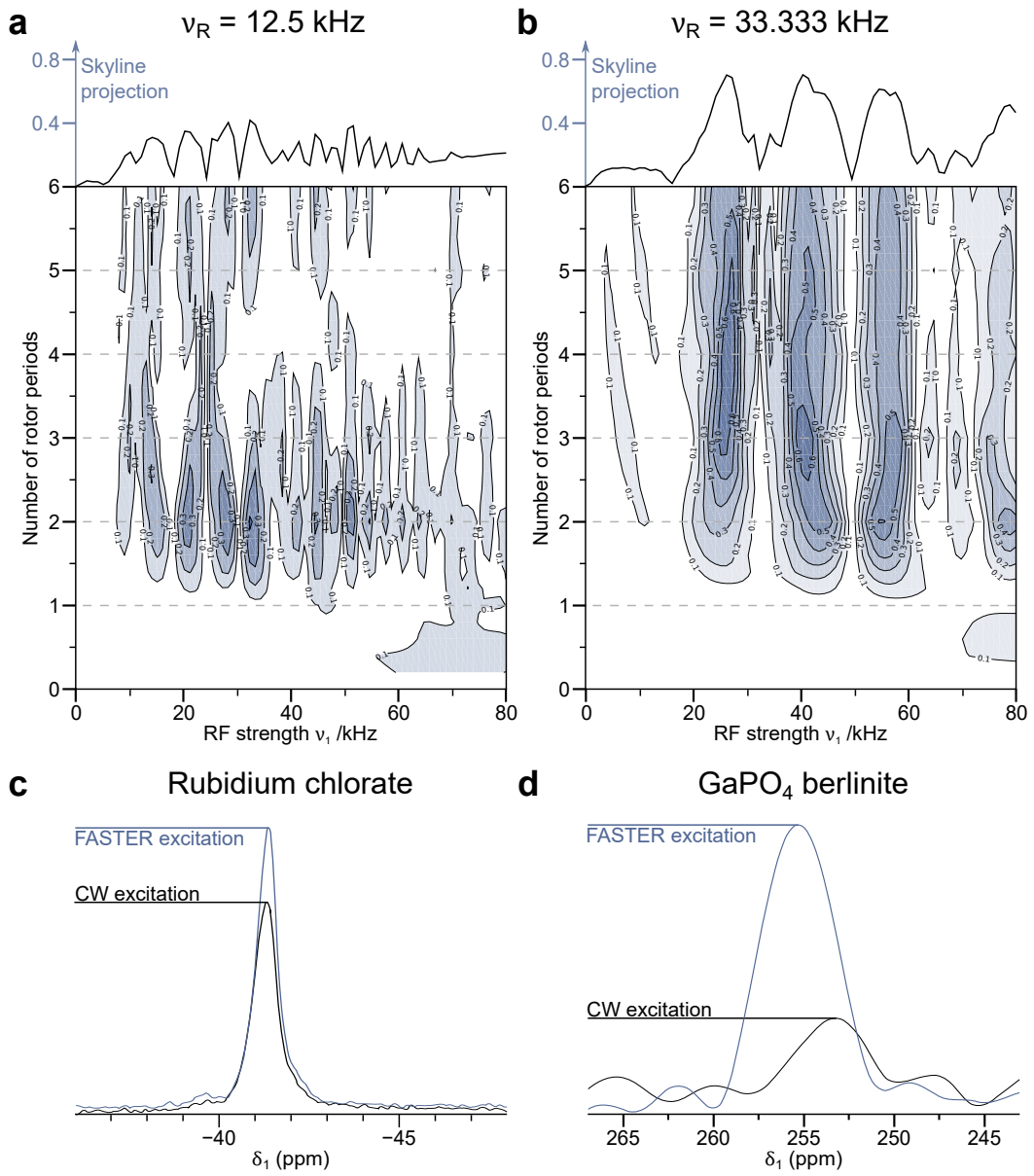

Figure 4.8: ***(a,b)****: Contour plots showing the amount of 3Q coherence | real part of ρ_{14} for ^{87}Rb ($I = 3/2$) during pulses applied at different RF field strengths as a function of the pulse duration given in number of rotor periods. Simulations were performed at B_0 = 14.1 T (ν_0 = 196.4 kHz) and used the quadrupolar parameters of $RbClO_4$ (C_Q = 3.2 MHz and η_Q = 0.16), for* ***(a)****: ν_R = 12.5 kHz and* ***(b)****: ν_R = 33.333 kHz.* ***(c,d)****: Projections of the indirect dimension of split-t_1 shifted-echo MQMAS spectra.* ***(c)****: ^{87}Rb spectra of $RbClO_4$ for B_0 = 14.1 T (ν_0 = 196.4 kHz), ν_R = 33.333 kHz, and ν_1 = 138.2 kHz for CW excitation and ν_1 = 55 kHz for FASTER excitation.* ***(d)****: ^{71}Ga spectra of $GaPO_4$ berlinite, plotted in magnitude, for B_0 = 14.1 T (ν_0 = 156.4 MHz), ν_R = 33.333 kHz, and ν_1 = 134 kHz for CW excitation and ν_1 = 105 kHz for FASTER excitation. See the extended caption in Appendix C.3 for further details.*

ν_R = 12.5 kHz	ν_R = 33.333 kHz
18 conditions found	13 conditions found
Condition no 1	Condition no 1
************************************	************************************
Intensity: 0.4185	Intensity: 0.70326
RF Strength: 33000 +– 2278 Hz	RF Strength: 41000 +– 3201 Hz
Duration: 156 us	Duration: 90 us
Duration in number of rotor periods: 1.95	Duration in number of rotor periods: 3
Condition no 2	Condition no 2
************************************	************************************
Intensity: 0.40389	Intensity: 0.70185
RF Strength: 29000 +– 1551 Hz	RF Strength: 27000 +– 2179 Hz
Duration: 160 us	Duration: 116.5012 us
Duration in number of rotor periods: 2	Duration in number of rotor periods: 3.8833
Condition no 3	Condition no 3
************************************	************************************
Intensity: 0.38324	Intensity: 0.61296
RF Strength: 52000 +– 1020 Hz	RF Strength: 55000 +– 3633 Hz
Duration: 160 us	Duration: 60 us
Duration in number of rotor periods: 2	Duration in number of rotor periods: 2

Table 4.1: *Output from simulations showing the three most intense RR conditions for ^{87}Rb ($I = 3/2$) for B_0 = 14.1 T (ν_0 = 196.4 kHz), and for ν_R = 12.5 kHz (left) and ν_R = 33.3 kHz, simulated with steps of 1 kHz from ν_1 = 1 to 80 kHz, using the quadrupolar parameters of $RbClO_4$ (C_Q = 3.2 MHz and η_Q = 0.16). The quantity referred to as the "intensity" corresponds to the amount of 3Q | real part of ρ_{14}, created from initial population state $\hat{I}_z$.*

the length of the pulse, with durations of multiples of the rotor period. Such simulations, presented under the form of contour diagrams, are presented in Figure 4.8a and 4.8b, for ^{87}Rb ($I = 3/2$) with quadrupolar parameters corresponding to those of $RbClO_4$, and for ν_R = 12.5 and 33.333 kHz, respectively. It is also possible to search for the maxima from these plots, and return a list of RR conditions sorted by amount of 3Q created. Examples are given in Table 4.1, for the two contour plots shown in Figures 4.8a and 4.8b. For comparison, the amount of 3Q created after a CW excitation at the maximum RF field strength available in experiment, ν_1 = 138.2 kHz, is 0.385. As observed from Figures 4.8a and 4.8b, there are more RR conditions at ν_R = 12.5 kHz, but none of them are significantly more efficient than CW excitation. Conversely, the theoretical improvement for the same spin system with ν_R = 33.333 kHz is more significant, with ratios reaching ×1.8 for the first RR condition. Furthermore, the precision with which the RF field strength ν_1 can be determined from the width of each of the RR conditions presented in Figures 4.8a and 4.8b. This relates to the MAS rate according to

$$\Delta\nu_1 = \pm\frac{\nu_R}{10} \quad . \tag{4.2.5}$$

Equation (4.2.5) shows the precision required on ν_1 decreases as ν_R increases. Even

so, a precision of ±1.25 kHz is difficult to achieve in practice, but a precision of ±6 kHz is much more feasible, showing that FASTER becomes increasingly attractive as ν_R increases.

Figures 4.8c and 4.8d show projections of MQMAS spectra recorded with FASTER used for 3Q excitation. In Figure 4.8c, the improvement observed between the CW and FASTER excitation is approximately ×1.35. Figure 4.8d has been performed for ^{71}Ga ($I = 3/2$) for $GaPO_4$ berlinite, which possesses a unique site with a large C_Q of 8.8 MHz, thus requiring fast MAS. Under these conditions, both the excitation and conversion pulses are very inefficient, making this sample one of the hardest MQMAS spectra to acquire in this work. Improvement of the conversion efficiency will be addressed in Section 6.1.1. Here, with FASTER, a theoretical improvement of the 3Q excitation of ×2.6 is predicted, and an experimental improvement of ×3.0 is observed in Figure 4.8d.

Even if an enhancement of the 3Q excitation efficiency has been observed with FASTER, many questions remain concerning the prediction of RR conditions. Experimentally, RR conditions often prove not to match well with those predicted using simulations, as in Figures 4.1a and 4.1b and Table 4.1, with improvement minor or non-existent on samples less challenging than $GaPO_4$ berlinite in ^{71}Ga. For example, the ^{87}Rb FASTER-3QF spectrum of $RbClO_4$ in Figure 4.8c has been obtained with the third RR condition listed in Table 4.1, while the first RR condition resulted in a decrease in signal intensity. Preliminary investigations provide insight into the reason for this discrepancies. It can be seen that there is a reasonable tolerance to variations of the RF field for FASTER, and also to changes of C_Q, but there is some sensitivity to changes in the offset $\Delta\omega_0$. Further investigations must be undertaken to unravel those last issues. However, this approach appears to be useful for samples with sites which exhibits a large quadrupolar interaction.

4.3 Approaches based on modulated pulses

The use of modulated pulses for signal improvement of MQMAS is perhaps the most popular method used to date. As instructed in Section 4.1.1, the MQ conversion pulse limits the sensitivity of MQMAS under standard conditions. Substituting the CW conversion pulse by a modulated pulse is an efficient, robust approach that is easy to implement, and typically improves signal by a ratio of ×2-3 relative to the two-pulse MQMAS experiment.[115]

Applying a modulation to a pulse consists of applying a shape so the pulse changes frequency with the application time, in order to perform adiabatic passages, as described in Appendix F using the vector model. One of the earliest examples of adiabatic pulses applied on quadrupolar nuclei was that of Vega and Naor.[183] Subsequently, Haase and Conradi showed that the population difference in the CT energy levels can be increased by manipulation of the population of the ST energy levels with modulated pulses, trough which the larger population difference in the 3Q energy levels can be moved to the CT levels, producing a signal improvement in MAS spectra (see Section 7.1).[19, 20, 308–310] The same method have been shown by Kentgens and Verhagen to work similarly to improve the transfer efficiency of MQ coherence to CT-1Q coherence,[311] which has subsequently led to the development of a number of modulated pulses for MQMAS experiments, as discussed in this section.

4.3.1 Inversion/saturation of the ST populations/coherences

To understand how modulated pulses can be used to improve the efficiency of MQ conversion, it is necessary to consider background theory. The expression of the Hamiltonian for a quadrupolar spin I submitted to a first-order truncated quadrupolar interaction (see Equation (2.3.20)), and a RF pulse field in Σ_{lab} is given by

$$\hat{H} = \hat{H}_z + \hat{H}_Q^{(1)} + \hat{H}_{\text{RF}} \quad . \tag{4.3.1}$$

In Sections 1.1.3 and 1.2.3, it has been seen that, if an RF pulse is applied off resonance, a term $\Delta\omega_0\hat{I}_z$ appears in the expression of the Hamiltonian in Equation (4.3.1), when it is written in Σ_{rot}. This gives

$$\hat{H}_\rho = \hat{H}_Q^{(1)} + \omega_1\hat{I}_x + \Delta\omega_0\hat{I}_z \quad , \tag{4.3.2}$$

when an RF field is applied along the $+x$ direction. A similar effect can be obtained by the application of a modulation of the RF pulse. A modulation is characterised by a (time-dependent) modulation frequency, $\omega_m(t)$, associated with a modulation phase $\phi_m(t)$ given by

$$\phi_m(t - t_0) = \int_{t_0}^{t} \omega_m(\tau).d\tau \quad . \tag{4.3.3}$$

This modulation is applied by a modification of the shape of the RF pulse, executing a further oscillation determined by the modulation frequency ω_m, resulting in the expres-

sion of $\hat{H}_{\mathrm{RF}}$ in Σ_{lab} as

$$\hat{H}_{\mathrm{RF}} = \omega_1 \hat{I}_x \cos\left(\omega_{\mathrm{RF}} t\right) . \exp\left(i\phi_m(t)\right) \quad , \tag{4.3.4}$$

and giving the Hamiltonian in Equation (4.3.2), written in Σ_{rot},

$$\hat{H}_\rho = \hat{H}_Q^{(1)} + \omega_1 \hat{I}_x + \left(\omega_m(t) + \Delta\omega_0\right) \hat{I}_z \quad . \tag{4.3.5}$$

The modulation applied in Equation (4.3.4) is designated as a FM[17], as only the phase, and not the amplitude, of the RF pulse is affected. Effectively, the RF Hamiltonian described in Equations (4.3.4) and (4.3.5) is identical to a pulse applied at an offset $\Delta\omega_0 + \omega_m(t)$. However, applying a FM to the RF field is a convenient way to produce a pulse with a time-dependant offset $\Delta\omega_0 + \omega_m(t)$, a requirement for adiabatic pulses as instructed in Appendix F. $\Delta\omega_0$ then becomes a "reference" offset, relative to which the modulation is applied. For a FM pulse written as in Equation (4.3.4), a SFS[18] is enabled when $\omega_m(t)$ is varied with time, affecting only one side of the carrier frequency ν_{RF}. Figure 4.9a shows how the energies of the eigenstates in Σ_{rot} of the Hamiltonian in Equation (4.3.5) are affected by ω_m, for the case where $\omega_1 \ll \Omega_Q$. As shown, if a SFS is applied with an offset sweeping from far below $-\Omega_Q$ to far above $+\Omega_Q$, and if the SFS is sufficiently slow for all the transfer to be adiabatic (see Equation (4.3.15)), a full, adiabatic inversion of the populations of all of the energy levels can be observed in Σ_{lab}.

For quadrupolar nuclei, it has been shown in Section 2.3.3 that the lineshape of the STs is symmetrical, so it is desirable to apply a pulse simultaneously at two offsets, symmetrical to the reference offset $\Delta\omega_0$. This results in a RF Hamiltonian in Σ_{lab} of

$$\hat{H}_{\mathrm{RF}} = \omega_1 \hat{I}_x \cos\left(\omega_{\mathrm{RF}} t\right) . \frac{1}{2} \left(\exp\left(i\phi_m(t)\right) + \exp\left(-i\phi_m(t)\right)\right) \tag{4.3.6a}$$

$$= \omega_1 \hat{I}_x \cos\left(\omega_{\mathrm{RF}} t\right) . \cos\phi_m(t) \quad . \tag{4.3.6b}$$

The application of two simultaneous offsets in Equation (4.3.6) turns the FM in Equation (4.3.4) into an AM[19], as the sweep is applied symmetrically relative to $\Delta\omega_0$ and the STs are affected in an identical manner. The sweep created by the variation of ω_m with time of Equation (4.3.6) is thus denoted a DFS[20]. The application of a sweep at two different offsets is possible, and will result in a RF pulse exhibiting both AM and FM. How-

[17] FM: *Frequency Modulation*
[18] SFS: *Single-Frequency Sweep*
[19] AM: *Amplitude Modulation*
[20] DFS: *Double Frequency Sweep*

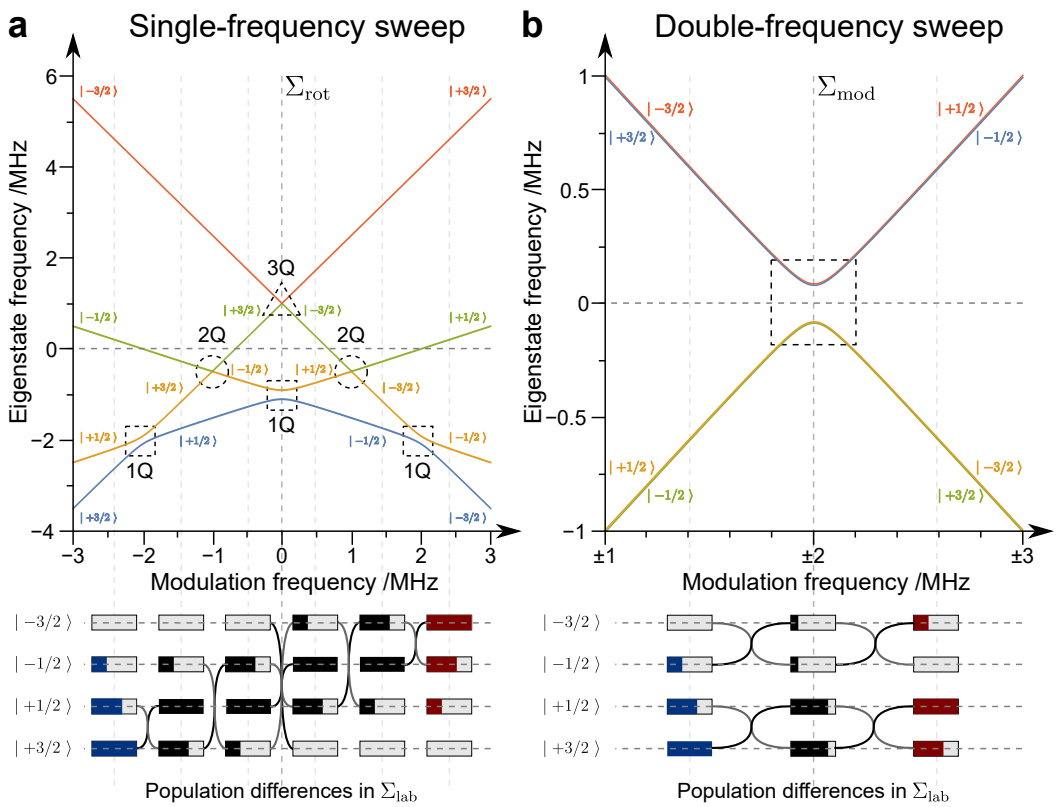

Figure 4.9: *Plots showing the evolution of the frequency of the quantum states of a spin $I = 3/2$ nucleus in the static case for ν_1 = 100 kHz and $\Delta\nu_0$ = 0, for a unique crystallite orientation $\alpha_{\mathrm{LP}} = \beta_{\mathrm{LP}} = 0$ such that $\Omega_Q(\alpha_{\mathrm{LP}}, \beta_{\mathrm{LP}})/2\pi = \omega_Q/2\pi$ = 1 MHz (e.g., in the limit $\omega_Q \gg \omega_1$) and the evolution of the populations differences in Σ_{lab} at different times during the sweep. Only first-order quadrupolar interaction is considered.* ***(a)****: Energy levels and populations during a single-frequency sweep as a function of the offset frequency in Σ_{rot}, obtained from the diagonalisation of Equation* (4.3.5). ***(b)****: Energy levels and populations during a double-frequency sweep as a function of the sweep frequency $\omega_m/2\pi$ in Σ_{mod}, obtained from the diagonalisation of Equation* (4.3.9)*. Plots inspired by [115, 309, 312].*

ever, it is clear that this is not necessary for quadrupolar nuclei owing to the symmetry of the ST lineshapes.

To understand the effect of DFS on the populations of the energy levels for a spin $I = 3/2$ nucleus, the theoretical description of Vega *et al.* is used here.[183] Re-expressing the Hamiltonian in Equation (4.3.1) using fictitious spin $I = 1/2$ operators (see Equation (3.2.11)), written in Σ_{rot} with $\Delta\omega_0$ = 0, and in the limit $\Omega_Q \ll \omega_1$, gives [115, 183, 312]

$$\hat{H}_\rho = 2\Omega_Q \left(\hat{I}_z^{1\text{-}2} - \hat{I}_z^{3\text{-}4}\right) + \omega_1 \cos\omega_m(t) \left(\sqrt{3}\hat{I}_y^{1\text{-}2} + 2\hat{I}_y^{2\text{-}3} + \sqrt{3}\hat{I}_y^{3\text{-}4}\right) \quad . \tag{4.3.7}$$

The time dependence of the RF field term in Equation (4.3.7) is eliminated by the transformation

$$U(t) = \exp\left(-i\omega_m(t)\left(\hat{I}_z^{1\text{-}2} - \hat{I}_z^{3\text{-}4}\right)\right) \quad , \tag{4.3.8}$$

transforming the Hamiltonian into the so-called modulation frame Σ_{mod}. The Hamiltonian written in Σ_{mod} is given by

$$\hat{H}_{\text{mod}} = \Delta\Omega_Q\left(\hat{I}_z^{1\text{-}2} - \hat{I}_z^{3\text{-}4}\right) + \frac{\sqrt{3}}{2}\omega_1\left(\hat{I}_x^{1\text{-}2} + \hat{I}_z^{3\text{-}4}\right) \quad , \tag{4.3.9}$$

where

$$\Delta\Omega_Q = 2\Omega_Q - \omega_m(t) \quad . \tag{4.3.10}$$

It should be noted that Equation (4.3.9) is time independent only in the static case for a constant $\omega_m(t)$. Ω_Q becomes time dependent under MAS as shown in Equation (2.3.29), and so does $\Delta\Omega_Q$ in Equation (4.3.10). Figure 4.9b shows the effect of ω_m on the energies of the eigenstates represented in Σ_{mod} of the Hamiltonian. As for a SFS, if the sweep is sufficiently slow for the transition to be adiabatic (see Equation (4.3.15)), the populations of the states $|3/2, \pm 3/2\rangle$ and $|3/2, \pm 1/2\rangle$ will be adiabatically inverted. A DFS pulse fulfilling the adiabaticity condition produces an effective, adiabatic, ST-selective 180° pulse.

For the purpose of signal improvement in MQMAS experiments, the transfer of most interest concerns the ”amount of 1Q coherence” created from initial 3Q coherence. The application of DFS and other methods for population inversion/saturation will be detailed in Chapter 7, but the mechanism by which the 3Q to 1Q transfer can be enhanced is identical for all the approaches. An initial pure 3Q coherence can be represented by a matrix $\hat{\rho} \propto \hat{O}_{j,i}$, as phase cycling ensures that only 3Q is present at the start of the conversion pulse (see Appendix D). The initial (symmetrical) $p = +3$ coherence and the desired $p = +1$ CT 1Q coherence are given by the density matrix elements ρ_{23} and ρ_{14} for spins $I = 3/2$ nuclei, ρ_{34} and ρ_{25} on spins $I = 5/2$ nuclei, *etc.* It should be noted that, in the pure state case defined in Section 1.2.2, the density matrix elements ρ_{ij} and ρ_{ji} are complex conjugates of each other, and so have same amplitudes and real parts. In matrix form, an adiabatic inversion of the 3Q coherence is represented by [115, 183, 312]

$$\begin{bmatrix} 0 & 0 & 0 & 1 \\ 0 & 0 & 0 & 0 \\ 0 & 0 & 0 & 0 \\ 1 & 0 & 0 & 0 \end{bmatrix} \xrightarrow[\text{of the STs}]{\text{Adiabatic inversion}} \begin{bmatrix} 0 & 0 & 0 & 0 \\ 0 & 0 & 1 & 0 \\ 0 & 1 & 0 & 0 \\ 0 & 0 & 0 & 0 \end{bmatrix} \quad . \tag{4.3.11}$$

However, Equation (4.3.11) shows an ideal case, with $\Omega_Q \gg \omega_1$ in a powdered solid.

There are crystallite orientations for which the condition $\Omega_Q \gg \omega_1$ is not fulfilled which can introduce non-adiabatic effects. As a result, another mechanism have been described, called saturation, where

$$\begin{bmatrix} 0 & 0 & 0 & 1 \\ 0 & 0 & 0 & 0 \\ 0 & 0 & 0 & 0 \\ 1 & 0 & 0 & 0 \end{bmatrix} \xrightarrow[\text{of the STs}]{\text{Saturation}} \begin{bmatrix} 0 & 0 & 0 & 1/2 \\ 0 & 0 & 1/2 & 0 \\ 0 & 1/2 & 0 & 0 \\ 1/2 & 0 & 0 & 0 \end{bmatrix} \quad . \tag{4.3.12}$$

Hence, whether a DFS results in an inversion or a saturation of the STs depends on Ω_Q, and there is significant debate on this matter in the literature.[313] Generally, it is assumed that both mechanisms take place, with some crystallites having populations inverted and some saturated, resulting overall in a signal improvement. The 3Q to 1Q transfer for a spin $I = 5/2$ nuclei is, in essence, identical to the case $I = 3/2$, with a different initial density matrix. In matrix representation, a full inversion results in

$$\begin{bmatrix} 0 & 0 & 0 & 0 & 0 & 0 \\ 0 & 0 & 0 & 0 & 1 & 0 \\ 0 & 0 & 0 & 0 & 0 & 0 \\ 0 & 0 & 0 & 0 & 0 & 0 \\ 0 & 1 & 0 & 0 & 0 & 0 \\ 0 & 0 & 0 & 0 & 0 & 0 \end{bmatrix} \xrightarrow[\text{of the innter STs}]{\text{Adiabatic inversion}} \begin{bmatrix} 0 & 0 & 0 & 0 & 0 & 0 \\ 0 & 0 & 0 & 0 & 0 & 0 \\ 0 & 0 & 0 & 1 & 0 & 0 \\ 0 & 0 & 1 & 0 & 0 & 0 \\ 0 & 0 & 0 & 0 & 0 & 0 \\ 0 & 0 & 0 & 0 & 0 & 0 \end{bmatrix} \quad . \tag{4.3.13}$$

The 5Q to 1Q transfer for a spin $I = 5/2$ will be addressed in Section 6.2.1.

4.3.2 DFS and FAM

In Section 4.3.1, is has been shown that a DFS is able to selectively invert (or saturate) the STs, converting 3Q coherence into CT 1Q coherence, and thus giving signal improvement relative a short CW conversion pulse. The term DFS refers to the concept of applying a pulse at two simultaneous offsets, and also refers to a specific pulse scheme, introduced by Kentgens and Verhagen, both for the enhancement of CT populations (see Chapter 7),[19] and for the substitution of the CW conversion pulse to enhance the sensitivity of MQMAS experiments.[311] By far the most common implementation of the DFS sweep is the linear sweep given by [311]

$$\omega_m(t) = \omega_s + \lambda_{\text{sw}} t \tag{4.3.14a}$$

$$= \omega_s + \frac{\omega_f - \omega_s}{\tau_p} t \quad . \tag{4.3.14b}$$

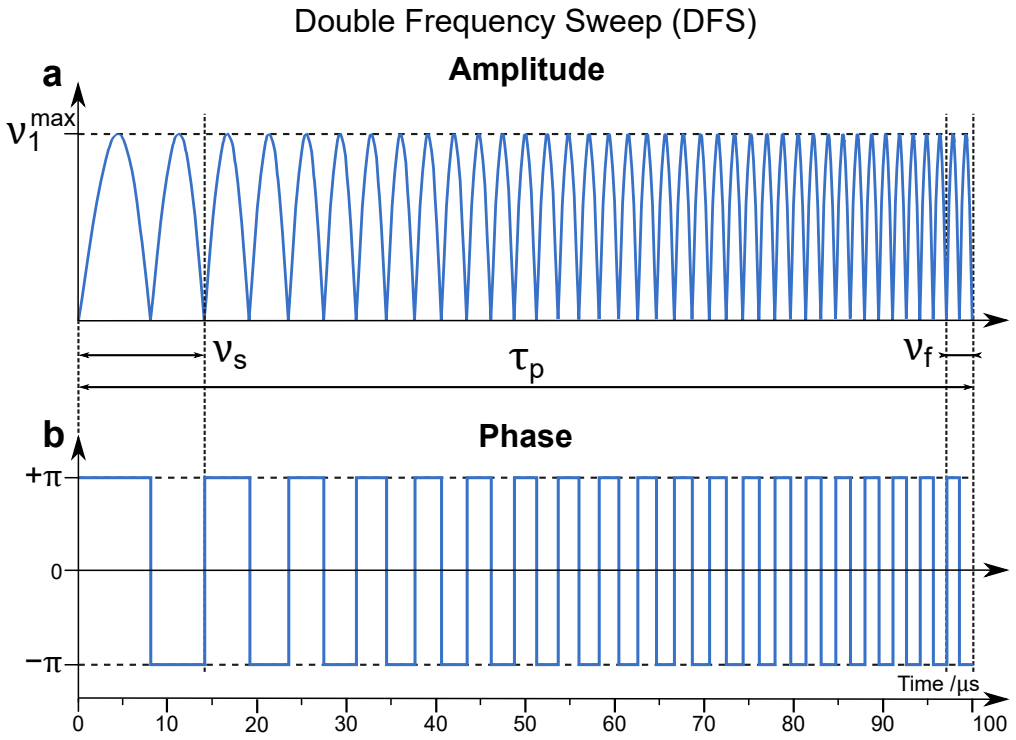

Figure 4.10: *Illustration of **(a)**: the amplitude and **(b)**: the phase of a DFS pulse executing a linear sweep from ν_s = 50 kHz and ν_f = 200 kHz for a duration τ_p = 100 µs, giving a sweep rate of λ_{sw} = 1.5×10^6 kHz.s^{-1} , here represented with an always positive amplitude and shifting phase.*

where

- ω_s and ω_f are the initial and final frequencies, respectively,
- τ_p is the pulse duration,
- λ_{sw} is known as the sweep rate, usually given in kHz.s^{-1}.

The linear sweep is the ”standard” sweep scheme used for DFS, even though other formulations have been reported in the literature.[314–316] An example of the shape of the amplitude and phase of a DFS pulse that executes a linear sweep is shown in Figure 4.10. The adiabaticity factor (see Equation (F.1.10)) can be rewritten is terms of the sweep rate, such that [309, 312]

$$\alpha = \frac{\omega_1^2}{4\lambda_{sw}} \quad . \tag{4.3.15}$$

Evidently, Equation (4.3.15) expresses that DFS is more adiabatic when applied with a slow sweep rate and for a strong RF.

The DFS pulse scheme is one of the most efficient approaches for improving the sensitivity of MQMAS experiments. It is versatile and robust with respect to most experimen-

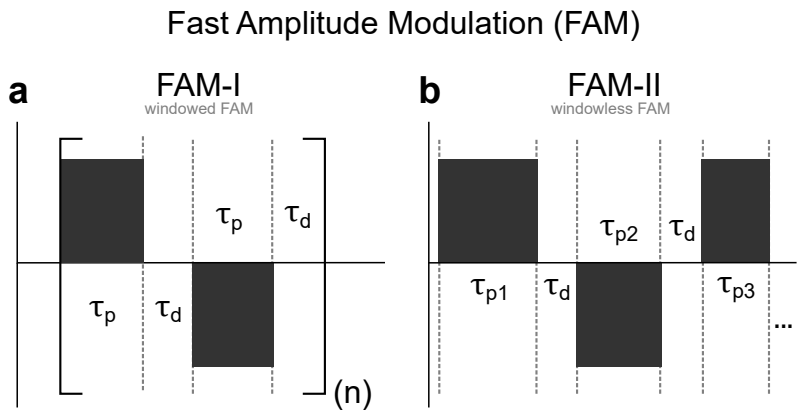

Figure 4.11: *Illustration of the FAM scheme in **(a)**: its windowed form (FAM-I) and **(b)**: its windowless form (FAM-II).*

tal parameters, including the offset $\Delta\omega_0$.[312, 317] Nevertheless, as discussed in Section 4.3.1, this type of pulse is only applicable to enhance the efficiency if MQ to 1Q transition, *i.e.*, can only be easily implemented in the shifted-echo MQMAS experiment (see Section 3.3.2) or in the alternative formulation of the z-filtered MQMAS experiment (see Figure 3.13b). Moreover, it is clear from Equation (4.3.14) that its experimental optimisation is demanding, requiring two independent quantities ω_s and ω_f to be optimised on (typically) low-sensitivity MQF spectra, while making sure the adiabaticity condition (see Equation (F.1.9)) in Equation (4.3.15) remains fulfilled.

The FAM[21] pulse scheme is a composite pulse scheme introduced by Madhu *et al.*,[18] that mimics the AM of DFS pulses by executing only the phase inversions shown in Figure 4.10b. This pulse scheme has been introduced as windowed version, termed FAM-I, and a windowless version, termed FAM-II, shown in Figures 4.11a and Figures 4.11b, respectively.[318] One advantage of FAM over DFS was that shaped-pulse capable hardware is not required and thus can be implemented in any spectrometer able to produce pulsed RF fields. A theoretical description of FAM pulses would be essentially identical to that for DFS pulses, and would lead to the similar observation. However, FAM offers less degree of freedom than DFS, reducing the maximum improvement achievable, in exchange for a greater ease of implementation and optimisation.[23, 237]

• The windowed FAM-I pulse train in Figure 4.11a has a clear resemblance to DFS, with the duration of each n block defining a unique modulation frequency given by

$$\omega_m = \frac{1}{2\tau_p + 2\tau_d} \quad . \tag{4.3.16}$$

[21] FAM: *Fast-Amplitude Modulation*

This pattern is repeated n times, allowing the modulation to be applied for a long duration. The modulation produced by FAM-I being fixed, this approach relies on the time dependence acquired by Ω_Q when under MAS to affect all of the crystallite orientations (see Section 7.1 for details). A sweep can be reintroduced by building a succession of FAM-I blocks with different τ_p,[319] or varying the τ_p during this application in a method termed sw-FAM[22].[320] In its non-swept variant, FAM-I has two parameter than DFS to optimise: τ_p and the number of blocks n.

• The windowless FAM-II in Figure 4.11b consists of a simple succession of oppositely phased pulses, again, mimicking the AM of DFS, but allowing the duration of each pulse to be set individually. As a result, the modulation frequency depends on the duration of each individual element, and so cannot be easily established for the general case. Even though this scheme may seems less advantageous than FAM-I or DFS at first sight, it was proven to be an efficient approach as it can very easily result in signal improvement, following a simple optimisation procedure consisting of the three following steps, established from experimental investigations.

1 Optimise a single-pulse conversion,
2 Add an second, oppositely-phased pulse and optimise this,
3 Return to the first pulse and re-optimise.

It has been established from experiments that the optimisation of FAM-II can be restricted to the two last pulses. Unlike the other methods presented here, FAM-II has the advantage not to require multiple-parameter optimisation, as the procedure detailed above can be performed with only one parameter at the time. In practice, however, one cannot expect to experimentally optimise more than 2 to 3 FAM-II pulses, as this would make it a very time-consuming procedure, and because any signal improvement become increasingly difficult to see in experimental spectra because of the noise.

4.3.3 FAM with N pulses (FAM-N)

The starting point for the design of a new method for the signal improvement of MQMAS is based on the observation that, although DFS pulses are able to produce significant signal improvement, the multiple parameters that required to be optimised is problematic in experiments. The optimisation of FAM-I or FAM-II is not as difficult, but more limited improvements can be observed.[23, 237] Therefore, an approach for easier optimisation procedures is to predict efficient 3Q to CT 1Q conversion pulses with

[22] sw-FAM: *frequency-SWept Fast-Amplitude Modulation*

numerical simulations, using one of the multiple simulation packages available: GAMMA,[321] SpinEvolution,[322] PyPULSAR,[323] pNMRsim,[324] or SIMPSON[23].[24] The simulation package SIMPSON has been used to perform the following simulations.

However, in simulations, the simultaneous optimisation of multiple parameters is challenging, as it requires multi-dimensional optimisation which are time-consuming, and it remains unclear whether the obtained pulse is "optimal" for a given set of experimental parameters. Here, we introduce a novel optimisation scheme for FAM-II pulses, that differs from previously introduced approaches (see Section 6.2.2 for details).[318, 325] This code executed the SIMPSON package using a home-written Matlab script,[326] that reads in the output files and sorts the step of the optimisation. The code performs the FAM-II optimisation procedure detailed in Section 4.3.2, and attemps to add additional pulses until no further signal improvement is obtained. The flowchart shown in Figure 4.12 details the execution process of the optimisation. Appendix I gives a more precise description of this optimisation program, together with some practical elements. Each step of the optimisation is described below, following the labels **(a)** to **(g)** of Figure 4.12.

Step (a) A first simulation generates the conversion profile, *i.e.*, amount of CT 1Q coherence | real part of ρ_{23} created as a function of the pulse duration for spins $I = 3/2$, of the short CW conversion pulse.

Step (b) At the point of maximum 1Q creation, a new SIMPSON input file is written in which a new oppositely-phase pulse is added just at the point of this maximum, and the computation is repeated.

Step (c) The program will then increase (or decrease) the length by the first pulse of one time increment, defined in the program, and the computation is repeated. Hopefully, the resulting maximum should again increase. The duration of the first pulse is increasingly incremented, until a point where the amount of 1Q coherence does not exhibit any further increase.

Step (d) At this point, a counter is enabled. The program will continue to increase the first pulse length, even if the signal is decreasing, for a fixed number of times, called `counter` in Figure 4.12. If the signal starts rising again, the counter is reset to zero. Once `counter` reached a value defined by `countmax`, the program stops incrementing, and compare the value of the maximum to

[23] SIMPSON: *SIMulation Package for SOlid-state Nmr*

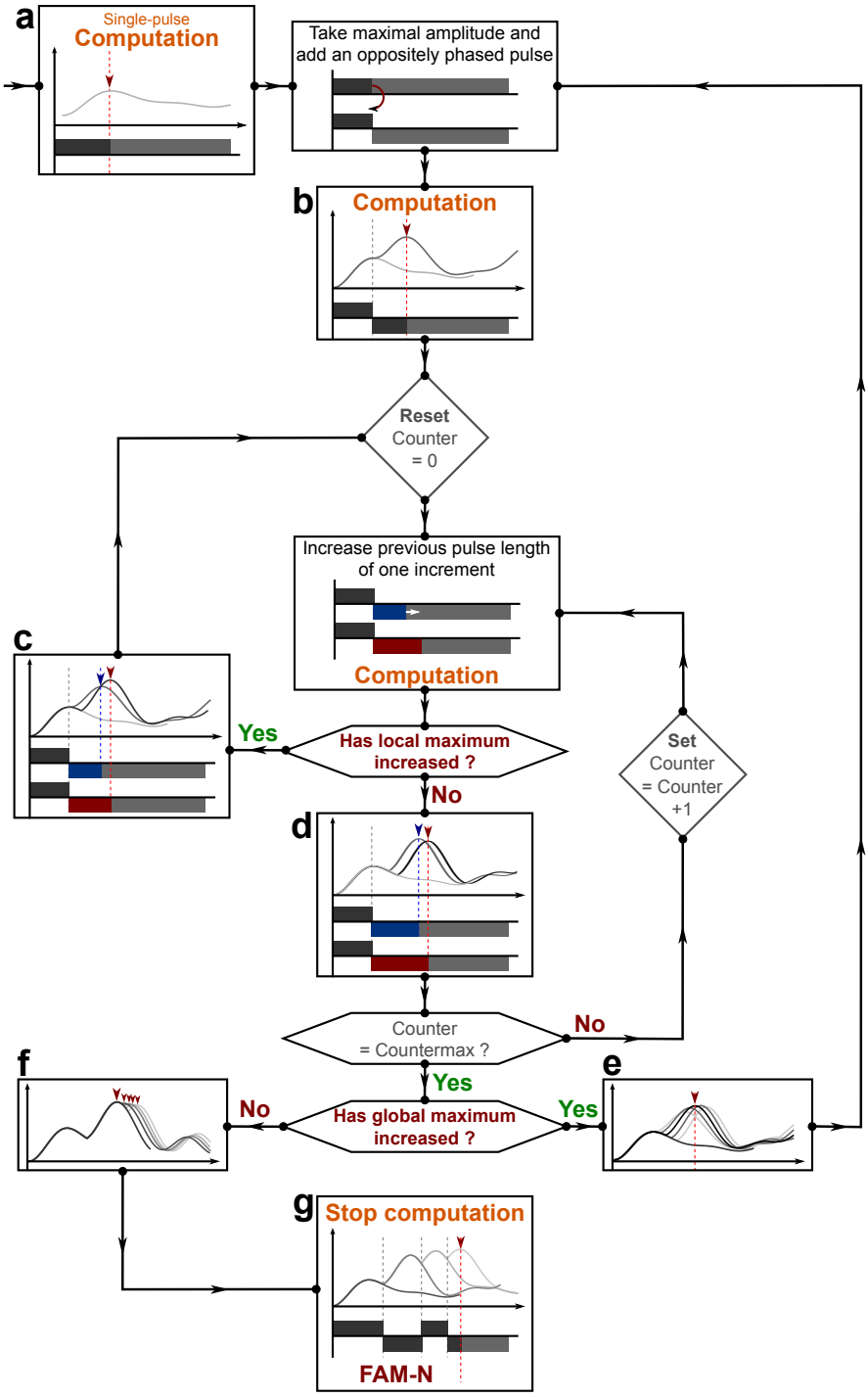

Figure 4.12: *Flow chart showing the optimisation procedure of FAM-N pulses.*

the one obtained from the CW conversion pulse.

Step (e) If an increase is observed, the program will take this new maximum, and add a third, oppositely-phased pulse at this point, and the previous operation is repeated.

Step (f) The process is repeated up to the point when, the recorded maximum using $N+1$ pulses is not higher than that observed using N pulses.

Step (g) At this points, the program stops. The composite pulse series is then saved in the form of a text file report and in the form of a matlab file. The program also writes a pulse programme that can be used directly in Bruker's Topspin.

The pulse optimised by this approach is called FAM-N[24], the new approach for the improvement of MQ to 1Q conversion introduced in this work.[23] Using the numerical optimisation procedure described in Figure 4.13, a composite pulse that can be considered as an "optimum" FAM-II pulse for a given set of parameters is produced. Initially conceived as a attempt to understand the characteristics of an efficient AM pulse (number of pulses, total duration, total flip angle, ...) FAM-N proved to be usable directly in experiments, as will be discussed in the following chapters.

A mentioned previously, with this optimisation procedure, only one parameter is optimised at a time. That is, the duration of the second last pulse,[25] which results in the optimisation been rapid, and the output FAM-N pulse to be reproducible with the knowledge of the input parameters. The process by which FAM-N pulses are obtained resembles that of the approach called optimal control,[327, 328] that consists of optimising in simulation a pulse optimised for a given coherence transfer with little constraints on the pulse shape.[329, 330] However, FAM-N imposes that the pulse is constituted of a series of rectangular-shaped pulses applied at a constant RF field ν_1, hence can be easily implemented in any spectrometer. While keeping these restrictions, because the durations of the FAM-N pulses is set free, so the modulation frequency sweep do not follow any particular scheme, which is an additional degree of freedom compared to DFS.

An example of a FAM-N pulse optimisation is shown in Figure 4.13, for ^{23}Na ($I = 3/2$), using standard conditions and a tolerance counter of 2.[26] In this example, the theoretical signal improvement ratio observed between the CW and FAM-N conversions is ×2.9. As often observed experimentally, the second pulse creates most of the signal enhance-

[24] FAM-N: *Fast-Amplitude Modulation* with *N* pulses

[25] It has been proven in the support information of [23] that subsequent re-optimisations of other pulses leads to little improvement.

[26] By default, the tolerance counter is set to 5 (see Appendix I.2). It is here reduced to 2 for readability reasons. See Figure I.2 for a unprocessed figure.

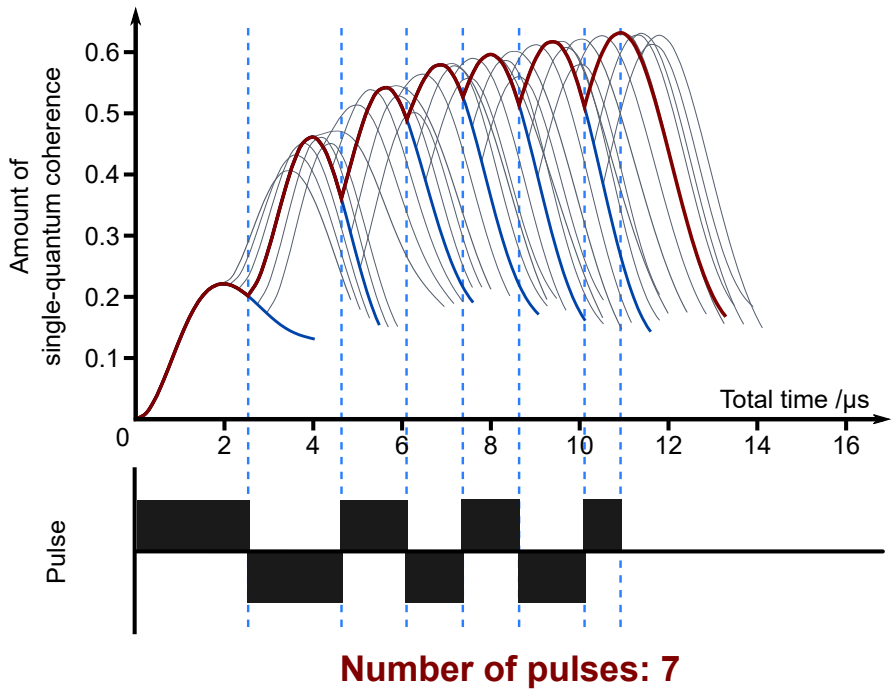

Figure 4.13: *Illustration of a FAM-N optimisation for ^{23}Na ($I = 3/2$) at B_0 = 14.1 T (ν_0 = 158.8 MHz), with ν_1 = 80 kHz and ν_R = 12.5 kHz. Each curve shows a step of the optimisation. Curves plot the evolution of the amount of CT 1Q coherence | real part of ρ_{23} as a function of time and of the pulse used in the simulation. Grey lines show the amount of CT 1Q coherence for all of the intermediate optimisation steps, the blue line are for the optimisations steps that were used for the subsequent steps of the FAM-N optimisation. The red line shows the evolution of ρ_{23} for the final FAM-N pulse. In the electronic version of this thesis, this figure is animated.*

ment in Figure 4.13 (×2.1). The following pulses result in a more limited increase when taken individually, but results in a substantial improvement compared to the same pulse truncated to two pulses (×1.4) when added together. By default, FAM-N is optimised using 66 crystallite orientations, and 4 γ-angles, no significant difference have been observed between FAM-N pulses have been observed when a higher number crystallite orientations. However, FAM-N pulses optimised for this amount of crystallite orientations and γ-angles can subsequently be used in a simulation with more crystallite orientations if a more precise theoretical improvement ratio is desired.[27] Figure 4.13 shows the maximum signal improvement is not obtained by a phase inversion at the point of maximum CT 1Q created, but is obtained by increasing the duration of the second last pulse. Cases where decreasing the previous pulse duration results in an enhancement were also observed but remain uncommon. FAM-N pulses are often observed as being ”conver-

[27] Usually 320 crystallite orientations and 20 γ-angles.

gent", *e.g.*, the frequency sweep is executed from a low to a high modulation frequency. The insertion of a new pulse by the FAM-N optimisation program appears to impose that the previous component executes a modulation at a lower frequency, which can be seen as adding a frequency component to the sweep executed by FAM-N.

The FAM-N pulse optimised using the procedure detailed above is able, in simulation, to enhance the efficiency of the 3Q to CT 1Q conversion step of the 3QF or MQMAS experiment. However, many questions still remain concerning the applicability of the approach in practice, and its efficiency compared to others the methods introduced above. In Chapters 5 and 6, the experimental implementation, the performances and robustness of FAM-N pulses applied on various systems and conditions.

Chapter 5

The FAM-N composite pulse

Introduction

Section 4.3.3 introduced a novel scheme for the sensitivity enhancement of the conversion pulse of MQMAS based on the FAM-II approach, denoted FAM-N. As the number of pulses and the length of each element is based solely on numerical simulations, the highest or near-highest possible improvement using this pulse scheme should be obtainable in practice. However, many questions about the actual efficiency and general applicability of the method remain to be resolved. The diversity of samples and quadrupolar nuclei, presenting different spin quantum numbers, quadrupolar moments, and with different sensitivities, means that FAM-N will need to be efficient over a wide range of conditions to be practically useful.

This chapter investigates the practical use of the method, based on theoretical investigations of the efficiency and robustness of the pulse when submitted to different experimental conditions. This will be confirmed by experiments performed on model compounds. In Section 5.1, general, in-depth investigations of the theoretical efficiency of FAM-N when applied under most of the usual experiment conditions, mainly performed with the SIMPSON simulation package,[24] will be presented and analysed. As introduced in Section 4.3.2, FAM, and in particular FAM-II, is a scheme that sacrifices some of the complexity of DFS for simplicity, but at the price of a lower efficiency. This is corroborated by several literature publications.[115, 312, 313, 316] The robustness of FAM-N, *i.e.*, how its efficiency is affected when applied with experimental conditions for which it is not optimised, will be presented in Section 5.2. This has been

accomplished by numerical simulations, simulating FAM-N for a certain conditions and applying it for others. Experimentally, FAM-N has been applied on samples containing multiple sites with different quadrupolar parameters. Finally, in Section 5.3, the efficiency of FAM-N compared to that of other MQMAS signal-enhancement techniques that replace the CW conversion pulse by a more efficient pulse scheme, *e.g.*, SPAM (Section 4.1.3), FAM-I, FAM-II and DFS (Section 4.3.2), will be investigated.

This chapter uses data published in H. Colaux *et al.*, *J. Phys. Chem. A*, 2014, **118**, 6018, DOI: 10.1021/jp505752c .[23]

5.1 Effect of the optimisation parameters on FAM-N

FAM-N pulses can be described as FAM-II type pulses with an undetermined durations and number of pulses, generated according to the numerical optimisation procedure described in Section 4.3.3, from user-defined experimental parameters, including B_0, ν_1, ν_R, C_Q, η_Q, *etc.*, described in detail in Appendix I.2. The FAM-N pulses produced, and the resulting sensitivity improvement of MQF, are different depending on the parameters of the simulation. The effect of these parameters on the type of the efficiency of FAM-N and on the FAM-N pulse trains will be analysed in this section. Indisputably, ν_1 and C_Q are the parameters that have the greatest effect on the FAM-N pulse generated, as they determine how the frequency sweep is executed. Other parameters, such as ν_R or η_Q, potentially have an impact on FAM-N pulses, yet this impact can be presumed to be more limited than that of C_Q or ν_1.

5.1.1 RF field and quadrupolar coupling constant

To gain insight into the impact of ν_1 and C_Q on the FAM-N efficiency, simulations have been performed for a range of C_Q and ν_1 values covering the entire range of realistic experimental conditions. For these simulations, C_Q and η_Q were incremented logarithmically for all half-integer spins up to $I = 9/2$, with a constant MAS rate used in the simulation. The amount of CT 1Q obtained from initial unit 3Q coherence obtained from CW and FAM-N are plotted under the form of a contour plot in Figure 5.1. To allow a direct comparison between simulations performed on different spins I, simulations have been performed for an identical range of ν_Q (see Equation (2.3.12)) for all spins, resulting in different C_Q ranges.

The first observation that can be made for the CW plots in Figures 5.1a, 5.1c, 5.1e and 5.1g is consistent with those made in Section 4.1.1, that, for all spins, the transfer efficiency increases as ν_1 increases and as C_Q gets smaller. Clearly, this efficiency is constant for a constant C_Q/ν_1 ratio. Overall, a similar observation can be made for FAM-N, as the efficiency eventually drops as C_Q gets higher. However, one striking observation is the existence of a set of conditions for which FAM-N is most efficient, forming a "band" in Figures 5.1b, 5.1d, 5.1f and 5.1h. This shows that there exists an optimum C_Q/ν_1 ratio for which FAM-N appears to be most efficient, which can be roughly expressed as

$$\nu_{1_{\text{opt}}} \approx \frac{\nu_Q}{6} \tag{5.1.1a}$$

$$\approx \left(\frac{3}{24I(2I-1)}\right) C_Q \quad . \tag{5.1.1b}$$

This band is present for all spin in Figure 5.1, for the same ν_Q/ν_1 ratio. Indeed, fundamentally, for the purpose of converting 3Q to 1Q coherence, FAM-N must have only an effect on the inner STs, while avoiding the outer STs. Yet, as shown in Section 2.3.3, C_Q relates to the total width of the static quadrupolar lineshape including all STs, while ν_Q can be linked to the width of individual ST lineshapes. However, the tendency in Equation (5.1.1) is only approximate as variations in the efficiencies can be observed in Figure 5.1. These can be attributed, at least partially, to computational accuracy, as FAM-N depends, to some extent, to the number of points and tolerance conditions chosen for the FAM-N simulations. Another interesting feature in all of the plots in Figure 5.1 is that the FAM-N efficiency is almost constant in the strong ν_1 and low C_Q region of the plots (bottom-right corners), with an amount of CT 1Q created being roughly 0.4 to 0.5. This shows that, in this region, FAM-N performs a transfer similar to the saturation described in Section 4.3.1, whereas, for the band described by Equation (5.1.1), the effect of FAM-N is closer to an inversion. In the opposite region, the amount of CT 1Q coherence created by FAM-N quickly drops in the weak ν_1 and low C_Q regions (top-right corners), although this decrease is not as significant as that observed in the CW plots. This observation is consistent with the simulations shown in Figure 4.1, predicting that a weak RF field creates 3Q coherence with low efficiency.

To illustrate the existence of the band of maximum efficiency, simulations were carried out, returning all the coefficients of the density matrix of ^{87}Rb ($I = 3/2$). The simulation

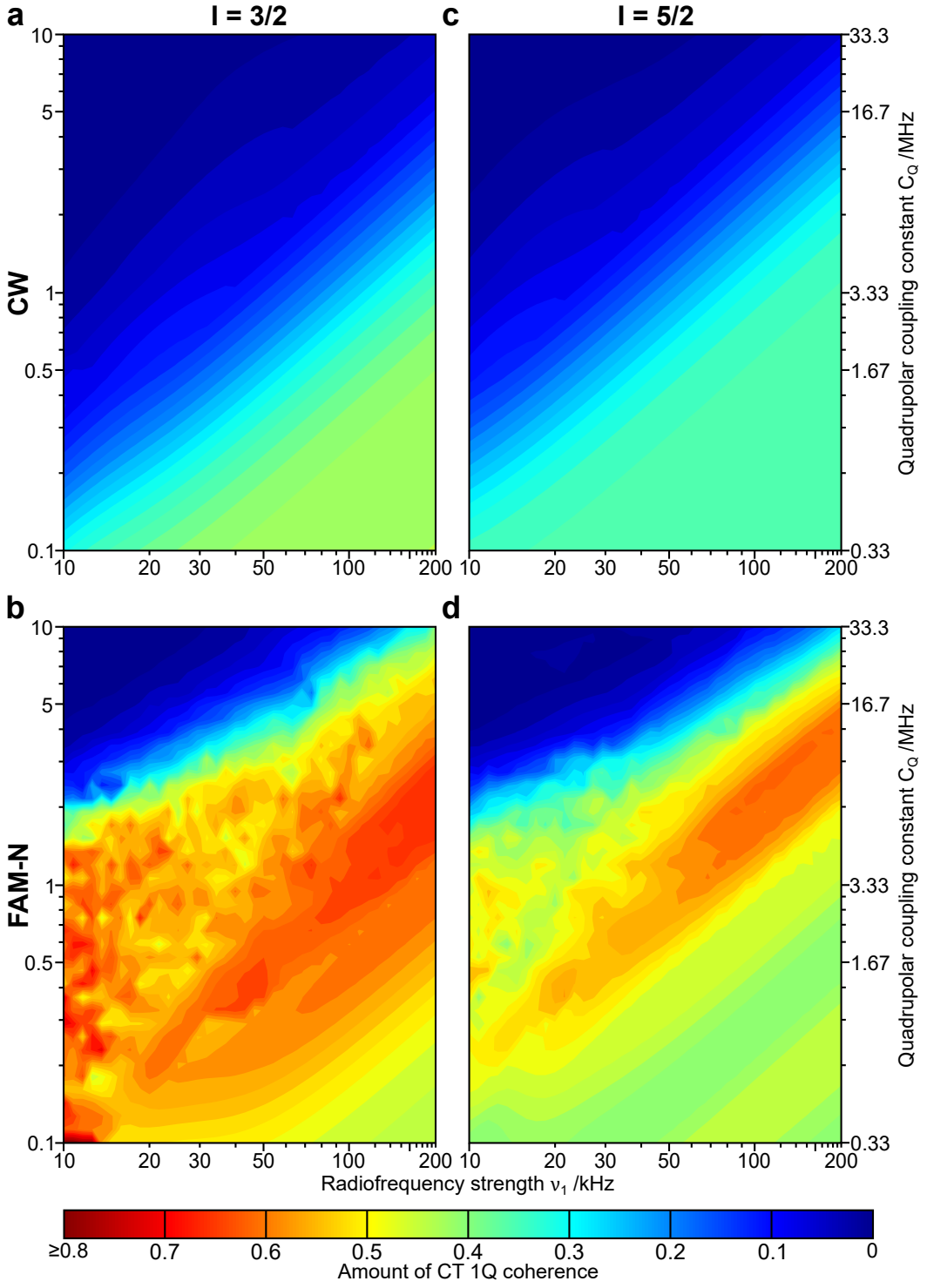

Figure 5.1: *Log-log contour plots showing the maximum amount of CT 1Q coherence created after **(a,c,e,g)**: CW and **(b,d,f,h)**: FAM-N conversion pulses for different values of C_Q and ν_1 for spin **(a,b)**: $I = 3/2$, **(c,d)**: $I = 5/2$, **(e,f)**: $I = 7/2$ and **(g,h)**: $I = 9/2$. ...*

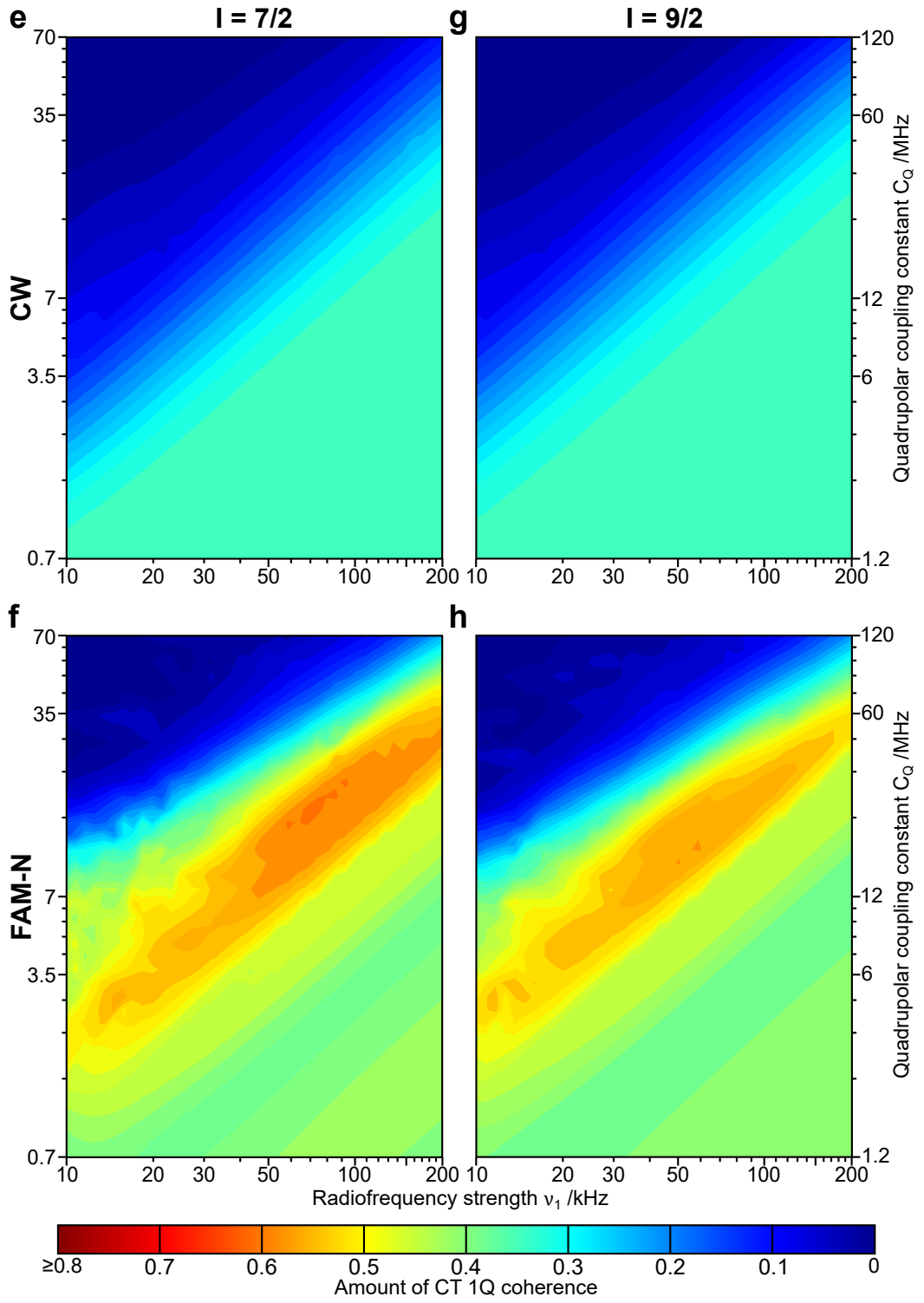

Cont.: *The contour levels are set to be identical in all plots to allow a direct comparison of the amount of CT 1Q coherence. All simulation have been performed for ν_0 = 196.4 MHz and ν_R = 12.5 kHz. C_Q values have been chosen such that the range of ν_Q is the same for the different spins. All simulations were performed for 66 crystallite orientations and 4 γ-angles.*

starts from an initial unit 3Q coherence, represented by the density matrix

$$\hat{\rho}(t_0) = \begin{bmatrix} 0 & 0 & 0 & +1 \\ 0 & 0 & 0 & 0 \\ 0 & 0 & 0 & 0 \\ 0 & 0 & 0 & 0 \end{bmatrix} , \tag{5.1.2}$$

where elements for populations are in black, initial 3Q coherence is in red, and the desired CT 1Q coherence is in blue. A simulation for C_Q = 1 MHz, η_Q = 0, ν_R = 12.5 kHz and ν_1 = 100 kHz gives the density matrix

$$\hat{\rho}(\tau_{p_{\text{FAM-N}}}) = \begin{bmatrix} +0.031 & -0.011 & +0.040 & +0.246 \\ +0.054 & -0.031 & +0.669 & +0.038 \\ -0.008 & +0.020 & -0.032 & -0.011 \\ +0.065 & +0.001 & +0.009 & -0.011 \end{bmatrix} , \tag{5.1.3}$$

$\tau_{p_{\text{FAM-N}}}$ being the total duration of the FAM-N pulse. The density matrix in Equation (5.1.3) is used as a reference to observe the effects of varying the RF field strength on the terms of the density matrix. Repeating the simulation with ν_1 = 30 kHz gives

$$\hat{\rho}(\tau_{p_{\text{FAM-N}}}) = \begin{bmatrix} -0.009 & -0.008 & -0.002 & +0.380 \\ +0.008 & +0.010 & +0.571 & +0.002 \\ 0.000 & +0.020 & +0.011 & -0.008 \\ +0.024 & +0.001 & +0.009 & -0.011 \end{bmatrix} . \tag{5.1.4}$$

Here, in Equation (5.1.4), the RF field is simply not strong enough to be efficient, leaving a large amount of 3Q coherence remaining. Finally, repeating this last simulation with ν_1 = 300 kHz gives

$$\hat{\rho}(\tau_{p_{\text{FAM-N}}}) = \begin{bmatrix} -0.049 & -0.103 & -0.161 & +0.244 \\ +0.060 & +0.049 & +0.597 & -0.161 \\ +0.040 & +0.060 & +0.049 & -0.103 \\ +0.099 & +0.040 & +0.060 & -0.049 \end{bmatrix} . \tag{5.1.5}$$

This shows that 3Q to 1Q conversion efficiency is not necessarily achieved with stronger RF for FAM-N. Nevertheless, for most spin $I = 3/2$ nuclei studied practically, experimental ν_1 typically ranges from 30 to 140 kHz and C_Q from 1 to 5 MHz. As a result, experimental conditions are such that the strongest RF field available will give the highest signal improvement.

In Figure 5.1, it can be observed that the amount of 1Q coherence created after FAM-N conversion slightly decreases as I increases. This can be illustrated by performing the full density matrix simulation for FAM-N conversion for a spin $I > 3/2$ nucleus, following the same approach as before. Equation (5.1.6) shows this matrix, obtained

from a simulation performed for ^{27}Al ($I = 5/2$) with C_Q = 6.66 MHz, η_Q = 0, ν_1 = 100 kHz and ν_R = 12.5 kHz, given by

$$\hat{\rho}(\tau_{p_{\text{FAM-N}}}) = \begin{bmatrix} +0.010 & -0.007 & +0.001 & -0.011 & -0.007 & +0.148 \\ +0.002 & +0.008 & +0.002 & +0.002 & +0.187 & -0.001 \\ -0.014 & +0.011 & -0.018 & +0.612 & +0.012 & -0.020 \\ 0.000 & +0.002 & +0.012 & -0.018 & 0.002 & -0.002 \\ 0.000 & +0.019 & +0.002 & +0.011 & +0.009 & -0.008 \\ +0.013 & 0.000 & 0.000 & -0.015 & +0.001 & +0.010 \end{bmatrix} . \tag{5.1.6}$$

It can be seen that in Equation (5.1.6), in addition to the desired coherence being created, additional unwanted coherences are also present in the density matrix, including a large amount of 5Q coherence (green density matrix element). As the spin quantum number I increases, the number of terms that can potentially be created by FAM-N also increases, leading to a drop of the desired term. This behaviour is also visible on the CW plots in Figure 5.1.

The full density matrices also explain why, in the weak RF region of the plot spin $I = 3/2$, FAM-N shows a very high efficiency which does not appear for higher-spin systems. FAM-N, which can be considered as a ST-selective pulse, has a different effect on spin $I = 3/2$ nuclei, which exhibit only one pair of STs, than on higher spins that possess multiple overlapping pairs of STs. That is, a modulated pulse cannot be perfectly selective to the inner STs for spins $I > 3/2$, resulting in unwanted 3Q to 5Q transfer as in Equation (5.1.6). As long modulated pulses giving rise to unwanted 3Q to MQ transfers, the FAM-N optimisation finds that a relatively low number of pulses gives the most efficient 3Q to 1Q conversion. However, for $I = 3/2$, modulated pulses affect only the STs, and the FAM-N optimisation program determines that longer pulse trains perform the most efficient conversion. It should be noted that the simulations do not take relaxation of the 3Q coherences during the pulse into account, which would inevitably results in discrepancies with experiments.[1] Further insight can be obtained from Figure 5.2, which plots the total number of pulses and pulse duration, given here as the flip angle of a CW pulse of equal duration, achieved by FAM-N pulses under the same ν_1 and C_Q ranges used in Figure 5.1. It can be observed, as predicted, that the number of pulses and total durations are higher for a spin $I = 3/2$ nucleus than for a spin $I = 5/2$ nucleus.

Figure 5.2 also shows that their is a similar relationship between ν_1 and ν_Q and the number of pulses and pulse durations of FAM-N pulses as was observed in Figure 5.1. In Figure 5.2, the region where the largest number of pulses and greatest total nutation

[1] This is one of the reasons why the FAM-N optimisation script includes the parameter `cmpt.MAXnopulses` to voluntarily restrict the maximum number of pulses of FAM-N. See Appendix I.2 for details.

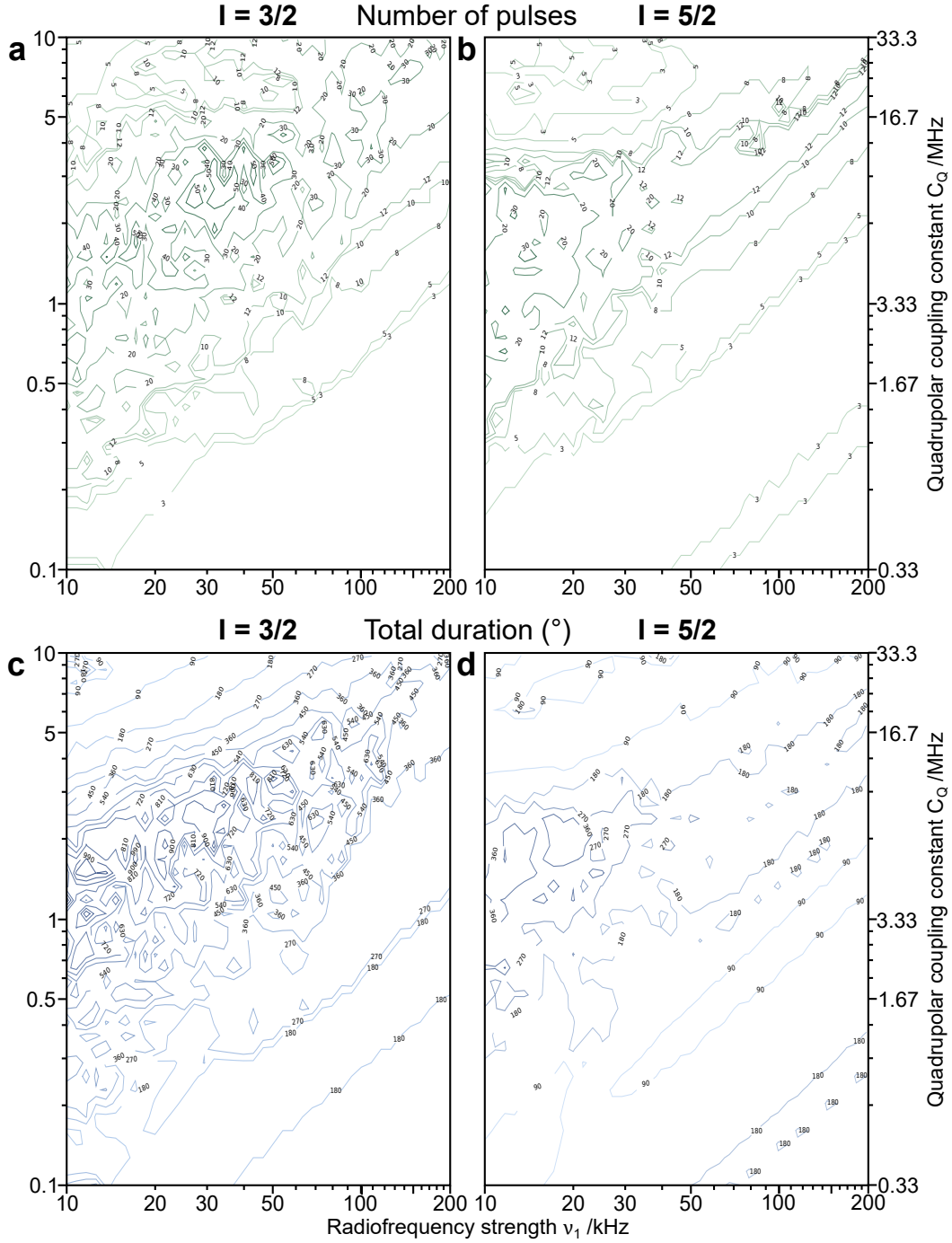

Figure 5.2: *Plots showing **(a,b)**: the total number of pulses of FAM-N, and **(c,d)**: the total duration of FAM-N expressed as the flip-angle achieved by a CW pulse of equal duration, obtained from the same simulations than those used to plot Figure 5.1b for $I = 3/2$ (**(a,c)**), and Figure 5.1d for $I = 5/2$ (**(b,d)**).*

are found from a band located to slightly higher C_Q values than the band observed in Figure 5.1 corresponding to the highest FAM-N efficiency, near the border determining whether the available RF field strength still allows an efficient 3Q to 1Q transfer (pale/-dark blue border in Figure 5.1). This also corresponds to a band where the theoretical improvement ratios between CW and FAM-N are the highest, as will be discussed in Section 5.1.2. As will be described in Section 5.2, the efficiency of long pulses is less tolerant to varying experimental conditions, so the enhancement predicted often cannot be perfectly reproduced in experiments (see Section 6.2.4). Finally, in the strong ν_1 and low C_Q region on Figures 5.2a and 5.2b, the optimisation stops after a low (2 to 3) number of pulses. That is, in this particular region, that FAM-N becomes of similar complexity than FAM-II and could be readily be optimised experimentally.

5.1.2 Theoretical signal improvement ratio

The amount of CT 1Q coherence created by CW and FAM-N shown in Figure 5.1 can be used to derive the so-called theoretical (signal) improvement ratio, used throughout this work, by dividing the amount of CT 1Q coherence created by FAM-N by that created by a CW pulse. In principle, this should predict the experimental signal improvement in 3QF/MQMAS spectra recorded with CW and FAM-N conversion, as this ratio gives a quantitative measurement of the efficiencies of both methods. This is also the only quantity easy to verify experimentally. The theoretical improvement ratios for all of the simulations in Figure 5.1 are shown in Figure 5.3 for all spins.

The existence of a band for which the theoretical improvement ratiois very high (×8 or more) for spin $I = 3/2$ can clearly be seen in Figure 5.3a,[2] corresponding to the region where FAM-N pulses are the longest (see Figure 5.2), slightly above the band of FAM-N maximum efficiency established in Equation (5.1.1). Although this band is present for all spins, the improvement ratio rapidly decreases with the spin quantum number I, to reach only ×5 over the same region for spin $I = 9/2$ nuclei in Figure 5.3d. As explained in Section 5.1.1, FAM-N pulse trains for spin $I > 3/2$ nuclei are typically shorter and become increasingly less efficient as I increases, owning to the presence of more than one pair of STs. For all spins, the improvement ratio decreases with ν_1 along this band. This is due to the creation of unwanted coherences in the density matrix discussed in Section 5.1.1, which increases with ν_1.

[2] In light of the experiments that will be presented in future sections, improvement ratios higher than ×8 can be considered unrealistic owing to multiple features detailed in Section 5.2.2, hence these have been omitted in Figure 5.3.

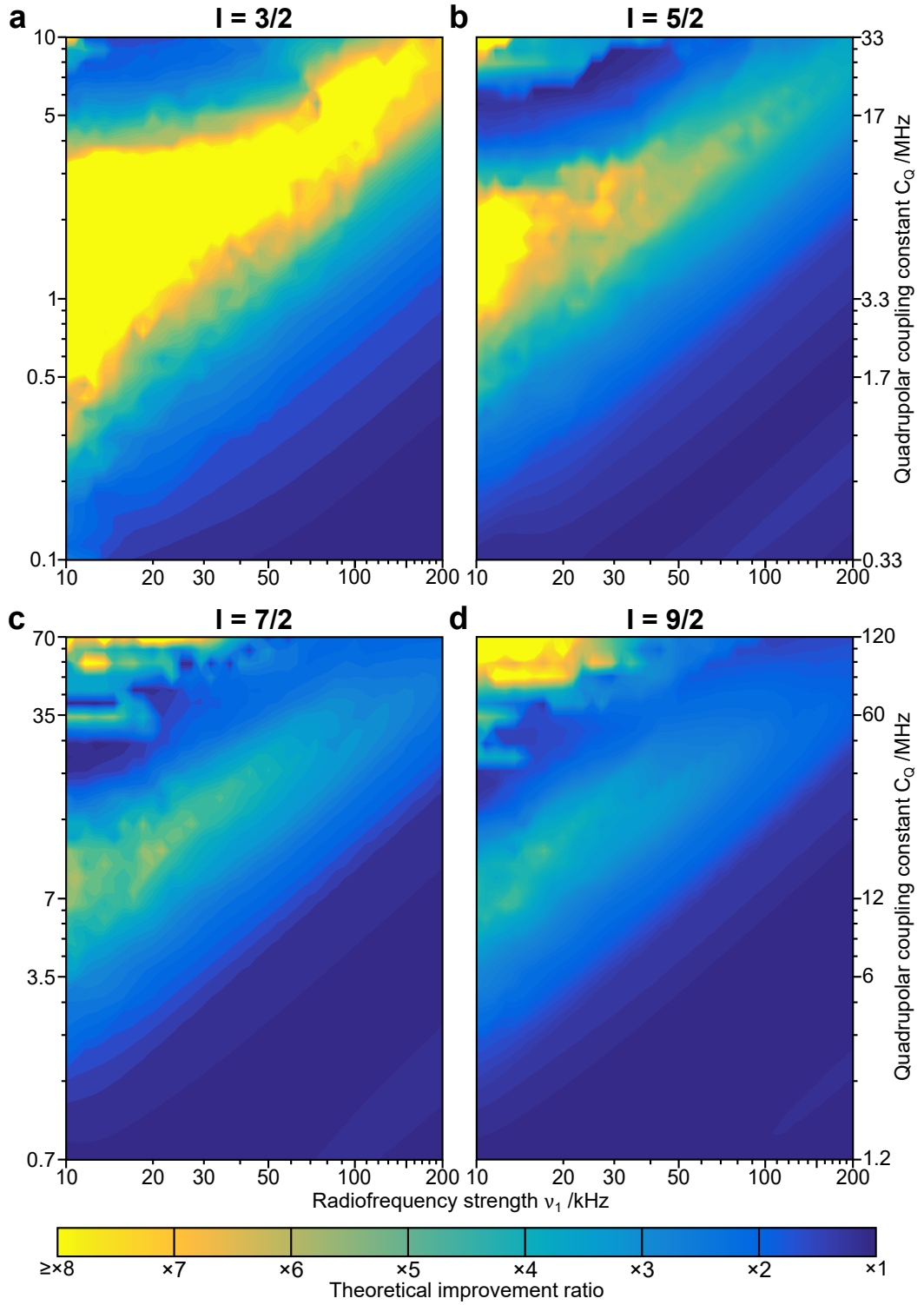

Figure 5.3: *Theoretical (signal) improvement ratio obtained by the division of the amounts of CT 1Q created by FAM-N and CW conversion from the corresponding points in the simulation Figure 5.1 for spins* ***(a)****:* $I = 3/2$ *(Figures 5.1a and 5.1b),* ***(b)****:* $I = 5/2$ *(Figures 5.1c and 5.1d),* ***(c)****:* $I = 7/2$ *(Figures 5.1e and 5.1f) and* ***(d)****:* $I = 9/2$ *(Figures 5.1g and 5.1h).*

In the high ν_1 and low C_Q region of Figure 5.3, the theoretical improvement is close to ×1.[3] Indeed, in this region, FAM-N is composed of a low number of pulses (2 or 3, see Figure 5.2), each resulting in a tiny theoretical improvement. This is typically the region for which FAM-N is not very attractive compared to CW, or even to an experimentally optimised FAM-II pulse. However, this case only applies to a very limited number of nuclei and materials, more realistic parameters being often located around the band corresponding to the maximum improvement ratios. Around this region, theoretical improvements of ×2 to ×4 are observed, which corresponds to signal improvement ratios observed in most experiments reported in this work (see Section 5.2.3).

Finally, in the opposite region, corresponding to low ν_1 and high C_Q, a small region of high efficiency is observed for all spins. Unlike the band discussed previously, this region expands as the spin quantum number I increases. In this region, FAM-N is composed of a low number of pulses, as visible in Figure 5.2. Presumably, under very strong C_Q and low ν_1 conditions, both CW and FAM-N only affect a small region around the carrier frequency, resulting in very low efficiencies. Furthermore, as CW affects only the region around the carrier frequency, the entire STs are affected in a similar way. However, FAM-N pulses cover a wider frequency range, permitting a much higher proportion of the inner STs to be affected. In the end, this gives a lower efficiency for CW but a similar efficiency for FAM-N as I increases, explaining why this region expands with the spin quantum number I. Owing to the extremely poor sensitivity after 3QF of experiments recorded under such conditions, it is almost impossible to verify the existence of this region by experiments.

5.1.3 Other parameters

This section analyses the impact on FAM-N efficiency and duration of other parameters, previously assumed to be of less importance to the outcome of the FAM-N simulation.

MAS rate

In Section 4.1.1, it was established that, unlike the MQ excitation pulse, the CW conversion pulse is virtually unaffected by the MAS rate for short pulse durations. A similar

[3] By definition, FAM-N cannot be less efficient in than CW in simulations, as FAM-N would be composed of only a single pulse if a second pulse does not result in a signal improvement, so be as efficient as CW. However, this does not apply to experimental results.

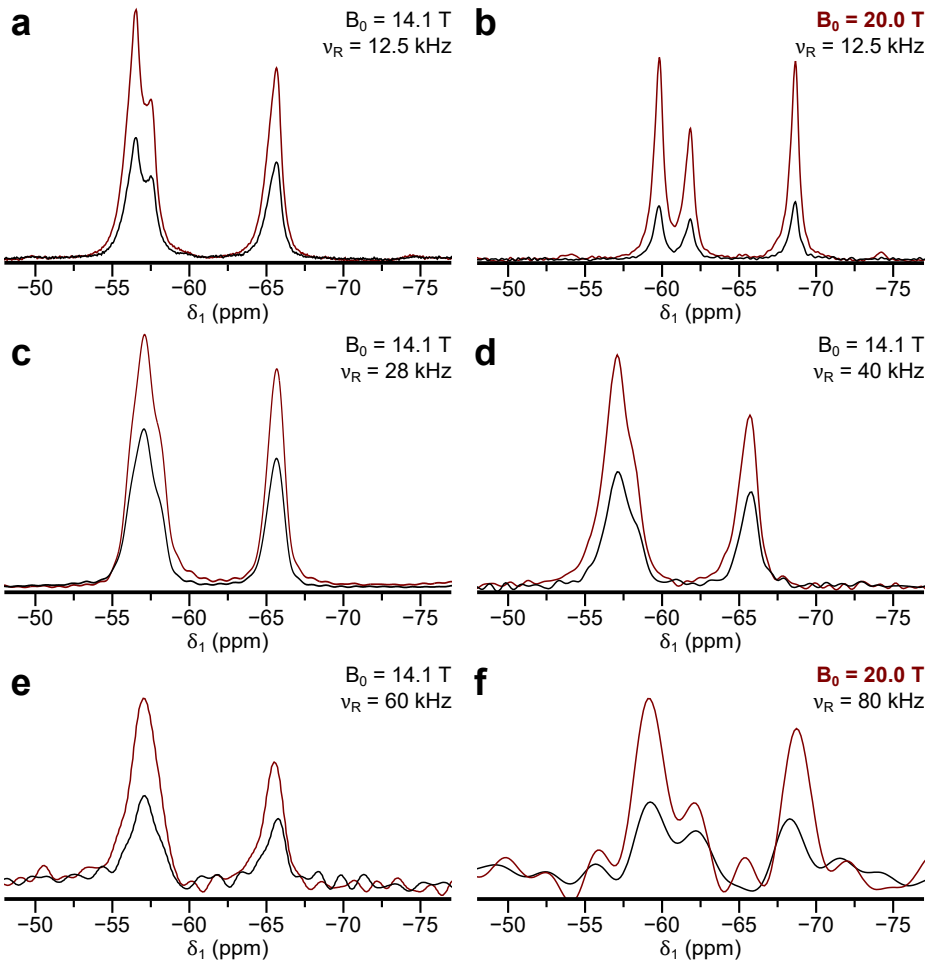

Figure 5.4: *Projections of the indirect dimension of ^{87}Rb split-t_1 shifted-echo MQMAS spectra of $RbNO_3$ recorded with CW (black lines) and FAM-N (red lines) conversion pulses for different MAS spinning rates ν_R and, unless otherwise mentioned, for B_0 = 14.1 T (ν_0 = 196.4 MHz).* ***(a)****: ν_R = 12.5 kHz,* ***(b)****: ν_R = 12.5 kHz and B_0 = 20.0 T (ν_0 = 278.2 MHz),* ***(c)****: ν_R = 28 kHz,* ***(d)****: ν_R = 40 kHz,* ***(e)****: ν_R = 60 kHz,* ***(f)****: ν_R = 80 kHz and B_0 = 20.0 T. See the extended caption in Appendix C.3 for further details.*

conclusion was also established for FAM-N. Few differences exist between FAM-N pulses optimised for different MAS rates, either in the pulse train itself, or in the resulting theoretical improvement. Only a few of the final pulses in the FAM-N pulse train are missing in the fast MAS case compared to the static case. This results in a very slight decrease in theoretical efficiencies, which seems impossible to reproduce experimentally. However, it is possible to verify the applicability of FAM-N optimised for different MAS rates.

Projections from the indirect dimensions of ^{87}Rb MQMAS spectra of $RbNO_3$ are shown

Figure 5.4	B_0 /T	ν_R /kHz	Improvement
(a)	14.1	12.5	×2.1
(b)	20.0	12.5	×3.4
(c)	14.1	28	×1.6
(d)	14.1	40	×1.8
(e)	14.1	60	×2.1
(f)	20.0	80	×2.2

Table 5.1: *Improvement ratios between CW and FAM-N conversion in the ^{87}Rb MQMAS spectra of $RbNO_3$ shown in Figure 5.4.*

in Figure 5.4,[4] and an estimate of the observed improvement is given in Table 5.1. As established by simulation, no definitive correlation can be established between ν_R and the signal improvement. The changes in the improvement ratios between CW and FAM-N can be attributed to other parameters, such as the amplifier, maximum available RF field, probe tuning or other factors that are difficult to estimate and that vary between probes and spectrometers. These experiments prove FAM-N to be equally applicable at all MAS rates. The MAS rate being a user defined parameter, a thorough investigation of the robustness of FAM-N to the MAS rate in unnecessary. However, differences in efficiency in simulations and experiments have been observed when FAM-N is applied at a MAS rate different from the MAS rate used for the FAM-N optimisation.

Asymmetry parameter

The asymmetry parameter of the quadrupolar interaction, η_Q, can be challenging to measure accurately in an MQMAS experiment as low SNR or lineshape distortions are often observed in MQMAS spectra. Besides, many literature articles simply quote the quadrupolar product P_Q if a lineshape fitting is impossible or not sufficiently precise. The effect of η_Q on FAM-N can be approached by a modification of the value of C_Q following Equation (2.3.36), *i.e.*, a FAM-N simulated for C_Q = 1 MHz and η_Q = 1 should be similar to one simulated for $C_Q \simeq 1.15$ MHz and η_Q = 0. That is, a relatively minor change, that is shown in Section 5.2 to be, generally speaking, tolerable if omitted in the FAM-N optimisation.

Figure 5.5 shows the amount of 1Q coherence created by FAM-N from initial 3Q coher-

[4]Two resonances on some spectra of Figure 5.4 appear to overlap. This is due to a difference in 3QF efficiencies between spectra that causes the resonances to appear as one single, asymmetric peak rather than two distinct resonances, and not to to differences in resolution in the indirect dimension.

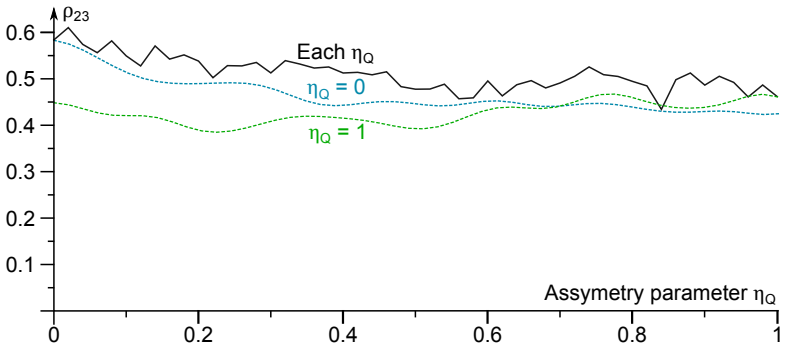

Figure 5.5: *Simulation of the amount of CT 1Q | real part of ρ_{23} created by FAM-N from initial 3Q coherence for ^{87}Rb ($I = 3/2$) and for B_0 = 14.1 T (ν_0 = 196.4 MHz), ν_1 = 100 kHz, ν_R = 12.5 kHz and C_Q = 3.2 MHz, optimised for each η_Q value of the horizontal scale (solid black curve), and with FAM-N optimised for η_Q = 0 and η_Q = 1 then applied to all η_Q values between 0 to 1 (dashed blue line and dashed green line, respectively). All FAM-N pulses were optimised for 66 crystallite orientations and 4 γ-angles, and this figure was obtained from applying these pulses for 320 crystallite orientations and 20 γ-angles.*

ence for each η_Q value (black line) for ^{87}Rb under a given set of conditions. It can be seen that the efficiency of FAM-N decreases as η_Q increases from 0 to 1. However, this is only because the simulation conditions happen to correspond to a region where the FAM-N efficiency decreases as C_Q increases (see Figure 5.1b). This drop is relatively limited, reaching 20% between η_Q = 01. Figure 5.5 also shows the efficiency of two FAM-N pulses optimised for η_Q = 0 and η_Q = 1, and applied across the range of η_Q. The FAM-N optimised for η_Q = 0 shows an efficiency that decreases by approximately 5% compared to a FAM-N optimised for each individual η_Q. The FAM-N optimised for η_Q = 1 is a little more efficient than the FAM-N optimised for η_Q = 0 if $\eta_Q > 0.65$, but much less efficient when applied for an η_Q value approaching 0.

Overall, the simulations shown in Figure 5.5 prove that the asymmetry parameter can be, to a first approximation, neglected in FAM-N simulations. However, if measured precisely, it can be used in the FAM-N optimisation, which will result in further signal improvement.

Static magnetic field

From simulations performed with identical conditions other than the strength of the static field B_0, optimised FAM-N pulses are independent B_0 under ”standard” conditions (not shown), *i.e.*, where $\nu_0 \gg \nu_Q$. This can be explained by the fact that the FAM-N modulation is designed to have an effect on the ST energy levels, *e.g.*, affecting a given range of frequencies that remain unaffected by the magnetic field. Differences can be

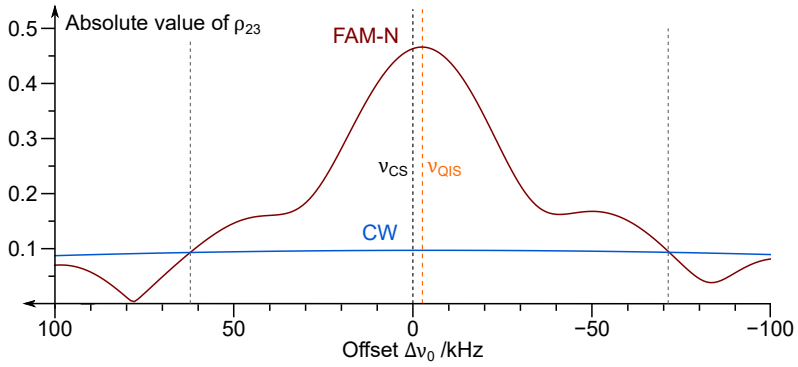

Figure 5.6: *Plot representing the variation of the amount of CT 1Q | absolute value of ρ_{23} as a function of the offset frequency on ^{87}Rb for B_0 = 14.1 T (ν_0 = 196.4 MHz), ν_1 = 100 kHz, ν_R = 12.5 kHz, ν_{CS} = 0, C_Q = 3.2 MHz and η_Q = 0. Here, the value of ρ_{23} is given in amplitude to remove the offset-induced phase. The FAM-N pulse was optimised for 66 crystallite orientations and 4 γ-angles, and this figure was obtained from applying these pulses for 320 crystallite orientations and 20 γ-angles.*

observed when FAM-N pulses are generated for values of ν_0 approaching ν_Q. Indeed, in the latter case, the Zeeman interaction cannot be considered dominant, and energy levels experience a large SOQE. As B_0 decreases, the CT lineshape gets broader (see Section 2.3.3, Equation (2.3.38)). In order to be truly ST-selective, FAM-N must also have a minimum effect on the CT lineshape, which causes changes in FAM-N when ν_0 is near ν_Q. In practice, this case is highly exceptional, and corresponds to situations where MQMAS is challenging, if not impossible. As with the MAS rate, B_0 is precisely given by the instrument, so robustness investigations are not necessary. In summary, the efficiency of FAM-N does not benefit directly from being used at high field, but this still permits a narrower SOQE and, therefore, a better sensitivity of all NMR spectra.

RF offset

Until this point, FAM-N optimisations have been performed assuming $\Delta\nu_0 = 0$ (see Equation (1.1.21)). It was shown in Section 2.3.3 that the quadrupolar interaction causes an isotropic shift of the resonance toward high-field, called the QIS. This leads to most experiments being conducted with a systematic offset from δ_{CS} of the order of a couple of kHz if the user chooses the offset to be on resonance with the observed lineshape. Furthermore, an offset is necessarily present for experiments on samples containing multiple sites. For this reason, simulations showing the impact of the offset of FAM-N were carried out. The result of this simulation is shown in Figure 5.6 and compared to CW conversion. It can be observed that FAM-N is more efficient that CW

over a far greater range than few kHz mentioned above. CW becomes more efficient in Figure 5.6 for an offset of −71 kHz and +62 kHz, thus presenting a width approximately equal to ν_1. The difference in absolute value between the positive and negative offsets can be explained by the asymmetry of the SOQE (see Section 2.3.3). Furthermore, the offset corresponding to the maximum FAM-N efficiency coincides with the CT QIS, which is $\nu_{\mathrm{QIS}} = -1.22$ kHz for the quadrupolar parameters in Figure 5.6. This implies that FAM-N is slightly more efficient when applied on resonance with the CT lineshape rather than with δ_{CS}, although the difference remains low. In conclusion, it was demonstrated that the offset $\Delta\nu_0$ is not typically an important parameter to consider, as will also be shown in Section 6.2.4.

5.2 Robustness investigations

Section 5.1 described the effects of various experimental parameters used for the optimisation of FAM-N pulses, on their efficiencies. However, in reality, a user is likely to apply FAM-N to mostly unknown systems, for which several of these parameters are unknown, or for systems that contain species with various C_Q or η_Q. The issue is that FAM-N relies on a numerical simulations, that require some knowledge of the studied system. As part of the strategy to validate the applicability of FAM-N on real samples, investigating the robustness, *e.g.*, the efficiency of FAM-N when applied to systems described by undetermined parameters, or these that deviate from the parameters used in the FAM-N optimisation, will be discussed.

5.2.1 Theoretical investigations

As discussed in Section 5.1, the static magnetic field and the MAS rate are defined by the user and the equipment, respectively, and therefore are known exactly for the FAM-N optimisation. Furthermore, it has also been proven that the asymmetry parameter and the offset both result in only a minor drop in the FAM-N efficiency in the general case, so can be neglected. This leaves potentially two unknown parameters, the ”inherent” RF field strength $\nu_{1_{\mathrm{inh}}}$ and the quadrupolar interaction. As established in Section 3.2.2, the quadrupolar interaction affects the RF nutation rate, resulting in an apparent nutation rate called the ”effective” nutation rate $\nu_{1_{\mathrm{eff}}}$. A consequence of this is that the inherent RF field is not systematically measured in practice, as it requires either a solution-state

reference, or a solid-state sample with zero- or near-zero-C_Q site. However, SIMPSON simulations require the inherent RF field strength to be specified. If C_Q is such that either $\nu_Q \gg \nu_{1_{\text{inh}}}$ or $\nu_Q \ll \nu_{1_{\text{inh}}}$, $\nu_{1_{\text{inh}}}$ can be deduced from $\nu_{1_{\text{eff}}}$ (see Section 3.2.2).

Nevertheless, the quadrupolar parameters are typically not known in advance. There are several strategies to obtain an approximate value for C_Q:

- A first strategy is to use the quadrupolar parameters of species similar to the sample of interest, *i.e.*, model compounds with similar structures if they are known.
- Another is to perform an analytical lineshape fitting of the MAS spectrum to give an idea of the order of magnitude of the quadrupolar interaction. When several sites are overlapped, this approach will give a very approximate C_Q value.
- First-principles calculation can be used to obtain an estimate of the quadrupolar parameters.
- Finally, a "typical" C_Q value for each nucleus can be used, that can be used as a last resort (see Appendix C.2 or Wasylishen *et al.*,[100] Table 2.1).

Any of the above approaches will only give an approximate, or "average" value for C_Q. For a sample with more than one site, there is no other option than to optimise FAM-N for a C_Q value that does not match that of all of the sites. Therefore, it is extremely important to understand the efficiency of FAM-N optimised for specific conditions, and then applied to others.

Figure 5.7 plots the efficiency of several FAM-N pulses, optimised for particular values of ν_1 (Figure 5.7a) and C_Q (Figure 5.7b) and thereafter applied for other C_Q and ν_1 values, respectively. In both plots, the efficiency of the most efficient CW conversion pulse for the considered ν_1 and C_Q values is shown.

RF field strength

Not only is a calibration of the RF field strength not systematically performed for quadrupolar nuclei in practice, it may change between different experiments or even over the duration of an experiment, depending on the probe tuning and other hardware-related parameters. It is important to determine how precisely the RF field must be calibrated, to ensure FAM-N still results in an improvement if the RF is not recalibrated each time.

Figure 5.7a shows that, for all the FAM-N pulses optimised for $\nu_1 \geq 75$ kHz, FAM-N is more efficient than CW conversion over the whole range chosen for ν_1, except in the low

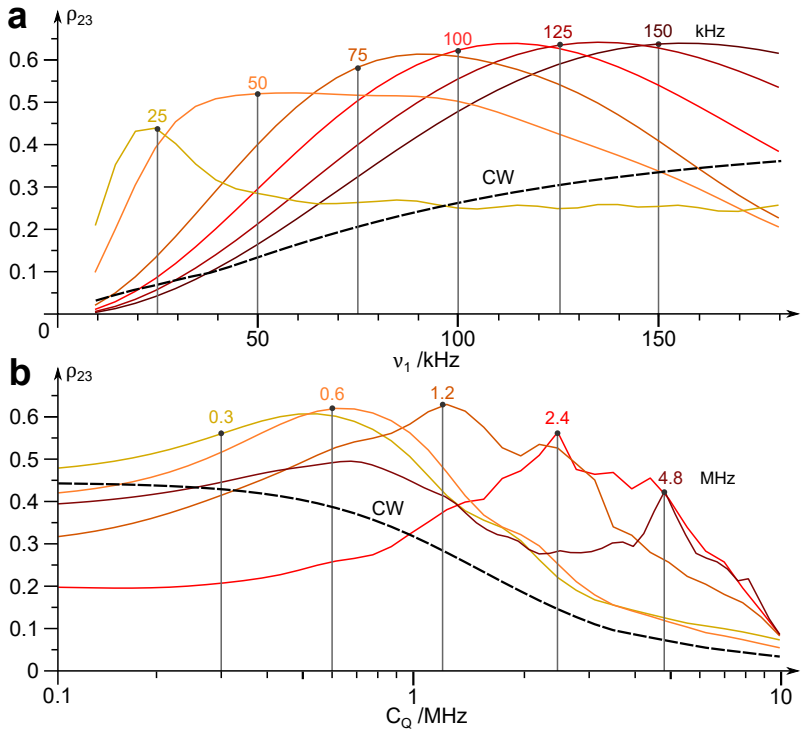

Figure 5.7: *Simulations of the amount of CT 1Q coherence | real part of ρ_{23} created by CW (dashed line) and several FAM-N pulses for ^{87}Rb ($I = 3/2$) with B_0 = 14.1 T (ν_0 = 196.4 MHz), ν_R = 12.5 kHz and η_Q = 0 as a function of* ***(a)****: the RF field strength ν_1 (38 points equally spaced from 10 to 180 kHz every 5 kHz), with ν_1 = 50, 75, 100, 125 and 150 kHz, and* ***(b)****: the quadrupolar coupling constant C_Q (40 points logarithmically spaced from 0.1 to 10 MHz), with ν_1 = 0.3, 0.6, 1.2, 2.4 and 4.8 MHz. For CW conversion, the value is the maximum observed at each point. For the FAM-N pulses, the pulse train has been kept the same as that determined by the FAM-N optimisation program (i.e., the pulse has not been re-optimised at each point). The FAM-N pulses were optimised for 66 crystallite orientations and 4 γ-angles, and applied on a same number of crystallite orientations and γ-angles.*

ν_1 regime, and that the efficiency remains approximately unchanged over a range of a few tens of kHz. For the FAM-N optimised for ν_1 = 50 kHz, the efficiency is essentially unchanged until ν_1 reaches 150 kHz. However, the form of the curve is different from that of the other FAM-N pulse, with an amount of CT 1Q coherence created remaining constant between ν_1 = 35 to 100 kHz. Finally, the curve for the FAM-N optimised for ν_1 = 25 kHz, which corresponds to the typical RF field strength achieved for low-γ nuclei, shows a much more uneven profile and a range of maximum efficiency of only a few kHz, which is still within the precision of the RF calibration.[5] However, this pulse is still more efficient than CW until applied with ν_1 above 100 kHz. Figure 5.7a suggests that the tolerable error on FAM-N parameters decreases as ν_1 gets lower, and, as shown in Section 5.1.1, that the improvement ratio overall gets higher as the RF field is low.

[5]The typical precision of a RF calibration can be estimated to be a maximum of 2 to 3 kHz.

Another point to make for Figure 5.7a is that several of the FAM-N pulses appear to be more efficient when applied at a slightly higher ν_1 than that used in the FAM-N optimisation. As investigated in Section 5.1.1, there are conditions for which the efficiency of FAM-N increases with ν_1. However, two FAM-N pulses optimised for very similar ν_1 values would not be significantly different, but one may be more efficient, explaining this observation. However, FAM-N optimised for a given ν_1 is always the most efficient FAM-N pulse for this particular ν_1 value. Nevertheless, even with the lowest RF field used in this figure, FAM-N retains a good efficiency, showing the RF field strength does not have to be precisely determined.

Quadrupolar coupling constant

Figure 5.7b, showing the efficiency of different FAM-N pulses when re-simulated using different C_Q values, exhibits multiple similarities to Figure 5.7a. First, the maxima in efficiency become sharper as C_Q increases, and so the FAM-N pulse becomes more specific to the parameters it was optimised for. All FAM-N pulses optimised for $C_Q \geq 1.2$ MHz are more efficient than CW conversion over most of the range of C_Q values chosen for the plot, with the exception of the low C_Q limit. The FAM-N pulse optimised for C_Q = 2.4 MHz is more efficient than CW for all C_Q values above 1 MHz, but is most efficient only for its optimisation C_Q value. This feature is even more pronounced for the FAM-N pulse optimised for C_Q = 4.8 MHz. As for ν_1, the simulations in Figure 5.7b show that FAM-N remains efficient over a sufficiently broad range of C_Q that only an approximative C_Q value can be used in the FAM-N simulation if a precise value is not known. Finally, as for Figure 5.7a, FAM-N optimised for C_Q = 0.3 MHz and C_Q = 0.6 MHz are most efficient for C_Q values slightly exceeding that of the C_Q used for the FAM-N optimisation. This can be explained as described above for ν_1: FAM-N is here constituted of only 2 pulses, meaning that FAM-II could be a more attractive approach.

5.2.2 Experimental investigations

The simulations discussed in Section 5.2.1 prove the robustness of FAM-N optimised for quadrupolar parameters differing from those for which it is applied experimentally. This potentially permits FAM-N to provide good enhancements for multiple sites in a same sample, even when these have very different quadrupolar parameters. A suitable way to verify this experimentally, is to apply FAM-N on samples presenting several

	Rb 1		Rb 2	
	Exp.	Sim.	Exp.	Sim.
FAM-N Rb 1	**×2.0**	**×3.4**	×2.5	×4.3
FAM-N Rb 2	×1.7	×2.7	**×2.7**	**×5.7**

Table 5.2: *Signal improvement ratios for FAM-N conversion over CW conversion for the two ^{87}Rb sites of Rb_2SO_4, measured experimentally from the MQMAS spectra shown in Figures 5.8b and 5.8c, and by simulation from Figure 5.8d for simulations. Bold values highlight for which C_Q value for which FAM-N was optimised.*

crystallographic sites.

Concerning the choice of the C_Q value used for FAM-N optimisations, the two following approaches are possible:

- choose C_Q to be an "average" value of that of all of the sites, or
- use the quadrupolar parameters for one of the site.

For the second approach, the most sensible quadrupolar parameters to choose for the optimisation are those of the less sensitive site, *i.e.*, in general, that exhibiting the highest P_Q (see Section 4.1.1). A suitable sample on which to test this approach is Rb_2SO_4 using ^{87}Rb NMR. In addition to the high sensitivity of ^{87}Rb, this particular material contains two distinct species, one with moderate C_Q and the other with high C_Q. A ^{87}Rb MAS spectrum of Rb_2SO_4 is shown in Figure 5.8a, showing the two sites Rb 1 (C_Q = 2.52 MHz, η_Q = 1.0) and Rb 2 (C_Q = 5.30 MHz, η_Q = 0.1).[45] Projections of the indirect dimension of 2D MQMAS spectra are shown in Figure 5.8b for Rb 1 and Figure 5.8c for Rb 2. Here, MQMAS was not needed to resolve the two sites, already well resolved in the MAS spectrum, but used to obtain sharp resonances for the two sites, thus increasing the accuracy of the signal comparison. Figures 5.8b and 5.8c compare the signal in MQMAS spectra recorded with a CW conversion (black line), FAM-N optimised for the quadrupolar parameters of Rb 1 (green line) and Rb 2 (red line), with the improvement ratios given in Table 5.2. Finally, Figure 5.8d shows simulations of the amount of CT 1Q created by the CW and FAM-N conversion pulses used in the experiment as a function of C_Q. As such, the effect of η_Q, which is different on the two sites, has been omitted.

As predicted in Figure 5.8d, Figures 5.8b and 5.8c show that CW conversion is more efficient for Rb 1 than Rb 2, as the latter possesses a higher C_Q value. Furthermore, and in agreement with the simulations presented in Section 5.2.1, the theoretical and experimental improvement is higher for Rb 2 than for Rb 1 for this same reason. Most importantly, the FAM-N pulse optimised for Rb 1 is most efficient on Rb 1, and the FAM-

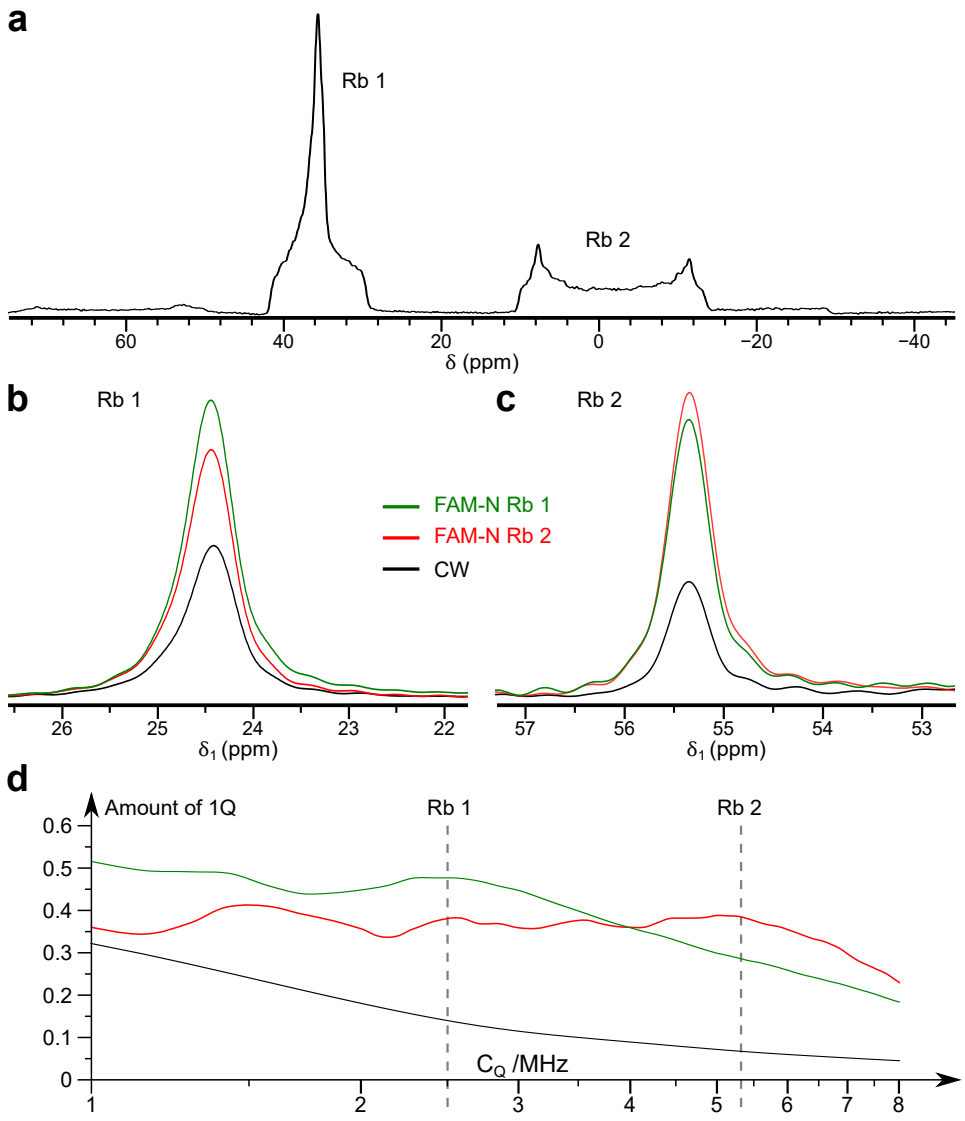

Figure 5.8: *^{87}Rb spectra of Rb_2SO_4, acquired for B_0 = 14.1 T (ν_0 = 196.4 kHz), ν_R = 12.5 kHz and ν_1 = 123 kHz.* ***(a)****: MAS spin-echo spectrum showing the two sites labelled Rb 1 and Rb 2.* ***(b,c)****: Projections of the indirect dimension of the MQMAS spectra, with expansions of the resonances for the sites* ***(b)****: Rb 1 and* ***(c)****: Rb 2, recorded using CW conversion (black line), FAM-N optimised with C_Q = 2.52 MHz and η_Q = 1.0 (green line), and with C_Q = 5.30 MHz and η_Q = 0.1 (red line).* ***(d)****: plots of the theoretical amount of 1Q | real part of ρ_{23} for the CW and FAM-N conversion pulses described previously, keeping the same colour scheme as in* ***(b,c)****. See the extended caption in Appendix C.3 for further details.*

N optimised for Rb 2 is most efficient on Rb 2, which is also successfully predicted by the simulations shown in Figure 5.8d. This last result suggests that FAM-N may also be used to selectively enhance one insensitive species, at the expense of reduced enhancement of the signal from other, more sensitive species. Finally, it can be observed there are considerable discrepancies between the theoretical and experimental improvements in Table 5.2. As discussed in Section 5.2.1, the longer the FAM-N pulse train, the less robust it is predicted to be experimentally. As discussed in Section 5.1.1, FAM-N tends to be much longer for spins $I = 3/2$ nuclei than for higher spin systems. However, the FAM-N used for the MQMAS experiments in Figure 5.8 are, indeed, rather long, with the following characteristics:

- The Rb 1 FAM-N has 14 pulses and lasts for 8.6 µs.
- The Rb 2 FAM-N has 26 pulses and lasts for 11.0 µs.

Under these conditions, the FAM-N pulses become more sensitive to experimental imperfections and inaccuracies. Furthermore, it must be remembered that there are many sources of signal loss in experiment, and many of these are hard or impossible to estimate. Other possible sources of signal loss include:

- Precision of the quadrupolar parameters used for the FAM-N optimisation,
- for temperature-sensitive nuclei, variations of the quadrupolar parameters due to sample heating during MAS experiments carried out with no temperature control,
- RF field inhomogeneities,
- probe detuning during the experiment and time variations of the RF field,
- ability of the amplifier to precisely generate the desired FAM-N pulse.

5.2.3 Experiments on various spins and samples

For further insight in the robustness of FAM-N pulses optimised for C_Q values differing from experiments, but also to experimentally verify the applicability of FAM-N conversion for any half-integer spin, FAM-N has been applied to various samples containing multiple sites with differing quadrupolar parameters. Projections of the indirect dimension of MQMAS spectra recorded on spins $I = 3/2$ (^{23}Na), $5/2$ (^{27}Al), $7/2$ (^{45}Sc) and $9/2$ (^{93}Nb) nuclei are shown in Figures 5.9a, 5.9c, 5.9e and 5.9g, respectively. Quadrupolar parameters and isotropic chemical shifts for the samples used are reported in Appendix C.2.

Following the same approach as in Figure 5.8d, Figures 5.9b, 5.9d, 5.9f and 5.9h show

simulations of the conversion efficiencies plotted against C_Q of CW (optimised on the spectrometer) and FAM-N pulses used in the corresponding experiment. The C_Q value used for the FAM-N optimisation is indicated by a solid black line, and the C_Q for each of the sites is represented by a dashed line. As explained below, some experiments were conducted using the C_Q and η_Q values of one of the sites, and some using an "average" C_Q value, according to the two approaches detailed in Section 5.2.2. As in Figure 5.8d, these plots do not show the effect of the asymmetry parameter, η_Q, leading to some systematic errors in the predicted signal improvement. It should be noted that the effect of the excitation pulse, whose efficiency also depends on the quadrupolar parameters, is not taken into account in the simulations, while this has an impact on the absolute intensities in experimental spectra. However, the relative signal between MQMAS spectra recorded using CW and FAM-N conversion is not affected by the excitation pulse, which is identical in the two experiments.

Finally, Table 5.3 reports the theoretical and experimental improvement ratios for all of the sites of the different compounds investigated here.

Sodium pyrophosphate

In $Na_4P_2O_7$, there are four ^{23}Na sites,[331] each of them having similar C_Q values (See Appendix C.2).[199] All sites are well resolved by MQMAS, as shown on Figure 5.9a, and an improvement ratio of approximately ×2 is observed between CW and FAM-N conversion. Following one of the approaches described in Section 5.2.2, the C_Q value used for the FAM-N optimisation was chosen to be an approximate value between the C_Q values of the different site present in the sample. FAM-N was optimised for

- C_Q = 2 MHz
- η_Q = 0

In Figure 5.9b, while the CW conversion efficiency steadily decreases over the range of C_Q values covered, the FAM-N efficiency shows some variation with a maximum at the value for which it has been optimised. In absolute value, the relative intensity of the different resonances in Figure 5.9a is overall consistent with Figure 5.9b with, in order of intensity, Na 3 > Na 1 > Na 2 > Na 4 for FAM-N, and Na 3 > Na 1 > Na 4 > Na 2 for CW. The differences can be explained by the effect of the excitation pulse, whose efficiency also depends on quadrupolar parameters. However, as the quadrupolar parameters are similar, the excitation is almost as efficient for all sites. Na 3, whose C_Q is the closest to that used for the FAM-N optimisation, is the most amplified. The

relative intensity does not perfectly follow the predicted relative intensities, but it can be see that the least enhanced resonance is Na 4 and those that are most enhanced are Na 1 and Na 3. The case of Na 1 is especially interesting: instinctively, one might think that its enhancement would be lower than of Na 4, as its C_Q value is further apart from the optimisation C_Q value. Figure 5.9b shows that the efficiency of FAM-N decreases until C_Q reaches approximately 2.5 MHz, then increases again to a new maximum at C_Q = 2.9 MHz, which results in the signal improvement predicted and observed for Na 1 being higher than that for Na 2 and Na 4.

Finally, it can be seen in Table 5.3 that there are large disparities between theoretical and experimental improvement ratios for all of the ^{23}Na sites of $Na_4P_2O_7$. As discussed in Section 5.1.1, FAM-N applied to spin $I = 3/2$ nuclei has some fundamental differences compared to FAM-N optimised for higher spin systems. The pulse trains are longer and possess more pulses, which can result FAM-N being less efficient in experiment than in simulations. This discrepancies have been previously observed for the ^{87}Rb MQMAS spectra of Rb_2SO_4 in Figure 5.8. Moreover, it can be seen from the other results in Table 5.3 that those differences are much smaller for higher spins. For this particular sample, reasons for the discrepancies between experiments and simulations will be investigated in Section 6.2.4, with simulations including additional parameters, such as η_Q, that were omitted in Figure 5.9b.

Kyanite

Among all quadrupolar nuclei commonly studied, ^{27}Al ($I = 5/2$) has one of the highest range of ν_Q values observed.[40, 100, 332] Kyanite (Al_2SiO_5) has four ^{27}Al sites, which are known to be difficult to resolve by 3QMAS,[260] with C_Q values ranging from 4 to 13 MHz.[260, 332–338] In the spectrum shown in Figure 5.9c, recorded at B_0 = 14.1 T, the resonances for Al 3 and Al 4 are only just resolved. As for $Na_4P_2O_7$, FAM-N was optimised for an arbitrary C_Q value that can be seen as a rough ”average” of the C_Q of the four sites. FAM-N was optimised with

- C_Q = 6 MHz
- η_Q = 0

The absolute intensities of the resonances in Figure 5.9c are very different from those predicted by the simulation of the conversion pulses in Figure 5.9d. Unlike the ^{23}Na sites in $Na_4P_2O_7$, the four ^{27}Al sites in kyanite have very different quadrupolar parameters, giving non-uniform 3Q excitation for all of the sites. However, the variation of the

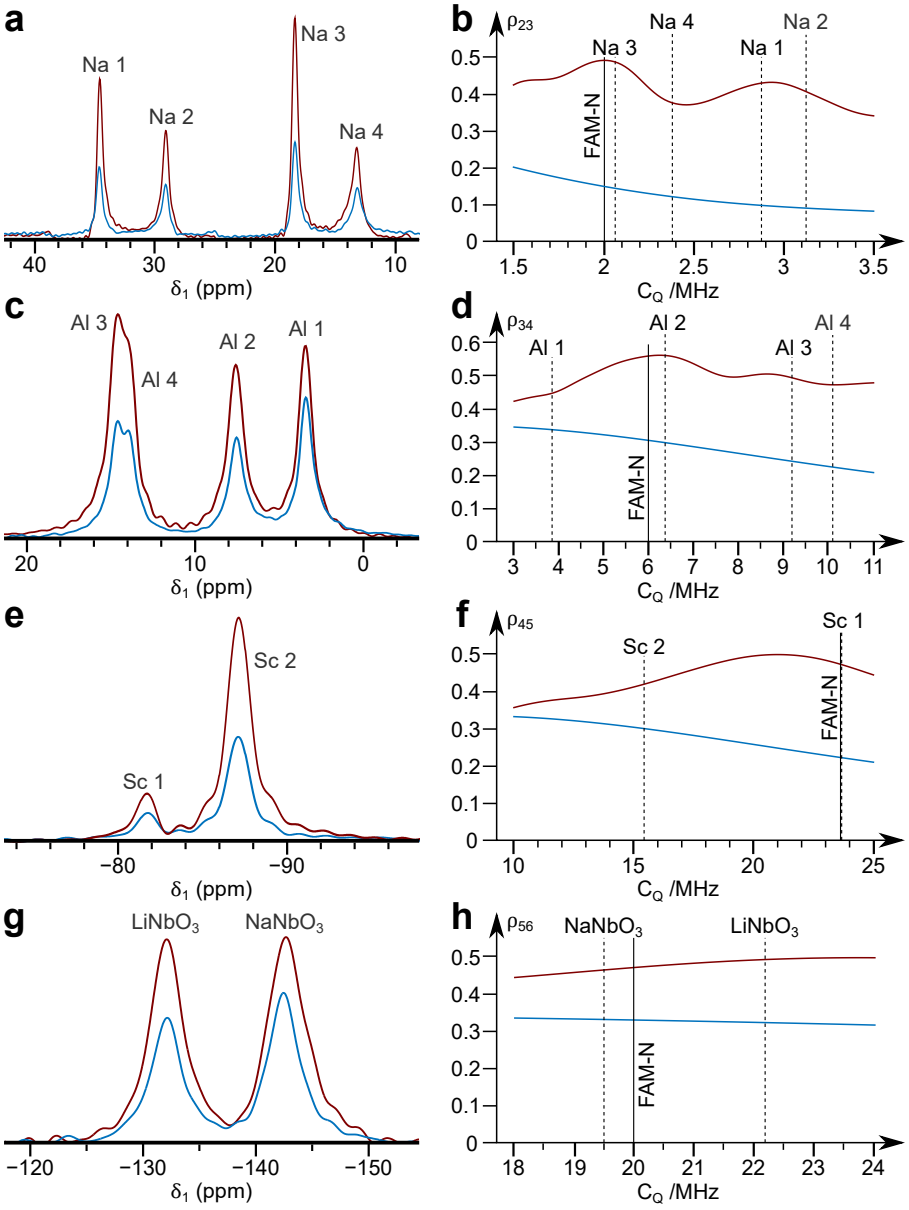

Figure 5.9: ***(a,c,e,g)**: Projections of the indirection dimension of split-t_1 shifted-echo MQMAS spectra recorded with CW (red line) and FAM-N (blue line) **(a)**: for ^{23}Na ($I = 3/2$) in sodium pyrophosphate $Na_4P_2O_7$ with B_0 = 14.1 T (ν_0 = 158.8 MHz), ν_1 = 95.8 kHz and ν_R = 12.5 kHz, **(c)** for ^{27}Al ($I = 5/2$) in kyanite Al_2SiO_5 with B_0 = 14.1 T (ν_0 = 156.4 MHz), ν_1 = 139 kHz and ν_R = 20 kHz, **(e)**: for ^{45}Sc ($I = 7/2$) in scandium oxide Sc_2O_3 with B_0 = 9.4 T (ν_0 = 97.2 kHz), ν_1 = 131 kHz and ν_R = 40 kHz, **(g)**: for ^{93}Nb in a 1:1 mixture in amount of substance of $LiNbO_3$ and $NaNbO_3$ with B_0 = 14.1 T (ν_0 = 146.8 MHz), ν_1 = 95 kHz and ν_R = 33.333 kHz. **(b,d,f,h)**: Numerical simulation of the amount of CT 1Q coherence created from initial unit 3Q coherence (the initial and detected matrix element depends on the spin quantum number I) after CW (blue lines) and FAM-N (red lines) conversion as a function of C_Q and with η_Q = 0, with all other conditions being identical to **(a,c,e,g)**, respectively. The C_Q value for which FAM-N was optimised is indicated by a solid line, and the C_Q values corresponding to each of the sites in the respective samples are indicated by dashed lines. See the extended caption in Appendix C.3 for further details.*

Sample	Site	Theoretical enhancement	Experimental enhancement
$Na_4P_2O_4$	Na 1	×4.4	×2.3
	Na 2	×4.4	×2.1
	Na 3	×3.4	×2.4
	Na 4	×3.1	×1.9
Al_2SiO_5	Al 1	×1.4	×1.4
	Al 2	×1.9	×1.7
	Al 3	×2.0	×2.0
	Al 4	×2.0	×1.7
Sc_2O_3	Sc 1	×2.1	×1.7
	Sc 2	×1.4	×2.1
Li/$NaNbO_3$	$LiNbO_3$	×1.5	×1.6
	$NaNbO_3$	×1.4	×1.4

Table 5.3: *Theoretical and experimental signal improvements between FAM-N and CW conversion pulse measured in Figure 5.9. As indicated in the main text, the theoretical improvements reported in this table do not take the asymmetry parameter η_Q into account.*

relative FAM-N efficiency with C_Q in Figure 5.9d resembles that of Figure 5.9b. FAM-N is most efficient for sites with parameters similar to these for which it is optimised, but this efficiency experiences some non-monotonic variations as C_Q changes, resulting in some oscillations and in an improvement higher for C_Q values further apart.

The improvement ratios between CW and FAM-N conversion for the four ^{27}Al sites are in good agreement with the simulations, as shown in Table 5.3, unlike the case of $Na_4P_2O_7$ discussed above. The improvement ratios for Al 3 and Al 1 are predicted exactly by the simulation, and are slightly overestimated in simulations for Al 4 and Al 2. The site with the closest C_Q to the FAM-N optimisation value, Al 2, is the most enhanced, and the site with the lowest C_Q, Al 1, despite being closer to the FAM-N optimisation C_Q than Al 3 and Al 4, is the least enhanced. However, it must be noted that, unlike the sites of $Na_4P_2O_7$, the range of C_Q for all the ^{27}Al sites of kyanite is large, resulting in the omitted parameters, such as η_Q, to cause less significant error between experiments and simulations.

Scandium oxide

^{45}Sc ($I = 7/2$) in scandium oxide is a system similar to $RbSO_4$ in Section 5.2.2: it possesses two sites, one with a C_Q much higher than the other.[339] The same approach as this last case has been employed. Instead of choosing an average C_Q value for the FAM-N optimisation, the quadrupolar parameters of the site most challenging to observed experimentally, here Sc 1, were chosen for the simulation. As a result, the improvement upon application of FAM-N is expected to be higher for Sc 1 than for Sc 2. FAM-N was optimised with the parameters

- C_Q = 23.4 MHz
- η_Q = 0.02

Owing to the large difference in C_Q for the two ^{45}Sc sites, a significant difference in their absolute intensities can be observed between the two sites in Figure 5.9f. As for the previous cases, this can be primarily attributed to the difference in efficiencies of the excitation pulse for the two sites. The improvement ratios given in Table 5.3 are of the right order of magnitude for the two sites. However, although simulation predicts the improvement upon using FAM-N to be higher for Sc 1 than Sc 2, experimentally, the opposite is observed. Although optimised for the quadrupolar parameters of Sc 1, the FAM-N pulse has a maximum conversion efficiency for a lower C_Q value of approximately 21 MHz. Two effects can explain this result. First, while Sc 1 has an asymmetry parameter near 0, whereas the asymmetry parameter for Sc 2 is η_Q = 0.62, which is not included in the simulations in Figure 5.9f. Performing a simulation to take into account this value of η_Q gives a higher improvement of ×1.6 for Sc 2. The second is the decreased robustness of FAM-N when applied for high C_Q, discussed in Section 5.2.1, where it was been shown that such FAM-N pulses are more specific for their optimisation values. Even if optimised for a given site, multiple factors can cause an error and affect the final experimental improvement as discussed previously.

Lithium and sodium niobate

^{93}Nb is one of the few sensitive $I = 9/2$ nuclei, with a high natural abundance and gyromagnetic ratio, and C_Q can be sufficiently small that MQMAS experiments are easily feasible. Here two compounds were studied, $LiNbO_3$ and $NaNbO_3$,[340, 341] which have a similar ^{93}Nb C_Q values,[340, 341] but different η_Q values (η_Q = 0.2 for $LiNbO_3$ and η_Q = 0.8 for $NaNbO_3$). As presented in Appendix C.2, commercial samples often

contain several polymorphs of $NaNbO_3$, each containing a unique site, whose C_Q values are slightly different. As a result, the C_Q value shown in Figure 5.9h for $NaNbO_3$ is that measured from a lineshape fitting of a ^{93}Nb MAS spectrum of the $NaNbO_3$ sample used, which gave C_Q = 19.5 MHz and η_Q = 0.8, similar to the quadrupolar parameters reported by Johnston *et al.*[342] The FAM-N pulse was optimised for a C_Q similar to that for ^{93}Nb in $NaNbO_3$, *e.g.*,

- C_Q = 20 MHz
- η_Q = 0

The FAM-N pulse produced using these parameters is composed of only two pulses, thus the relatively low improvement ratios observed in Table 5.3. In Figure 5.9h, the efficiency of FAM-N is steadily increasing while that of CW is steadily decreasing as C_Q increases, although by small amounts in either case. The theoretical improvement ratio is similar for $LiNbO_3$ and $NaNbO_3$, but the simulation predicted the improvement of the $LiNbO_3$ signal to be slightly higher. This is indeed observed in the experimental spectra in Figure 5.9g, and Table 5.3 shows that the experimental and experimental improvement ratios are very similar, even though the improvement is lower in simulation than in experiment. The theoretical improvement ratio does not change when η_Q is included if rounded up to two significant figures. Using more precise theoretical improvement ratios shows that including η_Q in a simulation results in only very small increases: +3% for $LiNbO_3$ and +1% for $NaNbO_3$. That is, the asymmetry parameter does not have any significant impact on the improvement given by FAM-N for this sample, which is as anticipated by the investigations conducted in Section 5.1.3 about the impact of η_Q on FAM-N pulse.

Conclusion

In conclusion, the robustness of FAM-N has been proven over a wide range of ν_1 and C_Q values, and it was demonstrated that FAM-N can be performed experimentally even when neither of these two parameters is known precisely, and for samples that contain multiple sites. This evaluation confirmed the validity of the two approaches described in Section 5.2.2, concerning the choice of an approximate C_Q value for the optimisation for samples with multiple sites, as both approaches produced appreciable signal improvement compared to CW conversion for all sites. However, the investigations conducted here brought to light some inconsistencies between and experimental signal improvements in some cases, as visible in Table 5.3. Therefore, uncertainties remain

concerning the ability of FAM-N to produce precisely and quantitatively a desired effect. However, in almost all practical cases, a signal enhancement will always be observed.

5.3 Comparing FAM-N to other methods

The previous sections prove that FAM-N enables more efficient 3Q to 1Q coherence transfer than CW conversion, both in simulation and experiment. However, it is now necessary to compare the efficiency of FAM-N with the other signal-enhancement methods presented in Section 4.3 to establish that FAM-N is a suitable alternative. The methods compared in this section are CW (as a reference), FAM,[6] DFS, as well as SPAM as this method is also applied by substituting the conversion pulse.

5.3.1 Theoretical investigations

To understand and assess how well each method performs the 3Q to 1Q coherence transfer step, SIMPSON simulations were carried out for each pulse type under a variety of conditions as shown in Figure 5.10. The CW and FAM-II pulses were obtained from the FAM-N optimisation program (see Section 4.3.3). For SPAM, a numerical optimisation of the high power part of the pulse was carried out. A numerical optimisation of FAM-I and DFS, both requiring multiple-variable optimisations, has been omitted from these simulations and will only be considered experimentally in Section 5.3.2. However, as these are based on the same principles, it can reasonably be assumed that the efficiency of DFS and FAM-I should approach that of FAM-N.

Figure 5.10a plots the amount of CT 1Q coherence created by different methods as a function of the RF field strength ν_1. CW conversion is always less efficient than the other methods but, as discussed in Section 5.1, its efficiency, in addition those of SPAM and FAM-II, increases with RF field strength. The relative improvement of SPAM compared to CW increases as the RF field strength increases. FAM-N can be seen to be more efficient than the other methods, especially at low RF. However, in the region corresponding to strong RF ($\nu_1 > 170$ kHz), FAM-N is best with only two pulses, as discussed in Section 4.3, thus the efficiency of FAM-N is that of FAM-II.

[6] Here composed of two pulses, optimised experimentally.

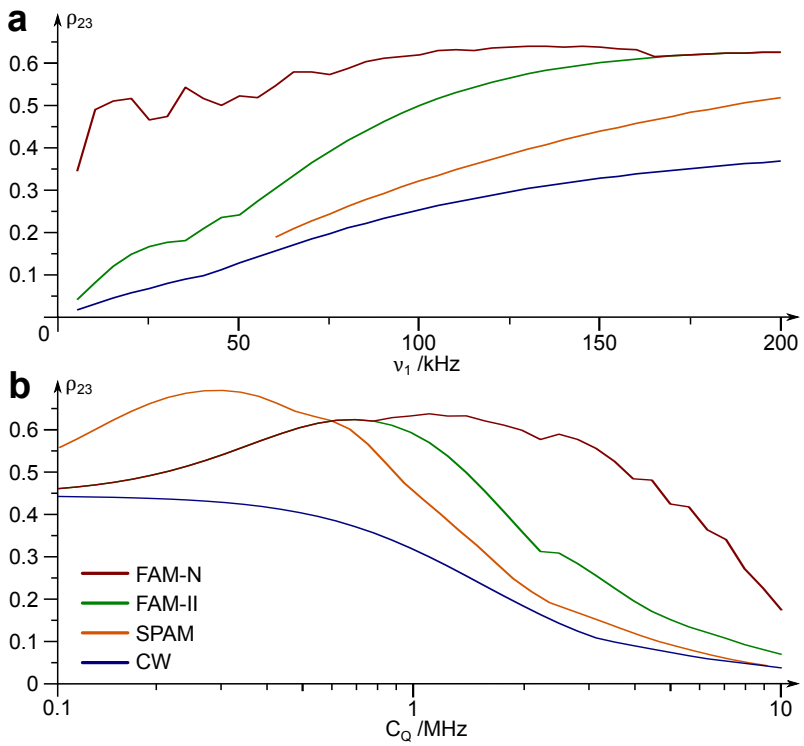

Figure 5.10: *Maximum amount of 1Q coherence | real part of ρ_{23} created from unit 3Q coherence, for ^{87}Rb ($I = 3/2$) with B_0 = 14.1 T (ν_0 = 196.4 MHz) and ν_R = 12.5 kHz,* ***(a)****: as a function of C_Q with ν_1 = 114 kHz, and* ***(b)****: as a function of ν_1 with C_Q = 1.2 MHz, for the following methods: CW (blue), FAM-II with two pulses (green), SPAM (orange), and FAM-N (red). The FAM-N pulses were optimised for 66 crystallite orientations and 4 γ-angles, and applied on a same number of crystallite orientations and γ-angles.*

Figure 5.10b reflects the same information as Figure 5.10a, but now plots the efficiency against C_Q. The efficiency of CW conversion decreases as C_Q increases, becoming negligible for C_Q = 10 MHz. As also established for Figure 5.10a, the FAM-N pulse consists only of two pulses at low C_Q, and its efficiency is identical to FAM-II for $C_Q \leq 1$ MHz. Above this, FAM-N remains the most efficient method. As previously, the efficiency of FAM-N and FAM-II is always superior than of CW. The SPAM pulse shows a maximum efficiency for $C_Q = 0.3$ MHz, and is more efficient than FAM-II and FAM-N for $C_Q \leq 1$ MHz. The improvement for SPAM drops rapidly as C_Q increases, and for $C_Q \geq 1$ MHz, the improvement then drops and becomes insignificant at high C_Q.

The simulations in Figure 5.10 shown that FAM-N exhibits significant sensitivity advantages over the other methods for a wide range of ν_1 and C_Q values. SPAM appears to be more suitable for sites with low C_Q, while FAM-II become as efficient as FAM-N in the high RF and low C_Q regimes, suggesting that FAM-N is especially interesting for sites with high C_Q, or when low RF field is available.

B_0	Site	SPAM	FAM-I	FAM-II	DFS	FAM-N
9.4 T	Rb 1	×1.40	×1.40	×1.50	×1.70	×1.90
	Rb 2	×1.40	×1.20	×1.40	×1.60	×1.95
	Rb 3	×1.45	×1.45	×1.45	×1.45	×1.95
14.1 T	Rb 1	×1.25	×1.25	×1.70	×1.90	×2.05
	Rb 2	×1.25	×1.25	×1.75	×1.90	×2.05
	Rb 3	×1.30	×1.25	×1.60	×1.75	×1.95
20.0 T	Rb 1	×1.95	×2.95	×2.40	×3.35	×3.40
	Rb 2	×1.90	×2.70	×2.20	×3.00	×3.35
	Rb 3	×1.90	×2.70	×2.20	×3.00	×3.35

Table 5.4: *Experimental signal improvement ratios for SPAM, FAM-II (two pulses), DFS and FAM-N conversion pulses relative to CW for the ^{87}Rb MQMAS spectra shown in Figures 5.11c, 5.11d and Figures 5.11e, where ×1 corresponds to no improvement.*

5.3.2 Experimental comparison to other methods

To experimentally investigate the efficiency of FAM-N, 3QF-MAS and MQMAS spectra were recorded comparing FAM-N to the other methods introduced in Chapter 4, for various spin systems and samples. To make the comparisons as reliable as possible, the different methods were optimised and the spectra were recorded back to back using identical hardware set-ups. The limit of these comparison lies arise from the difficulty of optimisation of specific methods. To this extent, SPAM and FAM-II, that are optimised with one parameter at the time, leading to the maximum improvement being obtained with almost no ambiguity, are the easiest methods to optimise experimentally. In contrast, FAM-I and DFS, and their multiple-parameter optimisations, leave some uncertainty over whether the signal improvement observed is the global maximum possible improvement for a given system. For this reason, it is not clear whether some methods are intrinsically more efficient than others, or if some further improvement could have been obtained by spending more time on their optimisation. However, it could be argued that the optimisations carried out in this study were already more rigorous and time consuming than would be carried out in a ”typical” spectroscopy experiment.

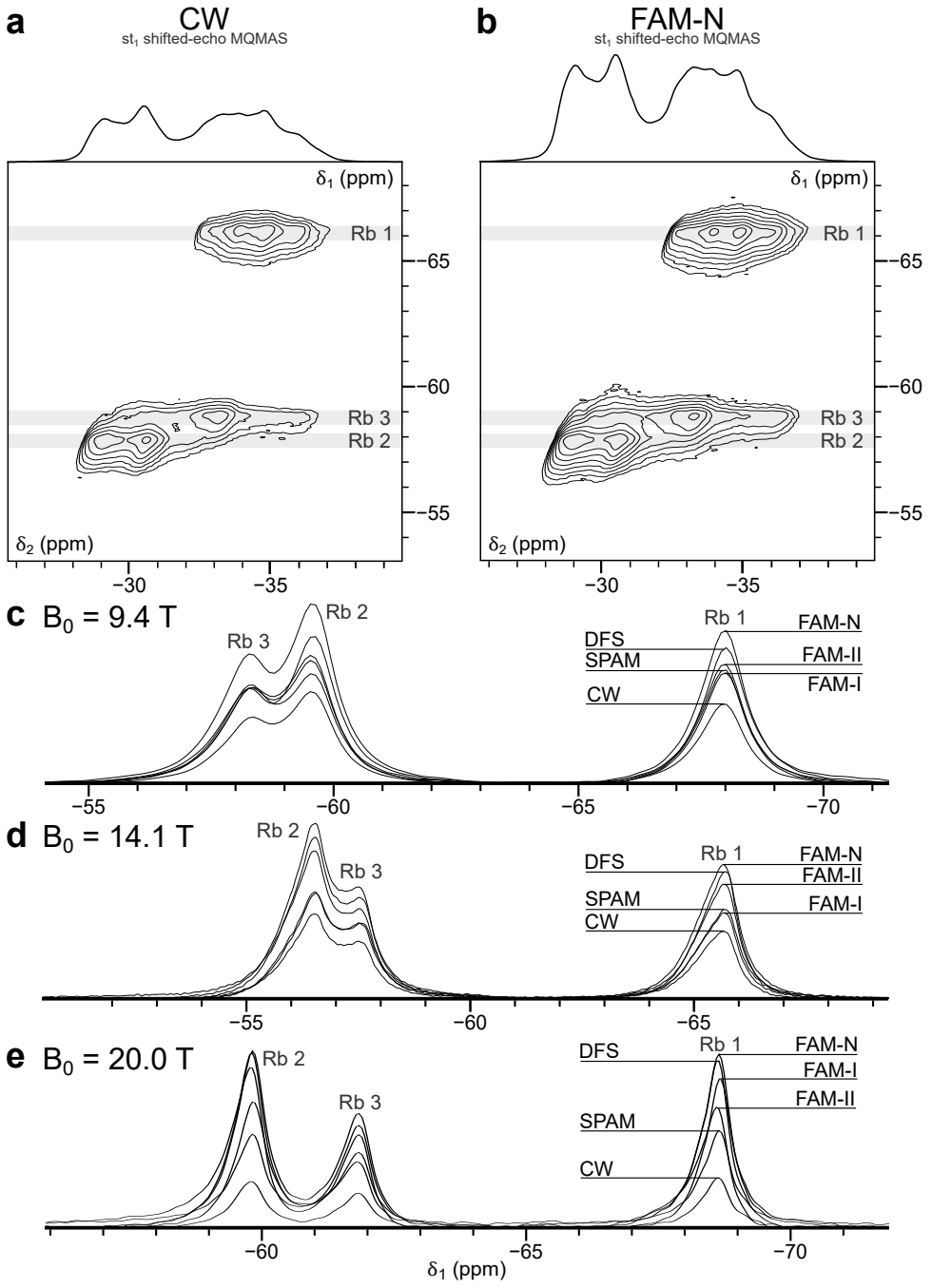

Figure 5.11: ***(a)*** *and* ***(b)****: ^{87}Rb MQMAS spectra of $RbNO_3$, showing projections of the direct dimension, recorded at B_0 = 14.1 T (ν_0 = 196.4 MHz), ν_1 = 114 kHz and ν_R = 12.5 kHz, with* ***(a)****: CW and* ***(b)****: FAM-N conversion pulses. Contour lines in* ***(a,b)*** *are identical to allow direct comparison.* ***(c,d,e)****: Projections of the indirect dimension of ^{87}Rb MQMAS spectra of $RbNO_3$, recorded with CW, SPAM, FAM-I, FAM-II, DFS and FAM-N conversion pulses, for ν_R = 12.5 kHz and* ***(c)****: B_0 = 9.4 T (ν_0 = 130.9 MHz) and ν_1 = 161 kHz,* ***(c)****: B_0 = 14.1 T (ν_0 = 196.4 MHz) and ν_1 = 114 kHz, and* ***(e)****: B_0 = 20.0 T (ν_0 = 278.2 MHz) and ν_1 = 76 kHz. See the extended caption in Appendix C.3 for further details.*

^{87}Rb spectra of $RbNO_3$

^{87}Rb MQMAS spectra of $RbNO_3$ are useful for the experimental comparison of the different methods, owing to the high sensitivity and fast T_1 relaxation of this nucleus. Figures 5.11a and 5.11b show two ^{87}Rb MQMAS spectra of $RbNO_3$ recorded with CW and FAM-N conversion, respectively, and Figures 5.11c, 5.11d and 5.11e show the projections of the indirect dimension of MQMAS spectra recorded with each different conversion pulses, for different B_0 field strengths. For all the spectra in Figure 5.11, FAM-N was not re-optimised experimentally, *e.g.*, the pulse was identical in the optimisation and in the experiment. The experimental improvement ratios measured on these projections are reported in Table 5.4 for each site. Each of the experiments have been performed independently multiple times, giving improvement ratios consistent with these reported in Table 5.4. Here, the experiments shown are acquired at different fields to determine if improvements ratios are consistent on different spectrometers.

As first sight, it seems that the improvement ratios for all sites increases with the magnetic field. In reality, as all spectra have been recorded with the maximum RF field strength available on a given spectrometer, the differences are due to the variations in the RF field available on the probes of each spectrometer, which happened to be the highest on the probe of the 9.4 T magnet and the lowest on the probe of the 20.0 T magnet (see the extended figure caption of Figure 5.11 for details). This implies that CW conversion is more efficient on the B_0 = 9.4 T spectrometer than on the B_0 = 20.0 T spectrometer.

The improvements observed for all sites, and on all spectrometers, are similar for all sites, with the differences in the absolute intensity explained by the efficiency of the excitation pulse. One important observation in Table 5.4 is that the improvement ratio given by FAM-II, DFS and FAM-N always seem to follow a same order, with FAM-N and DFS being the most efficient methods. However, it remains unclear whether this difference is due to FAM-N being intrinsically more efficient than DFS or to the practical difficulties in optimising DFS, which could potentially reach, or surpass, the efficiency of FAM-N if sufficient time and effort were spent on the optimisation. Furthermore, the differences between the improvements of DFS and FAM-N are often not sufficiently significant to be considered actual (typically 5 to 10%). FAM-II is consistently less efficient than DFS by several tens of percent, agreeing with the comparisons reported in the literature.[237] It can also be observed that the signal improvement obtained using FAM-I is much higher on the B_0 = 20.0 T spectrometer than on the others, where

FAM-II is more efficient. As discussed for Figure 5.2, FAM-N tends to be composed of a greater number of pulses as ν_1 decreases. This indicates that the windowed FAM-I would have a significant advantage over FAM-II, as it allows many pulses to be optimised simultaneously. As for DFS, the need for a multiple parameter optimisation for FAM-I may also explain some of the differences.

SPAM appears to produce lower improvements than the other methods, which is consistent with previously reported comparisons.[237, 297] It was established in Section 5.3.1 that SPAM is less efficient as the RF field strength of the high-power component of the pulse decreases. There is no correlation with the field B_0 observed in Table 5.4, with SPAM being most efficient on the B_0 = 20.0 T spectrometer, then on the B_0 = 9.4 T spectrometer, and finally on the B_0 = 14.1 T spectrometer. The mechanism of SPAM is different from the other methods and its efficiency depends on the CT-selective RF field strength. This dependency was not analysed in this work, and the CT-selective RF field has not been optimised as it would turn SPAM, described here as being the easiest method to optimise, into a method then dependent on multiple parameters. Nevertheless, the order of magnitude of the improvement ratios given by SPAM are sufficient to state that FAM-N and DFS are normally much higher.

Various samples

The set of experiments discussed above show that FAM-N is able to achieve signal improvements similar, or superior, to DFS and other MQ conversion methods for ^{87}Rb NMR of $RbNO_3$, which is a standard and sensitive model sample. For further insight, comparisons were performed for multiple samples with different spins and quadrupolar parameters. Figure 5.12 shows 3QF-MAS spectra recorded with CW, SPAM, FAM-II, DFS and FAM-N conversion, and the corresponding signal improvement ratios is given in Table 5.5. For these experiments, experimental re-optimisation of the FAM-N duration was performed and applied if significant signal improvement was observed. The high-power component of the SPAM pulse was also re-optimised. Nuclei with different spins I are considered here to ensure that the observations above, for $I = 3/2$, are also applicable to higher spins.

Figure 5.12a shows ^{23}Na ($I = 3/2$) spectra of sodium pyrophosphate ($Na_4P_2O_7$). This sample was introduced in Section 5.2.3, but studied using different experimental conditions. The conversion pulses, as well as the high-power part of the SPAM pulse, was applied for ν_1 = 53 kHz. The change in lineshape observed in Figure 5.12 between the

Nucleus	Spin I	SPAM	FAM-II	DFS	FAM-N
^{23}Na	$3/2$	×1.2	×2.6	×2.9	×3.4
^{17}O	$5/2$	×1.3	×1.8	×1.4	×2.0
^{85}Rb	$5/2$	×1.1	×2.0	×2.8	×3.9
^{45}Sc	$7/2$	×1.6	×2.1	×2.2	×2.5

Table 5.5: *Signal improvement ratios for SPAM, FAM-II (two pulses), DFS and FAM-N conversion pulses relative to CW for the spectra reported on Figure 5.12, where 1 corresponds to no improvement.*

different methods affects the precision of the improvement ratios reported in Table 5.5. For this sample, experimental re-optimisation of FAM-N was performed, but not applied in the spectra in Figure 5.12a as the observed improvement was insignificant. As discussed previously, ^{23}Na is a very sensitive nucleus, despite somewhat long T_1 relaxation times, and often exhibits sites with moderate C_Q, typically 1 MHz. It can be seen in Table 5.5 that the improvement achieved for FAM-N is greater than that for DFS, despite FAM-N being applied using its optimisation values while one to two hours of experimental optimisation was necessary for DFS. As explained above, it is not possible to state for certain that this is due to FAM-N being inherently more efficient than DFS, as DFS requires multiple parameters to be optimised. FAM-II also give an appreciable signal improvement, approaching that of DFS as the second pulse of a FAM train is generally responsible for most of the signal improvement, as discussed in Section 4.3.3. The improvement obtained for SPAM is much lower than for the other methods, even with the re-optimisation of the high-power component of the pulse.

Figures 5.12b and 5.12c show of 3QF-MAS spectra recorded for two spin $I = 5/2$ nuclei, ^{17}O in ^{17}O-enriched SIZ-4, a metal-organic framework,[343] and ^{85}Rb in $RbNO_3$. Both nuclei present some sensitivity limitations: ^{17}O has a moderate gyromagnetic ratio, but more importantly some level of isotopic enrichment is absolutely necessary for NMR spectroscopy to be carried out in a reasonable timescale. Here, the sample is enriched to 10%. ^{85}Rb is a low-γ nucleus, but benefits from relaxation times even faster than those reported for ^{87}Rb,[45] and a higher natural abundance than ^{87}Rb. However, for both of these samples, the low sensitivity of 3QF leads to a rather long optimisation process. The first consequence of those sensitivity limitations is for DFS, which requires extensive experimental optimisation. As shown in Figures 5.12b and 5.12c, the signal improvement ratios given by DFS is relatively lower than those observed for $Na_4P_2O_7$ in Figure 5.12a, where optimisation was easier. FAM-N was experimentally re-optimised for SIZ-4, and the process lasted for less than one hour. The change in the total

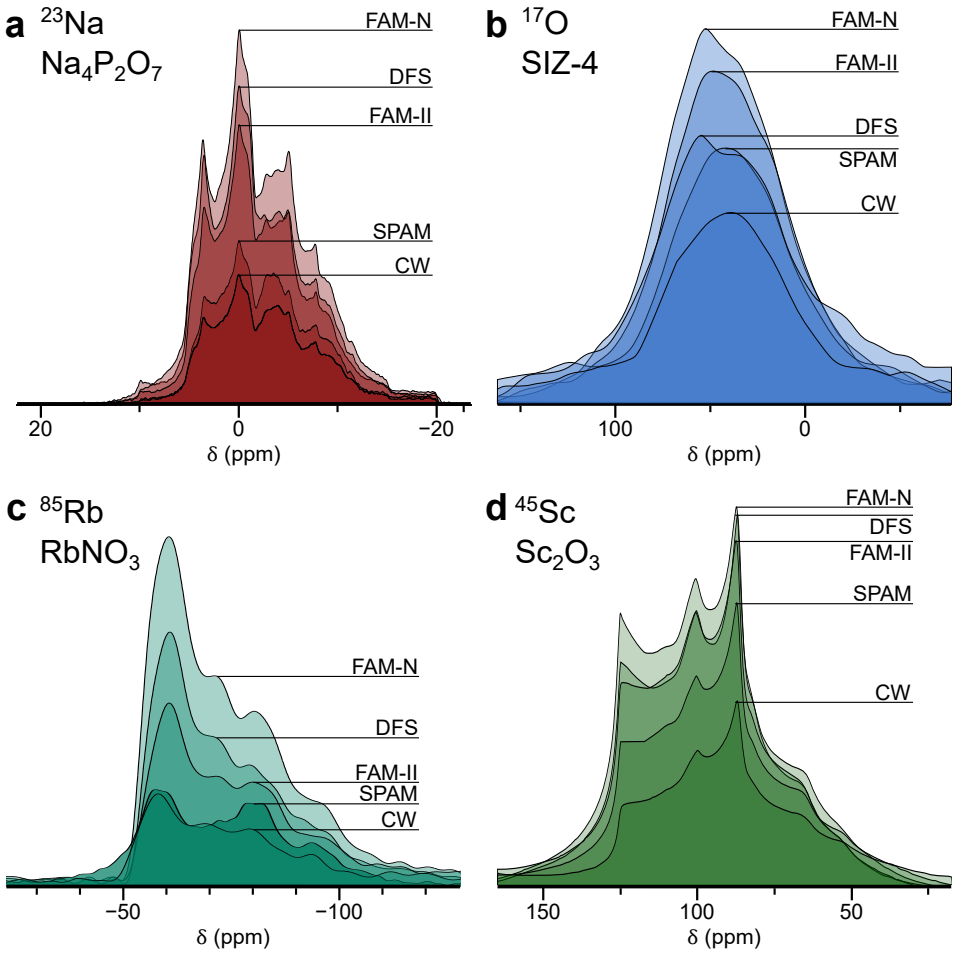

Figure 5.12: *3QF NMR spectra, recorded for B_0 = 14.1 T using five methods for 3Q to 1Q coherence conversion : CW, SPAM, FAM-II (two pulses), DFS and FAM-N, for ν_R = 12.5 kHz and on samples containing* ***(a)****: ^{23}Na ($I = 3/2$, ν_0 = 158.8 MHz),* ***(b)****: ^{17}O ($I = 5/2$, ν_0 = 81.4 MHz),* ***(c)****: ^{85}Rb ($I = 5/2$, ν_0 = 58.0 MHz) and* ***(d)****: ^{45}Sc ($I = 7/2$, ν_0 = 145.8 MHz). Details about the samples are given in Appendix C.2 and the experimental improvement ratios relative to CW are given Table 5.5. See the extended caption in Appendix C.3 for further details.*

duration of the FAM-N pulse after experimental re-optimisation is significant, changing from 38.4 to 10.2 µs, because the FAM-N pulse was optimised for dehydrated SIZ-4, but applied on wet SIZ-4, for which the quadrupolar parameters are not perfectly known (See Appendix C.2 for details). The DFS optimisation was carried out over several NMR time slots, taking a total of 8 h. FAM-N was not experimentally re-optimised for $RbNO_3$, and the more rapid T_1 relaxation of ^{85}Rb resulted in the DFS optimisation taking only several hours. Owing to these optimisation difficulties, DFS in Figure 5.12b gave less signal than FAM-II, even though it is normally expected to reach at least the same improvement. The improvement for SPAM is quite significant for SIZ-4, but very low for $RbNO_3$. In Figure 5.10, it was shown that the improvement given by SPAM relative to

CW decreases with the RF power level of the high-power component of the pulse. This is consistent with the improvements observed for SPAM on Figures 5.12b and 5.12c, as ^{85}Rb has a lower gyromagnetic ratio than ^{17}O and, hence, an inherently lower ν_1 for a given RF field B_1.

Finally, Figure 5.12d shows ^{45}Sc ($I = 7/2$) 3QF-MAS spectra of Sc_2O_3. This sample has been discussed previously in Section 5.2.3 for B_0 = 9.4 T. As for $Na_4P_2O_7$, the precision of the improvement ratios in Table 5.5 in Figure 5.12d is affected by the presence of several overlapped lineshapes. ^{45}Sc is a very sensitive nucleus, with fast relaxation rates, 100% natural abundance, and a low typical C_Q. This makes experimental optimisations reasonably rapid, which is reflected in the improvement ratio observed for DFS, which almost reaches that of FAM-N. A re-optimisation attempt was performed for the FAM-N pulse, giving an almost identical value to the optimisation value. The optimisation of DFS took between one and two hours. In spite of the time dedicated to DFS optimisation, a similar improvement was obtained with FAM-II. Finally, the improvement obtained for SPAM is quite high, as expected for a high-γ nucleus, as discussed previously.

5.3.3 Conclusion for each method

A summary of the experimental conditions under which a given method gives best results for 3Q to 1Q conversion in MQMAS experiment is given in Table 5.6. The conditions considered are denoted as ”average” and ”high” ν_1, and ”low”, ”moderate” and ”high” C_Q. The ease of optimisation reflects the time required to optimise properly the pulse parameters in experiments.[7,8]

SPAM SPAM is among the easiest methods to optimise, and in most cases result in an appreciable signal improvement. SPAM turns out to be increasingly more efficient as C_Q decreases, thus SPAM is probably the most suitable method in this case. However, re-optimisation of the high power part of the pulse may be necessary to achieve the highest improvement.

FAM-II FAM-II performs best for situations where only a few pulses are required, which cover most of the usual situations. FAM-II is most interesting when high RF field strength is available, and for species with low to moderate

[7] ν_1 and C_Q values are denoted by the qualitative term of ”low”, ”average” and ”high” as an objective definition of what constitutes a ”low”, ”average” and ”high” ν_1 or C_Q is complicated be established.

[8] ”Average” RF and ”high” RF denotes the RF used non central-transition selective pulses, in contrast to the lower RF, used for CT-selective pulses.

	ν_1		C_Q			Ease of
	Avrg	High	Low	Avrg	High	Optimisation
CW	−	∼	∼	∼	−	+
SPAM	−	+	+	∼	−	+
FAM-II	∼	+	∼	+	∼	∼
FAM-I	+	∼	−	∼	+	∼
DFS	+	+	∼	+	+	−
FAM-N	+	+	∼	+	+	+

Table 5.6: *Table showing qualitatively under which conditions CW, SPAM, FAM-I, FAM-II, DFS, and FAM-N conversion pulses are appropriate to use, "+" being "good", "∼" being "correct" and "−" being "poor".*

C_Q, although the SPAM approach appears to work best for low C_Q. Nevertheless, this method may still be useful at low RF or low C_Q, as the optimisation procedure is straightforward and the improvement almost guaranteed.

FAM-I FAM-I is more suitable than FAM-II for systems where a FAM-II train requires a large number of pulses. Those include species with high C_Q, or for low RF field strengths - which includes low-γ nuclei. This method is much less useful in other cases, as it requires a multiple parameters to be optimised.

DFS DFS is suitable for experiments at both moderate and high RF field. For the case of low RF field strength case, a wider sweep would be needed. In spite of DFS not being as efficient as SPAM for sites with low C_Q, DFS still gives an improvement, and performs best for species with moderate to high C_Q ; high C_Q also means that a wider sweep is required. The main drawback is the time required to correctly optimize the pulse. The optimisation process may be long, or even impossible, to carry out on samples with low sensitivity, because of the necessary time-consuming optimisation. Numerical simulations could also be challenging for this reason.

FAM-N FAM-N is suitable for species with a similar range of C_Q and RF values to DFS. The strength of the method is that the optimisation process is much more straightforward than DFS and the other methods discussed here, and, consequently FAM-N is more suitable for insensitive samples, that require time-consuming optimisations. The main drawback of FAM-N is the need

to know some of the system parameters in advance for the purpose of the optimisation, as discussed in Section 5.2.1.

In light of these results, it is safe to state that FAM-N is, generally speaking, more efficient than SPAM and FAM, and equally or slightly more efficient than DFS. However, FAM-N presents a significant advantage compared to DFS, as it requires no re-optimisation for similar signal improvements to DFS. This is particularly helpful when performing MQMAS on insensitive or challenging nuclei. An experimental re-optimisation of FAM-N which was observed to result in slightly more signal in the general case, when approximative values for ν_1 and C_Q are known. Therefore, this can be omitted when it is lengthy or challenging. Thorough investigation of this later case will be presented in Section 6.1.

Chapter 6

Applications of FAM-N to different systems

Introduction

Chapter 5 demonstrated that FAM-N was able to produce a significant improvement of the 3Q to 1Q conversion efficiency, comparable to the other methods reported in Chapter 4, for a wide range of model samples and for any half-integer spin. This method has also been shown to be robust towards miscalibration of experimental parameters, or if these are not known at all, potentially allowing FAM-N to be applied on samples about which little information is known. Finally, it has been shown that this improvement is possible without optimisation on the spectrometer.

These two last properties of FAM-N pulses are particularly attractive, as FAM-N should, in principle, enable good sensitivity enhancement for samples on which 3QF is extremely inefficient, without the need for a lengthy optimisation process. Section 6.1 presents MQMAS spectra recorded on a variety of samples that can be qualified as being ”challenging” owing to unfavourable properties such as a low gyromagnetic ratio (low-γ), low natural abundance, or that contain species exhibiting a very high C_Q. These investigations are necessary to prove that FAM-N, applied in Chapter 5 to mostly samples that have a high sensitivity in NMR, can be successfully employed on ”real” samples, that present a challenge for recording spectra with a good SNR in a reasonable time scale. Finally, miscellaneous investigations into others aspects of FAM-N pulses will be discussed in Section 6.2.

Section	Compound		Nucleus	High C_Q	Low-γ	Low natural abundance
6.1.1	Berlinite	$GaPO_4$	^{71}Ga	✗		
	Andalusite	Al_2SiO_5	^{27}Al	✗		
6.1.2	Potassium sulfate	K_2SO_4	^{39}K		✗	
	Enstatite	$MgSiO_3$	^{25}Mg		✗	✗
	Brucite	$Mg(OH)_2$	^{25}Mg		✗	✗
6.1.3	Forsterite	Mg_2SiO_4	^{25}Mg	✗	✗	✗

Table 6.1: *Table showing the unfavourable characteristics that apply to the samples investigated using the MQMAS experiment in this section.*

6.1 Applications of FAM-N to challenging systems

Systems referred as ”challenging” possess features that decrease the sensitivity either of 3QF, or indeed of any NMR experiment. There are multiple sources of signal loss, which include

Low natural abundance: In this case, all NMR experiments are very insensitive, and, the sensitivity problems associated with MQMAS are even more dramatic.

Low-γ: Not only are all NMR experiments insensitive, but, in addition, also the efficiency of the 3QF steps are greatly reduced as only weak RF field strengths are available for such a nucleus, as discussed in Section 4.1.1.

High C_Q: As established in Section 4.1.1, the efficiency of both the 3Q excitation and conversion are less efficient when C_Q is high. Moreover, the large SOQE result in a very broad CT lineshape, for which fast MAS is required. This not only results in a reduced sample volume (see Table C.1), buy also, fast MAS rates have been shown to reduce the 3Q excitation efficiency.

In this section, MQMAS spectra recorded with FAM-N conversion on several samples exhibiting one or more of the unfavourable properties described above are presented and analysed. For clarity, Table 6.1 summarises the different samples investigated in this section and shows which of the characteristics above apply. For all samples, the quadrupolar parameters have been obtained from literature as described in Appendix C.2.

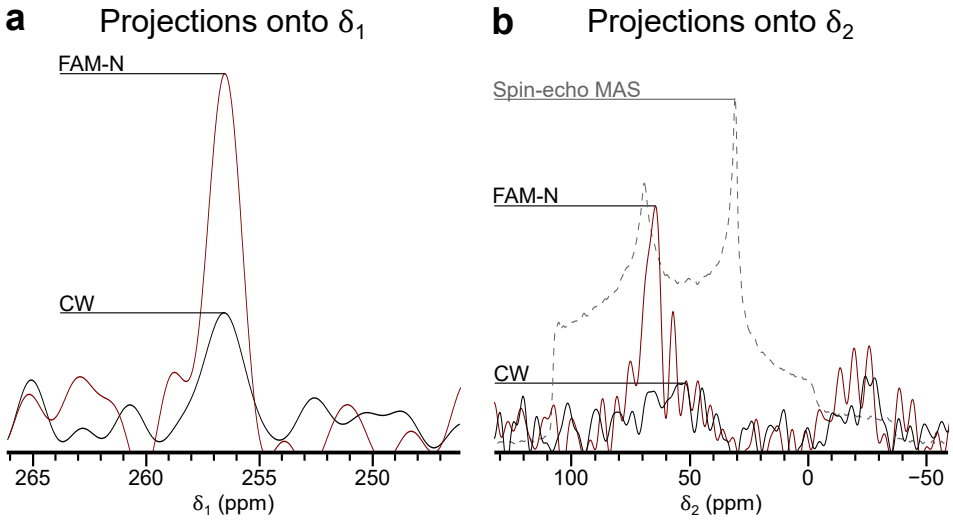

Figure 6.1: *Projections of ^{71}Ga split-t_1 shifted-echo MQMAS spectra of $GaPO_4$ berlinite, each recorded in 52 h, at B_0 = 14.1 T (ν_0 = 183.1 MHz) with ν_R = 30 kHz and ν_1 = 115 kHz.* ***(a)****: Projections of the indirect dimension and* ***(b)****: of the direct dimension of spectra recorded with CW (black lines) and FAM-N (red lines) conversion, with the MAS spin-echo spectrum being shown by a dashed grey line. See the extended caption in Appendix C.3 for further details.*

6.1.1 Strong quadrupolar coupling

$GaPO_4$ berlinite

^{71}Ga is a spin $I = 3/2$ nucleus that possesses an extremely high quadrupolar moment, giving a typical C_Q of 150 MHz according to Wasylishen *et al.*[100] Berlinite, possessing a single site with C_Q = 8.8 MHz corresponds to the upper C_Q limit for which MQMAS is recordable at B_0 = 14.1 T for $I = 3/2$.[344]

As stated previously, one difficulty of acquiring spectra for samples with high C_Q is that they require fast MAS to be used, limiting the efficiency of the 3Q excitation pulse. For $GaPO_4$, with a CT linewidth of $\Delta\nu_Q^{(2)}$ = 27.5 kHz at B_0 = 14.1 T, a fast MAS rate of ν_R = 33.333 kHz was absolutely necessary for this experiment. Figure 6.1a shows the projection onto the indirect dimension of MQMAS spectra recorded with CW and FAM-N conversion pulses. The difficulty of recording an MQMAS spectrum for ^{71}Ga in this system is clearly visible, considering the SNR observed in Figure 6.1a in spite of the long acquisition time. Furthermore, it is much more difficult to successfully observe signal in a MQMAS spectrum using CW conversion, which is the reason for the long acquisition time. On the other hand, signal can be observed in MQMAS spectra recorded with FAM-N after an overnight of acquisition. The use of MQMAS rather a 3QF-MAS experiment is useful to estimate the improvement ratio between CW and FAM-N conversion,

as the lineshapes for the latter experiment shown in Figure 6.1b exhibits very significant lineshape distortions. This results in a lineshape that is impossible to fit with fitting programs, giving P_Q as the only information that can be extracted from the spectrum. Moreover, the barycentre of the CW FAM-N spectrum is difficult to measure on the CW spectrum due to the low SNR observed. From the MQMAS spectrum recorded with FAM-N conversion, P_Q = 9.2 MHz, obtained using $\{\delta_1, \delta_2\} = \{255 \text{ ppm}, 20 \text{ ppm}\}$ in the equations given in Appendix E.1,[1] which is identical to the value reported in the literature.[345] It can be seen in Figure 6.1a that the signal obtained in the CW spectrum is barely above the noise to be able to determine precisely the position of the signal, which is not the case for the FAM-N spectrum. The improvement ratio between FAM-N and CW is estimated to ×3.0 from the spectrum in Figure 6.1a against ×3.6 in simulation. As is often observed, the improvement is lower in experiment than in practice, but in this case, the agreement is better than that observed for spin $I = 3/2$ nuclei in Chapter 5.

Andalusite

^{27}Al NMR of andalusite presents a similar challenge as ^{87}Rb NMR of Rb_2SO_4 shown in Section 5.2.2, as this sample possesses two ^{27}Al sites with very different quadrupolar parameters. As has been discussed previously for this case, FAM-N conversion has been optimised for the site with the highest C_Q value. This site is difficult to see in a MQMAS spectrum, mainly owing to of the width of the lineshape, $\Delta\nu_Q^{(2)}$ = 21 kHz at B_0 = 14.1 T. Most importantly, andalusite is one of the samples in which third-order quadrupolar interaction effects are important, and so STMAS experiments are not to be suitable for this particular sample.[136] As a result, MQMAS is the method that gives the best resolution.

An ^{27}Al spin-echo MAS spectrum of andalusite is shown in Figure 6.2a, showing that the two resonances are resolved at B_0 = 14.1 T. Figure 6.2b shows the projections of the indirect dimension of two MQMAS spectra recorded with CW and FAM-N conversion pulses. The improvement ratios between the two methods are ×1.3 for Al 1 and ×2.2 for Al 2. The theoretical improvement ratios were ×1.4 for Al 1 and ×2.1 for Al 2. Here, the theoretical improvement ratios agree very well with the experiments, and the highest improvement is achieved for the site with the quadrupolar parameters that were used for the FAM-N optimisation, as with Rb_2SO_4 in Section 5.2.2. The theoretical improvement

[1] δ_2 was obtained from the average between the position of the two peaks visible in Figure 6.1b.

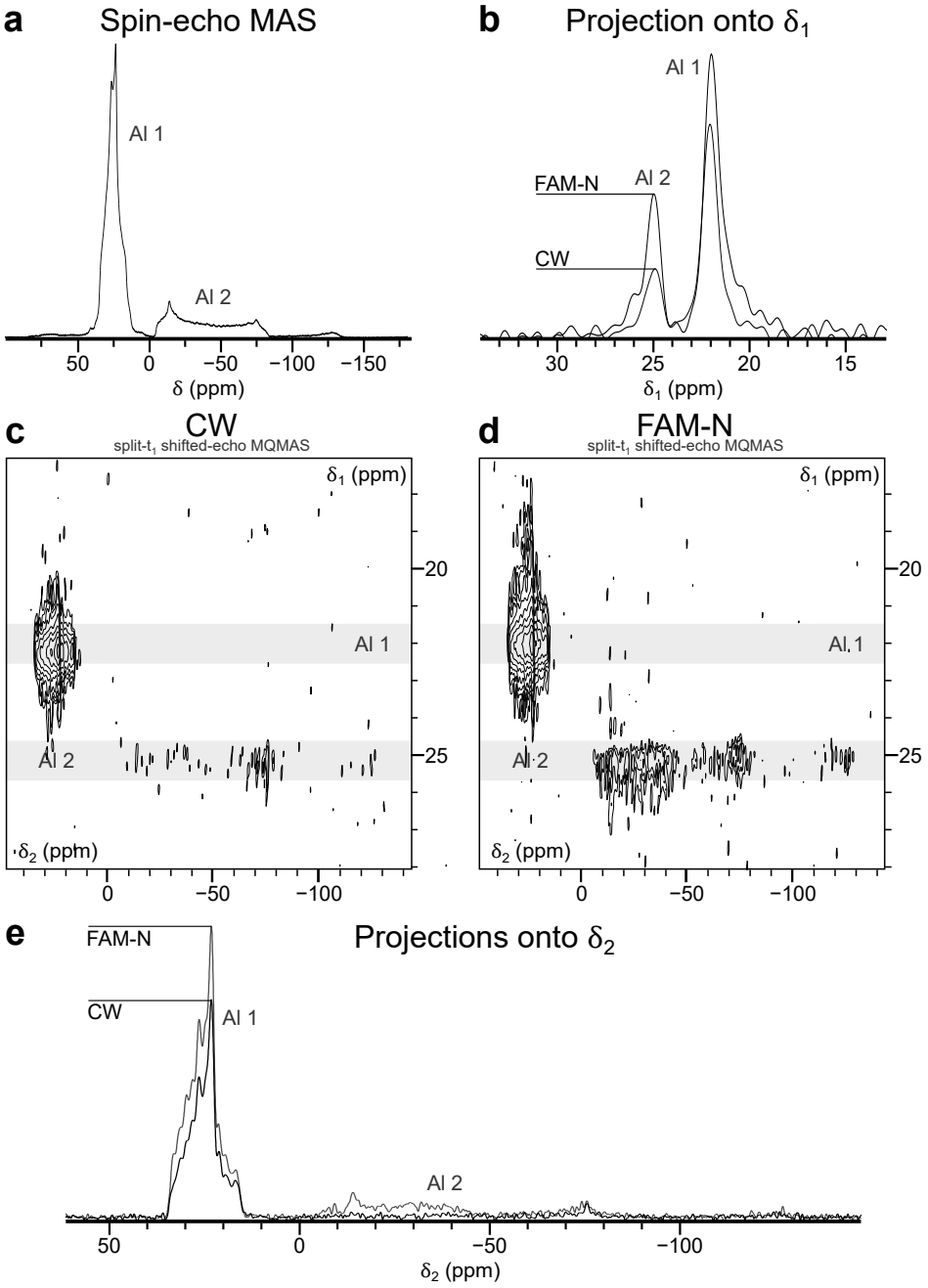

Figure 6.2: *^{27}Al spectra of Al_2SiO_5 andalusite recorded for B_0 = 14.1 T (ν_0 = 156.4 MHz), ν_R = 40 kHz and ν_1 = 97 kHz **(a)**: MAS spectrum showing the two sites Al 1 and Al 2. **(b)**: Projection onto the indirect dimension of the MQMAS spectra shown in **(c,d)**. **(c,d)**: split-t_1 shifted-echo MQMAS spectra recorded in 11 h each using **(c)**: CW and **(d)**: FAM-N conversion. Contour lines in **(c,d)** are identical to allow direct comparison. **(e)**: Projection onto the direct dimension of **(c,d)**. See the extended caption in Appendix C.3 for further details.*

ratio for Al 2 is slightly lower in experiment than in simulations, but it should be noted that the experimental improvement ratio observed for Al 2 is more likely to be affected by the noise in the spectrum in Figure 6.2b and the difficulty of adequately phasing the resonance.

The ^{27}Al MQMAS spectra of andalusite are shown in Figures 6.2c and 6.2d for CW and FAM-N conversion, respectively. As for berlinite, the signal in the CW MQMAS is just above the noise level in Figures 6.2c, whereas the signal observed in the FAM-N MQMAS spectrum in Figures 6.2d is clearly much higher than the noise. As a result, measuring the position of the barycentre of the lineshape in the direct dimension seems impossible from the CW MQMAS spectrum owing to the width of the lineshape of Al 2 and to the SNR of the spectrum. From the FAM-N MQMAS spectrum, a P_Q of 15.8 MHz can be obtained using $\{\delta_1, \delta_2\} = \{26\text{ ppm}, -50\text{ ppm}\}$ in the equations reported in Appendix E.1, in comparison to P_Q = 15.6 MHz from the literature.[206, 346] As visible in Figure 6.2e, in spite of the SNR in neither spectra not being sufficient for a precise lineshape fitting, the lineshape of Al 2 appears to be similar to the expected lineshape, and higher sensitivity would certainly allow lineshape fitting. Nevertheless, the MQMAS spectra shown in Figure 6.2 have been obtained in a relatively short amount of time (11 h each), and thus a longer acquisition would allow these to be recorded with a sufficiently high SNR for this fitting to be possible.

6.1.2 Nuclei with low gyromagnetic ratios

Potassium sulfate

Approximately 85% of NMR-active nuclei have gyromagnetic ratios lower than that of ^{13}C. This includes ^{39}K, which has an extremely low gyromagnetic ratio of $\gamma/2\pi$ = 1.99 MHz.T^{-1}, limiting the available RF field strength to a maximum of $\nu_1 \approx 25$ kHz on conventional probes. In many case, low-γ nuclei do not require fast MAS, but, with the low-sensitivity affecting every NMR experiment, recording MAS spectra or performing optimisations are, in general, time-consuming procedures. However, possessing a low gyromagnetic ratio is the only unfavourable characteristic of ^{39}K, as it has 93% natural abundance, and a low quadrupole moment, resulting in typical C_Q values equal to or below 1 MHz, therefore direct acquisition NMR experiments being fairly sensitive. However, the weak RF field available imposes severe efficiency limitations to 3QF.

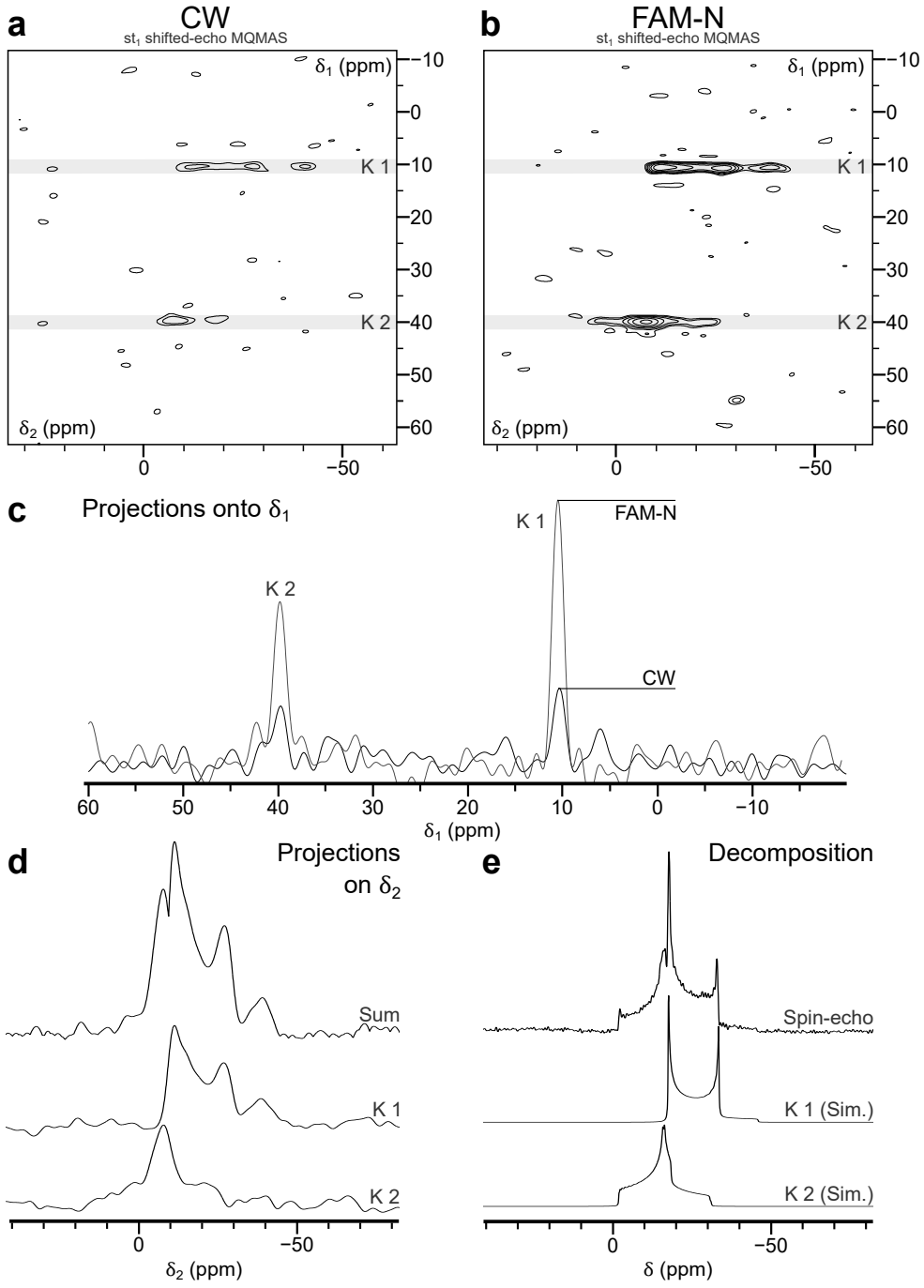

Figure 6.3: *^{39}K spectra of K_2SO_4 acquired for B_0 = 18.8 T (ν_0 = 37.3 MHz), ν_1 = 23 kHz and ν_R = 20 kHz.* ***(a,b)****: shifted-echo split-t_1 MQMAS spectra acquired in 33 h each with CW (grey line) and FAM-N (black line) conversion. Contour lines in* ***(a,b)*** *are identical to allow direct comparison.* ***(c)****: Projections of the indirect dimension of the two MQMAS spectra reported in* ***(a,b)****.* ***(d)****: Cross-sections taken parallel to the direct dimension of the FAM-N MQMAS spectrum in* ***(b)****, the top spectrum being the sum of the contributions of the resonances of K 1 and K 2.****(e)****: Spin-echo MAS spectrum (top), and the simulated contributions of the sites K 1 and K 2, with the parameters given in Table 6.2. See the extended caption in Appendix C.3 for further details.*

Fitted spectrum	Site	δ_{CS} (ppm)	C_Q /MHz	η_Q
MQMAS	K 1	−4.4	0.92	0.0
	K 2	+5.2	0.73	1.0
Spin-echo MAS	K 1	−4.283	0.943	0.00
	K 2	+9.197	0.831	0.96
Literature [347]	K 1	N/D	0.958	0.27
	K 2	N/D	0.864	0.90

Table 6.2: *Results of the lineshape fitting for the two ^{39}K sites of K_2SO_4, K 1 and K 2, obtained from measurement on the MQMAS spectrum shown in Figure 6.3b, on the spin-echo spectrum shown in Figure 6.3e, and in the literature,[347] giving the values for δ_{CS}, C_Q and η_Q.*

K_2SO_4 possesses two ^{39}K sites with similar quadrupolar parameters. FAM-N was optimised for

- C_Q = 0.9 MHz [2]
- η_Q = 0

The two MQMAS spectra recorded with CW and FAM-N conversion pulses are shown in Figures 6.3a and 6.3b, and Figure 6.3c shows a comparison of the projections of the indirect dimension in each case. The experimental improvement ratios are ×3.6 for K 1 and ×3.0 for K 2, compared with theoretical improvement ratios of ×4.0 for K 1 and ×3.5 for K 2. In this case, simulations are in good agreement with the experimental improvement ratios despite some reasonable variations. It can be seen that improvements are expected to be higher in the low-RF field strength regime as established in Section 5.1.1. This is also one of the few experiment recorded for a spin $I = 3/2$ nucleus for which the simulation predicts the signal improvement in experiments very accurately.

As visible in Figure 6.3a, the SNR obtained in the MQMAS spectrum recorded with CW conversion is just sufficient to accurately determine the number of sites, the isotropic chemical shift and the QIS for both sites. However, the SNR is not sufficiently high to allow a lineshape fitting. Figure 6.3d shows a projection of the direct dimension, and cross sections extract parallel to the this dimension, of the FAM-N MQMAS spectrum in Figure 6.3b. Despite some level of distortions, the quadrupolar lineshapes in Figure 6.3d are sufficiently close to the ideal lineshapes that a lineshape fitting is possible. This fitting resulted in the quadrupolar parameters and the isotropic chemical shifts shown

[2] corresponding to an average value for the two sites

in Table 6.2.

As seen previously in the literature,[254] lineshape fitting of MQMAS spectra can be used as an initial estimate of the quadrupolular parameters, which can be subsequently be refined through a fitting of a spin-echo MAS spectrum. A spin-echo MAS experiment and the lineshape obtained from fitting this spectrum are shown in Figure 6.3e. A comparison with Figure 6.3e confirms the absence of any major lineshape changes in the MQMAS spectrum. Fitting these lineshapes gives the quadrupolar parameters, reported on Table 6.2, that are very similar to literature values,[347] with the notable exception of η_Q for K 1. Some discrepancies are manifest between quadrupolar parameters extracted from the spin-echo MAS and the MQMAS spectra. However, this shows that the MQMAS spectrum can indeed be used to obtain an initial estimate of the quadrupolar parameters, that can subsequently be reported on a MAS spectrum for increased precision.

Enstatite and brucite

Enstatite [348–350] and brucite [351] are two inner-earth minerals, containing large amounts of magnesium.[349, 352, 353] ^{25}Mg ($I = 5/2$) NMR is particularly difficult, as this nucleus has low natural abundance (10%), a low gyromagnetic ratio ($\gamma/2\pi$ = −2.60 MHz.T^{-1}), and a high quadupolar moment (see Appendix C.2 for details).

Enstatite possesses two ^{25}Mg sites, thus the attempt to record an MQMAS spectrum instead of comparing the intensities in 3QF spectra. Projections of the direct dimension of ^{25}Mg 3QF-MAS spectra is shown in Figure 6.4a. However, one of the two sites possesses a very large C_Q of 14 MHz,[348] which results in an extremely low inefficient of 3QF and, therefore, this site is virtually impossible to see in an MQMAS spectrum. The existence of this second site was established from X-ray crystallography, and quadrupolar parameters were obtained by first-principles calculations.[348] As a result, the single peak visible in Figure 6.4a, that corresponds to the site with the lowest C_Q value. Brucite possesses only one ^{25}Mg site, therefore the efficiency FAM-N and CW 3Q conversion can be compared in a 3QF-MAS spectrum, shown in Figure 6.4b. For the latter sample, higher sensitivity has been obtained by using B_0 = 20.0 T.

The experimental improvement ratio between CW and FAM-N conversion is ×2.2 for enstatite, compared to a theoretical improvement of ×2.3 showing good agreement. For brucite, the experimental improvement ratio obtained from the integrated intensity[3]

[3]The severe lineshape distortions observed on the brucite spectrum in Figure 6.4b prevent the improvement

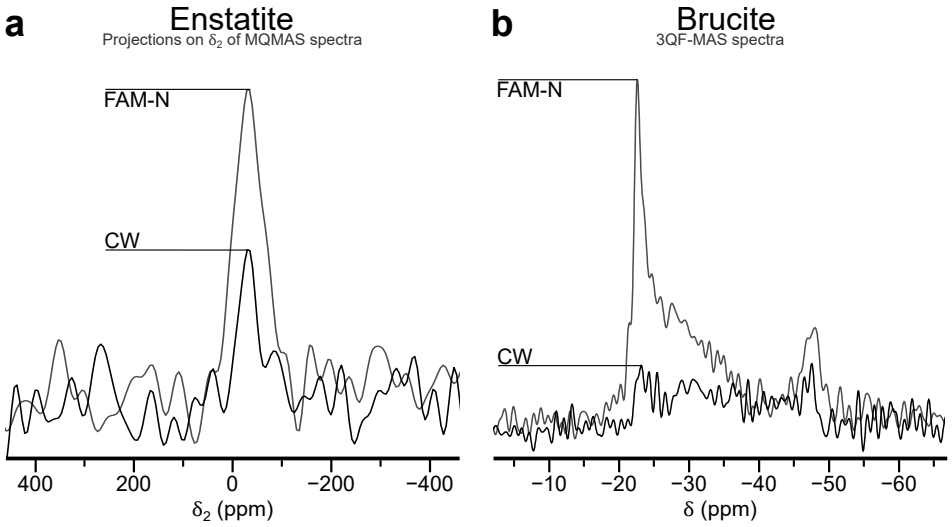

Figure 6.4: *^{25}Mg spectra recorded for ν_R = 12.5 kHz, with CW (black lines) and FAM-N (blue line) conversion.* ***(a)****: Projection of the direct dimension of shifted-echo split-t_1 MQMAS spectra of enstatite $MgSiO_3$, acquired in 64 h each at B_0 = 14.1 T (ν_0 = 36.75 MHz), with ν_1 = 33 kHz* ***(b)****: 3QF-MAS spectra of brucite $Mg(OH)_2$ recorded in 27 h each at B_0 = 20.0 T (ν_0 = 52.1 MHz), with ν_1 = 31.5 kHz. See the extended caption in Appendix C.3 for further details.*

of the two spectra is ×3.3, with the theoretical improvement being ×4.8. As observed for some samples in Section 5.2.3, the improvement ratio is considerably lower in experiment than in simulation. Nevertheless, the improvement obtained is important and appreciable, considering the SNR in the spectrum recorded with CW conversion in Figure 6.4b, and that no optimisation has been required for this result. There may be some concern about the level of lineshape distortions observed in Figure 6.4b for the FAM-N spectrum, as a fit of this lineshape would result in inaccurate quadrupolar parameters. More insight on this issue can be found in Section 6.2.3. The improvement observed for those samples is a further confirmation that FAM-N can be successfully applied to low-γ nuclei, and, furthermore, on samples with low sensitivity where experimental optimisation is not possible.

6.1.3 ^{25}Mg NMR of forsterite

Forsterite is an inner-earth silicate mineral and the magnesium-pure end member of the olivine family with a raw formula of Mg_2SiO_4.[354] Its structure has been extensively studied in the literature,[212, 354–364] and solid-state NMR has been one of the most common techniques applied for this purpose. Forsterite has been studied

ratio to be measured directly.

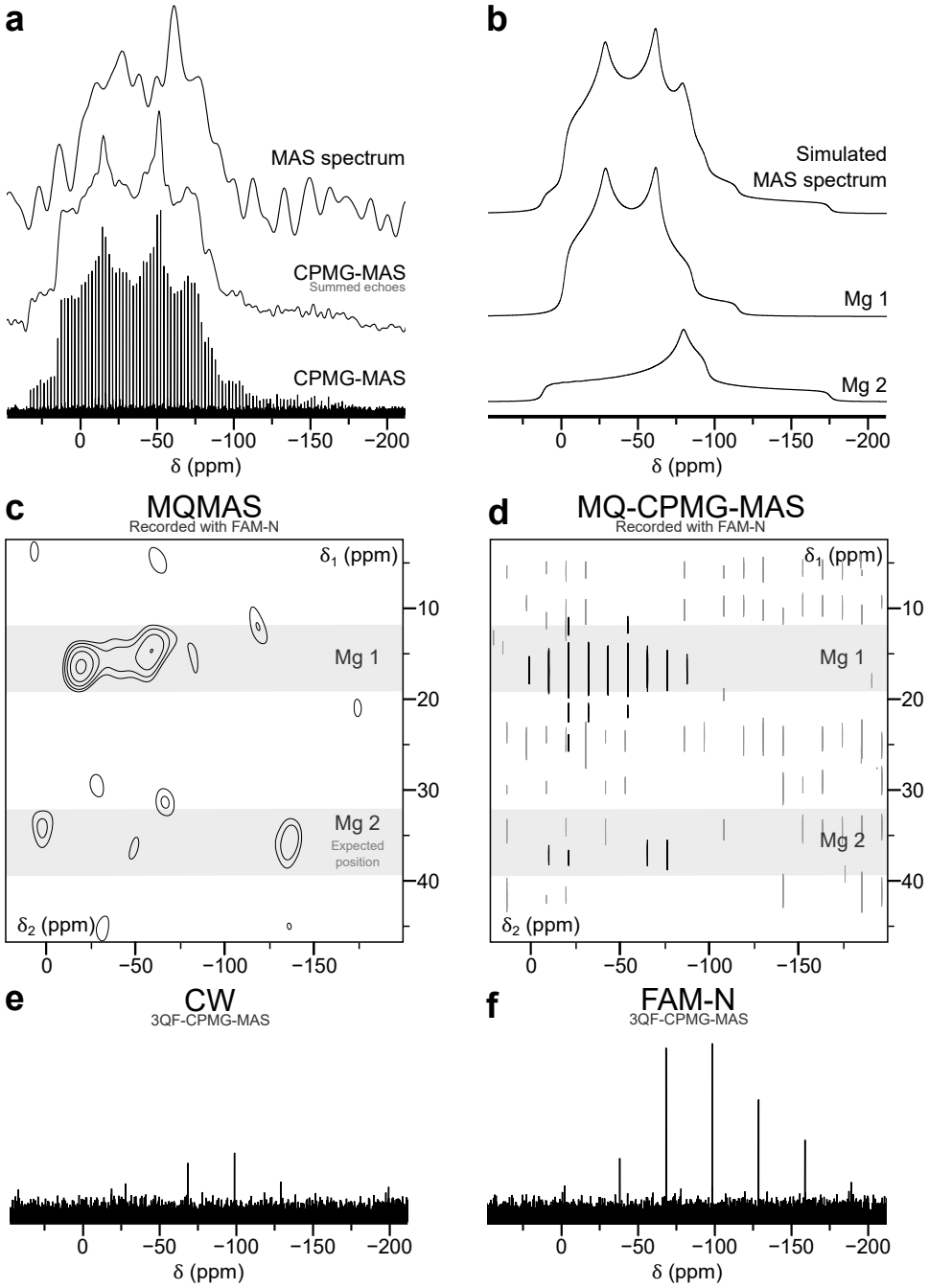

Figure 6.5: *Experimental and simulated ^{25}Mg spectra of forsterite Mg_2SiO_4. **(a)**: MAS, CPMG-MAS with summed echoes, and CPMG-MAS spectra acquired at B_0 = 18.8 T (ν_0 = 48.98 MHz). **(b)**: Spectral decomposition of the CPMG-MAS spectrum presented in **(a)**, showing the contribution of sites Mg 1 (middle) and Mg 2 (bottom) to the total lineshape (top), with the parameter given in the extended figure caption. **(c)**: Split-t_1 shifted-echo MQMAS spectrum acquired in 48 h at B_0 = 20.0 T (ν_0 = 52.05 MHz) for ν_1 = 35.0 kHz and ν_R = 14 kHz. **(d)**: split-t_1 MQ-CPMG-MAS spectrum, acquired in 88 h at B_0 = 20.0 T with ν_1 = 35.9 kHz and ν_R = 13.333 kHz. **(e,f)**: 3QF-CPMG-MAS spectra recorded using **(e)**: CW and **(f)**: FAM-N conversion pulses. Each spectrum is the sum of several spectra recorded for B_0 = 14.1 T (ν_0 = 36.75 MHz), ν_R = 13.333 kHz and ν_1 = 36.5 kHz in a total time of 38 h. See the extended caption in Appendix C.3 for further details.*

using ^{17}O and ^{29}Si NMR and experimental measurements have been compared to ab-initio calculations.[212, 359, 361, 364] The ^{25}Mg quadrupolar parameters have been initially measured using single-crystal NMR and DNP,[356] and obtained by *ab-initio* calculation.[355, 357, 360]

Unfortunately, for any of the three elements present in forsterite, all the NMR-active isotopes have low natural abundance, and isotropic enrichment is preferable, if not vital. The inherent sensitivity limitations of ^{25}Mg discussed in Section 6.1.2, combined with the inherently low sensitivity of MQMAS, result in a system known to be very challenging to record using ^{25}Mg NMR. Davis *et al.* successfully recorded a ^{25}Mg MQMAS spectrum at natural abundance, using a special probe able to apply very strong RF fields.[363] Using a standard probe, high B_0 fields are necessary to obtain MQMAS spectra with a sufficient SNR in a reasonable amount of time. Forsterite has two ^{25}Mg sites, overlapped in the MAS spectrum at B_0 = 14.1 T, as shown in Figure 6.5a. The two theoretical lineshapes of Mg 1 and Mg 2 are shown in Figure 6.5b, along with a simulated MAS spectrum. Observing MQMAS Mg 2 is much harder than Mg 1 in MQMAS spectra, as

- Mg 2 has a higher C_Q, so 3QF is less efficient,
- a higher η_Q of approximatively 1, causing the lineshape to be broader and less intense than that of Mg 1, and
- a much longer T_1 relaxation time, explaining the difference of intensities of the two ^{25}Mg sites in Figure 6.5b. Indeed, from the literature,[365] the relative integrated intensity ratio Mg 1:Mg 2 is expected to be 1:1, whereas 1.96:1 was measured from Figure 6.5b. The T_1 relaxation curve obtained from CPMG-saturation-recovery experiment (not shown) exhibits a double-exponential behaviour, but only T_1 = 25(6) s for Mg 1 could have been determined accurately. From this latter value, and considering the relative integrated intensities of Mg 1:Mg 2 in Figure 6.5b, that have been recorded with a recycle interval of 35 s, T_1 for Mg 2 can be estimated to 90 s.

A MQMAS spectrum recorded with FAM-N conversion in 48 h at B_0 = 20.0 T is shown in Figure 6.5c. While the signal for Mg 1 is clearly visible, there is no sign of the second site in the spectrum. Fortunately, the ”global” T_2 relaxation for the two sites has been measured by spin-echo experiments to exceed several hundreds of ms. As a result, it can be expected that CPMG would offer a potentially very high signal improvement on such a difficult sample. Furthermore, as no ^{1}H decoupling is necessary for this sample, acquisition can perfectly be carried out for such a long duration, allowing

multiple echoes to be recorded. This is confirmed by the CPMG-MAS spectrum shown in Figure 6.5a. As it can be seen, the SNR on the CPMG-MAS spectrum with added echoes, recorded in 5 h, is much higher than that of the MAS spectrum, recorded in 9 h. The very long T_2 relaxation time results in extremely sharp spikelets, with a width of 2 Hz, giving $T_2 \approx 0.5$ s.

The MQ-CPMG-MAS pulse sequence described in Section 4.1.2, Figure 4.2b was used to record the spectrum shown in Figure 6.5d. The resonance for Mg 2 is now more apparent, with a SNR of about 3 for the most intense spikelet. As visible, a sizeable number of spikelets from stimulated echoes appear on this spectrum, some of them being more intense than the Mg 2 spikelets. However, the perfect alignment of the Mg 1 and Mg 2 spikelets, along with their remarkably narrow width, enables the assignment without any ambiguity for the Mg 2 site. For visibility, stimulated echo spikelets have been represented in grey in Figure 6.5d. Traces of truncation are also visible in the indirect dimension for Mg 1. The shape of the Mg 2 lineshape in Figure 6.5d suggests significant lineshape distortion, but the chemical shift of the most intense spikelet still corresponds to the position of the maximum intensity expected for the Mg 2 resonance, which is located around −75 ppm. With the position of Mg 2 being visible on the MQMAS, an estimate of the QIS and P_Q is now possible. From the barycentre $\{\delta_1, \delta_2\}$ of the Mg 2 ridge, estimated to $\{37 \text{ ppm}, -77 \text{ ppm}\}$, P_Q has been calculated using the equations reported in Appendix E.2 to 6.4 MHz. This value is similar to that of 5.7 MHz established from the quadrupolar parameters reported by Derighetti *et al.*[356] The sources of error include the SNR observed in Figure 6.5d, but also the difficulty in identifying the center of the lineshape in the direct dimension δ_2 from the CPMG spikelets.

Considering the difficulty of acquiring the same MQ-CPMG-MAS experiment with CW conversion on a standard probe in a reasonable amount of time, the signal improvement ratio between CW and FAM-N conversion have been estimated from 3QF-CPMG-MAS spectra. These are shown in Figures 6.5e and 6.5f for CW and FAM-N conversion, respectively. The improvement is estimated to be ×2.0, which is consistent with those seen for the ^{25}Mg spectra in Section 6.1.2. However, it should be noted that this improvement mainly reflects the signal improvement for Mg 1, since the contribution of Mg 2 to the spikelets visible in Figures 6.5e is only minor. Simulation of the CW and FAM-N conversion pulses used in Figures 6.5e and 6.5f gave theoretical improvement ratios of ×2.4 for Mg 1 and ×2.0 for Mg 2, which are very similar to the experimental improvement ratio. Assuming these improvements are identical on the MQ-CPMG-MAS spectrum shown in Figure 6.5d, an equivalent SNR would have been obtained with CW

conversion in 352 h (15 days) despite the high field. In light of these results, it appears clear that this spectrum could not have been recorded in a reasonable amount of time of a standard MAS probe without the use of FAM-N.

6.2 Further investigation of FAM-N pulses

This section discusses a range of further investigations into FAM-N pulses, to verify some of the aspects of the method, and to highlight possible future developments. Section 6.2.1 describes some preliminary data concerning the application of FAM-N pulses for 5Q to 1Q conversion. Section 6.2.2 discusses a comparison between FAM-N and other computationally optimised FAM-II pulses reported in the literature,[318, 325] Section 6.2.3 analyses lineshape changes in 3QF-MAS spectra recorded with CW and FAM-N conversion, and Section 6.2.4 deals with possible sources of disparities between theoretical and experimental improvement ratios.

6.2.1 FAM-N for 5QMAS

The issue of the coherence order p to use for optimum resolution or sensitivity MQMAS has also been raised multiple times in the literature.[207, 212, 217, 220, 366, 367] As mentioned in Section 3.2.2, higher resolution has been reported in the literature when 5QMAS[4] [276, 368–377] or 7QMAS[5] [373, 378] experiments are employed instead of 3QMAS,[207, 212, 217, 220, 233, 244, 366] owing to the higher chemical shift differences for the 5Q or 7Q[6] transition compared to the 3Q transition. Wang *et al.* reported that a 5QMAS spectrum have permitted the assignment of a microporous material that was not possible from the 3QMAS spectrum, in which several resonances are overlapped.[379] However, as 3QF is the less inefficient transfer, 3QMAS remains the most widely used MQMAS method, while the use of the MQMAS experiments exploiting higher coherence orders remains comparatively low and decreases further as the order increases.

The conventional FAM pulse has been employed successfully in the literature to enhance the signal of 5QMAS spectra,[276, 368, 369, 380–383] and FAM-N, throughout this work,

[4] 5QMAS: *Quintuple-Quantum Magic-Angle Spinning*
[5] 7QMAS: *Septuple-Quantum Magic-Angle Spinning*
[6] 7Q: *Septuple-Quantum*

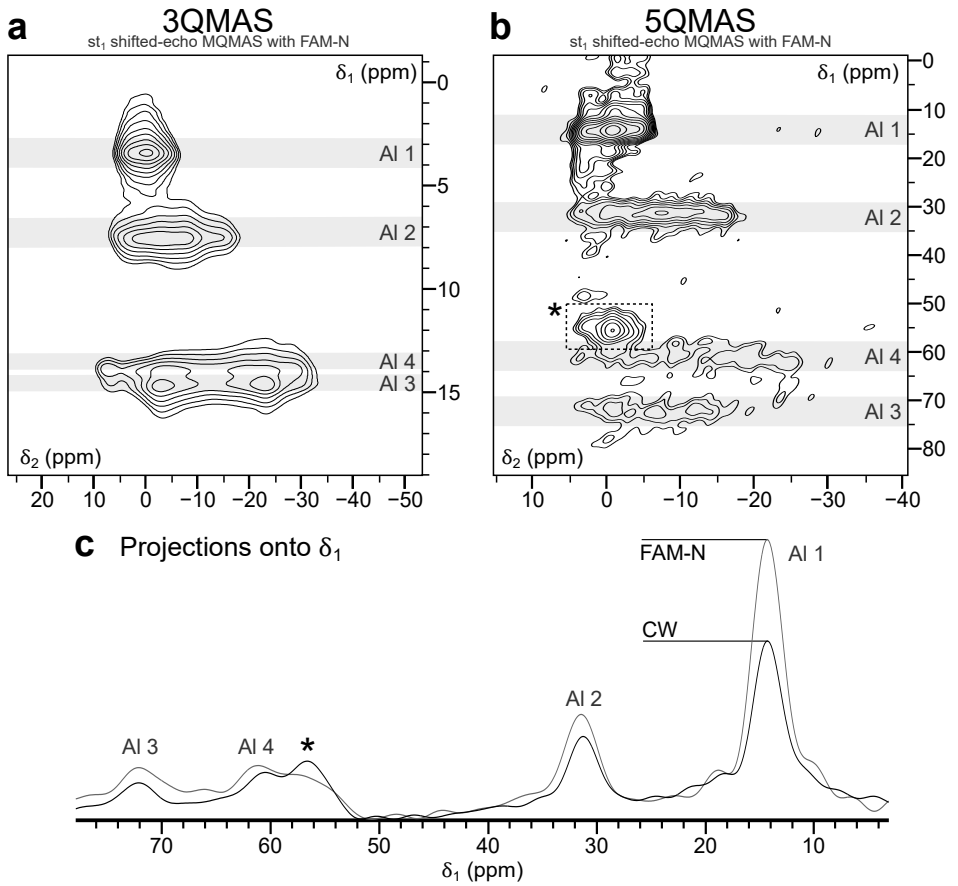

Figure 6.6: *^{27}Al MAS spectra of Al_2SiO_5 kyanite, recorded at B_0 = 14.1 T (ν_0 = 156.4 kHz) and ν_R = 20 kHz.* ***(a)****: Split-t_1 shifted-echo 3QMAS spectrum recorded with FAM-N for ν_1 = 139 kHz (reported from Figure 5.9c).* ***(c)****: Split-t_1 shifted-echo 5QMAS spectrum recorded with FAM-N for ν_1 = 133 kHz.* ***(c)****: Projections of the indirect dimension of* ***(b)*** *and of a 5QMAS spectrum recorded with CW conversion. The signal marked by "*" is a spinning sideband of Al 1. See the extended caption in Appendix C.3 for further details.*

has so far only utilised to enhance the efficiency of the $p = \pm 3 \rightarrow p = \pm 1$ transfer. The applicability of FAM-N for 5QMAS experiments is discussed below.

^{27}Al 5QMAS of kyanite

Executing the FAM-N optimisation program for a $p \neq \pm 3 \rightarrow \pm 1$ transfer only requires little modification, therefore this option is already implemented (see Appendix I.2, Code I.2). The optimisation procedure remains identical in every respect to that described in Section 4.3.3, and results in FAM-N pulses that exhibit a clear resemblance to 3Q-FAM-N pulses. For ^{27}Al NMR of kyanite, studied in Section 5.3.2, is an adequate sample to test the applicability of FAM-N to higher coherence orders, owing to the variety and the

	Simulation		Experiment	
	3Q	5Q	3Q	5Q
Al 1	×1.4	×2.2	×1.4	×1.6
Al 2	×1.9	×2.6	×1.7	×1.3
Al 3	×2.0	×3.3	×2.0	×1.4
Al 4	×2.0	×3.2	×1.7	×1.3

Table 6.3: *Experimental and theoretical improvement ratios, reported from the spectra in Figure 5.9c and Table 5.3 for the 3Q experiments and simulations, measured from Figure 6.6b for the 5Q experiments, and from simulations using identical parameters as in Figure 6.6b.*

multiplicity of the ^{27}Al sites in this sample. Furthermore, the two sites Al 3 and Al 4 are overlapped in the 3QMAS projection shown in Figure 5.9c. To serve as an example, kyanite 3QMAS and 5QMAS spectra are shown in Figures 6.6a and 6.6b, respectively, with FAM-N optimised for the same parameters as the 3QMAS spectrum in Figure 5.9c, *i.e.*,

- C_Q = 6 MHz,
- η_Q = 0.

The optimised FAM-N pulse consists of 7 pulses for a total duration of 6.6 µs. It can be observed that, as predicted, the resolution of the 5QMAS is significantly better than that of the 3QMAS spectrum, and that the two ridges for Al 3 and Al 4 are now resolved. However, the SNR is clearly inferior in the 5QMAS spectrum to that of the 3QMAS spectrum, despite the fact that the 5QMAS spectrum was acquired for a longer duration. For such SNR levels, fitting the ridges would result in inaccurate quadrupolar parameters. Furthermore, the separation of the four sites is now larger than the MAS rate in the indirect dimension, resulting in spinning sidebands appearing in Figure 6.6b, with that for Al 1 being clearly visible.

Figure 6.6c shows projections of the indirect dimension of two 5QMAS spectra recorded with CW and FAM-N conversion, and the experimental improvements ratios between the two conversion pulses are reported in Table 6.3, along with the theoretical improvement ratios obtained from simulations. Also shown are the experimental and theoretical improvement ratios for the 3QMAS spectrum in Figure 5.9. In Section 5.2.3, it was established that there was an excellent agreement between the theoretical and experimental improvement ratios between CW and FAM-N conversion in the 3QMAS spectra of kyanite. In contrast, significant discrepancies between the experimental and theoretical improvement ratios are observed for 5QMAS. While the theoretical improvement ratios increases between Al 1 and Al 4, the experimental maximum for Al 1, and Al 2 to

	Excitation		CW conv.		FAM-N conv.	
	3Q	5Q	3Q	5Q	3Q	5Q
Al 1	0.64	0.23	0.35	0.12	0.48	0.28
Al 2	0.67	0.16	0.29	0.08	0.51	0.20
Al 3	0.64	0.09	0.24	0.05	0.52	0.16
Al 4	0.62	0.08	0.22	0.04	0.48	0.14

Table 6.4: *Simulations of the amount of 3Q coherence | real part of ρ_{25} created from population, and 5Q | real part of ρ_{16} created from population by the excitation pulse, and amounts of 1Q coherence | real part of ρ_{34} created from initial 3Q or 5Q coherence created by the CW and FAM-N pulses, using the excitation, CW and FAM-N pulses and the conditions of Figures 6.6a and 6.6b.*

Al 4 are improved by only very small amounts. Further investigation would be necessary to understand these discrepancies, such as repeating the robustness investigations shown in Section 5.2 for 5Q FAM-N. Nevertheless, it can be noted that FAM-N results in an improvement for all of the sites.

A final observation from Figures 6.6a and 6.6b is that the signal intensity dramatically decreases between Al 1 and Al 4 in the 5QMAS spectrum, *e.g.*, as C_Q increases, while little difference in signal intensity are found in the 3QMAS spectrum. Table 6.4 reports the absolute ”efficiencies” of the 3Q and 5Q excitation and conversion pulses for kyanite. It is clear from this table that, while the efficiency of the 3Q excitation pulse is approximately similar for all sites, the 5Q excitation pulse experiences a large decrease in efficiency as C_Q increases. A similar observation can be made for the 3Q and 5Q CW conversion pulses; while the efficiency of the 3Q CW pulse decreases with C_Q as discussed in Section 5.2.3, that of the 5Q CW pulse is relatively much higher. Conversely, no decrease with C_Q is observed for the 3Q FAM-N pulse. The 5Q FAM-N efficiency decreases as C_Q increases, but at a slower rate than the 5Q CW pulse, thus the increase of the theoretical improvement ratios with C_Q reported in Figure 6.6.

Different approaches for the optimisation of 5Q FAM-N pulses

Although further investigations is required to understand 5Q MQMAS, this first example on kyanite provides initial proof that the optimisation process described in Section 4.3.3 can be used to generate FAM-N pulse to improve the sensitivity of 5QMAS. However, population or coherence transfer is often described in the literature as a succession of adiabatic population of coherence transfers performed by separated pulses. FAM-N pulses have been described in Section 5.1.1 as performing some inversion of the

inner ST transitions, resulting in the improvement observed. Nevertheless, the action of modulated pulses on spin $I = 5/2$ nuclei have often been described in the literature as consisting of two separated steps.[115, 312, 316] The first executes a $p = \pm5 \rightarrow \pm3$ transfer through the application of the modulation near the frequency of the outer ST (ST_2)

$$\hat{\rho} = \begin{bmatrix} 0 & 0 & 0 & 0 & 0 & 1 \\ 0 & 0 & 0 & 0 & 0 & 0 \\ 0 & 0 & 0 & 0 & 0 & 0 \\ 0 & 0 & 0 & 0 & 0 & 0 \\ 0 & 0 & 0 & 0 & 0 & 0 \\ 1 & 0 & 0 & 0 & 0 & 0 \end{bmatrix} \xrightarrow[\text{near } ST_2]{p=\pm5\rightarrow\pm3} \hat{\rho} = \begin{bmatrix} 0 & 0 & 0 & 0 & 0 & 0 \\ 0 & 0 & 0 & 0 & 1 & 0 \\ 0 & 0 & 0 & 0 & 0 & 0 \\ 0 & 0 & 0 & 0 & 0 & 0 \\ 0 & 1 & 0 & 0 & 0 & 0 \\ 0 & 0 & 0 & 0 & 0 & 0 \end{bmatrix} , \tag{6.2.1}$$

followed by a $p = \pm3 \rightarrow \pm1$ step through by the application of the modulation near the inner satellites

$$\hat{\rho} = \begin{bmatrix} 0 & 0 & 0 & 0 & 0 & 0 \\ 0 & 0 & 0 & 0 & 1 & 0 \\ 0 & 0 & 0 & 0 & 0 & 0 \\ 0 & 0 & 0 & 0 & 0 & 0 \\ 0 & 1 & 0 & 0 & 0 & 0 \\ 0 & 0 & 0 & 0 & 0 & 0 \end{bmatrix} \xrightarrow[\text{near } ST_1]{p=\pm3\rightarrow\pm1} \hat{\rho} = \begin{bmatrix} 0 & 0 & 0 & 0 & 0 & 0 \\ 0 & 0 & 0 & 0 & 0 & 0 \\ 0 & 0 & 0 & 1 & 0 & 0 \\ 0 & 0 & 1 & 0 & 0 & 0 \\ 0 & 0 & 0 & 0 & 0 & 0 \\ 0 & 0 & 0 & 0 & 0 & 0 \end{bmatrix} . \tag{6.2.2}$$

When applied for the $p = \pm5 \rightarrow \pm1$ transfer, it can be assumed that FAM-N is optimised to simultaneously perform the two transfers represented in Equations 6.2.1 and 6.2.1. However, it is possible that changing the optimisation procedure to perform multiple successive steps, as described in the literature, might result in further signal enhancement. For insight about this problem, several FAM-N optimisation approaches have been performed and compared. These are:

- **Direct optimisation**

  FAM-N is optimised directly for the $p = \pm5 \rightarrow p = \pm1$ transfer.
- **Concatenated independent optimisations**

  FAM-N pulses independently optimised for the $p = \pm5 \rightarrow p = \pm3$ and the $p = \pm3 \rightarrow p = \pm1$ transfers are combined sequentially.
- **Two-step optimisation**

  A FAM-N pulse is first optimised for the $p = \pm5 \rightarrow p = \pm3$, which is subsequently used as an initial pulse train in an optimisation observing $p = \pm1$.

The sample chosen to verify the theoretical predictions experimentally is $Al(acac)_3$, as it has a single ^{27}Al site. Figure 6.7 shows the FAM-N optimisation curves obtained from the FAM-N pulses using the three approaches described above, using the experimental

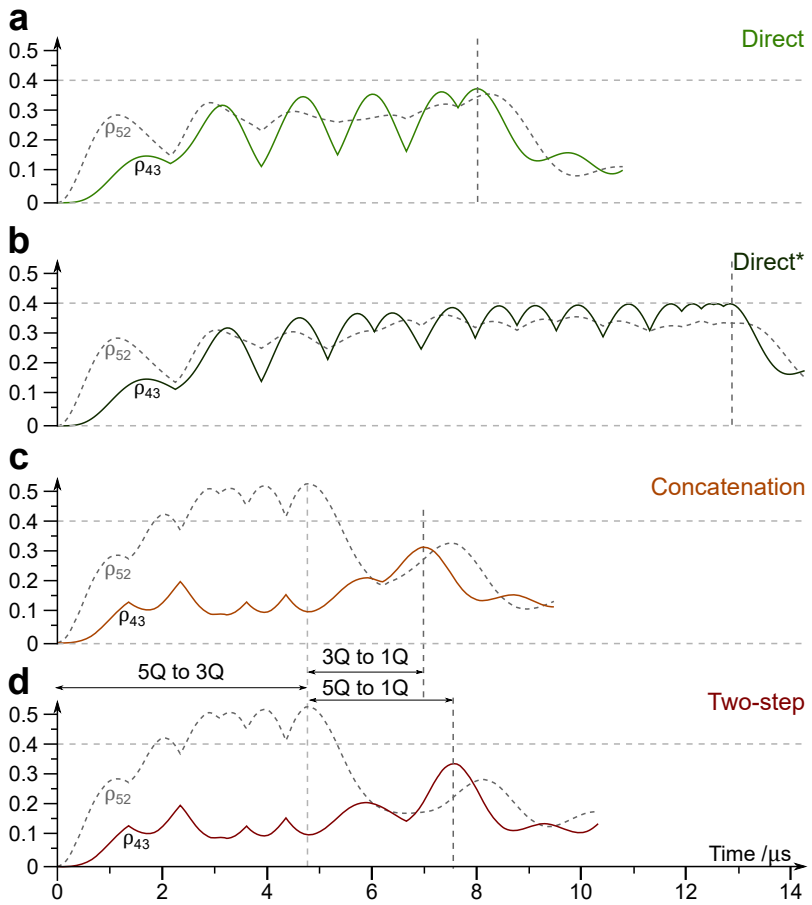

Figure 6.7: *Simulations showing the amount of symmetrical CT 1Q coherence | real part of ρ_{43} (solid coloured lines) and the amount of 3Q coherence | real part of ρ_{52} (grey dashed lines) created by FAM-N pulses optimised using **(a)**: the direct optimisation approach, **(b)**: the direct optimisation approach using a large number of crystallite orientations (320 crystallite orientations and 20 γ-angles) **(c)**: the concatenated independent optimisations approach, and **(d)**: the two-step optimisation approach, described in the main text. Simulations have been performed on ^{27}Al with B_0 = 14.1 T (ν_0 = 156.4 MHz), ν_1 = 133 kHz and ν_R = 20 kHz, C_Q = 6 MHz and η_Q = 0.*

parameters of Figure 6.6d in the simulations. Table 6.5 reports the amount of 1Q coherence created from initial 5Q coherence using the FAM-N pulses optimised according to the three approaches described previously. The optimised FAM-N pulses were put into practice in the 5QF[7]-MAS spectra shown in Figure 6.8. The experimental improvement ratios are given in Table 6.5.

Direct: The effect of the pulse obtained using the direct optimisation approach is shown in Figure 6.7a, with the final pulse consisting of 6 pulses for a total duration of 7.1 µs. As discussed previously, the ”direct” optimisation approach produces a sweep that simultaneously affects the ST_1 and the ST_2. This interpretation is confirmed

[7] 5QF: *Quintuple-Quantum Filtration*

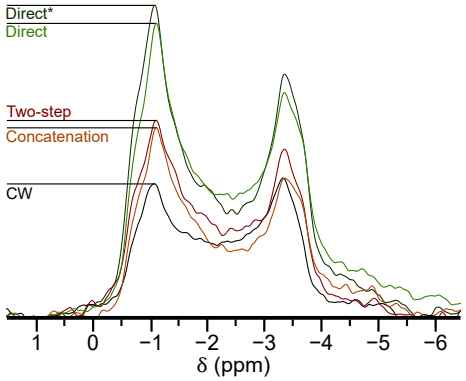

Figure 6.8: *^{27}Al 5QF-MAS spectra of Al(acac)$_3$ recorded with CW conversion and the FAM-N pulses optimised according to the different approaches detailed in the main text, for B_0 = 14.1 T (ν_0 = 156.4 MHz), ν_R = 20 kHz and ν_1 = 133 kHz. The improvement ratios are reported in Table 6.5. See the extended caption in Appendix C.3 for further details.*

Method	Improvement ratio	
	Sim.	Exp.
Direct	×2.4	×1.9
Direct*	×2.6	×2.0
Concatenation	×2.1	×1.3
Two-step	×2.3	×1.5

Table 6.5: *Theoretical (measured from Figure 6.7) and experimental (measured from Figure 6.8) improvement ratios between CW conversion and the FAM-N pulses optimised according to the different approaches detailed in the main text.*

by Figure 6.7a, where the amount of 3Q coherence produced at any stage is similar to that seen for 3Q coherence. This pulse results in an improvement in experiment similar to that in simulation (see Table 6.5).

Direct*: Contrary to what has been observed for 3Q FAM-N pulses, significant differences were observed between the 5Q FAM-N pulse optimised using the direct approach for the standard number of crystallites (66 crystallite orientations and 4 γ-angles) and the FAM-N pulse optimised with a larger number of crystallites (here, 320 crystallite orientations and 20 γ-angles).[8] The effect of this pulse, labelled "Direct*", is shown in Figure 6.7b and is now composed of 15 pulses for a total duration of 11.4 µs. As for the FAM-N pulse optimised with a lower number of crystallites, the variation in amount of 3Q coherence roughly follows that of the CT 1Q coherence. The additional pulses small in a slight further enhancement in simulations and in experiments.

Concatenation: The FAM-N pulse optimised using this approach is composed of 8 pulses for a total duration of 6.1 µs, as shown in Figure 6.7c. The $p = \pm5 \rightarrow p = \pm3$ FAM-N pulse is composed of 6 pulses for a total duration of 4.3 µs. The $p = \pm3 \rightarrow p = \pm1$ FAM-N pulse is composed of 2 pulses for a total duration of 1.8 µs. The two components of the total FAM-N pulse is here striking when

[8] No significant effect of the number of crystallite orientation was observed for the FAM-N pulses optimised using either the concatenated independent optimisations approach or the two-step optimisation approach.

looking at the amounts of CT 1Q and 3Q coherences. The $p = \pm5 \rightarrow p = \pm3$ FAM-N creates large amounts of 3Q coherence, which is thereafter dramatically reduced by the $p = \pm3 \rightarrow p = \pm1$ FAM-N pulse. The total FAM-N pulse exhibits little resemblance to any of the direct FAM-N pulses and results in a lower theoretical improvement compared to any of these. This is perhaps expected, as the optimisation of each of the two FAM-N pulses was carried out assuming initial pure 5Q or 3Q coherence is present. In experiments or in simulations, unless an additional phase cycling step is applied to filter all coherences but $p = +3$ or $p = -3$ after the $p = \pm5 \rightarrow p = \pm3$ FAM-N pulse, the density matrix contains multiple elements. Since the $p = \pm3 \rightarrow p = \pm1$ is not optimised for such a transfer, it follows that differences arise between this FAM-N pulse and a FAM-N pulse specifically optimised for this transfer, as will be discussed for the two-step optimisation approach. However, it should be noted that this may not be as important for any experimental conditions. In Section 5.2.1, the existence of an optimum RF field strength for the conversion of 3Q, sufficiently strong for the desired coherence to be created in large amounts while avoiding large amounts of unwanted coherences to be created (see Equation (5.1.6)) has been highlighted. As a result, there might be conditions for which the absence of the phase cycling $p = \pm5 \rightarrow p = \pm3 \rightarrow p = \pm1$ during the conversion has little or no effect, resulting in this approach being equally efficient. In experiment, the improvement ratio is much more limited than in simulations, although the simulation successfully predicted this FAM-N pulse as being the less efficient approach.

Two-step: The FAM-N pulse optimised in this was consists of 8 pulses for a total duration of 6.7 µs as shown in Figure 6.7d. It utilises the $p = \pm5 \rightarrow p = \pm3$ FAM-N pulse described for the concatenation approach above. This optimisation results in 2 additional pulses, giving the same total number of pulses as the FAM-N pulse obtained using the concatenated approach, but these two pulses have a significantly different duration compared to this last approach, resulting in a slightly higher theoretical improvement. This could perhaps have been predicted, as, unlike the FAM-N pulse obtained from concatenation, the optimisation does not start from a density matrix composed of pure 3Q. However, this approach does not result in a higher theoretical improvement than any of the directly optimised FAM-N. The experimental improvement ratio is higher to that observed using the concatenated FAM-N. However, this approach also results in a much lower improvement ratio in experiments than in simulations.

Conclusion

In summary, no strong evidence has been established that 5Q FAM-N conversion can be improved for this system using an alternative, multiple-step optimisation approach. All of the FAM-N pulses obtained give an efficiency improvement for the ^{27}Al 5QF experiments of Al(acac)$_3$, although the direct optimisation is much easier to perform. The simulations did not predict the experimental enhancement with precision, the efficiency of the different approaches follow the order that are observed in the simulation, with the direct approaches being the most efficient, followed by the concatenation approach, then the two-step approach.

However, the investigations conducted here are only valid for Al(acac)$_3$. Similar investigations conducted for kyanite gave different results, with the concatenated FAM-N or the two-step FAM-N being equally or more efficient depending on the number of crystallite orientations used for the optimisations. This indicates that further investigations is needed to determine whether the ”direct” optimisation approach can be improved by a multiple step approach, and whether using a larger number of crystallite orientations is required to obtain efficient 5Q FAM-N pulses. When FAM-N conversion is used, the step limiting the sensitivity of 5QMAS experiments become the excitation pulse, as seen in Table 6.4, therefore investigations should also be carried out on this pulse. An unsuccessful attempt to increase the efficiency of the excitation pulse using RIACT (see Section 4.2.1) is reported in Section 7.2.3. FASTER (see Section 4.2.2) may also give appreciable enhancement.

6.2.2 Comparing FAM-N to previously-introduced methods

Numerically-optimised FAM-II pulses have been published in literature,[318, 325] differing from FAM-N by their optimisation procedure and by the pulse produced. This section reports the investigation conducted in the Supporting Information of Colaux *et al.*,[23] Section S.2. Two previous attempts have been made in the literature to improve the efficiency of pulses based on FAM-II.[318, 325]

In the approach of Goldbourt *et al.*,[318] the length of the initial pulse was varied until a maximum in conversion efficiency was reached, at which point a second pulse was added with opposite phase. The length of the second pulse was incremented until a maximum in conversion efficiency was reached, and then a third pulse of opposing phase was added. This approach was continued with up to four pulses of opposing phase reported

in the original work and with an enhancement factors of ∼3 reported, relative to the most efficient single-pulse conversion.

In the approach of Morais *et al.*,[325] it was noted that, for spin $I = 3/2$, the optimum length of the first pulse corresponded to an inherent flip angle of 90°, *i.e.*, the point of the echo/antiecho crossing, and this value was used as a constraint. While the precise details of the remainder of the optimisation procedure are somewhat unclear from the original work, composite pulses were generated, comprised of up to six oppositely-phased pulses, and yielding signal enhancement factors slightly higher than those obtained by Goldbourt *et al.*[318] One possible reason for the improved efficiency of the optimised pulses of Morais *et al.*, relative to those of Goldbourt *et al.*, is the removal of the constraint that the phase must be inverted whenever an efficiency maximum is obtained. Morais *et al.* demonstrated that, by increasing the length of the preceding pulse beyond an efficiency maximum, greater overall efficiency could be achieved by the following pulse. The pulses developed in this way appear to be essentially invariant with both the RF nutation frequency and the magnitude of the quadrupolar coupling (See, for example, Table 1 of the original work,[325]) suggesting that they may have essentially universal applicability (at least under the conditions explored). However, the optimisation procedure of Morais *et al.* still appears to have been constrained so that each pulse is shorter than the preceding pulse.

In this work, we carried out a procedure conceptually similar to that of Morais *et al.*, but with no constraint on the relative lengths or efficiencies of the individual pulses, and with the pulse durations simply optimised to obtain the overall maximum efficiency. For ^{87}Rb (B_0 = 9.4 T, C_Q = 1 MHz, ν_R = 15 kHz, ν_1 = 100 kHz), Table 6.6 shows the durations of the individual oppositely-phased pulses obtained by optimisation of the pulse lengths using the methods of Goldbourt *et al.*, Morais *et al.* and FAM-N. The optimisations using the Goldbourt method were carried out for this work, whereas there was insufficient information in the work of Morais *et al.* [325] to generate a comparable composite pulse optimised for the specific parameters considered here, and the pulse optimised for ν_Q/ν_1 = 5 in the original work was used.

It can be seen that both the composite pulses of Goldbourt *et al.* and Morais *et al.* are shorter than the FAM-N pulse. In addition, it is clear that FAM-N does not represent merely an extension to either of the earlier pulse schemes, as the lengths of the first four individual pulses of the FAM-N scheme do not resemble those of either of the other two schemes. Table 6.6 also shows the overall efficiency of the three different pulses,

Method	Pulse duration /μs							Relative efficiency
	1	2	3	4	5	6	Total	
CW	2.14	×	×	×	×	×	2.14	0.460
Goldbourt *et al.* [318]	2.14	1.65	×	×	×	×	3.79	0.744
Morais *et al.* [325]	2.52	1.75	0.97	0.50	×	×	5.75	0.953
FAM-N	2.39	1.78	1.06	0.89	1.00	0.56	7.67	1.000

Table 6.6: *The durations and efficiencies (relative to FAM-N) of the conversion pulses described in the text, when applied to ^{87}Rb at B_0 = 9.4 T with C_Q = 1 MHz, ν_R = 15 kHz and ν_1 = 100 kHz.*

and it can be seen that efficiency of the FAM-N pulse optimised as described in this work is 1.33 times greater than that of the pulse optimised using the method of Goldbourt *et al.* and 1.05 times greater than that of the pulse optimised by Morais *et al.* (see Table 1 of the original work [325] for further details). However, all composite pulses were between 60% and 120% more efficient than CW conversion.

6.2.3 Does FAM-N cause lineshape changes ?

Lineshape distortion is a fundamental and recurrent issue in MQMAS experiments. As reported in Section 3.2.2, the orientation-dependent Ω_Q term in Equation (3.2.13) causes the 3Q nutation rate to be orientation dependent, resulting in the 3QF to be more or less efficient with different crystallite orientations. The presence of distortions in spectral lineshapes results in a reduction in the precision with which quadrupolar parameter can be measured. This is an important consideration, as quadrupolar parameters are often extracted from MQMAS spectra and are subsequently used as initial guesses for a more precise extraction of the quadrupolar parameters for MAS spectra, as discussed in Section 6.1.2. Two striking examples in this work are the ^{71}Ga MQMAS spectrum of $CaPO_4$ berlinite shown in Figure 6.1 and the ^{25}Mg 3QF-MAS spectrum of brucite shown in Figure 6.4. However, a lineshape comparison is not feasible owing to the very low SNR observed for the CW spectra. In this section, theoretical investigations are conducted to investigate whether the distortion level is more pronounced on spectra recorded with FAM-N conversion than with CW conversion for these two examples.

First, it has been verified that SIMPSON is able to successfully reproduce experimental lineshape changes. In Figures 6.9a and 6.9d, experimental MAS spectra and simulated ideal MAS spectra are shown as a reference for the lineshape changes observed in 3QF-MAS spectra. The simulated MQMAS and 3QF spectra are shown in Figures 6.9b and 6.9e for brucite and berlinite, respectively, and the corresponding experimental spectra

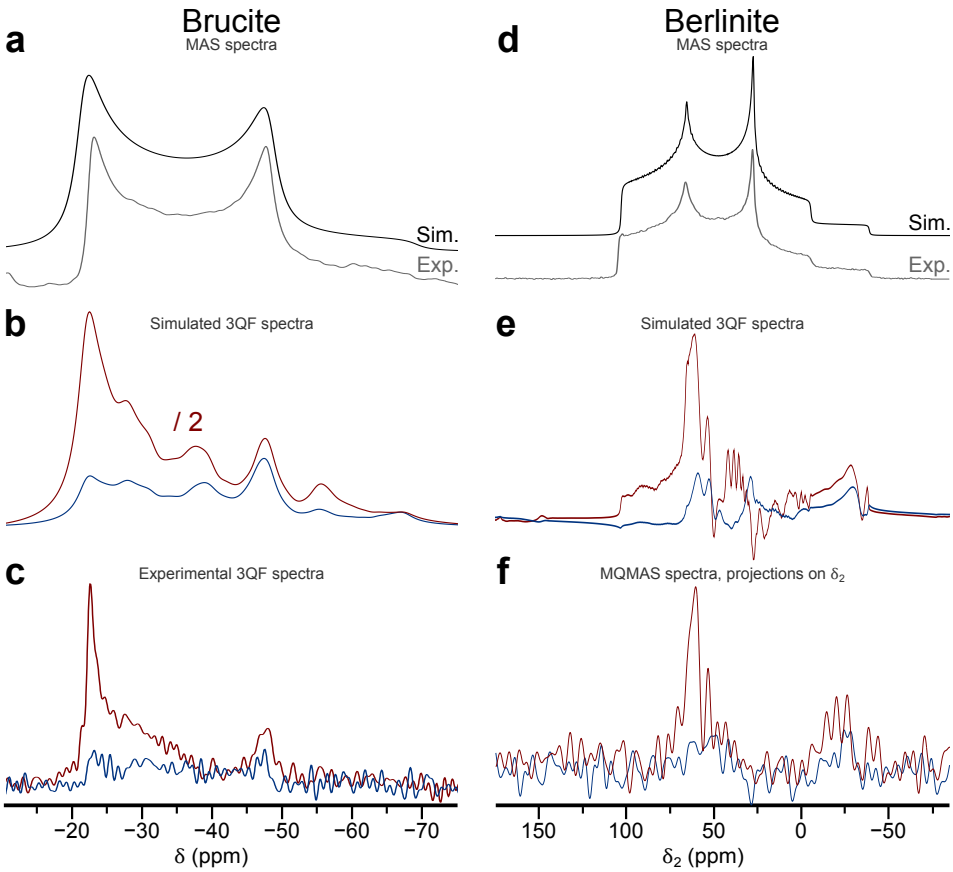

Figure 6.9: *Experimental and simulated spectra obtained for B_0 = 14.1 T, with simulation parameters chosen to be identical to the experimental parameters.* ***(a,b,c)****: ^{25}Mg spectra of brucite recorded/simulated with ν_1 = 31.5 kHz and ν_R = 14 kHz.* ***(d,e,f)****: ^{71}Ga spectra of Berlinite recorded with ν_1 = 115 kHz and ν_R = 40 kHz.* ***(a,d)****: Experimental (black) and simulated (grey) MAS spectra.* ***(b,e)****: Simulated 3QF-MAS spectra using CW (blue line) and FAM-N (red line) conversion. The lineshapes were simulated using 75 024 cristallite orientations and 20 γ-angles.* ***(c)****: Experimental 3QF-MAS spectra recorded with CW (blue line) and FAM-N (red line) conversion, already reported in Figure 6.4.* ***(f)****: projections of the direct dimension of MQMAS spectra recorded with CW (blue line) and FAM-N (red line) conversions, already reported in Figure 6.1.*

in Figures 6.9c and 6.9f. Clearly, the simulated and experimental 3QF-MAS spectra resemble each other well for both brucite and berlinite. In particular, it can be observed that the positions of the intense spectral features are almost identical between the experimental and simulated spectra. The experimental MAS spectra are also close to the ideal lineshapes. However, even on the simulated spectra in Figures 6.9b and 6.9e, it remains difficult to determine whether distortions are more pronounced for the spectrum recorded with CW or FAM-N conversion. The home-written ODD[9] script, detailed in Appendix H, allows the "amount of distortion" of a given lineshape to be quantified, by defining it as the standard-deviation of $\langle \hat{I}^{CT} \rangle$ with respect to the crystallite orienta-

[9] ODD: *Orientation-Dependant Distortions*

Brucite				
Pulse	Amplitude	Standard deviation		Phase
CW	0.119	$\pm$ 0.045	(37.9 %)	±7.39°
FAM-N	0.534	$\pm$ 0.218	(40.7 %)	±16.2°

Berlinite				
Pulse	Amplitude	Standard deviation		Phase
CW	7.01×10^{-3}	$\pm 7.78 \times 10^{-3}$	(110 %)	±86.4°
FAM-N	2.52×10^{-2}	$\pm 2.24 \times 10^{-2}$	(88.8 %)	±106.3°

Table 6.7: *Average and standard deviations in amplitude and phase returned by the ODD script for the simulated 3QF-MAS spectra of brucite, reported in Figure 6.9b, and berlinite, reported in Figure 6.9e, representing the amount of distortion in each lineshape. The ODD histogram plots for brucite are shown in Figure 6.10.*

tions. The standard deviation in both amplitude and phase are reported in Table 6.7.

For brucite, the standard deviations in amplitude are higher for FAM-N than for CW in absolute value, but are very similar when taken as a percent of the total intensity. This shows that the level of distortion in amplitude for both cases are almost identical. In Figures 6.9b and 6.9c, even though the most intense features of the spectral lineshapes differ between the CW and FAM-N spectra, the overall ”amount” of distortion is similar when referenced to their intensities. The phase distortions are higher for FAM-N than for CW conversion, which is consistent with the fact that FAM-N pulse are longer than CW, causing further relaxation, *e.g.*, further losses of coherence between the magnetic moments before the acquisition. However, the amount of phase distortions is low for both CW and FAM-N and tolerable in practice. As an illustration, the histogram plots returned by the ODD script for brucite are shown in Figure 6.10. The plot of amplitude for CW (Figure 6.10a) shows that most of the bars are located around 0.1, whereas the plot for FAM-N (Figure 6.10b) shows that the bars appears to be more scattered between 0.1 and 1. However, this gives overall a similar percentage of distortions in amplitude, as reported in Table 6.7. The histogram for the phase for CW (Figures 6.10c) and FAM-N (Figure 6.10d) are very similar, as shown in Table 6.7.

For berlinite, it can be seen that the lineshapes in the 3QF-MAS spectra in Figures 6.9e and 6.9f are extremely distorted and differ significantly from the ideal lineshape shown in 6.9d. This is also reflected in Table 6.7, where the standard deviation in amplitude gets above a 100% for CW, and near a 100% for FAM-N. This indicates that the amplitudes for

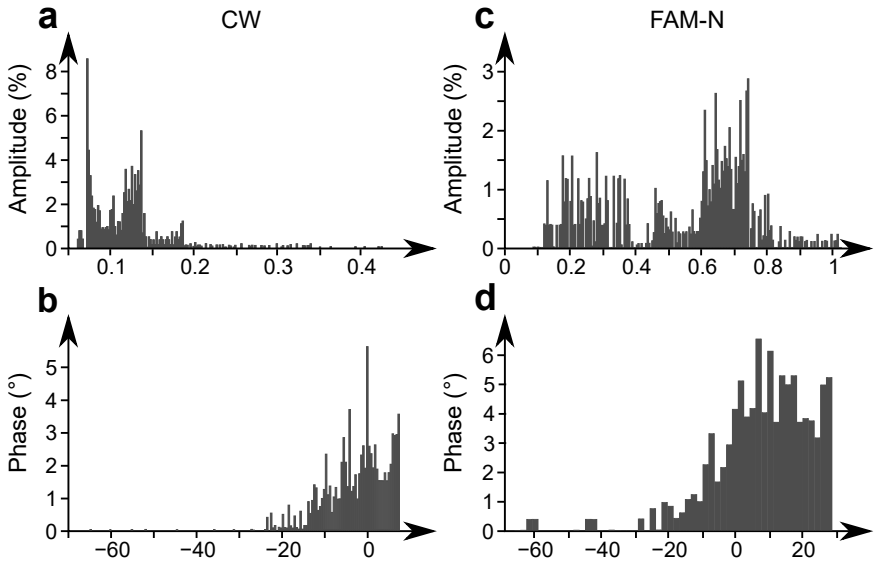

Figure 6.10: *ODD histograms for ^{25}Mg 3QF-MAS experiments on Brucite recorded with **(a,b)**: CW and **(c,d)**: FAM-N conversion pulses. All plots gives the proportion of all of the crystallite orientations as a function of **(a,c)**: the amplitude, and **(c,d)**: the phase of the detected operator $\langle \hat{I}_x^{\mathrm{CT}} \rangle$. Numerical values are given in Table 6.7. The phase origin is arbitrary.*

each of the crystallites are widely distributed around the average amplitude in a highly asymmetric manner. Phases distortions are also large, as clearly visible in Figure 6.9c, with those for FAM-N being slightly higher. Nevertheless, the amount of distortions is similar between the CW and FAM-N spectra. Moreover, no noticeable difference in the amount of phase distortions can be observed between the experimental and simulated CW and FAM-N spectra.

In conclusion, there is no strong evidence that FAM-N results in more lineshape distortion than CW conversion in MQMAS experiments. Despite an apparent difference in the lineshape changes between CW and FAM-N experimental spectra in Figures 6.9c and 6.9f, these appear to be only due to the lower signal intensities observed on CW spectra when plotted with FAM-N spectra for those two examples.

6.2.4 Difference between simulations and experiments

In this work, multiple comparison of CW and FAM-N conversion pulses for which the theoretical improvement ratios are very different to those seen experimentally have been presented. The robustness of FAM-N to variation of ν_1 and C_Q have been assessed in Section 5.2, and it has been concluded that only an approximate knowledge of those quantities is sufficient to observe signal improvement. However, discrepancies

		Ideal	Including				
			C_Q	η_Q	δ	$T_{2_{3Q}}$	Filtration
Na 1	CW	0.15	0.10	0.11	0.11	0.11	0.09
	FAM-N	0.49	0.43	0.38	0.37	0.36	0.29
	Ratio	×3.3	×4.3	×3.5	×3.4	×3.3	×3.4
			+1.1	−0.8	−0.1	−0.1	+0.1
Na 2	CW	0.15	0.09	0.10	0.10	0.10	0.08
	FAM-N	0.49	0.38	0.34	0.34	0.33	0.26
	Ratio	×3.3	×4.4	×3.4	×3.4	×3.3	×3.3
			+1.0	−0.9	0	−0.1	0
Na 3	CW	0.15	0.14	0.14	0.15	0.15	0.12
	FAM-N	0.49	0.49	0.43	0.43	0.41	0.33
	Ratio	×3.3	×3.4	×2.9	×2.9	×2.8	×2.9
			+0.1	−0.5	0	−0.1	+0.1
Na 4	CW	0.15	0.13	0.14	0.14	0.14	0.11
	FAM-N	0.49	0.40	0.37	0.36	0.34	0.28
	Ratio	×3.3	×3.1	×2.6	×2.6	×2.5	×2.5
			−0.2	−0.5	0	−0.1	0

Table 6.8: *Evolution of the amount of CT 1Q coherence | real part of ρ_{23} and of the theoretical improvement ratios between CW and FAM-N conversion pulses on each of the ^{23}Na site in $Na_4P_2O_7$ when various additional parameters are included in the simulation, from left to right. All simulations were performed for the FAM-N pulse used in Figures 5.9a and 5.9b, using 320 crystallite orientations and 20 γ-angles.*

between the parameters used in the optimisation and the experimental parameters will inevitably result in experimental improvement ratios that are lower, or at least different, to the theoretical ones. In addition, numerous possible instrument-related sources of signal loss have been mentioned in Section 5.2. In Figures 5.8 and 5.9, the amount of 1Q coherence created by CW and FAM-N conversion pulses was plotted against C_Q, using the experimental parameters in simulations, to illustrate the variation of the experimental improvements ratios measured on the different sites in a sample containing multiple species. It was concluded that, even though C_Q is the most important parameter, other parameters that have been neglected in the optimisation may have a significant impact on the improvement obtained. This section attempts to explore further the causes of the differences between the improvement ratios between simulation and experiment.

The ^{23}Na spectra of $Na_4P_2O_7$ shown in Figure 5.9a are a particularly intriguing example, as the theoretical improvement is halved in the experiments compared to the sim-

ulations, even when taking into account the variation of C_Q, as shown in Figure 5.9b and Table 5.4. Table 6.8 shows the amount of 1Q coherence created from initial 3Q coherence by the CW and FAM-N conversion pulses used to record the spectra shown in Figure 5.9a. Their ratio is used to derive the theoretical enhancement ratio for the four sites, adding one parameter at a time to bring the simulation closer to reality. The column ”Ideal”, shown in Table 6.8, gives the theoretical improvement ratio between CW and FAM-N obtained from a simulation that uses the optimisation parameters of FAM-N in a simulation. These are

- B_0 = 14.1 T (ν_0 = 158.8 MHz)
- C_Q = 2 MHz
- η_Q = 0
- ν_1 = 95.8 kHz
- ν_R = 12.5 kHz

The FAM-N pulse optimised using these parameters is composed of 12 pulses and has a total duration of $\tau_{p_{\text{FAM-N}}}$ = 9.59 µs. The CW pulse, optimised experimentally, has a duration $\tau_{p_{\text{CW}}}$ = 1.5 µs and is similar to that optimised in simulation ($\tau_{p_{\text{CW}}}$ = 1.4 µs). It should be noted that these two pulses are not changed when other parameters are included, *e.g.*, a new FAM-N optimisation is not carried out when a parameter is included, but the effect of pulses described previously are re-simulated including additional parameters.

Quadrupolar coupling constant

The column ”C_Q” of Table 6.8 shows the changes of the theoretical improvement ratios when FAM-N is simulated for the C_Q value of the four ^{23}Na sites, assuming η_Q = 0. This gives the same information as in Figure 5.9b. This column also shows that the improvement increases when only C_Q is taken into account for all sites except Na 4. Although the efficiency of FAM-N decreases for most sites, the efficiency of the CW conversion changes by different amounts, resulting in the changes in the theoretical improvement ratios given in Table 6.8.

Asymmetry parameters

Taking into account the effect of η_Q in the simulation for each of the sites is the most obvious next step to be considered, as it affects the FAM-N pulses is a similar way to a small change in C_Q (see Figure 5.5). The effect of this, shown in the column ”η_Q” of

Table 6.8, are quite important, with the FAM-N efficiency for all sites decreasing by a maximum amount of 20%, while that of CW remain essentially unchanged, resulting in the end in a decrease of the theoretical improvement ratios. The data presented here are consistent with the simulations previously performed in Figure 5.5, where changes by similar amounts were predicted. As all of the theoretical improvement ratios decrease as a result, these are now closer to the experimental improvement ratios.

Offsets and isotropic chemical shifts

A FAM-N pulse is not applied perfectly on resonance has been proven in Section 5.1.3 to be less and less efficient as the offset $\Delta\nu_0$ increases, although to a limited extent in the usual cases. The experimental offset, as well as the isotropic chemical shifts for each of the four sites, can be taken into account in the simulation, and these results are reported in the column δ ($= \Delta\nu_0 + \nu_{\mathrm{CS}}$) of Table 6.8. To compensate for the phase change induced by the offset, zero-order phase corrections of $-4.5°$ and $-22.1°$ have been applied respectively to the final amount of CT 1Q obtained after CW and FAM-N conversion. However, including $\Delta\nu_0$ and ν_{CS} results in very minor changes, with a decrease of -0.1 only for Na 1.

Relaxation during FAM-N

FAM-N pulses are longer than CW conversion pulses. As a result, it can be assumed that signal losses can occur due to the relaxation process taking place during the application of the FAM-N pulse. Estimated relaxation times during 3Q evolution have been derived from the linewidth of each of the four resonances in $Na_4P_2O_7$ from the indirect dimension of the MQMAS spectra in Figure 5.9a, and are denoted $T_{2_{3Q}}$. It is assumed that only this relaxation process take place during the whole duration of the FAM-N pulse. To account for this relaxation, the amount of 1Q coherence created by FAM-N has been multiplied by

$$\exp\left(-\frac{\tau_{\text{FAM-N}} - \tau_{\text{CW}}}{T_{2_{3Q}}}\right) \quad , \tag{6.2.3}$$

and the results reported in the column of Table 6.8 labelled $T_{2_{3Q}}$. This inclusion also results in small changes of -0.1 for all of the sites. The highest loss is observed for Na 4, which has the broader resonance, as visible in Figure 5.9a.

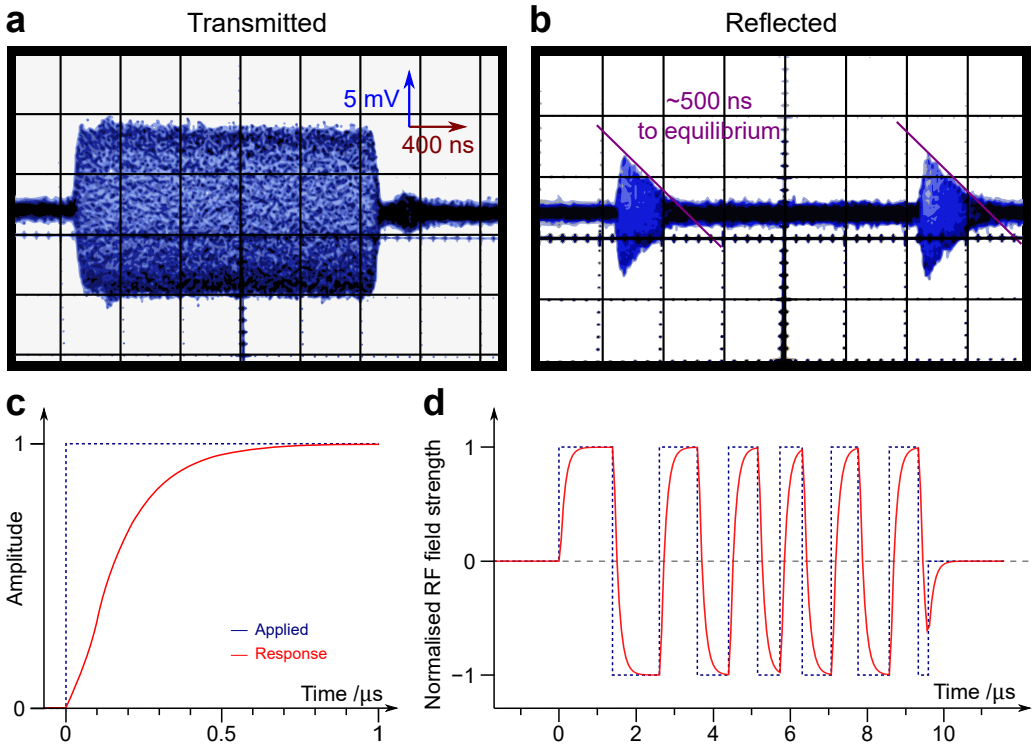

Figure 6.11: *Screen captures of an oscilloscope showing **(a)**: the voltage transmitted to the probe used that have been used to acquire the MQMAS spectra in Figure 5.9,[10] and **(b)**: the voltage reflected by the probe for a pulse modulated by ν_{RF} = 158.8 MHz (Larmor frequency of ^{23}Na at B_0 = 14.1 T) of duration 2 µs and power of 0.5 W. **(c,d)**: Illustration on the effect of the filter described by H_F in the main text on **(c)**: a Heaviside function and **(d)**: the (demodulated) FAM-N pulse of interest in this section.*

Filtration

As stated in Section 5.2, the efficiency of FAM-N is also reduced by hardware-related factors. While most of them are difficult or impossible to take into account in a simulation (*e.g.*, ability of the probe amplifier to accurately generate the FAM-N pulse, the error in RF calibration, detuning of the probe during an experiment, *etc.*), the effect of the probe itself is fairly simple to include. As instructed in Section 1.3.2, a probe can be simplified to a bandpass RLC circuit characterised by a resonance frequency, ω_{RF}, as well as a passband-width. The effect of an electronic filter on a alternating voltage at a frequency ω is described by a transfer function H, defined as

$$H(\omega) = \frac{U_s(\omega)}{U_e(\omega)} \quad , \tag{6.2.4}$$

where U_e and U_s, represented in Figure 1.8b, are the voltages applied by the amplifier and observed on the terminals of the RF coil, respectively. The typical maximum ex-

citation bandwidth of a regular NMR probe can be estimated to 200 kHz.[160] However, FAM-N imposes fast phase changes, which are equivalent to the application of a frequency remote from ω_{RF}, thus attenuated by the probe. This gives rise to a certain period, called the rise-time, necessary for a voltage applied by the amplifier to appear at the terminals of the RF coil, which can affect the efficiency of RF pulses. To deduce the transfer function for the electronics of the probe that was used to record the MQMAS spectra shown in Figure 5.9[10] is difficult due to its complexity. An easier approach is to experimentally measure the rise-time of the probe using an oscilloscope, then to build a transfer function that reproduces this rise-time. Screen captures of the oscilloscope show the transmitted (Figure 6.11a) and the reflected voltage (Figure 6.11b) observed for the probe used. It can be established from Figure 6.11b that only after 500 ns from a voltage change does the reflected power vanish completely.[11]

A suitable transfer function can be obtained from the Matlab function `fdesign`. Instead of a bandpass filter centred on ω_{RF} applied on FAM-N pulse modulated by ω_{RF}, a lowpass filter applied on the demodulated FAM-N pulse was used with the characteristics[12]

- Passband frequency: 200 kHz
- Passband attenuation: 0.1 dB
- Stopband frequency: 8 MHz
- Stopband attenuation: 12 dB

These parameters define a transfer function set internally in Matlab, termed H_{F}. From Equation (6.2.4), it can be deduced that the response of the RF coil in the time domain $\widetilde{U}_s$ when a voltage $\widetilde{U}_e$ is applied is expressed as[13]

$$\widetilde{U}_s(t) = \left(\widetilde{H}_{\mathrm{F}} * \widetilde{U}_e\right)(t) \quad , \tag{6.2.5}$$

where $\widetilde{H}_{\mathrm{F}} = \mathrm{FT}\left(H_{\mathrm{F}}\right)$ is the FT of the transfer function H_{F}, thus expressed in the time domain, and $*$ denotes the convolution product (see Appendix G.1, Property G.4). The response of a probe modelled by H_{F} to a Heaviside function shaped voltage is shown in Figure 6.11c, and reveals that the rise-time is indeed of approximately 500 ns. The effect of H_{F} on the experimental FAM-N pulse is shown in Figure 6.11d. The altered CW and FAM-N pulses are then used in SIMPSON input files, which gives the improvement reported in the column "Filtration" in Table 6.8.

[10] Spectrometer 1, probe (b) in Appendix C.1

[11] On spectrometer 1, probe (a) in Appendix C.1, this time is slightly lower, calibrated to 350 ns.

[12] It should be noted that the passband and stopband frequencies used for the `fdesign` function were 100 kHz and 4 MHz, as they describe the spacing between the zero-frequency and the applied frequency.

[13] In Matlab, Equation (6.2.5) is applied using the function `filter`.

There is a very visible effect of the filter on the FAM-N pulse in Figure 6.11d, with the rise time discussed previously necessary for the response voltage/RF field strength to reach the applied value. This has a considerable effect on the 3Q to 1Q conversion efficiencies of both CW and FAM-N conversion, as reported in Table 6.8, whose efficiency decrease by a large amount. However, the theoretical improvement ratio is left almost unchanged despite a small increase for Na 1 and Na 3, as the loss in efficiencies of the FAM-N pulses are proportionality equal to that of the CW pulses. From this result, it can be concluded that the theoretical improvement of the probe filtration, despite a manifest effect on the FAM-N pulse shape, has little effect on the relative efficient of CW and FAM-N pulses. However, this affects the absolute intensities obtained for spectra recorded with CW and FAM-N, but also other modulated pulses such as FAM-I, FAM-II or DFS.

Other sources

After taking into account the parameters discussed previously, the theoretical improvement ratios in Table 6.8 are still significantly higher than the experimental improvement reported in Table 5.3. The other potential sources of signal loss remaining are the hardware related problems listed in Section 5.2, which are mostly impossible to analyse by simulation. One final verification can be performed experimentally. The FAM-N pulse investigated in this section is composed of 12 pulses. In Section 5.2.1, it was shown that ”long” FAM-N pulses tends to be more ”specific” to their optimisation parameters, resulting in a theoretical maximum being difficult to attain, as experimental parameters unavoidably differ slightly from theoretical ones. Moreover, this effect seems to be more important for spins $I = 3/2$ nuclei, as discussed in Section 5.1.1. This is also reflected in Table 5.3, where the discrepancies between theoretical and experimental improvement ratios are the highest for ^{23}Na. For further insight, it can be determined experimentally whether the FAM-N optimisation is an accurate representation of reality by reducing the number of pulses used in FAM-N, in order to ensure that all pulses contribute to the signal increase.

Figure 6.12a shows the FAM-N optimisation curve, plotting the amount of CT 1Q coherence observed during the application of FAM-N, and showing the amount of CT 1Q coherence expected from applying FAM-N with a reduced number of pulses. Projections of the indirect dimension of ^{23}Na MQMAS spectra obtained using these FAM-N pulses are shown in Figure 6.12b. It should be noted that Figures 6.12a and 6.12b are not comparable, as Figure 6.12a is only valid for the parameters at which FAM-N was optimised,

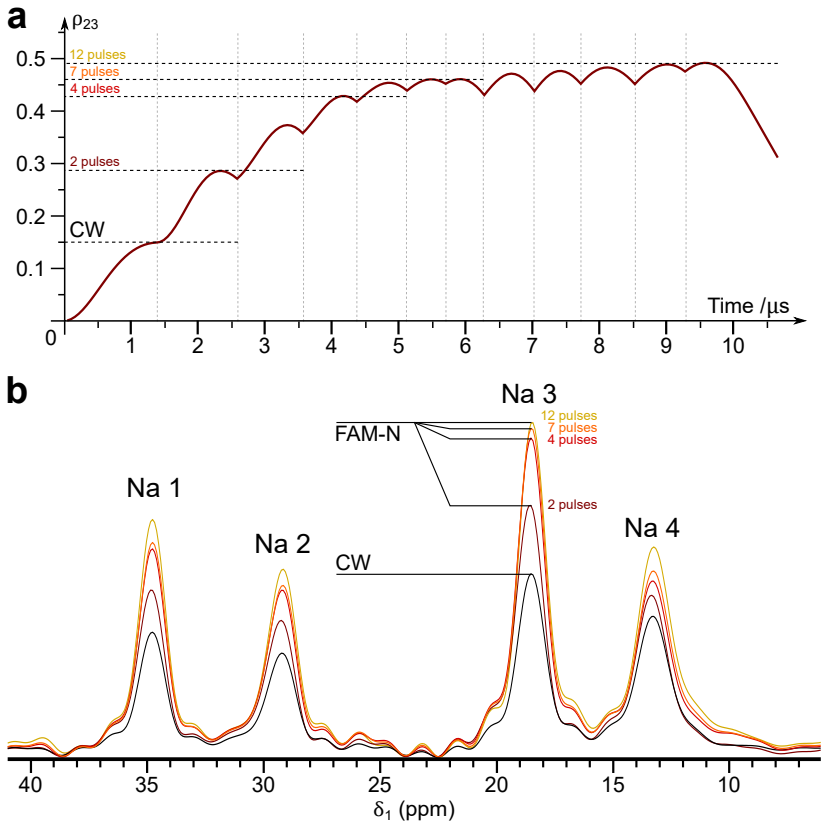

Figure 6.12: ***(a)****: Simulation showing the amount of CT 1Q coherence | real part of ρ_{23} created by FAM-N as a function of time from initial 3Q coherence for ^{23}Na at B_0 = 14.1 T (ν_0 = 158.8 MHz) with ν_1 = 95.8 kHz, ν_R = 12.5 kHz, C_Q = 2 MHz and η_Q = 0, showing the theoretical efficiencies of FAM-N and CW for the spectra shown in* ***(b)****. The points of phase inversion are indicated by light grey dashed lines, and the position and corresponding amounts of 1Q coherence created by FAM-N with a reduced number of pulses is indicated by dark grey dashed lines.* ***(b)****: Projections of the indirect dimension of ^{23}Na MQMAS spectra recorded at B_0 = 14.1 T (ν_0 = 158.8 MHz) with ν_1 = 96.5 kHz and ν_R = 12.5 kHz, for CW (black line) and the FAM-N shown in* ***(a)*** *with 2 (dark red line), 4 (light red line), 7 (orange line), and 12 (yellow line) pulses. See the extended caption in Appendix C.3 for further details.*

so precise theoretical and experimental improvement ratios are reported in Table 6.9.

It can be seen that all FAM-N pulses in Figure 6.12b contribute to a signal increase for all sites, even for these with quadrupolar parameters that differ greatly from those used in the FAM-N optimisation. However, the improvement given by each group of pulses is different between the four sites. Indeed, Na 3, whose quadrupolar parameters are the closest from the FAM-N optimisation values, experiences a large improvement in intensity from FAM-N truncated to 2 and 4 pulses, while the following pulses only result in a minor improvement. The same observation is provided by the theoretical improvement ratios in Table 6.9, although the final group of pulses result in a slight signal loss in simulations. On the contrary, Na 4, which exhibits the lowest improvement of all the

Site	Number of pulses	Experiment	Simulation
Na 1	2	×1.4	×1.8
	4	×1.7	×2.6
	7	×1.7	×3.1
	12	×1.9	×3.5
Na 2	2	×1.3	×1.8
	4	×1.6	×2.8
	7	×1.7	×3.0
	12	×1.8	×3.4
Na 3	2	×1.4	×1.9
	4	×1.7	×2.6
	7	×1.8	×3.0
	12	×1.8	×2.9
Na 4	2	×1.2	×1.5
	4	×1.3	×1.8
	7	×1.3	×2.4
	12	×1.5	×2.6

Table 6.9: *Table reporting the theoretical and experimental improvement ratios, obtained from simulation of the 3Q conversion (third column), and the intensities of the resonances for the four ^{23}Na species of $Na_4P_2O_7$ measured from the MQMAS spectra shown in Figure 6.12b, using the FAM-N pulses shown in Figure 6.12a with a reduced number of pulses.*

^{23}Na sites (as established in Figure 5.9 and in Table 6.8), is improved by small amounts, but in an almost identical amount, by each group of FAM-N pulses. This suggests that the signal on this site would experience a further increase with a longer FAM-N pulse, which would be obtained from a FAM-N optimisation using the quadrupolar parameters of Na 4. The two other sites, Na 1 and Na 2, appear to correspond to an intermediate case. The first 2 and 4 pulses of FAM-N give the highest improvement, the first 7 pulse to a very tiny additional improvement, and the total FAM-N give a larger additional improvement. For all of the sites, although the theoretical improvement ratios are quantitatively not consistent with the experiments, qualitatively, it can be noted that there is a consistency between simulation and experiment. Nevertheless, even though the experiments shown in Figure 6.12b confirm that the FAM-N simulations are accurate, this shows that the long duration of the FAM-N pulse is not responsible of the discrepancy between theoretical and experimental improvement ratios. The fact that the duration of the CW conversion pulse has been obtained from an experimental optimisation, while FAM-N is applied directly with its optimisation value do not explain this disparity, as the

CW conversion has a duration of 1.5 µs, and the first pulse of FAM-N has a duration of 1.4 µs.

Conclusion

Different causes of possible signal loss in experiment have been analysed, resulting in the conclusion that most induce only minor changes in the efficiency of FAM-N conversion pulses on $Na_4P_2O_7$. Taking into account η_Q for each site results in the highest diminution of the efficiency of the FAM-N pulses. This illustrates that including η_Q in the FAM-N optimisation, whenever possible, is useful. Including offsets and relaxation have a negligible impact on the improvement for this sample. However, this may not be the case for every sample, as some may contain sites with a higher chemical shift dispersion or faster relaxation. The effect of the filtration, although reducing the efficiencies of both FAM-N and CW conversion, leave the improvement ratios essentially unchanged for all sites. In summary, the investigation conducted establishes a set of experimental parameters that are not responsible for the discrepancies observed between theoretical and experimental improvements. While the reasons of these observations remain unclear, most parameters that can be included in simulations have been taken into account here, leaving mainly the contribution of some more complex hardware-related problems as the cause of the differences.

Part III

Other methods for quadrupolar nuclei

« La faiblesse humaine est d’avoir des curiosités d’apprendre ce qu’on ne voudrait pas savoir.»

”Human weakness is to have the curiosity to learn what we would not want to know.”

Molière, Amphitryon

Chapter 7

Enhancing the CT signal for quadrupolar nuclei

Introduction

Section 4.3 described the phenomenon by which ST-selective AM pulses enable more efficient 3Q to 1Q conversion and thus more sensitive MQMAS experiments, and Chapters 5 and 6 analysed the enhancements offered by FAM-N and other methods. This chapter describes how AM pulses can be utilised to improve the amplitude of the CT signal through the inversion, or the saturation, of the ST populations. Pound was the first to demonstrate that modulated pulses can be used to manipulate the ST populations of ^{23}Na for a single crystal of $NaNO_3$,[114] followed by Vega and Naor who performed the inversion of the ST populations on the same sample.[183] Subsequently, the AM pulses were used as a signal enhancement technique for MAS and spin-echo spectra,[27, 308, 384–397] as well as CPMG [398–402], DOR [403] and RIACT-MQMAS [22, 275, 298–300, 389, 404] spectra of quadrupolar nuclei, with many examples in the literature.

This chapter explores the performance of several AM pulses existing in the literature. Section 7.1 describes the methods that will be investigated in this chapter, and Section 7.2 reports the results of the investigations conducted on the HS[1] pulse scheme. Section 7.2.1 presents a general investigation of HS, with a particular focus on its performance under fast MAS. Section 7.2.2 reports the studies of the relative efficiency

[1] HS: *Hyperbolic Secant*

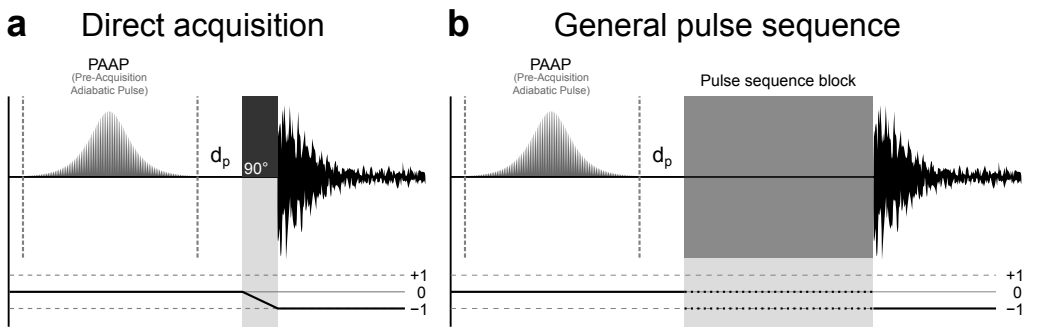

Figure 7.1: *Pulse sequence and CTPs including a PAAP for* ***(a)****: a direct acquisition experiment, and* ***(b)*** *for any pulse sequence, where d_p is a short delay.*

of HS compared to other methods, and Section 7.2.3 shows the implementation of HS prior to a RIACT experiment (see Section 4.2.1) for the purpose of signal improvement in MQMAS experiments.

7.1 CT signal enhancement methods

This section describes a brief overview, that is complementary to that in Section 4.3.1, discussing the concept of AM pulses for the inversion of ST populations, although this latter focussed primarily on the MQ to 1Q transfer. All methods reported in this section apart from COMPACT[2] in Section 7.1.4 are applied using a common pulse sequence presented in Figure 7.1a for a direct acquisition experiment, and in Figure 7.1b for the general case: a shaped pulse followed by a short delay d_p before a 90° pulse is applied for direct acquisition (Figure 7.1a), or any pulse sequence (Figure 7.1b) on which these pulses may have a positive effect, *e.g.*, spin-echo, CPMG, or RIACT-MQMAS (see Section 7.2.3) experiments. The shaped pulses effectively execute an adiabatic inversion of the ST magnetisation by 180° (see the description of an AFP[3] in Appendix F). As such pulses are positioned before the acquisition 90° pulse, or before the pulse sequence, here we define the acronym PAAP[4] to refer to these pulses.

7.1.1 General considerations

As with the improvement of MQ to 1Q conversion in Section 4.3.1, a ST inversion can be illustrated by the density matrices before and after the sweep. The initial density matrix

[2]COMPACT: *COMposite Pulses Adapted for Central Transitions*
[3]AFP: *Adiabatic Full Passage*
[4]PAAP: *Pre-Acquisition Adiabatic Pulse*

is always given by $\langle \hat{I}_z \rangle$. In the general case, the action of a pulse with an AM and/or a FM modulation is expressed by the Hamiltonian

$$\hat{H}_{\mathrm{RF}} = \hat{I}_x . \omega_1(t) \exp\left(i\phi_m(t - t_0)\right) \quad , \tag{7.1.1}$$

where $\omega_1(t)$ is the time-dependent RF field strength, *e.g.*, the AM part of the RF Hamiltonian, and ϕ_m is the modulation phase

$$\phi_m(t - t_0) = \int_{t_0}^{t} \Delta\omega(\tau) d\tau \quad , \tag{7.1.2}$$

with $\Delta\omega(\tau)$ being the time-dependent offset, *e.g.*, the FM part of the RF Hamiltonian, both described in Appendix F. As discussed in Section 4.3.1, symmetrical double-offset pulses are purely amplitude modulated and are, therefore, expressed by a cos function. A pulse performing a perfect ST inversion on a spin $I = 3/2$ results in the transfer [115, 183, 312]

$$\begin{bmatrix} +3/2 & 0 & 0 & 0 \\ 0 & +1/2 & 0 & 0 \\ 0 & 0 & -1/2 & 0 \\ 0 & 0 & 0 & -3/2 \end{bmatrix} \xrightarrow[\text{of the ST populations}]{\text{Adiabatic inversion}} \begin{bmatrix} +1/2 & 0 & 0 & 0 \\ 0 & +3/2 & 0 & 0 \\ 0 & 0 & -3/2 & 0 \\ 0 & 0 & 0 & -1/2 \end{bmatrix} \quad . \tag{7.1.3}$$

As it can be observed from Equation (7.1.3), a perfect inversion would result in the amount of population in the two energy levels of the 3Q transition being transferred to the CT energy levels, resulting in ×3 the original population difference in the CT, and thus an equivalent amount of signal improvement on a MAS spectrum. For any spin I, this improvement is given by

$$\epsilon = 2I \quad . \tag{7.1.4}$$

As discussed from Section 4.3.1, it is common in practice that a transfer does not result in a perfect inversion for all of the crystallite orientations, giving improvements lower than that in Equation (7.1.4) in a powdered solid. For some crystallites, saturation rather than inversion of the ST populations may take place, resulting in the population transfer for a spin $I = 3/2$ nucleus of [115, 183, 312]

$$\begin{bmatrix} +3/2 & 0 & 0 & 0 \\ 0 & +1/2 & 0 & 0 \\ 0 & 0 & -1/2 & 0 \\ 0 & 0 & 0 & -3/2 \end{bmatrix} \xrightarrow[\text{of the ST populations}]{\text{Adiabatic saturation}} \begin{bmatrix} +1 & 0 & 0 & 0 \\ 0 & +1 & 0 & 0 \\ 0 & 0 & -1 & 0 \\ 0 & 0 & 0 & -1 \end{bmatrix} \quad , \tag{7.1.5}$$

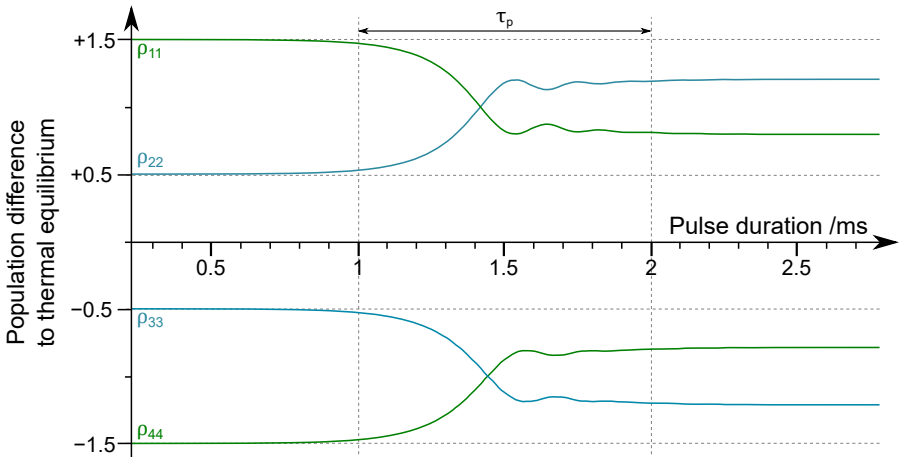

Figure 7.2: *Illustration of the population transfers during the application of a PAAP in Σ_{lab}, averaged over a statistical ensemble of crystallite orientations. Plot of the density matrix elements corresponding to the population of the two 3Q energy levels $|3/2,+3/2\rangle$ and $|3/2,-3/2\rangle$ (green lines), and the two CT energy levels $|3/2,+1/2\rangle$ and $|3/2,-1/2\rangle$ (blue lines) for ^{87}Rb ($I = 3/2$) on $RbClO_4$, here using a HS pulse (see Section 7.1.3) with τ_p = 1 ms in Equation (7.1.17), using in simulation the same parameters for simulation as for the ν_R = 10 kHz spectrum of $RbClO_4$ in Figure 7.11. Simulations performed on 320 crystallite orientations and 10 γ-angles, with a digitisation of 120 ns.*

giving the maximum expected improvement for a full saturation of ×2 on spin $I = 3/2$. On any spin I, the maximum improvement after ST saturation is given by

$$\epsilon = I + {}^1\!/_2 \quad . \tag{7.1.6}$$

Figure 7.2 illustrates the population transfer for a spin $I = 3/2$ nucleus during the application of a PAAP in Σ_{lab}, averaged over a statistical ensemble of crystallite orientations. Here, the observed improvement is ×2.4, higher than the theoretical maximum for a saturation, but lower than that of a full inversion. Figure 7.2 illustrates, as stated in Section 4.3.1, that whether one mechanism or the other takes place depends upon the relative orientation of Σ_{rot} and the PAF of the quadrupolar interaction for each crystallite, and the total improvement observed over an ensemble of orientations would be reflected by the contribution of both mechanisms.[313] A comparison of Equations (7.1.4) and (7.1.6) shows that the inversion of the ST population results in the highest improvement, and therefore is the desired transfer.

7.1.2 The RAPT and DFS pulses

DFS, already introduced in Section 4.3.2 and investigated in Section 5.3, is a method that can be also be applied to invert the ST populations, as reflected by the multiple

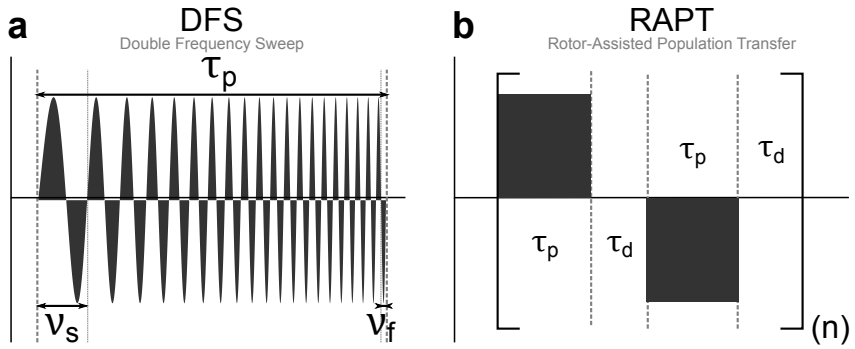

Figure 7.3: *Illustration of **(a)**: the DFS scheme and **(b)**: the RAPT scheme.*

examples in the literature reporting successful experiments recorded with the help of DFS for difficult nuclei,[272, 314, 315, 394, 395, 398–401, 405, 406] such as ^{43}Ca.[395, 405]

The RF Hamiltonian for the DFS pulse is given for $\phi_m(t) = 0$ in Equation (7.1.1), and

$$\omega_1(t) = \omega_1^{\max} \cos \omega_m(t) \quad , \tag{7.1.7}$$

where $\omega_m(t)$ is the modulation frequency introduced in Section 4.3.1. Here, only the linear sweep, already defined in Equation (4.3.14b), is considered, which is

$$\omega_m(t) = \omega_s + \frac{\omega_f - \omega_s}{\tau_p} t \quad . \tag{7.1.8}$$

This results in the RF Hamiltonian

$$\hat{H}_{\mathrm{RF}} = \hat{I}_x \omega_1^{\max} \cos \omega_m(t) \quad . \tag{7.1.9}$$

It should be noted that Goswami *et al.* reported an alternative DFS scheme, termed ssDFS[5] [315] obtained by multiplying the linearly swept DFS in Equation (7.1.8) with a $\sin^2$ function, which was proven to be more suitable for the improvement of the CT signal, without increasing the complexity of the original DFS pulse.[314]

When DFS is applied as a PAAP, Equation (7.1.8) is best when re-formulated using the form

$$\omega_m(t) = \Delta\omega_c + \lambda \left[\frac{2t}{\tau_p} - 1 \right] \quad , \tag{7.1.10}$$

where

$$\Delta\omega_c = \frac{\omega_s + \omega_f}{2} \tag{7.1.11}$$

[5] ssDFS: *Sideband-Selective Double-Frequency Sweep*

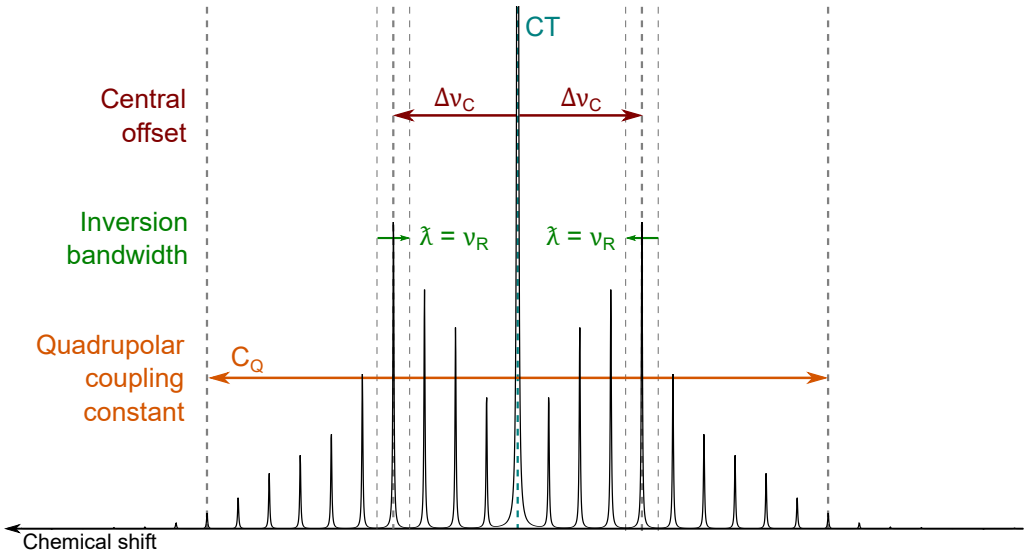

Figure 7.4: *Schematic of the inversion executed on one spinning sideband of the MAS lineshape of the STs of a quadrupolar nucleus, according to the inversion bandwidth ƛ and the offset frequency $\Delta\nu_c$.*

is the central offset,[6] and corresponds to the frequency at which the DFS pulse is applied, and

$$\lambda = \frac{|\omega_f - \omega_s|}{2} \tag{7.1.12}$$

is the half-inversion bandwidth, here given in rad.s^{-1}. It can also be defined the more convenient full-inversion bandwidth in Hz, ƛ, given by

$$\text{ƛ} = \frac{|\omega_f - \omega_s|}{2\pi} \tag{7.1.13}$$

$$= \frac{\lambda}{\pi} \quad . \tag{7.1.14}$$

Expressing the sweep with these parameters allows an easy visualisation of how they relate to the static lineshape or the spinning sideband manifold of the ST transitions. This is shown in Figure 7.4. If it is possible to observe the full MAS manifold of the STs, signal enhancement is at a maximum when placing the central offset $\Delta\nu_c$ on the spinning sideband with the highest intensity as illustrated in Figure 7.4.[396, 407] Otherwise, an optimisation of the offset frequency can be carried out, which would result in an identical answer if only the CT signal is visible.

For the inversion bandwidth ƛ, it might be expected that the inversion has to cover the entire lineshape in the static case, or the entire spinning sideband manifold under

[6] Or $\Delta\nu_c$ when expressed in Hz.

MAS. However, it has been shown by several authors that this is not necessary under MAS,[390, 408] as $\Omega_Q(t)$ (see Equation (2.3.29)) associated with each of the crystallite is swept across the entire width of the ST lineshape by the spinning of the rotor (see Figure 3.7). It follows that best results are obtained when λ is set to the MAS rate ν_R, which can be pictured as the inversion being executed over the spacing between spinning sidebands as illustrated in Figure 7.4. This is the main difference with modulated pulses introduced in Section 4.3, which are more efficient when performing the inversion over the entire ST lineshape.

The RAPT[7] pulse is a method introduced by Yao *et al.*,[27] which has a form identical to FAM-I pulses,[8] but has been adapted for the adiabatic inversion of the ST populations rather than MQ to 1Q. This pulse scheme is also popular,[27, 169, 275, 385, 387–389, 398, 406, 409, 410] owing to its greater simplicity compared to DFS and for its ease of implementation on spectrometers that do not support the generation of complex shaped pulses. As with FAM, RAPT possesses less degrees of freedom than DFS, therefore a lower efficiency should be expected. In spite of the absence of a frequency sweep in the formulation of RAPT, signal enhancement by this method is enabled by the sweeping of the crystallite orientations under MAS, as described previously. Therefore, the STs for all of the crystallite orientations can be affected even without an effective sweep.[20, 316] Removing the window of RAPT, *e.g.*, as in FAM-II shown in Figure 4.11b, proved not to be an efficient approach as experimentally optimising RAPT pulse by pulse eventually results in series of pulses with almost identical durations.

7.1.3 The HS pulse

The HS pulse is a shaped pulse scheme originally proposed as an analytical solution to the Bloch equations (see Equation (1.3.14)),[411] and has been first introduced for applications in two-level laser spectroscopy.[25] Later, it has been used as efficient adiabatic inversion pulses for MRI (see Appendix F).[26, 412] The use of HS pulses for the improvement of the CT transition populations was extensively investigated by Siegel *et al.*,[384, 390–393] who reported signal improvement near the theoretical maximum of $2I$ for a full inversion in Equation (7.1.4) on model samples. HS pulses are one of the most common approaches for signal improvement of the CT signal for quadrupolar nuclei,[169, 384, 386, 396, 401] with applications on insensitive nuclei such as ^{33}S demon-

[7] RAPT: *Rotor-Assisted Population Transfer*
[8] Hence, the technique is sometimes referred to as being RAPT/FAM.[300, 382]

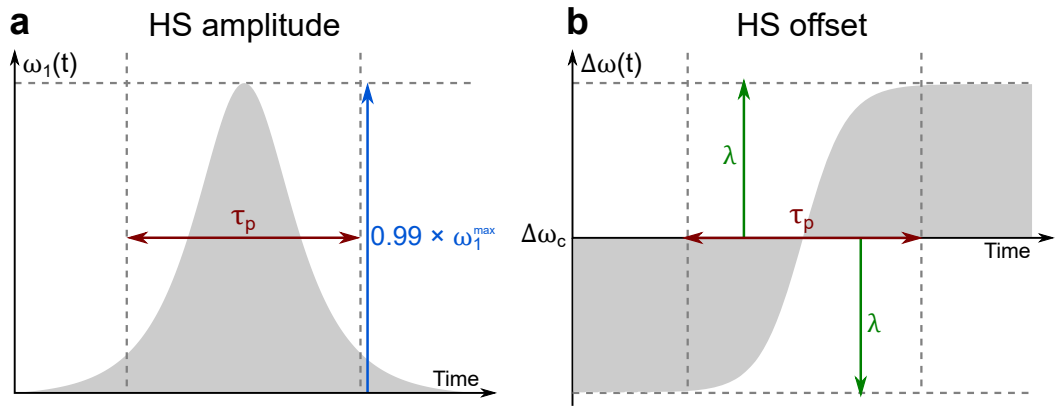

Figure 7.5: *Schematic representations of **(a)**: the shape of $\omega_1(t)$ and **(b)**: of $\Delta\omega(t)$ for the HS pulse according to the parameters given in Equation* (7.1.17a) *and (7.1.17b).*

strated.[169, 384, 386]

A HS pulse consists of a hyperbolic secant function "sec" as the AM part

$$\text{sec} : x \rightarrow \text{sec}(x) = \frac{1}{\text{ch}(x)} = \frac{2}{\exp(x) + \exp(-x)} \quad , \tag{7.1.15}$$

and a hyperbolic tangent "tanh" function as the FM part

$$\tanh : x \rightarrow \tanh(x) = \frac{\sinh(x)}{\cosh(x)} = \frac{\exp(x) - \exp(x)}{\exp(x) + \exp(-x)} \quad . \tag{7.1.16}$$

The HS pulse is often expressed in the following convenient form in the literature, with the RF field amplitude $\omega_1(t)$ and the phase/offset $\Delta\omega(t)$ in Equations (7.1.1) and (7.1.2) being defined as [26, 391, 413, 414]

$$\omega_1(t) = \omega_1^{\max} \cos\left(\Delta\omega_c + \lambda\left[\frac{2t}{\tau_p} - 1\right]\right) \text{sec}\left(\beta\left[\frac{2t}{\tau_p} - 1\right]\right) \quad , \tag{7.1.17a}$$

and

$$\Delta\omega(t) = \Delta\omega_\phi + \lambda.\tanh\left(\beta\left[\frac{2t}{\tau_p} - 1\right]\right) \quad , \tag{7.1.17b}$$

represented in Figures 7.5a and 7.5b, respectively. This corresponds to a modulation phase of

$$\phi_m(t) = \Delta\omega_\phi t + \left(\frac{\lambda\tau_p}{2\beta}\right) \ln\left(\cosh\left(\beta\left[\frac{2t}{\tau_p} - 1\right]\right)\right) \quad . \tag{7.1.17c}$$

It can clearly be seen that the AM is produced by the "cos" function of Equation (7.1.17a) The shape and the nature of the sweep of the HS pulse are given in Equation (7.1.17) using the parameters of Equation (7.1.10). Those are

- the pulse duration τ_p,
- the half-inversion bandwidth λ,
- the maximum RF field strength $\omega_1^{\max}$,
- the truncation factor β, set to 5.3 to limit the maximum amplitude of $\omega_1(t=0)$ to $\simeq 0.99 \times \omega_1^{\max}$.
- the central AM offset frequency $\Delta\omega_c$,
- the central FM offset frequency $\Delta\omega_\phi$.

As for DFS, a HS pulse can be expressed using an inversion bandwidth λ and offset frequencies. In the literature, HS is often expressed with two frequency offsets, here denoted $\Delta\omega_c$ and $\Delta\omega_\phi$ for the AM and FM respectively. As discussed in Section 4.3.1, a FM only introduces an asymmetry relative to the carrier frequency in the two simultaneous offsets at which the pulse is applied, which is not relevant given the symmetry of the ST lineshape.[407] The effect of the HS pulse is an adiabatic inversion for the signal located at $\omega_{\text{RF}} + \Delta\omega_c$ and $\omega_{\text{RF}} - \Delta\omega_c$. As for DFS, the AM is swept linearly, following the relation in Equation (7.1.10). HS was also used to enhance the sensitivity of MQMAS experiments. However, Siegel *et al.* showed that the efficiency of HS pulse for MQ to 1Q coherence transfer is roughly similar to that reported for DFS, and that HS is more efficient than DFS for the signal improvement of the CT intensity.[392]

7.1.4 The COMPACT pulse

COMPACT is a composite pulse [291, 292] published by Carnevale and Bodenhausen for signal improvement of the CT of quadrupolar nuclei.[28] It consists of a succession of oppositely-phased hard pulses, with durations that are successive multiples of the first pulse duration τ_p

$$(1 \times \tau_p)_{+\phi} \mid (2 \times \tau_p)_{-\phi} \mid (3 \times \tau_p)_{+\phi} \mid \ldots \mid (n \times \tau_p)_{\pm\phi} \quad , \tag{7.1.18}$$

with the method termed COMPACT-n when n pulses are employed.[9] The main benefit of COMPACT over the PAAPs previously described is that it enables signal improvement of the CT signal with no additional effort than a direct acquisition spectrum. It could be argued that the optimum number of pulses is also to be optimised (generally 3 or 5, shown in Figures 7.6a and 7.6b, respectively). However, varying the number of pulses is not of vital importance, but further improvement might be obtained *via* optimisation if the aim is the maximum signal improvement. The COMPACT pulse can be seen as a

[9] In this work, only COMPACT-3 pulses have been utilised.

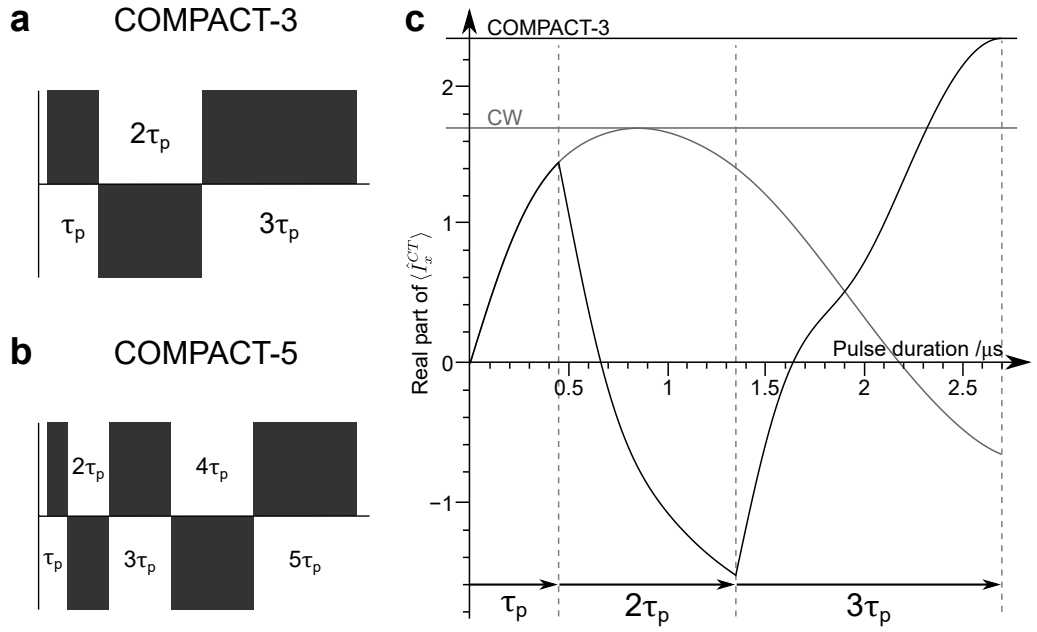

Figure 7.6: ***(a,b)****: Illustration of* ***(a)****: the COMPACT-3 and* ***(b)****: the COMPACT-5 pulse schemes.* ***(c)****: Simulation plotting the amount of CT 1Q coherence | the real part of* $\langle \hat{I}_x^{\mathrm{CT}} \rangle$ *obtained as a function of time during the application of a CW and a* τ_p *= 0.45 µs COMPACT-3 pulse, for* ^{87}*Rb at* B_0 *= 14.1 T (*ν_0 *= 196.4 MHz),* ν_1 *= 146.2 kHz*ν_R *= 12.5 kHz, and the quadrupolar parameters of* $RbClO_4$ *given in Appendix C.2.*

simplified version of the pulse optimised by O'Dell *et al.* using optimal control,[415] as it combines both the effects of an AM pulse, manipulating populations and resulting in some signal improvement, and of the 90° acquisition pulse, and hence is applied directly in one single block. This pulse scheme has been proven by simulations to produce signal improvements of roughly ×1.3 to ×1.4 for spins $I = 3/2$, $5/2$ and $7/2$ on model samples, to be usable in both static and MAS conditions, and to induce no noticeable lineshape distortions. However, its disadvantage it that these signal improvements of 1.3 to 1.4 are lower than those typically obtained using PAAPs.[28, 392]

Figure 7.6c shows the evolution of $\langle \hat{I}_x^{\mathrm{CT}} \rangle$ during hard CW and COMPACT pulses, where it can clearly be observed that the final $\langle \hat{I}_x^{\mathrm{CT}} \rangle$ is higher using COMPACT-3 than for the CW pulse. The authors also showed that the pulse scheme reduced the intensity of the STs signal, which is the origin of the observed signal improvement. However, COMPACT does not perform an adiabatic inversion/saturation of the satellite populations unlike the methods introduced previously, and therefore must not be confused with a PAAP. Nevertheless, it serves the same purpose of CT signal improvement and is very easy to implement. As such, COMPACT can be compared to PAAPs.

7.2 Investigating the efficiency of HS pulses

In light of the large signal improvements of the CT signal reported to the literature for HS, it has been decided to conduct more in-depth investigations, with applications on materials that require expensive isotropic enrichment of low natural abundance nuclei such as ^{17}O, ^{25}Mg or ^{43}Ca in mind. These are found in a wide range of materials, such as high-pressure glasses, zeolites and minerals.[279, 378, 416–418] The effect of fast MAS on the efficiency of HS and other PAAPs have not been extensively investigated in the literature. Therefore, the discussion remains on whether the shape of the spinning sideband manifold and the constant width of each individual spinning sideband for different MAS rates has a major impact on the performance of PAAPs. Figure 7.7 illustrates this last point, showing that an inversion is performed over an inversion bandwitdh λ equal to the MAS rate ν_R, but it is not trivial to conclude that inversions performed at different MAS rates are identical as the most intense spinning sideband may change with ν_R, while it keeps the same width dictated by SOQE. However, no major differences are expected between standard and fast MAS rate, but this is a pertinent interrogation as fast MAS is a necessity for sites with high C_Q and at low to moderate B_0 fields. Investigations of the performance of HS pulses will be conducted, both experimentally and in simulation, at various MAS rates for model samples (^{87}Rb in $RbClO_4$ for spin $I = 3/2$ and ^{27}Al in $Al(acac)_3$ for spin $I = 5/2$), to unravel this issue.

7.2.1 HS applied under fast MAS

Even though it might appear complicated to optimise HS pulses experimentally owing to the large number of parameters defining its shape, this is in reality relatively straightforward after some consideration. The truncation parameter β, used to prevent the amplifier to reach exactly $\omega_1^{\max}$, is normally set by convention to 5.3 and thus is not to be optimised.[390] As mentioned in Section 7.1.2, under MAS, most efficient improvements can be obtained when the inversion bandwidth λ is set to the MAS rate ν_R.

The adiabaticity of the pulse must also be considered. As discussed in Appendix F for spin $I = 1/2$ nuclei, pulses described in this section are subject to an adiabatic condition (see Equation (F.1.10)). If this condition is fulfilled, an adiabatic pulse will result in a magnetisation flip independent of the RF field strength ν_1 and pulse duration τ_p. Expressing adiabatic conditions for quadrupolar nuclei is more complex owing to the presence of the quadrupolar interaction. A general adiabatic factor has been expressed by

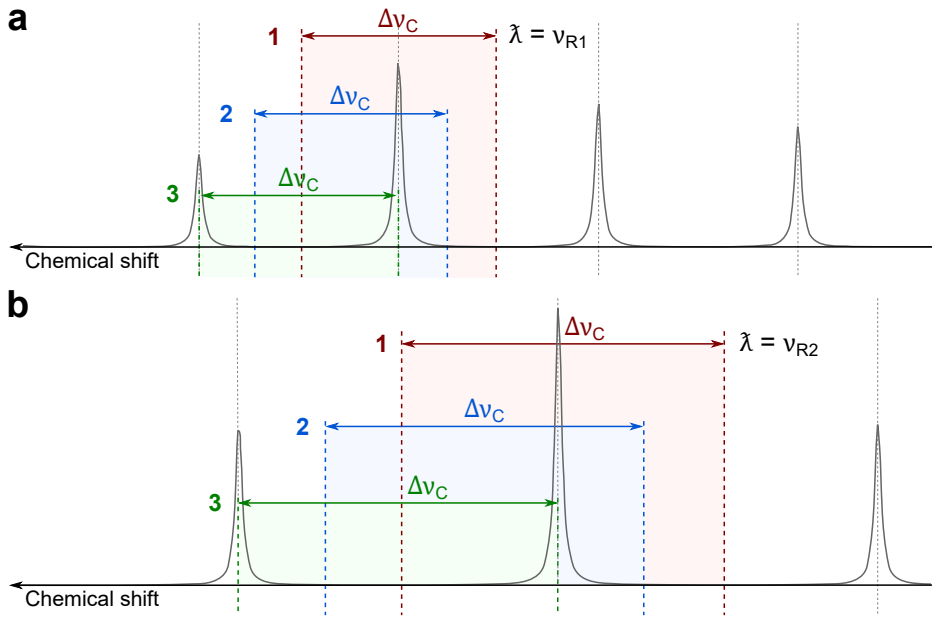

Figure 7.7: *Schematic representation of two ST spinning sideband manifolds at two different spinning speeds* ***(a):*** ν_{R1} *and* ***(b):*** ν_{R2}*, illustrating different positions of the central offset* $\Delta\nu_c$ *relative to this spinning sideband manifold, with the inversion bandwidth being* ***(a)****:* $\tilde{\lambda} = \nu_{R1}$ *and* ***(b)****:* $\tilde{\lambda} = \nu_{R2}$*.* ***(1)****: Offset placed on the top of the most intense spinning sideband,* ***(2)****: offset placed away from the most intense spinning sideband, and* ***(3)****: offset placed in between the most intense spinning sideband and the next spinning sideband.*

Schäfer *et al.*,[316] showing a dependence on the orientation of the quadrupolar interaction PAF, and the "effective" RF field strength $\omega_{1_{\text{eff}}}$ (see Section 3.2.2), not trivial to express as it is also dependant on the strength of the quadrupolar interaction.[309, 393] This adiabaticity factor is

$$A = \frac{\omega_{1_{\text{eff}}}^2(t)}{p\frac{d}{dt}\left(\Omega_Q(\beta_{\text{PR}}, \gamma_{\text{PR}}, t) - \Delta\omega(t)\right)} \quad , \tag{7.2.1}$$

where p is the coherence order of the CT and the symmetrical MQ transition(s) affected by the pulse. The adiabaticity of HS pulses for quadrupolar nuclei have been discussed by several authors in the literature.[309, 393, 414, 419] It is clear that the time and orientation dependence of Equation (7.2.1) does not make it very practical to derive a mathematical expression of the adiabaticity factor. In practice, to make sure pulses are in the adiabatic regime, optimisation of τ_p and ν_1 have been conducted to ensure that the improvement remains unchanged as these two quantities are varied. Finally, among the offsets $\Delta\omega_c$ and $\Delta\omega_\phi$ given in Equation (7.1.17), $\Delta\omega_c$, only the AM central offset $\Delta\omega_c$ needs to be considered for quadrupolar nuclei as discussed in Section 7.1.3. This leaves in end only one parameter to optimise, assuming the adiabatic condition is fulfilled.

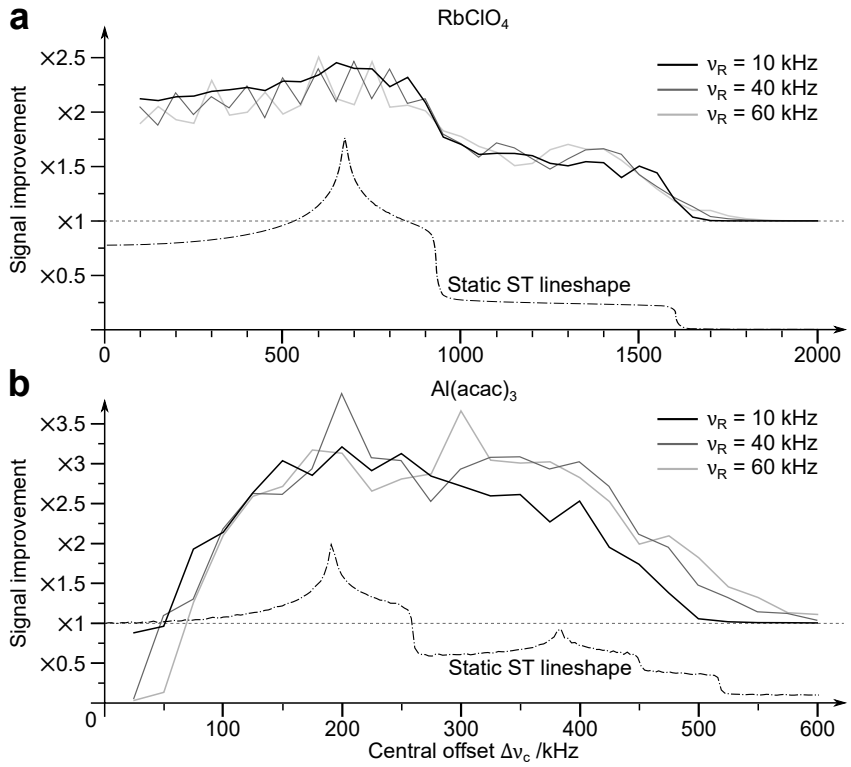

Figure 7.8: *Simulated signal improvement obtained using HS as a PAAP as a function of the central offset $\Delta\nu_c$, for conditions simulated with the ^{87}Rb and ^{27}Al quadrupolar parameters of **(a)**: $RbClO_4$ and **(b)**: $Al(acac)_3$, performed for ν_R = 10 kHz (black lines), ν_R = 40 kHz (dark grey lines) and ν_R = 60 kHz (light grey lines). All of the simulations performed on 320 crystallite orientations and 10 γ-angles, at $B_0 = 14.1$ T (ν_0 = 196.4 MHz for ^{87}Rb and ν_0 = 156.4 MHz for ^{27}Al), $\nu_1 = 22$ kHz with $\Delta\nu_c$ increments of 50 kHz for **(a)** and 25 kHz for **(b)**.*

Figures 7.8a and 7.8b shows the signal improvement in simulation of varying $\Delta\nu_c$ for ^{87}Rb in $RbClO_4$ and for ^{27}Al in $Al(acac)_3$, respectively, with ν_R = 10, 40 and 60 kHz. It can be seen that the two curves simulated for the two MAS rates are very similar, with the improvement being maximum for $\Delta\nu_c$ = 600 to 900 kHz in Figure 7.8a, and 200 to 300 kHz in Figure 7.8b. As established by Siegel *et al.* and as illustrated in Figure 7.8, each of the plots of signal improvement resembles the static lineshapes of the STs, with the maximum improvement being obtained when the offset is placed at the point of maximum intensity of the static lineshape.[391] For $\Delta\nu_c > C_Q/2$, the pulses leads to no improvement. Besides some oscillations, the curves for the three MAS rates are essentially identical in Figure 7.8a, but a higher improvement starts to be visible for $\Delta\nu_c > 250$ kHz in Figure 7.8b, where the offset is applied in a region where the ST_2 spinning sidebands are mostly affected. As visible in Figure 2.5, even though the spinning sideband manifold resembles the static lineshape, the intensity of the spinning sideband manifold does not strictly follow that of the static lineshape and spinning sidebands can appear

outside from the static lineshape. A simulation (not presented here) of the MAS spectrum of the ST for $Al(acac)_3$ shows that the spinning sidebands are about as intense on either side of the first "horn" of the static lineshape with ν_R = 60 kHz, while these spinning sidebands are significantly smaller on a MAS spectrum simulated for ν_R = 10 kHz compared to the spectrum simulated for ν_R = 60 kHz. This does not apply for ^{87}Rb of $RbClO_4$, as spin $I = 3/2$ nuclei have only one pair of STs.

In Figures 7.8a and 7.8b, a larger number of peaks in the plots of signal improvement are observed for certain values of $\Delta\nu_c$ when ν_R = 40 kHz or ν_R = 60 kHz, in comparison to when ν_R = 10 kHz. These oscillations can be understood by considering Figure 7.9. This figure plots the theoretical signal improvement for $RbClO_4$ as a function of $\Delta\nu_c$ using a small increment, for ν_R = 10 kHz (Figure 7.9a), ν_R = 40 kHz (Figure 7.9b) and ν_R = 60 kHz (Figure 7.9c). There is a clear pseudo-periodicity in this figure for all plots and both in the simulations and in the experiments. The improvement oscillates between minimum and maximum values for every half rotor period. These oscillation can be attributed to the position of the central offset $\Delta\nu_c$ relative that of the spinning sidebands. In Figure 7.7, three cases have been presented:

1. $\Delta\nu_c$ is applied exactly on a given spinning sideband (red),
2. $\Delta\nu_c$ is applied away from a given spinning sideband (blue),
3. $\Delta\nu_c$ is applied exactly in between two given spinning sideband (green).

The half-rotor period periodicity of the improvement in Figure 7.9 can be interpreted in terms of these three cases. The signal improvement is a maximum when $\Delta\nu_c$ is applied either exactly on a spinning sideband, or exactly in between (cases 1 and 3, respectively), and is a minimum when it is not the case (case 2). Furthermore, in Figures 7.9b and 7.9c, different maximum signal intensities are seen in the experimental spectra, corresponding to case 1 for the most intense maxima, and case 3 for the less intense maxima. The same effect can be seen in the simulations, but is clearly less important. Therefore, it appears that, case 1 is slightly more favourable than case 3, *e.g.*, applying $\Delta\nu_c$ on a spinning sideband results in a more efficient transfer than exactly in between two sidebands. The apparently random position of the peaks is due to the large interval used for $\Delta\nu_c$ of 50 kHz for Figure 7.8a and 25 kHz for Figure 7.8b. Choosing a narrower interval would result in the same periodicity as in Figure 7.9 to be visible.

Finally, Figure 7.10 plots the theoretical improvement ratios for HS pulses applied with a constant offset in Figure 7.10a and a variable offset in Figure 7.10b, adjusting the inversion bandwidth λ to correspond to the MAS rate ν_R in each case. In the region of

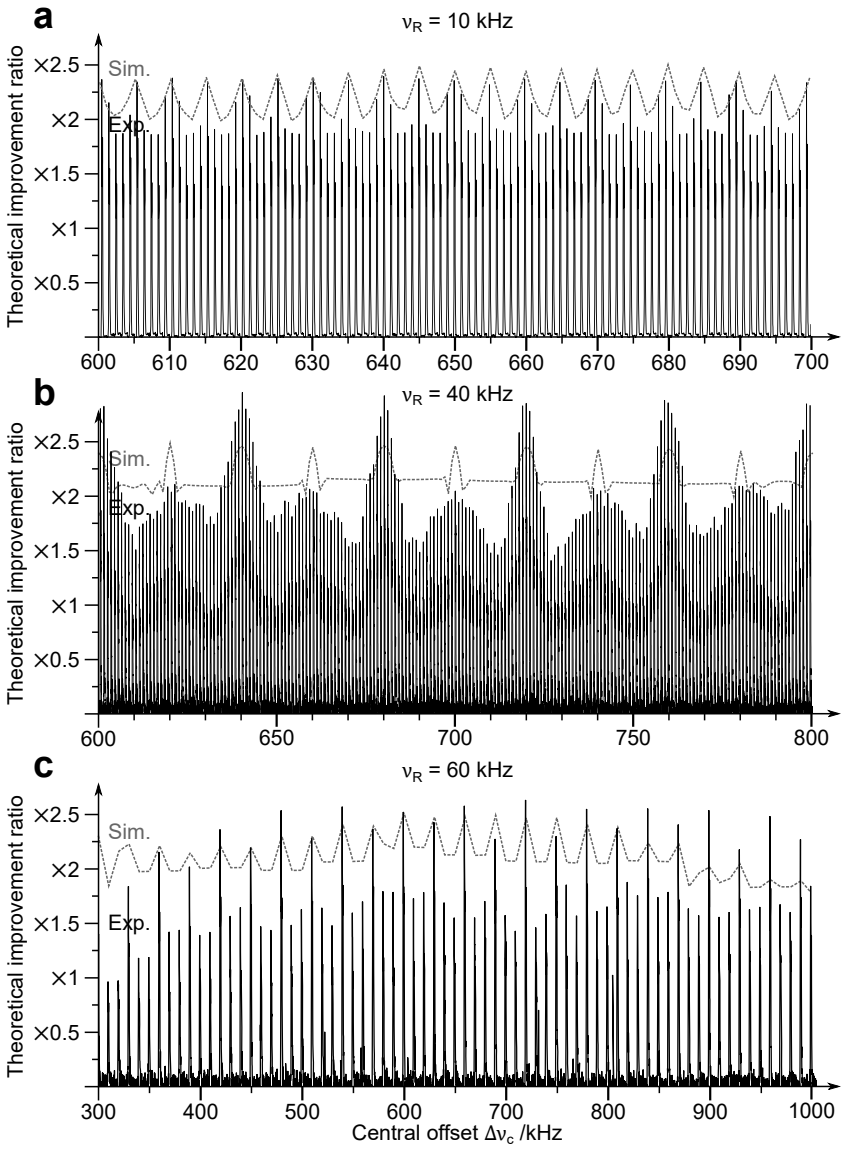

Figure 7.9: *Simulated signal improvement obtained using a HS pulse as a PAAP as a function of the offset in simulation (grey line) and in experiment (black lines) for ^{87}Rb in $RbClO_4$ for B_0 = 14.1 T (ν_0 = 196.4 MHz) for **(a,c)** and B_0 = 9.4 T (ν_0 = 130.9 MHz) for **(b)**, with HS being applied for ν_1 = 22 kHz and **(a)**: ν_R = 10 kHz, **(b)**: ν_R = 40 kHz and **(c)**: ν_R = 60 kHz. Both experiments and simulations have been performed by increments of **(a)**: 1 kHz = $\tau_R/10$, **(b)**: 1 kHz = $\tau_R/40$ and **(c)**: 10 kHz = $\tau_R/6$. Spectra recorded by Dr. Nasima Kanwal. See the extended caption in Appendix C.3 for further details.*

slow MAS for both plots, it can be observed that the improvement increases between ν_R = 0 and ν_R = 10 kHz. This is particularly visible for $Al(acac)_3$ in Figure 7.10a, where the improvement rises from ×2 to ×3 in this region. It has been discussed in Section 7.1.2 that inversion of the ST populations requires a sweep across the entire width of the STs in the slow MAS rate regime (or in the static case), but under standard or fast MAS, the sweep only needs to cover an inversion bandwidth equal to the MAS rate. The signal improvement rise between ν_R = 0 to 10 kHz corresponds to the transition between the two regimes. For higher MAS rates than ν_R = 10 kHz, the improvement is steady overall, with approximately ×2 for $RbClO_4$ and ×3 for $Al(acac)_3$. Some sudden rises of the theoretical improvement ratio is clearly visible for specific MAS rates in Figure 7.10a. As the offset has been kept constant for all the data points in Figure 7.10a while the spinning sideband manifold changes, the sweep is applied randomly at cases corresponding to 1, 2 or 3 described in Figure 7.7. As discussed previously, the improvement is a maximum for either case 1 or 3. As a result, higher improvement ratios compared to that reported in Figure 7.10a are possible by re-optimising the offset $\Delta\nu_c$ in simulation for all MAS rates.

A range of HS pulses with different offset have been simulated, and that giving the highest improvement was plotted in Figure 7.10b. In Figure 7.10b, most of the sudden rises of efficiency disappear for $RbClO_4$, and the ”average” improvement ratio increases from ×2 to ×2.5 compared to Figure 7.10a. On the contrary, the number of peaks in the improvement ratio increases for $Al(acac)_3$, as the sampling in $\Delta\nu_c$ is relatively better for $RbClO_4$ than for $Al(acac)_3$, for which it remains too large. Nevertheless, the improvement rises from ×3 to ×4 for most MAS rates, and it can clearly be foreseen that reducing the increment in $\Delta\nu_c$ in Figure 7.10b would result in more constant improvement ratios for all the MAS rates. However, this is difficult on a standard computer, owing to the simulation time that would be required.

In conclusion, it can be deduced from the investigations conducted that the improvement able to be obtained by HS pulses is, essentially, not affected by the MAS rate. Some differences were highlighted between spin $I = 3/2$ and $I = 5/2$, due to the coexistence of ST_1 and ST_2 at same frequencies. Following the approach discussed in Section 6.2.1 for FAM-N optimised for $p = \pm5 \rightarrow \pm1$ transition, further improvement for spin $I = 5/2$ nuclei is possible by performing the adiabatic inversion using a succession of two HS pulses, one applied to the outer ST_2, followed by another applied to the inner ST_1. However, this would require the optimisation of two offsets $\Delta\nu_c$, hence significantly complicating the optimisation procedure either in simulation or in

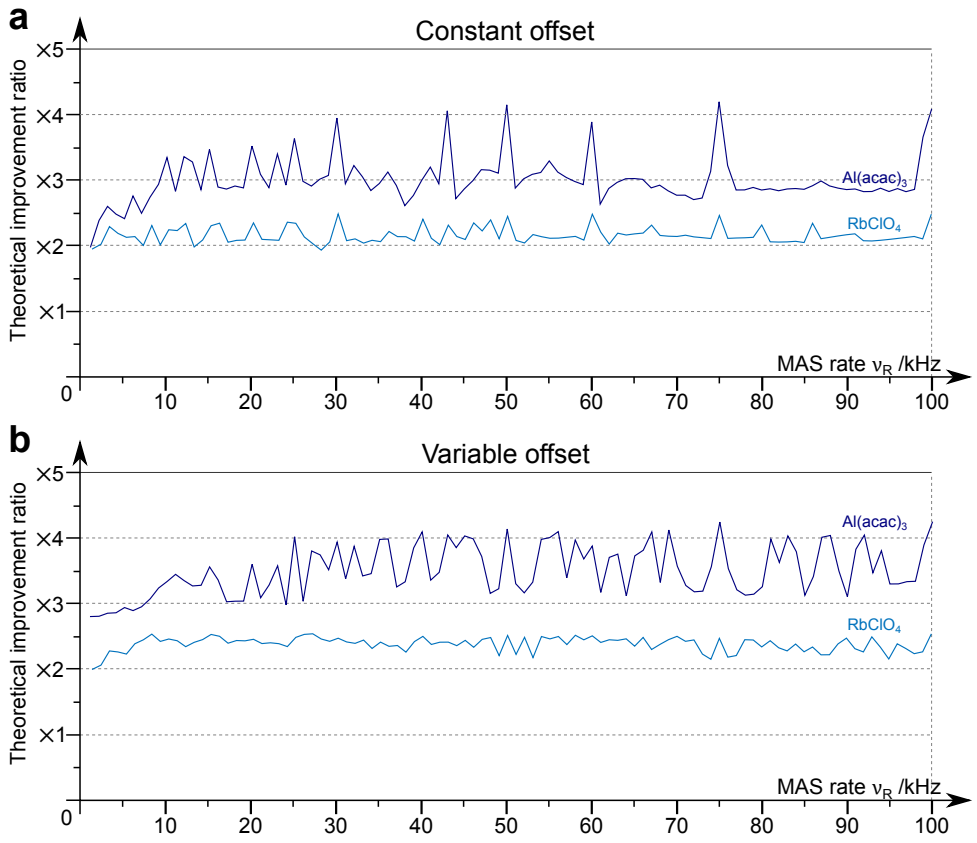

Figure 7.10: *Simulations of the impact of the MAS on the CT signal improvement given by HS pulses used as PAAPs for ^{87}Rb ($I = 3/2$) in $RbClO_4$ (light blue lines) and for ^{27}Al ($I = 5/2$) in $Al(acac)_3$ (dark blue line) using the quadrupolar parameters of both these compounds reported in Appendix C.2.* ***(a)****: HS applied with constant offsets of $\Delta\nu_c$ = ±600 kHz for ^{87}Rb and $\Delta\nu_c$ = ±300 kHz for ^{27}Al.* ***(b)****: HS applied with "variable" offsets: HS simulations have been performed for a range of offsets for the two nuclei, and the improvement plotted on the figure corresponds to the HS pulse that gives the highest improvement. $\Delta\nu_c$ have been varied from ±500 kHz to ±900 kHz by increments of 25 kHz for ^{87}Rb, and from ±100 kHz to ±500 kHz by increments of 25 kHz for ^{27}Al. The simulations were performed for 168 crystallite orientations and 10 γ-angles and for B_0 = 14.1 T (ν_0 = 196.4 MHz for ^{87}Rb and ν_0 = 156.4 MHz for ^{27}Al), and ν_1 = 22 kHz for HS.*

experiment. Moreover, the simulations presented in Figures 7.9 and 7.10 show that, even though large improvement ratios were observed over a large range of $\Delta\nu_c$ in Figure 7.8, the improvement is very sensitive to the central offset $\Delta\nu_c$, with significant changes in signal improvements being observed for very small offset variations, leading to time-consuming optimisation processes being necessary either in simulations or in experiments to obtain the maximum signal improvement. As discussed previously about Figure 7.8, the improvement ratio plotted as a function of the offset roughly resembles the static lineshape, so the offset for maximum improvement stays in a same range of $\Delta\nu_c$ for all MAS rates. Nonetheless, a precise offset recalibration must be performed for each MAS rate to reach the maximum signal improvement available.

7.2.2 Comparing the efficiencies of different PAAPs

This section investigates the experimental efficiencies of the different methods reported in Section 7.1, with ν_R = 10, 20, 40 and 60 kHz. As instructed in Section 7.1.2, there are alternative formulations for RAPT and DFS pulses than those reported in this section. For DFS, the formulation termed ssDFS has been shown to result in improvements similar to HS.[315] Likewise, literature studies showed that RAPT can be more efficient if a frequency sweep is introduced.[389] In this work, only the RAPT pulse with no frequency sweep and the ”standard” DFS pulse were considered, in order to gain insight in the efficiency for methods executing different sorts of sweeps. The experimental spectra for ν_R = 10 and 60 kHz are shown in Figure 7.11, and the measured improvements for all spinning speeds are given in Table 7.1. The ^{87}Rb spectra on $RbNO_3$ were recorded for insight into the signal improvement given by HS for sample containing multiple different species.

From all spectra shown in Figure 7.11, HS appears to be the most efficient of CT enhancement method on both samples and for all MAS rates, with an average experimental improvements of approximately ×2.5 for $RbClO_4$, and ×3 for $Al(acac)_3$. As predicted in the simulations in Section 7.2.1, the spectra recorded for $RbClO_4$ clearly show enhancements near the theoretical adiabatic inversion (Equation (7.1.4)), while the improvement for $Al(acac)_3$ is closer to a saturation (Equation (7.1.6)). The second most efficient method is DFS, followed by RAPT. This shows a clear hierarchy in the efficiency of the different approaches, with, in order, HS (double frequency sweep + shaped pulse), DFS (double frequency sweep + non-shaped pulses), and RAPT (single frequency sweep), despite requiring similar optimisation time and effort.

Inconsistencies in the efficiencies of the different methods for different MAS are visible in Table 7.1. As for the investigation conducted on FAM-N pulses in Section 5.3, it remains unclear whether the observed differences in efficiency for the different methods are due to a fundamental difference in the efficiency of the methods, or are due to of optimisation difficulties or imprecision, complex features in the probe design, errors in the estimation of the signal improvement or the stability with time of the calibrated experimental conditions. A reasonable amount of time has been dedicated to experimentally optimise each of the methods, therefore the observed efficiencies can be assumed to be approximately those obtained by a typical spectroscopist optimising the method. However, Table 7.1 shows that, as predicted in Section 7.2.1, HS and the other pulses are applicable at any MAS rates, with consistent improvement ratios found for different

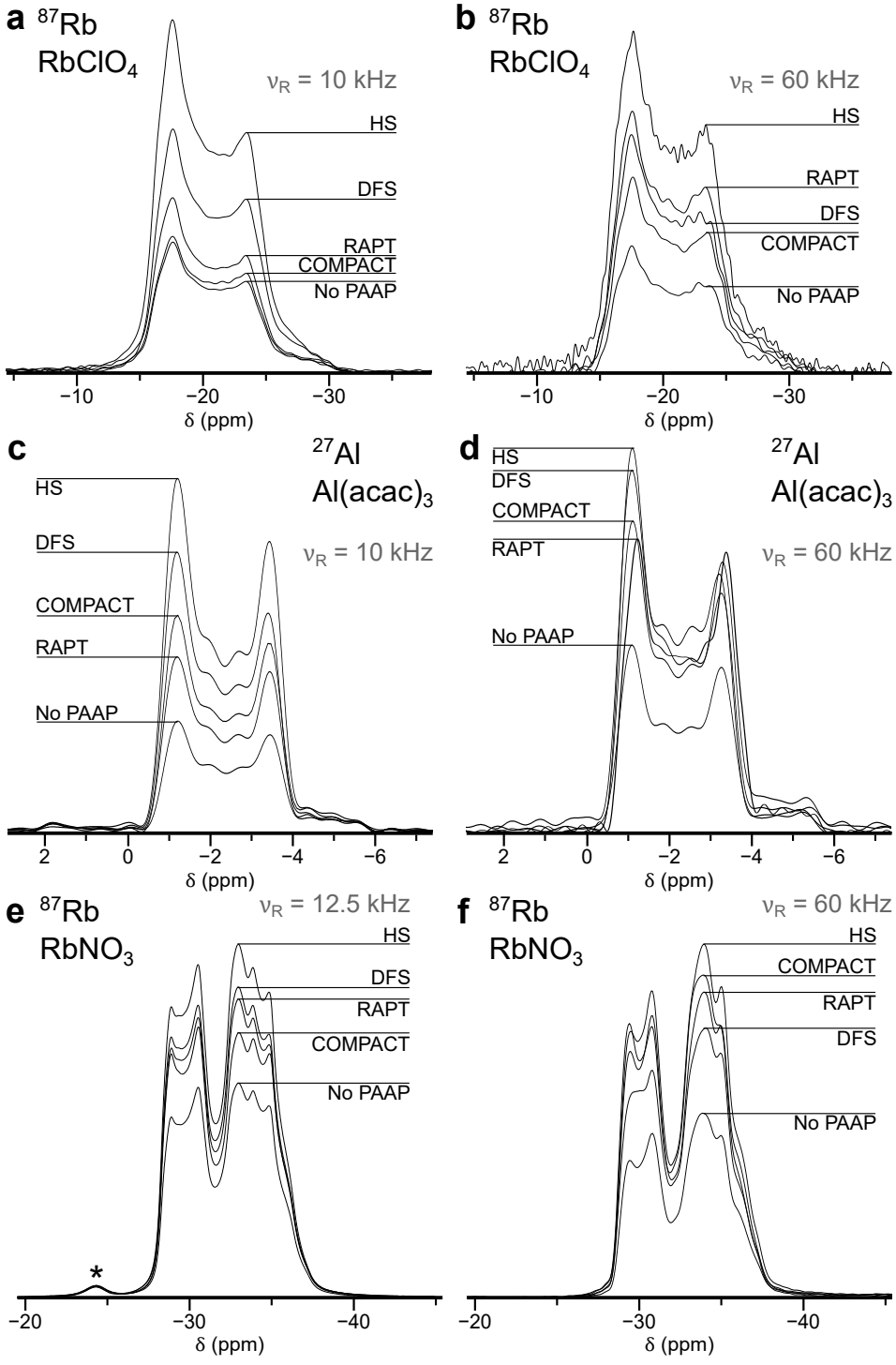

Figure 7.11: *MAS spectra acquired at B_0 = 14.1 T (ν_0 = 196.4 MHz for ^{87}Rb and ν_0 = 156.4 MHz for ^{27}Al), with no PAAP, COMPACT, and with RAPT, DFS, and HS. All PAAPs were applied for ν_1 = 22 kHz, and COMPACT was applied at the maximum RF field strength available.* ***(a,b)****: ^{87}Rb spectra of $RbClO_4$ recorded at ν_R = 10 and 60 kHz, respectively.* ***(c,d)****: ^{27}Al spectra of $Al(acac)_3$ recorded at ν_R = 20 and 60 kHz, respectively.* ***(e,f)****: ^{87}Rb spectra of $RbNO_3$ recorded at ν_R = 12.5 and 60 kHz, respectively. See the extended caption of Table 7.1 for further details about the spectra shown in this figure. $RbClO_4$ and $Al(acac)_3$ spectra recorded by Dr. Nasima Kanwal.*

Sample	ν_R /kHz	COMPACT	RAPT	DFS	HS	Sim. HS
$RbClO_4$	10	×1.1	×1.4	×1.9	×2.6	×2.4
	20	×1.3	×1.3	×1.9	×2.7	×2.5
	40	×1.1	×1.6	×2.0	×2.8	×2.4
	60	×1.5	×2.0	×1.8	×2.6	×2.5
$Al(acac)_3$	10	×1.7	×1.8	×2.4	×2.5	×3.2
	20	×2.0	×1.6	×2.6	×3.2	×3.9
	40	×1.7	×1.6	×2.3	×2.5	×3.1
	60	×1.7	×1.6	×1.9	×2.1	×2.9
$RbNO_3$	12.5	×1.3	×1.3	×1.4	×1.6	N/A
	60	×1.7	×1.6	×1.4	×1.9	N/A

Table 7.1: *Improvement ratios of the CT signal measured for the MAS spectra in Figure 7.11, reported relative to the intensity of the MAS spectrum recorded with no PAAP. The improvement ratios were measured from the left horn of the signal for $RbClO_4$ at −17 ppm, and from the right horn of the signal for $Al(acac)_3$ at −3.6 ppm. See the extended caption in Appendix C.3 for further details.*

MAS rates.

In general, Figure 7.11 shows that COMPACT pulses, except for some cases ($Al(acac)_3$ for ν_R = 20 kHz, and ^{87}Rb for ν_R = 60 kHz), give the lowest improvement ratios, compensated by their ease of optimising. The limit of the comparison of COMPACT to PAAPs comes from the RF field strength ν_1. As seen in Section 7.1.1, the efficiency of PAAPs is, neglecting relaxation processes, not affected by the RF field strength or the pulse duration as long as the adiabaticity condition is fulfilled, and thus PAAPs are in practice applied for long durations at moderate RF field strengths. On the other hand, COMPACT benefits from being applied with strong RF. For consistency with what an average user would do in practice, the improvements reported for COMPACT in Table 7.1 are the maximum RF field strengths available on the hardware used for the acquisition. The improvement ratios observed for COMPACT applied at ν_1 = 22 kHz, *e.g.*, the RF strength used for all the PAAPs, is given in the extended caption of Table 7.1. Unlike other methods, the improvements reported in Table 7.1 would not be transferable to low-γ nuclei, on which COMPACT would show decreased signal improvements, while PAAPs should remain essentially unaffected, assuming that the adiabatic condition remains fulfilled. Improvements observed for COMPACT applied at the same power as the PAAPs in Table 7.1 oscillate between ×1.0 and ×1.2 (see the extended caption of Table 7.1).

Some level of distortion in the lineshape of the MAS spectra recorded with PAAP were

		MAS rate ν_R /kHz			
		10	20	40	60
$RbClO_4$	No PAAP	0.3%	0.2%	0.1%	0.2%
	COMPACT	11%	7.7%	11%	6.6%
	HS	20%	19%	25%	21%
$Al(acac)_3$	No PAAP	1.3%	0.6%	<0.1%	0.6%
	COMPACT	4.7%	7.4%	6.8%	6.5%
	HS	30%	18%	19%	21%

Table 7.2: *Amount of distortion in amplitude obtained with ODD (see Appendix H) of the lineshapes for the spectra the $RbClO_4$ and $Al(acac)_3$ spectra shown in Figure 7.11 and Table 7.1. All simulations have been performed for 80 α-angles and 40 β-angles.*

reported in the litterature.[396, 415] In the spectra reported in Figure 7.11, only a few noticeable lineshape distortions can be observed using COMPACT or any of the PAAP on any of the spectra of Figure 7.11. This means that, the STs are affected in an almost identical manner for each crystallite orientations for all of the presented methods, resulting in signal improvements being almost identical for all crystallite orientations, and thus no lineshape distortions arise from the use of any of the methods. This is an important property, as lineshape decomposition is often performed on MAS spectra of quadrupolar nuclei. The near absence of noticeable distortion improves the precision of the parameters extracted from lineshape fitting. However, some tiny lineshape changes can be observed, particularly for the $RbNO_3$ spectra Figures 7.11e and 7.11f as it is composed of several similar but different sites.

For a more in-depth analysis of the lineshape distortions created by PAAPs, the ODD script introduced earlier and presented in Appendix H. Table 7.2 shows the amount of distortion in amplitude[10] obtained with the ODD script for simulated spectra of $RbClO_4$ and $Al(acac)_3$, simulated with no PAAP, COMPACT and HS, using the experimental parameters from the spectra of Table 7.1 and Figure 7.11. Being based on the same phenomenon, the amount of distortion given by the HS pulses should also give an indication of the amount of distortion that would be obtained using other PAAPs. However, the distortion for COMPACT must be calculated separately.

Small variations between the values for the level of distortion obtained for different pulses at the different spinning speeds can be observed in Table 7.2, that can reasonably be assumed not to be related to the MAS rate, but to $\Delta\nu_c$, which is slightly

[10] Distortions in phase proved to never exceed 1° for all the cases presented in Table 7.2, and thus have not been reported.

different in each acquired experiment. Overall, distortion levels are similar for the same method applied at different spinning speeds. Spectra recorded with no PAAP exhibit extremely low levels of distortion for both samples. This indicates that spectra reported in Figure 7.11 recorded with no PAAP contain lineshapes that are very similar to the ideal lineshapes. With COMPACT, these distortions increase to between 6% for 11% for $RbClO_4$, and between 5% and 7% for $Al(acac)_3$. Distortions are also slightly lower than for ^{27}Al than for ^{87}Rb. These values are higher than the distortions found for the spectra acquired with no PAAP, but this level is still very small. With HS, distortions rise to between 19% and 25% for $RbClO_4$ and 18% to 30% for $Al(acac)_3$. These distortions are visible on the experimental spectra in Figure 7.11, particularly when comparing the relative intensities of the two horns, or the intensity of the dip between the horns. However, despite being higher than the two other methods, the distortions are reasonable and almost not observable in the experimental spectra.

7.2.3 Implementing HS pulses in RIACT experiments

The RIACT experiment presented in Section 4.2.1 was initially reported as a method to obtain more quantitative MQMAS spectra for spins $I = 3/2$ nuclei,[22] but it can be also used as a signal improvement method when combined with a PAAP.[275, 298–300, 382, 389, 404] As briefly discussed in Section 4.2.1, PAAPs cannot be employed to enhance the efficiency of MQMAS experiment with a hard CW pulse used for excitation, as these pulses are used to promote 3Q coherence from the populations of the 3Q (or MQ) energy levels. Conversely, RIACT creates 3Q coherence from initial CT 1Q coherence. Subsequently, RIACT would benefit from a higher initial difference in the population of the CT energy levels, therefore PAAP can be employed. This offers signal improvement at a limited experimental cost, as the experimental optimisation of a PAAP, or of the CT-selective 90° or 180° pulse, does not require MQF. Furthermore, the two excitation and conversion SL pulses have a fixed duration of a quarter of a rotor period as instructed in Section 4.2.1 and in the literature.[22] A possible extension would be to implement FAM-N as the conversion pulse in a (PAAP +) RIACT-I experiment.

^{87}Rb 3QF-MAS spectra of $RbNO_3$ were recorded using different combinations of excitation and conversion approaches, *i.e.*, CW, SL excitation and conversion, and FAM-N conversion, with and without PAAP, which are shown in Figures 7.12a, 7.12b and 7.12c. The signal improvement ratios observed for each of the approaches are reported in Table 7.3. FAM-N conversion results in a signal improvement of ×1.7 in a Table 7.3,

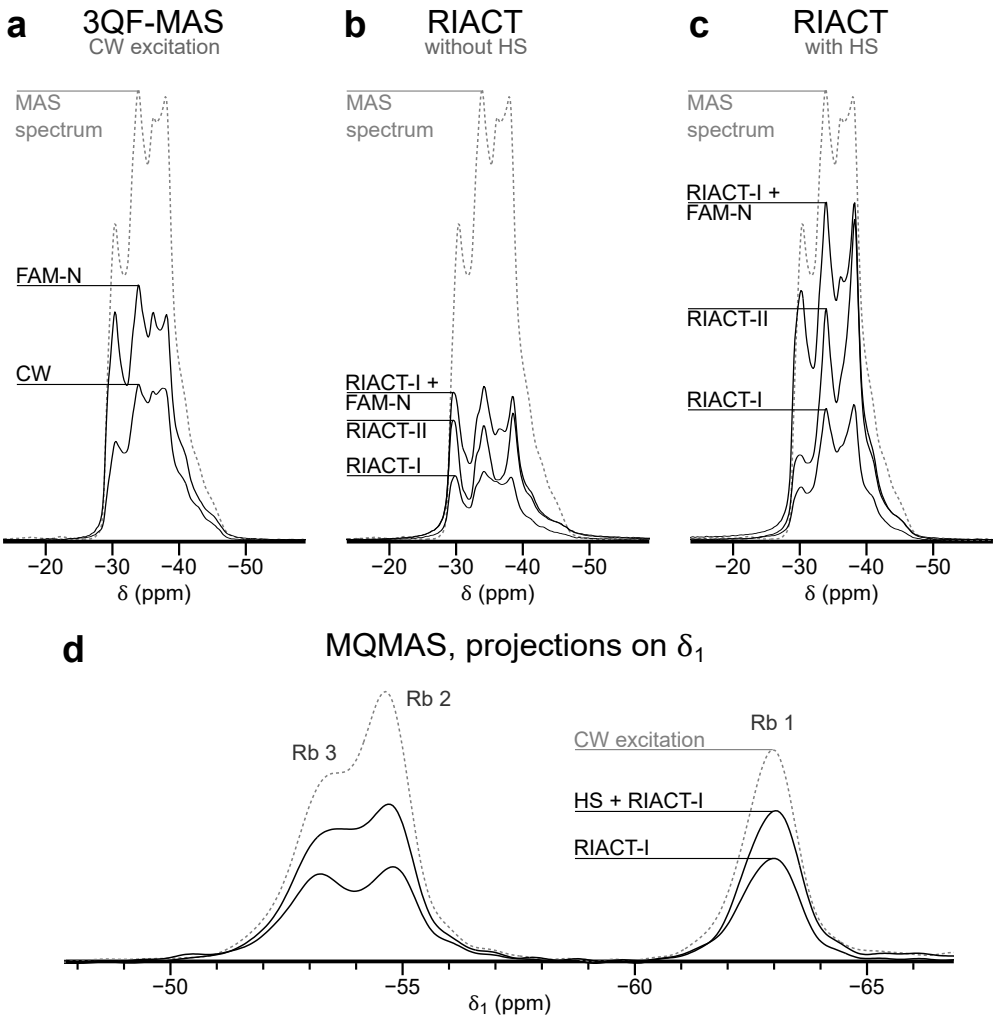

Figure 7.12: *^{87}Rb spectra of $RbNO_3$ recorded at B_0 = 9.4 T (ν_0 = 130.9 MHz), with ν_1 = 107 kHz and ν_R = 12.5 kHz.* ***(a,b,c)****: 3QF-MAS spectra recorded with different 3Q excitation and conversion schemes. All spectra are plotted on the same intensity scale to allow comparisons of the signal intensity. The dashed grey line corresponds to the experimental MAS spectrum, plotted to compare lineshape distortions.* ***(a)****: Short pulse CW 3Q excitation.* ***(b,c)****: SL 3Q excitation, with CW (RIACT-I), SL (RIACT-II) and FAM-N 3Q conversion, and* ***(b)****: without HS and* ***(c)****: with HS as a PAAP.* ***(d)****: Comparison of the projections onto the indirect dimension of split-t_1 shifted-echo MQMAS spectra recorded using the RIACT-I, HS + RIACT-I techniques and FAM-N (dashed grey line). This latter spectrum only serves the purpose of comparing the relative intensity of the three sites and is not scaled in intensity. See the extended caption in Appendix C.3 for further details.*

PAAP	3Q excitation method	3Q conversion method	Improvement ratio
N/A	CW	FAM-N	×1.7
No	SL	CW	×0.5
	SL	SL	×0.8
	SL	FAM-N	×1.7
HS	SL	CW	×0.7
	SL	SL	×1.4
	SL	FAM-N	×2.1

Table 7.3: *Table reporting the sensitivity improvements of spectra shown in Figure 7.12, measured from the integrated intensity of each spectrum.*

and the use of HS results in ×2.1 in a MAS spectrum. Similar improvements can be observed in Table 7.3 for the MQMAS spectra where CW is substituted by FAM-N, or for the RIACT spectra where HS is added as a PAAP. Variations can be attributed to small changes in the baseline or in the phasing. It can be observed in Table 7.3b that the use of RIACT instead of two CW pulses for 3Q excitation and conversion results in a loss of signal, more pronounced when compared to CW excitation and FAM-N conversion. However, when HS is introduced in Table 7.3, only RIACT-I results in less signal than the two pulse experiment, and RIACT-II gives an improvement approaching that of CW + FAM-N. Furthermore, the use of FAM-N instead of CW for the conversion pulse results in a further signal improvement compared to the SL conversion, with no significant lineshape distortions being visible in Figure 7.12c compared to the MAS spectrum. This proved, for a model sample, that PAAP + RIACT-I + FAM-N MQMAS is a valid combination for the improvement of MQMAS. Figure 7.12d illustrates one of the advantages of RIACT-I over CW excitation discussed in Section 4.2.1, is that it offers increased quantitativity for the MQMAS spectra in the indirect dimension compared to MQMAS spectra recorded with CW excitation. In spite of the presence of sites with similar quadrupolar parameters, MQMAS spectra exhibits peaks with different intensities in the indirect dimension in this latter spectrum, whereas the RIACT spectra shows very similar intensities for all three sites.

Among the potentially interesting applications of RIACT is the possibility of sensitivity improvement for 5QMAS in spin $I = 5/2$ nuclei.[420] In Section 4.2.1, it has been shown that the amount of CT 1Q coherence and the highest possible coherence for a given spin system are adiabatically transferred during the sample rotation, if the adiabaticity con-

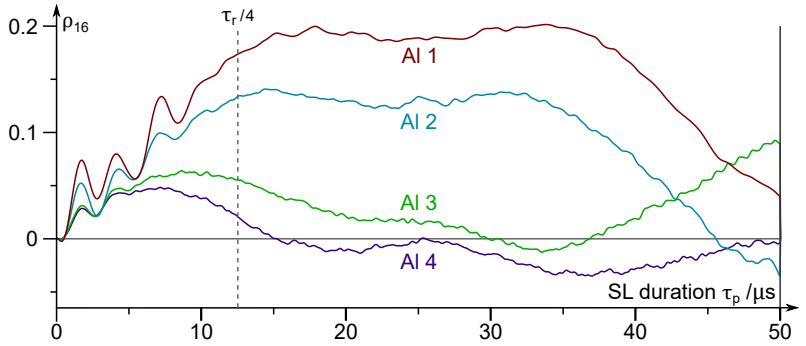

Figure 7.13: *Evolution of the amounts of 5Q coherences | real part of ρ_{16} during SL on ^{27}Al ($I = 5/2$), for B_0 = 14.1 T (ν_0 = 156.4 MHz), ν_1 = 133 kHz and ν_R = 20 kHz, using the quadrupolar parameters of the four sites of kyanite. Simulation from initial $\hat{I}_z$ after a 90° pulse of duration 4.5 µs applied at ν_1 = 22 kHz. The SL curves are plotted for site 1 (red line), site 2 (cyan line), site 3 (green line) and site 4 (purple line), whose quadrupolar parameters are reported in Appendix C.2. The vertical dashed line shows $\tau_c = \tau_R/4$ = 12.5 µs, which corresponds to the point where the SL has been stopped in the experiments (no shown here) and in Table 7.3. The amounts of 5Q coherence at this contact time are given in Table 7.4.*

dition is fulfilled (see Equation (3.2.8)). In Section 6.2.1, it has been shown that FAM-N can be used to enhance the efficiency of the 5Q to 1Q conversion. However, in this last section, the sensitivity problems and the dependence of the efficiency of the CW excitation pulse on the quadrupolar parameters were brought to light through ^{27}Al experiments of kyanite. Here, the efficiency of RIACT in performing the same experiment is investigated.

Experimentally recording a PAAP-RIACT-I-FAM-N MQMAS or a PAAP-RIACT-II MQMAS spectrum in a reasonable time proved to be impossible at B_0 = 14.1 T, with only two of the four sites seen above out of the noise after 16 h of acquisition. SL simulations for the 1Q to 5Q excitation after a CT-selective 90° pulse were performed using the quadrupolar parameters of the four ^{27}Al sites with ν_R = 20 kHz, as shown in Figure 7.13 for a maximum contact time of 50 ms (one rotor period). As discussed in Section 4.2.1, RIACT exhibits good efficiency when the SL is stopped for $\tau_p = \tau_R/4$. Table 7.4 reports the amount of 5Q coherence as a function of the SL duration, and shows values which are comparable to those reported in Table 6.4. The amount of 5Q coherence in Table 7.4 shows that the SL efficiency greatly depends on the quadrupolar parameters, with the amount of 5Q coherence created dramatically decreasing as C_Q increases. Moreover, the ridges for Al 3 and Al 4 are broader on the MQMAS spectrum, which results these resonances not being observable at all.

To conclude, the use of FAM-N combined with a PAAP + SL excitation/RIACT-I has been shown for $RbNO_3$ as a potentially attractive method for obtaining further signal

Site	Amounts of 5Q coherence
Al 1	0.172
Al 2	0.132
Al 3	0.055
Al 4	0.021

Table 7.4: *Amount of 5Q coherence | real part of ρ_{16} measured from Figure 7.13 for a contact time $\tau_c = \tau_R/4$ (vertical dashed line in Figure 7.13).*

improvement for 3QMAS than CW + FAM-N on spins $I = 3/2$ nuclei. More in-depth investigations would be required to confirm this for the general case. RIACT for 5QMAS on spin $I = 5/2$ nuclei suffers from the same problem as the standard method, *i.e.*, that the SL excitation efficiency depends significantly on quadrupolar parameters, so approaches to solve this problem should be considered. In particular, it has been shown that FAM-N can be adapted for the conversion 1Q to MQ,[11,12] which has been shown by theoretical and experimental investigations to result in a more efficient transfer. Nevertheless, it should be recalled that no experimental optimisation with MQF for RIACT, as the CT-selective 90° pulse and the PAAP can be obtained from direct acquisition experiments. In addition to the signal improvement, the quantitative nature of 5QMAS spectra, and the lineshape changes in the direct dimension of the spectrum needs to be investigated. The efficiency of the SL on the quadrupolar nucleus must also be considered in order to predict the maximum enhancement available.

[11] See the parameter `cmpt.exc_conv` in Appendix I.2

[12] Modulated pulses cannot be used to improve the population to MQ transfer, as discussed in Section 4.3 for the inverse transfer.

Chapter 8

CP from I = 1/2 to S > 1/2 nuclei

Introduction

CP between spins $I = 1/2$ and $S > 1/2$ nuclei is a useful technique for spectral editing as many materials have pairs of spins I and S in close proximity, for which dipolar interaction takes place. One of the earliest examples of the successful application of CP to quadrupolar nuclei can be attributed to Amoureux *et al.*, who showed that CP from ^{1}H or ^{19}F to ^{27}Al can be successfully employed to edit the intensities of the ^{27}Al resonances of a fluorinated aluminophosphate compound with respect to their spatial proximity to ^{1}H or ^{19}F.[421] Such a CP experiment is carried out with the same pulse sequence as for spin $I = S = 1/2$ nuclei, presented in Section 3.1.3, Figure 3.4, but the additional energy levels of the spin S, as well as the presence of the quadrupolar interaction which affects the effective nutation rates of all transitions (see Section 3.2.2), dramatically complicate the theoretical description of the experiment. As a result, there remains a lack of understanding regarding the mechanism by which CP takes place between spins $I = 1/2$ and $S > 3/2$ nuclei, and the optimum conditions for these experiments.

Unlike CP between spins $I = S = 1/2$ nuclei, CP to $S > 1/2$ is in practice rarely used for the enhancement of the NMR signal of the S spin, as it is often not observed.[422–424] Nonetheless, it remains a powerful method to investigate spatial proximities between two nuclei, hence giving structural information. The large number of literature studies in which CP has been used to investigate proximities with quadrupolar nuclei such

as ^{11}B,[425, 426] ^{23}Na,[427–432] ^{27}Al,[30, 209, 367, 427, 430, 433–442] ^{17}O,[443–445], ^{43}Ca,[446] or ^{95}Mo,[447], shows how useful this experiment is in practice. The combination of CP with the MQMAS experiment has also been used to resolve the quadrupolar lineshapes of the spin S, but in spite of numerous successful applications[367, 442, 448–451], the range of application is very limited due to considerable sensitivity limitations.

To understand the changes of the Hartmann-Hahn matching conditions when a quadrupolar nucleus is involved in CP, and to predict the efficiency of the CP transfer, is crucial for the acquisition of NMR experiments with a reasonable sensitivity. Theoretical models to understand the CP dynamics for acquisition nucleus were reported in the literature,[180, 181, 448, 452] but most theoretical approaches limit the range of investigation to static CP, owing to the additional difficulties of including MAS in a theoretical description. After reviewing the main points of theory of CP for static samples in Section 8.1, CP simulations for both the static case and under MAS will be presented, compared and discussed in Section 8.2.

8.1 The theory of CP for quadrupolar nuclei

This section introduces essential theoretical elements for the CP transfer to a quadrupolar nucleus as presented previously by Ashbrook and Wimperis.[452] As described in Section 3.2.2, the quadrupolar interaction affects the nutation rates of the CT and 3Q transitions, giving rise to the necessary distinction between the ”inherent” RF field strength, $\nu_{1_{\text{inh}}}$, and the ”effective” RF field strengths, $\nu_{1_{\text{eff}}}$. When a quadrupolar nucleus is involved in a CP transfer, the Harmtmann-Hahn condition consists in matching the RF field strength of I to the effective RF field strength of S. However, the nutation rate of the 3Q transition depends on Ω_Q (see Equation (2.3.21)), and therefore on the strength of the quadrupolar interaction and on the orientation between Σ_{lab} and the PAF of the quadrupolar interaction. Moreover, it initially would appear that CP transfer can be performed between the unique transition of the spin I nucleus to any of the $2S(S + 1/2)$ transitions of the spin S, illustrating the complexity of the problem.

8.1.1 Hartmann-Hahn conditions for quadrupolar nuclei

To establish the Hartmann-Hahn matching condition for CP to a quadrupolar nucleus, it is first necessary to establish the effect of quadrupolar interaction on the nutation frequencies for all of the transitions of the quadrupolar nucleus. Following the same approach as in Section 3.1.3, the Hamiltonian is expressed in a double rotating frame $\Sigma_{\text{rot}}^{(\times 2)}$, in which the time-dependence of the Hamiltonian during the application of two simultaneous RF pulses on both spins I and S is removed. The total Hamiltonian $\hat{H}$ expressed in $\Sigma_{\text{rot}}^{(\times 2)}$ is given by

$$\hat{H}_{\rho\times 2} = \hat{H}_I + \hat{H}_S \quad , \tag{8.1.1}$$

where

$$\hat{H}_I = \omega_{1_I} \hat{I}_x \tag{8.1.2a}$$

$$\hat{H}_S = \omega_{1_S} \hat{S}_x + \hbar\Omega_Q \left(\frac{\hat{S}_z^2}{\hbar^2} - \frac{S(S+1)}{3} \hat{1}_N \right) \quad , \tag{8.1.2b}$$

where ω_{1_S} refers to the inherent RF field strength applied on S. The second-order quadrupolar interaction is omitted from the theoretical developments presented in this section. The effective nutation rates for the spin S can be obtained by diagonalisation of the Hamiltonian describing this spin. The matrix that diagonalises $\hat{H}_S$ is denoted $\hat{V}$, which gives

$$\hat{H}_S^D = V.\hat{H}_S.V^{-1} \quad . \tag{8.1.3}$$

The diagonalised Hamiltonian is termed $\hat{H}_S^D$, and the frame in which $\hat{H}_S$ is diagonal is denoted Σ_V. The diagonalisation matrix for a $S = 3/2$ nucleus has been given analytically in the literature, and is [29, 453, 454]

$$V = \frac{1}{\sqrt{2}} \begin{bmatrix} -\sin\alpha_1 & +\cos\alpha_1 & -\cos\alpha_1 & +\sin\alpha_1 \\ -\sin\alpha_2 & +\cos\alpha_2 & +\cos\alpha_2 & -\sin\alpha_2 \\ -\cos\alpha_1 & -\sin\alpha_1 & +\sin\alpha_1 & +\cos\alpha_1 \\ +\cos\alpha_2 & +\sin\alpha_2 & +\sin\alpha_2 & +\cos\alpha_2 \end{bmatrix} \quad , \tag{8.1.4}$$

where α_1 and α_2 are two angles given by

$$\alpha_1 = \frac{1}{2}\tan^{-1}\frac{\sqrt{3}\omega_{1_S}}{2\Omega_Q + \omega_{1_S}} \tag{8.1.5a}$$

$$\alpha_2 = \frac{1}{2}\tan^{-1}\frac{\sqrt{3}\omega_{1_S}}{2\Omega_Q - \omega_{1_S}} \quad . \tag{8.1.5b}$$

The spin S nutation rates for any given transition between the two energy levels r and s can be obtained from the r, r and s, s diagonal elements of $\hat{H}_S^D$, which are[1]

$$\hbar\omega_{r,s} = \left(\hat{H}_S^D\right)_{s,s} - \left(\hat{H}_S^D\right)_{r,r} \quad . \tag{8.1.6}$$

As discussed in Section 3.1.3, CP is enabled only when a dipolar interaction is present between I and S. In the latter case, the dipolar interaction Hamiltonian must be added to the expression of $\hat{H}_{\rho\times 2}$ to enable magnetisation exchange. $\hat{H}_{\rho\times 2}$ then becomes

$$\hat{H}_{\rho\times 2} = \hat{H}_I + \hat{H}_S + \hat{H}_{D_{IS}} \quad , \tag{8.1.7}$$

where $\hat{H}_{D_{IS}}$ is the heteronuclear dipolar interaction Hamiltonian, expressed in the PAF (see Equation (2.2.21)). This Hamiltonian is expressed in $\hat{H}_{\rho\times 2}$ as

$$\hat{H}_{D_{IS}} = 2\frac{d_{IS}}{\hbar}\hat{I}_z\hat{S}_z \quad , \tag{8.1.8}$$

which becomes in Σ_V

$$\hat{H}_{IS}^D = -2\frac{d_{IS}}{\hbar}\hat{I}_x V \hat{S}_z V^{-1} \quad . \tag{8.1.9}$$

$\hat{H}_{IS}^D$ can be conveniently expressed in terms of the fictitious $S = 1/2$ operators introduced in Section 3.2.2 for the description of MQF. For example, this gives the expression of $\hat{H}^D$ for $S = 3/2$ as [93, 182, 183]

$$\hat{H}_{IS}^D = -\frac{d_{IS}}{\hbar}\hat{I}_x\left(C_{1,2}\hat{S}_x^{1,2} + \hat{C}_{2,3}\hat{S}_x^{2,3} + C_{3,4}S_x^{3,4} + C_{1,4}\hat{S}_x^{1,4}\right) \quad , \tag{8.1.10}$$

where the coefficients $C_{r,s}$, termed the dipolar coefficients, are given by

$$C_{r,s} = \sum_{k=1}^{k=2S+1} V_{r,k}V_{s,k}(\sigma_z)_{k,k} \quad , \tag{8.1.11}$$

$(\sigma_z)_{k,k}$ being the k, k element of the Pauli's spin matrix σ_z. Equation (8.1.10) can be used to express the effective nutation rates in Equation (8.1.6) for any transition between

[1] V as expressed in Equation (8.1.4) guarantees that the eigenvalues of $\hat{H}_S^D$ are sorted by increasing energy, thus the nutation rates given in Equation (8.1.6) are positive if $\omega_{1_S} > 0$.

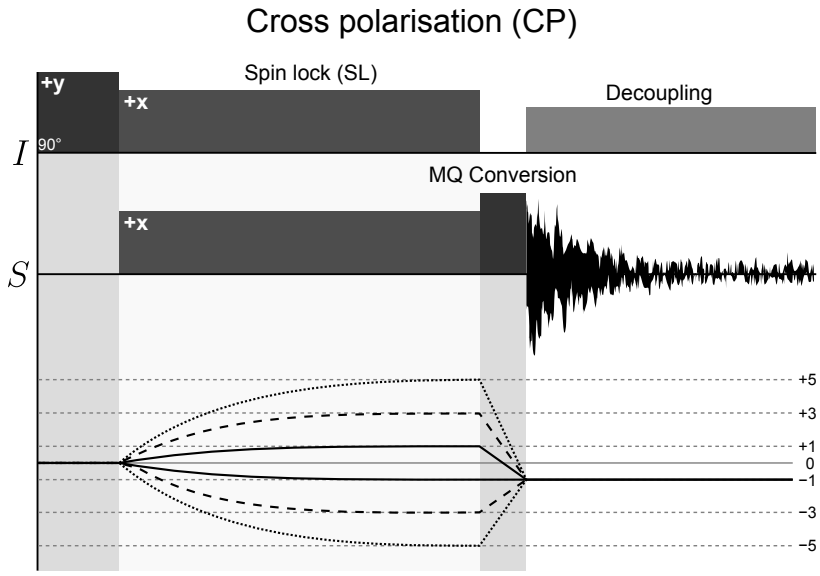

Figure 8.1: *Pulse sequence and CTPs for the CP experiment for quadrupolar nuclei. The phase diagram shows the different CTP where $p = \pm 1$ 1Q (solid line), $p = \pm 3$ 3Q (dashed line) and $p = \pm 5$ 5Q (dotted line) coherences are selected.*

levels r and s. As stated previously, a general Hartmann-Hahn condition between I and S is expressed as[2]

$$\omega_{1_I} = \omega_{r,s} \quad . \tag{8.1.12}$$

Equation (8.1.10) indicates that a CP transfer is not possible to all of the transition of S, but for only four of them. These are, the $\{r, s\} = \{1, 2\}$, $\{2, 3\}$, $\{3, 4\}$, and $\{1, 4\}$ transitions of Σ_V. As a result, the number of match conditions allowing magnetisation transfer are, for any spin S,

$$(S + 1/2)^2 \tag{8.1.13}$$

of the $2S(S + 1/2)$ possible transitions of a spin S nucleus.

8.1.2 The CP transfer

When one of the nutation rates of S, for which a CP transfer is allowed between I and S spins, is matched to ω_{1_S}, *e.g.*, when one of the Hartmann-Hahn conditions expressed in Equation (8.1.12) is fulfilled, magnetisation is transferred between I and S, between the two energy levels on the spin I, and the two r, s energy levels on the spin S in Σ_V.

[2]It should be notated that the labels r and s do not refer to the Zeeman energy levels given in $\Sigma_{\text{rot}}^{\times 2}$ in the general case, but to the energy levels in Σ_V.

However, the process by which this is enabled is not of vital importance, as, irrespective of the CP parameters, magnetisation on I and S ultimately reach an equilibrium value, independent of the values of d_{IS} and $C_{r,s}$,[3] under a certain number of assumptions:

- All expressions are given in the static case, so the Hamiltonian in Equation (8.1.7) is time independent in $\Sigma_{\mathrm{rot}}^{(\times 2)}$,
- the magnetisation rise-time (see Equation (3.1.20)) is much shorter than the contact time τ_C, and
- no significant relaxation, such as $T_{1\rho}$ relaxation, takes place during the contact time.

Under these assumptions, the density matrix ρ^D, expressed in Σ_V at the end of the CP contact time, can be shown to be proportional to $\hat{S}_z$, *e.g.*,

$$\rho^D(\tau_C) = a\hat{S}_z^{r,s} \quad , \tag{8.1.14}$$

where $a \in \mathbb{R}$. Equation (8.1.14) is valid for any spins with any quantum number. The expression of the density matrix ρ in $\Sigma_{\mathrm{rot}}^{(\times 2)}$ can be obtained performing the reverse transformation by V, given by

$$\rho(\tau_C) = V^{-1}\rho^D(\tau_C)V \quad . \tag{8.1.15}$$

The elements of the density matrix ρ can consequently be expressed as

$$\rho_{ij}(\tau_C) = \frac{a}{2}\left(V_{r,i}V_{r,j} - V_{s,i}V_{s,j}\right) \quad . \tag{8.1.16}$$

As stated previously, CP can only be performed between the transition of I and four of the transitions of S in Σ_V. When $S = 3/2$, the main elements of interest of the density matrix are $\rho_{23} = \rho_{32}^*$ (CT 1Q coherence) and $\rho_{14} = \rho_{41}^*$ (3Q coherence). The case when $\omega_Q \gg \omega_1$ has been widely discussed in the literature for spin $S = 3/2$ nuclei, as an analytical expression for the Harmann-Hahn condition can be obtained in this case.[29, 180–182] In this limit, $C_{1,2} = C_{3,4} = 0$, and the nutation rates $\omega_{1,2}$ and $\omega_{3,4}$, already established in Equation (3.2.13), are[4]

$$\omega_{1,2} = 2\omega_{1_S} \tag{8.1.17a}$$

$$\omega_{3,4} = \frac{3}{8}\frac{\omega_{IS}^3}{\Omega_Q^2} \quad . \tag{8.1.17b}$$

[3] provided that either of the two numbers are not zero or close to zero

[4] The values of $\omega_{1,2}$ and $\omega_{3,4}$ in Equation (8.1.17) would be inverted if $\omega_Q < 0$.

The density matrices after the CP contact are, in $\Sigma_{\text{rot}}^{(\times 2)}$,

$$\hat{\rho}(\tau_C) = -\frac{a}{2}\hat{S}_x^{2,3} \tag{8.1.18a}$$

$$\hat{\rho}(\tau_C) = -\frac{a}{2}\hat{S}_x^{1,4} \quad , \tag{8.1.18b}$$

when $\omega_{1,2}$ and $\omega_{3,4}$ are matched, respectively. As a result, magnetisation can be either transferred to pure CT 1Q (Equation (8.1.18a)) or to pure 3Q transitions (Equation (8.1.18b)) when observed in $\Sigma_{\text{rot}}^{(\times 2)}$. In general, compared to the CP pulse sequence betweens two spins $I = S = 1/2$ nuclei in Figure 3.4, several CTPs are possible when a quadrupolar nucleus is involved, as shown in Figure 8.1, in which case an additional MQ conversion pulse is necessary to observed the MQ coherence created during the CP transfer. In the limit $\omega_Q \gg \omega_1$, the match condition ω_{1_I} to $\omega_{1,2}$ results in a very efficient CP transfer, as it is independent of the orientation of the quadrupolar interaction PAF with respect to $\Sigma_{\text{rot}}^{\times 2}$ and it requires a strong RF field strength to be applied on I, which enables an efficient SL to be maintained for I. In contrast, matching ω_{1_I} to $\omega_{3,4}$ is less efficient, as this Hartmann-condition is now orientation dependant because of its dependence upon Ω_Q. Moreover, in the limit $\omega_Q \gg \omega_1$, the nutation rate in Equation (8.1.17b) is clearly small, with, for example, $\omega_{3,4}/2\pi$ = 1.5 kHz for $\Omega_Q/2\pi$ = 0.5 MHz and ν_{1_S} = 100 kHz, which may not be sufficient to maintain the magnetisation of the spin I during SL. For either of the two matching conditions, the weak RF limit only holds for certain crystallites, as particular orientations present a small Ω_Q value for which the condition $\Omega_Q \gg \omega_1$ does not hold. For this reason, direct CP transfer to 3Q is possible. This also means that, in general, matching only one Hartmann-Hahn condition can be used to create more than one transition on the spin S in $\Sigma_{\text{rot}}^{\times 2}$. The amounts of the different coherences created greatly depends mainly upon the Hartmann-Hahn condition chosen and the ω_{1_I} ratio, and upon various other parameters, as investigated by Ashbrook and Wimperis.[452]

More generally, the effective nutation rate of the $\{r, s\} = \{2n-1, 2n\}$ ($n \in \mathbb{N}^\star$) transition is Σ_V is given by [29, 30, 452]

$$\omega_{2n-1,2n} = K\frac{\omega_1^n}{\Omega_Q^{n-1}} \quad , \tag{8.1.19}$$

where K is a constant defined

$$K = \frac{2^{1-n}}{((n-1)!)^2}.\frac{(S+n/2)!}{(S-n/2)!} \quad . \tag{8.1.20}$$

From Equation (8.1.19), the previous discussion can be extended for any spin quantum number S. $\omega_{1,2}$ correspond to a nutation rate of $\omega_{1,2} = 2\omega_{1_{\text{inh}}}$ for spin $S = 3/2$ nuclei, $\omega_{1,2} = 3\omega_{1_{\text{inh}}}$ for spins $S = 5/2$ nuclei, *etc*, which is the nutation rate of the CT 1Q transition of S when observed in $\Sigma_{\text{rot}}^{\times 2}$. $\omega_{3,4}$ has a dependence proportional to $1/\Omega_Q$, $\omega_{5,6}$ is proportional to $1/\Omega_Q^2$, *etc*. This dependence in $1/\Omega_Q^n$ of the nutation rate $\omega_{2n-1,2n}$ causes that a very low nutation rate for the spin I being required. As a result, matching ω_{1_S} to $\omega_{2n-1,2n}$ becomes increasingly difficult in $\Sigma_{\text{rot}}^{\times 2}$ as n increases. Finally, $\omega_{2n-1,2n}$ correspond to the nutation rate of the symmetrical n-quantum transition in $\Sigma_{\text{rot}}^{\times 2}$ when in the limit $\Omega_Q \gg \omega_1$.

8.2 Simulating CP under static and MAS conditions

As discussed previously, the quadrupolar interaction becomes time-dependent under MAS (see the definition of $\Omega_Q(t)$ in Equation (2.3.29)), which severely increases the complexity of a theoretical description of a CP transfer to a quadrupolar nuclei.[455] Furthermore, even though analytical models exist for CP to spins $S = 3/2$ nuclei, no analytical solution for spins $S > 3/2$ nuclei is available in the literature. Hence, numerical simulation appears to be necessary for further understanding of CP to quadrupolar nuclei, particularly under MAS.

SIMPSON simulations of CP transfers were carried out as a function of three parameters: the RF field strength for I, $\nu_1(^1\text{H})$, the inherent RF field strengths for S, $\nu_1(^{23}\text{Na})$ for $S = 3/2$ or $\nu_1(^{27}\text{Al})$ for $S = 5/2$, and the CP contact τ_C varying from 5 to 500 µs by increments of 10 µs. The simulations were performed for $\nu_1(^{23}\text{Na})$ and $\nu_1(^{27}\text{Al})$ ranging from 10 to 200 kHz, and $\nu_1(^1\text{H})$ ranging from 20 to 400 kHz for the ^{23}Na simulation, or 10 to 600 kHz for the ^{27}Al simulations, all in steps of 2 kHz. The maximum RF field strength on ^{1}H is double that of ^{23}Na, and triple that of ^{27}Al, in order to observe the match conditions $\nu_1(^1\text{H}) = 2\nu_{1_{\text{inh}}}(^{23}\text{Na})$ and $\nu_1(^1\text{H}) = 3\nu_{1_{\text{inh}}}(^{27}\text{Al})$ in the limit $\omega_1 \ll \omega_Q$ (see Equation (8.1.19)). The ^{1}H-^{23}Na and ^{1}H-^{27}Al dipolar coupling frequency $d_{\text{IS}}/2\pi$ has been arbitrarily set to 6.5 kHz and η_Q to 0. In view of the large C_Q value chosen for the simulations, second-order quadrupolar corrections as expressed in Section 2.3.2, Equation (2.3.26) are taken into account. All simulations were performed for 320 crystallite orientations and 1 γ-angle for the static case or 5 γ-angles for the MAS case, and at B_0 = 14.1 T, resulting in ν_0 = 600.0 MHz for ^{1}H, ν_0 = 158.7 MHz for ^{23}Na, and ν_0 = 156.3 MHz for ^{27}Al.

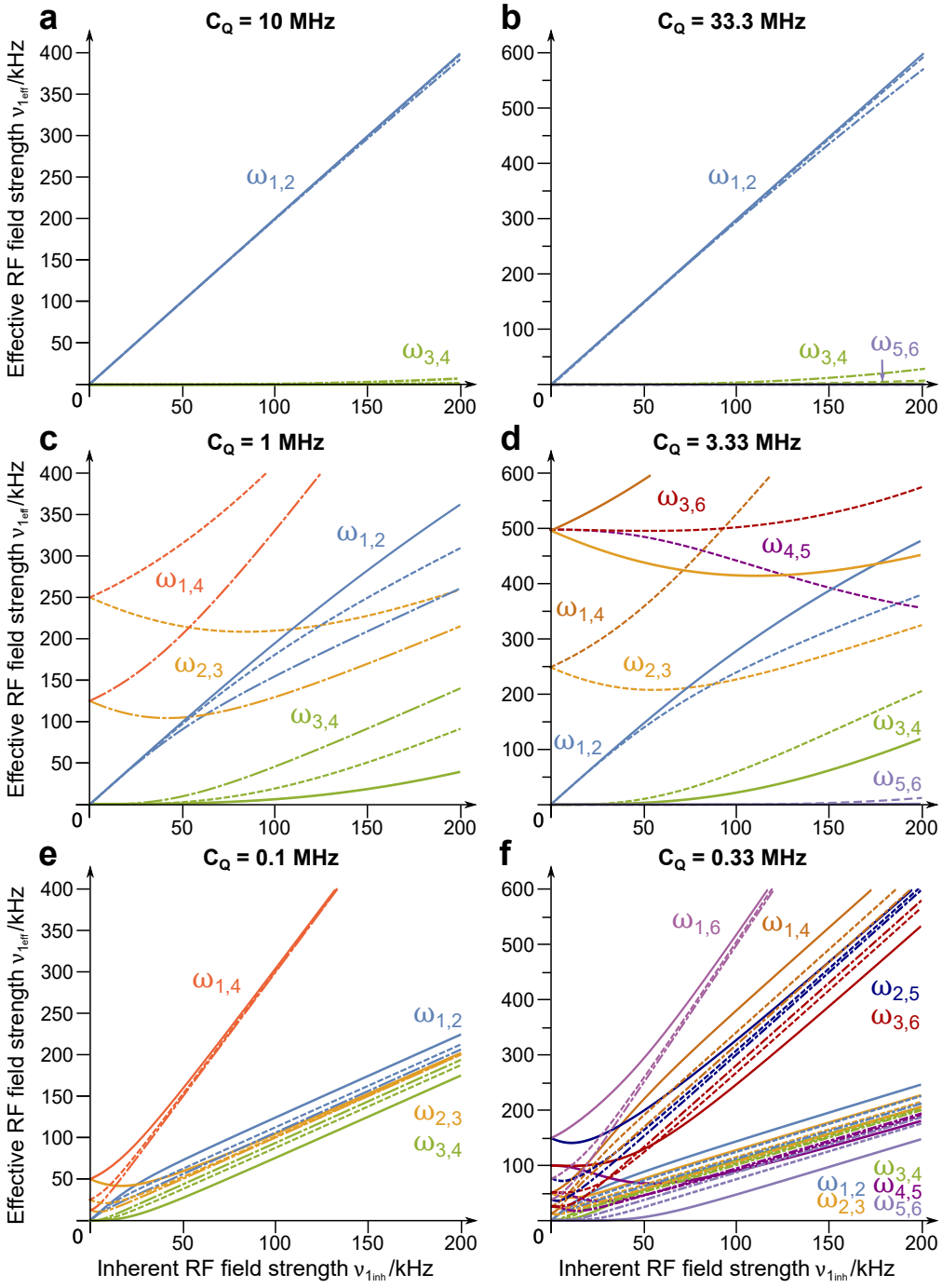

Figure 8.2: *Plots of the effective RF nutation rate $\nu_{1_{\text{eff}}}$ observed on a spin S as a function of the inherent RF nutation rate $\nu_{1_{\text{inh}}}$ applied on S, obtained from the analytical diagonalisation of the Hamiltonian given in Equation* (8.1.2b)*, for all the transitions that can give rise to a CP transfer (see Equation* (8.1.13)*) for* ***(a,c,e)****: $S = 3/2$, and* ***(b,d,f)****: $S = 5/2$, and for C_Q =* ***(a)****: 10 MHz,* ***(b)****: 33.3 MHz,* ***(c)****: 1 MHz,* ***(d)****: 3.33 MHz,* ***(e)****: 0.1 MHz, and* ***(f)****: 0.33 MHz. All transitions are labelled according of the labels r, s of the nutation rates $\omega_{r,s}$ in Σ_V (see Equation* (8.1.12)*). Each line corresponds to one single crystallite orientation. Solid lines correspond to a crystallite orientation such that $\Omega_Q/2\pi = \nu_Q$, dashed lines to $\Omega_Q/2\pi = \nu_Q/2$ and dashed and dotted lines to $\Omega_Q/2\pi = \nu_Q/4$.*

The simulations are plotted in the form of contour plots, showing the expectation value of the CT 1Q coherence of the spin S, *e.g.*, $\langle \hat{S}_x^{\text{CT}} \rangle$, as a function of the contact time τ_c, $\nu_1(^1\text{H})$, and $\nu_1(^{23}\text{Na})$ or $\nu_1(^{27}\text{Al})$. It should be noted that CP is often applied with a "ramp" of the SL on the I nucleus, with the consequence of broader Hartmann-Hahn conditions. Here, CP is executed with two conventional rectangular pulses as shown in Figure 8.1, giving sharp match conditions. The effect of the contact time τ_c is presented by an animation of the corresponding figures in the electronic version of this thesis. These animations can be played on any operating system using Acrobat Reader[5] or PDF-XChange,[6] but not all PDF readers are able to play the animations. When the animation is not played, or cannot be played, the figures display the contour plot for a fixed value of τ_C, indicated in the corresponding figure.

As discussed in Section 8.1.2, the efficiency of the magnetisation transfer *via* the dipolar coupling between spin I and S significantly depends on the ability of the RF pulse to maintain the magnetisation along a fixed direction in $\Sigma_{\text{rot}}^{(\times 2)}$, with an inefficient SL resulting in an inefficient CP transfer. However, although the SL of ^{1}H can be assumed to be at a maximum efficient for all the values of $\nu_1(^1\text{H})$ chosen for the simulation apart, perhaps, for the lowest values, maintaining SL on a quadrupolar, particularly under MAS, is much more complicated owing to the presence of the quadrupolar interaction, as discussed in Section 3.2.1 and by several authors.[180, 181, 185, 186] Simulations showing $\langle \hat{S}_x^{\text{CT}} \rangle$ during a SL, referred to as the SL efficiency, for the same powder average as the CP simulations and for the same pulse durations, are plotted underneath each of the CP plots as a function of $\nu_1(^{23}\text{Na})$ or $\nu_1(^{27}\text{Al})$. Those plots are also animated in the electronic version of this thesis as a function of τ_c, and played simultaneously with the CP animations.

In order to assign the different match conditions observed on the CP simulations to the labels r, s defined in Equation (8.1.12), Figure 8.2 plots the effective RF field strength $\nu_{1_{\text{eff}}} = \omega_{1_{\text{eff}}}/2\pi$ against the inherent RF field strength $\nu_{1_{\text{inh}}} = \omega_{1_{\text{inh}}}/2\pi = \omega_{1_S}/2\pi$ applied on S under different conditions and for several crystallites. The effective RF field strengths were obtained from the diagonalisation of $\hat{H}_S$ given in Equation (8.1.2b). However, it should be noted that the plots in Figure 8.2 do not provide any information about the amount of each of the coherences created by the CP transfer.

[5] https://acrobat.adobe.com/uk/en/products/pdf-reader.html
[6] http://www.tracker-software.com/product/pdf-xchange-viewer

8.2.1 The case of strong quadrupolar coupling

The first case discussed in this section corresponds to the situation where $\omega_1 \ll \omega_Q$ discussed in Section 8.1.2, for which the Hartmann-Hahn conditions are given in Equations (8.1.17) and (8.1.19) and illustrated in Figures 8.2a and 8.2b for $S = 3/2$ and $S = 5/2$, respectively. For $S = 3/2$, as discussed previously, matching $\omega_1(^1\text{H})$ to $\omega_{2,3}$ or $\omega_{1,4}$ results in no CP transfer, as $C_{2,3} = C_{1,4} = 0$ in the limit $\omega_1 \ll \omega_Q$, meaning that these matches would results in inefficient CP in simulations. Furthermore, the nutation rates $\omega_{2,3}$ and $\omega_{1,4}$ are very high, on the order of several MHz for the crystallite orientations considered in Figure 8.2, therefore simply do not appear either in Figure 8.2a or in the CP simulation curves. Similar observations can be made for the $S = 5/2$ case, where most of the nine nutation rates that can result in CP transfer not appearing in Figure 8.2b and in the CP simulation shown below. The principal difference with the spin $S = 3/2$ case is the existence of the $\omega_{5,6}$ nutation rate on the plot. However, this nutation rate exhibits a dependence on $1/\Omega_Q^2$, and hence is extremely small for most crystallite orientations when ω_Q is large. As a result, $\omega_{5,6}$ is overlapped with the horizontal axis for any of the crystallite orientations plotted in Figure 8.2b. The nutation rate $\omega_{1,2}$ for both cases, behave exactly according to Equation (8.1.19), with $\omega_{1,2} \simeq 2\omega_{1_{\text{inh}}}$ for $S = 3/2$ and $\omega_{1,2} \simeq 3\omega_{1_{\text{inh}}}$ for $S = 5/2$.

S = 3/2

The first simulation, presented in Figure 8.3 and performed for C_Q = 10 MHz, shows that only two possible matches are $\omega_1(^1\text{H})$ to $\omega_{1,2}$ or $\omega_{3,4}$, are observed. The matching condition to $\omega_{1,2}$ appears, as predicted by the theory in Section 8.1.2, as a single, sharp and intense feature in the static case (Figure 8.3a) lying along a straight line such that $\nu_1(^1\text{H}) = 2\nu_{1_{\text{inh}}}(^{23}\text{Na})$. In the region of low RF field strength for both ^{1}H and ^{23}Na, poor CP transfers can be observed, due to an inefficient SL on ^{23}Na for $\nu_1(^{23}\text{Na})$ < 30 kHz. For $\nu_1(^{23}\text{Na})$ > 30 kHz, the efficiency of the SL is steady, and so is the amount of 1Q CT coherence created from CP, after a contact time of $\tau_c \approx$ 150 µs, the time necessary for the complete CP build-up. The Hartmann-Hahn condition $\omega_1(^1\text{H})$ to $\omega_{3,4}$ is not visible in the static case because it has a intensity too low to be drawn with the lowest contour available in a Figure 8.3.

In the MAS case (Figure 8.3b), the matching condition to $\omega_{1,2}$ splits, as expected, into multiple modified Hartmann-Hahn conditions (see Equation (3.1.21)). The build-up is

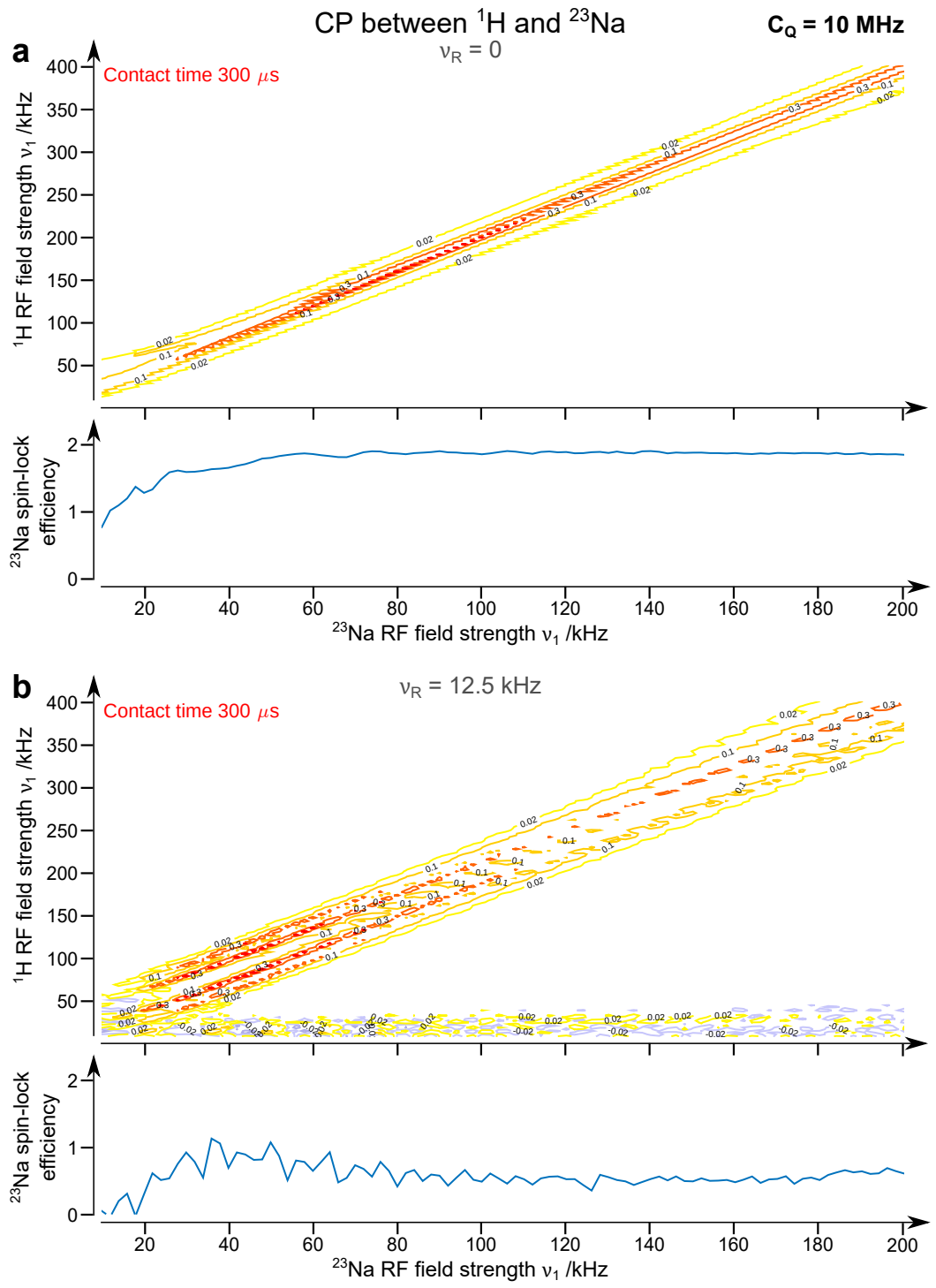

Figure 8.3: *^{23}Na ($I = 3/2$) CP and SL simulations carried out for C_Q = 10 MHz (ν_Q = 2.5 MHz) and **(a)**: in the static case and **(b)**: ν_R = 12.5 kHz (τ_R = 80 µs).*

complete after a contact time of $\tau_c \approx 300$ µs. The CT 1Q intensity varies greatly with the contact time. For 150 µs < τ_c < 200 µs, only two modified Hartmann-Hahn conditions exhibit an efficiency that is drawn with a dark red contour, while four conditions are at this level for 200 µs < τ_c < 400 µs. For τ_c > 400 µs, the four modified Hartmann-Hahn conditions become sparse throughout the positions of the four modified Hartmann-Hahn conditions discussed previously. The SL is overall very inefficient over the range of $\nu_1(^{23}\text{Na})$ plotted, with a strong initial dephasing (see Section 3.2.1) taking place, lasting for approximately 100 µs, during which $\langle \hat{S}_x^{\text{CT}} \rangle$ is more than halved. As for the static case, poor CP transfer is observed in the region corresponding to low ^{1}H and ^{23}Na RF field strengths, due to the extremely inefficient ^{23}Na SL. It can also be noted that a less efficient CP transfer is observed for $\nu_1(^{23}\text{Na}) \approx 120$ kHz. As discussed in Section 3.2.2, the SL on a quadrupolar nucleus is efficient if the adiabaticity factor α verifies either $\alpha \gg 1$ or $\alpha \ll 1$. When $\nu_1(^{23}\text{Na}) \approx 120$ kHz precisely corresponding to the region where $\alpha \approx 1$ for many crystallite orientations. Moreover, for $\nu_1(^{23}\text{Na})$ > 120 kHz, the SL plot exhibits a small ”peak” every rotor period, confirming some level of adiabaticity.

Finally, the transfer for $\omega_1(^1\text{H})$ to $\omega_{3,4}$ is visible under MAS conditions in Figure 8.3b. As predicted in Equation (8.1.17b) and as seen in Figure 8.2a, this condition is orientation dependent, and appears for large values of ν_Q and for very low values of $\nu_1(^1\text{H})$. Even though it is clear that the efficiency of the CP transfer is enhanced by MAS, it appears in Figure 8.3b with a very low intensity. As discussed by Ashbrook and Wimperis,[452] in $\Sigma_{\text{rot}}^{\times 2}$, matching $\omega_{3,4}$ essentially results, in almost pure 3Q transition while matching $\omega_{1,2}$ results in pure CT-1Q coherence in Σ_V. That is, the match to $\omega_{3,4}$ is expected to result in a low amount of CT-1Q and a large amount of 3Q transition. The transfer is negative at some places and positive at some others. The sign of the CT 1Q coherence is essentially unchanged for τ_c > 200 µs. As predicted in Figure 8.2, the condition is visible for a broader range of $\omega_1(^1\text{H})$ when $\omega_1(^{23}\text{Na})$ is large.

When C_Q is large, and as discussed in Section 8.1.2, the most efficient CP transfer is accomplished using the Hartman-Hahn condition $\omega_1(^1\text{H}) = \omega_{3,4} = 2\omega_1(^{23}\text{Na})$. The presence of multiple modified Hartmann-Hahn conditions observed in Figure 8.3b suggests that the efficiency of the transfer could be improved by the use of ramped CP contact pulse, sweeping $\nu_1(^1\text{H})$ throughout the modified Hartmann-Hahn conditions present.

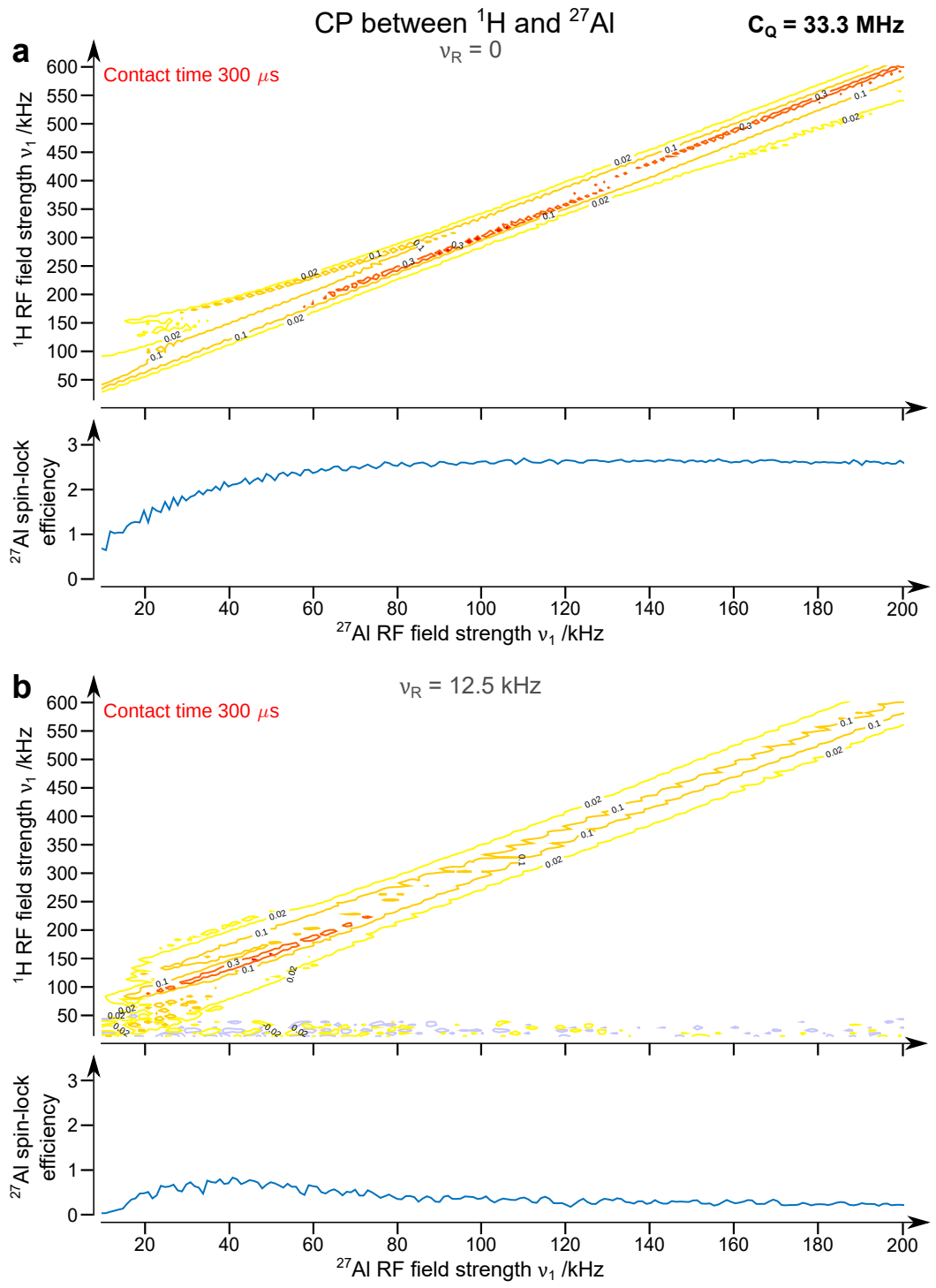

Figure 8.4: *^{27}Al ($I = 5/2$) CP and SL simulations carried out for C_Q = 33.33 MHz (ν_Q = 2.5 MHz) and **(a)**: in the static case and **(b)**: ν_R = 12.5 kHz (τ_R = 80 µs).*

S = 5/2

The CP plot for the case of high C_Q for ^{27}Al, shown in Figure 8.4, exhibits many similar features to the corresponding ^{23}Na case shown in Figure 8.3, as discussed previously. The build-up is complete after a contact time of τ_c = 120 µs. The most important feature observed in the static case in Figure 8.4a is the match condition to $\omega_{1,2}$ which, as predicted previously, lies along a straight line such that $\nu_1(^1\text{H}) \simeq 3\nu_{1_{\text{inh}}}(^{23}\text{Na})$. The SL for ^{27}Al is at a high level for $\nu_1(^{27}\text{Al})$ > 60 kHz. For $\nu_1(^{27}\text{Al})$ < 60 kHz, the SL is less efficient, and so is the CP transfer. Moreover, in this region, the single line splits into several components, reflecting some level of orientation dependence in the CP transfer. The same feature also appears for the nutation rates in Figure 8.2b and, although with a lower intensity, in Figure 8.3. The match conditions to $\omega_{3,4}$ and $\omega_{5,6}$ do not appear in the plot for the static case, which makes sense as these conditions give respectively almost pure symmetrical 3Q and 5Q coherence.

When under MAS as in Figure 8.4b, the SL experiences a dramatic drop in efficiency. For $\nu_1(^{27}\text{Al})$ < 40 kHz region, the magnetisation is not maintained at all during the SL, resulting in little or no CP transfer. A drop in the SL efficiency can be observed for $\nu_1(^{27}\text{Al})$ > 40 kHz, which is reflected by a less efficient CP transfer in this region. As for ^{23}Na, the point where $\nu_1(^{27}\text{Al}) \approx 120$ kHz corresponds to the change between sudden and adiabatic passage for some of the crystallite orientations, *e.g.*, α = 1, although an increase in SL efficiency is not very visible in Figure 8.4b. As for the static case, the build-up is complete after a contact time τ_c = 120 µs. A split of the apparently unique Hartmann-Hahn condition in the static case to several modified Hartmann-Hahn conditions is visible. Only one of these appear as a red contour, for $\nu_1(^{27}\text{Al}) \approx 40$ kHz and τ_c > 120 µs. This condition then becomes more sparsely distributed for τ_c > 400 µs.

In an extension to the above discussion for the $S = 3/2$ case, matching $\omega_{3,4}$ results in almost pure symmetrical 3Q transition, and $\omega_{5,6}$ to pure 5Q transition, in $\Sigma^{\times 2}_{\text{rot}}$.[452] Under MAS, a very small amount of CT 1Q coherence is created for low values of $\nu_1(^1\text{H})$ by the $\omega_{3,4}$ and $\omega_{5,6}$ match conditions. Although it may seem unclear which of the two conditions results in the observed CT 1Q coherence, matching to the $\omega_{5,6}$ condition required, for $\nu_1(^{27}\text{Al})$ = 200 kHz and $\Omega_Q/2\pi = \nu_Q/4$, requires $\nu_1(^1\text{H})$ = 4.1 kHz, for which the SL on ^{1}H cannot be maintained. Therefore, this condition is unlikely to have any significant contribution to the CT coherence observed in Figure 8.4b. In can be concluded that, for $S = 5/2$ when $\omega_Q \gg \omega_1$, the most efficient transfer to the CT is accomplished by the Hartmann-Hahn condition $\omega_1(^1\text{H}) = \omega_{3,4} = 3\omega_1(^{27}\text{Al})$.

8.2.2 The case of weak quadrupolar coupling

This section discusses CP transfer in the opposite case to that of Section 8.2.1, *i.e.*, $\omega_1 \gg \omega_Q$. When C_Q decreases, the matching conditions that were out of range in the case of high C_Q case in Figures 8.2a and 8.2b, now appear within the range of plotted RF field strengths, as shown in Figures 8.2c and 8.2d for $S = 3/2$ and $S = 5/2$, respectively. The $\omega_{1,2}$ and $\omega_{3,4}$ nutation rates come closer to a line such that $\omega_{1_{\text{eff}}} = \omega_{1_{\text{inh}}}$ as C_Q decreases. In the limit $\omega_1 \gg \omega_Q$, shown in Figures 8.2e and 8.2f, respectively for $S = 3/2$ and $S = 5/2$, it can be noted that the r, s labels now correspond to the labels of the Zeeman energy levels, where $\omega_{1,2}$, $\omega_{2,3}$, $\omega_{3,4}$, $\omega_{4,5}$ and $\omega_{5,6}$ are the nutation rates of the 1Q transitions, $\omega_{1,4}$, $\omega_{2,5}$ and $\omega_{3,6}$ to that of the 3Q transitions, and $\omega_{1,6}$ to that of the 5Q transition. In the limit C_Q = 0, the nutation rates of the 1Q transitions all lie along a line such that $\nu_{1_{\text{eff}}} = \nu_{1_{\text{inh}}}$, the 3Q nutation rates along $\nu_{1_{\text{eff}}} = 3\nu_{1_{\text{inh}}}$, and the 5Q nutation rates to $\nu_{1_{\text{eff}}} = 5\nu_{1_{\text{inh}}}$. In the cases given in Figures 8.2e and 8.2f, C_Q is not exactly zero, and so some level of orientation dependence is visible. However, it can be noted that the nutation rates for the symmetrical CT, 3Q and 5Q transitions are orientation dependant only for low values of $\nu_{1_{\text{inh}}}$. As all those nutation rates overlap, an increased complexity compared to the high case of C_Q is expected for the low C_Q case.

S = 3/2

The CP simulations performed for C_Q = 0.1 MHz are shown in Figure 8.5. The SL-efficiency is maintained to its highest level for most of the range of $\nu_1(^{23}\text{Na})$, except for $\nu_1(^{23}\text{Na})$ < 30 kHz, for which the SL is relatively inefficient, as is the CP transfer as a result. As discussed previously, in the limit $\omega_1 \gg \omega_Q$, all of the 1Q nutation rates are approximately identical, each giving a significant amount of CT 1Q coherence. For the static case in Figure 8.5a, this results in a complex CP transfer along a line such that $\nu_1(^1\text{H}) \simeq \nu_1(^{23}\text{Na})$. The nutation rate $\omega_{2,3}$, discussed previously to be orientation independent for high $\nu_1(^1\text{H})$ values, appears as a sharp feature in Figure 8.5a by a red contour. Some level of orientation dependence can be spotted for low values of $\nu_1(^{23}\text{Na})$. The nutation rates $\omega_{1,2}$ and $\omega_{3,4}$, that show some level of orientation dependence, appear as slightly broaden features in Figure 8.5a, with an approximate width $\Delta\nu_1(^1\text{H}) \approx 50$ kHz, measured from the orange contours seen for $\nu_1(^{23}\text{Na})$ = 100 kHz. Matching $\omega_{1,4}$, lying along a line such that $\nu_1(^{23}\text{Na}) \simeq 3\nu_1(^1\text{H})$, is clearly visible in the static case for low values of $\nu_1(^{23}\text{Na})$, and gives a small but visible amount of CT 1Q coherence. However, matching this condition would result in large amounts of 3Q coherence.

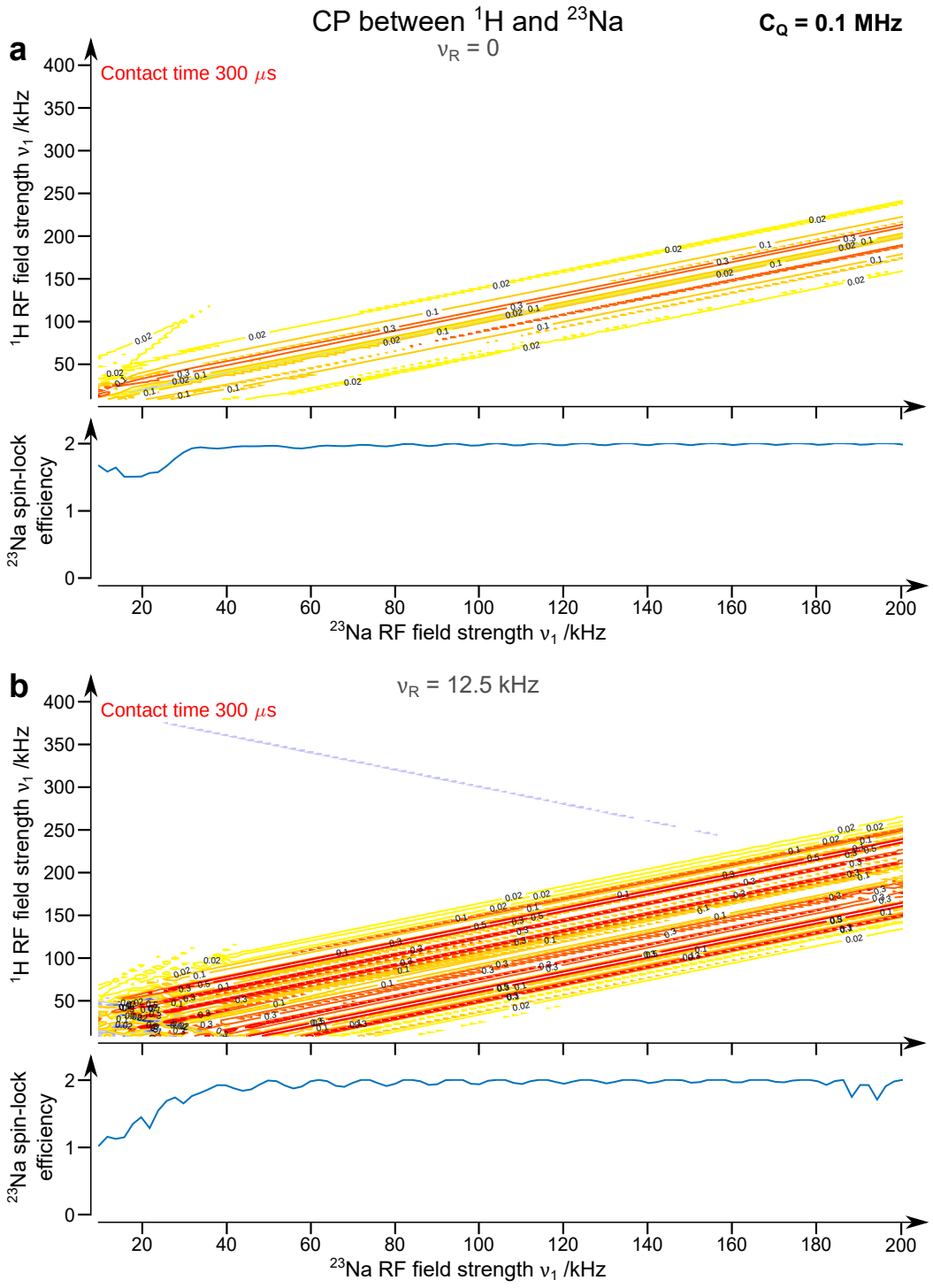

Figure 8.5: *^{23}Na ($I = 3/2$) CP and SL simulations carried out for C_Q = 0.1 MHz (ν_Q = 25 kHz) and **(a)**: in the static case and **(b)**: ν_R = 12.5 kHz (τ_R = 80 µs).*

In the case of CP under MAS, shown in Figure 8.5b, the maximum signal is reached after $\tau_c \approx 150$ µs. The SL is maintained to the maximum level for $\nu_1(^{23}\text{Na}) > 30$ kHz, while the CP for $\nu_1(^{23}\text{Na}) < 30$ kHz is less efficient. The match conditions to the 1Q transitions of ^{23}Na, which are overlapped as discussed previously, split into multiple modified Hartman-Hahn conditions, while the non-modified Hartmann-Hahn condition, *i.e.*, $\nu_1(^1\text{H}) \simeq \nu_1(^{23}\text{Na})$, leads to only a low CP transfer efficiency. The intensity of these matches can be seen to be much larger than that observed for the static case in Figure 8.5a. As before, the complexity observed around the line such that $\nu_1(^1\text{H}) = \nu_1(^{23}\text{Na})$ is due to the multiple and almost overlapped matches to the nutation rates $\omega_{1,2}$, $\omega_{2,3}$ and $\omega_{3,4}$. The match condition to $\omega_{1,4}$ also splits into a set of modified Harmann-Hahn conditions, although this is particularly visible for the maximum contact time of Figure 8.5b, *i.e.*, τ_c = 500 µs. The origin of a weak negative match condition at the top of the CP plot in Figure 8.5b, visible from τ_c = 280 µs, is unclear, and does not correspond to any of the nutation rates identified in Figure 8.2e. Therefore, this is either a computational artefact, or a result from a weak magnetisation transfer produced by phenomena other than CP.

It is clear in Figure 8.5b that the efficiency of CP in this case would greatly benefit from a ramp for an efficient transfer to the CT under MAS. Sweeping $\nu_1(^1\text{H})$ to $\nu_1(^{23}\text{Na}) \pm \nu_Q$ to $\nu_1(^1\text{H})$ from $\nu_1(^{23}\text{Na}) \mp \nu_Q$ would enable all the modified Hartman-Hahn conditions to contribute to the CT signal. The same approach could also be used to created 3Q coherence when matching to $\omega_{1,4}$ (not shown here).

S = 5/2

The CP plot for $S = 5/2$ nuclei, shown in Figure 8.6, is different from the $S = 3/2$ case previously discussed in the sense that five Hartmann-Hahn conditions now lie along a line such that $\nu_1(^1\text{H}) \simeq \nu_1(^{27}\text{Al})$, three along the line such that $\nu_1(^1\text{H}) \simeq 3\nu_1(^{27}\text{Al})$, and one along the line $\nu_1(^1\text{H}) \simeq 5\nu_1(^{27}\text{Al})$. The match to the CT, here $\omega_{3,4}$, is almost not orientation dependent and appears as a sharp feature in Figure 8.6, mostly visible for τ_c = 100 µs. However, the matches to the other 1Q nutation rates exhibit a visible orientation dependence. This results in further complexity of the static CP plot in Figure 8.6a. The SL efficiency for ^{27}Al is at its maximum level for most of the range of $\nu_1(^{27}\text{Al})$, providing an efficient CP transfer. Finally, the Hartmann-Hahn conditions to the 1Q transitions span along a width $\Delta\nu_1(^1\text{H}) \approx 50$ kHz, taken from the width of the orange contour for τ_c = 300 µs and $\nu_1(^{27}\text{Al})$ = 100 kHz. The other major difference from the $S = 3/2$

case is the presence of a small amount of CT 1Q transition created from the match condition to $\omega_{1,6}$, *e.g.*, the 5Q transition in the low C_Q case. As discussed for Figure 8.2f, matching $\omega_{2,4}$ results mainly in symmetrical 3Q coherence in $\Sigma^{\times 2}_{\text{rot}}$, and $\omega_{1,6}$ in 5Q coherence. No other major differences from the $S = 3/2$ case can be observed in Figure 8.6a, concerning the amount of CT 1Q transition created by this match, in spite of the presence of the three nutation rates that enable the transfer.

Under MAS, in Figure 8.6b, a large number of modified Hartmann-Hahn conditions appear along a line where $\nu_1(^1\text{H}) = \nu_1(^{27}\text{Al})$, and the non-modified Hartmann-Hahn condition result in an inefficient CP transfer. Under MAS, the SL level remains at a maximum efficiency for $\nu_1(^1\text{H})$ > 50 kHz, but is slightly less efficient for $\nu_1(^1\text{H})$ < 50 kHz. Above this last value, the match to the 1Q nutation rates exhibit a complex pattern composed of multiple modified Hartmann-Hahn conditions, with intensities much larger those that observed for the static case in Figure 8.5a, apart from the match to the non-modified Hartmann-Hahn condition, which gives only small amount of CT 1Q coherence. The match conditions to the MQ transitions results to almost no CT 1Q transition in the MAS case. These give a pattern of modified Hartmann-Hahn spinning sidebands for low values of $\nu_1(^1\text{H})$, clearly visible from τ_c > 200 µs. It can be noted that a similar unexplained weak negative match condition, as seen in Figure 8.5b, appears in Figure 8.6b, although it is only visible for τ_c > 300 µs.

As for the $S = 3/2$ case, the most efficient transfer to the CT is obtained from matching the 1Q transitions, *e.g.*, choosing $\nu_1(^1\text{H}) \simeq \nu_1(^{27}\text{Al})$. A ramped SL pulse from $\nu_1(^1\text{H})$ to $\nu_1(^{27}\text{Al}) \pm \nu_Q$ to $\nu_1(^1\text{H})$ from $\nu_1(^{23}\text{Al}) \mp \nu_Q$ would certainly be very beneficial for the obtained signal.

8.2.3 The case of intermediate quadrupolar coupling

The values of C_Q chosen for the "intermediate" C_Q case correspond to realistic values for many common $S = 3/2$ nuclei (^{23}Na, ^{87}Rb,...) and $S = 5/2$ nuclei (^{17}O, ^{27}Al,...). However, the complexity of the CP behaviour is greatly increased in this regime. The nutation rates are given in Figures 8.2c and 8.2d for the $S = 3/2$ and $S = 5/2$ cases, respectively. The nutation rate $\omega_{1,2}$ progressively moves from a slope such that $\nu_{1_{\text{eff}}} = 2\nu_{1_{\text{inh}}}$ in Figure 8.2c (as in Figure 8.2a), or a slope $\nu_{1_{\text{eff}}} = 3\nu_{1_{\text{inh}}}$ in Figure 8.2d (as in 8.2b), to a slope $\nu_{1_{\text{eff}}} = \nu_{1_{\text{inh}}}$ in Figures 8.2e and 8.2f. This change is even more pronounced for low values of Ω_Q. $\omega_{3,4}$ and $\omega_{5,6}$ exhibit nutation rates decreasing as Ω_Q increases, to the extent that $\omega_{5,6}$ is only visible for one of the crystallite orientation plotted in Figure 8.2d.

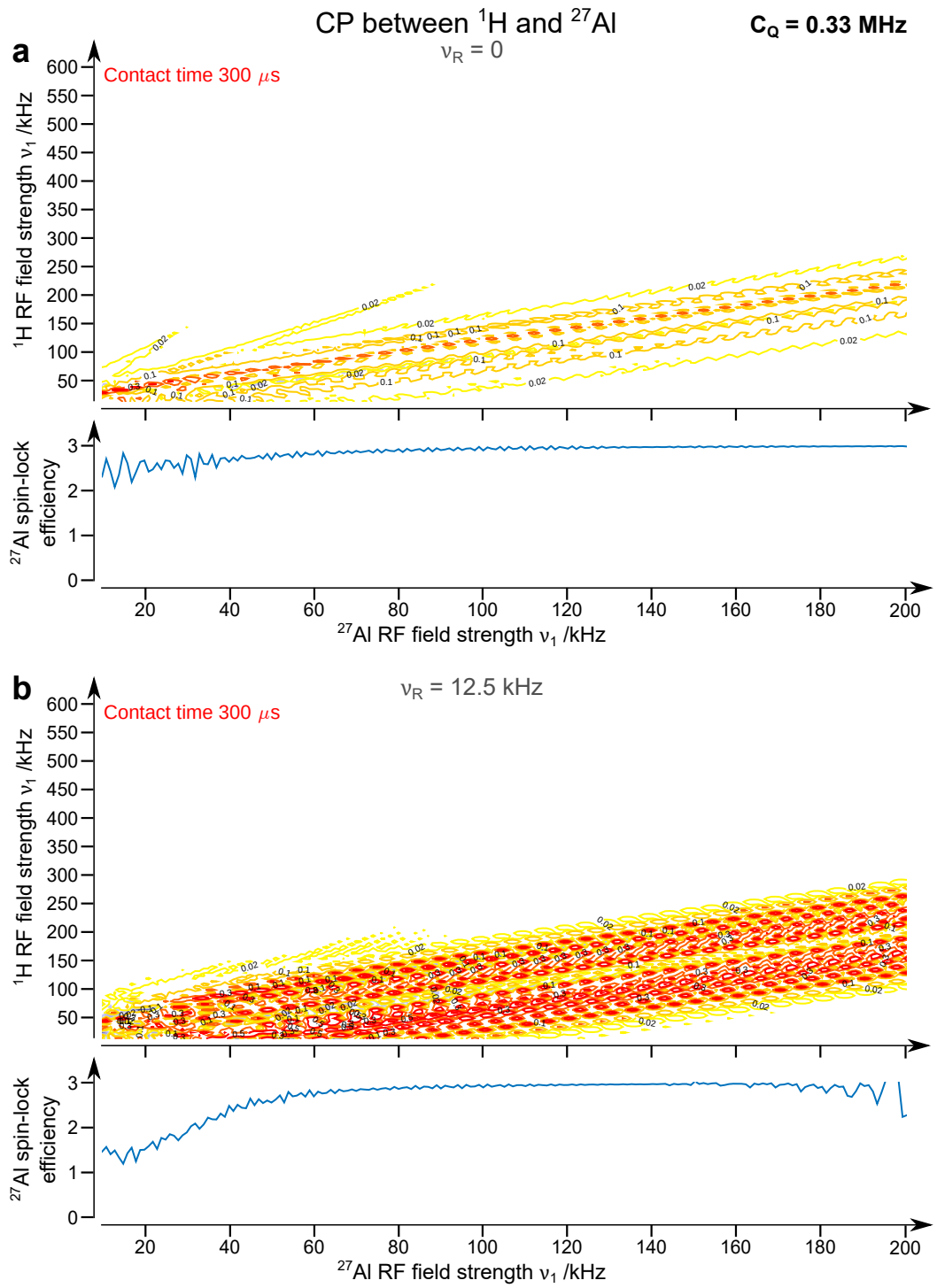

Figure 8.6: *^{27}Al ($I = 5/2$) CP and SL simulations carried out for C_Q = 0.33 MHz (ν_Q = 25 kHz) and **(a)**: in the static case and **(b)**: ν_R = 12.5 kHz (τ_R = 80 µs).*

For the nutation rates $\omega_{1,2}$, $\omega_{3,4}$ and $\omega_{5,6}$, the orientation dependence increases significantly with $\nu_{1_{\text{inh}}}$. Finally, the other nutation rates $\omega_{2,3}$ and $\omega_{1,4}$ in Figure 8.2c show a considerable orientation dependence, notably increasing as Ω_Q increases, and not appearing at all in Figure 8.2c for an orientation such that $\Omega_Q/2\pi = \nu_Q$. In the CP plots, matching these nutation rates will certainly give rise to inefficient CP transfer. An identical observation can be made in Figure 8.2d for the nutation rates $\omega_{2,3}$, $\omega_{1,4}$, $\omega_{3,6}$, $\omega_{4,5}$, $\omega_{2,5}$ and $\omega_{1,6}$, with the latter two not appearing at all for all of the considered crystallite orientations. However, it should be noted that for a crystallite orientation such that $\Omega_Q/2\pi = \nu_Q/4$, not plotted for Figure 8.2d because of the lack of readability that would have resulted, the nutation rates $\omega_{2,5}$ and $\omega_{1,6}$ appear within the plotted range, therefore would contribute to a limited extent to the CP transfer. In the end, it results from this that the nutation rates that are expected to result in an efficient CP transfer when observing CT 1Q coherences on the spin S are $\omega_{1,2}$ and $\omega_{3,4}$. As discussed in the literature for similar values of ν_Q,[452] matching $\omega_{1,2}$ results in mainly CT 1Q coherence and matching $\omega_{3,4}$ mainly to 3Q coherence in $\Sigma_{\text{rot}}^{\times 2}$ for the considered C_Q values.

S = 3/2

The CP plot for an intermediate C_Q value and $S = 3/2$ is shown in Figure 8.7. It can first be noted that, in the static case in Figure 8.7a, the SL levels remains close to its maximum for the entire range of $\nu_1(^{23}\text{Na})$ values plotted. As before, build-up is complete after a contact time of τ_c = 120 µs. For τ_c = 300 µs, the plots shows considerable complexity, but most of the features of the plot have been plotted in Figure 8.2c and discussed previously. The match to $\omega_{1,2}$ appears clearly, following the slopes described previously. The CP transfer using this condition, appearing at the level of the red contours for $\nu_1(^{23}\text{Na})$ < 70 kHz, becomes less efficient when $\nu_1(^{23}\text{Na})$ > 70 kHz, owing to the increase of the orientation-dependence of the nutation rate $\omega_{1,2}$ as $\nu_{1_{\text{inh}}}$ increases. It can also be noted that the intensity of this match condition varies dramatically with contact times for $\nu_1(^{23}\text{Na})$ > 100 kHz, due to the oscillation of the build-up at a frequency $d_{IS}/2\pi$ during contact. The match to $\omega_{3,4}$ appears, as in Figure 8.3b, for low values of $\nu_1(^1\text{H})$, and results in low amounts of CT 1Q transition. As predicted in Figure 8.2c, this conditions appears very broad due to the orientation-dependence of the $\omega_{3,4}$ nutation rate. However, unlike in the case of high C_Q shown in Section 8.2.1, matching to this conditions is feasible, as it requires $\nu_1(^1\text{H})$ to be of the order of several tens of kHz. The match condition to $\omega_{2,3}$ is clear in Figure 8.7, resulting in small

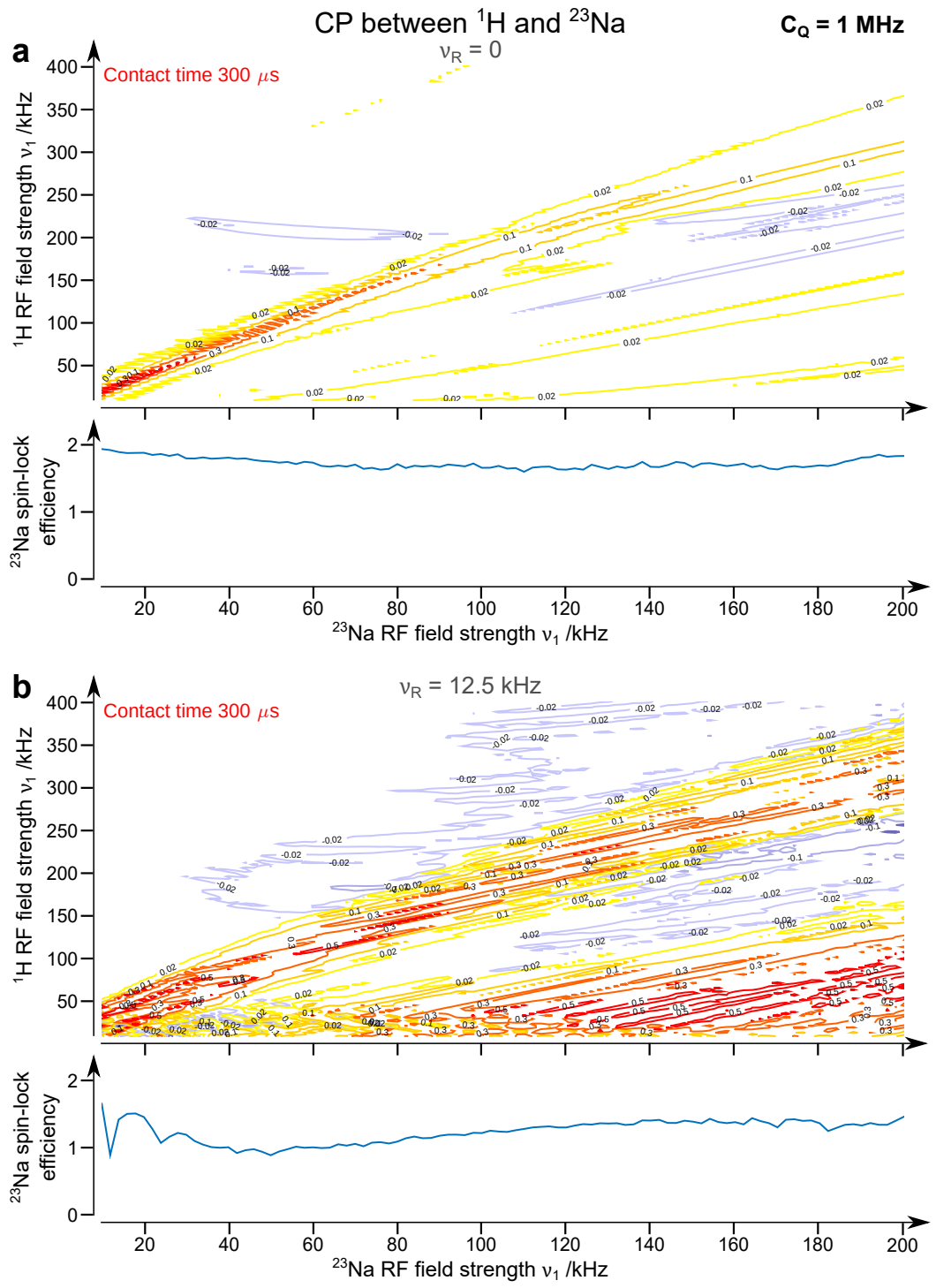

Figure 8.7: *^{23}Na ($I = 3/2$) CP and SL simulations carried out for C_Q = 1 MHz (ν_Q = 0.25 MHz) and **(a)**: in the static case and **(b)**: ν_R = 12.5 kHz (τ_R = 80 µs).*

amounts of negative 1Q CT coherence, visible around $\nu_1(^1\text{H}) \approx 200$ kHz. Finally, the contribution of $\omega_{1,4}$ to the CP plot is subtle, visible only as a sharp ridge present in the top of the plot with a low intensity from τ_c > 280 µs.

In the MAS case in Figure 8.7b, the CP plot increases even further in complexity. The SL remains at an average level for the range of $\nu_1(^{23}\text{Na})$ plotted. The two maxima in SL efficiency, discussed in Section 3.2.1, clearly appear every half of the rotor period ($\tau_R = 80$ µs), showing that the SL is applied in the adiabatic regime, except for $\nu_1(^{23}\text{Na})$ < 20 kHz. The Hartmann-Hahn condition to $\omega_{1,2}$ splits into multiple modified Hartmann-Hahn conditions, clearly visible in the range 50 kHz < $\nu_1(^{23}\text{Na})$ < 150 kHz for τ_c = 300 µs, while the non-modified Hartmann-Hahn condition remains as efficient. Unlike the static case, few changes are observed with contact time. A surprising feature in Figure 8.7b is the remarkably large amount of CT 1Q coherence created by matching $\omega_{3,4}$. Although the orientation dependence of this condition is clear, it is more efficient than the match condition to $\omega_{1,2}$ for $\nu_1(^{23}\text{Na})$ > 80 kHz. This is probably a consequence of the ^{23}Na SL being in the adiabatic regime, for which, as discussed in Section 3.2.1, exchange between 1Q and 3Q coherences occurs at several points during the rotation of the rotor. Using a ramped CP contact pulse, it is certainly possible to obtain tremendous signal from a match to this condition. As for $\omega_{1,2}$, few changes in the amount of CT 1Q coherence can be observed with the contact time. The match condition to $\omega_{2,3}$, only visible from a small number of ridges in Figure 8.7a, now appears spread over a wider range of $\nu_1(^1\text{H})$ and $\nu_1(^{23}\text{Na})$ between $\omega_{1,2}$ and $\omega_{3,4}$, and above $\omega_{1,2}$ with a low intensity. This larger spread is certainly contributing to the loss in efficiency of a match to $\omega_{1,2}$. Finally, the contribution of $\omega_{1,4}$ almost disappears in Figure 8.7b, and is only slightly visible for τ_c > 360 µs at a similar position as in Figure 8.7a.

In the end, several Hartman-Hahn conditions are possible to obtain efficient CP transfer to the CT for $S = 3/2$, with intermediate C_Q. For CP from ^{1}H or ^{19}F, for which large RF field strengths are available, matching $\omega_{1,2}$ certainly remains the best solution, but for CP from a nucleus for which only lower RF field strengths are available, such as ^{31}P, using a ramped CP SL pulse for moderate ν_{1_I} values to match $\omega_{3,4}$ may result in more CT signal.

S = 5/2

The CP plot for when $S = 5/2$ is given in Figure 8.8 for an intermediate C_Q value. Unlike all the cases discussed previously, owing to the complexity of the nutation rates shown

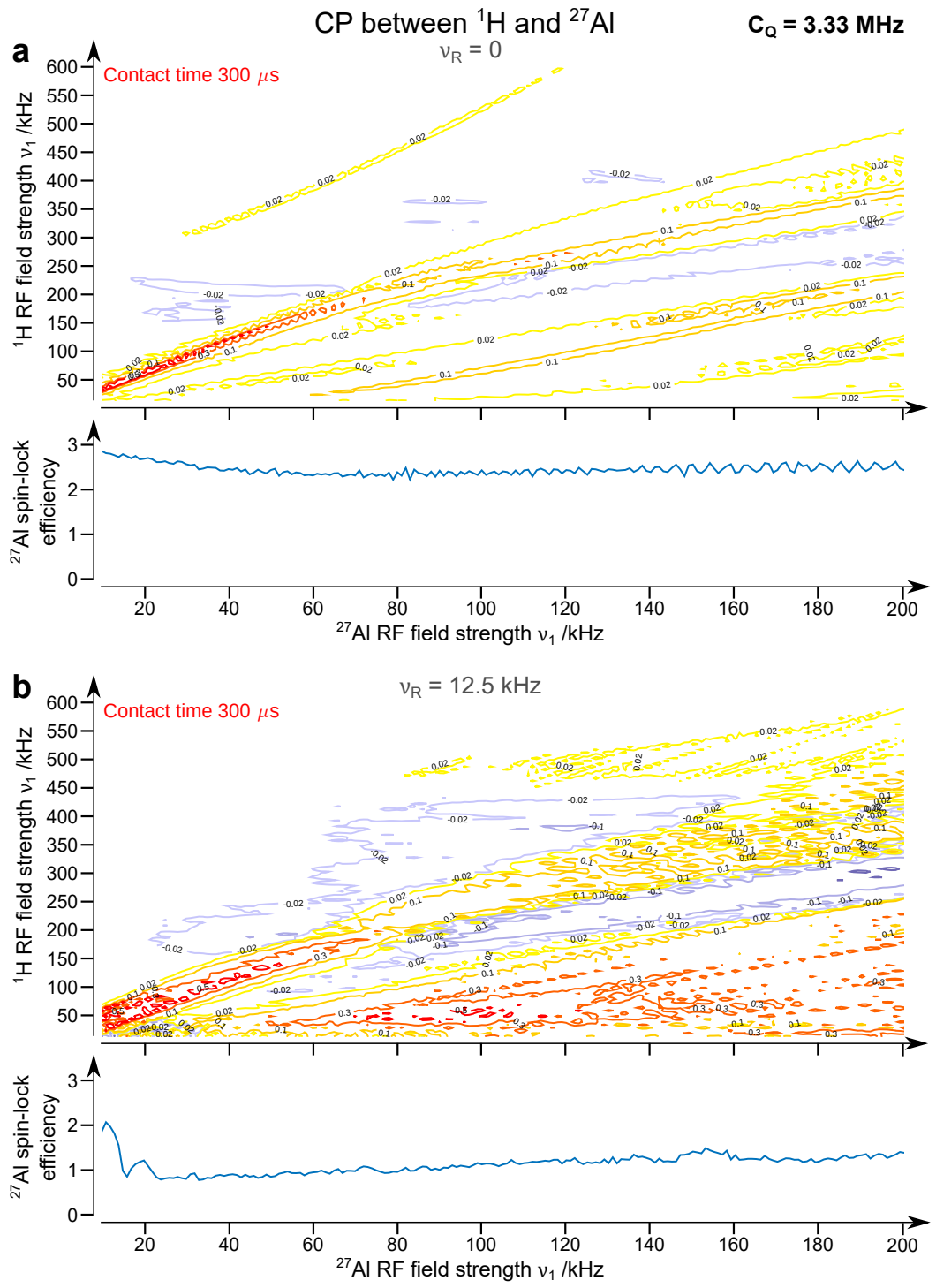

Figure 8.8: *^{27}Al ($I = 5/2$) CP and SL simulations carried out for C_Q = 3.33 MHz (ν_Q = 0.25 MHz) and **(a)**: in the static case and **(b)**: ν_R = 12.5 kHz (τ_R = 80 µs).*

in Figure 8.2d, it is impossible to assign unambiguously some of the features observed in Figure 8.8 to only one of nutation rate, as many of them appear to arise from the superposition of several Hartmann-Hahn conditions. In the static case in Figure 8.8a, and as for the $S = 3/2$ case, the SL on ^{23}Na remains very high for all values of $\nu_1(^{27}\text{Al})$. The Hartmann-Hahn match to $\omega_{1,2}$ gives an efficient transfer for $\nu_1(^{27}\text{Al})$ < 70 kHz, but becomes less efficient above this limit as $\omega_{1,2}$ acquires a significant orientation dependence. The match condition to $\omega_{3,4}$ appears for low values of $\nu_1(^1\text{H})$, and is spread over a large range of values of $\nu_1(^1\text{H})$. It results in a surprisingly large amount of CT 1Q coherence even in the static case. It is particularly striking that the match to $\omega_{1,2}$ is less efficient, and that to $\omega_{3,4}$ is more efficient, in creating CT coherence when the ^{27}Al SL is in the adiabatic regime. As for the high C_Q case in Section 8.2.1, the extent of the contribution of the match condition to $\omega_{5,6}$ is unclear, as it requires low values of $\nu_1(^1\text{H})$. For a crystallite orientation such that $\Omega_Q/2\pi = \nu_Q/4$ and for $\nu_1(^{27}\text{Al})$ = 100 kHz, $\omega_{5,6}/2\pi$ = 6 kHz. This illustrates that there is certainly some effect of this condition in Figure 8.8a, but its contribution cannot be separated from that of $\omega_{3,4}$. While most of the negative CT 1Q coherence created certainly arises from a match to $\omega_{2,3}$ as for the $S = 3/2$ case in Figure 8.7a, other transfers, such as that to $\omega_{4,5}$, may also contributed to the features observed. Moreover, the apparition of two ridges at a very short contact time ($\tau_c \approx$ 50 µs) tends to support this statement. Finally, one ridge, similar to that assigned to a match to $\omega_{1,4}$ in Figure 8.7a, appear from a contact time $\tau_c \approx$ 180 µs. Other Hartmann-Hahn conditions are certainly not visible in Figure 8.8a.

As in Figure 8.7b, the SL in Figure 8.8b is maintained at an average levels for all values of $\nu_1(^{27}\text{Al})$, and the peaks every half of the rotor period appearing clearly for $\nu_1(^{27}\text{Al})$ > 20 kHz, which is characteristic of the adiabatic regime. The Hartmann-Hahn conditions splits into a complex pattern of modified Hartmann-Hahn conditions. As before, each feature in Figure 8.8b most certainly arises from the overlapping of several contributions. The CP plot shows few changes with contact times above τ_c > 120 µs. The match condition to $\omega_{1,2}$, as in the static case, is more efficient for $\nu_1(^{27}\text{Al})$ < 60 kHz, after which it acquires a significant orientation dependence. The transfer to $\omega_{3,4}$ (or $\omega_{5,6}$) results, as in Figure 8.7b, in the creation of large amounts of CT 1Q, despite the strong orientation dependence of the condition, although this amount if relatively lower than that observed in Figure 8.7. Matching this condition with a ramped CP pulse should result, in practice, in a large amount of CT signal. The negative CT coherence, previously attributed to $\omega_{2,3}$, and spread over large portions of the plot in Figure 8.8b, is located between the $\omega_{1,2}$ and $\omega_{3,4}$ conditions. The apparition of a positive match condition for high

values of $\nu_1(^1\mathrm{H})$ and $\nu_1(^{27}\mathrm{Al})$, which was not visible in the static case in Figure 8.8a, can be noted. Due to the orientation dependence of the nutation rates previously discussed, it is not possible to associate this feature to a match to just one of the nutation rates observed in Figure 8.2, but the slope of the modified Hartmann-Hahn conditions in this plot suggests that this could arise mainly from matching $\omega_{1,4}$. This conditions was visible in the static case only as one, low intense ridge.

As discussed for the $S = 3/2$ case, matching $\omega_{1,2}$, *i.e.*, the nutation rate of the CT, might not give the most efficient transfer under MAS, as the match to $\omega_{3,4}$ appears to result in significant amounts of CT 1Q transitions. This could be further enhanced using a ramped CP pulse, and can be considered particularly when only moderate RF field strengths are available for the spin I.

8.2.4 CP under fast MAS

The plots described previously highlighted some differences in the CP transfer efficiencies between the static and MAS cases for the CP to quadrupolar nuclei. In particular, it has been shown that the match condition to $\omega_{3,4}$ results in a surprisingly large amount of CT 1Q coherence in the average C_Q case for both spins. In light of these results, the question exists as to whether further CT 1Q coherence would be obtained from employing even faster MAS rates. Therefore, the CP simulations performed for ν_Q = 0.25 MHz in Figure 8.7 for $S = 3/2$ and Figure 8.8 for $S = 5/2$ have been repeated for ν_R = 50 kHz (τ_R = 25 µs), and are shown in Figures 8.9 and 8.10, respectively. These simulations are plotted for τ_c = 2 to 300 µs, with τ_c = 200 µs for the static figure, with an increment of τ_c = 5 µs. Unlike most of the CP plots shown so far, those two plots are very complex, as all of the Hartman-Hahn conditions now split into modified Hartman-Hahn conditions, separated by ν_R = 50 kHz. As a result, the CP transfers now give intense features that appear at multiple position in the plots.

S = 3/2

The CP plot performed under fast MAS for ^{23}Na is shown in Figure 8.9. The fast MAS rate decreases the adiabaticity factor of the SL (see Equation (3.2.8)) compared to Figure 8.7b, *e.g.*, the SL becomes less adiabatic, resulting in the SL peak being more intense and the CP transfer less efficient. As stated previously, the resulting plot is now extremely complex, with all of the modified Hartmann-Hahn conditions now appearing

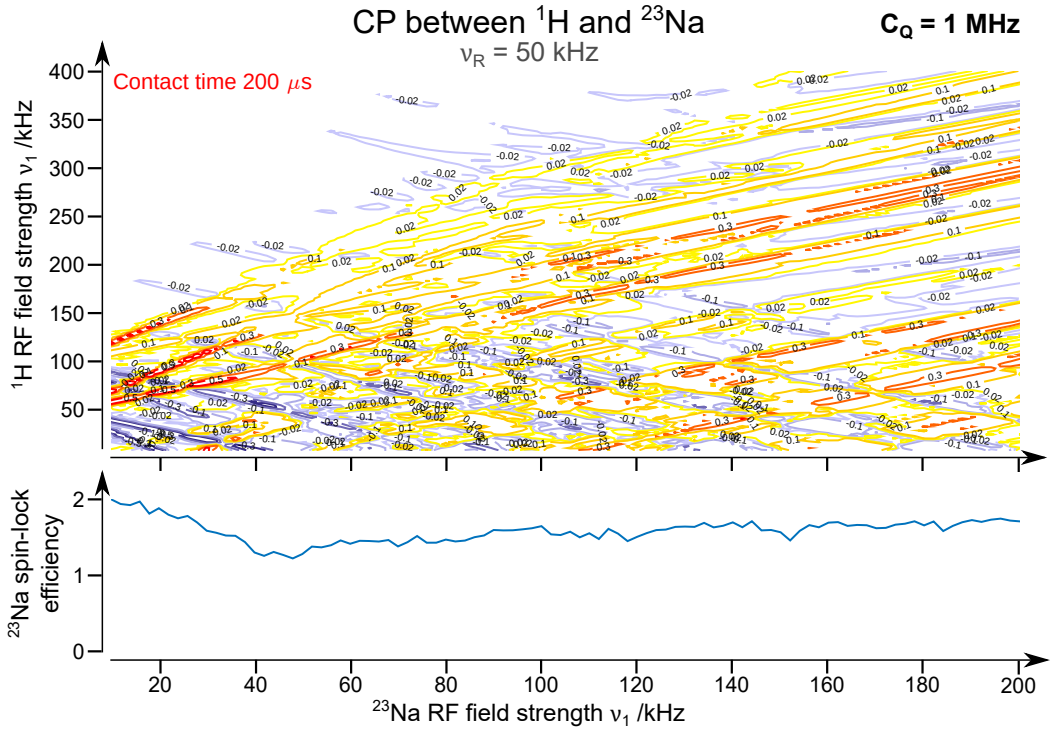

Figure 8.9: *^{23}Na ($I = 3/2$) CP and SL simulations carried out for C_Q = 1 MHz (ν_Q = 0.25 MHz) and ν_R = 50 kHz (τ_R = 25 µs).*

in various parts of the plots. Overall, the efficiency of the CP transfer decreases, as the dipolar coupling is averaged more efficiently by MAS. At a first glance, it would appear that an efficient CP transfer to the CT can be obtained for any values of $\nu_1(^{1}\mathrm{H})$ and $\nu_1(^{23}\mathrm{Na})$, especially if a ramped SL pulse is employed. It is possible to observe the spacing between the modified Hartmann-Hahn conditions for $\nu_1(^{23}\mathrm{Na})$ = 10 kHz, where two strong match condition to $\omega_{1,2}$, separated by exactly ν_R = 50 kHz, can be observed. The number of efficient modified Hartmann-Hahn conditions for $\omega_{1,2}$ increases as $\nu_1(^{23}\mathrm{Na})$ increases. A striking feature of Figure 8.9 is the spread of the match condition to $\omega_{2,3}$, which is now distributed across the entire plot. This is particularly visible for τ_c > 300 µs. The effect of matching $\omega_{1,4}$ in the plot, if any, cannot be formally identified in the plot for any of the contact times.

The match condition to $\omega_{3,4}$ also appears at a series modified Hartmann-Hahn conditions, mostly visible for high $\nu_1(^{23}\mathrm{Na})$ values. Matching $\omega_{3,4}$ does not result in increased CT 1Q coherence compared to the ν_R = 12.5 kHz case in Figure 8.8. No major changes in the amount of CT 1Q arising from matching to $\omega_{3,4}$ or $\omega_{1,2}$. occur in Figure 8.9 for τ_c > 250 µs. Furthermore, the amount of CT 1Q coherence is not increased between ν_R

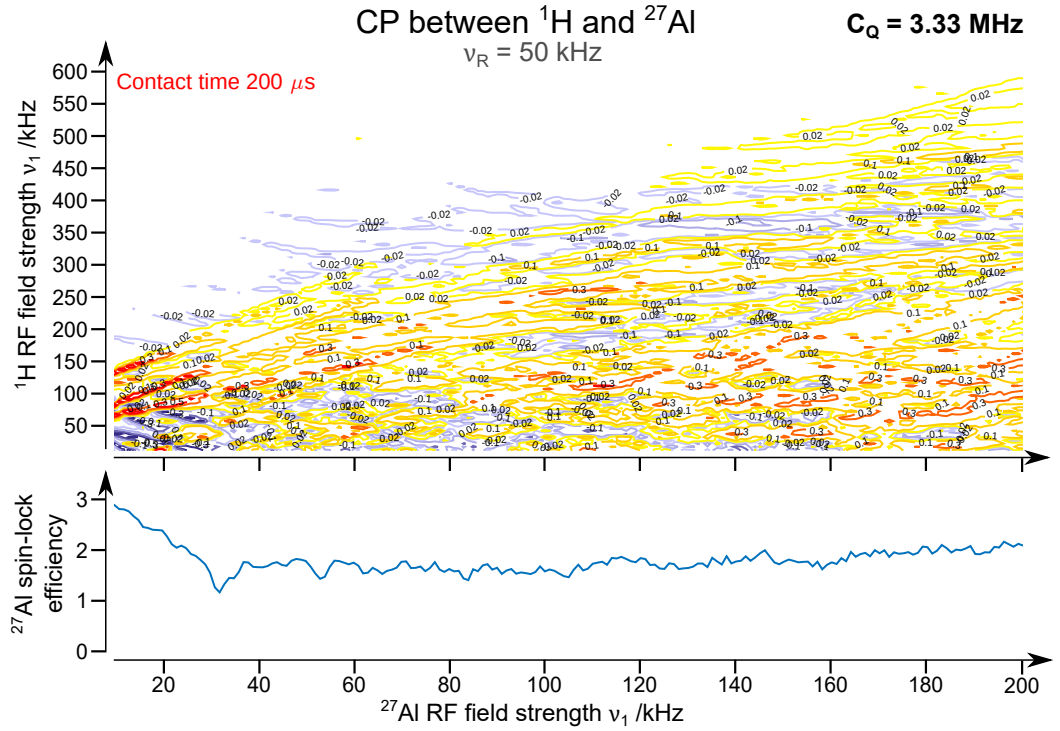

Figure 8.10: *^{27}Al ($I = 5/2$) CP and SL simulations carried out for C_Q = 3.33 MHz (ν_Q = 0.25 MHz) and ν_R = 50 kHz (τ_R = 20 µs).*

= 12.5 and 50 kHz when matching $\omega_{3,4}$, but there are several match conditions to $\omega_{1,2}$ that are more efficient for ν_R = 50 kHz than for ν_R = 12.5 kHz. This suggests that there are now two possible options for an efficient CP to the CT, provided that a sufficiently strong RF field is available for ^{1}H.

S = 5/2

The $S = 5/2$ case for fast MAS and intermediate C_Q, shown in Figure 8.10, exhibits even further complexity than that for the $S = 3/2$ case, with the match conditions to $\omega_{1,2}$ or $\omega_{3,4}$ being now almost impossible to identify as every feature of the plot is a combination of the contribution of multiple match conditions. However, as in Figure 8.9, two efficient match conditions to $\omega_{1,2}$ separated by ν_R = 50 kHz can be observed for $\nu_1(^{27}\text{Al})$ = 10 kHz. It can also be noted the contribution of the match conditions to $\omega_{2,3}$ that appears in the upper-right region of Figure 8.10. The effect of the match to $\omega_{2,3}$ (or $\omega_{3,6}$) is also visible for high values of $\nu_1(^{1}\text{H})$ from τ_c = 240 µs.

It is difficult to establish from Figure 8.10 any value of $\nu_1(^{1}\text{H})$ and $\nu_1(^{27}\text{Al})$ to any of the

other match conditions, but several intense features appear for weak $\nu_1(^1\mathrm{H})$ and strong $\nu_1(^{27}\mathrm{Al})$ can be observed, that have been assigned in Figure 8.8b to mainly $\omega_{3,4}$. The amounts of CT 1Q coherence observed are approximately identical between Figure 8.8b and Figure 8.10 in the regions that have been assigned to matches to $\omega_{1,2}$ and $\omega_{3,4}$ in Figure 8.8b. However, strong and positive features are more common in the region of the match condition to $\omega_{3,4}$ than to $\omega_{1,2}$ for $\nu_1(^{27}\mathrm{Al})$ > 80 kHz, while more strong and positive features can be observed for the region of the match condition to $\omega_{1,2}$ when $\nu_1(^{27}\mathrm{Al})$ < 80 kHz. This suggests that an efficient transfer could be obtained using a ramped CP pulse, choosing the region of $\omega_{1,2}$ or $\omega_{3,4}$ according to the RF field strength available for ^{27}Al.

8.2.5 Summary

This chapter illustrated the complexity of performing a CP experiment to a quadrupolar nucleus. Indeed, there are multiple nutation rates to which the RF field of ^{1}H / the spin I can be matched to, which depend significantly on the relative orientation of the quadrupolar interaction PAF and $\Sigma_{\mathrm{rot}}^{\times 2}$ for most of them, and which result in various amounts of different coherences on the spin S. Furthermore, one needs to consider the efficiency of the SL for the quadrupolar nucleus. The performed simulation provided new insight into the efficiency of a CP transfer to CT 1Q coherence, although it must be recalled that all of the simulations presented here assumed that no $T_{1\rho}$ relaxation takes place during the contact time, and that the quadrupolar spin S is coupled to only one spin I. This complexity will be even further increased if the two spins I and S are both quadrupolar.

First, the two extreme cases, when $\omega_Q \gg \omega_1$ and $\omega_Q \ll \omega_1$, have been discussed as a verification of literature predictions for the static case.[452] When $\omega_Q \gg \omega_1$, the match condition to $\omega_{1,2}$ results in almost pure CT 1Q coherence, and so does the match condition to the 1Q transitions of S (*i.e.*, $\omega_{1,2}$, $\omega_{2,3}$, $\omega_{3,4}$, $\omega_{4,5}$ and $\omega_{5,6}$) when $\omega_Q \ll \omega_1$. The case of intermediate C_Q is complicated, but it has been shown that matching $\omega_{1,2}$ results in significant amounts of CT 1Q coherence, still in the static case.

The problem becomes even more complex under MAS, which introduces a mixing of the states created in Σ_V under static conditions. This resulted in a large amount of CT 1Q coherence being observed for either spin $S = 3/2$ or spin $S = 5/2$ nuclei when matching to $\omega_{3,4}$ (or $\omega_{5,6}$) for the intermediate or large C_Q case. Moreover, MAS causes the match conditions to split into a large number of modified Hartmann-Hahn conditions. As such, the efficiency of CP when a ramped SL pulse is employed on ^{1}H / the spin I can also

be investigated in simulations to determined what would be, in practice, the efficiency of the transfer. The simulations shown can be used in experiment for initial guesses of suitable values for ν_{1_I} and ν_{1_S} for a CP transfer.

General conclusion

Despite a significant gain in popularity in the last twenty years, NMR of quadrupolar nuclei still remains the ”poor relation” of NMR spectroscopy. This is mainly due to the presence of the often strong quadrupolar interaction, that standard line-narrowing methods, such as MAS, are unable to completely suppress. Recording high-resolution NMR spectra of quadrupolar nuclei without dedicated hardware has only been made possible by the relatively recent introduction of the MQMAS experiment,[11] and subsequently, the STMAS experiment.[121] Nevertheless, the first experiment inherently present drastic sensitivity limitations, and the latter experiment is a significant challenge to experimentally implement. The challenge is further exacerbated by the poor natural abundance of many NMR-active isotopes, hence sometimes requiring expensive isotropic enrichment, which may not be possible at all in the case of natural samples. Efficient signal improvement methods for MQMAS or direct acquisition experiments, are a much more convenient and economical alternative, as many elements that are vital to explain the properties of compounds of scientific interest have only quadrupolar isotopes which would, otherwise, be impossible to observe by NMR spectroscopy.

The present work introduced a novel composite pulse scheme for the improvement of MQMAS experiments, termed FAM-N, based on a numerical optimisation routine, which possesses multiple advantages. The optimisation procedure allows a quick, single-parameter optimisation process, enabling its application after a minimum waiting time for the user. FAM-N consisting of a succession of rectangular pulses, the method is available for any spectrometer, even those that cannot easily handle complicated shaped pulses. FAM-N has been proven to be equally or more efficient than SPAM, FAM, and DFS (see Section 5.3), even when no optimisation on the spectrometer is conducted. There have been almost no cases for which FAM-N is less efficient than CW conversion. The robustness of FAM-N, *i.e.*, its efficiency when applied to systems

that have parameters differing from those used in the optimisation, have been shown to be very good, providing great flexibility in the systems to which it can be used (see Section 5.2). Simulations and experiments proved that the FAM-N pulse is applicable for any half-integer spin (see Section 5.2.3), for any MAS rate (see Section 5.1.3) and for samples with multiple sites (see Section 5.1.3). Furthermore, experiments on challenging samples have shown that, not only is FAM-N equally applicable on challenging samples, where no experimental optimisation is even possible, but also that FAM-N is particularly attractive in this case. As investigated in Section 5.1.2, the improvement relative to MQMAS recorded with CW conversion is higher for sites with large C_Q and at low RF field, which are precisely the sorts of systems on which a signal improvement method is most useful. For these reasons, we believe that FAM-N is a great addition to MQMAS, as it can extended the range of samples for which MQMAS is possible, thus filling the sensitivity gap with the challenging STMAS experiment.

There are several ways in which the FAM-N method can be further improved.

- Most of the investigations conducted here aimed to show the applicability and efficiency of FAM-N over the CW pulse in 3QMAS experiments. As explained in Section 6.2.1, 5QMAS, or MQMAS with higher orders, can be interesting on particular systems to increase the resolution of MQMAS spectra. However, this comes at a significant cost in terms of sensitivity compared to 3QMAS. Because of this, 5QMAS is often carried out only after 3QMAS experiments when the resolution of the latter is not sufficient. As shown in Section 6.2.1, FAM-N can be used to improve 5QMAS, but further investigation is necessary to determine whether the efficiency of FAM-N is still comparable to that of other methods, or whether the pulse scheme can be further improved by modifying the optimisation procedure. For example, 3QMAS could provide initial guesses for quadrupolar parameters, which can then be used for 5QMAS with FAM-N conversion adapted for the conversion of 5Q, improving the sensitivity of this latter approach.

- In its current form, the FAM-N optimisation program re-simulates completely all pulses that have been previously optimised. A possible efficiency improvement for the FAM-N optimisation program would be to modify the program in such a way that only the currently optimised pulse is being simulated. This could be achieved by obtaining the full density matrix at each point of the simulation, and then propagating from this at each new pulse inversion. Such an approach would allow simulations to run faster, or with a larger number of orientations. FAM-N has been

successfully tested for 3QMAS despite the use of a low number of 66 crystallite orientations and 4 γ-angles in the simulation, and few differences have been observed for FAM-N pulses optimised with a larger number of crystallites for the $p = \pm 3 \rightarrow \pm 1$. Nevertheless, increasing this number of crystallites would be interesting for a higher precision of the pulses of FAM-N, and more accurate theoretical improvement ratios.

- Throughout this work, a new FAM-N optimisation has been executed for every new set of experiments to account for the time-variation of the RF field strength. To avoid having to perform a new optimisation for each experiment or for different samples, a possible extension of the current concept would be to identify FAM-N pulses whose efficiency could be guaranteed over a wide range of experimental conditions. The origin of this idea comes from the band discussed in Section 5.1, Figure 5.1, showing the FAM-N efficiency to be approximately linked to the ν_1/ν_Q ratio for all spins I (see Equation (5.1.1)), showing that there might be some similarities between the FAM-N pulses optimised for these conditions. This idea is also used by Morais *et al.*,[325] where the simulated FAM-II schemes are expressed in executed nutation according to the ν_1/ν_Q ratio. Something similar could be established for FAM-N. As discussed in Section 5.1.3, the Larmor frequency ν_0 has little or no effect on FAM-N for standard conditions, the offset $\Delta\omega_0$ has a very limited impact on the FAM-N efficiency, and the asymmetry parameter η_Q and the MAS rate ν_R could perhaps be omitted in a first instance, leaving the ν_1/ν_Q ratio as the only parameter FAM-N is dependent on. The investigations conducted in Section 5.2.1 show that FAM-N remains efficient over a large range of C_Q and ν_1 values, and suggest that a series of 4-5 FAM-N pulses, expressed in achieved nutation, would be sufficient to describe most experimental conditions. This would remove the need for a new FAM-N simulation every time the experimental condition changes.

- For the purpose of sensitivity improvement for MQMAS, FAM-N has been proven to give satisfactory results under most experimental conditions. However, there are conditions under which the excitation pulse become the major source of sensitivity loss. For further sensitivity enhancement, the improvement of the excitation pulse, especially under fast MAS conditions, is logically the next step. Two existing approaches, RIACT and FASTER, have been evaluated in Section 4.2.2 and Section 7.2.3 with some success, but also several failures and inconsistencies. Further investigations are in order to guarantee that using one of these more

complex methods will result in a signal improvement compared to CW excitation, particularly at fast MAS. More recent approaches can also be included in this comparison, such as FASTER pulses optimised using optimal control,[330] or the recently introduced SFAM[7] pulse scheme.[304] The combination of any of these methods with FAM-N could also be investigated.

- FAM-N can also be adapted to enhance the $p = \pm 1 \rightarrow \pm 3$ transfer. It has been shown in simulations that a modulated pulse can be substituted in the SL excitation step of RIACT, increasing the efficiency of the transfer. Although essentially untested, this possibility has been implemented in the FAM-N optimisation program (see the parameter `cmpt.exc_conv` in Appendix I.2). Such an approach could potentially be used to solve the efficiency limitations of some MQMAS experiments, when performed under fast MAS.
- Finally, the relative specificity of FAM-N, examined in Section 5.2.2, could be used to selectively enhance certain sites, predicted in first-principles calculations, but not observed in experimental MQMAS spectra.

One of the other aspect investigated in this work is the improvement of the NMR signal for the CT of quadrupolar nuclei (see Chapter 7), where the use of HS pulses under fast MAS rates has been an important part. The investigations performed have proven that HS is equally applicable at either standard and fast MAS rates, with efficiencies on spins $I = 3/2$ and $I = 5/2$ nuclei approaching the theoretical maximum.

- One of the possible extensions to this work would be to analyse the efficiency of multiple-step HS for spin $I > 3/2$ nuclei. As shown in Section 7.2.2, the signal improvement observed for ^{27}Al on Al(acac)$_3$ slightly differs from the theoretical maximum of ×5 for spins $I = 5/2$, with ×3-4 being observed in experiments and simulations. To improve the CT signal further, the effect of two successive HS pulses, one applied on ST$_2$, followed by one applied on ST$_1$, could be assessed.
- The concept of the COMPACT pulse, presented in Section 7.1.4, as well as the pulse scheme proposed by O'Dell *et al.*,[415] obtained using optimal control, suggests that the FAM-N optimisation program could be adapted to produce pulses that enhance the CT signal. However, this last transfer may not be as interesting as the $p = \pm 3 \rightarrow \pm 1$ transfer for several reasons. HS, but also ssDFS and other PAAP schemes, already enable significant CT signal improvement, and their

[7] SFAM: *Shifted Fast-Amplitude Modulation*

optimisation can be reduced to one single parameter in the MAS case. In light of the signal enhancements given by COMPACT in Section 7.2.2, it is uncertain whether a similar or higher improvement would be possible. However, because it would only be composed of rectangular pulse, this pulse would be easier to implement. FAM-N applied for a transfer from population to CT 1Q coherence would be certainly quicker to numerically optimise than HS, but certainly slower than FASTER.

Finally, simulations of CP between $I = 1/2$ and $S > 1/2$ nuclei provided new insight into the description of CP from a spin $I = 1/2$ to a quadrupolar nucleus. In particular, it has been observed that MAS enables surprisingly large amounts of CT 1Q for cases of intermediate C_Q, when $\omega_{3,4}$ is matched.

- All of the simulations shown in Section 8.2 were performed with rectangular contact pulses. Considering that most of the matching conditions are orientation dependent, and thus appear over large ranges in ν_{1I} and ν_{1S}, simulations of the effect of a ramped CP pulse for ^{1}H / the spin I could be used to estimate the signal that would be obtained in experiments. This could result in some improvement of the efficiency of CP transfer, particularly when CP is performed under MAS.
- Finding efficient match conditions for the CP transfer to 3Q coherence rather than to CT 1Q coherence could be of considerable interest for the combination of CP with MQMAS. If 3Q coherence on the spin S can be directly created by CP, the combination with MQMAS would, as a result, be much easier, with only an additional $p = \pm 3 \rightarrow \pm 1$ conversion pulse being required. Moreover, this might permit higher sensitivity than an experiment composed of CP creating 1Q on the spin S, followed by MQMAS. If conditions for efficient CP transfer to 3Q coherence cannot be found, or are difficult to put into practice, the investigation of an efficient scheme for the $p = \pm 1 \rightarrow \pm 3$ transfer on spin S, could help in resolving some of the sensitivity issues of CP to quadrupolar nuclei. Finally, CP transfer to 3Q coherence or higher orders could also be investigated.

Throughout this manuscript, it has been demonstrated, as stated in the general introduction of this work, that NMR is a unique, powerful and versatile analytical technique, whose major limitation is, indeed, sensitivity. When quadrupolar nuclei are involved, the sensitivity issue of NMR is even greater, and the outcome of this work is such that

one can find experiments for samples previously out of reach. Combined with high magnetic field spectrometers, very fast MAS probes and DNP techniques becoming more widely accessible, signal improvement methods such as FAM-N and HS allow NMR to be extended to more challenging samples, enabling the extraction of NMR parameters and, hence, the properties of these materials to be solved.

一寸先は闇

”Issun saki wa yami.”

One inch ahead is darkness.

Japanese proverb

Appendices

”I dettagli fanno la perfezione e la perfezione non è un dettaglio.”

« Les détails font la perfection et la perfection n’est pas un détail.»

”Details make perfection and perfection is not a detail.”

Leonardo da Vinci / Léonard de Vinci

Appendix A

French abstract - Résumé

Titre :

Méthodes pour l'amélioration du signal des noyaux quadripolaires en résonnance magnétique nucléaire de l'état solide.

L'étude des noyaux quadripolaires par spectroscopie RMN a connu un gain de popularité considérable vers la fin du XX^{e} siècle, avec l'apparition de méthodes permettant l'acquisition de spectres soustraits de l'effet de l'interaction quadripolaire, qui provoque un élargissement significatif des formes de raie du signal RMN que la technique de giration à l'angle magique de l'échantillon (MAS) n'est pas capable de complètement supprimer, à l'inverse de la plupart des autres interactions en RMN. La première technique qui, sans besoin de matériel dédié, permit la suppression de cette interaction, fut l'expérience *Multiple-Quantum* (MQ)MAS. Celle-ci devint rapidement très populaire dans la communauté scientifique comme le montrent de nombreuses applications couronnées de succès dans la littérature. Cependant, la très inefficace filtration par les multiple-quanta, sur laquelle cette expérience est basée, impose des limitations drastiques en termes de signal, ce qui en restreint l'application aux noyaux les plus réceptifs.

L'utilisation de méthodes d'amélioration du signal s'avère donc nécessaire pour l'utilisation de la méthode MQMAS sur les noyaux peu actifs en RMN. De nombreuses méthodes publiées dans la littérature permettent cela, mais souvent au prix de processus d'optimisation très chronophages, voire impossibles dans le cas des noyaux

les moins sensibles. Ces recherches ont abouti à l'introduction d'un nouveau schéma d'impulsion composite pour l'amélioration du signal pour l'expérience MQMAS, baptisé FAM-N. Son optimisation étant uniquement basée sur des simulations de l'évolution de l'opérateur densité, effectuées sous SIMPSON, aucune optimisation sur le spectrométre ne s'est avèrée nécessaire pour obtenir une amélioration du signal égale, voire supérieure, à celles produites par d'autres méthodes très courantes. Afin de prouver la validité de l'approche pour virtuellement n'importe quel système, FAM-N a été étudié par simulation et testé sur un grand nombre d'échantillons modèles, ainsi que sur des échantillons connus pour être difficiles à observer par RMN.

Ces recherches portent également sur plusieurs autres aspects de la RMN des noyaux quadripolaires. L'inversion adiabatique des populations satellites est une approche courante pour améliorer le signal de la transition central des spectres RMN. Un éventail de différentes méthodes a été étudié, et une attention particulière a été portée aux impulsions de forme sécante hyperbolique, dont les performances ont été analysées. Finalement, de nouveaux élements sur la technique de polarisation croisée entre un spin $I = 1/2$ et un noyau quadripolaire a été introduits. Après une revue de la théorie dans le cas statique, des simulations ont été effectuées sous MAS afin de d'identifier les conditions permettant des transferts efficaces d'aimantation entre les deux noyaux, avec pour but l'édition spectrale ou la combinaison avec MQMAS.

Appendix B

Useful elements for NMR theory

B.1 Representation of Pauli's spin matrices

This appendix gives Pauli's spin matrices for all half-integer spins up to spin $I = 9/2$.[58] As given in Section 1.2.1, Pauli's matrices are related to the spin observables along the direction $k = x$, y, or z, according to the equation

$$\hat{I}_k = \frac{\hbar}{2}\sigma_k \quad . \tag{B.1.1}$$

Spin 1/2

$$\sigma_x = \begin{bmatrix} 0 & 1 \\ 1 & 0 \end{bmatrix} \qquad \sigma_y = \begin{bmatrix} 0 & -i \\ i & 0 \end{bmatrix} \qquad \sigma_z = \begin{bmatrix} 1 & 0 \\ 0 & -1 \end{bmatrix}$$

Spin 3/2

$$\sigma_x = \begin{bmatrix} 0 & \sqrt{3} & 0 & 0 \\ \sqrt{3} & 0 & 2 & 0 \\ 0 & 2 & 0 & \sqrt{3} \\ 0 & 0 & \sqrt{3} & 0 \end{bmatrix} \qquad \sigma_y = \begin{bmatrix} 0 & -i\sqrt{3} & 0 & 0 \\ i\sqrt{3} & 0 & -2i & 0 \\ 0 & 2i & 0 & -i\sqrt{3} \\ 0 & 0 & i\sqrt{3} & 0 \end{bmatrix}$$

$$\sigma_z = \begin{bmatrix} 3 & 0 & 0 & 0 \\ 0 & 1 & 0 & 0 \\ 0 & 0 & -1 & 0 \\ 0 & 0 & 0 & -3 \end{bmatrix}$$

Spin 5/2

$$\sigma_x = \begin{bmatrix} 0 & \sqrt{5} & 0 & 0 & 0 & 0 \\ \sqrt{5} & 0 & \sqrt{8} & 0 & 0 & 0 \\ 0 & \sqrt{8} & 0 & 3 & 0 & 0 \\ 0 & 0 & 3 & 0 & \sqrt{8} & 0 \\ 0 & 0 & 0 & \sqrt{8} & 0 & \sqrt{5} \\ 0 & 0 & 0 & 0 & \sqrt{5} & 0 \end{bmatrix}$$

$$\sigma_y = \begin{bmatrix} 0 & -i\sqrt{5} & 0 & 0 & 0 & 0 \\ i\sqrt{5} & 0 & -i\sqrt{8} & 0 & 0 & 0 \\ 0 & i\sqrt{8} & 0 & -3i & 0 & 0 \\ 0 & 0 & 3i & 0 & -i\sqrt{8} & 0 \\ 0 & 0 & 0 & i\sqrt{8} & 0 & -i\sqrt{5} \\ 0 & 0 & 0 & 0 & i\sqrt{5} & 0 \end{bmatrix}$$

$$\sigma_z = \begin{bmatrix} 5 & 0 & 0 & 0 & 0 & 0 \\ 0 & 3 & 0 & 0 & 0 & 0 \\ 0 & 0 & 1 & 0 & 0 & 0 \\ 0 & 0 & 0 & -1 & 0 & 0 \\ 0 & 0 & 0 & 0 & -3 & 0 \\ 0 & 0 & 0 & 0 & 0 & -5 \end{bmatrix}$$

Spin 7/2

$$\sigma_x = \begin{bmatrix} 0 & \sqrt{7} & 0 & 0 & 0 & 0 & 0 & 0 \\ \sqrt{7} & 0 & 2\sqrt{3} & 0 & 0 & 0 & 0 & 0 \\ 0 & 2\sqrt{3} & 0 & \sqrt{15} & 0 & 0 & 0 & 0 \\ 0 & 0 & \sqrt{15} & 0 & 4 & 0 & 0 & 0 \\ 0 & 0 & 0 & 4 & 0 & \sqrt{15} & 0 & 0 \\ 0 & 0 & 0 & 0 & \sqrt{15} & 0 & 2\sqrt{3} & 0 \\ 0 & 0 & 0 & 0 & 0 & 2\sqrt{3} & 0 & \sqrt{7} \\ 0 & 0 & 0 & 0 & 0 & 0 & \sqrt{7} & 0 \end{bmatrix}$$

$$\sigma_y = \begin{bmatrix} 0 & i\sqrt{7} & 0 & 0 & 0 & 0 & 0 & 0 \\ -i\sqrt{7} & 0 & -2i\sqrt{3} & 0 & 0 & 0 & 0 & 0 \\ 0 & 2i\sqrt{3} & 0 & -i\sqrt{15} & 0 & 0 & 0 & 0 \\ 0 & 0 & i\sqrt{15} & 0 & -4i & 0 & 0 & 0 \\ 0 & 0 & 0 & 0 & 4i & 0 & -i\sqrt{15} & 0 \\ 0 & 0 & 0 & 0 & i\sqrt{15} & 0 & -2i\sqrt{3} & 0 \\ 0 & 0 & 0 & 0 & 0 & 2i\sqrt{3} & 0 & -i\sqrt{7} \\ 0 & 0 & 0 & 0 & 0 & 0 & i\sqrt{7} & 0 \end{bmatrix}$$

$$\sigma_z = \begin{bmatrix} 7 & 0 & 0 & 0 & 0 & 0 & 0 & 0 \\ 0 & 5 & 0 & 0 & 0 & 0 & 0 & 0 \\ 0 & 0 & 3 & 0 & 0 & 0 & 0 & 0 \\ 0 & 0 & 0 & 1 & 0 & 0 & 0 & 0 \\ 0 & 0 & 0 & 0 & -1 & 0 & 0 & 0 \\ 0 & 0 & 0 & 0 & 0 & -3 & 0 & 0 \\ 0 & 0 & 0 & 0 & 0 & 0 & -5 & 0 \\ 0 & 0 & 0 & 0 & 0 & 0 & 0 & -7 \end{bmatrix}$$

Spin 9/2

$$\sigma_x = \begin{bmatrix} 0 & 3 & 0 & 0 & 0 & 0 & 0 & 0 & 0 & 0 \\ 3 & 0 & 4 & 0 & 0 & 0 & 0 & 0 & 0 & 0 \\ 0 & 4 & 0 & \sqrt{21} & 0 & 0 & 0 & 0 & 0 & 0 \\ 0 & 0 & \sqrt{21} & 0 & 2\sqrt{6} & 0 & 0 & 0 & 0 & 0 \\ 0 & 0 & 0 & 2\sqrt{6} & 0 & 5 & 0 & 0 & 0 & 0 \\ 0 & 0 & 0 & 0 & 5 & 0 & 2\sqrt{6} & 0 & 0 & 0 \\ 0 & 0 & 0 & 0 & 0 & 2\sqrt{6} & 0 & \sqrt{21} & 0 & 0 \\ 0 & 0 & 0 & 0 & 0 & 0 & \sqrt{21} & 0 & 3 & 0 \\ 0 & 0 & 0 & 0 & 0 & 0 & 0 & 4 & 0 & 3 \\ 0 & 0 & 0 & 0 & 0 & 0 & 0 & 0 & 4 & 0 \end{bmatrix}$$

$$\sigma_y = \begin{bmatrix} 0 & -3i & 0 & 0 & 0 & 0 & 0 & 0 & 0 & 0 \\ 3 & 0 & -4i & 0 & 0 & 0 & 0 & 0 & 0 & 0 \\ 0 & 4 & 0 & -i\sqrt{21} & 0 & 0 & 0 & 0 & 0 & 0 \\ 0 & 0 & \sqrt{21} & 0 & -2i\sqrt{6} & 0 & 0 & 0 & 0 & 0 \\ 0 & 0 & 0 & 2\sqrt{6} & 0 & -5 & 0 & 0 & 0 & 0 \\ 0 & 0 & 0 & 0 & 5 & 0 & -2i\sqrt{6} & 0 & 0 & 0 \\ 0 & 0 & 0 & 0 & 0 & 2\sqrt{6} & 0 & -i\sqrt{21} & 0 & 0 \\ 0 & 0 & 0 & 0 & 0 & 0 & \sqrt{21} & 0 & -3i & 0 \\ 0 & 0 & 0 & 0 & 0 & 0 & 0 & 4 & 0 & -3i \\ 0 & 0 & 0 & 0 & 0 & 0 & 0 & 0 & 4 & 0 \end{bmatrix}$$

$$\sigma_z = \begin{bmatrix} 9 & 0 & 0 & 0 & 0 & 0 & 0 & 0 & 0 & 0 \\ 0 & 7 & 0 & 0 & 0 & 0 & 0 & 0 & 0 & 0 \\ 0 & 0 & 5 & 0 & 0 & 0 & 0 & 0 & 0 & 0 \\ 0 & 0 & 0 & 3 & 0 & 0 & 0 & 0 & 0 & 0 \\ 0 & 0 & 0 & 0 & 1 & 0 & 0 & 0 & 0 & 0 \\ 0 & 0 & 0 & 0 & 0 & -1 & 0 & 0 & 0 & 0 \\ 0 & 0 & 0 & 0 & 0 & 0 & -3 & 0 & 0 & 0 \\ 0 & 0 & 0 & 0 & 0 & 0 & 0 & -5 & 0 & 0 \\ 0 & 0 & 0 & 0 & 0 & 0 & 0 & 0 & -7 & 0 \\ 0 & 0 & 0 & 0 & 0 & 0 & 0 & 0 & 0 & -9 \end{bmatrix}$$

B.2 Rotating matrices and operators

The rotation of a vector $\vec{r}$ of the $\mathbb{R}^3$ space by an angle ϕ_R around an axis defined by a unit vector $\vec{u}_R$, in the general case, can be written as [456]

$$\vec{r}' = \cos\phi_R.\vec{r} + (1 - \cos\phi_R)(\vec{r}.\vec{u}_R).\vec{u}_R + \sin\phi_R.\vec{r} \wedge \vec{u}_R \quad , \tag{B.2.1}$$

where $\vec{r}'$ is the rotated vector. In the case relevant to Section 1.1, where the rotation goes around $\vec{u}_z$ and the plane $(\vec{u}_x, \vec{u}_y)$ is complex, the rotated vector becomes

$$\vec{r}' = \exp(i\phi_R).\vec{r} \quad . \tag{B.2.2}$$

Although Equation (B.2.1) shows that a rotation can be expressed with a single angle ϕ_R, it is often more convenient to express the rotation around the base vector. In a orthonormal Cartesian base $(\vec{u}_x, \vec{u}_y, \vec{u}_z)$, two rotation angles are necessary to describe any possible rotation, often termed θ and ϕ called the spherical angle (as used in Section 1.1).[457] A vector in a spherical frame defined by $\vec{u}_\xi$ is given by

$$\vec{r} = r.\vec{u}_\xi \tag{B.2.3a}$$

$$= r\cos\theta\sin\phi.\vec{u}_x + r\sin\theta\sin\phi.\vec{u}_y + r\cos\phi\vec{u}_z \tag{B.2.3b}$$

A rotation between two frames is more conveniently written under the form of an order-two matrix R, representing the base vectors expressed in one base expressed in another. The relation between $\vec{u}'_R$ and $\vec{u}_R$ becomes

$$\vec{u}'_R = R.\vec{u}_R \quad , \tag{B.2.4}$$

with

$$R = \begin{array}{c} \\ \vec{u}_x \\ \vec{u}_y \\ \vec{u}_y \end{array} \begin{array}{c} \begin{array}{ccc} \vec{u}'_x & \vec{u}'_y & \vec{u}'_z \end{array} \\ \begin{bmatrix} R_{xx'} & R_{xy'} & R_{yz'} \\ R_{yx'} & R_{yy'} & R_{yz'} \\ R_{zx'} & R_{zy'} & R_{zz'} \end{bmatrix}_n \end{array} \quad , \tag{B.2.5}$$

$\{\vec{u}'_x, \vec{u}'_y, \vec{u}'_z\}$ being the rotated base. The elements R_{ij} are undetermined for any rotation, but in the special case of a rotation of ϕ_R around one of the basis vectors, R can be written

$$R_x(\phi_R) = \begin{bmatrix} 1 & 0 & 0 \\ 0 & \cos\phi_R & -\sin\phi_R \\ 0 & \sin\phi_R & \cos\phi_R \end{bmatrix} \quad , \tag{B.2.6a}$$

$$R_x(\phi_R) = \begin{bmatrix} \cos\phi_R & 0 & \sin\phi_R \\ 0 & 1 & 0 \\ -\sin\phi_R & & \cos\phi_R \end{bmatrix} \quad , \tag{B.2.6b}$$

$$R_z(\phi_R) = \begin{bmatrix} \cos\phi_R & -\sin\phi_R & 0 \\ \sin\phi_R & \cos\phi_R & 0 \\ 0 & 0 & 1 \end{bmatrix} \quad . \tag{B.2.6c}$$

The rotation matrix R is associated with a rotation operator $\hat{R}$. The rotation of a vector as written in Equation (B.2.4) is still valid in the quantum formalism introduced in Chapter 1.2. Operators can be rotated using

$$\hat{A}_\rho = \hat{R}^{-1}.\hat{A}.\hat{R} \quad , \tag{B.2.7}$$

with $\hat{A}_\rho$ being the rotated operator, and $\hat{R}^{-1}$ referring to the operator executing the opposite rotation of $\hat{R}$, *i.e.*,

$$\hat{R}^{-1}(\phi_R) = \hat{R}^{\dagger *}(\phi_R) = \hat{R}(-\phi_R) \quad . \tag{B.2.8}$$

The case of the rotation of the magnetic momentum observables $\{\hat{I}_x, \hat{I}_y, \hat{I}_z\}$ is especially interesting, as the rotation operators can be proven to be equal to [37]

$$\begin{aligned} \hat{R}_x(\phi_R) &= \exp\left(-\frac{i}{\hbar}\phi_R \hat{I}_x\right) \\ \hat{R}_y(\phi_R) &= \exp\left(-\frac{i}{\hbar}\phi_R \hat{I}_y\right) \\ \hat{R}_z(\phi_R) &= \exp\left(-\frac{i}{\hbar}\phi_R \hat{I}_z\right) \quad . \end{aligned} \tag{B.2.9}$$

It follows that, if $\hat{I}_1$, $\hat{I}_2$ and $\hat{I}_3$ are any of the three components of $\hat{I}$ that verify the equation

$$\left[\hat{I}_1, \hat{I}_2\right] = i\hbar\hat{I}_3 \quad , \tag{B.2.10}$$

then

$$\exp\left(+\frac{i}{\hbar}\phi_R\hat{I}_1\right).\hat{I}_2.\exp\left(-\frac{i}{\hbar}\phi_R\hat{I}_1\right) = \hat{I}_2.\cos\phi_R + \hat{I}_3.\sin\phi_R \quad . \tag{B.2.11}$$

B.3 Euler angles

In this section, the convention changes and the previously defined θ and ϕ angles are now α and β, respectively. To describe the rotation of an object in space, such as a tensor, a third angle, γ, must be added to the two angles α and β defined previously, which allows a "spinning" of the object around any given axis defined by α and β. Euler angles refer to the set of three angles (α, β, γ) that are used to define the rotation of one frame compared to another, by three successive angles α β and γ. Steps of the rotation are shown in Figure B.1. Starting from an initial frame $(O, \vec{u}_x, \vec{u}_y, \vec{u}_z)$ represented a Figure B.1

1 Figure B.1b: Precession by an angle α around $\vec{u}_z$, giving an intermediate rotated frame $(O, \vec{u}_u, \vec{u}_v, \vec{u}_z)$,
2 Figure B.1c: Nutation by an angle β around $\vec{u}_u$, giving an intermediate rotated frame $(O, \vec{u}_u, \vec{u}_w, \vec{u}_{z'})$,
3 Figure B.1d: Gyration by an angle γ around $\vec{u}_{z'}$, giving the final rotated frame $(O, \vec{u}_{x'}, \vec{u}_{y'}, \vec{u}_{z'})$.

The final frame is represented Figure B.1e. The total rotation can be defined as the successive application of three rotation matrices according to

$$\hat{R}(\alpha, \beta, \gamma) = \hat{R}_{z'}(\gamma).\hat{R}_u(\beta).\hat{R}_z(\alpha) \quad , \tag{B.3.1}$$

where each individual matrix is defined as

$$R_z(\alpha) = \begin{bmatrix} \cos\alpha & -\sin\alpha & 0 \\ \sin\alpha & \cos\alpha & 0 \\ 0 & 0 & 1 \end{bmatrix} \quad , \tag{B.3.2a}$$

$$R_u(\beta) = \begin{bmatrix} 1 & 0 & 0 \\ 0 & \cos\beta & -\sin\beta \\ 0 & \sin\beta & \cos\beta \end{bmatrix} \quad , \tag{B.3.2b}$$

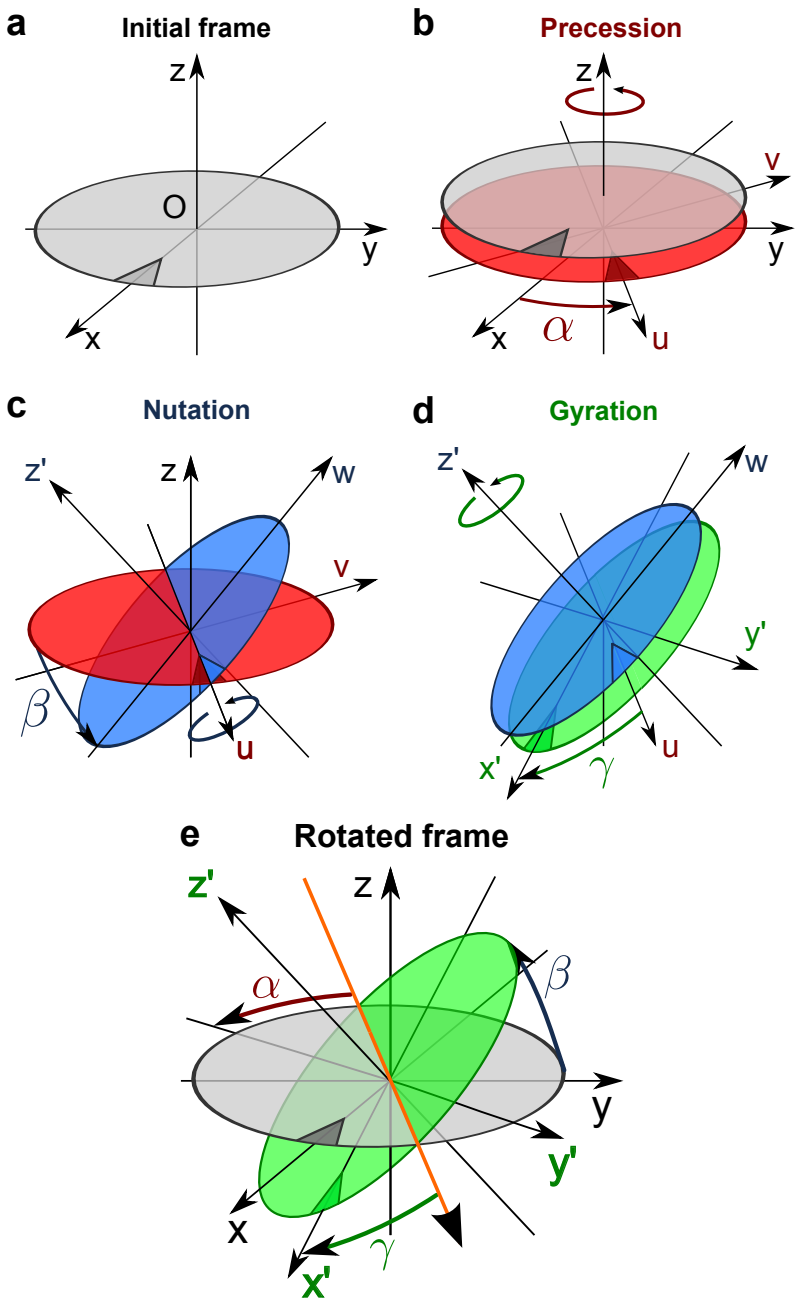

Figure B.1: ***(a)****: Initial frame,* ***(b)****: frame formed after a rotation of α around $\vec{u}_z$ (precession),* ***(c)****: of β around $\vec{u}_u$ (nutation), and* ***(d)****: of γ around $\vec{u}_{z'}$ (gyration).* ***(e)****: Representation of the rotated frame relative to the initial frame.*

$$R_{z'}(\gamma) = \begin{bmatrix} \cos\gamma & -\sin\gamma & 0 \\ \sin\gamma & \cos\gamma & 0 \\ 0 & 0 & 1 \end{bmatrix} \quad . \tag{B.3.2c}$$

It should be noted that other definitions of the Euler angles exist. Some of them simply define the three rotations described previously relative to other axis than the (z, u, z') axis used here, and some use indirect frames, meaning that the angles defined here would be oppositely signed in this later convention.

B.4 Reduced Wigner rotation matrix elements

Wigner's rotation d-matrices relevant for this work are introduced in this appendix. From Equation (2.1.12), the d-matrix relates to Wigner's D-matrices according to

$$D^l_{m,m'}(\alpha,\beta,\gamma) = \exp(-im'\alpha).d^{(l)}_{m,m'}(\beta).\exp(-im\gamma) \quad , \tag{B.4.1}$$

where $m, m' \in \mathbb{I}^2$, and α, β and γ are the Euler angles described in Appendix B.3. These quantities as defined here are used by several authors,[458–460] but some others use their transconjugate instead.[118, 461] It can be noted the following properties

$$d^{(l)}_{m,m'} = d^{(l)}_{m',m} \tag{B.4.2a}$$

$$= d^{(l)}_{l-m,m'} \tag{B.4.2b}$$

$$= d^{(l)}_{m,l-m'} \quad . \tag{B.4.2c}$$

The first-order, second-order and a selection of fourth-order order d-matrices are reported in Table B.1, Table B.3 and Table B.2, respectively.

		m		
		1	0	-1
m'	1	$^1/_2\,(1+\cos\beta)$	$^1/\sqrt{2}\sin\beta$	$^1/_2\,(1-\cos\beta)$
	0	$^1/\sqrt{2}\sin\beta$	$\cos\beta$	$^1/\sqrt{2}\sin\beta$
	-1	$^1/_2\,(1-\cos\beta)$	$^1/\sqrt{2}\sin\beta$	$^1/_2\,(1+\cos\beta)$

Table B.1: *Order-1 reduced Wigner d-matrices.*

		m
		0
m'	4	$\sqrt{70}/128\,(\cos 4\beta - 4\cos 2\beta + 3)$
	2	$-\sqrt{10}/128\,(14\cos 4\beta - 8\cos 2\beta - 6)$
	0	$^1/_8\left(35\cos^4\beta + 30\cos^2\beta + 3\right)$
	-2	$-\sqrt{10}/128\,(14\cos 4\beta - 8\cos 2\beta - 6)$
	-4	$\sqrt{70}/128\,(\cos 4\beta - 4\cos 2\beta + 3)$

Table B.2: *Selection of order-4 reduced Wigner d-matrices.*

m' \ m	2	1	0	−1	−2
2	$^1/_4(1+\cos\beta)^2$	$-^1/_2(1+\cos\beta)\sin\beta$	$\sqrt{^3/_8}\sin^2\beta$	$-^1/_2(1-\cos\beta)\sin\beta)$	$^1/_4(1-\cos\beta)^2$
1	$^1/_2(1+\cos\beta)\sin\beta$	$\left(\cos^2\beta-^1/_2(1-\cos\beta)\right)$	$-\sqrt{^3/_8}\sin 2\beta$	$\left(^1/_2(1+\cos\beta)-\cos^2\beta\right)$	$^1/_2(1-\cos\beta)\sin\beta$
0	$-\sqrt{^3/_8}\sin^2\beta$	$\sqrt{^3/_8}\sin 2\beta$	$^1/_2\left(3\cos^2\beta-1\right)$	$-\sqrt{^3/_8}\sin 2\beta$	$-\sqrt{^3/_8}\sin^2\beta$
−1	$^1/_2(1-\cos\beta)\sin\beta$	$\left(^1/_2(1+\cos\beta)-\cos^2\beta\right)$	$\sqrt{^3/_8}\sin 2\beta$	$\left(\cos^2\beta-^1/_2(1-\cos\beta)\right)$	$^1/_2(1+\cos\beta)\sin\beta$
−2	$^1/_4(1-\cos\beta)^2$	$-^1/_2(1-\cos\beta)\sin\beta)$	$\sqrt{^3/_8}\sin^2\beta$	$-^1/_2(1+\cos\beta)\sin\beta)$	$^1/_4(1+\cos\beta)^2$

Table B.3: *Order-2 reduced Wigner d-matrices*

Appendix C

Samples and experimental details

Introduction

This appendix contains useful additional informations about the content of this thesis, such as technical details about the spectrometers used to record the experiments (Appendix C.1), the different nuclei and samples investigated (Appendix C.2), and extended figure captions giving more details about the experiments and simulation presented (Appendix C.3), describing more in detail the acquisition or simulation and processing parameters that has been used for figures shown in the main text or other appendices.

C.1 Spectrometers and probes

All the solid-state NMR spectra presented in this work were recorded using one of the spectrometers and the probes presented below. All samples were packed into standard zirconia MAS rotors. The maximum MAS rate available for each rotor size is given in Table C.1.

1 Bruker Avance III spectrometer equipped with wide-bore superconducting magnet with B_0 = 14.1 T (ν_0 = 600 MHz for ^{1}H) from the university of St Andrews. The probes used on this spectrometer were

   (a) Bruker 4 mm WB HX probe

Rotor diameter	Typical max. MAS rate	Typical sample volume
7 mm	5 to 8 kHz	200 to 400 µl
4 mm	10 to 15 kHz	60 to 80 µl
3.2 mm	20 to 24 kHz	∼30 µl
2.5 mm	30 to 35 kHz	∼10 µl
1.9 mm	40 to 45 kHz	∼4 µl
1.3 mm	50 to 60 kHz	∼2 µl
1 mm	60 to 80 kHz	∼0.7 µl

Table C.1: *Table showing typical maximum MAS rates achievable and sample enclosing volume for rotors of different diameter.*

(b) Bruker ”new” 4 mm WB HX probe
(c) Bruker 4 mm low-γ WB HX probe
(d) Bruker 4 mm WB HXY probe
(e) Bruker 3.2 mm WB HX probe
(f) Bruker 2.5 mm mm WB HX probe
(g) Bruker 1.9 mm mm WB HX probe
(h) Bruker 1.3 mm mm WB HX probe

2 Bruker Avance II spectrometer equipped with wide-bore superconducting magnet with B_0 = 9.4 T (ν_0 = 400 MHz for ^{1}H) from the university of St Andrews. The probes used on this spectrometer were

(a) Bruker 4 mm WB HX probe
(b) Bruker ”new” 4 mm WB HX probe
(c) Bruker 1.9 mm WB HX probe

3 Bruker Avance III spectrometer equipped with wide-bore superconducting magnet with B_0 = 20.0 T (ν_0 = 850 MHz for ^{1}H) from the UK NMR national facility in Coventry. The probes used on this spectrometer were

(a) Bruker 4 mm WB HX probe
(b) Bruker 4 mm low-γ WB HX probe
(c) Jeol 1 mm WB HX probe

4 Bruker Avance III spectrometer equipped with narrow-bore superconducting magnet with B_0 field strength of 18.8 T (^{1}H Larmor frequency of 800 MHz) from the University of Lille. The only probe used on this spectrometer was a Bruker 3.2 mm NB HX probe.

C.2 Samples

This section details the main characteristics of recorded nuclei (sorted by number of masses) and recorded samples. Spin quantum numbers I, gyromagnetic ratios and natural abundances were obtained from Harris *et al.*[50] Most typical C_{Q} values for each element were quoted from Wasylishen *et al.*,[100] Table 2.1. The same source precise that any actual value for C_{Q} would not differ from this value by more than a ratio of 3-4. Quadrupole moments were obtained from Pyykkö.[462] The reference compounds and reference chemical shifts used are given on a case-by-case basis, but most were obtained from MacKenzie and Smith.[40]

Recorded in $^{17}0$

Spin: $I = 5/2$

Gyromagnetic ratio: -5.77 MHz.T^{-1}

Natural abundance: 0.038%

Quadrupole moment: -2.558×10^{-30} m^2

Typical C_{Q}: 7 MHz

Reference sample: $H_2O_{(l)}$ or $D_2O_{(l)}$, peak at 0 ppm [40, 50]

SIZ-4 / AlPO-34 (calcined)

Raw formula: N/A

Reference: Griffin *et al.* [274]

Origin: Home-made as described in [274]

Enrichment: $\sim$10%

Remark: Quadrupolar parameters are here reported for the four sites of dried SIZ-4. Quadrupolar parameters for wet SIZ-4, as recorded and presented in Section 5.3.2, Figure 5.12b, are not perfectly determined.

Site	δ_{CS} (ppm)	C_{Q} /MHz	η_Q
O 1	61.7	6.37	0.1
O 2	50.7	6.45	0.11
O 3	52.2	6.48	0.11
O 4	63.7	6.32	0.7

Recorded in ^{23}Na

Spin: $I = 3/2$

Gyromagnetic ratio: -11.26 MHz.T^{-1}

Natural abundance: 100%

Quadrupole moment: 10.4×10^{-30} m^2

Typical C_Q: 2 MHz

Reference sample: $NaCl_{(s)}$, peak at -7.9 ppm [266]

Sodium pyrophosphate

Raw formula: $Na_4P_2O_7$

Reference: Engelhardt *et al.* [199]

Origin: Alfa Aesar, reference *7758-29-4*.

Site	δ_{CS} (ppm)	C_Q /MHz	η_Q
Na 1	-1.69	2.08	0.26
Na 2	3.20	2.90	0.47
Na 3	-5.25	2.30	0.70
Na 4	-0.85	3.22	0.56

Recorded in ^{25}Mg

Spin: $I = 5/2$

Gyromagnetic ratio: -2.60 MHz.T^{-1}

Natural abundance: 10.0%

Quadrupole moment: 19.94×10^{-30} m^2

Typical C_Q: 5 MHz [1]

Reference sample: $MgO_{(s)}$, peak to 26 ppm [365, 463]

Brucite

Raw formula: $Mg(OH)_2$

Reference: Bastow,[347] Pallister *et al.* [365]

Origin: Home-made

[1] Typical value non-existent in [100] for ^{25}Mg, estimated from [40] instead.

Site	δ_{CS} (ppm)	C_{Q} /MHz	η_Q
Mg 1	-14.1	3.056	0

Enstatite

Raw formula: $MgSiO_3$

Reference: Griffin *et al.* [348]

Origin: Home-made

Remark: Three polymorphs for $MgSiO_3$ have been identified and investigated by Griffin *et al.*[348] Here are only approximative values, sufficient for FAM-N optimisations.

Site	δ_{CS} (ppm)	C_{Q} /MHz	η_Q
Mg 1	~ 8	~ 3	~ 0.6
Mg 2	~ 8	~ 14	~ 0.2

Forsterite

Raw formula: Mg_2SiO_4

Reference: Derighetti *et al.* [356]

Origin: From collaborator

Site	δ_{CS} (ppm)	C_{Q} /MHz	η_Q
Mg 1	N/D	4.313	0.396
Mg 2	N/D	4.996	0.943

Recorded in ^{27}Al

Spin: $I = 5/2$

Gyromagnetic ratio: 11.09 MHz.T^{-1}

Natural abundance: 100%

Quadrupole moment: 14.66×10^{-30} m^2

Typical C_{Q}: 1 to 20 MHz

Reference sample: $Al(acac)_3$, left horn to -1.1 ppm at B_0 = 14.1 T, centre of gravity to -5.2 ppm at B_0 = 9.4 T.

Aluminum acetylacetonate, or Al(acac)$_3$

Raw formula: $Al(C_5H_7O_2)_3$
Reference: Schurko *et al.* [464]
Origin: Sigma-Aldrich, reference 208248

Site	δ_{CS} (ppm)	C_Q /MHz	η_Q
Al 1	N/D	3.0	0.15

Kyanite

Raw formula: Al_2SiO_5
Reference: Alemany *et al.* [334], Lee and Bray [465]
Origin: From collaborator
Remark: Sites are sorted by increasing values of C_Q for this sample.

Site	δ_{CS} (ppm)	C_Q /MHz	η_Q
Al 1	4.0	3.8	0.85
Al 2	5.7	6.4	0.70
Al 3	5.9	9.2	0.38
Al 4	13.0	10.1	0.27

Andalusite

Raw formula: Al_2SiO_5
Reference: Bryant *et al.*,[206] Hafner *et al.* [346]
Origin: From collaborator
Remark: As observed by Gan *et al.*,[136] third-order quadrupolar interaction effects are present for this sample in ^{27}Al.

Site	δ_{CS} (ppm)	C_Q /MHz	η_Q
Al 1	N/D	5.9	0.7
Al 2	N/D	15.6	0.08

Recorded in ^{39}K

Spin: $I = 3/2$
Gyromagnetic ratio: 1.99 MHz.T^{-1}
Natural abundance: 100 %
Quadrupole moment: 5.85×10^{-30} m^2
Typical C_Q: 1 MHz
Reference sample: $KBr_{(s)}$, maximum at 55.1 ppm [466]

Potassium sulphate

Raw formula: K_2SO_4
Reference: Bastow,[347] Dowell *et al.* [254]
Origin: Sigma-Aldrich, reference P0772

Site	δ_{CS} (ppm)	C_Q /MHz	η_Q
K 1	N/D	0.958	0.27
K 2	N/D	0.864	0.90

Recorded in ^{45}Sc

Spin: $I = 7/2$
Gyromagnetic ratio: 10.34 MHz.T^{-1}
Natural abundance: 100%
Quadrupole moment: -22.0×10^{-30} m^2
Typical C_Q: 3 MHz
Reference sample: $LaScO_{4(s)}$, maximum at 162 ppm [467]
Remark: Despite the C_Q of $LaScO_{4(s)}$ not being zero, no significant SOQE on the lineshape are visible at 9.4 T or 14.1 T at regular RF strength. Furthermore, no significant difference on the RF calibration have been observed on

Scandium oxide

Raw formula: Sc_2O_3
Reference: Kim *et al.* [339]

Origin: Sigma-Aldrich, reference *307874*

Site	δ_{CS} (ppm)	C_{Q} /MHz	η_Q
Sc 1	108.0	23.4	0.02
Sc 2	128.2	15.3	0.63

Recorded in ^{71}Ga

Spin: $I = 3/2$

Gyromagnetic ratio: 10.22 MHz.T^{-1}

Natural abundance: 39.89 %

Quadrupole moment: 10.7×10^{-30} m^2

Typical C_{Q}: 150 MHz

Reference sample: $Ga_2(SO_4)_3$, peak to −87 ppm [345]

$GaPO_4$ berlinite

Raw formula: $GaPO_4$

Reference: Amri *et al.* Supporting information [344]

Origin: Home-made according to Dawson [42]

Site	δ_{CS} (ppm)	C_{Q} / MHz	η_Q
Ga 1	111	8.8	0.5

Recorded in ^{85}Rb

Spin: $I = 5/2$

Gyromagnetic ratio: 4.11 MHz.T^{-1}

Natural abundance: 72.17%

Quadrupole moment: 27.6×10^{-30} m^2

Typical C_{Q}: 20 MHz [2]

Reference sample: $RbCl_{(s)}$, peak at +123 ppm [45]

Remark: All samples recorded in ^{85}Rb are those described in the section on ^{87}Rb. ^{85}Rb quadrupolar parameters can be obtained by multiplying the C_Q values for ^{87}Rb by ×2.07.

Recorded in ^{87}Rb

Spin: $I = 3/2$

Gyromagnetic ratio: 13.98 MHz.T^{-1}

Natural abundance: 27.84%

Quadrupole moment: 13.35×10^{-30} m^2

Typical C_Q: 10 MHz [2]

Reference sample: $RbCl_{(s)}$, peak at +128 ppm [45]

Remark: ^{87}Rb, as well as ^{85}Rb, is know from Skibsted and Jakobsen to have temperature dependant chemical shifts and quadrupolar parameters.[468] Non of the ^{87}Rb NMR spectra presented in this work have been recorded using controlled temperature, so variation of the lineshape positions between experiments recorded on different days are normal and to be expected. No significant variations should be observed on spectra during a same NMR time slot.

Rubidium chlorate

Raw formula: $RbClO_4$

Reference: Cheng *et al.* [45]

Origin: Alfa Aesar, reference 11628

Site	δ_{CS} (ppm)	C_Q /MHz	η_Q
Rb 1	3.8	3.2	0.16

Rubidium nitrate

Raw formula: $RbNO_3$

Reference: Skibsted and Jakobsen [468]

Origin: Sigma-Aldrich, reference 289299

Remark: $T_1 = T_2 \simeq 70$ ms

[2] These are the values tabulated in [100] for ^{85}Rb an ^{87}Rb, but more suitable values would be 6 MHz for ^{85}Rb and 3 MHz for ^{87}Rb, for the samples studied in this work.

Site	δ_{CS} (ppm)	C_{Q} /MHz	η_Q
Rb 1	-26.2	1.83	0.77
Rb 2	-26.8	2.07	0.12
Rb 3	-30.9	1.85	1

Rubidium sulphate

Raw formula: Rb_2SO_4

Reference: Cheng *et al.* [45]

Origin: Sigma-Aldrich, reference 289280

Site	δ_{CS} (ppm)	C_{Q} /MHz	η_Q
Rb 1	46.6	2.6	0.89
Rb 2	3.0	3.2 [3]	0.13

Recorded in ^{93}Nb

Spin: $I = 9/2$

Gyromagnetic ratio: 10.45 MHz.T^{-1}

Natural abundance: 100%

Quadrupole moment: -32×10^{-30} m^2

Typical C_{Q}: 50 MHz

Reference sample: Taken directly from fitting the $LiNbO_3$ lineshape.

Lithium niobate

Raw formula: $LiNbO_3$

Reference: Prasad *et al.*,[340] Lapina *et al.*,[341] Lapina *et al.* [469]

Origin: Sigma-Aldrich, reference *254290*

Site	δ_{CS} (ppm)	C_{Q} /MHz	η_Q
Nb 1	-1004	22.2	0.2

[3] The value observed for C_Q and η_Q is closer for that reported by Skibsted and Jakobsen,[468] *e.g.* $P_Q \simeq$ 5.3 MHz.

Sodium niobate

Raw formula:	$NaNbO_3$
Reference:	Johnston *et al.* [342]
Origin:	Alfa Aesar, reference *10872*
Remark:	Commercial samples are often a mixture of the two crystallographic structures below, that possess slightly different NMR parameters.

Phase	Site	δ_{CS} (ppm)	C_Q /MHz	η_Q
Pbcm	Nb 1	−1078	19.5	0.7
$P_{21}ma$	Nb 1	−1078	20.3	0.7

C.3 Extended table and figure captions

This section details further the conditions for which the figures shown in the main text have been recorded/simulated. All simulation and simulated spectra were carried out with SIMPSON.[24] The data for all of the simulations and experiments presented in this work can be found in the disk enclosed with this thesis.

Chapter 2

Figure 2.9, **page 93**: All spectra were simulated for 75024 orientations, and, for MAS spectra, with 20 γ-angles.

- **(a)**: ^{23}Na simulation with B_0 = 14.1 T (ν_0 = 158.7 MHz) and first-order truncated quadrupolar interaction.
- **(b)**: ^{87}Rb simulations for different MAS rates ν_R with C_Q = 5.2 kHz and η_Q = 0.1, corresponding to the approximative quadrupolar parameters for the Rb 2 site of $RbSO_4$ (see Appendix C.2).
- **(c)**: ^{87}Rb simulations performed for different B_0 fields, with ν_R = 12.5 kHz, C_Q = 2 MHz and η_Q = 0.
- **(d)**: ^{87}Rb simulations performed for different C_Q , with B_0 = 9.4 T (ν_0 = 130.9 MHz), η_Q = 0 and ν_R = 12.5 kHz.
- **(e)**: Lineshapes generated for ^{23}Na using SOLA for different values of η_Q, with B_0 = 14.1 T (ν_0 = 158.7 MHz), ν_R= 12.5 kHz and C_Q = 2 MHz.

Chapter 3

Figure 3.12, **page 124**: Additional information about the NMR spectra:

(a): Recorded on Spectrometer 1, Probe (a). Original data: `130701_Original_MQMAS_RbNO3/23`. The spectrum were acquired by averaging 1024 transients with a recycle interval of 0.25 s, for 256 increments of 50 µs. 3Q excitation and conversion were carried out using pulse durations of 3 µs and 0.9 µs, respectively.

(b): Recorded on Spectrometer 1, Probe (a). Original data: `130701_Original_MQMAS_RbNO3/23`. The spectrum were acquired by averaging 512 transients with a recycle interval of 0.25 s, for 256 increments of 50 µs. 3Q excitation and conversion were carried out using pulse durations of 3 µs and 0.9 µs, respectively. The 90° CT-selective pulse was applied at ν_1 = 6 kHz for a duration of 15 µs.

(c): Recorded on Spectrometer 1, Probe (a). Original data: `130701_Original_MQMAS_RbNO3/1025` (echo) and `130701_Original_MQMAS_RbNO3/1024` (anti-echo). Both spectra were acquired by averaging 1024 transients with a recycle interval of 0.25 s, for 280 increments of 50 µs. 3Q excitation and conversion were carried out using pulse durations of 3 µs and 0.9 µs, respectively. The 180° CT-selective pulse was applied at ν_1 = 6 kHz for a duration of 24 µs using an echo period of t_e = 10 ms.

(d): Recorded on Spectrometer 1, Probe (a). Original data: `130708_RbNO3/3005`. The spectrum were acquired by averaging 2048 transients with a recycle interval of 0.25 s, for 200 increments of 142 µs. 3Q excitation and conversion were carried out using pulse durations of 4 µs and 1.2 µs, respectively. The 180° CT-selective pulses was applied at ν_1 = 8 kHz for a duration of 25.8 µs using an echo period of t_e = 15 ms.

Figure 3.19, **page 135**: Additional information about the NMR spectra:

(c): Recorded on Spectrometer 1, Probe (a). Original data: `131015_RbNO3_STMAS/2002`. The spectrum were acquired by averaging 384 transients with a recycle interval of 0.25 s, for 180 increments of 151.11 µs. ST excitation and ST to CT conversion were carried out using pulse durations of 2 µs and 0.75 µs, respectively. The 180° CT-selective pulse was applied at ν_1 = 8 kHz for a duration of 28.46 µs.

(d): Spectrum reproduced from Figure 3.12d.

Chapter 4

Figure 4.3, **page 147**: Recorded on Spectrometer 1, Probe (b). Original data: `151109_RbNO3_Figures_2`. The spectrum was acquired by averaging 96 transients, for 120 increments of 142 µs. The 3Q excitation was carried out using a pulse duration of 4 µs, and the 3Q conversion when carried out using a FAM-N pulse numerically optimised for C_Q = 1.8 MHz and η_Q = 0, resulting in 9 pulses for a total duration of 6.9 µs. The 180° CT-selective pulses were applied at ν_1 = 10 kHz for a duration of 27 µs

(a): The spectrum was acquired with a recycle interval of 0.25 s using an echo period of t_e = 6 ms. Original data: `1009`.

(b): The spectrum was acquired from 100 CPMG echoes with an echo period of t_e = 8 ms and a recycle interval of 40 ms. Original data: `1010`.

Figure 4.8, **page 155**: Additional information about the experimental spectra:

(c): Recorded on Spectrometer 1, Probe (g). Original data: `150719_RbClO4_FASTER`. The reference in the indirect dimension has been correct relative to the original data to account for spectral folding. Both spectra were acquired by averaging 192 transients with a recycle interval of 0.25 s, for 128 increments of 163 µs. 3Q conversion was carried out using FAM-N, numerically optimised for C_Q = 3.2 MHz and η_Q = 0.16, resulting in 8 pulses for a total duration of 6.4 µs. The 180° CT-selective pulse was applied at ν_1 = 13 kHz for a duration of 21 µs using an echo period of t_e = 5 ms.

- The CW excitation was carried out for a pulse duration of 5 µs. Original data: `2005`.
- The FASTER excitation was carried out with ν_1 = 55 kHz ($n = 2$) for a duration of 60 µs ($m = 2$). Original data: `2006`.

(d): Recorded on Spectrometer 1, Probe (g). Original data: `141101_GaPO4_Berlinite_TestRR`. Both spectra were acquired by averaging 960 transients with a recycle interval of 3 s, for 24 increments of 53.3 µs. 3Q conversion was carried out using FAM-N, numerically optimised for C_Q = 8.8 MHz and η_Q = 0.5, resulting in 7 pulses for a total duration of 7.5 µs. The 180° CT-selective pulse was applied at ν_1 = 134.4 kHz for a duration of 2.9 µs using an echo period of t_e = 1.2 ms.

- The CW excitation was carried out for a pulse duration of 8 µs. Original data: `3012`.
- The FASTER excitation was carried out with ν_1 = 107 kHz ($n = 4$) for a duration of 45 µs ($m = 1.5$). Original data: `3013`.

Chapter 5

Figure 5.4, **page 184**: Additional information about the MQMAS spectra:

(a): Recorded on Spectrometer 1, Probe (a). Original data: `130708_RbNO3`. The spectrum was acquired by averaging 192 transients with a recycle interval of 0.25 s, for 200 increments of 142 µs. 3Q excitation was carried out using pulse durations of 4 µs for ν_1 = 114 kHz. The 180° CT-selective pulse was applied at ν_1 = 5 kHz for a duration of 25.8 µs using an echo period of t_e = 15 ms. The 3Q conversion pulses were applied at ν_1 = 114 kHz.

- The CW conversion pulse was applied for 1.2 µs.
- The FAM-N conversion pulse was numerically optimised for C_Q = 1.8 MHz and η_Q = 0, resulting in 11 pulses for a total duration of 7.8 µs. The referencing of the indirect dimension was corrected for the figure.

(b): Recorded on Spectrometer 3, Probe (a). Original data: `HC_131007_RbNO3_FAMN`, `2004` for CW and `2006` for FAM-N conversion. The two spectra were acquired bply averaging 384 transients with a recycle interval of 0.25 s, for 70 increments of 23.70 µs. 3Q excitation was carried out using pulse durations of 7.5 µs for ν_1 = 88 kHz. The 180° CT-selective pulse was applied at ν_1 = 13 kHz for a duration of 35 µs using an echo period of t_e = 15 ms. The 3Q conversion pulses were applied at ν_1 = 88 kHz.

- The CW conversion pulse was applied for 3 µs.
- The FAM-N conversion pulse was numerically optimised for C_Q = 1.9 MHz and η_Q = 0, resulting in 19 pulses for a total duration of 19.3 µs.

(c): Recorded on Spectrometer 1, Probe (f). Original data: `130813_RbNO3_MAS28kHz`, `3004` for CW and `3009` for FAM-N conversion. The spectrum was acquired by averaging 288 transients with a recycle interval of 0.25 s, for 175 increments of 434 µs. 3Q excitation was carried out using pulse durations of 3.75 µs for ν_1 = 130 kHz. The 180° CT-selective pulse was applied at ν_1 = 15 kHz for a duration of 16.4 µs using an echo period of t_e = 15 ms. The 3Q conversion pulses were applied at ν_1 = 130 kHz.

- The CW conversion pulse was applied for 1.1 µs.
- The FAM-N conversion pulse was numerically optimised for C_Q = 1.9 MHz and η_Q = 0, resulting in 5 pulses for a total duration of 5.9 µs.

(d): Recorded on Spectrometer 1, Probe (g). Original data: `140215_RbNO3_40kHz`, `1003` for CW and `1010` for FAM-N conversion. The spectrum was acquired by averaging

192 transients with a recycle interval of 0.25 s, for 140 increments of 44.4 µs. 3Q excitation was carried out using pulse durations of 3.5 µs for ν_1 = 115 kHz. The 180° CT-selective pulse was applied at ν_1 = 8 kHz for a duration of 35 µs using an echo period of t_e = 4.5 ms. The 3Q conversion pulses were applied at ν_1 = 115 kHz.

- The CW conversion pulse was applied for 1.2 µs.
- The FAM-N conversion pulse was numerically optimised for C_Q = 1.9 MHz and η_Q = 0, resulting in 12 pulses for a total duration of 8.5 µs.

(e): Recorded on Spectrometer 1, Probe (h). Original data: `131016_RbNO3_60kHz`, `2003` for CW and `2007` for FAM-N conversion. The spectrum was acquired by averaging 192 transients with a recycle interval of 0.25 s, for 150 increments of 59.2 µs. 3Q excitation was carried out using pulse durations of 2.75 µs. The 180° CT-selective pulse was applied at ν_1 = 15.2 kHz for a duration of 37.5 µs using an echo period of t_e = 10 ms. The 3Q conversion pulses were applied at ν_1 = 103 kHz.

- The CW conversion pulse was applied for 1.2 µs.
- The FAM-N conversion pulse was numerically optimised for C_Q = 1.9 MHz and η_Q = 0, resulting in 8 pulses for a total duration of 7.6 µs. The 3Q conversion pulses were optimised for ν_1 = 88 kHz.

(f): Recorded on Spectrometer 3, Probe (a). Original data: `HC_131008_RbNO3_FAMN`, `2004` for CW and `2006` for FAM-N conversion. The two spectra were acquired by averaging 384 transients with a recycle interval of 0.25 s, for 70 increments of 23.70 µs for ν_1 = 88 kHz. 3Q excitation was carried out using pulse durations of 3 µs. The 180° CT-selective pulse was applied at ν_1 = 12 kHz for a duration of 39.60 µs using an echo period of t_e = 12 ms. The 3Q conversion pulses were applied at ν_1 = 88 kHz.

- The CW conversion pulse was applied for 5 µs.
- The FAM-N conversion pulse was numerically optimised for C_Q = 1.9 MHz and η_Q = 0, resulting in 15 pulses for a total duration of 16.6 µs.

Figure 5.8, **page 193**: All FAM-N pulses have been optimised for 66 crystallite orientations and 4 γ-angles, using the parameters detailed below. **(d)** was obtained from applying these pulses for 320 crystallite orientations and 20 γ-angles. All spectra were recorded on Spectrometer 1, Probe (a).

(a): Original data: `140310_Rb2SO4/3`.The spectrum was acquired from averaging 1200 transients with a recycle interval of

(b): Original data: `140315_Rb2SO4_12.5kHz_NEW4mm`, `1002` for the MQMAS spectrum

recorded with CW conversion, `1007` for that with FAM Rb 1 pulse, and `1008` for that with FAM Rb 2 pulse. All spectra were acquired by averaging 192 transients with a recycle interval of 0.25 s, for 160 increments of 71.1 µs. The 3Q excitation was carried out using a pulse duration of 4.75 µs. The 180° CT-selective pulse was applied at ν_1 = 13 kHz for a duration of 20.9 µs using an echo period of t_e = 7.5 ms. The 3Q conversion pulses were applied at the same RF field strength as before.

- The CW conversion pulse was applied for 1.50 µs.
- The FAM-N Rb 1 conversion pulse was numerically optimised for C_Q = 2.52 MHz and η_Q = 1.0, resulting in 14 pulses for a total duration of 8.5 µs.
- The FAM-N Rb 2 conversion pulse was numerically optimised for C_Q = 5.30 MHz and η_Q = 0.11, resulting in 26 pulses for a total duration of 11.0 µs.

Figure 5.9, **page 197**: All simulations were performed using the FAM-N pulses described below. All FAM-N pulses have been optimised for 66 crystallite orientations and 4 γ-angles. **(b,d,e,h)** were obtained from applying these pulses for different C_Q values for 320 crystallite orientations and 20 γ-angles. Additional information about the NMR spectra:

(a): Recorded on Spectrometer 1, Probe (b). Original data: `150815_Na4P2O7`, `1013` for the MQMAS spectrum recorded with FAM-N conversion, and `1014` for that with CW conversion. The two spectra were acquired by averaging 96 transients with a recycle interval of 8 s, for 88 increments of 142.2 µs. 3Q excitation was carried out using a pulse duration of 10 µs. The 180° CT-selective pulse was applied at ν_1 = 15.8 kHz for a duration of 16.8 µs using an echo period of t_e = 10.2 ms. The 3Q conversion pulses were applied at the same power level as the excitation pulses.

- The CW conversion pulse was applied for 1.5 µs.
- The FAM-N conversion pulse was numerically optimised for C_Q = 2 MHz and η_Q = 0, resulting in 12 pulses for a total duration of 9.6 µs.

(c): Recorded on Spectrometer 1, Probe (e). Original data: `141201_Kyanite`, `2007` for the MQMAS spectrum recorded with CW conversion, and `2008` for that with FAM conversion. The two spectra were acquired by averaging 384 transients with a recycle interval of 1 s, for 80 increments of 128.2 µs. 3Q excitation was carried out using a pulse duration of 3 µs. The 180° CT-selective pulse was applied at ν_1 = 14.2 kHz for a duration of 12.9 µs using an echo period of t_e = 2 ms. The 3Q conversion pulses were applied at the same power level as the excitation pulses.

- The CW conversion pulse was applied for 0.75 µs.

- The FAM-N conversion pulse was numerically optimised for C_Q = 6 MHz and η_Q = 0, resulting in 5 pulses for a total duration of 3.35 µs.

(e): Recorded on Spectrometer 2, Probe (b). Original data: `150323_45Sc_Sc2O3`, `1020` for the MQMAS spectrum recorded with CW conversion, and `1035` for that with FAM conversion. The two spectra were acquired by averaging 3840 transients with a recycle interval of 0.5 s, for 80 increments of 81.1 µs. 3Q excitation was carried out using a pulse duration of 2.00 µs. The 180° CT-selective pulse was applied at ν_1 = 34.5 kHz for a duration of 4.75 µs using an echo period of t_e = 0.4 ms. The 3Q conversion pulses were applied at the same power level as the excitation pulses.

- The CW conversion pulse was applied for 2 µs.
- The FAM-N conversion pulse was numerically optimised for C_Q = 23.4 MHz and η_Q = 0.02, resulting in 6 pulses for a total duration of 2.4 µs.

(g): Recorded on Spectrometer 1, Probe (g). Original data: `160405_LiNbO3_NaNbO3`, `2005` for the MQMAS spectrum recorded with CW conversion, and `2004` for that with FAM conversion. The two spectra were acquired by averaging 1728 transients with a recycle interval of 0.5 s, for 34 increments of 105.83 µs. 3Q excitation was carried out using a pulse duration of 2 µs. The 180° CT-selective pulse was applied at ν_1 = 30.0 kHz for a duration of 3.8 µs using an echo period of t_e = 0.7 ms. The 3Q conversion pulses were applied at the same power level as the excitation pulses.

- The CW conversion pulse was applied for 0.6 µs.
- The FAM-N conversion pulse was numerically optimised for C_Q = 20 MHz and η_Q = 0, resulting in 2 pulses for a total duration of 1.64 µs.

Figure 5.11, **page 204**: Additional information about the NMR spectra:

(a): See **(d)**

(b): See **(d)**

(c): Recorded on Spectrometer 2, Probe (a). Original data: `140707_RbNO3_FAMN`. These experiments were recorded on a space-restricted sample. All spectra were acquired by averaging 96 transients with a recycle interval of 0.25 s, for 200 increments of 71.1 µs. 3Q excitation was carried out using a pulse duration of 3.50 µs. The 180° CT-selective pulse was applied at ν_1 = 8 kHz for a duration of 31.5 µs using an echo period of t_e = 10 ms.

- The CW conversion pulse was applied for 1.00 µs. Original data: `2005`.
- The high-power part of the SPAM conversion pulse was applied for 1.40 µs,

and the low-power part for 14 µs at ν_1 = 8 kHz. Original data: `2008`.

- The FAM-I conversion pulse was composed of 6 blocks with τ_p = 0.50 µs. Original data: `2010`.
- The FAM-II conversion pulse was composed of two pulses of durations 1.1 µs and 0.7 µs. Original data: `2006`.
- The DFS conversion pulse was applied with a sweep from 75 kHz to 2000 kHz for 80 µs. Original data: `2016`.
- The FAM-N conversion pulse was numerically optimised for C_Q = 1.9 MHz and η_Q = 0, resulting in 8 pulses for a total duration of 5.6 µs. Original data: `2017`.

(d): Recorded on Spectrometer 1, Probe (a). Original data: `130807_RbNO3_1stpaper_bis`. The referencing of the indirect dimension of the MQMAS spectra have been corrected when plotting the figure. All spectra were acquired by averaging 192 transients with a recycle interval of 0.25 s, for 280 increments of 142 µs. 3Q excitation was carried out using a pulse duration of 4.25 µs. The 180° CT-selective pulse was applied at ν_1 = 8 kHz for a duration of 27.2 µs using an echo period of t_e = 15 ms.

- The CW conversion pulse was applied for 4.25 µs. Original data: `2005`.
- The high-power part of the SPAM conversion pulse was applied for 1.5 µs, and the low-power part for 13.6 µs at ν_1 = 8 kHz. Original data: `2007`.
- The FAM-I conversion pulse was composed of 3 blocks with τ_p = 0.8 µs. Original data: `2016`.
- The FAM-II conversion pulse was composed of two pulses of durations 1.7 µs and 0.8 µs. Original data: `2006`.
- The DFS conversion pulse was applied with a sweep from 175 kHz to 850 kHz for 20 µs. Original data: `2013`.
- The FAM-N conversion pulse was numerically optimised for C_Q = 1.8 MHz and η_Q = 0, resulting in 11 pulses for a total duration of 7.8 µs. Original data: `3003`.

(e): Recorded on Spectrometer 3, Probe (a). Original data: `HC_131007_RbNO3_FAMN`. All spectra were acquired by averaging 192 transients with a recycle interval of 0.25 s, for 150 increments of 71.1 µs. 3Q excitation was carried out using a pulse duration of 7.5 µs. The 180° CT-selective pulse was applied at ν_1 = 11 kHz for a duration of 35 µs using an echo period of t_e = 15 ms.

- The CW conversion pulse was applied for 3 µs. Original data: `2006`.

- The high-power part of the SPAM conversion pulse was applied for 2.6 µs, and the low-power part for 17.5 µs at ν_1 = 11 kHz. Original data: `2012`.
- The FAM-I conversion pulse was composed of 6 blocks with τ_p = 0.8 µs. Original data: `2013`.
- The FAM-II conversion pulse was composed of two pulses of durations 2.4 µs and 1.2 µs. Original data: `2008`.
- The DFS conversion pulse was applied with a sweep from 100 kHz to 600 kHz for 2.6 µs. Original data: `2029`.
- The FAM-N conversion pulse was numerically optimised for C_Q = 1.9 MHz and η_Q = 0, resulting in 19 pulses for a total duration of 19.2 µs. Original data: `2010`.

Figure 5.12, **page 208**: Additional information about the NMR spectra:

(a): Recorded on Spectrometer 1, Probe (a). Original data: `130427_Na4P2O7`. All spectra were acquired by averaging 2160 transients with a recycle interval of 3 s. The 3Q excitation pulse was applied for a duration of 4 µs for ν_1 = 95 kHz. All of the 3Q conversion pulses were applied for ν_1 = 60 kHz.

- The CW conversion pulse was applied for 3.00 µs. Original data: `1004`.
- The high-power part of the SPAM conversion pulse was applied for 3 µs, and the low-power part for 12 µs at ν_1 = 7 kHz. Original data: `1007`.
- The FAM-II conversion pulse was composed of two pulses of durations 3.0 µs and 2 µs. Original data: `1005`.
- The DFS conversion pulse was applied with a sweep from 150 kHz to 500 kHz for 13.3 µs. Original data: `1010`.
- The FAM-N conversion pulse was numerically optimised for C_Q = 0.6 MHz and η_Q = 0, resulting in 7 pulses for a total duration of 15 µs. The pulse was applied for for ν_1 = 60 kHz. Original data: `1008`.

(b): Recorded on Spectrometer 1, Probe (a). Original data: `130520_017_SIZ-4`. All spectra were acquired by averaging 7200 transients with a recycle interval of 1 s. The 3Q excitation pulse was applied for a duration of 6 µs for ν_1 = 56 kHz. Unless otherwise stated, all of the 3Q conversion pulses were applied for ν_1 = 56 kHz.

- The CW conversion pulse was applied for 1.4 µs. Original data: `1010`.
- The high-power part of the SPAM conversion pulse was applied for 2.1 µs, and the low-power part for 8 µs at ν_1 = 10 kHz. Original data: `1010`.
- The FAM-II conversion pulse was composed of two pulses of durations 2 µs and 1 µs. Original data: `1012`.

- The DFS conversion pulse was applied with a sweep from 150 kHz to 500 kHz for 20 µs at ν_1 = 50 kHz. Original data: `1013`.
- The FAM-N conversion pulse was numerically optimised for C_Q = 6 MHz and η_Q = 0, resulting in 10 pulses for a total duration of 10.2 µs. Original data: `1005`.

(c): Recorded on Spectrometer 1, Probe (b). Original data: `140207_RbNO3_Rb85`. All spectra were obtained from projections on the indirect dimension of MQMAS spectra, expect the spectrum from SPAM, that is a 3QF-MAS spectrum. All spectra but the SPAM spectrum was acquired by averaging 960 transients with a recycle interval of 0.25 s, for 100 increments of 184 µs. The 180° CT-selective pulse was applied at ν_1 = 28 kHz for a duration of 26 µs using an echo period of t_e = 2.5 ms. The 3Q excitation pulse was applied for a duration of 21 µs.

- The CW conversion pulse was applied for 2.2 µs. Original data: `1003`.
- The high-power part of the SPAM conversion pulse was applied for 3.0 µs at ν_1 = 50 kHz, and the low-power part for 8.9 µs at ν_1 = 11 kHz. Original data: `151204_RbNO3_RbCl_Rb85/117`.
- The FAM-II conversion pulse was composed of two pulses of durations 2.4 µs and 1.2 µs. Original data: `1007`.
- The DFS conversion pulse was applied with a sweep from 30 kHz to 400 kHz for 16 µs. Original data: `1017`.
- The FAM-N conversion pulse was numerically optimised for C_Q = 3.9 MHz, η_Q = 0 and ν_1 = 40 kHz, resulting in 13 pulses for a total duration of 15.7 µs. Original data: `1110`.

(d): Recorded on Spectrometer 1, Probe (a). Original data: `130524_ScSO4`. All spectra were acquired by averaging 21 600 transients with a recycle interval of 0.25 s. The 3Q excitation pulse was applied for a duration of 2.75 µs for ν_1 = 100 kHz. All of the 3Q conversion pulses were applied for ν_1 = 100 kHz.

- The CW conversion pulse was applied for 0.8 µs. Original data: `1006`.
- The high-power part of the SPAM conversion pulse was applied for 1.0 µs, and the low-power part for 4.8 µs at ν_1 = 14 kHz. This particular spectrum was recorded during a different NMR slot, hence the lineshape difference observed. Original data: `1008`.
- The FAM-II conversion pulse was composed of two pulses of durations 1.4 µs and 0.8 µs. Original data: `1009`.
- The DFS conversion pulse was applied with a sweep from 100 kHz to 500 kHz

for 5.3 µs. Original data: `1014`.

- The FAM-N conversion pulse was numerically optimised for C_Q = 6 MHz and η_Q = 0, resulting in 2 pulses for a total duration of 1.8 µs. Original data: `10 20`.

Chapter 6

Figure 6.1, **page 215**: All spectra were recorded on Spectrometer 1, Probe (g). Original data: `140903_GaPO4_Berlinite`.

(a): Original data: `2010` for the MQMAS spectrum recorded with CW conversion, and `1011` for that with FAM conversion. The reference in the indirect dimension has been correct relative to the original data to account for spectral folding. Both were acquired by averaging 2400 transients with a recycle interval of 3 s, for 21 increments of 106 µs. 3Q excitation were carried out using a pulse duration of 8 µs, and the CT-selective 180° pulse was applied for 2.8 µs for ν_1 = 115 kHz using an echo period of t_e = 1.2 ms.

- The CW conversion pulse was applied for 2.70 µs.
- The FAM-N conversion pulse was numerically optimised for C_Q = 8.8 MHz and η_Q = 0, resulting in 19 pulses for a total duration of 8.8 µs.

(b): Original data for the MAS spin-echo spectrum: `1005`. The spectrum was acquired with pulse durations for the 90° and 180° conversion pulse of 1.5 µs and 2.8 µs, respectively, for t_e = 27.9 µs and ν_1 = 115 kHz.

Figure 6.2, **page 217**: All spectra were recorded on Spectrometer 1, Probe (g). Original data: `150126_27Al_Andalusite`.

(a): Original data: `1011`. The spectrum was acquired with pulse durations for the 90° and 180° conversion pulse of 1 µs and 2.5 µs, respectively, for t_e = 48.3 µs and ν_1 = 97 kHz.

(b): Original data: `4022` for the MQMAS spectrum recorded with FAM-N conversion, and `4023` for that with CW conversion. Both spectra were acquired by averaging 1.00 transients with a recycle interval of 1 s, for 124 increments of 64.6 µs. 3Q excitation was carried out using a pulse duration of 1 µs, and the CT-selective 180° pulse was applied for 2.8 µs for ν_1 = 115 kHz.

- The CW conversion pulse was applied for 1 µs.
- The FAM-N conversion pulse was numerically optimised for C_Q = 15.261 MHz and η_Q = 0.1029, resulting in 7 pulses for a total duration of 4.1 µs.

(c): see **(b)**

(d): see **(c)**

Figure 6.3, **page 219**: All spectra were recorded on Spectrometer 4. Original data: `800.HColaux-150518-39K`.

(a): Original data: `5001`. The spectrum was acquired by averaging 288 transients with a recycle interval of 5 s, for 80 increments of 177 µs. 3Q excitation was carried out using a pulse duration of 9.50 µs, and the CT-selective 180° pulse was applied for 11 µs for ν_1 = 23 kHz using an echo period of t_e = 25 ms. The FAM-N conversion pulse was numerically optimised for C_Q = 0.9 MHz and η_Q = 0, resulting in 19 pulses for a total duration of 53.0 µs. The full echoes were processed with 1 kHz Gaussian broadening.

(b): Original data: `5002`. The CW conversion pulse was applied for 5.00 µs. The others parameters are identical to **(a)**.

(c): see **(a)** and **(b)**.

(e): Original data: `1009`. The spectrum was acquired with pulse durations for the 90° and 180° pulses of 5.00 µs and 100 µs, respectively, for t_e = 42.5 µs and ν_1 = 25 kHz. The fitted lineshapes are located in `1009/100` for the sum of the sites K 1 and K 2, `1009/101` for K 1 and `1009/102` for K 2.

Figure 6.4, **page 222**: Additional information about the NMR spectra:

(a): Recorded on Spectrometer 1, Probe (c). Original data: `131212_25Mg`, `1` for FAM-N and `3` for CW. Both spectra were acquired by averaging 5760 transients with a recycle interval of 1 s, for 40 increments of 206 µs. 3Q excitation was carried out using a pulse duration of 8 µs. The 180° CT-selective pulse was applied at ν_1 = 33 kHz for a duration of 5.5 µs using an echo period of t_e = 0.3 ms.

- The CW conversion pulse was applied for 5.5 µs.
- The FAM-N conversion pulse was numerically optimised for C_Q = 3.091 MHz, η_Q = 0.65 and ν_R = 0, resulting in 9 pulses for a total duration of 16.1 µs.

(b): Recorded on Spectrometer 3, Probe (b). Original data: `HC_140221_25Mg_Mg(OH)2_4mmLow-G`, `204` for FAM-N and `207` for CW conversion. Both spectra were acquired by averaging 93 600 transients with a recycle interval of 1 s. The 3Q excitation and were carried out using a pulse duration of 16.00 µs.

- The CW conversion pulse was applied for 5.5 µs.
- The FAM-N conversion pulse was numerically optimised for C_Q = 3.091 MHz, η_Q = 0 and ν_1 = 31 kHz, resulting in 9 pulses for a total duration of 15.4 µs.

Figure 6.5, **page 223**: Additional information about the NMR spectra:

(a): Recorded on Spectrometer 4. Original data: `800.HColaux-150518`, `1105` for the MAS spectrum, `1106` for the CPMG-MAS spectrum with summed echo, and `1107` for the original CPMG-MAS spectrum. These spectra were acquired with pulse durations for the 90° and 180° pulses of 5.1 µs and 10.2 µs, respectively, for t_e = 63.78 µs and ν_1 = 16.3 kHz.

(b): Original data: `800.HColaux-150518/1009`, `900` for the simulated total lineshape, `901` for Mg 2 and `902` for Mg 1. The spectrum was fitted using the quadrupolar parameters of Derighetti *et al.* [356] as initial value. The lineshape were obtained using the following parameters:

- **Mg 1**: δ_{CS} = 4.33 ppm, C_Q = 4.31 MHz, η_Q = 0.40, and an exponential line broadening of 200 Hz.
- **Mg 2**: δ_{CS} = 12.7 ppm, C_Q = 5.08 MHz, η_Q = 1.00, and an exponential line broadening of 200 Hz.

(c): Recorded on Spectrometer 3, Probe (b). Original data: `HC_140909_25Mg_Fosterite/36`. The spectrum was acquired by averaging 1440 transients with a recycle interval of 5 s, for 24 increments of 185 µs. 3Q excitation was carried out using a pulse duration 14 µs. The 5.66° CT-selective pulse was applied at ν_1 = 32.5 kHz for a duration of 5.66 µs using an echo period of t_e = 571 ms. The FAM-N conversion pulse was numerically optimised for C_Q = 5 MHz and η_Q = 0, resulting in 8 pulses for a total duration of 11.4 µs.

(d): Recorded on Spectrometer 3, Probe (b). Original data: `HC_151001_25Mg_Forsterite/1002`. The spectrum was acquired by averaging 48 transients with a recycle interval of 5 s, for 75 increments of 193 µs. 3Q excitation was carried out using a pulse duration of 13.00 µs, respectively. The 180° CT-selective pulse was applied at ν_1 = 17.5 kHz for a duration of 33.40 µs. The FAM-N conversion pulse was numerically optimised for C_Q = 4.996 MHz and η_Q = 0.943, resulting in 6 pulses for a total duration of 11.6 µs. 1500 CPMG echoes were recorded, and 750 were processed, with an echo period of 6.2 µs.

(e): Recorded on Spectrometer 1, Probe (c). Original data: `150630_MG2SiO4_3QF_CPMG/30000`. The total spectrum was acquired by averaging 3658 transients with a recycle interval of 35 s. 3Q excitation and conversion were carried out using pulse durations of 14.00 µs and 2.2 µs, respectively. CPMG was carried out using a 180° pulse of duration 4.56 µs for ν_1 = 36.5 kHz, with 1600 recorded, and with an echo period of t_e = 370 µs.

(f): Recorded on Spectrometer 1, Probe (c). Original data: `150630_MG2SiO4_3QF_CPMG/30001`. The FAM-N conversion pulse was numerically optimised for C_Q = 4.996 MHz and η_Q = 0.943 , resulting in 6 pulses for a total duration of 16.1 µs.

Figure 6.6, **page 227**: Additional information about the experimental spectra.

(a): See Figure 5.9c.

(b): Recorded on Spectrometer 1, Probe (e). Original data: `160226_Kyanite5Q`. The spectrum was acquired by averaging 1600 transients with a recycle interval of 1 s, for 42 increments of 51.4 µs. 5Q excitation was carried out using a pulse duration of 3 µs. The 180° CT-selective pulse was applied at ν_1 = 21 kHz for a duration of 8.7 µs using an echo period of t_e = 2.5 ms. The spectra was processed with 500 kHz of Gaussian broadening in the direct dimension and with 200 kHz of exponential broadening in the indirect dimension.

(c):
- The CW conversion pulse was applied for 1.5 µs. Original data: `6006`.
- The FAM-N conversion pulse was numerically optimised for C_Q = 6 MHz and η_Q = 0, resulting in 7 pulses for a total duration of 6.6 µs. Original data: `6007`.

Figure 6.8, **page 232**: Recorded on Spectrometer 1, Probe (e). Original data: `160314_Al(acac)5Q`, `104` for CW excitation, `109` for the direct FAM-N pulse, `106` for the direct* FAM-N pulse, `108` for the concatenated FAM-N pulse, and `107` for the FAM-N pulse optimised in two steps. Both spectra were acquired by averaging 800 transients with a recycle interval of 3 s. The 5Q excitation and CW conversion were carried out using pulse durations of 3 µs and 1.5 µs, respectively. The FAM-N pulses are described in the main text.

Figure 6.12, **page 246**:

(b): Recorded on Spectrometer 1, Probe (b). Original data: `160210_Na4P2O7_New4mm`, `1006` for the spectrum recorded with CW conversion, and `1007`, `1008`, `1009` and `1005` for the spectra recorded with FAM-N truncated to 2, 4, 7, and 12 (full) pulses, respectively. The spectra were acquired by averaging 96 transients with a recycle interval of 4 s, for 32 increments of 142.22 µs. 3Q excitation for all spectra were carried out using pulse durations of 5.00 µs, and 3Q conversion for the CW spectrum was carried out using pulse durations of 1.5 µs. The 180° CT-selective pulse was applied at ν_1 = 15.1 kHz for a duration of 17.43 µs. An exponential line broadening of 100 Hz have been applied to all spectra.

Chapter 7

Figure 7.9, **page 267**: Simulations and experiments performed for B_0 = 14.1 T (ν_0 = 196.4 MHz for ^{87}Rb and ν_0 = 156.4 MHz for ^{27}Al), with ν_1 = 22 kHz.

(a): Recorded on Spectrometer 1, Probe (b). Original data: `87RbClO4-06-05-2015-4mm-HX-new/6`. Each step of the procedure consists of a spectrum acquired for 8 transients with a recycle interval of 1 s and a 90° pulse duration of 9 µs for ν_1 = 7 kHz.

(b): Recorded on Spectrometer 2, Probe (c). Original data: `RbClO4-04-03-2016-1.9mmHFX-all, 20, 997`. Each step of the procedure consists of a spectrum acquired for 8 transients with a recycle interval of 1 s and a 90° pulse duration of 6 µs for ν_1 = 5 kHz.

(c): Recorded on Spectrometer 1, Probe (h). Original data: `87RbClO4-03-09-2015-1.3mm/8`. Each step of the procedure consists of a spectrum acquired for 4 transients with a recycle interval of 1 s and a 90° pulse duration of 8 µs for ν_1 = 6 kHz.

Table 7.1, **page 272**: Additional information about the ^{87}Rb spectra of $RbClO_4$:

- ν_R = 10 kHz: Recorded on Spectrometer 1, Probe (c). Original data: `87RbClO4-19-11-2015-4_mm-HX-new-all`. Each spectrum was acquired by averaging 8 transients with a recycle interval of 1 s. The 90° CT-selective pulse was applied at ν_1 = 8 kHz for a duration of 6 µs. Original data for the CW spectrum: `4`.
  - COMPACT was applied of ν_1 = 98 kHz with τ_p = 0.75 µs. COMPACT applied for ν_1 = 22 kHz with τ_p = 3 µs resulted in a signal improvement of ×1.05. Original data: `15` and `16`.
  - RAPT was applied for 18 blocks with τ_p = 0.45 µs. Original data: `18`.
  - DFS was applied for a duration of 100 µs with $\omega_s/2\pi$ = ±700 kHz and $\omega_f/2\pi$ = ±600 kHz. Original data: `9`.
  - HS was applied for a duration of 3 ms with $\Delta\nu_c$ = ±640 kHz. Original data: `5`.
- ν_R = 20 kHz: Recorded on Spectrometer 1, Probe (e). Original data: `87RbClO4-05-11-2015-3.2mm`. Each spectrum was acquired by averaging 4 transients with a recycle interval of 1 s. The 90° CT-selective pulse was applied at ν_1 = 5 kHz for a duration of 6 µs. Original data for the CW spectrum: `103`.
  - COMPACT was applied of ν_1 = 146 kHz with τ_p = 0.4 µs. COMPACT applied for ν_1 = 22 kHz with τ_p = 3 µs resulted in a signal improvement of ×1.1. Original data: `18` and `104`.

  - RAPT was applied for 11 blocks with τ_p = 6 µs. Original data: `101`.
  - DFS was applied for a duration of 83.3 µswith $\omega_s/2\pi$ = ±950 kHz and $\omega_f/2\pi$ = ±350 kHz. Original data: `100`.
  - HS was applied for a duration of 3 ms with $\Delta\nu_c$ = ±620 kHz. Original data: `102`.
- ν_R = 40 kHz: Recorded on Spectrometer 1, Probe (g). Original data: `87RbClO4-20-11-2015-1.9_mm_HX-all`. Each spectrum was acquired by averaging 8 transients with a recycle interval of 1 s. The 90° CT-selective pulse was applied at ν_1 = 14 kHz for a duration of 6 µs. Original data for the CW spectrum: `3`.
  - COMPACT was applied of ν_1 = 91 kHz with τ_p = 0.75 µs. COMPACT applied for ν_1 = 22 kHz with τ_p = 4 µs resulted in a signal improvement of ×1. Original data: `26` and `24`.
  - RAPT was applied for 6 blocks with τ_p = 7.5 µs. Original data: `18`.
  - DFS was applied for a duration of 25 µs with $\omega_s/2\pi$ = ±600 kHz and $\omega_f/2\pi$ = ±600 kHz. Original data: `9`.
  - HS was applied for a duration of 3 ms with $\Delta\nu_c$ = ±600 kHz. Original data: `5`.
- ν_R = 60 kHz: Recorded on Spectrometer 1, Probe (h). Original data: `87RbClO4-03-09-2015-1.3mm`. Each spectrum was acquired by averaging 16 transients with a recycle interval of 1 s. The 90° CT-selective pulse was applied at ν_1 = 19 kHz for a duration of 8 µs. Original data for the CW spectrum: `6`.
  - COMPACT was applied of ν_1 = 129 kHz with τ_p = 0.4 µs. COMPACT applied for ν_1 = 22 kHz with τ_p = 3 µs resulted in a signal improvement of ×1.2. Original data: `15` and `14`.
  - RAPT was applied for 10 blocks with τ_p = 6.3 µs. Original data: `12`.
  - DFS was applied for a duration of 166.7 µs with $\omega_s/2\pi$ = ±1600 kHz and $\omega_f/2\pi$ = ±400 kHz. Original data: `24`.
  - HS was applied for a duration of 3 ms with $\Delta\nu_c$ = ±720 kHz. Original data: `9`.

Additional information about the ^{27}Al spectra of Al(acac)$_3$:

- ν_R = 10 kHz: Recorded on Spectrometer 1, Probe (c). Original data: `Al(Acac)3-hs-19112015-4mmHX-new-all`. Each spectrum was acquired by averaging 4 transients with a recycle interval of 3 s. The 90° CT-selective pulse was applied at ν_1 = 6 kHz for a duration of 9 µs. Original data for the CW spectrum: `4`.
  - COMPACT was applied of ν_1 = 85 kHz with τ_p = 0.75 µs. COMPACT applied

for ν_1 = 22 kHz with τ_p = 1.5 µs resulted in a signal improvement of ×1.3. Original data: `22` and `19`.

- RAPT was applied for 10 blocks with τ_p = 2 µs. Original data: `16`.
- DFS was applied for a duration of 5 ms with $\omega_s/2\pi$ = ±350 kHz and $\omega_f/2\pi$ = ±300 kHz. Original data: `10`.
- HS was applied for a duration of 3 ms with $\Delta\nu_c$ = ±290 kHz. Original data: `8`.

- ν_R = 20 kHz: Recorded on Spectrometer 1, Probe (e). Original data: `Al(Acac)3-27102015-3.2mmHX`. Each spectrum was acquired by averaging 8 transients with a recycle interval of 3 s. The 90° CT-selective pulse was applied at ν_1 = 8 kHz for a duration of 4 µs. Original data for the CW spectrum: `105`.
  - COMPACT was applied of ν_1 = 98 kHz with τ_p = 0.70 µs. COMPACT applied for ν_1 = 22 kHz with τ_p = 0.70 µs resulted in a signal improvement of ×1.3. Original data: `104` and `103`.
  - RAPT was applied for 6 blocks with τ_p = 9 µs. Original data: `151204_Al(acac)3_RAPT/2005`.
  - DFS was applied for a duration of 5 ms with $\omega_s/2\pi$ = ±600 kHz and $\omega_f/2\pi$ = ±300 kHz. Original data: `101`.
  - HS was applied for a duration of 3 ms with $\Delta\nu_c$ = ±260 kHz. Original data: `102`.
- ν_R = 40 kHz: Recorded on Spectrometer 1, Probe (g). Original data: `Al(Acac)3-20112015-1.9mmHX-all`. Each spectrum was acquired by averaging 8 transients with a recycle interval of 3 s. The 90° CT-selective pulse was applied at ν_1 = 22 kHz for a duration of 4 µs. Original data for the CW spectrum: `4`.
  - COMPACT was applied of ν_1 = 85 kHz with τ_p = 1.5 µs. COMPACT applied for ν_1 = 22 kHz with τ_p = 1.5 µs resulted in a signal improvement of ×1.3. Original data: `18` and `19`. RAPT was applied for 6 blocks with τ_p = 6.8 µs. Original data: `22`.
  - DFS was applied for a duration of 25 µs with $\omega_s/2\pi$ = ±350 kHz and $\omega_f/2\pi$ = ±300 kHz. Original data: `10`.
  - HS was applied for a duration of 2 ms with $\Delta\nu_c$ = ±320 kHz. Original data: `11`.
- ν_R = 60 kHz: Recorded on Spectrometer 1, Probe (h). Original data: `Al(Acac)3-22062015-1.3mmHX`. Each spectrum was acquired by averaging 8 transients with a recycle interval of 3 s. The 90° CT-selective pulse was applied at ν_1 = 22 kHz for a duration of 4 µs. Original data for the CW spectrum: `5`.

- COMPACT was applied of ν_1 = 100 kHz with τ_p = 0.5 µs. COMPACT applied for ν_1 = 22 kHz with τ_p = 1.5 µs resulted in ×0.3 of the signal recorded with no PAAP. Original data: `33` and `34`.
- RAPT was applied for 3 blocks with τ_p = 3 µs. Original data: `15`.
- DFS was applied for a duration of 417 µs with $\omega_s/2\pi$ = ±1200 kHz and $\omega_f/2\pi$ = ±400 kHz. Original data: `32`.
- HS was applied for a duration of 2 ms with $\Delta\nu_c$ = ±540 kHz. Original data: `1 1`.

Additional information about the ^{87}Rb spectra of $RbNO_3$:

- ν_R = 12.5 kHz: Recorded on Spectrometer 1, Probe (a). Original data: `150304_RbNO3_Misctests`. Each spectrum was acquired by averaging 2880 transients with a recycle interval of 0.25 s. The 90° pulse was applied at ν_1 = 147 kHz for a duration of 1 µs. Original data for the CW spectrum: `1013`.
  - COMPACT was applied of ν_1 = 147 kHz with τ_p = 0.5 µs. COMPACT was not applied with ν_1 = 22 kHz for this dataset.
  - RAPT was applied for 32 blocks with τ_p = 1.15 µs. Original data: `1015`.
  - DFS was applied for a duration of 1 ms with $\omega_s/2\pi$ = ±1500 kHz and $\omega_f/2\pi$ = ±200 kHz. Original data: `1024`.
  - HS was applied for a duration of 5 ms with $\Delta\nu_c$ = ±400 kHz. Original data: `1 066`.
- ν_R = 60 kHz: Recorded on Spectrometer 1, Probe (h). Original data: `151218_RbNo3_RbCl_PAAP`. Each spectrum was acquired by averaging 1800 transients with a recycle interval of 0.25 s. The 90° CT-selective pulse was applied at ν_1 = 12 kHz for a duration of 12 µs. Original data for the CW spectrum: `1011`.
  - COMPACT was applied of ν_1 = 128 kHz with τ_p = 0.5 µs. COMPACT applied for ν_1 = 22 kHz with τ_p = 3.2 µs resulted in a signal improvement of ×1.2. Original data: `1012` and `1017`.
  - RAPT was applied for 8 blocks with τ_p = 4.2 µs. Original data: `1013`.
  - DFS was applied for a duration of 3 ms with $\omega_s/2\pi$ = ±150 kHz and $\omega_f/2\pi$ = ±210 kHz. Original data: `1016`.
  - HS was applied for a duration of 3 ms with $\Delta\nu_c$ = ±180 kHz. Original data: `1 014`.

Figure 7.12, **page 275**: Recorded on Spectrometer 2, Probe (b).

(a), **(b)** and **(c)**: All spectra were acquired by averaging 3600 transients with a recycle interval of 0.25 s. Original data: `150920_RbNO3_FAMN_test_RIACT_FAM`, `10`

05 to 1015.

- The MAS spectrum was acquired using a 90° pulse applied at ν_1 = 107 kHz for 1.5 µs. Original data: 1012.
- The HS pulse was applied at ν_1 = 34 kHz and $\Delta\nu_c$ = ±400 kHz for a duration of 5 ms. Original data: 1005.
- The CW excitation pulse was applied for a duration of 5.5 µs.
- The CW conversion pulse was applied for a duration of 1.75 µs
- The FAM-N conversion pulse was numerically optimised for C_Q = 2 MHz and η_Q = 0, resulting in 11 pulses for a total duration of 8.4 µs.
- The SL excitation and conversion pulses were applied for a duration of 20 µs = $\tau_R/4$.

(d): The spectrum was acquired by averaging 288 transients with a recycle interval of 0.25 s, for 62 increments of 142 µs. The 180° CT-selective pulse was applied at ν_1 = 15 kHz for a duration of 19.5 µs using an echo period of t_e = 12.9 ms. The others acquisition parameters are identical to those presented for the 3QF spectra in **(a)**, **(b)** and **(c)**. Original data: 2010 for the RIACT-I spectrum, 2011 for the HS + RIACT-I spectrum, and 2013 for the CW excitation spectrum.

Appendix D

Phase cycling

Introduction

The concept of phase cycling comes from a simple observation about NMR experiments. It is assumed that the signal produced by a given pulse sequence is $S = S_0 + S_1$ where S_0 is the desired part of the signal and S_1 is an error or an undesired part of the signal. Because of the nature of NMR experiment, it is often very easy to design an second pulse sequence that produces exactly the opposite error while leaving the desired part unchanged, *e.g.*, $S' = S_0 - S_1$. Adding those two experiments will result in a signal free from undesired errors $S'' = S + S' = 2S_0$, with the inconvenience of two acquisition being required. Likewise, if an experiment produces a total signal, with one desired part and N desired part, N+1 experiments would allow the retrieval of only the desired part of the signal while cancelling the others.

The design of such experiments is executed by the adjustment of the relative phase of the different pulses in a multi-pulse experiment. This is made possible by the coherence orders of the different constituents of the quantum states of the magnetisation (Section 1.2.2, Equation (1.2.37)). NMR experiments are designed with an associated CTP[1] that insures that the experiment produces the desired effect. Phase cycling allows the selection of the constituents of the CTP through constructive interferences, while suppressing all others through destructive interferences.

[1] CTP: *Coherence Transfer Pathway*

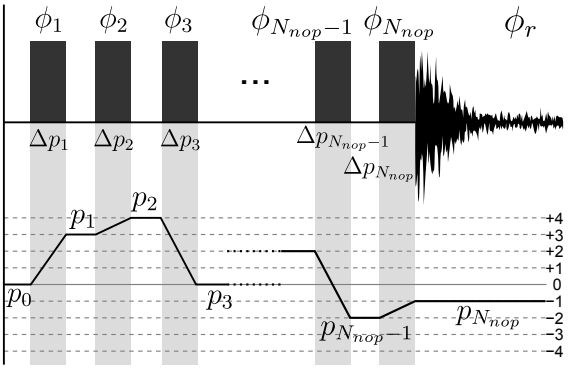

Figure D.1: *Illustration of a general pulse sequence and associated CTP.*

A schematic pulse sequence composed of N_{nop} pulses and its CTP can be presented as in Figure D.1, illustrating the following important points:

- Magnetisation at the beginning of the pulse sequence has a coherence $p_0 = 0$.
- By convention, recorded magnetisation is always $p_{\text{nop}} = -1$ (see Section 1.3.2).
- Because initial and final coherences are settled, phase cycling it only necessary on $N_{\text{nop}} - 1$ pulses.

The CTP defines a number of desired coherence changes Δp_k. To select only the desired CTP, the k-th pulse is incremented by N_k steps with an associated phase $\phi_{k,l}$, $l \in [1, N_k]$. Phase cycling consists in multiplying the non-phased signal (*e.g.*, all $\phi_{k,l} = 0$) during the l-th step by a factor P_c defined

$$\begin{aligned} P_c &= \exp\left(i\phi_{r_l}\right) \prod_{k=1}^{k=N_{\text{nop}}} \exp\left(i\Delta p_k \phi_{k,l}\right) \\ &= \exp\left(i\phi_{r_l} + i \sum_{k=1}^{k=N_{\text{nop}}} \Delta p_k \phi_{k,l}\right) \end{aligned} \quad , \tag{D.0.1}$$

with ϕ_{r_l} referring to the phase of the receiver during the l-th step. The receiver phase is a user-controlled parameter that corresponds to the angle from which the magnetisation is observed, and can be interpreted as being equivalent the rotating frame Σ_{rot}, with θ_{RF} being the difference angle between the position of $\vec{B}_1$ and a reference axis of the rotating frame (See Chapter 1). The minimum total number of steps necessary for all the pulses to accomplish their cycle at least once is

$$N_{\text{nos}} = \prod_{k=1}^{k=N_{\text{nop}}} N_k \tag{D.0.2}$$

This appendix introduces the approach for phase cycling termed ”nested phase cycling”,[41, 56, 148, 470, 471] while the other common approach, the ”cogwheel phase

cycling",[472] which offers the advantage of requiring a lower N_{nos} than in Equation (D.0.2), will not be detailed in this appendix.

D.1 Compensating for acquisition artefacts

A first application of phase-cycled pulse programs aims at compensating instrumental problems, that cause artefacts to appear on recorded spectra. Even for a simple direct acquisition pulse sequence (Chapter 3.1.1), artefacts may appear on recorded spectra when quadrature detection is being employed, known as quadrature artefacts. Ideally, a signal should be expressed as

$$s(t) = s_0 \exp(i\omega_0 t) \quad , \tag{D.1.1}$$

as illustrated in Figure D.2.

Continuous current components

Continuous current components arise from the two following reasons (Illustrated Figure D.2). Because of an electronic miscalibration, a continuous component $A\exp(i\phi_A)$ is added to the recorded signal in one of the two channels (or both) resulting in an artefact at the carrier frequency, which appears in the middle of the spectrum (Figure D.2b). The complex signal s obtained from the non-phase-cycled pulse sequence is

$$s(t) = A\exp(i\phi_A) + s_0\exp(i\omega_0 t) \quad . \tag{D.1.2}$$

Recording the signal with the pulse phased at 180°,

$$s'(t) = A\exp(i\phi_A) - s_0\exp(i\omega_0 t) \quad . \tag{D.1.3}$$

Finally, setting the receiver phase to 180° gives

$$s''(t) = -A\exp(i\phi_A) + s_0\exp(i\omega_0 t) \quad . \tag{D.1.4}$$

Adding s to s'', the obtained signal is

$$S(t) = 2s_0\exp(i\omega_0 t) \quad , \tag{D.1.5}$$

e.g., the effect of the continuous component is no longer present.

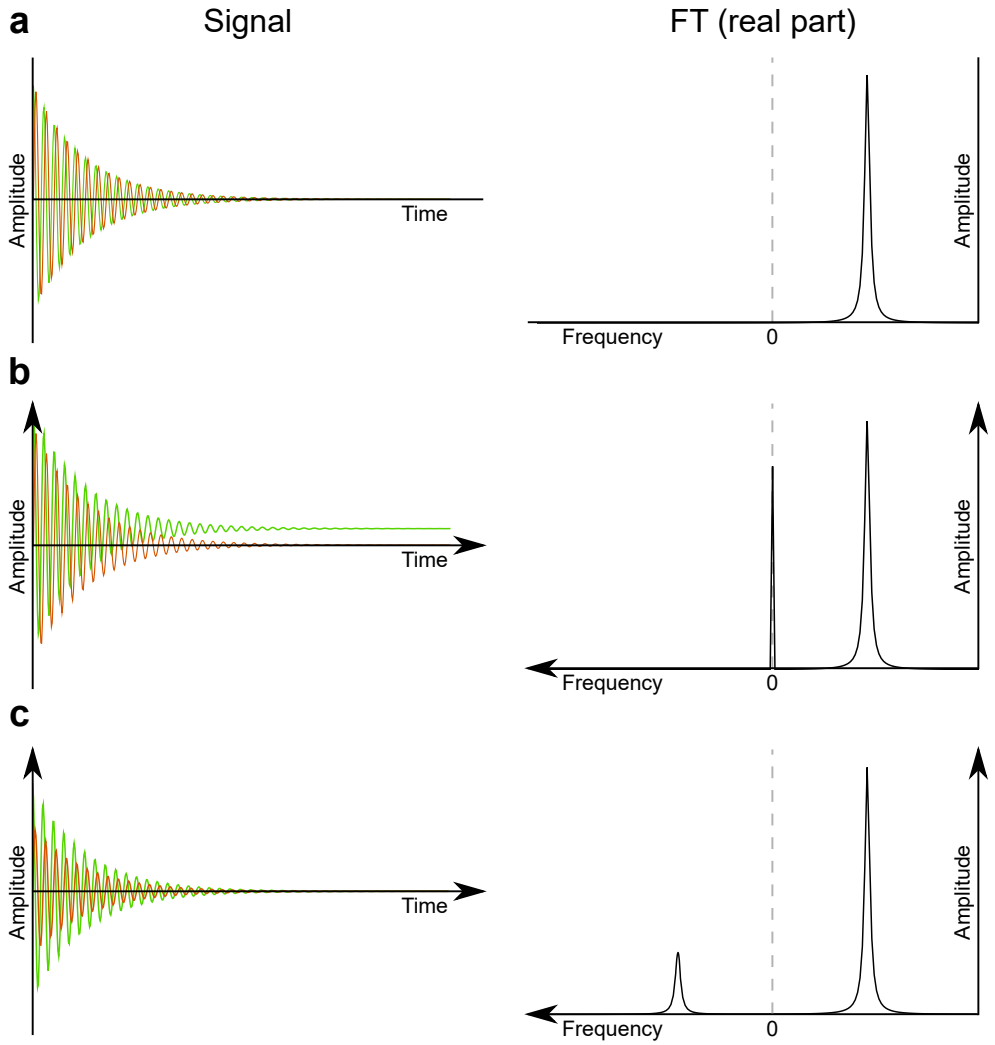

Figure D.2: *Illustration of possible artefacts in NMR spectra. On the left-hand side of the figure are plotted simulated FIDs (oscillating decay, see Appendix G.2), with the green line representing being its real part (or the x channel) and the orange line representing its imaginary part (or the y channel). Their FT are shown on the left-hand side as a function of the central frequency ω_0.* ***(a)****: Ideal case.* ***(b)****: Continuous component difference between the two channel.* ***(c)****: Gain difference between the two channels.*

Gain difference between the two channels

The gain between the two channels is not identical, causing a mirror image relative to the carrier frequency of the recorded resonances to appear in the spectrum (Figure D.2c). Noting α the gain ratio between the channel x y, the recorded signal is

$$s(t) = s_0 \cos(\omega_0 t) + i\alpha.s_0 \sin(\omega_0 t) \quad . \tag{D.1.6}$$

Shifting the pulse phase by 90°,

$$s'(t) = s_0 \sin(\omega_0 t) - i\alpha.s_0 \cos(\omega_0 t) \quad . \tag{D.1.7}$$

and shifting the receiver phase by 90°,

$$s''(t) = \alpha.s_0 \cos(\omega_0 t) + is_0 \sin(\omega_0 t) \quad . \tag{D.1.8}$$

Adding s to s'' gives a signal for which the gain is seemingly identical in the two channels

$$S(t) = s(t) + s''(t) = (1+\alpha).\exp(i\omega_0 t) \quad , \tag{D.1.9}$$

thus removing the artefact. In summary, a four-step phase cycle is necessary to remove all possible artefacts. This is the reason why the direct acquisition normally requires a phase cycling of four steps to guarantee that no artefact is present.

D.2 Nested phase cycling

This approach of phase cycling is summarized by two rules expressed by Bodenhausen *et al.* [453] :

1 *"If the phase of a pulse or group of pulses is shifted by ϕ, then a coherence undergoing a change in coherence order of $\Delta p = p'$–p experiences a phase shift of –$\phi\Delta p$."*

In other words, the term P_c in Equation (D.0.1) should be equal to 1 if the considered coherence belongs to the CTP, and 0 if not. Generally speaking, the phase on each pulse undergoes a regular phase permutation and therefore can be expressed as

$$\phi_{k,l} = \frac{2\pi l \Delta p_k}{N_k} \quad . \tag{D.2.1}$$

P_c in Equation (D.0.1) is thus expressed

$$P_c = \exp\left(i \sum_{l=1}^{l=N_{\text{nos}}} \left(\phi_{r_l} + \sum_{k=1}^{k=N_{\text{nop}}} \frac{2\pi l \Delta p_k}{N_k} \right) \right) \quad . \tag{D.2.2}$$

P_c is equal to 1 for the desired CTP if the receiver phase for the step l has the form

$$\phi_{r_l} = -\sum_{k=1}^{k=N_{\text{nop}}} \frac{2\pi l \Delta p_k^{\text{CTP}}}{N_k} \quad , \tag{D.2.3}$$

where Δp_k^{CTP} is the desired coherence changes in the CTP. Equation (D.2.3) becomes

$$P_c = \exp\left(i \sum_{l=1}^{l=N_{\text{nos}}} \sum_{k=1}^{k=N_{\text{nop}}} \frac{2\pi l \left(\Delta p_k - \Delta p_k^{\text{CTP}}\right)}{N_k} \right) \quad . \tag{D.2.4}$$

In can be observed from Equation (D.2.4) that P_c is equal to 1 if $\Delta p_k = \Delta p_k^{\text{CTP}}$, $\forall k \in [1, N_{\text{nop}}]$. Any other non-specific value of Δp_k would cause P_c to sum up to 0.

2 *"If a phase cycle uses steps of $360°/N$, then, along with the desired pathway Δp, pathways $\Delta p \pm n.N$, where $n = 1, 2, 3 \ldots$, will also be selected. All other pathways will be suppressed."*

Considering in Equation (D.2.4) the particular case when Δp_k has the form

$$\Delta p_k = \Delta p_k^{\text{CTP}} + m_k N_k \quad , \tag{D.2.5}$$

with $m_k \in \mathbb{I}$, Equation (D.2.4) becomes

$$\begin{aligned} P_c \quad &= \exp\left(i \sum_{l=1}^{l=N_{\text{nos}}} \sum_{k=1}^{k=N_{\text{nop}}} 2\pi l m_k \right) \\ &= 1 \quad , \forall m_k \in \mathbb{I} \quad . \end{aligned} \tag{D.2.6}$$

This illustrates this second rule of phase cycling. If Δp_k has the form expressed in Equation (D.2.5), then P_c equals 1, otherwise it vanishes. The desired CTP is selected, along with some undesired ones.

The design of phase cycling consists of the determination of the number of steps required to filter unwanted coherences on each pulse, then the determination of the resulting receiver phase. Even though very high coherence orders can in principle be created on a real multiple-spin system, many of them are actually negligible and can be omitted to keep the minimum required number of steps as low as possible. Coherences qualified as undesired previously are in reality desired when multiple CTPs are needed as the same time for certain experiments, as in for example the z-filtered MQMAS pulse sequence detailed in Chapter 3.3.2.

Appendix E

Useful parameters for MQMAS spectra

Introduction

This section introduces useful gradients and ratios observed on MQMAS spectra, related to theoretical elements introduced in Section 2.3. These quantities have been obtained from [33, 233].

E.1 Gradients in unsheared MQMAS spectra

As instructed in Section 3.3.3, unsheared, or non split-t_1, MQMAS spectra exhibit ridges tilted by a gradient $R = \Delta\omega_1/\Delta\omega_2$ that depends on the spin I of the investigated nucleus, and on the CTP used for the MQMAS experiment. This inclination can be corrected applying Equation (3.3.14) on the two dimension of an MQMAS spectrum. The values for the gradients R are listed in Table E.1. It should be noted that those gradients are always negative when the highest MQ transition for a given spin system is used, and positive if it is not the case.

Spin I	Coherence order $\pm p$	$R(I,p)$
$3/2$	3	$-7/9$
$5/2$	3	$19/12$
	5	$-25/12$
$7/2$	3	$101/45$
	5	$19/11$
	7	$-161/45$
$9/2$	3	$91/36$
	5	$95/36$
	7	$7/18$
	9	$-31/6$

Table E.1: *Gradients $R = \Delta\omega_1/\Delta\omega_2$ of the ridges on unsheared MQMAS spectra as a function of the spin quantum number I and the coherence order p used in the MQMAS experiment.*

E.2 Position of the ridges in MQMAS spectra

The coordinates of the barycentre (δ_I, δ_D) of the ridges in MQMAS spectra is related to the isotropic CS[1], δ_{CS} (see Equation (2.2.12)), and to the QIS[2], δ_{QIS} (see Equation (2.3.37)), according to the equations given in Table E.2.

[1] CS: *Chemical Shift*
[2] QIS: *Quadrupolar Induced Shift*

Spin I	MQ order	Dimension	Unsheared MQMAS	Sheared or split-t_1 MQMAS
$3/2$	$3Q$	δ_I	$3.\delta_{CS} + (^{6}/_{5}).\delta_{QIS}$	$(^{17}/_{8}).\delta_{CS} + (^{1}/_{2}).\delta_{QIS}$
		δ_D	$\delta_{CS} - (^{2}/_{5}).\delta_{QIS}$	$\delta_{CS} - (^{2}/_{5}).\delta_{QIS}$
$5/2$	$3Q$	δ_I	$3.\delta_{CS} - (^{4}/_{5}).\delta_{QIS}$	$(^{17}/_{31}).\delta_{CS} + (^{32}/_{93}).\delta_{QIS}$
		δ_D	$\delta_{CS} - (^{16}/_{15}).\delta_{QIS}$	$\delta_{CS} - (^{16}/_{15}).\delta_{QIS}$
	$5Q$	δ_I	$5.\delta_{CS} + (^{20}/_{3}).\delta_{QIS}$	$(^{85}/_{37}).\delta_{CS} + (^{160}/_{111}).\delta_{QIS}$
		δ_D	$\delta_{CS} - (^{16}/_{15}).\delta_{QIS}$	$\delta_{CS} - (^{16}/_{15}).\delta_{QIS}$
$7/2$	$3Q$	δ_I	$3.\delta_{CS} - (^{54}/_{15}).\delta_{QIS}$	$(^{17}/_{73}).\delta_{CS} + (^{20}/_{73}).\delta_{QIS}$
		δ_D	$\delta_{CS} - 2.\delta_{QIS}$	$\delta_{CS} - 2.\delta_{QIS}$
	$5Q$	δ_I	$5.\delta_{CS} + 2.\delta_{QIS}$	$(^{17}/_{10}).\delta_{CS} + 2.\delta_{QIS}$
		δ_D	$\delta_{CS} - 2.\delta_{QIS}$	$\delta_{CS} - 2.\delta_{QIS}$
	$7Q$	δ_I	$7.\delta_{CS} + (^{98}/_{5}).\delta_{QIS}$	$(^{238}/_{103}).\delta_{CS} + (^{280}/_{103}).\delta_{QIS}$
		δ_D	$\delta_{CS} - 2.\delta_{QIS}$	$\delta_{CS} - 2.\delta_{QIS}$
$9/2$	$3Q$	δ_I	$3.\delta_{CS} - (^{36}/_{5}).\delta_{QIS}$	$(^{17}/_{127}).\delta_{CS} + (^{32}/_{127}).\delta_{QIS}$
		δ_D	$\delta_{CS} - (^{16}/_{5}).\delta_{QIS}$	$\delta_{CS} - (^{16}/_{5}).\delta_{QIS}$
	$5Q$	δ_I	$5.\delta_{CS} - 4.\delta_{QIS}$	$(^{85}/_{131}).\delta_{CS} + (^{160}/_{131}).\delta_{QIS}$
		δ_D	$\delta_{CS} - (^{16}/_{5}).\delta_{QIS}$	$\delta_{CS} - (^{16}/_{5}).\delta_{QIS}$
	$7Q$	δ_I	$7.\delta_{CS} + (^{56}/_{5}).\delta_{QIS}$	$(^{119}/_{25}).\delta_{CS} + (^{224}/_{25}).\delta_{QIS}$
		δ_D	$\delta_{CS} - (^{16}/_{5}).\delta_{QIS}$	$\delta_{CS} - (^{16}/_{5}).\delta_{QIS}$
	$9Q$	δ_I	$9.\delta_{CS} + (^{216}/_{5}).\delta_{QIS}$	$(^{85}/_{37}).\delta_{CS} + (^{160}/_{37}).\delta_{QIS}$
		δ_D	$\delta_{CS} - (^{16}/_{5}).\delta_{QIS}$	$\delta_{CS} - (^{16}/_{5}).\delta_{QIS}$

Table E.2: *Relation between the centre of gravity of the ridges, (δ_I, δ_D), in a MQMAS spectrum, to the isotropic chemical shift and the QIS, δ_{CS} and δ_{QIS}.*

Likewise, Table E.2 can be rearranged to establish δ_{CS} and δ_{QIS} as a function of the coordinates of the barycentre of the quadrupolar lineshape. Those are given in Table E.3.

Spin I	MQ order	Quantity	Unsheared MQMAS	Sheared or split-t_1 MQMAS
$3/2$	$3Q$	δ_{CS}	$(1/6).\delta_I + (1/2).\delta_D$	$(8/27).\delta_I + (10/27).\delta_D$
		δ_{QIS}	$(5/12).\delta_I - (5/4).\delta_D$	$(40/54).\delta_I - (85/54).\delta_D$
$5/2$	$3Q$	δ_{CS}	$(4/9).\delta_I - (1/3).\delta_D$	$(31/27).\delta_I + (10/27).\delta_D$
		δ_{QIS}	$(5/12).\delta_I - (15/12).\delta_D$	$(155/144).\delta_I - (85/144).\delta_D$
	$5Q$	δ_{CS}	$(4/45).\delta_I + (5/9).\delta_D$	$(37/135).\delta_I + (10/27).\delta_D$
		δ_{QIS}	$(1/12).\delta_I - (5/12).\delta_D$	$(37/144).\delta_I - (85/144).\delta_D$
$7/2$	$3Q$	δ_{CS}	$(5/6).\delta_I - (3/2).\delta_D$	$(73/27).\delta_I + (10/27).\delta_D$
		δ_{QIS}	$(5/12).\delta_I - (1/12).\delta_D$	$(73/54).\delta_I - (17/54).\delta_D$
	$5Q$	δ_{CS}	$(15/36).\delta_I - (15/36).\delta_D$	$(10/27).\delta_I + (10/27).\delta_D$
		δ_{QIS}	$(1/12).\delta_I - (5/12).\delta_D$	$(5/27).\delta_I - (17/54).\delta_D$
	$7Q$	δ_{CS}	$(15/252).\delta_I + (197/252).\delta_D$	$(103/378).\delta_I + (20/54).\delta_D$
		δ_{QIS}	$(5/168).\delta_I - (1/72).\delta_D$	$(103/756).\delta_I - (238/378).\delta_D$
$9/2$	$3Q$	δ_{CS}	$(4/3).\delta_I - 3.\delta_D$	$(127/27).\delta_I + (10/27).\delta_D$
		δ_{QIS}	$(5/12).\delta_I - (5/4).\delta_D$	$(635/432).\delta_I - (85/432).\delta_D$
	$5Q$	δ_{CS}	$(4/15).\delta_I - (1/3).\delta_D$	$(131/135).\delta_I + (10/27).\delta_D$
		δ_{QIS}	$(1/12).\delta_I - (5/12).\delta_D$	$(131/432).\delta_I - (85/432).\delta_D$
	$7Q$	δ_{CS}	$(2/7).\delta_I - \delta_D$	$(25/189).\delta_I + (70/189).\delta_D$
		δ_{QIS}	$(5/56).\delta_I - (35/56).\delta_D$	$(125/3024).\delta_I - (85/432).\delta_D$
	$9Q$	δ_{CS}	$(2/45).\delta_I + (27/45).\delta_D$	$(37/135).\delta_I + (10/27).\delta_D$
		δ_{QIS}	$(1/72).\delta_I - (1/8).\delta_D$	$(37/432).\delta_I - (85/432).\delta_D$

Table E.3: *Relation between the isotropic chemical shift and the QIS, δ_{CS} and δ_{QIS}, to the centre of gravity of the ridges, (δ_I, δ_D), in a MQMAS spectrum.*

Data for sheared/split-t_1 MQMAS spectra reported in Table E.2 and Table E.3 uses the convention established by Pike *et al.*,[220] in which a ppm corresponds to a same variation in frequency in both dimensions. The values in those tables would differ from that using the convention from Amoureux and Fernandez [217] (see Section 3.3.3).

E.3 Scaling factors for MQMAS and STMAS

The scaling factors ξ defined in Equation (3.3.16) for MQMAS are reported in Table E.4 for all half-integer spin quantum numbers I and all coherence orders p of the MQMAS.

The STMAS scaling factors are also reported for comparison, using the labels defined in Section 2.3.2, Figure 2.7. As a comparison, the scaling factor of a DAS experiment is $\xi = +1.0$.[248]

Spin I	Coherence order p	$\xi(I,p)$	
$3/2$	-3	$+17/8$	$\simeq +2.125$
$5/2$	$+3$	$-17/31$	$\simeq -0.548$
	-5	$+85/37$	$\simeq +2.297$
$7/2$	$+3$	$-17/73$	$\simeq -0.233$
	$+5$	$-17/10$	$\simeq -1.700$
	-7	$+238/103$	$\simeq +2.311$
$9/2$	$+3$	$-17/127$	$\simeq -0.134$
	$+5$	$-85/131$	$\simeq -0.649$
	$+7$	$-119/25$	$\simeq -4.760$
	-9	$85/37$	$\simeq +2.297$

Table E.4: *Scaling factors $\xi(I,p)$ for MQMAS as a function of the spin I and of the coherence order p.[220]*

Spin I	ST label	$\xi(I,p)$	
$3/2$	ST_1	1	
$5/2$	ST_1	$17/31$	$\simeq 0.548$
	ST_2	1	
$7/2$	ST_1	$17/73$	$\simeq 0.233$
	ST_2	1	
	ST_3	1	
$9/2$	ST_1	$17/127$	$\simeq 0.134$
	ST_2	$17/19$	$\simeq 0.895$
	ST_3	1	
	ST_4	1	

Table E.5: *Scaling factors $\xi(I,p)$ for STMAS as a function of the spin I and the ST label.[257]*

E.4 Split-t_1 coefficients for MQMAS

Table E.6 reports the split-t_1 coefficients, deduced from Table E.1, where t_1 is defined

$$t_1 = t_{\mathrm{MQ}} + t_{1\mathrm{Q}} \quad . \tag{E.4.1}$$

t_{MQ} and $t_{1\mathrm{Q}}$ are respectively the MQ and 1Q evolution period, given by

$$\begin{cases} t_{\mathrm{MQ}} = \dfrac{1}{1+R(I,p)}.t_i & \text{(E.4.2a)} \\ t_{1\mathrm{Q}} = \dfrac{R(I,p)}{1+R(I,p)}.t_i \quad . & \text{(E.4.2b)} \end{cases}$$

It can be noted that the definition of the MQ and 1Q evolution periods differ from the definition given in Equation (3.3.19).

Spin I	Evolution period	Coherence order p			
		3	5	7	9
$3/2$	$t_{1\mathrm{Q}}$	$7/16$	N/A	N/A	N/A
	t_{MQ}	$9/16$	N/A	N/A	N/A
$5/2$	$t_{1\mathrm{Q}}$	$19/31$	$25/37$	N/A	N/A
	t_{MQ}	$12/31$	$12/37$	N/A	N/A
$7/2$	$t_{1\mathrm{Q}}$	$101/146$	$11/20$	$161/206$	N/A
	t_{MQ}	$45/146$	$9/20$	$45/206$	N/A
$9/2$	$t_{1\mathrm{Q}}$	$91/127$	$95/131$	$7/25$	$31/37$
	t_{MQ}	$36/127$	$36/131$	$18/25$	$6/37$

Table E.6: *Coefficients for the split-t_1 MQMAS experiments.*

Appendix F

Adiabatic pulses

Introduction

The original NMR experiments [1–3] were performed using a magnetic field $\vec{B}_0$ varied in amplitude, submitted to a constant RF field $\vec{B}_1$. The flip angle achieved by the magnetisation with this approach is mostly insensitive to the amplitude of the magnetic field B_1.

In order to reach magnetic fields strong enough to produce high-resolution spectra on insensitive nuclei (*e.g.*, ^{13}C or ^{15}N), the resistive magnets have now been replaced, in most NMR facilities, by superconducting magnets to produce the static magnetic field $\vec{B}_0$, while resistive magnets having applications mainly in relaxometry or for high-resolution spectra of only very sensitive nuclei such as ^{1}H. However, the nature of a superconducting magnet makes it impossible to vary the static magnetic field, so the flipping of the magnetisation is produced by a pulsed RF field (as detailed in Section 1.3.2), chosen to excite the spectral region of interest.

It is possible to reproduce the robustness-to-B_1 aspect of the original experiments with pulsed RF field by varying the frequency carrier of the pulse during its application. These pulses are termed ”adiabatic pulses” and constitute a broad category of shaped pulses. Primarily, the aim of adiabatic pulses is to nutate the magnetisation by precise, broadband, and/or B_1-insensitive flip angles, with applications mostly found in the fields of in-vivo NMR and MRI.[26, 473–475] This thesis only deals with the application of adiabatic pulses as a signal improvement method for experiments involving quadrupolar nuclei, but the mechanism involved to produce either of those effects is identical and

will be introduced briefly in this appendix.

This appendix was mainly inspired from Tannús and Garwood.[53, 414, 419]

F.1 Off-resonance effects

Adiabatic pulses can be visualised in the rotating frame Σ_{rot} introduced Section 1.1. This frame is defined as rotating at the same frequency ω_{RF} as any applied RF field, which results in the magnetisation nutating anticlockwise around a magnetic field $\vec{B}_{\text{eff}}$, given in Equation (1.1.20),[1] and expressed in Σ_{rot} as

$$\vec{B}_{\text{eff}} = \Delta\omega_0.\vec{u}_z + \omega_1 \exp(i\theta_{\text{RF}}).\vec{u}_\rho \quad , \tag{F.1.1}$$

defining the offset frequency $\Delta\omega_0$ as the difference between the RF frequency and the Larmor frequency

$$\Delta\omega_0 = \omega_0 - \omega_{\text{RF}} \quad , \tag{F.1.2}$$

three cases can be distinguished:

1 The RF field is on resonance or close to resonance, *e.g.* $\mid \Delta\omega_0 \mid \ll \mid \omega_1 \mid$, resulting in

$$\vec{B}_{\text{eff}} \simeq -\frac{\omega_1}{\gamma} \exp(i\theta_{\text{RF}}).\vec{u}_\rho \quad , \tag{F.1.3}$$

2 The RF field is far off resonance, *e.g.* $\mid \Delta\omega_0 \mid \gg \mid \omega_1 \mid$, resulting in

$$\vec{B}_{\text{eff}} \simeq \frac{\Delta\omega_0}{\gamma}.\vec{u}_z \quad , \tag{F.1.4}$$

3 The RF field is close to resonance and $\mid \Delta\omega_0 \mid \approx \mid \omega_1 \mid$, resulting in

$$\vec{B}_{\text{eff}} = \frac{\Delta\omega_0}{\gamma}.\vec{u}_z - \frac{\omega_1}{\gamma} \exp(i\theta_{\text{RF}}).\vec{u}_\rho \quad . \tag{F.1.5}$$

It follows that there is an angle between $\vec{B}_0$ and $\vec{B}_{\text{eff}}$ given by

$$\phi = \tan^{-1}\left(\frac{\omega_1}{\Delta\omega_0}\right) \quad . \tag{F.1.6}$$

As illustrated Figure F.1, the consequence of the application of a pulse at a constant offset is, if applied significantly off resonance, $\phi \neq 90°$ and the nutation does not go though

[1] It can be noted that the expression of $\vec{B}_{\text{eff}}$ in Equation (F.1.1) is oppositely signed compared to that of Equation (1.1.20).

the $-z$ axis. This situation can occur if a sample contains several species with very different Larmor chemical shifts. All adiabatic pulses have a common feature of being applied at applied with a time-dependant offset $\Delta\omega(t)$, (*e.g*, FM), or a time-dependant B_1 amplitude (*e.g.*, AM), or both (see Section 4.3.1). An AM and FM modulated pulse would have a $\vec{B}_1(t)$ (See Equation (1.1.14)) expressed in Σ_{rot} as

$$\vec{B}_1(t) = -\frac{\omega_1(t)}{\gamma} \exp\left(i\phi_{\text{RF}}t\right).\vec{u}_\rho \quad , \tag{F.1.7}$$

where $\phi_{\text{RF}}(t)$ is the time-dependant phase of the RF pulse and can be related to the offset $\Delta\omega_0(t)$ by

$$\phi_{\text{RF}}(t) = \int_{t_0}^{t} \Delta\omega_0(\tau).d\tau \quad , \tag{F.1.8}$$

where t_0 is the moment when the pulse is initially applied. A pulse exhibiting an AM, an FM, or both, will result in the angle ϕ changing over time. A similar effect would be produced by sweeping the magnetic field B_0 in amplitude, as in classical NMR experiments. Magnetisation $\vec{M}$ will continue nutating around (or perpendicular to) any time-dependant $\vec{B}_{\text{eff}}$ magnetic field, providing that its motion is slow enough for the magnetisation to follow at any moment of the pulse. Mathematically, this condition can be written [476]

$$\left| \frac{d\phi(t)}{dt} \right| \ll \left| \gamma B_{\text{eff}} \right| \quad , \forall t \quad . \tag{F.1.9}$$

The condition in Equation (F.1.9) is known as the adiabaticity condition. It can be derived from this condition the adiabaticity factor α, given by

$$\alpha = \left| \frac{\gamma B_{\text{eff}}}{d\phi(t)/dt} \right| \quad , \tag{F.1.10}$$

with the adiabaticity condition now being $\alpha \gg 1$. This adiabaticity condition can be defined for any pulse and can be expressed in a more exhaustive manner, *i.e.* expressed as a function pulse length, RF field strength, offset-sweep width *etc.* with analytical expressions for $B_1(t)$ and $\Delta\omega_0(t)$. Qualitatively, the adiabaticity condition is considerer fulfilled if B_1 is sufficiently strong, and if the sweep is sufficiently slow and narrow. As long as the adiabatic condition is fulfilled, magnetisation will be flipped by a same flip angle, independent of the amplitude of $\vec{B}_1$.

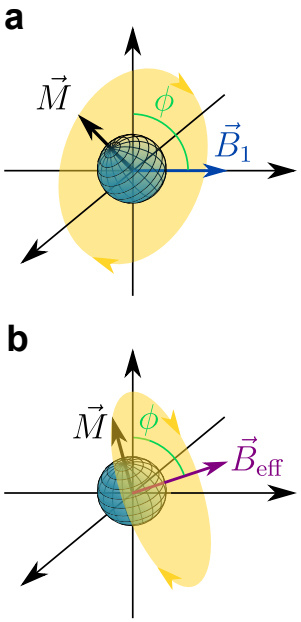

Figure F.1: *Schematic representation of the nutation plane when **(a)**: the RF field is fully on resonance ($\alpha = 90$ °), and **(b)**: when off-resonance effects are significant ($\alpha \neq 90$°).*

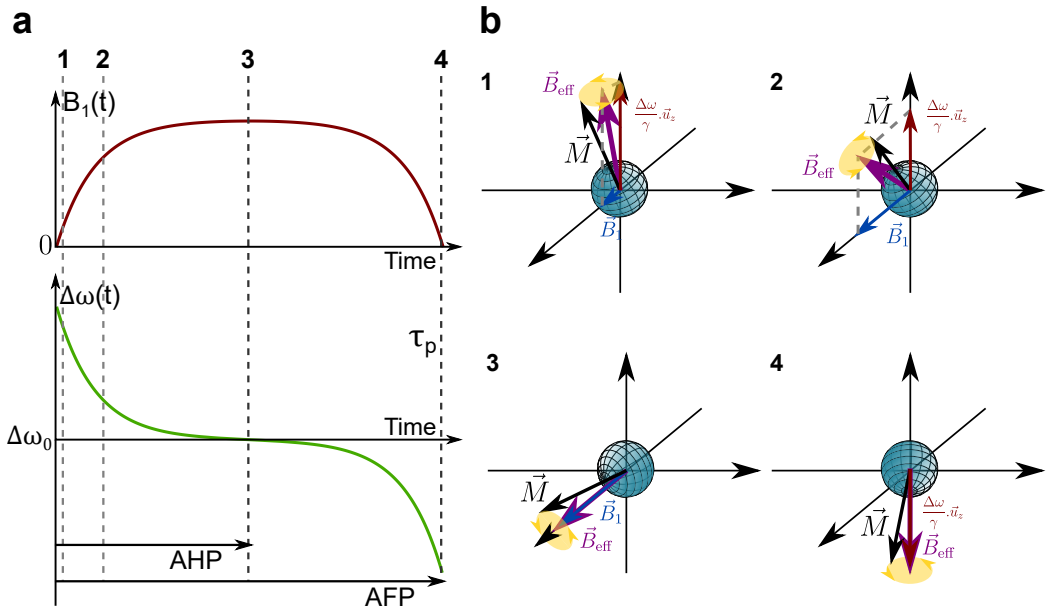

Figure F.2: ***(a)****: Schematic representation of the variation of $B_1(t)$ and $\Delta\omega_0(t)$ as a function of time during the application of a pulse of duration τ_p performing an AHP or an AFP .* ***(b)****: Representation of the bulk magnetisation vector $\vec{M}$ and the effective magnetic field $\vec{B}_{\text{eff}}$ at several moments of the application of the pulse. These moments are represented in* ***(a)*** *with dashed lines. $\vec{M}$ is represented nutation around $\vec{B}_{\text{eff}}$ and is shown as a yellow circle.*

In practice, only a relatively weak RF field strength can fulfil the adiabaticity condition in most cases, resulting in methods being in general very robust to RF inhomogeneities, versatile and easy to experimentally optimise. Apart from complexity and technical implementation issues, the main drawback of those methods is their long application duration (typically several milliseconds or longer), implying that samples with long relaxations (see Section 1.3.1) is required to avoid sensitivity or quantitativity problems as a result.

F.2 The AHP and AFP classes

The terms AHP[2] and AFP[3] refer to a large class of adiabatic pulses, primary designed to flip the magnetisation of a constant angle independent of the frequency offset $\Delta\omega_0$ and of the chemical shifts of the different species, or field gradients.[53] ω_1 and $\Delta\omega_0$ can be

[2]AHP: *Adiabatic Half Passage*
[3]AFP: *Adiabatic Full Passage*

expressed as

$$\begin{cases} \omega_1(t) = \omega_1^{\max} F_1(t) & \text{(F.2.1a)} \\ \Delta\omega(t) = (\Delta\omega_0 - \Delta\omega_0^{\max})\, F_2(t) \quad , & \text{(F.2.1b)} \end{cases}$$

where $F_1(t)$ and $F_2(t)$ are two dimensionless and normalized functions, $\omega_1^{\max}$ is the maximum RF field strength the pulse is applied at, $\Delta\omega_0^{\max}$ is half of the maximum offset of the sweep of the pulse, and $\Delta\omega_0$ the central offset, *i.e.*, the frequency around which the adiabatic passage is executed. For example, the simplest adiabatic pulse available termed "Chirp" defines [310, 477, 478]

$$\begin{cases} F_1(t) = 1 & \text{(F.2.2a)} \\ F_2(t) = \lambda t \quad , & \text{(F.2.2b)} \end{cases}$$

and the HS pulse introduced in Section 7.1.3 defines

$$\begin{cases} F_1(t) = \text{sec}(t) & \text{(F.2.3a)} \\ F_2(t) = \tanh(t) \quad . & \text{(F.2.3b)} \end{cases}$$

Various other shapes are available in the literature.[53] A pulse that describes an AFP begins far off resonance with $\Delta\omega_0(0) = -\Delta\omega_0^{\max}$ and $\omega_1(t = 0) = 0$ (Figure F.2b.1), and finish far off resonance with $\Delta\omega_0(\tau_p) = -\Delta\omega_0^{\max}$ and $\omega_1(\tau_p) = 0$ (Figure F.2b.4); The middle of the AFP (Figure F.2b.3) is applied on resonance, with $\omega_1(\tau_p/2) = \omega_1^{\max}$. A pulse describing an AHP stops at $t = \tau_p/2$, as shown in Figure F.2a. As long as the adiabaticity condition (Equation (F.1.9)) is fulfilled at any time, the magnetisation vector $\vec{M}$ for entities will be flipped or inverted by a constant angle throughout the inversion bandwidth if their respective chemical shifts is comprised between $\Delta\omega_0 - \Delta\omega_0^{\max}$ and $\Delta\omega_0 + \Delta\omega_0^{\max}$.

Appendix G

Fourier transformation and applications

Introduction

This appendix introduces the FT[1], used to separate components of a signal composed of multiple oscillating decays. For any typical FID recorded by NMR, the signal usually consists of a sum of several decaying oscillating components. Although it is possible to measure the frequency (or pseudo-frequency) of a signal consisting of only one frequency, it becomes increasingly difficult, if not possible, when the signal consists of a large number of components. The first proposition to use the Fourier transform for NMR analysis was reported by Ernst and Anderson.[76] Since then it has become routinely used for NMR spectroscopy.

This appendix was mainly inspired from the course of Barbier.[479]

G.1 Continuous FT: definition and properties

Definition G.1: Continuous Fourier Transform

The FT relates a complex function s to another complex function S following the definition

$$S(\omega) = \mathrm{FT}[s](\omega) = \int_{-\infty}^{+\infty} s(t)\exp(-i\omega t).dt \quad , \tag{G.1.1}$$

[1] FT: *Fourier Transform*

where t and ω are two real variables, associated with time and angular frequency, respectively.

Definition G.2: Fourier Transform in frequency

Spectroscopists often prefer the definition in frequency (e.g., in Hz) rather than in angular frequency (e.g., in rad.s^{-1}), which is

$$S(\nu) = \mathrm{FT}[s](\nu) = \int_{-\infty}^{+\infty} s(t) \exp(-i2\pi\nu t).dt \quad , \tag{G.1.2}$$

where ν is a frequency.

The real and imaginary FT can also be introduced. These are given by

$$S(\omega) = S_{\Re}(\omega) + iS_{\Im}(\omega) \quad , \tag{G.1.3}$$

where

$$S_{\Re}(\omega) = \int_{-\infty}^{+\infty} s(t) \cos(i\omega t).dt \tag{G.1.4a}$$

$$S_{\Im}(\omega) = \int_{-\infty}^{+\infty} s(t) \sin(i\omega t).dt \quad . \tag{G.1.4b}$$

Property G.1: Linearity of the FT

The FT of a sum of functions s_n, $n \in \mathbb{N}$, is equal to the sum of the FT of each of the functions s_n, i.e.,

$$\int_{-\infty}^{+\infty} \sum_n s_n(t) \exp(i\omega t).dt = \sum_n \int_{-\infty}^{+\infty} s_n(t) \exp(i\omega t).dt \quad . \tag{G.1.5}$$

Property G.1 is very important for NMR, as FT of a signal composed of several oscillating components is equal to the sum of the FT of its component. This property is the source of the ability of the FT to separate the components of a signal by their frequency, as shown in Figure G.1.

Property G.2: Fourier transform of even and odd functions

It can be easily deduced from Equations (G.1.4a) and (G.1.4b) the properties presented in Table G.1.

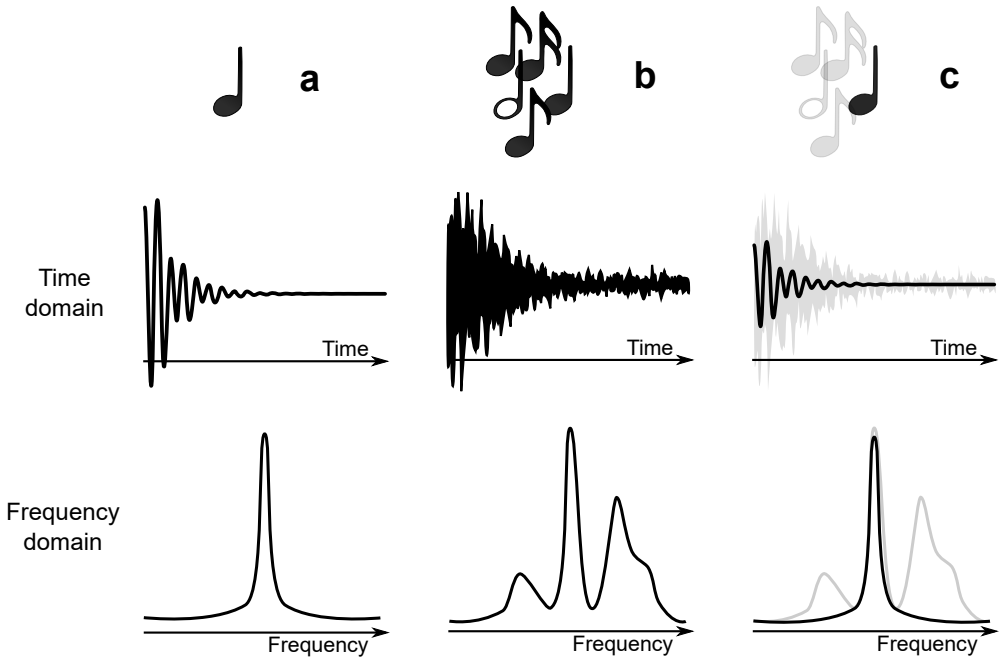

Figure G.1: *Illustration of the relation between time domain and frequency domain for several signals and their FT for* ***(a)****: a single oscillating decay,* ***(b)****: a sum of several oscillating decays, and* ***(c)****: one of the multiple decays of* ***(b)****.*

s is even, *i.e.*, $s(t) = s(-t)$:	if s is real	then S is real and even
	if s is imaginary	then S is imaginary and even
	if s is complex	then S is complex and even
s is odd, *i.e.*, $s(t) = -s(-t)$:	if s is real	then S is imaginary and odd
	if s is imaginary	then S is real and odd
	if s is complex	then S is complex and odd

Table G.1: *Properties of the FT of even and odd functions.*

Property G.3: Translation of the FT

Upon applying the translation $t \to t - t_0$*, the relation between* $\mathrm{FT}[s(t)]$ *and* $\mathrm{FT}[s(t - t_0)]$ *is*

$$\mathrm{FT}[s(t - t_0)](\omega) = e^{i\omega t_0}\mathrm{FT}[s(t)](\omega) \quad . \tag{G.1.6}$$

Many usual functions present possess symmetrical properties and thus can be represented as even/odd functions using a simple translation of the time origin, simplifying the calculation of the FT.

Definition G.3: Inverse Fourier Transform

The IFT[2], i.e., the transformation that returns the original function for its FT, is defined

$$s(t) = \text{IFT}[S](\omega) = \frac{1}{2\pi} \int_{-\infty}^{+\infty} S(t).\exp(+i\omega t).dt \quad , \tag{G.1.7}$$

when given in angular frequency units (e.g., in rad.s^{-1}), and

$$s(t) = \text{IFT}[S](\nu) = \int_{-\infty}^{+\infty} S(t).\exp(+i2\pi\nu t).dt \quad , \tag{G.1.8}$$

when given in frequency units (e.g., in Hz).

It can be noted that the $1/2\pi$ normalisation factor is necessary to obtain $s = \text{IFT}(\text{FT}(s))$. The definition in frequency rather than in angular frequency is convenient as the normalisation factor disappears in both the expressions of the direct and inverse FT, given in Equation (G.1.8). It is straightforward to demonstrate that the properties established in Appendix G.1 for the direct transform are all valid for the inverse transform. In particular, the symmetry properties given in Table G.1 are also valid for the IFT.

Definition G.4: Convolution product
The operation, noted $*$, defined

$$(s_1 * s_2)(t) = \int_{-\infty}^{+\infty} s_1(t-\tau)s_2(t).d\tau \quad , \tag{G.1.9}$$

is called convolution product of the two functions s_1 and s_2.

Property G.4: Relation to the Fourier space
Two functions that are multiplied in one domain will be convoluted in the other domain

$$\text{FT}[s_1.s_2] = \text{FT}[s_1] * \text{FT}[s_2] \quad . \tag{G.1.10}$$

G.2 Applications for several typical NMR signals

Non-decaying oscillation

First, consider a signal s consisting of a single complex non-decaying oscillating, that thus can be written

[2] IFT: *Inverse Fourier Transform*

$$s(t) = s_0 \exp(i2\pi\nu_0 t) \quad , \tag{G.2.1}$$

where ν_0 is the signal frequency, *i.e.*, the Larmor frequency. The FT of s is given by

$$S(\nu) = s_0.\delta(\nu - \nu_0) \quad , \tag{G.2.2}$$

where δ is Dirac's delta function, defined as, $\forall x \in \mathbb{R}$,

$$\delta(x) = \begin{cases} +\infty & \text{if } x = 0 \\ 0 & \text{if } x \neq 0 \quad . \end{cases} \tag{G.2.3}$$

As a result, the FT of an oscillating signal exhibit a peak for $\nu = \nu_0$. This example illustrates the utility of the FT, as its application on a oscillating signal results in a function peaking at the Larmor frequency of the original signal.

Oscillating decay

More realistically, the NMR signal presents some decay, thus can be written

$$s(t) = s_0 \exp(i\omega_0 t) \exp\left(-t/T_2^\star\right) \exp\left(i\phi\right) \quad , \tag{G.2.4}$$

where $T_2^\star$ is a time constant characterising the signal decay (see Section 3.1.1), associated with the spin-spin relaxation, and ϕ is the phase of the signal. The FT of s leads to the following real and imaginary parts of the resulting complex transform of the signal

$$S(\omega)/s_0 = \Re(\omega)\cos\phi + i\Im(\omega)\sin\phi \quad , \tag{G.2.5}$$

where

$$\Re(\omega) = \frac{1/T_2^\star}{(1/T_2^\star)^2 + (\omega - \omega_0)^2} \quad , \tag{G.2.6a}$$

and

$$\Im(\omega) = -\frac{\omega - \omega_0}{(1/T_2^\star)^2 + (\omega - \omega_0)^2} \quad . \tag{G.2.6b}$$

Equation (G.2.6a) is called an absorptive Lorentzian (Figure G.2a). Its opposite is an emissive Lorentzian (Figure G.2c). Equation (G.2.6b) is called an dispersive Lorentzian (Figure G.2b). Its opposite is a negative dispersive Lorentzian (Figure G.2d). The module, shown in Figure G.2e, is given by

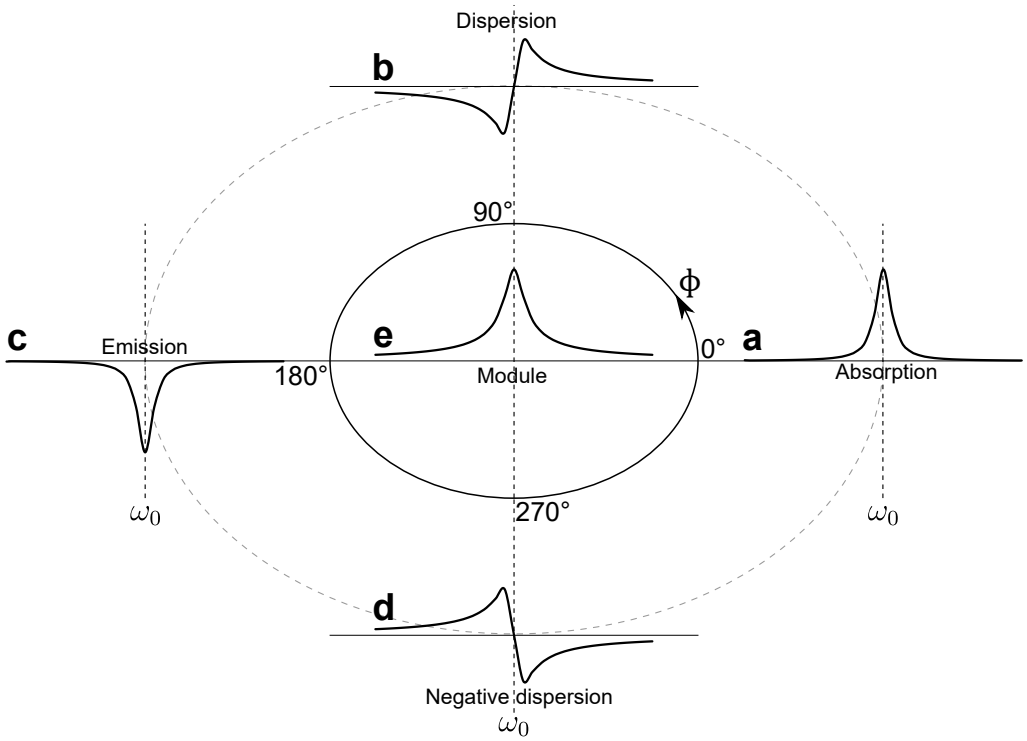

Figure G.2: *Representation of the lineshape of different Lorentzian functions according to the phase ϕ.* ***(a)****: represents an absorptive Lorentzian,* ***(b)****: a dispersive Lorentzian,* ***(c)****: a emissive Lorentzian,* ***(d)*** *a negative dispersive Lorentzian and* ***(e)*** *the module of the Lorentzian.*

$$|S(\omega)| = \sqrt{\frac{T_2^{\star 2}}{1 + T_2^{\star 2}(\omega - \omega_0)^2}} \quad . \tag{G.2.7}$$

The width at half of the maximal amplitude for $S(\omega)$ is

$$\begin{cases} \Delta\Re = 2/T_2^\star & \text{(G.2.8a)} \\ \Delta\Im = 1/T_2^\star & \text{(G.2.8b)} \\ \Delta|S| = 2\sqrt{3}/T_2^\star \quad . & \text{(G.2.8c)} \end{cases}$$

The Lorentzian lineshape corresponds to an ideal case where the signal relaxation can be assumed mono-exponential as in Equation (G.2.4), which is the case when mobility and collision is the main cause of the relaxation. That is, in the liquid, solution, or gas state. In the solid state, where particles are rigid and where interaction partners do not change over time, different relaxation mechanisms take place, giving rise to a lineshape which is best described with a Gaussian function.[480] This lineshape is defined as in

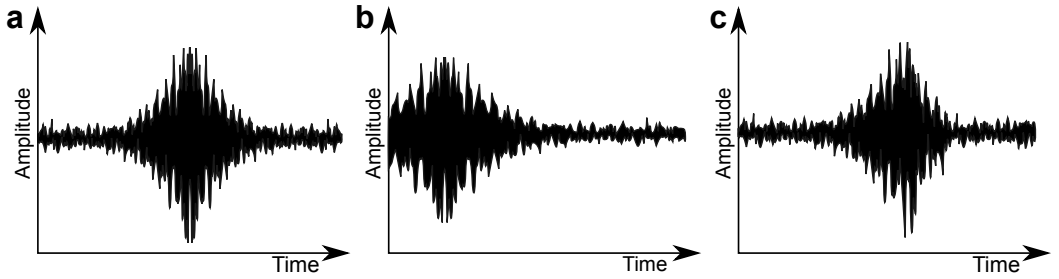

Figure G.3: *Representation of **(a)**: a full-echo, **(b)**: a incomplete echo, and **(c)**: a distorted echo.*

Equation (G.2.5), with

$$\Re(\omega) = \frac{1/T_2^\star}{\sqrt{2\pi}} \exp\left[\frac{1}{2}\left(\frac{\omega-\omega_0}{T_2^\star}\right)^2\right] \quad , \tag{G.2.9a}$$

and

$$\Im(\omega) = \frac{\omega-\omega_0}{\sqrt{2\pi}} \exp\left[\frac{1}{2}\left(\frac{\omega-\omega_0}{T_2^\star}\right)^2\right] \quad . \tag{G.2.9b}$$

A Gaussian lineshape is similar to a Lorentzian lineshape. Both are maximum for $\omega = \omega_0$ and steadily decrease to zero as $|\omega - \omega_0|$ increases, but the half-width of a Gaussian is narrower than that of a Lorentzian. Some fitting programs use Lorentzian/Gaussian hybrid functions.[242]

Full-echo

An full-echo, shown in Figure G.3a, is the signal acquired for several different types of NMR experiments. It has several useful properties compared to a normal exponential, such as refocussing broadened resonances arising from fast relaxation. It is the signal recorded for the shifted-echo MQMAS experiment (Section 3.3.2). An echo can be represented by the following function:

$$s(t) = s_0 \exp(i\omega_0 t) \exp\left(-|t|/T_2^\star\right) \quad . \tag{G.2.10}$$

A whole echo can be phased to be and even in the real dimension (Figure G.3a). Using the properties reported in Table G.1, the FT of s is

$$S(\omega) = \frac{2T_2^\star}{T_2^{\star 2}(\omega+\omega_0)^2 + 1} \quad . \tag{G.2.11}$$

It can be seen that the imaginary part of the FT signal is zero, meaning that the observed lineshape in the frequency domain is purely absorptive (as in Figure G.2a).

The key importance of the echo symmetry can be seen when establishing this result. Experimentally, this may be no longer the case, especially when an incomplete echo is recorded (Figure G.3b), or when relaxation affects the shape of the echo (Figure G.3c). In these cases, imaginary components are reintroduced. Moreover, a first-order phase correction must be applied to compensate for the time origin not being at the symmetry point of the full-echo. This correction can be deduced Property G.3 and is performed by the multiplication of the FT signal by $\exp(i\omega t_e)$, where t_e is the echo delay (see Section 3.1.1). This is expressed for the digitalised signal (see Appendix G.3) as $\exp(i\phi_{1C}\omega)$, where ϕ_{1C} is called the first-order phase correction, and is given by

$$\phi_{1C} = 360° \times \frac{t_e}{2T_{Rec}} \quad , \tag{G.2.12}$$

where T_{Rec} is the dwell time, *i.e.*, which is the time interval between two adjacent complex points of the signal (see Equation (G.3.2)).

G.3 Discrete FT

Experimental FIDs are not continuous functions as described previously, and must be digitalised. The description and properties of the FTD[3], *e.g.*, the *FT* applied for digitalised signal is described here.

Definition G.5: Dirac comb

A Dirac comb is a function with Dirac's delta function (see Equation (G.2.3)) regularly spaced in time, according to the definition

$$\text{Ш}_{f_{rec}}(t) = \sum_{k=-\infty}^{k=+\infty} \delta\left(t - \frac{k}{f_{rec}}\right) \quad , \tag{G.3.1}$$

where $k \in \mathbb{I}$. f_{rec} is called the sampling frequency or sampling rate, i.e., the number of points of the digitalisation per unit of time, i.e., the number of Dirac's delta function per unit of time. The time spacing between each of the delta function is given by

$$T_{Rec} = \frac{1}{f_{rec}} \quad , \tag{G.3.2}$$

where T_{rec} is called the dwell time.

[3] FTD: *Discrete Fourier Transform*

Definition G.6: FT of the Dirac comb
The FT of the Dirac comb is given by

$$\mathrm{FT}(\text{Ш}_{f_{\mathrm{rec}}})(\nu) = f_{\mathrm{rec}} \sum_{k=-\infty}^{k=+\infty} \delta\left(\nu - k f_{\mathrm{rec}}\right) \quad . \tag{G.3.3}$$

Mathematically speaking, digitalising (or sampling) a signal corresponds to the multiplication of any given continuous signal by a Dirac comb. The digitalised signal s_{dig} associated with the continuous signal s is expressed as

$$s_{\mathrm{dig}}(t) = s(t) \times \text{Ш}_{f_{\mathrm{rec}}}(t) \quad , \tag{G.3.4}$$

and its FT, S_{dig}, is given by

$$S_{\mathrm{dig}}(\nu) = \left(s * \mathrm{FT}[\text{Ш}_{f_{\mathrm{rec}}}]\right)(\nu) \tag{G.3.5a}$$

$$= s(\nu) * f_{\mathrm{rec}} \sum_{k=-\infty}^{k=+\infty} \delta\left(\nu - k f_{\mathrm{rec}}\right) \quad , \tag{G.3.5b}$$

where $*$ is the convolution product defined in Definition G.4. Furthermore, an FID cannot be recorded for an infinite time, and thus must be truncated, and recorded using a finite N number of points. The total time them become $T_{\mathrm{rec}} = {}^{N}/_{f_{\mathrm{rec}}}$. This additional condition defines the FTD, which applies on a complex sequence s containing N terms and results in a complex sequence S containing N terms.

Definition G.7: Discrete Fourier Transform
In frequency units, the definition of the FTD is

$$S(\nu_n) = \mathrm{FT}_{\mathrm{D}}[s(t_n)] = A \sum_{k=1}^{k=N} s\left(t_n\right) \exp -\frac{i2\pi kn}{N} \quad , \tag{G.3.6}$$

where A is an arbitrary normalisation factor that does not affect the properties of the function and that is usually set to 1, ${}^{1}/_{\sqrt{N}}$ or ${}^{1}/_{N}$, and t_n and ν_n, $n \in \mathbb{N}$, are respectively sequences for times and frequencies expressed as

$$\begin{cases} t_n = \dfrac{n}{N} T_{\mathrm{rec}} & \text{(G.3.7a)} \\ \nu_n = \dfrac{n}{N} f_{\mathrm{rec}} \quad . & \text{(G.3.7b)} \end{cases}$$

Definition G.8: Inverse Discrete Fourier Transform

In frequency units, the IFTD[4] *is given by*

$$s(t_n) = \mathrm{IFT_D}\left[S(\nu_n)\right] = \frac{1}{NA}\sum_{k=1}^{k=N} S\left(\nu_n\right).\exp\frac{i2\pi kn}{N} \quad . \tag{G.3.8}$$

The FTD keeps all the properties of the continuous FT introduced in Appendix G.1, including linearity (Property G.1). However, because of the digitalisation, several properties are introduced. The digitisation of the signal in the time domain results in three important properties.

Property G.5: Range in the frequency domain

If a signal is recorded for a duration T_{rec}*, then the sampling in the frequency domain is* $1/T_{\mathrm{rec}}$ *(Figure G.4).*

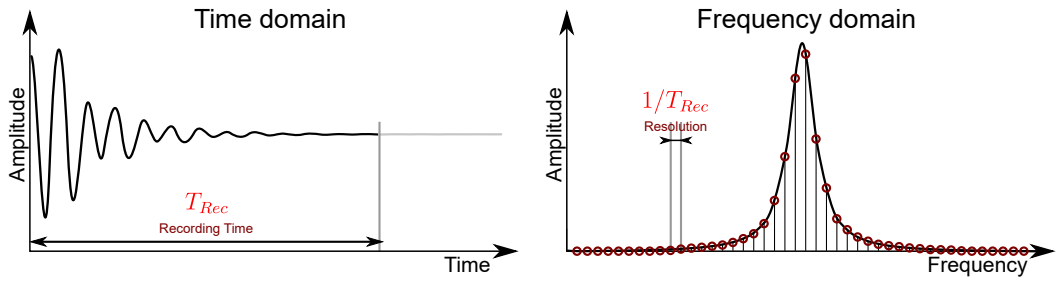

Figure G.4: *Illustration of the effect of the acquisition time on the resolution in the frequency domain.*

As a result of Property G.5, increasing the number of points in the FID without changing T_{rec} will only result in the broadening of the observed range of frequency (the ”spectral width” of the spectrum).

Property G.6: Sampling in the frequency domain

If the sampling frequency, i.e., the number of points recorded per unit of time is f_{rec}*, then the spectral width in the frequency domain is* $1/f_{\mathrm{rec}}$*, e.g., from* $-1/2f_{\mathrm{rec}}$ *to* $1/2f_{\mathrm{rec}}$ *around the central frequency (Figure G.5).*

[4] IFTD: *Discrete Inverse Fourier Transform*

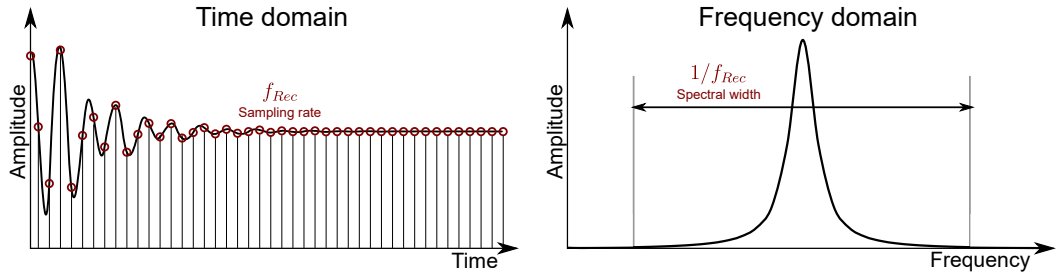

Figure G.5: *Illustration of the effect of the sampling frequency rate in the time domain on the spectral width in the frequency domain.*

Property G.7: Folding in the frequency domain

Every frequency f_{unfold} *outside the spectral width will be folded to appear in the frequency domain, at a frequency of* $f_{\text{fold}} = f_{\text{unfold}} - N/T_{\text{rec}}$*, with* $N \in \mathbb{I}$ *chosen such that* $f_{\text{fold}} \in [-1/2f_{\text{rec}}, +1/2f_{\text{rec}}]$ *(Figure G.6).*

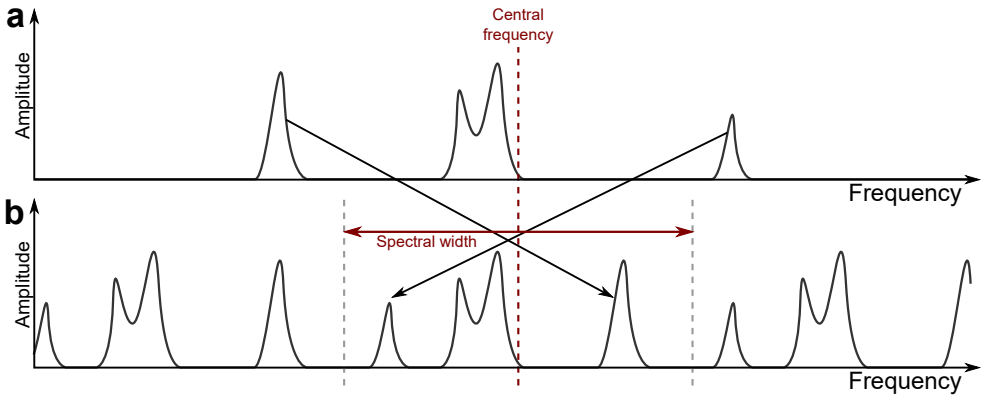

Figure G.6: ***(a)*** *Illustration of a continuous FT, with four components around the central frequency.* ***(b)*** *Illustration of the same four resonance when processed by a FTD. It can be observed the apparition of a frequency window around the central frequency. All resonances outside this spectral width are folded into the spectral width.*

Property G.7 in a direct consequence of Nyquist-Shannon theorem.[481] It leads to the problem of spectrum folding when the sampling frequency is not sufficiently high. As modern digitisers are able to sustain a sampling frequency much larger than generally required, this is often not a problem for conventional 1D experiments> However, it is an important consideration for multi-dimensional NMR experiments, where increasing the sampling frequency results in an increased experimental time.

G.4 The applications of the FT in NMR

In NMR, the FT of a FID can be interpreted as the amount of signal at each frequency. By convention, only the real part of the FT is displayed. The module, despite dealing with phase problems, is in practice rarely used because of the additional broadening of the signal (see Equation (G.2.7) and Figure G.2), as well as the loss of sign discrimination.

In practice, FT is performed using the FFT[5] algorithm,[482, 483] which allows a much faster processing that conventional FT algorithms, but requires the number of points of the signal, N, to be a power of 2. For example, the time required to perform the FT of a 1D spectrum composed of N points would be proportional to N^2 for a normal FT algorithm, and $N \times \log N$ for a FFT algorithm. This property is highly useful when processing multi-dimensional spectra.

Carrier frequency

In NMR, the frequency measured is not the absolute frequency. The Larmor frequency is dependant on the chemical environment due to the chemical shielding interaction described in Chapter 1. But experiments shows that these variations of the Larmor frequency are all within a restricted range of frequencies. As a result, a translation of the central frequency is performed, given a FT now being

$$S(\nu) = \frac{1}{2\pi} \int_{-\infty}^{+\infty} s(t) \exp\left(i2\pi(\nu - \nu_C)t\right) .dt \quad . \tag{G.4.1}$$

where ν_C is called the carrier or central frequency. This way, the observed frequency is the difference of the absolute frequency compared to the carrier frequency, *i.e.* ν_C, which corresponds to its frequency in the rotating frame. This way, many fewer points have to be recorded, taking much less storage space. In practice the technique consists in multiplying the raw signal by a synthesised wave that can take the form $\cos(2\pi\nu_C t + \phi_C)$, where ϕ_C is the recording phase. Writing the recorded signal $s(t) = A.\cos(2\pi\nu_0 t + \phi_L)$, the multiplication of the two signals, also called the mixing of the two frequencies ν_0 and ν_C, is given by

[5] FFT: *Fast Fourier Transform*

$$A.\cos(2\pi t\nu_0+\phi_L).\cos(2\pi t\nu_C+\phi_C) = {}^{A}/_{2}.\cos\left(2\pi t \quad \overbrace{(\nu_0+\nu_C)}^{\text{High-frequency part}} \quad +\phi_L+\phi_C\right) + {}^{A}/_{2}.\cos\left(2\pi t \quad \underbrace{(\nu_0-\nu_C)}_{\text{Low-frequency part}} \quad +\phi_C-\phi_L\right) \quad . \tag{G.4.2}$$

If ν_C is chosen to be closed to the observed frequency ν_0 (or all the observed frequencies), the frequency of the signal after multiplication will be low, and only few points will be required to record the signal. The resulting frequency exactly corresponds to the frequency the original signal would have in a rotating frame Σ_{rot} rotating at a frequency ν_C as introduced in Section 1.1.3. The high frequency part of Equation (G.4.2) can be removed using a low-pass filter.

Quadrature detection

Among the consequences of Table G.1 is that, if the recorded signal is real, which is the case when the magnetisation is recorded only along one axis, the real part of the FT will be even, thus two symmetrical peaks would be observed on either side of the carrier frequency. Moreover, in Equation (G.4.2), it can be noted that the two frequencies $\nu_0 = \nu_C + A$ and $\nu_0 = \nu_C - A$, where A is a small frequency, result in the same mixed signal, therefore these two frequencies cannot be distinguished.

The solution is to recorded the signal along two orthogonal axis, which is called quadrature detection. This set-up enables the retrieval of the sign of the signal frequency with respect to the carrier, and to remove the symmetry of the signal in the frequency domain. In practice, this is achieved using only one coil. The detected signal is split into two channels. One of them is multiplied by $\cos(2\pi t\nu_C+\phi_C)$, giving the real part of the signal ; the other is multiplied by a signal with a phase different of 90°, *i.e.*, $\sin(2\pi t\nu_C+\phi_C)$, giving the imaginary part of the signal. The complex signal can thus being reconstituted after application of the low-pass filter. It follows that the symmetry of the FT is removed.

Multi-dimensional FT

2D NMR experiments constitute a large category of highly successful experiments.[216] The signal of a 2D experiment is given by

$$s(t_1, t_2) = \exp(i\omega_I t_1).\exp(i\omega_D t_2) \tag{G.4.3}$$

where t_2 is the time associated with the FID (constituting the direct dimension), t_1 is an incremented delay (constituting the indirect dimension), ω_I is the angular frequency associated with the indirect dimension and ω_D to the direct dimension. The signal in Equation (G.4.3) is processed with two successive FTs, giving

$$\mathrm{FT}\left[s(t_1, t_2)\right](\nu_1, \nu_2) = \int_{-\infty}^{+\infty} \exp(i2\pi\nu_1 t_1) \left(\int_{-\infty}^{+\infty} s(t_1, t_2).\exp(i2\pi\nu_2 t_2).dt_2 \right) .dt_1 \tag{G.4.4a}$$

$$= \iint_{-\infty}^{+\infty} s(t_1, t_2).\exp(i2\pi\nu_1 t_1 + i2\pi\nu_2 t_2).dt_1.dt_2 \quad . \tag{G.4.4b}$$

Equation (G.4.4) can easily be extended to 3D[6] signals, or above. For some experiments, such as the saturation-recovery experiment (see Section 3.1.1), the FT is only applied along the direct dimension so the decay of the signal with the relaxation delay can be observable. As discussed previously, in practice, a FFT is normally performed for multidimensional datasets for rapidity.

[6] 3D: *Three-Dimensional*

Appendix H

Orientation-Dependant Distortions (ODD)

Introduction

Similarly to other NMR methods, the 3QF step in MQMAS experiments (see Section 3.3.1) is known to cause distortions of the lineshape in the direct dimension. These distortions are limited usually small, but are much more pronounced, for example, on low-γ nuclei or for samples possessing sites with high C_Q sites. The Matlab script ODD[1] has been written to visualise and to quantify the lineshape distortions of spectra simulated with SIMPSON.

H.1 Description

The program, denoted `ODD_function`, uses any SIMPSON input file that simulates a NMR experiment. SIMPSON usually takes a crystal file *.cry* as an input parameter. This crystal file contains all the crystallite orientations for which the simulation will be executed, expressed in terms of Euler angles (see Appendix B.3). A crystal file has the form

Crystal_file.cry

[1] ODD: *Orientation-Dependant Distortions*

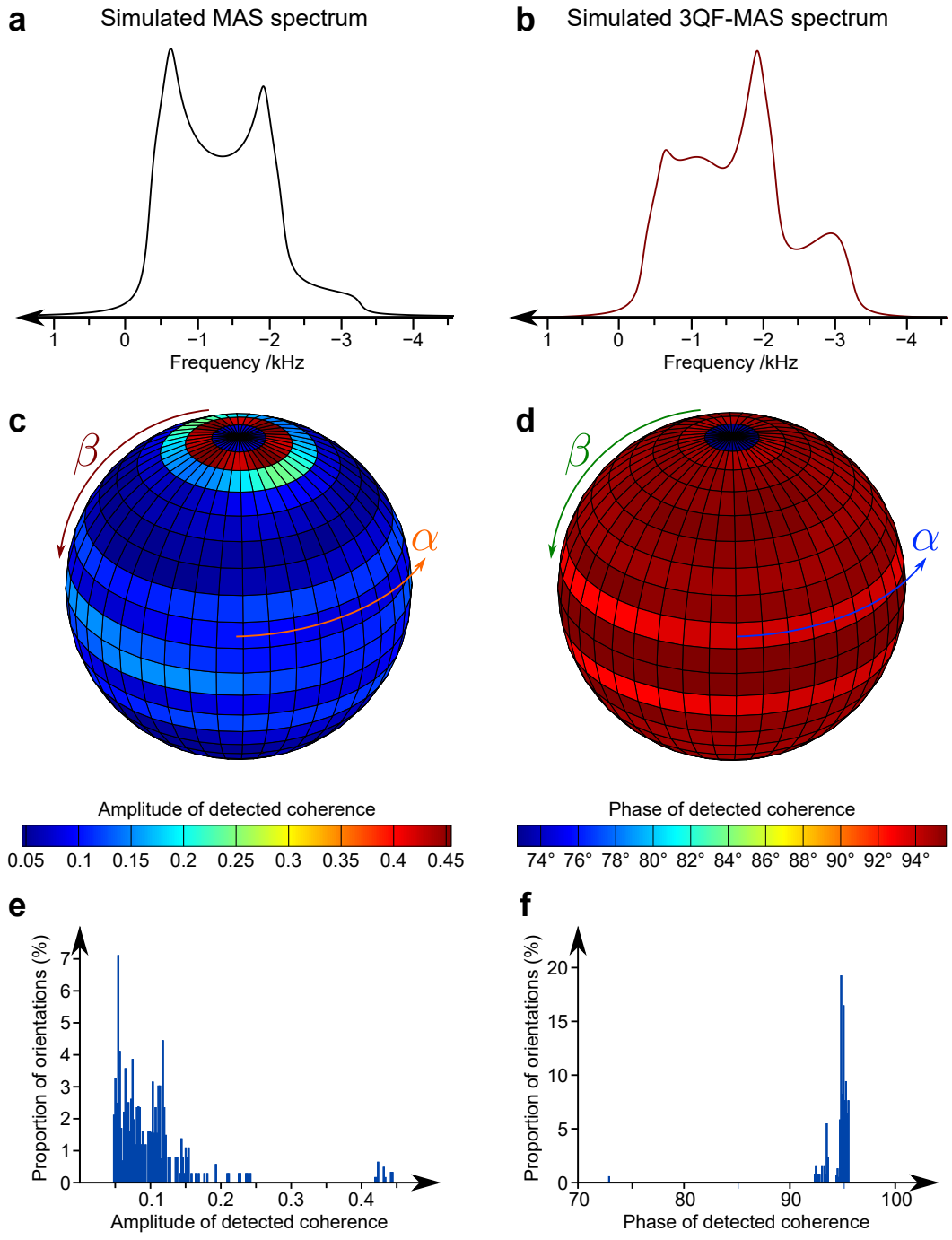

Figure H.1: ***(a)*** *and* ***(b)****: ^{87}Rb simulated spectra of $RbClO_4$ at a MAS rate ν_R = 12.5 kHz and an RF field strength ν_1 = 181.2 kHz.* ***(a)****: Ideal spectrum* ***(b)****: 3QF-MAS spectrum (Section 3.2.2).* ***(c)****: amplitude and* ***(d)****: phase sphere plots corresponding to spectrum* ***(b)****.* ***(e)****: amplitude and* ***(f)****: phase histogram plots corresponding to* ***(b)***

```
>1  alpha-angle[1]  beta-angle[1]   Proportion[1]
>2  alpha-angle[2]  beta-angle[2]   Proportion[2]
>3  alpha-angle[3]  beta-angle[3]   Proportion[3]
>4  ...
>5  alpha-angle[n]  beta-angle[n]   Proportion[n]
```

The program rewrites the SIMPSON input file, changing the crystal file to `ODD.cry` in the input parameters, then executes in a loop the SIMPSON input file, changing the content of the `ODD.cry` file at each iteration, and reading the first point (or any other point defined by the user) of the `.fid` file produced by the simulation. This way, it is possible to simulate the experiment for only one crystallite at the time. The file takes the form

ODD.cry

```
>1  alpha-angle  beta-angle  1
```

The programme features the following input arguments

ODD_char_function(*'filename'*,$n_{\alpha_{\mathrm{LP}}}$,$n_{\beta_{\mathrm{LP}}}$,N_{FID},N_{Hist})

where

- *'filename'* is the name of the SIMPSON input file. Matlab's current folder must be moved to the location of this file,
- $n_{\alpha_{\mathrm{LP}}}$ is the number of α_{LP}-angles for the simulation,[2]
- $n_{\beta_{\mathrm{LP}}}$ is the number of β_{LP}-angles for the simulation,[2]
- (Optional) N_{FID} is the point of the FID to be read by Matlab, the default being 1,
- (Optional) N_{Hist} is the number of bars in the histogram plot, the default being 100.

Usually, the number of α_{LP}-angles would be set as double the number of β_{LP}-angles. Firstly, the program generates two linear scales for α_{LP}- and β_{LP}-angles, from 0 to 180°, and from 0 to 90°, respectively. After the simulation, a Matlab array of the read FID points is obtained for all combinations of α_{LP}- and β_{LP}-angles in the two scales. Thereafter, all points can be normalised by the quantity $N(\beta_{\mathrm{LP}})$, which depends only on the β_{LP}-angle the corresponding have been simulated with, defined as

$$N(\beta_{\mathrm{LP}}) = \frac{d\alpha_{\mathrm{LP}}.d\beta_{\mathrm{LP}}}{4\pi}\cos\left(\beta_{\mathrm{LP}} - \frac{d\beta_{\mathrm{LP}}}{2}\right) \tag{H.1.1}$$

where $d\alpha_{\mathrm{LP}}$ and $d\beta_{\mathrm{LP}}$ are the increment in α_{LP}- and β_{LP}- angles, respectively. After normalisation, each FID point or the Matlab array reflects the total proportion of the crystallite orientations in a powder.

[2] or $n_{\alpha_{\mathrm{RP}}}$ and $n_{\beta_{\mathrm{RP}}}$ in the MAS case.

H.2 Results

`ODD_function` produces four graphical outputs, two plotting the amplitude of the detected element and two plotting its phase. An example of a simulated ^{87}Rb 3QF-MAS spectrum of $RbClO_4$ is shown Figure H.1b. SIMPSON is able to produce quadrupolar lineshape completely free from distortion, setting both the initial and detected operators to the CT + 1Q coherence, or equivalent. The ideal lineshape for $RbClO_4$ is presented Figure H.1a for comparison, which shows that Figure H.1b presents visible lineshape distortions.

Sphere plot

The amplitude and phase of the detected operator are colour-coded and plotted on a sphere as a function of the α_{LP} and β_{LP} angles of the orientation (Figures H.1c and H.1d). α_{LP} is plotted longitudinally, and β_{LP} latitudinally. The surface of each tile represents a proportion of crystallite orientations. Other examples can be found in the literature.[115]

Histogram plot

The proportion of the orientations that has an amplitude or phase of a similar amount contribute to the height of the bars of an histogram plot, presented in Figures H.1e and H.1f for amplitude and phase, respectively, after the normalisation described in Equation (H.1.1). These graphics represent the proportion of orientations that has the intensity labelled on the horizontal axis.

Amount of distortion

Ideally, a pulse sequence would produce an FID whose intensity is completely independent of the crystallite orientation. This would result in a sphere plot where all the tiles are coloured the same way, and an histogram plot where all the points sum up in one unique bar, to make exactly 100%. With this in mind, a suitable quantity to represent the ”amount of distortions” of a lineshape would be the standard deviation of the distribution of the normalised FID points. Below is an example of the output produced by `ODD_function` for the simulated 3QF-MAS spectrum shown in Figure H.1b

```
>> ------------------------------------------------
------------------------------------------------
Average amplitude: 0.10322
Span: 0.40783
Standard deviation: 0.070724
Standard deviation (%): 68.5206%

------------------------------------------------
Average phase: 94.6692 deg
Span: 22.8679 deg
Standard deviation: 1.9008 deg
```

The lineshape is quite distorted, as evidenced by a 68.5% standard deviation, and as it can be observed in Figure H.1b. The phase is however only very slightly distorted. It can be observed from Figures H.1c and H.1d that distortion are much greater when the crystallite is orientated along the axis of the magnetic field, which is reflected on Figures H.1e and H.1f where a small number of orientations have an amplitude/phase very different from all the other orientation.

Under some rare conditions, a 3QF would produce a lineshape distorted to such an extent that the standard deviation would be above 100%. This case reflects extremely high level of asymmetry in the phase or amplitude distribution.

Appendix I

Optimising FAM-N

Introduction

As instructed in Chapter 4.3.3, FAM-N pulses are obtained by executing a Matlab script,[326] and the density matrix evolution package SIMPSON [24] when necessary. This appendix details the input file and all useful elements to help with producing (or reproducing) FAM-N pulses.

Before using this program, one must make sure that SIMPSON is installed and ready to run on your system. SIMPSON is released under GPL[1] license v3 [2] and can be downloaded from `http://nmr.au.dk/software/simpson/`. The program should run on any computer that can execute both Matlab and SIMPSON. To make sure SIMPSON is installed and ready to run, the command **`simpson`** can be executed in a terminal/console/command prompt, and should return (as for version 4.1.1)

```
[Linux] Henri@chpc-hfc3 ~$ simpson
[MacOS] Douglass-iMac:~ henri$ simpson
[Windows] C:/Users/Henri/simpson

SIMPSON version 4.1.1, Copyright (C)
1999-2000 Mads Bak and Jimmy T. Rasmussen
2001 Mads Bak and Thomas Vosegaard
2002-2007 Thomas Vosegaard
2008-2009 Zdenek Tosner, Thomas Vosegaard, and Niels Chr. Nielsen
2009 plus Rasmus Andersen
2010-2014 Zdenek Tosner, Niels Chr. Nielsen, Thomas Vosegaard
SIMPSON comes with ABSOLUTELY NO WARRANTY, for details
read the COPYING file included in this distribution.
```

[1] GPL: GNU *General Public License*
[2] `https://gnu.org/licenses/gpl-3.0.en.html`

```
This is free software, and you are welcome to redistribute
it under certain conditions according to the GNU General Public License.

Please specify an inputfile, optionally with other arguments.

[Linux] Henri@chpc-hfc3 ~$
[MacOS] Douglass-iMac:~ henri$
[Windows] C:/Users/Henri/
```

To cite FAM-N: [23] H. Colaux *et al.*, *J. Phys. Chem. A*, 2014, **118**, 6018, DOI: 10.1021/jp505752c

To cite SIMPSON: [24] M. Bak *et al.*, *J. Magn. Reson.*, 2000, **147**, 296, DOI: 10.1006/jmre.2000.2179

SIMPSON example files: http://nmr.au.dk/software/simpson-code-examples/

Further readings: [484] T. Vosegaard *et al.*, *The flexibility of SIMPSON and SIMMOL for numerical simulations in solid-and liquid-state NMR spectroscopy*, Springer, 2003, DOI: 10.1007/978-3-7091-3715-4_5

[485] M. Bak *et al.*, *J. Magn. Reson.*, 2011, **213**, 366, DOI: 10.1016/j.jmr.2011.09.008

Matlab help: [326] http://uk.mathworks.com/help/matlab/

TOPSPIN user guide: [243] http://sites.uclouvain.be/sc-rmn/Manuels/Topspin_users_guide.pdf

I.1 FAM-N for the impatient

The FAM-N optimisation program with all necessary functions are enclosed in a folder. This section details the minimum, but sufficient, amount of information and practical details to be able to use the FAM-N optimisation script.

Install simpson and FAM-N

1 Download SIMPSON from http://nmr.au.dk/software/simpson/ ,
2 Follow the instructions and install the program,
3 Check that SIMPSON is installed by typing **simpson** in the terminal/console/command prompt,

4 Open the FAM-N folder, making sure that the `FUNCTIONS` folder is present in the same folder. Alternatively, to install permanently, make sure that the content of `FUNCTIONS` is in the permanent Matlab search path.

Execute the FAM-N optimisation

1 Locate the file `FAMN_TEMPLATE.m`,

2 Copy it, rename it `*userfilename*` and open in Matlab, or open it in Matlab and "Save as", `*userfilename*`,[3]

3 Modify the values of the arguments[4]

- `cmpt.nuclei`: `'23Na'`, `'27Al'`, *etc.*,
- `cmpt.proton_frequency`: ^{1}H Larmor frequency, ν_0, $\omega_0/2\pi$ (in Hz),
- `cmpt.RF`: RF field strength, ν_1, $\omega_1/2\pi$ (in Hz),
- `cmpt.SR`: MAS rate, ν_R, $\omega_R/2\pi$ (in Hz),
- `cmpt.CQ`: Quadrupolar coupling constant, C_Q, SOQE (in Hz),
- `cmpt.asym`: Asymmetry parameter η_Q of the quadrupolar interaction (0 to 1),

4 Run the script by pressing the "`Run`" button in the Matlab editor

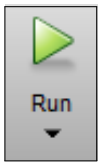

If this window appears, press `"Change Folder"` or `"Add to Path"`

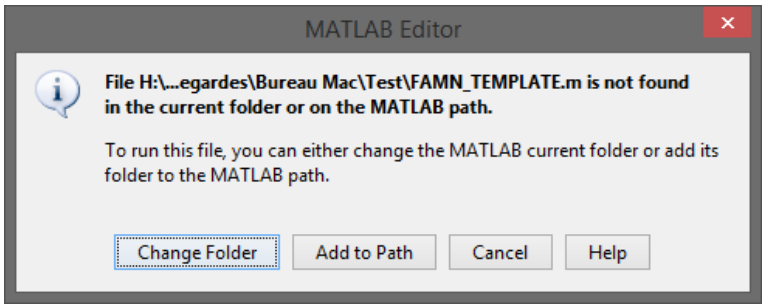

The following lines should appear in the Matlab command window as the calculation progresses

```
>> FAMN_TEMPLATE
```

[3] By default, output files will be given the same names as the input file. Keep it short, as TOPSPIN do not process pulse program names above 50 characters.

[4] The rest of the parameters should have a default value suitable for a general use. See Appendix I.2 for details.

```
********************************
**** Optimisation Parameters ****
********************************
Nuclei: 23Na
Proton frequency: 600000000 Hz
MAS rate: 12500 Hz
Quadrupolar coupling constant: 2000000 Hz
Asymmetry parameter: 0
RF strenght: 80000 Hz
Matrix start element: {{4 1}}
Matrix detected element: {{2 3}}
Crystal file: rep66
Number of gamma angles: 4
********************************
Number of pulses: 1
Current pulse duration: 1.5278us
Current pulse duration: 1.5972us
Current pulse duration: 1.6667us
Current pulse duration: 1.7361us
Current pulse duration: 1.8056us
Current pulse duration: 1.875us
********************************
**** Optimisation Parameters ****
********************************
Nuclei: 23Na
Proton frequency: 600000000 Hz
MAS rate: 12500 Hz
Quadrupolar coupling constant: 2000000 Hz
Asymmetry parameter: 0
RF strenght: 80000 Hz
Matrix start element: {{4 1}}
Matrix detected element: {{2 3}}
Crystal file: rep66
Number of gamma angles: 4
********************************
Number of pulses: 2
Current pulse duration: 0.97222us
Current pulse duration: 1.0417u
...
```

Remark: `Ctlr + C` can be used at any time to abort the simulation.

At the end of the computation, the program should display in the command window the line

```
...
Optimisation completed successfully
```

Use FAM-N

1 Locate the 3QF pulse program (named "`TQSetup_*userfilename*`") and the split-t_1 shifted-echo MQMAS[5] (named "`TQST*transition*_*userfilename*`"),[6]

2 Copy those file in the `pp/user/` folder of Topspin,[7]

3 Start a new experiment and set one of the two pulse program in the `PULPROG` field and compile,

4 Set `cnst1` to the value given in the parameter comment, *e.g.*

DE [µsec]	10.00	Pre-scan-delay
CNST1	20.9722004	FAM-N duration (should be 20.9722 us)
D1 [sec]	5.00000000	Recycle Delay

5 Optimise and set the other parameters.

Remark: FAM-N, like FAM, DFS and HS, executes pulses with fast modulations, applying frequencies exceeding the frequency range of a standard probe (see Section 4.3 and Section 6.2.4). Therefore, reflected power must be expected, but there is unlikely to be any risk for the probe as the application of FAM-N is short.

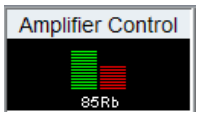

I.2 Folder content and input script

This section gives a more detailed overview of the content of the FAM-N optimisation program folder and of the input parameters. The folder containing all necessary MATLAB functions to permit FAM-N to function are contained in a folder that should present the tree view shown in Figure I.1, and described below.

Folder content

`FAMN_FUNCTIONS` This folder contains all function necessary to execute the optimisation program. This folder has to be in the search path of matlab, or in a

[5] The correct split-t_1 corresponding the nucleus/transition used in the numerical simulation are automatically implanted in the pulse program.

[6] One can use the contents of either `*userfilename*_PULSE_LIST.txt` (pulse list in Topspin pulse program style) or `*userfilename*_results.txt` (all simulation parameters and results) to implement FAM-N in other pulse programs.

[7] By default, this folder should be located in `TopSpin/exp/stan/nmr/lists/pp/user` .

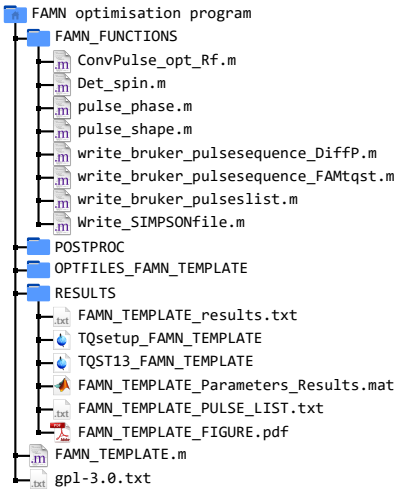

Figure I.1: *Tree view of the content of the FAM-N optimisation program folder.*

subfolder of the executed optimisation script (Here `OPTFILES_FAMN_TEMPLATE.m`) to function.

- `ConvPulse_opt_Rf.m` is the main function, executed by `OPTFILES_FAMN_TEMPLATE.m`. It organises the execution of the other functions, commands the writing of the SIMPSON file, executes and reads the SIMPSON file, and determines when to increase (or decrease) the current pulse length and when to inverse the phase accordingly. This function is described in more details in this section.
- `Det_spin.m` returns the spin of the nucleus defined by the argument `cmpt.nuclei`.
- `pulse_phase.m` returns an array that indicates where to inverse the phase.
- `pulse_shape.m` allows the application of a modulation to the RF pulse. By default, this function does nothing and returns the input RF.
- `write_bruker_pulsesequence_DiffP.m` writes the 3QF, or MQF (see Figure 3.8) pulse program for Topspin .
- `write_bruker_pulsesequence_FAMtqst.m` writes the split-t_1 shifted-echo MQMAS (see Figure 3.16) pulse program for Topspin. The phase cycling and split-$_1$ coefficients are implemented according to the nucleus spin (returned by `Det_spin.m` from `cmpt.nuclei`) and the transition used for the MQMAS (given by

`cmpt.transition`).

- `write_bruker_pulseslist.m` returns a pulse list in Topspin format for easier implementation of FAM-N in pulse programs not generated by the program.
- `Write_SIMPSONfile.m` writes the SIMPSON input file, according to the pulse duration and phase inversions given by `ConvPulse_opt_Rf.m`

`POSTPROC` This folder contains advanced functions for the post-processing analysis of FAM-N pulses. Its content is not necessary for the execution of FAM-N and can be erased if not needed. The content of this folder is variable, and the functions it contains will not be detailed here.

`OPTFILES_FAMN_TEMPLATE` Folder where the program writes the executed SIMPSON files detailed in Appendix I.4. By default, these files self-destruct during the optimisation process, and the folder is erased once the optimisation in complete. This folder may remain if the simulation has been aborted or if `cmpt.keepSIMfiles=1`.

`RESULTS` This folder contains the outputs of the program. All ouput files are presented in more details in Appendix I.3.

- `FAMN_TEMPLATE_results.txt` recalls input parameters and encloses different lists describing the output FAM-N pulse (For an example, see Table I.1).
- `TQsetup_FAMN_TEMPLATE` MQF pulse program for Topspin.[8]
- `TQST13_FAMN_TEMPLATE` split-t_1 shifted-echo MQMAS pulse program for Topspin.[8]
- `FAMN_TEMPLATE_Parameters_Results.mat` is a Matlab file containing the values for all the variables used for the FAM-N simulation. It is useful to verify all parameters after the optimisation. It can also be used for post-processing and analysis of FAM-N pulses in Matlab.
- `FAMN_PULSE_LIST.txt` Pulse list in Topspin format for implementation in pulse programs different from the two above.
- `FAMN_TEMPLATE_FIGURE.pdf` Picture showing the FAM-N optimi-

[8] The prefixes `TQsetup` and `TQST` become `QQsetup/QQST`, `SQsetup/SQST` and `NQsetup/NQST` if FAM-N is optimised for conversion from 5Q, 7Q and 9Q[9] coherence, respectively. See the parameter `cmpt.transition` for details.

sation (see Appendix I.3).

Input file: `FAMN_TEMPLATE.m`

The file most relevant file for the general user is the optimisation script named by default. `FAMN_TEMPLATE.m`, as this file defines all the optimisation parameters and is used to run the optimisation. All parameters are described below.

Code I.1: *`FAMN_TEMPLATE.m`, lines 1 to 7.*

```
>1  %%%%%%%%%% FAM-N optimisation input script %%%%%%%
>2  % Script to run FAM-N optimisation.
>3  %
>4  % FAM-N (Fast Amplitude Modulation - N pulses) is a composite pulse
        that
>5  % exploits the phenomenon of inversion/saturation of satellite
        transtion into the central
>6  % transition to enhance the efficiency of the conversion pulse in MQMAS
>7  % experiments, improving the overall sensitivity of the experiment.
```

Lines 1 to 57 (Code I.1) of ***`FAMN_TEMPLATE.m`*** gives a general description of the program, references and GPL license related information.

Code I.2: *`FAMN_TEMPLATE.m`, lines 59 to 62: System parameters.*

```
>59 % System parameters
>60 cmpt.nuclei='23Na'; % Nucleus of interest. As written in SIMPSON,
>61                     % i.e. under the form [Atomic number][Element]. Ex:
                             7Li, 23Na, 27Al ...
>62 cmpt.transition=3; % State desired transition : 3 for 3-quantum to
        single-quantum,
```

Lines 59 to 62 (Code I.2) allow the user to select the nucleus and transition.

`cmpt.nuclei` Defines the nucleus. It must be written as a string[10] following the SIMPSON convention '{Atomic Number}{Element symbol}'.
Example: `'23Na'`, `'27Al'` *etc.*

`cmpt.transition` This parameter allows the user to choose if FAM-N is to be optimised for a 3QMAS (the standard MQMAS experiment), 5QMAS or higher (see Section 6.2.1). It must be one of the numbers `3`, `5`, `7` or `9`. It should be noted that the code has not been extensively tested for CTPs other than 3QF, but all CTPs

[10] In Matlab, a string is enclosed between the quotation marks `' '`

are all implemented and have been shown to function in the general case. The default is `cmpt.\aca transition\aca =3`.

Code I.3: *FAMN_TEMPLATE.m, lines 69 to 74: Experimental Parameters.*

```
>69 %%%%%%%%%% Experimental Parameters
>70 cmpt.proton_frequency=6e8; % 1H Larmor frequency (Hz)
>71 cmpt.RF=80000; % Radio-frequency (RF) field strength (Hz)
>72 cmpt.SR=12500; % MAS rate (Hz)
>73 cmpt.CQ=2e6; % Quadrupolar coupling constant / CQ (Hz)
>74 cmpt.asym=0; %  Asymmetry parameter / eta.
```

Lines 69 to 74 (Code I.3) lists all the principle experimental parameters.

`cmpt.proton_frequency`	^{1}H Larmor frequency, ν_0, $\omega_0/2\pi$ (in Hz)
`cmpt.RF`	RF field strength, ν_1, $\omega_1/2\pi$ (in Hz)
`cmpt.SR`	MAS spin, ν_R, $\omega_R/2\pi$ (in Hz)
`cmpt.CQ`	Quadrupolar coupling constant, C_Q, SOQE (in Hz)
`cmpt.asym`	Asymmetry parameter η_Q (0 to 1)

All these parameters except `cmpt.proton_frequency` can be inserted as a list, to allow multiple successive optimisations.[11,12] The format are available in the following formats

- Plain numbers.
  Examples: `114000`, `114e3`, ...
- Plain number lists.
  Examples: `[20000,50000,80000]`, `[20e3,50e3,80e3]`, ...
- Incremented list.
  Examples: `30e3:10e3:120e3` returns a list of values from 30×10^3 to 120×10^3 separated by an increment of 10×10^3.
- Using the Matlab functions `linspace` or `logspace`.
  Examples:
  - `linspace[1e5,1e7,40]` returns a list of 40 linearly-spaced values between 10^5 and 10^7,
  - `logspace[5,7,40]` returns a list of 40 logarithmically-spaced values between 10^5 and 10^7.

The issues of RF calibration and obtaining C_Q approximations have been tackled in Section 3.2.2 and Section 5.2.1, respectively, and approaches to get values for RF and C_Q

[11] The loop will be executed for all possible combinations of the parameters written as a list.
[12] For a loop optimisation, file's name will be suffixed `_N*Noopt*`, where `Noopt` is an arbitrary index number. If `cmpt.custom_name` is set to `0`, the file will be name according to the optimisation parameters.

are addressed in Section 5.2.1.

Code I.4: *FAMN_TEMPLATE.m, lines 80 to 95: Computational parameters.*

```
>80 %%%%%%%%%% Computation Parameters
>81 cmpt.nop120=60; % Number of points for the first simulation, i.e.
       continuous wave
>82                 % The higher it is, the more precise each pulse would
                       be.
>83                 % Typical value of around 60.
>84 cmpt.tol_compt=5; % Tolerance counter. Set the number of time
       increments
>85                 % the programme carries on calculation despite a
                       decreasing
>86                 % amount of single quantum.
>87                 % Typical value of around 5.
>88 cmpt.tol_compt_minus=3; % Tolerance counter for decreasing pulse
       durations.
>89 %%%%%%%%%%%%%%%%
>90 cmpt.comspd=1;  % =1 Use a pre-set number of crystallites and gamma
       angles.
>91                 % Set to some other value to choose custom cristal
                       files and
>92                 % gamma angles that can be chosen using the two
                       parameters
>93                 % below.
>94 cmpt.crystfile=''; % Custom cristal file. Default is 'rep66'.
>95 cmpt.nogamma=1; % Custom number of gamma angles. Default is 4.
```

Lines 80 to 95 (Code I.4) contain some computation parameters.

`cmpt.nop120` Defines the number of points of the initial CW simulation, whose duration depends on **`cmpt.RF`**, and the inherent total nutation depends on the spin I and the coherence p taken for the nutation, as summarised in this table[13]

		Coherence order p			
		3	5	7	9
Spin I	3/2	120°	N/A	N/A	N/A
	5/2	75°	120°	N/A	N/A
	7/2	55°	75°	120°	N/A
	9/2	45°	55°	75°	120°

This number of points also describes the duration increment during FAM-N optimisations, as FAM-N pulses are incremented by 1 point at a time (see Section 4.3.3).

[13] These values have been chosen to be slightly longer than the expected duration of a MQ conversion observed in simulation and reported in the literature for a given spin I and coherence order p.[325]

`cmpt.tol_compt` Tolerance counter for increasing duration. Set the number of times the optimisation will continue despite the maximum amount of 1Q decreasing as the current pulse duration become longer (see Section 4.3.3). The default value is `=5`. Increasing it could allow longer, thus potentially more efficient, FAM-N pulses to be reached, but the default value is sufficient under normal conditions. The tolerance counter must be increased by the same proportion than `cmpt.nop120`.

`cmpt.tol_compt_minus` Same as `cmpt.tol_compt`, but sets the tolerance for decreasing pulse duration. The default value is `=0`, because the optimum points of inversion have been observed to be after the maximum in the vast majority of cases (see Section 4.3.3), although not always (see the description of `FAMN_TEMPLATE_results.txt` in Appendix I.3). This parameter should be set to `≠0` to optimise $p = \pm 1$ to $p = \pm M$ FAM-N pulses with the parameter `cmpt.exc_conv`.

`cmpt.comspd` (*Boolean*) Let the user choose whether to use the default crystal file and number of γ-angles (`=1`), or if he would rather use another crystal file and number of γ-angle (`=1`). By default, the crystal file is *`'rep166'`* and the number of gamma angles is `4`.

`cmpt.crystfile` Custom crystal file name. Must be written as a string. Unused if `cmpt.comspd=1`.
Examples: *`'rep166'`*, *`'rep320'`*, *etc.*

`cmpt.nogamma` Custum number of γ-angles. Unused if `cmpt.comspd=1`.

Code I.5: *`FAMN_TEMPLATE.m`, lines 100 to 123: Options.*

```
>100 %%%%%%%%%% Options %%%%%%%%%%%%%%%%%%%%%
>101 cmpt.num_cores=1; % ONLY FOR SIMPSON 4.x. For other versions set to 0.
>102                   % Number of threads used for computation.
>103 cmpt.filename=mfilename; % Name the output files the same way as this
         file.
>104 % For a custom name, remove mfilename for  a string name like '
         Hc_Rb87_RbNO3'.
>105 cmpt.pl=1; % Write pulse list (=1)
>106
>107 cmpt.ppw=1; % Write Topspin pulse programs (=1).
>108              % The pulse programs will appear in a folder called [
                     RESULTS]
>109 cmpt.copypath=''; % Path for the Bruker pulse program folder.
```

```
>110 %cmpt.copypath='C:\Bruker\TopSpin3.1p16\exp\stan\nmr\lists\pp\user';
>111 cmpt.figplot=1;  % Show and save optimisation pictures (=1)
>112
>113 cmpt.figclose=1; % Leave the picture opened after the simulation (=1)
>114
>115 cmpt.keepSIMfiles=1; % Keep SIMPSON intermediate optimisation files
        (=1)
>116
>117 cmpt.exc_conv=0; % UNTESTED! Calculate excitation instead of conversion
         (=1)
>118                  % Set cmpt.tol_compt_minus to a value above 2.
>119 cmpt.custom_name=1; % Use a custom name (=1).
>120                     % Else files will be given a standart name
>121 cmpt.MAS_maxdt_ratio=20; % Ratio between MAS period and maxdt in
        SIMPSON
>122
>123 cmpt.MAXnopulses=26; % Maximum number of pulses the simulation is
        allowed to reach.
```

Lines 100 to 123 (Code I.5) contain advanced options to modify some aspects of the optimisation or the output of the program.

`cmpt.num_cores` From version 4.0, SIMPSON allows the user to set the number of CPU threads/cores on which the simulation is carried out. This is set by the argument `num_cores` in SIMPSON, which is transferred by `cmpt.num_cores`. Default is `num_cores=1`, which is sufficient for most optimisation on a regular computer. If an earlier version of SIMPSON is installed, set `num_cores=0`, which will result in the argument being omitted in the SIMPSON input file.

`cmpt.filename` By default, this parameter is set to `cmpt.filename=mfilename`, giving the output files the same names as the current file. As instructed in Appendix I.1, it is best to keep the name short as Topspin does not process pulse program with long names.

`cmpt.pl` (*Boolean*) Enables (`=1`) or disables (`=0`) the output of the pulse list `FAMN_PULSE_LIST.txt`.

`cmpt.ppw` (*Boolean*) Enables (`=1`) or disables (`=0`) the output of the pulse programs `TQsetup_FAMN_TEMPLATE` and `TQST13_FAMN_TEMPLATE`.

`cmpt.copypath` If a path is specified, automatically copies the two pulse programs `TQsetup_FAMN_TEMPLATE` and `TQST13_FAMN_TEMPLATE` to the path given in argument. Unused if `cmpt.pl=0`. Must be

written as a string.
Example: `'C:\Bruker\TopSpin3.1p16\exp\stan\nmr\lists\pp\user'`

`cmpt.figplot` (*Boolean*) Plot and save the figure showing the FAM-N optimisation (see Figure I.2) if `=1`, or not if `=0`.

`cmpt.figclose` (*Boolean*) Leave the figure open once the computation is complete (`=0`) or close it (`=1`). It is a good idea to set this parameter to `=1` if you wish to loop optimisations.

`cmpt.keepSIMfiles` (*Boolean*) By default (`=1`), all SIMPSON input and output files `OPTFILES_*userfilename*` (see Appendix I.4) produced by the simulation are erased after use, as they are numerous, cumbersome, and their contents is saved in `FAMN_TEMPLATE_Parameters_Results.mat`. Set to `0` if you want to keep those files after the simulation.

`cmpt.exc_conv` (*Boolean*) This feature is implemented but essentially untested. By default (`=0`), FAM-N is optimised for a $+p \rightarrow +1$ conversion. Setting `=1` optimises FAM-N for the $+1 \rightarrow +p$ excitation. Those pulses could find applications, for example in RIACT. Generated pulses are very different, so it is advised for excitation to set `cmpt.tol_compt_minus`$\neq$`0`.

`cmpt.custom_name` (*Boolean*) By default (`=1`), the outputs will be named after the value of the argument `cmpt.filename`. If set to `=0`, files will be given a name reflecting the values of the input parameters, given by
`filename '_T'* '_RF_'* '_SR_'* '_CQ_'* '_AS_'*`.

`cmpt.MAS_maxdt_ratio` Adjust the value of the SIMPSON parameter `maxdt` to a value related to the MAS period τ_R, `maxdt` being a short time (Typically 0.1 to 100 µs) during which an time-dependent Hamiltonian can be approximated by a time-independent Average Hamiltonian (see Section 2.1.2). Under standard conditions, only minor changes in the optimised FAM-N cannot be observed when above `12`, so this value is set by default to `20`. See Appendix I.4 for details.

`cmpt.MAXnopulses` Set the maximum number of pulses that FAM-N is allowed to reach. The optimisation will stop at the number of pulses after which no further improvement is observed, or if the number of pulses defined by `cmpt.MAXnopulses` is reached. The default is `=26`. It should be noted that Topspin cannot handle more than a total of 64 individual pulses, so `cmpt.MAXnopulses` should always be at a maximum of `60` to account for the other pulses. of the MQMAS pulse sequence.

Code I.6: *FAMN_TEMPLATE.m, lines 121 to 136: Execution.*

```
>128 [pathstr, ~, ~] = fileparts(mfilename('fullpath'));
>129 cd(pathstr)
>130 cmpt.simc=1;
>131 for r=cmpt.asym
>132     for l=cmpt.CQ
>133         for p=cmpt.RF
>134             for q=cmpt.SR
>135             addpath(genpath(pwd))
>136             ConvPulse_opt_Rf(p,q,l,r,cmpt);
>137             rmpath(genpath(pwd))
>138             cmpt.simc=cmpt.simc+1;
>139             end
>140         end
>141     end
>142 end
```

Lines 121 to 136 executes the file `ConvPulse_opt_Rf.m` according to the input parameters given above. The cascade of `for` statements loops the execution of `ConvPulse_opt_Rf.m` if `cmpt.RF`, `cmpt.SR`, `cmpt.CQ` or `cmpt.asym` are defined as arrays. The command `addpath(genpath(pwd))` adds the folders and the subfolders contained in the folder of the optimisation script to the search path of matlab, which are removed after the execution of `ConvPulse_opt_Rf.m`.

Main function `ConvPulse_opt_Rf.m`

Being the main function of the program, `ConvPulse_opt_Rf.m` is long, so only some important elements of the code will be detailed here.

Code I.7: *ConvPulse_opt_Rf.m, lines 1 to 10.*

```
>1 function[]=ConvPulse_opt_Rf(RF,SR,CQ,AS,cmpt)
>2
>3 %%%%%%%%%%%%%%%%%%%%%%%%%%%%%
>4 % Definition of each variable %
```

```
>5  %%%%%%%%%%%%%%%%%%%%%%%%%%%%%%%%
>6  % alt_pm: Number that alternates between +1 and -1. +1 means a the
        previous
>7  %           pulse will be made longer, whereas -1 means it will be made
>8  %           shorter.
>9  % comptrawdata: Counts the number of executed simulation for storage of
        the
>10 %           raw results in the rawdata.signal array, saved at the end
        of
```

Lines 1 to 131 (Code I.7) gives a description for most internal variables.

Code I.8: *ConvPulse_opt_Rf.m, lines 136 to 170.*

```
>163 switch cmpt.transition
>164     case 3 %%%%%%%%%%%%%%%%%%%%%
>165     switch cmpt.spin
>166       case '3/2'
>167       param.flipang=120;
>168       PPParam.SE=[4,1];
>169       PPParam.PE=[2,3];
>170       case'5/2'
```

Lines 163 to 240 (Code I.8) sets the start and detected matrix density elements for the SIMPSON simulation. These depend of the spin I and the transition order p, and are summarised in this table.

		Coherence order p			
		3	5	7	9
Spin I	3/2	$\rho_{41} \rightarrow \rho_{32}$	N/A	N/A	N/A
	5/2	$\rho_{52} \rightarrow \rho_{43}$	$\rho_{61} \rightarrow \rho_{43}$	N/A	N/A
	7/2	$\rho_{63} \rightarrow \rho_{54}$	$\rho_{72} \rightarrow \rho_{54}$	$\rho_{81} \rightarrow \rho_{54}$	N/A
	9/2	$\rho_{74} \rightarrow \rho_{65}$	$\rho_{83} \rightarrow \rho_{65}$	$\rho_{92} \rightarrow \rho_{65}$	$\rho_{104} \rightarrow \rho_{65}$

Code I.9: *ConvPulse_opt_Rf.m, lines 305 to 312.*

```
>305 function[newData1]=importfile(fileToRead1)
>306 % Function that imports simpson output files into Matlab
>307 newData1 = importdata(fileToRead1);
>308 vars = fieldnames(newData1);
>309 for i = 1:length(vars)
>310     assignin('base', vars{i}, newData1.(vars{i}));
>311 end
>312 end
```

Lines 305 to 312 (Code I.9) are the function `importfile`, whose function is to import the output SIMPSON file into Matlab after its execution. Imported data is contained in a sub-container named `data`.

Code I.10: *ConvPulse_opt_Rf.m, line 511.*

```
>511 for NofFAM_temp=1:NofFAM-1
```

Line 511 (Code I.10) begin of the loop that increases the number of pulse, where the current number of pulses is `NofFAM_temp` and the maximum number of pulses that FAM-N is allowed to reach is `NofFAM` defined by the input parameter `cmpt.MAXnopulses`. This loop may be broken if adding another pulse to FAM-N does not further increase the amount of 1Q (see Code I.16). Else, the loop while stop when `cmpt.MAXnopulses = NofFAM_temp`.

Code I.11: *ConvPulse_opt_Rf.m, lines 305 to 312.*

```
>526 if tol_compt>1 || tol_compt_minus>1
>527 while compt_test<tol_compt || compt_test_minus<tol_compt_minus
```

Lines 526 to 527 (Code I.11) are the start of a `while`-loop that instructs Matlab to continue attempting to increase (or decrease) the duration of the pulse until both tolerance counters `compt_test` and `compt_test_minus` (counter for increasing and decreasing pulse durations, respectively) reach their maximum value given by `tol_compt` and `tol_minus_compt`, respectively (see input parameters `cmpt.tol_compt` and `cmpt.tol_compt_minus`). Line 526 is a verification that at least one counter is set to a value greater than `1`.

Code I.12: *ConvPulse_opt_Rf.m, lines 305 to 312.*

```
>650 Write_SIMPSONfile(filename,spinsys,PPParam,param,FAMdata,NofFAM_temp)
>651 unix(['simpson␣' filename '.in']);
>652 data=importfile(filename);
```

Lines 650 to 653 (Code I.12) are the part of the code that executes the SIMPSON simulation.

- `Write_SIMPSONfile` writes the SIMPSON file according to the input parameters, and to the characteristics of the current FAM-N pulse (duration, points of the phase inversion, *etc.*),
- `unix` executes SIMPSON for the file named `filename`,[14]
- `importfile` reads in the file outputted by SIMPSON.

Code I.12 is reproduced twice in the file: Lines 450 to 503 for the initial CW simulation, and lines 504 to 683 for the FAM-N simulations. Executed simulations are, in order:

[14] Despite being called `unix`, this function executes a command in the terminal/console/command prompt on any operating system.

- `nop120`
- `MAX1 || nop120`
- `MAX1 + 1 || nop120 + 2`
- `MAX1 - 1 || nop120 - 2`
- `MAX1 + 2 || nop120 + 4`
- `MAX1 - 2 || nop120 - 4`
- ...
- `MAX1 || MAX2 || nop120`
- `MAX1 || MAX2 + 1 || nop120 + 2`
- `MAX1 || MAX2 - 1 || nop120 - 2`
- `MAX1 || MAX2 + 2 || nop120 + 4`
- ... ...
- `MAX1 || MAX2 || ... || MAXN-1 || nop120`
- `MAX1 || MAX2 || ... || MAXN-1 +1 || nop120 +2`
- ... ...
- `MAX1 || MAX2 || ... || MAXN-1 || MAXN || nop120`

`nop120` is the number of points of the CW conversion, `MAXk` is the position of the maximum for the k^{th} pulse, and `||` is a phase inversion. Hence, the final FAM-N pulse is `MAX1 || MAX2 || ... || MAXN-1 || MAXN` .

Code I.13: *`ConvPulse_opt_Rf.m`, lines 574 to 594.*

```
>574  if currentmax>previousmax
>575     previousmax=currentmax;
>576     previousmaxpos=currentpos;
>577     nopotp=FAMdata(3,NofFAM_temp);
>578     FAMdata(3,NofFAM_temp+1)=FAMdata(3,NofFAM_temp);
>579
>580     if alt_pm==1
>581     compt_test=1;
>582     elseif alt_pm==-1
>583     compt_test_minus=1;
>584     end
>585
>586     keptdata=data.data(:,1);
>587     keptNP=param.np;
>588  else
>589     if alt_pm==1
>590     compt_test=compt_test+1;
>591     elseif alt_pm==-1
>592     compt_test_minus=compt_test_minus+1;
>593     end
>594  end
```

Lines 574 to 594 (Code I.13) are the part of the code that compares the maximum formed by increasing (or decreasing) the current pulse by `1` point, with the maximum formed by

the unaltered pulse. It resets the tolerance counter for increasing (or decreasing) pulse if the newly formed maximum is higher than the previous one, or increases its value by 1 if it is not.

Code I.14: *ConvPulse_opt_Rf.m, lines 687 to 691.*

```
>619 if alt_pm==-1
>620     if compt_test<tol_compt
>621         Store_FAMdata3_minus=FAMdata(3,NofFAM_temp);
>622         FAMdata(3,NofFAM_temp)=Store_FAMdata3_plus+1;
>623         Store_np_minus=param.np;
>624         param.np=Store_np+2;
>625         alt_pm=1;
>626     elseif compt_test_minus<tol_compt_minus
>627         FAMdata(3,NofFAM_temp)=FAMdata(3,NofFAM_temp)-1;
>628         alt_pm=-1;
>629         param.np=param.np-2;
>630     end
>631 elseif alt_pm==1
>632     if compt_test_minus<tol_compt_minus
>633         Store_FAMdata3_plus=FAMdata(3,NofFAM_temp);
>634         FAMdata(3,NofFAM_temp)=Store_FAMdata3_minus-1;
>635         Store_np=param.np;
>636         param.np=Store_np_minus-2;
>637         alt_pm=-1;
>638     elseif compt_test<tol_compt
>639         FAMdata(3,NofFAM_temp)=FAMdata(3,NofFAM_temp)+1;
>640         alt_pm=1;
>641         param.np=param.np+2;
>642     end
>643 end
```

Lines 619 to 643 (Code I.14) are the part of the code that alternates increasing and decreasing pulse durations if both of the tolerance counters are set to a non-zero value. Furthermore, if one of the counters reaches the value of either one of the tolerance counters `compt_test` or `compt_test_minus`, but not the other, no further attempt to increase or decrease the pulse duration will be undertaken until the other counter also reaches its maximum.

Code I.15: *ConvPulse_opt_Rf.m, lines 687 to 691.*

```
>662 if currentmax>previousmax
>663    keptdata=data.data(:,1);
>664    keptNP=param.np;
>665    previousmax=currentmax;
>666    previousmaxpos=currentpos;
>667    nopotp=FAMdata(3,NofFAM_temp);
>668    FAMdata(3,NofFAM_temp+1)=FAMdata(3,NofFAM_temp);
>669 else
>670    nopotp=0;
>671 end
```

Lines 662 to 671 (Code I.15) are the part of the code that compares the maximum obtained from optimising the current pulse to that obtained from optimising the previous pulse. If an improvement is observed, the new maximum is saved and the optimisation continues. If not, the variable `nopotp` is set to `0`.

Code I.16: *`ConvPulse_opt_Rf.m`, lines 697 to 699.*

```
>697    if nopotp==0
>698        disp(['No␣more␣improvement␣after␣' num2str(NofFAM_temp) '␣
               pulses'])
>699        break
```

Lines 697 to 699 (Code I.16) order the breaking of the `for`-loop defined in Code I.10 with the command `break` if `nopotp` has been set to `0` by Code I.16, thus finishing the optimisation and returning the final FAM-N pulse.

Code I.17: *`ConvPulse_opt_Rf.m`, lines 687 to 691.*

```
>687 %%%%%%%%%% Write data
>688 FAMdata(3,NofFAM_temp)=nopotp;
>689 FAMdata(1,NofFAM_temp+1)=previousmax;
>690 FAMdata(2,NofFAM_temp+1)=previousmaxpos;
>691 FAMdata(3,NofFAM_temp+1)=FAMdata(2,NofFAM_temp+1);
```

Lines 687 to 691 (Code I.17) save the final FAM-N parameters.

Subsequent lines terminate the function `ConvPulse_opt_Rf.m`, write the output files, pulse programs and figures, and save the variables in a `.mat` file.

I.3 Output files

This section details the files returned by the execution of the FAM-N optimisation program upon completion (briefly described at the beginning of Appendix I.2). Here, the output files obtained by executing the code detailed in Appendix I.2 are taken as an example. The six main parameters are

- ^{23}Na
- B_0 = 14.1 T (ν_0 = 158.8 MHz)
- ν_1 = 80 kHz
- ν_R = 12.5 kHz
- C_Q = 2 MHz
- η_Q = 0

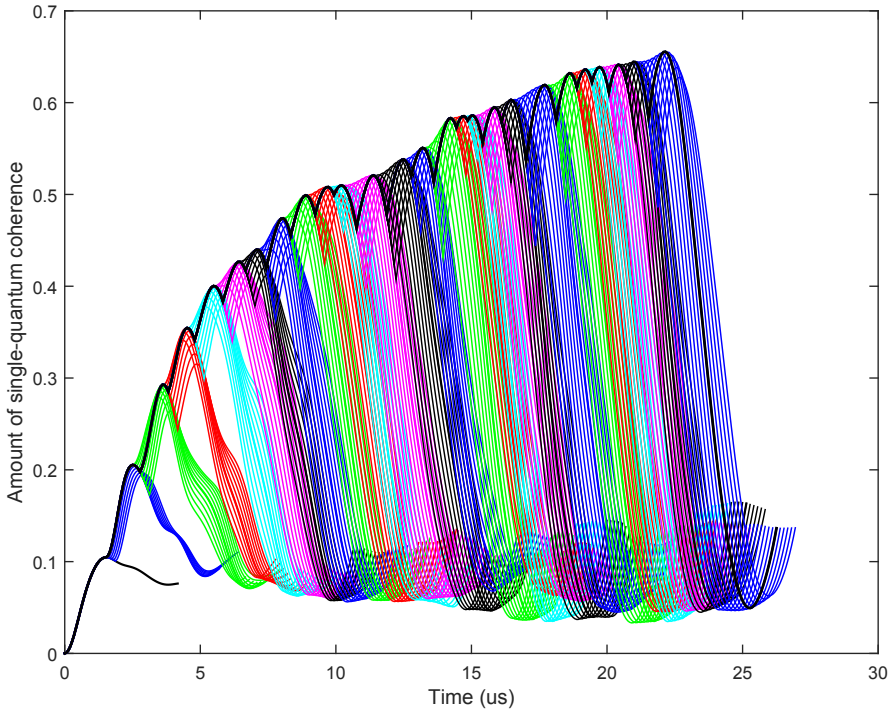

Figure I.2: *FAMN_TEMPLATE_FIGURE.pdf*

The knowledge of only those six parameters is sufficient to uniquely reproduce any of the FAM-N pulses used in this work.[15] The FAM-N pulse produced is described in several files presented in this section.

Figure `FAMN_TEMPLATE_FIGURE.pdf`

The optimisation outputs a figure presenting the FAM-N optimisation steps, here `FAMN_TEMPLATE_FIGURE.pdf`. The figure obtained with the parameters taken as an example is displayed in Figure I.2. The pulse retained as the final FAM-N is shown in a black bold line, and the intermediate simulations are shown using normal lines. For readability, the line colour changes for each step of the optimisation, cycling following the sequence black, blue, green, red, cyan, purple. This figure provides an easy way to visualise the expected signal improvement for each steps of the optimisation, should the user want to reduce the number of pulses of FAM-N. As stated in Section 4.3.3 and as it can be seen in Figure I.2, the first step is a simulation of the MQ to 1Q conversion efficiency of CW

[15] Unless otherwise stated, it is assumed that FAM-N pulses have been generated for 3QF (`cmpt.transition=3`) and with the default number of crystallites and γ-angles (`cmpt.crystfile='rep66'` and `cmpt.nogamma=4`).

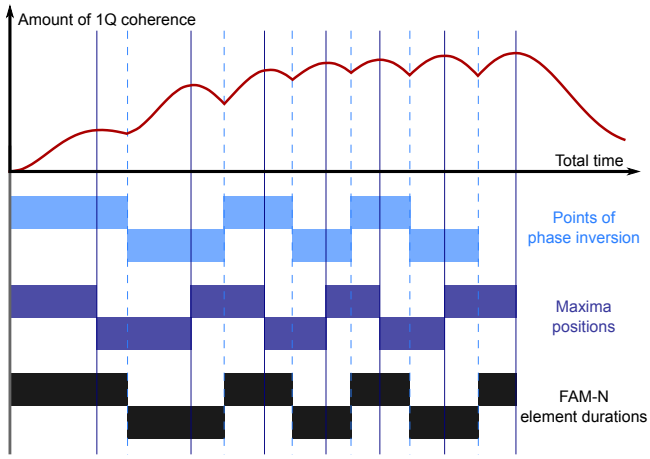

Figure I.3: *Illustration of the different elements of Table I.1 relative to the FAM-N optimisation curve* `FAMN_TEMPLATE_FIGURE.pdf` *in Figure I.2. For readability, here the plotted FAM-N does not correspond to the example taken for this section, but that of Figure 4.13.*

(black line on the bottom left), with following simulations making increments from the observed maximum of the previous pulse.

Results .txt file `FAMN_TEMPLATE_results.txt`

This `.txt` file is the most important file produced by the FAM-N optimisation program, as it contains all necessary informations and describes the durations of the elements of FAM-N.

Code I.18: `FAMN_TEMPLATE_results.txt`*, input parameters.*

```
>1  **************************
>2  FAM Optimisation Results
>3  **************************
>4  **** Input Parameters ****
>5  **************************
>6  Nuclei: 23Na
>7  Proton frequency: 600000000 Hz
>8  MAS rate: 12500 Hz
>9  Quadrupolar coupling constant: 2000000 Hz
>10 Asymmetry parameter: 0
>11 RF strength: 80000 Hz
>12 Matrix start element: {{4 1}}
>13 Matrix detected element: {{2 3}}
>14 Crystal file: rep66
>15 Number of gamma angles: 4
>16 MAS period/maxdt in SIMPSON: 20
```

Lines 1 to 16 (Code I.18) recall the input simulation parameters, crystal file, and start

and detected elements.

Code I.19: *FAMN_TEMPLATE_results.txt, results overview.*

```
>18 *****************
>19 **** Results ****
>20 *****************
>21 Number of pulses: 25
>22 Time increment: 0.069444 µs
>23 Total number of points: 302
>24 Total time: 20.9722 µs
```

Lines 18 to 24 (Code I.19) give a general overview of the FAM-N pulse generated, giving the number of pulses, time increment per point, and total duration. Lines below describe the final FAM-N pulse train, reported in Table I.1. Quantities are expressed in number of points, related to the time increment given in the result overview (Code I.19). The schematic representation of the relationship between the numbers in Table I.1 is shown in Figure I.3.

- *Phase inversion* provides the position of the phase inversions that enable the most efficient conversion of the start operator into the detect element.
- *Maxima position* provides, for each pulse, the position of the maximum of the detected operator for each successive pulses of the FAM-N train. As investigated in Section 4.3.3 and observed in Table I.1, positions of phase inversion are generally located after the maxima. In the case presented in this section, the point of the first maximum appears to coincide with the first phase inversion. This corresponds to a rare case when best conversion is obtained when the inversion is performed before the maximum. This can be adjusted by setting the `cmpt.tol_compt_minus` parameters to a non-zero value.
- *Amplitude of maxima* gives the amount of detected element at each of the maxima given in the previous list of numbers. All are normalised to `1` as it corresponds to the initial unit amount of the start operator. This may be used to derive the theoretical signal improvement ratio (see Section 5.1.2).
- *Element durations* gives the duration of the FAM-N elements, in points for the first series of numbers (fourth column of Table I.1), and in µs the second series of numbers (fifth column of Table I.1). As maxima often do not correspond to the points of phase inversion, the duration of the last FAM-N pulse corresponds to the time between the last phase inversion and the next maximum as illustrated in Figure I.3, *e.g.*, manually reducing the number of pulse of a FAM-N cannot be

Phase inversion (In number of points)	Maxima positions (In number of points)	Amplitude of maxima (Theoretical maximum is 1)	Element durations (In number of points)	Element durations (In µs)
22	22	0.10472	22	1.5278
40	36	0.20537	18	1.2500
55	52	0.29281	15	1.0417
69	65	0.35454	14	0.97222
84	79	0.40025	15	1.0417
96	93	0.42666	12	0.83333
107	102	0.43999	11	0.76389
120	116	0.47401	13	0.90278
133	128	0.49908	13	0.90278
143	140	0.50807	10	0.69444
155	147	0.50983	12	0.83333
171	164	0.52081	16	1.1111
184	180	0.53825	13	0.90278
196	190	0.55069	12	0.83333
208	205	0.58317	12	0.83333
214	212	0.5853	6	0.41667
222	217	0.58587	8	0.55556
232	228	0.59499	10	0.69444
245	237	0.60306	13	0.90278
261	255	0.61925	16	1.1111
272	268	0.63205	11	0.76389
280	276	0.63593	8	0.55556
289	284	0.63878	9	0.6250
298	294	0.64139	9	0.6250
N/A	302	0.64442	4	0.27778

Table I.1: *Lists of numbers written in* `FAMN_TEMPLATE_results.txt`*, detailing the durations and maxima of the FAM-N pulse. Code I.19 gives the total number of pulses and the time increment.*

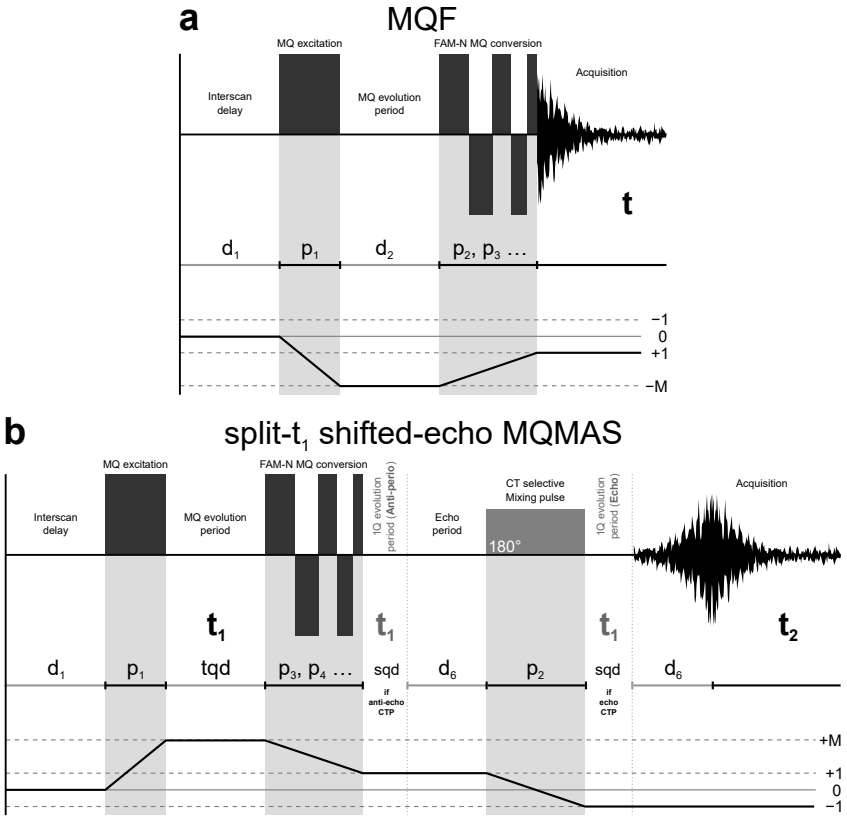

Figure I.4: *Pulse sequences, CTPs and definition of the different delays and pulse durations of **(a)**: the MQF pulse program and **(b)**: the split-t₁ shifted-echo MQMAS pulse sequence generated by the FAM-N optimisation program.*

made simply by removing final pulses, and the duration of the final FAM-N pulse must be corrected according to the point of maximum amount of 1Q given by the ”maxima position” section of `FAMN_TEMPLATE_results.txt`.

Pulse programs `TQsetup_FAMN_TEMPLATE`, `TQST13_FAMN_TEMPLATE`

FAM-N is most commonly used to increase the efficiency of the conversion pulse of a split-t₁ shifted-echo MQMAS experiment (see Section 3.3.2), as FAM/DFS cannot enhance the efficiency of the conversion $p = \pm 3$ to $p = 0$ (see Section 4.3). For this reason, the program also outputs directly pulse programs for Topspin so it can be quickly used after the FAM-N optimisation.

The two pulse programs created are an MQF pulse program (Figure I.4a), here called `TQsetup_FAMN_TEMPLATE`, and a split-t₁ shifted-echo MQMAS pulse program, here called `TQST13_FAMN_TEMPLATE`, represented in Figure I.4 with all pulses and delays. In either

pulse sequence

- `d1` is the recycle interval (1 to $5\times T_1$),
- `p1` is the MQ excitation pulse, generating $p = \pm M$ coherence from population.
- `cnst1` is the total duration of FAM-N in µs.

`cnst1` must be entered manually by setting its value to the one indicated in the comment of the `cnst1` parameter in Topspin, unless it has been experimentally optimised or re-optimised.

`TQsetup_FAMN_TEMPLATE`

The MQF pulse program, whose pulse sequence is given in Figure I.4a, is meant to be used for the optimisation of the excitation, and the re-optimisation of FAM-N if desired,[16] or to evaluate the amount of signal on the MQMAS while avoiding potential signal losses due to the spin-echo for optimisations. Its pulses and delays are

- `p2`, `p3`,... are the elements of the FAM-N pulse, effecting the $p = -M$ to $p = -1$ conversion.
- `d2` is a short MQ evolution delay (2 to 3 µs)

The total phase cycling for the MQF pulse programs are:

- **12** for 3QF / TQSetup
- **20** for 5QF / QQSetup
- **28** for 7QF[17] / SQSetup
- **36** for 9QF[18] / NQSetup

`TQST13_FAMN_TEMPLATE`

The split-t_1 shifted-echo MQMAS experiment pulse program has the following pulses and delays presented in Figure I.4b:

- `p2` is a CT-selective 180° (applied with ν_1 comparable to the total width of all the resonances on a MAS spectrum), effecting the $p = -M$ to $p = -1$ conversion and give rise to an echo.
- `p2`, `p3`,... are the elements of the FAM-N pulse, effecting the $p = +M$ to $p = +1$ conversion.

[16] Experience suggests that re-optimising FAM-N is not generally necessary, as obtained enhancements would be minor if the optimisation parameters used for FAM-N are close to the experimental parameters.
[17] 7QF: *Septuple-Quantum Filtration*
[18] 9QF: *Nonuple-Quantum Filtration*

- `d6` is the echo delay (under good conditions, this is the period necessary for the FID to decay to zero in the noise on a direct-acquisition or a spin-echo experiment).
- `sqd` and `tqd` are the two period of the split-t_1.

The total phase cycling for the st$_1$ shifted-echo MQMAS pulse programs:

- **96** for 3QMAS / TQST
- **160** for 5QMAS / QQST
- **224** for 7QMAS / SQST
- **288** for 9QMAS[19] / NQST

Split-t$_1$

As discussed in Section 3.3.3, split-t$_1$ does not present any disadvantages other than those inherent to the shifted-echo MQMAS experiment, thus is automatically included used in the pulse program. The t_1 delay, represented in Figure I.4b, is expressed in the pulse programs by two delays called `sqd` and `tqd`[20] such that

$$t_1(\texttt{d0}) = \texttt{tqd}(\texttt{d0}) + \texttt{sqd}(\texttt{d0}) \quad , \tag{I.3.1}$$

where

$$\begin{cases} \texttt{tqd} = \dfrac{1}{1+R(I,p)}\texttt{d0} & \text{(I.3.2a)} \\ \texttt{sqd} = \dfrac{R(I,p)}{1+R(I,p)}\texttt{d0} \quad , & \text{(I.3.2b)} \end{cases}$$

The values of $R(I,p)$ are tabulated in Appendix E.1, Table E.1, and the values of `sqd`/`d0` and `tqd`/`d0` Appendix E.4, Table E.6, and `d0` is the incremented time period in the indirect dimension. It is advised to rotor synchronised `tqd`, so the spinning sidebands in the indirect dimension would fold on the top of eachother, increasing the sensitivity. That is

$$\texttt{Inf} = \texttt{In0} = N\tau_R\left(1+R(I,p)\right) \quad , \tag{I.3.3}$$

where $N\tau_R$, $N \in \mathbb{N}^\star$, is a multiple or divisor of the rotor period τ_R. It is important to keep `Inf` and `In0` identical to avoid referencing problems.

[19] 9QMAS: *Nonuple-Quantum Magic-Angle Spinning*

[20] It should be noted that the MQ evolution delay is called `tqd` independently of the coherence order used for MQMAS.

Matlab data file `FAMN_TEMPLATE_Parameters_Results.mat`

This file contains a copy of all optimisation parameters, many internal variables not given in the output `.txt` file, and FAM-N results. This file can also be loaded into Matlab to use one the post-processing functions contained in the `POSTPROC` folder.

`cmpt` Contains most of the optimisation parameters (B_0, ν_1, C_Q, η_Q ...), nucleus, transition, number of points and tolerance counter(s), and the value of the options.

`FAM.data` Contains the final FAM-N pulses (see Table I.1)

1. The first line contains the amplitudes of the maxima in simulated 1Q coherence,
2. the second line contains the positions of the maxima,
3. the third line contains the points of phase inversion.

`FAM.data` is modified at all steps of the optimisation in the function `ConvPulse_opt_Rf.m`.

`param` Contains variables written in the parameter section of the SIMPSON files (section **`par`** of the SIMPSON input file).

`PPParam` Contains variables written in the pulse sequence section of the SIMPSON files section (section **`pulseq`** of the SIMPSON input file).

`rawdata` Contains a copy of the output SIMPSON files at each step of the optimisation.

`spinsys` Contains variables written in the pulse sequence section (section **`spinsys`** of the SIMPSON input file) of the SIMPSON files.

I.4 Executed SIMPSON file

This section describes the SIMPSON files generated and executed by the FAM-N program. The file taken as an example executes the simulation for the final FAM-N pulse obtained for the parameters given in Appendix I.3.

As instructed in Appendix I.2, the FAM-N program rewrites the SIMPSON file at every step of the simulation, causing the evolution of the matrix density to be re-simulated at every step. A possible improvement of the code would be to start the propagation from

the last non-optimised pulse (the second-last pulse) for better performance. Nevertheless, the code in its current form is still able to perform most optimisations in a few minutes on any modern computer.

SIMPSON files are given the name

`*userfilename*_NoFAM_*NOFP*_*CurPulse*_*Curpoint*`

where

- `*NOFP*` in the current number of FAM-N elements,
- `*CurPulse*` in the index of the incremented pulse,
- `*Curpoint*` is the index of the point of last inversion.

The execution of this file would give the return the bold black curve presented in Figure I.2, *i.e.*, would simulate the final FAM-N pulse.

Code I.20: *FAMN_TEMPLATE_NofFAM_25-26_298.m, lines 1 to 5.*

```
>1 spinsys {
>2    channels 23Na
>3    nuclei 23Na
>4    quadrupole 1 2 2000000 0 0 0 0
>5 }
```

The `spinsys` section in lines 1 to 5 in Code I.20 defines the nuclei to be simulated, and sets C_Q and η_Q for the second-order truncated quadrupolar interation for this nucleus *via* the field `quadrupolar`.

Code I.21: *FAMN_TEMPLATE_NofFAM_25-26_298.m, lines 7 to 18.*

```
 >7 par {
 >8   spin_rate        12500
 >9   method        cheby1
>10   variable tsw     0.069444
>11   variable RF      80000
>12   sw               1.0e6/tsw
>13   np               363
>14   crystal_file     rep66
>15   gamma_angles     4
>16   proton_frequency 600000000
>17   verbose          0
>18 }
```

The `par` section in lines 7 to 18 in Code I.21 defines experimental parameters and other options. The method `cheby1` is used here for improved stability in the execution of SIMPSON, but another method can be used instead, or the field can simply be omitted. `verbose` is set to `0` to disable the display of the ongoing simulation in the Matlab

window. The other fields are common to any SIMPSON input file, and can be found, for example, in the original paper.[24] This section may also contain the command **num_cores**, allowing the user to set the number of cores on which the computation will be performed (see parameter **cmpt.num_cores** in Appendix I.2).

Code I.22: *FAMN_TEMPLATE_NofFAM_25-26_298.m, lines 20 to 25.*

```
>20 proc pulseq {} {
>21   global par
>22   maxdt 4
>23   matrix set start elements {{4 1}}
>24   matrix set detect elements {{2 3}}
>25 reset
```

The **pulseseq** section is used to set the pulse sequence. Before the pulses, the following functions are called in lines 20 to 25 (Code I.22):

- `global` **par** is used to set all variables in the **par** section as global.
- **maxdt** is a short time (typically 0.1 to 100 µs) during which a time-dependent Hamiltonian can be approximated by a time-independent average Hamitonian (see Section 2.1.2). In Code I.22, it is set to $\tau_R/20$.
- The start element ρ_{41} is set by the command **matrix** `set` **start elements {{4 1}}**, and **matrix** `set` **detect elements {{2 3}}** sets the detect element to ρ_{32}.

It can be observed that the index orders are inverted with the command for the detect element, as SIMPSON uses internally Equation (1.2.34) to determine a density matrix element. Finally, **reset** sets those start and detected elements into the program memory.

Code I.23: *FAMN_TEMPLATE_NofFAM_27-26_298.m, lines 143 to 153*

```
>143 for {set i 0} {$i < 9 } {incr i 1} {
>144    pulse $par(tsw) $par(RF) -x
>145   acq
>146 }
>147
>148 for {set i 0} {$i < 64 } {incr i 1} {
>149    pulse $par(tsw) $par(RF) x
>150   acq
>151 }
>152
>153 }
```

Lines 143 to 153 (Code I.23) show the two final pulses of the FAM-N pulse train taken as an example in this section. Each defines a variable `i`, incremented from `0` (first curly brackets) to `8` and `63`, respectively (second curly brackets) by increments of `1` point (third curly bracket). The pulse itself is created by the command **pulse**, whose arguments are,

in order, the time increment (`tsw`), the RF strength ν_1 (`RF`), and the phase of the pulse (Here `x`). It can be seen that the last pulse is composed of `64` points, as it has a duration of at least `cmpt.nop120`.

Code I.24: *FAMN_TEMPLATE_NofFAM_27-26_298.m*

```
>155 proc main {} {
>156   global par
>157    fsave [fsimpson] $par(name)
>158 }
```

The section `main` in lines 155 to 158 (Code I.24) is used to set post-simulation processing. The evolution of the detected operator is printed in a file named after the SIMPSON file name by the command `fsave`, here with no file extension.

Bibliography

[1] I. I. Rabi, J. R. Zacharias, S. Millman and P. Kusch, *Phys. Rev.*, 1938, **53**, 318, DOI: 10.1103/PhysRev.53.318 (*Cited on pages 27, 35, 385*).

[2] F. Bloch, *Phys. Rev.*, 1946, **70**, 460, DOI: 10.1103/PhysRev.70.460 (*Cited on pages 27, 35, 60, 385*).

[3] E. M. Purcell, H. C. Torrey and R. V. Pound, *Phys. Rev.*, 1946, **69**, 37, DOI: 10.1103/PhysRev.69.37 (*Cited on pages 27, 35, 385*).

[4] H. Y. Carr and E. M. Purcell, *Phys. Rev.*, 1954, **94**, 630, DOI: 10.1103/PhysRev.94.630 (*Cited on pages 27, 104*).

[5] S. Meiboom and D. Gill, *Rev. Sci. Instrum.*, 1958, **29**, 688, DOI: 10.1063/1.1716296 (*Cited on pages 27, 104*).

[6] S. R. Hartmann and E. L. Hahn, *Phys. Rev.*, 1962, **128**, 2042, DOI: 10.1103/PhysRev.128.2042 (*Cited on pages 27, 106, 108*).

[7] A. Pines, M. Gibby and J. S. Waugh, *J. Chem. Phys.*, 1972, **56**, 1776, DOI: 10.1063/1.1677439 (*Cited on pages 27, 106, 107*).

[8] T. R. Carver and C. P. Slichter, *Phys. Rev.*, 1953, **92**, 212, DOI: 10.1103/PhysRev.92.212.2 (*Cited on page 27*).

[9] Q. Z. Ni, E. Daviso, T. V. Can, E. Markhasin, S. K. Jawla, T. M. Swager, R. J. Temkin, J. Herzfeld and R. G. Griffin, *Acc. Chem. Res.*, 2013, **46**, 1933, DOI: 10.1021/ar300348n (*Cited on pages 27, 142*).

[10] E. R. Andrew, *Philos. T. R. Soc. A*, 1981, **299**, 505, DOI: 10.1098/rsta.1981.0032 (*Cited on pages 27, 81*).

[11] L. Frydman and J. S. Harwood, *J. Am. Chem. Soc.*, 1995, **117**, 5367, DOI: 10.1021/ja00124a023 (*Cited on pages 28, 119, 313*).

[12] A. Medek, J. Harwood and L. Frydman, *J. Am. Chem. Soc.*, 1995, **117**, 12779, DOI: 10.1021/ja00156a015 (*Cited on pages 28, 90, 115, 119, 123*).

[13] A. Samoson, E. Lippmaa and A. Pines, *Mol. Phys.*, 1988, **65**, 1013, DOI: 10.1080/00268978800101571 (*Cited on pages 29, 134*).

[14] A. Llor and J. Virlet, *Chem. Phys. Lett.*, 1988, **152**, 248, DOI: 10.1016/0009-2614(88)87362-7 (*Cited on pages 29, 134*).

[15] Z. Gan, *J. Am. Chem. Soc.*, 2000, **122**, 3242, DOI: 10.1021/ja9939791 (*Cited on pages 29, 135, 136*).

[16] Z. Gan and H.-T. Kwak, *J. Magn. Reson.*, 2004, **168**, 346, DOI: 10.1016/j.jmr.2004.03.021 (*Cited on pages 29, 148–150*).

[17] P. K. Madhu, A. Goldbourt, L. Frydman and S. Vega, *J. Chem. Phys.*, 2000, **112**, 2377, DOI: 10.1063/1.480804 (*Cited on pages 29, 153*).

[18] P. K. Madhu, A. Goldbourt, L. Frydman and S. Vega, *Chem. Phys. Lett.*, 1999, **307**, 41, DOI: 10.1016/S0009-2614(99)00446-7 (*Cited on pages 29, 164*).

[19] A. P. M. Kentgens, *J. Magn. Reson.*, 1991, **95**, 619, DOI: 10.1016/0022-2364(91)90179-W (*Cited on pages 29, 158, 162*).

[20] J. Haase and M. S. Conradi, *Chem. Phys. Lett.*, 1993, **209**, 287, DOI: 10.1016/0009-2614(93)80109-3 (*Cited on pages 29, 158, 259*).

[21] T. Vosegaard, P. Florian, D. Massiot and P. Grandinetti, *J. Chem. Phys.*, 2001, **114**, 4618, DOI: 10.1063/1.1333407 (*Cited on pages 29, 154*).

[22] G. Wu, D. Rovnyak and R. G. Griffin, *J. Am. Chem. Soc.*, 1996, **118**, 9326, DOI: 10.1021/ja9614676 (*Cited on pages 29, 151–153, 253, 274*).

[23] H. Colaux, D. M. Dawson and S. E. Ashbrook, *J. Phys. Chem. A*, 2014, **118**, 6018, DOI: 10.1021/jp505752c (*Cited on pages 29, 164, 165, 168, 174, 234, 414*).

[24] M. Bak, J. Rasmussen and N. Nielsen, *J. Magn. Reson.*, 2000, **147**, 296, DOI: 10.1006/jmre.2000.2179 (*Cited on pages 29, 166, 173, 349, 413, 414, 441*).

[25] S. L. McCall and E. L. Hahn, *Phys. Rev.*, 1969, **183**, 457, DOI: 10.1103/PhysRev.183.457 (*Cited on pages 30, 259*).

[26] M. S. Silver, R. I. Joseph and D. I. Hoult, *J. Magn. Reson.*, 1984, **59**, Data about adiabatic pulses., 347, DOI: 10.1016/0022-2364(84)90181-1 (*Cited on pages 30, 259, 260, 385*).

[27] Z. Yao, H.-T. Kwak, D. Sakellariou, L. Emsley and P. J. Grandinetti, *Chem. Phys. Lett.*, 2000, **327**, 85, DOI: 10.1016/S0009-2614(00)00805-8 (*Cited on pages 30, 253, 259*).

[28] D. Carnevale and G. Bodenhausen, *Chem. Phys. Lett.*, 2012, **530**, 120, DOI: 10.1016/j.cplett.2012.01.058 (*Cited on pages 30, 261, 262*).

[29] S. Vega, *Phys. Rev. A*, 1981, **23**, 3152, DOI: 10.1103/PhysRevA.23.3152 (*Cited on pages 30, 111, 283, 286, 287*).

[30] S. E. Ashbrook and S. Wimperis, *J. Magn. Reson.*, 2000, **147**, 238, DOI: 10.1006/jmre.2000.2174 (*Cited on pages 30, 282, 287*).

[31] I. I. Rabi, The Nobel Prize in Physics, 1944, http://www.nobelprize.org/nobel_prizes/physics/laureates/1944/ (*Cited on page 35*).

[32] F. Bloch and E. M. Purcell, The Nobel Prize in Physics, 1952, http://www.nobelprize.org/nobel_prizes/physics/laureates/1952/ (*Cited on page 35*).

[33] S. E. Ashbrook, Ph.D. Thesis, Hertford College, Oxford, 2000 (*Cited on pages 36, 65, 89, 90, 99, 120, 146, 377*).

[34] M. J. Duer, *Solid-state NMR spectroscopy: principles and applications*, Wiley.com, 2008, DOI: 10.1002/9780470999394 (*Cited on pages 36, 49, 65, 70, 71, 76, 79, 85, 86, 89, 99, 108*).

[35] D. C. Apperley, R. K. Harris and P. Hodgkinson, *Solid state NMR: basic principles & practice*, Momentum, 2012, DOI: 10.5643/9781606503522 (*Cited on page 36*).

[36] D. Carnevale, Ph.D. Thesis, University of St Andrews, 2010, http://library.st-andrews.ac.uk/record=b1689900~S5 (*Cited on pages 36, 65*).

[37] C. Cohen-Tannoudji, B. Diu and F. Laloë, *Mécanique quantique Tome 1*, ISBN: 978-2-7056-6074-1, Hermann, 1977 (*Cited on pages 36, 44–47, 65, 331*).

[38] A. Abragam and L. C. Hebel, *Am. J. Phys*, 1961, **29**, 860, DOI: 10.1119/1.1937646 (*Cited on pages 36, 85, 86, 89, 115*).

[39] C. P. Slighter, *Principles of magnetic resonance*, Hafer and Row, 1963 (*Cited on page 36*).

[40] K. J. MacKenzie and M. E. Smith, *Multinuclear solid-state nuclear magnetic resonance of inorganic materials*, Elsevier, 2002, vol. 6 (*Cited on pages 36, 75, 85, 145, 196, 341, 342*).

[41] P. Hore, J. Jones and S. Wimperis, *NMR, the toolkit*, Oxford University Press, 2000, vol. 92 (*Cited on pages 36, 99, 100, 370*).

[42] D. M. Dawson, Ph.D. Thesis, University of St Andrews, 2014, http://library.st-andrews.ac.uk/record=b2053964~S5 (*Cited on pages 36, 99, 346*).

[43] S. E. Ashbrook, D. M. Dawson and J. M. Griffin, *Solid-state NMR spectroscopy*, School of Chemistry, University of St Andrews, 2012, DOI: 10.1002/9781118681909.ch1 (*Cited on page 36*).

[44] A. Comment, *Résonance Magnétique Nucléaire, "théorie et manuel pratique"*, 2013 (*Cited on page 36*).

[45] J. T. Cheng, J. C. Edwards and P. D. Ellis, *J. Phys. Chem.*, 1990, **94**, 553, DOI: 10.1021/j100365a014 (*Cited on pages 36, 192, 207, 346–348*).

[46] R. K. Harris, *Nuclear Magnetic Resonance Spectroscopy: A physicochemical view*, ed. P. London, ISBN : 9780273016847 0273016849, 1983 (*Cited on page 36*).

[47] R. L. Mössbauer, *Z. Phys.*, 1958, **151**, 124, DOI: 10.1007/BF01344210 (*Cited on page 36*).

[48] N. N. Greenwood and T. C. Gibb, *Mössbauer spectroscopy*, Chapman and Hall London, 1971 (*Cited on page 36*).

[49] J. D. Jackson, *Classical electrodynamics third edition*, ISBN-13: 978-0471309321, 2009 (*Cited on pages 36, 65, 78, 83, 85*).

[50] R. K. Harris, E. D. Becker, S. C. de Menezes, R. Goodfellow and P. Grangere, 2000, http://old.iupac.org/reports/provisional/abstract01/harris_prs_noopt.pdf (*Cited on pages 38, 341*).

[51] R. K. Harris, E. D. Becker, S. M. C. D. Menezes, R. Goodfellow and P. Granger, *Concepts Magn. Reson.*, 2002, **14**, 326, DOI: 10.1002/cmr.10035 (*Cited on page 38*).

[52] B. D. Cullity and C. D. Graham, *Introduction to magnetic materials*, ISBN: 978-0-471-47741-9, John Wiley & Sons, 2011 (*Cited on page 38*).

[53] A. Tannús and M. Garwood, *NMR Biomed.*, 1997, **10**, 423, DOI: 10.1002/(SICI)1099-1492(199712)10:8<423::AID-NBM488>3.0.CO;2-X (*Cited on pages 41, 386, 388, 389*).

[54] H. D. Zeh, *Found. Phys.*, 1970, **1**, 69, DOI: 10.1007/BF00708656 (*Cited on page 43*).

[55] L. De Broglie, Ph.D. Thesis, 1924, https://tel.archives-ouvertes.fr/tel-00006807 (*Cited on page 43*).

[56] M. H. Levitt, *Spin dynamics: basics of nuclear magnetic resonance*, ISBN-13: 978-0470511176, John Wiley & Sons, 2001 (*Cited on pages 44, 45, 65, 74, 79, 99, 370*).

[57] P. A. M. Dirac, *The principles of quantum mechanics, 4th edn. Clarendon*, 1958 (*Cited on page 45*).

[58] W. Pauli Jr, *Z. Phys.*, 1927, **41**, 81, DOI: 10.1007/BF01391920 (*Cited on pages 46, 327*).

[59] R. L. Liboff, *Introductory quantum mechanics*, Holden-Day San Francisco, 1980 (*Cited on page 46*).

[60] L. Landau and L. Lifschitz, *Physique théorique, Tome 1, mécanique*, Editions Mir, 1966 (*Cited on page 51*).

[61] E. Schrödinger, *Phys. Rev.*, 1926, **28**, 1049, DOI: 10.1103/PhysRev.28.1049 (*Cited on page 51*).

[62] E. Schrödinger, *Bull. Amer. Math. Soc.*, 1933, **39**, 854, 854, DOI: 10.1090/S0002-9904-1933-05739-7 (*Cited on page 51*).

[63] J. E. Campbell, *P. Lond. Math. Soc.*, 1897, **1**, 14 (*Cited on page 52*).

[64] H. Poincaré, *Compt. Rend. Acad. Sci. Paris*, 1899, **128**, 1065 (*Cited on page 52*).

[65] H. F. Baker, *P. Lond. Math. Soc.*, 1901, **1**, 347 (*Cited on page 52*).

[66] F. Hausdorff, *Ber. Verh. Kgl. SÃ¤chs. Ges. Wiss. Leipzig., Math.-phys. Kl.*, 1906, **58**, 19 (*Cited on page 52*).

[67] J. Neumann and R. T. Beyer, *Mathematical foundations of quantum mechanics*, Princeton university press, 1955 (*Cited on page 52*).

[68] P. Zeeman, *Versl. Kon. Ak. Wet*, 1896, **5**, 181 (*Cited on pages 53, 75*).

[69] B. Cagnac and J. C. Pebay-Peyroula, *Physique atomique: introduction à la physique quantique et structure de l'édifice atomique*, ISBN-13: 978-2100504619, Dunod, 1971, vol. 1 (*Cited on pages 57, 75*).

[70] C. Kittel, *Introduction to solid state physics*, Wiley, 2005 (*Cited on page 58*).

[71] S. A. Smith, W. E. Palke and J. T. Gerig, *Concepts Magn. Reson.*, 1994, **6**, 137, DOI: 10.1002/cmr.182006020 (*Cited on page 60*).

[72] D. Sakellariou, C. Hugon, A. Guiga, G. Aubert, S. Cazaux and P. Hardy, *Magn. Reson. Chem.*, 2010, **48**, 903, DOI: 10.1002/mrc.2683 (*Cited on page 60*).

[73] Z. Gan, P. Gor'kov, T. A. Cross, A. Samoson and D. Massiot, *J. Am. Chem. Soc.*, 2002, **124**, 5634, DOI: 10.1021/ja025849p (*Cited on pages 60, 119*).

[74] V. R. Cross, R. K. Hester and J. S. Waugh, *Rev. Sci. Instrum.*, 1976, **47**, 1486, DOI: 10.1063/1.1134560 (*Cited on page 60*).

[75] M. E. Stoll, A. J. Vega and R. W. Vaughan, *Rev. Sci. Instrum.*, 1977, **48**, 800, DOI: 10.1063/1.1135159 (*Cited on page 60*).

[76] R. R. Ernst and W. A. Anderson, *Rev. Sci. Instrum.*, 1966, **37**, 93, DOI: 10.1063/1.1719961 (*Cited on pages 62, 391*).

[77] S. A. Smith, W. E. Palke and J. T. Gerig, *Concepts Magn. Reson.*, 1992, **4**, 107, DOI: 10.1002/cmr.1820040202 (*Cited on pages 65, 66, 71, 77, 79*).

[78] J. M. Griffin, Ph.D. Thesis, University of Warwick (*Cited on page 65*).

[79] J. Trébosc, Ph.D. Thesis, Université de Lille 1, 2003, https://ori-nuxeo.univ-lille1.fr/nuxeo/site/esupversions/b7be3605-e232-47a8-8056-0350b4e9923c (*Cited on page 65*).

[80] N. S. Barrow, Ph.D. Thesis, University of Warwick, 2009, http://wrap.warwick.ac.uk/3617/1/WRAP_THESIS_Barrow_2009.pdf (*Cited on page 65*).

[81] C. Cohen-Tannoudji, B. Diu and F. Laloë, *Mécanique quantique Tome 2*, ISBN: 2-10-002427-2, Hermann, 1977 (*Cited on pages 65, 71–73*).

[82] P. W. Atkins and R. S. Friedman, *Molecular quantum mechanics*, Oxford university press, 2012, DOI: 10.1080/00107514.2012.678277 (*Cited on pages 65, 72*).

[83] S. A. Smith, W. E. Palke and J. T. Gerig, *Concepts Magn. Reson.*, 1992, **4**, 107, DOI: 10.1002/cmr.1820040302 (*Cited on pages 65, 66, 76*).

[84] A. Jerschow, *Prog. Nucl. Magn. Reson. Spectrosc.*, 2005, **46**, 63, DOI: 10.1016/j.pnmrs.2004.12.001 (*Cited on pages 65, 94, 99*).

[85] L. J. Mueller, *Concepts Magn. Reson. A*, 2011, **38**, 221, DOI: 10.1002/cmr.a.20224 (*Cited on pages 65, 66*).

[86] R. F. Schneider, *J. Chem. Phys.*, 1968, **48**, 4905, DOI: 10.1063/1.1668154 (*Cited on page 67*).

[87] A. E. Hansen and T. D. Bouman, *J. Chem. Phys.*, 1985, **82**, 5035, DOI: 10.1063/1.448625 (*Cited on page 68*).

[88] R. Paquin, P. Pelupessy, L. Duma, C. Gervais and G. Bodenhausen, *J. Chem. Phys.*, 2010, **133**, 034506, DOI: 10.1063/1.3445777 (*Cited on page 68*).

[89] C. Bonhomme, C. Gervais, F. Babonneau, C. Coelho, F. Pourpoint, T. Azais, S. E. Ashbrook, J. M. Griffin, J. R. Yates, F. Mauri *et al.*, *Chem. Rev.*, 2012, **112**, 5733, DOI: 10.1021/cr300108a (*Cited on page 68*).

[90] U. Haeberlen, *Advances in magnetic resonance*, Academic Press, 1976, vol. 1 (*Cited on page 68*).

[91] M. Mehring, *Principles of high resolution NMR in solids*, Springer Science and Business Media, 1983, DOI: 10.1007/978-3-642-68756-3 (*Cited on page 68*).

[92] H. W. Spiess, in *Dynamic NMR Spectroscopy*, Springer, 1978, pp. 55–214, DOI: 10.1007/978-3-642-66961-3_2 (*Cited on page 68*).

[93] A. Wokaun and R. R. Ernst, *J. Chem. Phys.*, 1977, **67**, 1752, DOI: 10.1063/1.435038 (*Cited on pages 69, 284*).

[94] O. W. Sørensen, *Prog. Nucl. Magn. Reson. Spectrosc.*, 1989, **21**, 503, DOI: 10.1016/0079-6565(89)80006-8 (*Cited on page 69*).

[95] N. Müller, G. Bodenhausen and R. R. Ernst, *J. Magn. Reson.*, 1987, **75**, 297, DOI: 10.1016/0022-2364(87)90038-2 (*Cited on page 69*).

[96] E. Wigner, *Gruppentheorie und ihre Anwendungen auf die Quantenmechanik der Atomspektren*, 1931 (*Cited on page 70*).

[97] H. E. White, *Phys. Rev.*, 1931, **37**, 1416, DOI: 10.1103/PhysRev.37.1416 (*Cited on page 70*).

[98] R. N. Zare, *Angular momentum: understanding spatial aspects in chemistry and physics*, Wiley-Interscience, 2013 (*Cited on page 70*).

[99] H. A. Buckmaster, *Can. J. Phys.*, 1964, **42**, 386, DOI: 10.1139/p64-036 (*Cited on page 70*).

[100] R. E. Wasylishen, S. E. Ashbrook and S. Wimperis, *NMR of quadrupolar nuclei in solid materials*, John Wiley & Sons, 2012 (*Cited on pages 70, 84, 85, 89, 189, 196, 215, 341, 342, 347*).

[101] G. De Nockere and G. Prévost, *Tables numériques des polynômes de Legendre*, Palais des académies, 1949 (*Cited on page 70*).

[102] W. Magnus, *Commun. Pure Appl. Math.*, 1954, **7**, 649, DOI: 10.1002/cpa.3160070404 (*Cited on page 71*).

[103] M. Goldman, P. J. Grandinetti, A. Llor, Z. Olejniczak, J. R. Sachleben and J. W. Zwanziger, *J. Chem. Phys.*, 1992, **97**, 8947, DOI: 10.1063/1.463321 (*Cited on pages 72, 89, 90, 115*).

[104] E. L. Hahn and D. E. Maxwell, *Phys. Rev.*, 1952, **88**, 1070, DOI: 10.1103/PhysRev.88.1070 (*Cited on page 74*).

[105] F. H. Köhler, in *eMagRes*, John Wiley & Sons, Ltd, 2007, ISBN: 9780470034590, DOI: 10.1002/9780470034590.emrstm1229 (*Cited on page 75*).

[106] N. F. Ramsey, *Phys. Rev.*, 1950, **78**, 699, DOI: 10.1103/PhysRev.78.699 (*Cited on pages 75, 82*).

[107] R. M. Silverstein, F. X. Webster, D. Kiemle and D. L. Bryce, *Spectrometric identification of organic compounds*, John Wiley & Sons, 2014 (*Cited on page 75*).

[108] W. Kemp, *Organic spectroscopy*, 1991, vol. 7, p. 11 (*Cited on page 75*).

[109] G. E. Pake, *J. Chem. Phys.*, 1948, **16**, 327, DOI: 10.1063/1.1746878 (*Cited on page 78*).

[110] M. M. Maricq and J. S. Waugh, *J. Chem. Phys.*, 1979, **70**, 3300, DOI: 10.1063/1.437915 (*Cited on page 82*).

[111] M. H. Levitt, *J. Magn. Reson.*, 1989, **82**, 427, DOI: 10.1016/0022-2364(89)90050-4 (*Cited on page 82*).

[112] R. K. Harris and A. Sebald, *Magn. Reson. Chem.*, 1987, **25**, 1058, DOI: 10.1002/mrc.1260251208 (*Cited on page 82*).

[113] T. P. Das and E. L. Hahn, *Nuclear quadrupole resonance spectroscopy*, Academic Pr, 1958 (*Cited on page 84*).

[114] R. V. Pound, *Phys. Rev.*, 1950, **79**, 685, DOI: 10.1103/PhysRev.79.685 (*Cited on pages 84, 253*).

[115] D. Iuga, Ph.D. Thesis, University of Nijmegen, 2003, http://repository.ubn.ru.nl/bitstream/handle/2066/19215/19215_nuclmares.pdf?sequence=1 (*Cited on pages 85, 99, 153, 157, 160, 161, 173, 230, 255, 410*).

[116] M. Munowitz, *Coherence and NMR*, Wiley New York, 1988 (*Cited on page 85*).

[117] M. J. Duer and I. Farnan, *Solid State NMR Spectroscopy: Principles and Applications*, 2008, 179 (*Cited on page 85*).

[118] D. Freude and J. Haase, *NMR Basic Principles and Progress, Vol. 29*, 1993 (*Cited on pages 88, 334*).

[119] R. Tycko and S. J. Opella, *J. Chem. Phys.*, 1987, **86**, 1761, DOI: 10.1063/1.452176 (*Cited on pages 89, 115*).

[120] A. D. Bain, *Chem. Phys. Lett.*, 2012, **531**, 267, DOI: 10.1016/j.cplett.2012.02.035 (*Cited on pages 89, 90*).

[121] Z. Gan, *J. Chem. Phys.*, 2001, **114**, 10845, DOI: 10.1063/1.1374958 (*Cited on pages 89, 134, 136, 313*).

[122] A. Goldbourt and P. K. Madhu, *Annu. Rep. NMR Spectrosc.*, 2004, **54**, 81, DOI: 10.1016/S0066-4103(04)54003-6 (*Cited on page 89*).

[123] P. P. Man, *eMagRes*, 2007, DOI: 10.1002/9780470034590.emrstm0429 (*Cited on page 89*).

[124] P. P. Man, *Phys. Rev. B*, 1997, **55**, 8406, DOI: 10.1103/PhysRevB.55.8406 (*Cited on page 89*).

[125] D. Freude and J. Haase, in *Special Applications*, Springer, 1993, pp. 1–90, DOI: 10.1007/978-3-642-50046-6 (*Cited on pages 89, 94, 95*).

[126] A. Medek, J. R. Sachleben, P. Beverwyk and L. Frydman, *J. Chem. Phys.*, 1996, **104**, 5374, DOI: 10.1063/1.471777 (*Cited on pages 89, 132*).

[127] T. Charpentier, C. Fermon and J. Virlet, *J. Chem. Phys.*, 1998, **109**, 3116, DOI: 10.1063/1.476903 (*Cited on page 89*).

[128] R. Hajjar, Y. Millot and P. P. Man, *Prog. Nucl. Magn. Reson. Spectrosc.*, 2010, **57**, 306, DOI: 10.1016/j.pnmrs.2010.05.003 (*Cited on pages 89, 126*).

[129] A. Llor, *Chem. Phys. Lett.*, 1992, **199**, 383, DOI: 10.1016/0009-2614(92)80136-Y (*Cited on page 89*).

[130] U. Haeberlen, *High Resolution NMR in solids selective averaging: supplement 1 advances in magnetic resonance*, Elsevier, 2012, vol. 1 (*Cited on page 89*).

[131] M. Goldman, *J. Magn. Reson. A*, 1993, **102**, 173, DOI: 10.1006/jmra.1993.1087 (*Cited on page 89*).

[132] C. A. Flask, *J. Magn. Reson. Imaging*, 2002, **16**, 327 (*Cited on page 89*).

[133] H.-J. Behrens and B. Schnabel, *Physica B+ C*, 1982, **114**, 185, DOI: 10.1016/0378-4363(82)90036-5 (*Cited on pages 89, 95*).

[134] S. P. Brown and S. Wimperis, *J. Magn. Reson.*, 1997, **128**, 42, DOI: doi:10.1006/jmre.1997.1217 (*Cited on pages 89, 119, 120, 123, 125, 129–131*).

[135] J.-P. Amoureux, *Solid State Nucl. Magn. Reson.*, 1993, **2**, 83, DOI: 10.1016/0926-2040(93)90066-V (*Cited on pages 89, 90, 120*).

[136] Z. Gan, P. Srinivasan, J. R. Quine, S. Steuernagel and B. Knott, *Chem. Phys. Lett.*, 2003, **367**, 163, DOI: 10.1016/S0009-2614(02)01681-0 (*Cited on pages 90, 216, 344*).

[137] A. D. Bain, *J. Magn. Reson.*, 2006, **179**, 308, DOI: 10.1016/j.jmr.2006.01.007 (*Cited on page 90*).

[138] S. E. Ashbrook and M. J. Duer, *Concepts Magn. Reson. A*, 2006, **28**, 183, DOI: 10.1002/cmr.a.20053 (*Cited on page 92*).

[139] K. Narita, J. Umeda and H. Kusumoto, *J. Chem. Phys.*, 1966, **44**, 2719, DOI: 10.1063/1.1727118 (*Cited on page 94*).

[140] D. Müller, *Ann. Phys.*, 1982, **494**, 451, DOI: 10.1002/andp.19824940607 (*Cited on pages 94, 95*).

[141] A. Samoson, *Chem. Phys. Lett.*, 1985, **119**, 29, DOI: 10.1016/0009-2614(85)85414-2 (*Cited on page 94*).

[142] G. Ajoy and J. Ramakrishna, *Solid State Nucl. Magn. Reson.*, 1995, **4**, 125, DOI: 10.1016/0926-2040(94)00043-C (*Cited on page 95*).

[143] A. Samoson, E. Kundla and E. Lippmaa, *J. Magn. Reson.*, 1982, **49**, 350, DOI: 10.1016/0022-2364(82)90201-3 (*Cited on page 95*).

[144] K. T. Mueller, Y. Wu, B. F. Chmelka, J. Stebbins and A. Pines, *J. Am. Chem. Soc.*, 1991, **113**, 32, DOI: 10.1021/ja00001a006 (*Cited on page 95*).

[145] M. H. Cohen and F. Reif, *Solid State Phys.*, 1957, **5**, 321 (*Cited on page 95*).

[146] D. Massiot, EPJ Web of Conferences, 2012, vol. 30, p. 02002, http://cea-proceedings.edpsciences.org/articles/epjconf/pdf/2012/12/epjconf_NMR2011_02002.pdf (*Cited on page 99*).

[147] L. Frydman, *Encyclopedia of nuclear magnetic resonance*, 2002, **9**, 262, http://www.researchgate.net/profile/Lucio_Frydman/publication/238107091_Fundamentals_of_Multiple-Quantum_Magic-Angle_Spinning_NMR_on_Half-Integer_Quadrupolar_Nuclei/links/54a4f7b80cf256bf8bb32a95.pdf (*Cited on pages 99, 127*).

[148] J. Keeler, *Understanding NMR spectroscopy*, ISBN: 978-0-470-74608-0, John Wiley & Sons, 2011 (*Cited on pages 100, 370*).

[149] E. L. Hahn, *Phys. Rev.*, 1950, **80**, 580, DOI: 10.1103/PhysRev.80.580 (*Cited on page 102*).

[150] V. I. Bakhmutov, *Solid State Nucl. Magn. Reson.*, 2009, **36**, 164, DOI: 10.1016/j.ssnmr.2009.10.002 (*Cited on page 102*).

[151] E. D. Becker, J. A. Ferretti, R. K. Gupta and G. H. Weiss, *J. Magn. Reson.*, 1980, **37**, 381, DOI: 10.1016/0022-2364(80)90045-1 (*Cited on page 104*).

[152] K. K. Dey, J. T. Ash, N. M. Trease and P. J. Grandinetti, *J. Chem. Phys.*, 2010, **133**, 054501, DOI: 10.1063/1.3463653 (*Cited on pages 104, 106*).

[153] F. H. Larsen, H. J. Jakobsen, P. D. Ellis and N. C. Nielsen, *J. Phys. Chem. A*, 1997, **101**, 8597, DOI: 10.1021/jp971547b (*Cited on page 104*).

[154] S. E. Shore, J.-P. Ansermet, C. P. Slichter and J. H. Sinfelt, *Phys. Rev. Lett.*, 1987, **58**, 953, DOI: 10.1103/PhysRevLett.58.953 (*Cited on page 104*).

[155] S. M. De Soto, C. P. Slichter, A. Kini, H. H. Wang, U. Geiser and J. M. Williams, *Phys. Rev. B*, 1995, **52**, 10364, DOI: 10.1103/PhysRevB.52.10364 (*Cited on page 104*).

[156] N. A. Farrow, R. Muhandiram, A. U. Singer, S. M. Pascal, C. M. Kay, G. Gish, S. E. Shoelson, T. Pawson, J. D. Forman-Kay and L. E. Kay, *Biochemistry*, 1994, **33**, 5984, DOI: 10.1021/bi00185a040 (*Cited on page 104*).

[157] D. G. Davis, M. E. Perlman and R. E. London, *J. Magn. Reson.*, 1994, **104**, 266, DOI: 10.1006/jmrb.1994.1084 (*Cited on page 104*).

[158] D. M. Korzhnev, E. V. Tischenko and A. S. Arseniev, *J. Biomol. NMR*, 2000, **17**, 231, DOI: 10.1002/jmri.20490 (*Cited on page 104*).

[159] G. S. Pell, R. S. Briellmann, A. B. Waites, D. F. Abbott, D. P. Lewis and G. D. Jackson, *J. Magn. Reson. Imaging*, 2006, **23**, 248, DOI: 10.1002/jmri.20490 (*Cited on page 104*).

[160] I. Hung and Z. Gan, *J. Magn. Reson.*, 2010, **204**, 256, DOI: 10.1016/j.jmr.2010.03.001 (*Cited on pages 105, 106, 244*).

[161] F. H. Larsen, H. J. Jakobsen, P. D. Ellis and N. C. Nielsen, *Chem. Phys. Lett.*, 1998, **292**, 467, DOI: 10.1016/S0009-2614(98)00777-5 (*Cited on page 105*).

[162] L. A. O'Dell and R. W. Schurko, *Phys. Chem. Chem. Phys.*, 2009, **11**, 7069, DOI: 10.1039/B906114B (*Cited on page 105*).

[163] J. T. Cheng and P. D. Ellis, *J. Phys. Chem.*, 1989, **93**, 2549, DOI: 10.1021/j100343a061 (*Cited on page 105*).

[164] F. H. Larsen and I. Farnan, *J. Phys. Chem. B*, 2004, **108**, 9764, DOI: 10.1021/jp049603d (*Cited on pages 105, 141, 146–148*).

[165] F. H. Larsen, J. Skibsted, H. J. Jakobsen and N. C. Nielsen, *J. Am. Chem. Soc.*, 2000, **122**, 7080, DOI: 10.1021/ja0003526 (*Cited on page 105*).

[166] F. H. Larsen, S. Rossano and I. Farnan, *J. Phys. Chem. B*, 2007, **111**, 8014, DOI: 10.1021/jp071539n (*Cited on pages 105, 141*).

[167] F. H. Larsen and I. Farnan, *Chem. Phys. Lett.*, 2002, **357**, 403, DOI: 10.1016/S0009-2614(02)00520-1 (*Cited on page 105*).

[168] A. S. Lipton, R. W. Heck, S. Primak, D. R. McNeill, D. M. Wilson III and P. D. Ellis, *J. Am. Chem. Soc.*, 2008, **130**, 9332, DOI: 10.1021/ja0776881 (*Cited on page 105*).

[169] L. A. O'Dell, K. Klimm, J. Freitas, S. Kohn and M. E. Smith, *Appl. Magn. Reson.*, 2009, **35**, 247, DOI: 10.1007/s00723-008-0159-8 (*Cited on pages 105, 259, 260*).

[170] A. J. Rossini, R. W. Mills, G. A. Briscoe, E. L. Norton, S. J. Geier, I. Hung, S. Zheng, J. Autschbach and R. W. Schurko, *J. Am. Chem. Soc.*, 2009, **131**, 3317, DOI: 10.1021/ja808390a (*Cited on page 105*).

[171] F. H. Larsen, H. J. Jakobsen, P. D. Ellis and N. C. Nielsen, *J. Magn. Reson.*, 1998, **131**, 144, DOI: 10.1006/jmre.1997.1341 (*Cited on pages 106, 147*).

[172] O. W. Sørensen, M. Rance and R. R. Ernst, *J. Magn. Reson.*, 1984, **56**, 527, DOI: 10.1016/0022-2364(84)90317-2 (*Cited on pages 106, 123*).

[173] I. Solomon, *Comptes Rendus Acad. Sci. Paris, 248, 92 (1959)*, 1959 (*Cited on page 107*).

[174] D. Rovnyak, *Concepts Magn. Reson. A*, 2008, **32A**, 254, DOI: 10.1002/cmr.a.20115 (*Cited on page 108*).

[175] P. Bertani, J. Raya, P. Reinheimer, R. Gougeon, L. Delmotte and J. Hirschinger, *Solid State Nucl. Magn. Reson.*, 1999, **13**, 219, DOI: 10.1016/S0926-2040(98)00093-9 (*Cited on page 108*).

[176] M. H. Levitt, D. Suter and R. R. Ernst, *J. Chem. Phys.*, 1986, **84**, 4243, DOI: 10.1063/1.450046 (*Cited on page 108*).

[177] L. Müller, A. Kumar, T. Baumann and R. R. Ernst, *Phys. Rev. Lett.*, 1974, **32**, 1402, DOI: 10.1103/PhysRevLett.32.1402 (*Cited on page 109*).

[178] W. Kolodziejski and J. Klinowski, *Chem. Rev.*, 2002, **102**, 613, DOI: 10.1002/chin.200221281 (*Cited on page 109*).

[179] G. Metz, X. L. Wu and S. O. Smith, *J. Magn. Reson. A*, 1994, **110**, 219, DOI: 10.1006/jmra.1994.1208 (*Cited on page 110*).

[180] A. J. Vega, *Solid State Nucl. Magn. Reson.*, 1992, **1**, 17, DOI: 10.1016/0926-2040(92)90006-U (*Cited on pages 111, 115, 282, 286, 290*).

[181] A. J. Vega, *J. Magn. Reson.*, 1992, **96**, 50, DOI: 10.1016/0022-2364(92)90287-H (*Cited on pages 111, 114, 115, 151, 282, 286, 290*).

[182] S. Vega, *J. Chem. Phys.*, 1978, **68**, 5518, DOI: 10.1063/1.435679 (*Cited on pages 111, 115, 151, 284, 286*).

[183] S. Vega and Y. Naor, *J. Chem. Phys.*, 1981, **75**, 75, DOI: 10.1063/1.441857 (*Cited on pages 111, 115, 143, 151, 158, 160, 161, 253, 255, 284*).

[184] A. J. Vega, *J. Magn. Reson.*, 1985, **65**, 252, DOI: 10.1016/0022-2364(85)90006-X (*Cited on page 111*).

[185] S. E. Ashbrook and S. Wimperis, *J. Chem. Phys.*, 2009, **131**, 194509, DOI: 10.1063/1.3263904 (*Cited on pages 111, 290*).

[186] S. E. Ashbrook and S. Wimperis, *J. Chem. Phys.*, 2004, **120**, 2719, DOI: 10.1063/1.1638995 (*Cited on pages 111, 115, 290*).

[187] S. Hayashi, *Solid State Nucl. Magn. Reson.*, 1994, **3**, 93, DOI: 10.1016/0926-2040(94)90027-2 (*Cited on page 111*).

[188] J.-P. Amoureux and M. Pruski, *Mol. Phys.*, 2002, **100**, 1595, DOI: 10.1080/00268970210125755 (*Cited on page 111*).

[189] C. A. Fyfe, H. Grondey, K. T. Mueller, K. C. Wong-Moon and T. Markus, *J. Am. Chem. Soc.*, 1992, **114**, 5876, DOI: 10.1021/ja00040a069 (*Cited on page 113*).

[190] S. Vega and A. Pines, *J. Chem. Phys.*, 1977, **66**, 5624, DOI: 10.1063/1.433884 (*Cited on page 115*).

[191] A. Samoson and E. Lippmaa, *Phys. Rev. B*, 1983, **28**, 6567, DOI: 10.1103/PhysRevB.28.6567 (*Cited on page 118*).

[192] A. Samoson and E. Lippmaa, *J. Magn. Reson.*, 1988, **79**, 255, DOI: 10.1016/0022-2364(88)90218-1 (*Cited on page 118*).

[193] A. P. M. Kentgens, *Prog. Nucl. Magn. Reson. Spectrosc.*, 1998, **32**, 141 (*Cited on page 118*).

[194] T. Nakashima, K. J. Harris and R. Wasylishen, *J. Magn. Reson.*, 2010, **202**, 162, DOI: 10.1016/j.jmr.2009.11.002 (*Cited on page 118*).

[195] T. L. Spencer, G. R. Goward and A. D. Bain, *Can. J. Chem.*, 2011, **89**, 764, DOI: 10.1139/v11-024 (*Cited on page 118*).

[196] R. V. SubbaRao, D. Srivastava and R. Ramachandran, *Phys. Chem. Chem. Phys.*, 2013, **15**, 2081, DOI: 10.1039/C2CP43103C (*Cited on page 118*).

[197] T. L. Spencer, G. R. Goward and A. D. Bain, *Solid State Nucl. Magn. Reson.*, 2013, **53**, 20, DOI: 10.1016/j.ssnmr.2013.03.002 (*Cited on page 118*).

[198] C. A. Fyfe, H. M. zu Altenschildesche and J. Skibsted, *Inorg. Chem.*, 1999, **38**, 84, DOI: 10.1021/ic980524o (*Cited on pages 119, 141*).

[199] G. Engelhardt, A. P. M. Kentgens, H. Koller and A. Samoson, *Solid State Nucl. Magn. Reson.*, 1999, **15**, 171, DOI: 10.1016/S0926-2040(99)00054-5 (*Cited on pages 119, 134, 141, 195, 342*).

[200] K. H. Lim and C. P. Grey, *J. Am. Chem. Soc.*, 2000, **122**, 9768, DOI: 10.1021/ja001281d (*Cited on pages 119, 141*).

[201] J. M. Egan and K. T. Mueller, *J. Phys. Chem. B*, 2000, **104**, 9580, DOI: 10.1021/jp992999m (*Cited on pages 119, 141*).

[202] J. Skibsted, M. Brorson, J. Villadsen and H. J. Jakobsen, *Inorg. Chem.*, 2000, **39**, 4130, DOI: 10.1021/ic000309j (*Cited on pages 119, 141*).

[203] S. R. Jansen, H. T. Hintzen, R. Metselaar, J. W. de Haan, L. J. M. van de Ven, A. P. M. Kentgens and G. H. Nachtegaal, *J. Phys. Chem. B*, 1998, **102**, 5969, DOI: 10.1021/jp981224v (*Cited on pages 119, 141*).

[204] L. Delevoye, S. Liu, M. D. Welch, C. Fernandez, J.-P. Amoureux and J. Klinowski, *J. Chem. Soc., Faraday Trans.*, 1997, **93**, 2591, DOI: 10.1039/A701848G (*Cited on pages 119, 141*).

[205] T.-H. Chen, B. H. Wouters and P. J. Grobet, *Eur. J. Inorg. Chem.*, 2000, **2000**, 281, DOI: 10.1002/(SICI)1099-0682(200002)2000:2<281::AID-EJIC281>3.0.CO;2-I (*Cited on pages 119, 141*).

[206] P. L. Bryant, C. R. Harwell, K. Wu, F. R. Fronczek, R. W. Hall and L. G. Butler, *J. Phys. Chem. A*, 1999, **103**, 5246, DOI: 10.1021/jp990374i (*Cited on pages 119, 141, 218, 344*).

[207] C. Fernandez and J.-P. Amoureux, *Chem. Phys. Lett.*, 1995, **242**, 449, DOI: 10.1016/0009-2614(95)00768-Y (*Cited on pages 119, 141, 226*).

[208] S. Wang and J. F. Stebbins, *J. Non-Cryst. Solids*, 1998, **231**, 286, DOI: 10.1016/S0022-3093(98)00703-0 (*Cited on pages 119, 141*).

[209] J. Rocha, S. W. Carr and J. Klinowski, *Chem. Phys. Lett.*, 1991, **187**, 401, DOI: 10.1016/0009-2614(91)80272-Y (*Cited on pages 119, 141, 282*).

[210] R. Iwamoto, C. Fernandez, J.-P. Amoureux and J. Grimblot, *J. Phys. Chem. B*, 1998, **102**, 4342, DOI: 10.1021/jp980291m (*Cited on pages 119, 141*).

[211] P. R. Bodart, M. Pruski, A. Bailly, C. Fernandez *et al.*, *Magn. Reson. Chem.*, 1999, **37**, S69, DOI: 10.1002/(SICI)1097-458X(199912)37:13<S69::AID-MRC533>3.0.CO;2-8 (*Cited on pages 119, 141*).

[212] S. E. Ashbrook, A. J. Berry and S. Wimperis, *Am. Mineral.*, 1999, **84**, 1191, DOI: 10.1016/0009-2614(90)87223-E (*Cited on pages 119, 128, 141, 222, 224, 226*).

[213] P. J. Dirken, S. C. Kohn, M. E. Smith and E. R. H. van Eck, *Chem. Phys. Lett.*, 1997, **266**, 568, DOI: 10.1016/S0009-2614(97)00041-9 (*Cited on pages 119, 141*).

[214] G. Wu, D. Rovnyak, P. C. Huang and R. G. Griffin, *Chem. Phys. Lett.*, 1997, **277**, 79, DOI: 10.1016/S0009-2614(97)00873-7 (*Cited on pages 119, 141*).

[215] S. Wang and J. F. Stebbins, *J. Am. Ceram. Soc.*, 1999, **82**, 1519, DOI: 10.1111/j.1151-2916.1999.tb01950.x (*Cited on pages 119, 141*).

[216] R. R. Ernst, G. Bodenhausen and A. Wokaun, *Clarendon*, 1987, ISBN-13: 978-0198556473 (*Cited on pages 119, 125, 403*).

[217] J.-P. Amoureux and C. Fernandez, *Solid State Nucl. Magn. Reson.*, 1998, **10**, 211, DOI: 10.1016/S0926-2040(97)00027-1 (*Cited on pages 119, 121, 128, 226, 380*).

[218] K. J. Pike, S. E. Ashbrook and S. Wimperis, *Chem. Phys. Lett.*, 2001, **345**, 400, DOI: 10.1016/S0009-2614(01)00912-5 (*Cited on pages 119, 136*).

[219] S. P. Brown, S. J. Heyes and S. Wimperis, *J. Magn. Reson. A*, 1996, **119**, 280, DOI: 10.1006/jmra.1996.0088 (*Cited on page 120*).

[220] K. J. Pike, R. P. Malde, S. E. Ashbrook, J. McManus and S. Wimperis, *Solid State Nucl. Magn. Reson.*, 2000, **16**, 203, DOI: 10.1016/S0926-2040(00)00081-3 (*Cited on pages 122, 128, 226, 380, 381*).

[221] S. P. Brown, Ph.D. Thesis, Merton College, Oxford, 1997, http://www2.warwick.ac.uk/fac/sci/physics/research/condensedmatt/nmr/members/steven/cv/thesis.pdf (*Cited on pages 123, 125*).

[222] J. Amoureux, C. Fernandez and L. Frydman, *Chem. Phys. Lett.*, 1996, **259**, 347, DOI: 10.1016/0009-2614(96)00809-3 (*Cited on pages 123, 132, 141, 143, 150*).

[223] D. Massiot, B. Touzo, D. Trumeau, J. Coutures, J. Virlet, P. Florian and P. Grandinetti, *Solid State Nucl. Magn. Reson.*, 1996, **6**, 73, DOI: 10.1016/0926-2040(95)01210-9 (*Cited on pages 123, 125, 130*).

[224] J.-P. Amoureux, C. Fernandez and S. Steuernagel, *J. Magn. Reson. A*, 1996, **123**, 116, DOI: 10.1006/jmra.1996.0221 (*Cited on page 123*).

[225] G. Wu, D. Rovnyank, B. Sun and R. G. Griffin, *Chem. Phys. Lett.*, 1996, **249**, 210, DOI: 10.1016/0009-2614(95)01376-8 (*Cited on page 123*).

[226] D. J. States, R. A. Haberkorn and D. J. Ruben, *J. Magn. Reson.*, 1982, **48**, 286, DOI: 10.1016/0022-2364(82)90279-7 (*Cited on pages 125, 147*).

[227] D. Marion and K. Wuthrich, *Biochem. Biophys. Res. Commun.*, 1983, **113**, 967, DOI: 10.1016/0006-291X(83)91093-8 (*Cited on pages 125, 147*).

[228] W. R. Hamilton, *Elements of quaternions*, Longmans, Green, & Company, 1866 (*Cited on page 125*).

[229] T. A. Ell and S. J. Sangwine, Signal Processing Conference, 2000 10th European, ISBN: 978-952-1504-43-3, 2000, pp. 1–4 (*Cited on page 125*).

[230] P. Grandinetti, J. H. Baltisberger, A. Llor, Y. K. Lee, U. Werner, M. Eastman and A. Pines, *J. Magn. Reson. A*, 1993, **103**, 72, DOI: 10.1006/jmra.1993.1132 (*Cited on pages 125, 134*).

[231] A. P. M. Kentgens, *Geoderma*, 1997, **80**, 271, DOI: 10.1016/S0016-7061(97)00056-6 (*Cited on pages 127, 146*).

[232] P. R. Bodart, *J. Magn. Reson.*, 1998, **133**, 207, DOI: 10.1006/jmre.1998.1426 (*Cited on page 127*).

[233] P. P. Man, *Phys. Rev. B*, 1998, **58**, 2764, DOI: 10.1103/PhysRevB.58.2764 (*Cited on pages 128, 226, 377*).

[234] Y. Millot and P. P. Man, *Solid State Nucl. Magn. Reson.*, 2002, **21**, 21, DOI: 10.1006/snmr.2001.0043 (*Cited on page 128*).

[235] C. Fernandez and J.-P. Amoureux, *Solid State Nucl. Magn. Reson.*, 1995, **5**, 315, DOI: 10.1016/0926-2040(95)01197-8 (*Cited on page 128*).

[236] S. P. Brown, S. E. Ashbrook and S. Wimperis, *J. Phys. Chem. B*, 1999, **103**, 812, DOI: 10.1021/jp9824858 (*Cited on pages 128, 141*).

[237] J. Kanellopoulos, D. Freude and A. P. M. Kentgens, *Solid State Nucl. Magn. Reson.*, 2007, **32**, 99, DOI: 10.1016/j.ssnmr.2007.09.003 (*Cited on pages 130, 150, 164, 165, 205, 206*).

[238] T. Vosegaard, P. Florian, P. J. Grandinetti and D. Massiot, *J. Magn. Reson.*, 2000, **143**, 217, DOI: 10.1006/jmre.1999.1993 (*Cited on page 130*).

[239] J. H. Baltisberger, S. L. Gann, E. W. Wooten, T. H. Chang, K. T. Mueller and A. Pines, *J. Am. Chem. Soc.*, 1992, **114**, 7489, DOI: 10.1021/ja00045a023 (*Cited on pages 131, 134*).

[240] G. Engelhardt and H. Koller, *Magn. Reson. Chem.*, 1991, **29**, 941, DOI: 10.1002/mrc.1260290914 (*Cited on page 132*).

[241] M. Hanaya and R. K. Harris, *J. Phys. Chem. A*, 1997, **101**, 6903, DOI: 10.1021/jp971108c (*Cited on pages 132, 141, 145*).

[242] D. Massiot, F. Fayon, M. Capron, I. King, S. Le Calvé, B. Alonso, J.-O. Durand, B. Bujoli, Z. Gan and G. Hoatson, *Magn. Reson. Chem.*, 2002, **40**, 70, ISSN: 1097-458X, DOI: 10.1002/mrc.984 (*Cited on pages 132, 397*).

[243] *TOPSPIN Users Guide*, Bruker, http://sites.uclouvain.be/sc-rmn/Manuels/Topspin_users_guide.pdf (*Cited on pages 132, 414*).

[244] C. Fernandez, J.-P. Amoureux, J. Chezeau, L. Delmotte and H. Kessler, *Microporous Mater.*, 1996, **6**, 331, DOI: 10.1016/0927-6513(96)00040-5 (*Cited on pages 133, 226*).

[245] B. Q. Sun, J. H. Baltisberger, Y. Wu, A. Samoson and A. Pines, *Solid State Nucl. Magn. Reson.*, 1992, **1**, 267, DOI: 10.1016/0926-2040(92)90047-D (*Cited on page 134*).

[246] G. Engelhardt, H. Koller, P. Sieger, W. Depmeier and A. Samoson, *Solid State Nucl. Magn. Reson.*, 1992, **1**, 127, DOI: 10.1016/0926-2040(92)90013-Y (*Cited on page 134*).

[247] K. Mueller, B. Sun, G. Chingas, J. Zwanziger, T. Terao and A. Pines, *J. Magn. Reson.*, 2011, **213**, 298, DOI: 10.1016/j.jmr.2011.08.034 (*Cited on page 134*).

[248] J.-P. Amoureux, C. Huguenard, F. Engelke and F. Taulelle, *Chem. Phys. Lett.*, 2002, **356**, 497, DOI: 10.1016/S0009-2614(02)00398-6 (*Cited on pages 134, 136, 381*).

[249] J.-P. Amoureux, L. Delevoye, G. Fink, F. Taulelle, A. Flambard and L. Montagne, *J. Magn. Reson.*, 2005, **175**, 285, DOI: 10.1016/j.jmr.2005.05.002 (*Cited on pages 135, 136, 150*).

[250] T. Takahashi, K. Kanehashi, Y. Shimoikeda, T. Nemoto and K. Saito, *J. Magn. Reson.*, 2009, **198**, 228, DOI: 10.1016/j.jmr.2009.02.015 (*Cited on pages 135, 145*).

[251] J. Trébosc, J.-P. Amoureux and Z. Gan, *Solid State Nucl. Magn. Reson.*, 2007, **31**, 1, DOI: 10.1016/j.ssnmr.2006.09.002 (*Cited on pages 135, 136, 141, 145*).

[252] J. Trébosc, HDR, Habilitation à Diriger des Recherches, Université de Lille 1, 2013 (*Cited on pages 135, 136*).

[253] S. E. Ashbrook and S. Wimperis, *J. Magn. Reson.*, 2003, **162**, 402, DOI: 10.1016/S1090-7807(03)00016-8 (*Cited on pages 135, 136*).

[254] N. G. Dowell, S. E. Ashbrook and S. Wimperis, *J. Phys. Chem. B*, 2004, **108**, 13292, DOI: 10.1021/jp047868m (*Cited on pages 135, 221, 345*).

[255] S. E. Ashbrook and S. Wimperis, *J. Magn. Reson.*, 2002, **156**, 269, DOI: 10.1006/jmre.2002.2557 (*Cited on pages 135, 136*).

[256] H.-T. Kwak and Z. Gan, *J. Magn. Reson.*, 2003, **164**, 369, DOI: 10.1016/S1090-7807(03)00246-5 (*Cited on page 136*).

[257] S. E. Ashbrook and S. Wimperis, *Prog. Nucl. Magn. Reson. Spectrosc.*, 2004, **45**, 53, DOI: 10.1002/chin.200451275 (*Cited on pages 136, 145, 381*).

[258] J.-P. Amoureux, A. Flambard, L. Delevoye and L. Montagne, *Chem. Commun.*, 2005, 3472, DOI: 10.1039/B502840J (*Cited on pages 136, 150*).

[259] C. Huguenard, F. Taulelle, B. Knott and Z. Gan, *J. Magn. Reson.*, 2002, **156**, 131, DOI: 10.1006/jmre.2002.2548 (*Cited on page 136*).

[260] S. E. Ashbrook and S. Wimperis, *J. Am. Chem. Soc.*, 2002, **124**, 11602, DOI: 10.1021/ja0203869 (*Cited on pages 136, 196*).

[261] S. Antonijevic, S. E. Ashbrook, S. Biedasek, R. I. Walton, S. Wimperis and H. Yang, *J. Am. Chem. Soc.*, 2006, **128**, 8054, DOI: 10.1021/ja057682g (*Cited on pages 136, 141*).

[262] S. E. Ashbrook, A. J. Berry, D. J. Frost, A. Gregorovic, C. J. Pickard, J. E. Readman and S. Wimperis, *J. Am. Chem. Soc.*, 2007, **129**, 13213, DOI: 10.1021/ja074428a (*Cited on pages 136, 141*).

[263] M. J. Thrippleton, T. J. Ball and S. Wimperis, *J. Chem. Phys.*, 2008, **128**, 034507, DOI: 10.1063/1.2813892 (*Cited on page 136*).

[264] J.-P. Amoureux, M. Pruski, D. Lang and C. Fernandez, *J. Magn. Reson.*, 1998, **131**, 170, DOI: 10.1006/jmre.1997.1275 (*Cited on pages 141, 145, 148*).

[265] F. H. Larsen and N. C. Nielsen, *J. Phys. Chem. A*, 1999, **103**, 10825, DOI: 10.1021/jp992798i (*Cited on pages 141, 146, 147*).

[266] R. Tabeta and H. Saito, *Chem. Lett.*, 1984, **13**, 293, DOI: 10.1246/cl.1984.293 (*Cited on pages 141, 342*).

[267] S.-J. Hwang, C. Fernandez, J. P. Amoureux, J.-W. Han, J. Cho, S. W. Martin and M. Pruski, *J. Am. Chem. Soc.*, 1998, **120**, 7337, DOI: 10.1021/ja9800481 (*Cited on page 141*).

[268] H. Yang, R. I. Walton, S. Antonijevic, S. Wimperis and A. C. Hannon, *J. Phys. Chem. B*, 2004, **108**, 8208, DOI: 10.1021/jp037887g (*Cited on page 141*).

[269] S. Antonijevic, S. E. Ashbrook, R. I. Walton and S. Wimperis, *J. Mater. Chem.*, 2002, **12**, 1469, DOI: 10.1039/B201581C (*Cited on page 141*).

[270] S. E. Ashbrook, L. Le Pollès, R. Gautier, C. J. Pickard and R. I. Walton, *Phys. Chem. Chem. Phys.*, 2006, **8**, 3423, DOI: 10.1039/b604520k (*Cited on page 141*).

[271] J. V. Hanna, M. E. Smith and H. J. Whitfield, *J. Am. Chem. Soc.*, 1996, **118**, 5772, DOI: 10.1021/ja960016i (*Cited on page 141*).

[272] A. P. M. Kentgens, D. Iuga, M. Kalwei and H. Koller, *J. Am. Chem. Soc.*, 2001, **123**, 2925, DOI: 10.1021/ja005917c (*Cited on pages 141, 257*).

[273] S. E. Ashbrook, A. J. Berry and S. Wimperis, *J. Phys. Chem. B*, 2002, **106**, 773, DOI: 10.1021/jp0130362 (*Cited on page 142*).

[274] J. M. Griffin, L. Clark, V. R. Seymour, D. W. Aldous, D. M. Dawson, D. Iuga, R. E. Morris and S. E. Ashbrook, *Chem. Sci.*, 2012, **3**, 2293, DOI: 10.1039/C2SC20155K (*Cited on pages 142, 341*).

[275] S. Prasad, T. M. Clark, R. Sharma, H.-T. Kwak, P. J. Grandinetti and H. Zimmermann, *Solid State Nucl. Magn. Reson.*, 2006, **29**, 119, DOI: 10.1016/j.ssnmr.2005.10.007 (*Cited on pages 142, 253, 259, 274*).

[276] P. Zhao, P. Neuhoff and J. Stebbins, *Chem. Phys. Lett.*, 2001, **344**, 325, DOI: 10.1016/S0009-2614(01)00786-2 (*Cited on pages 142, 226*).

[277] G. Wu and S. Dong, *J. Am. Chem. Soc.*, 2001, **123**, 9119, DOI: 10.1021/ja0102181 (*Cited on page 142*).

[278] G. Wu, *Prog. Nucl. Magn. Reson. Spectrosc.*, 2008, **52**, 118, DOI: 10.1016/j.pnmrs.2007.07.004 (*Cited on page 142*).

[279] L. Peng, H. Huo, Z. Gan and C. P. Grey, *Microporous Mesoporous Mater.*, 2008, **109**, 156, DOI: 10.1016/j.micromeso.2007.04.039 (*Cited on pages 142, 263*).

[280] D. Rovnyak, C. Filip, B. Itin, A. S. Stern, G. Wagner, R. G. Griffin and J. C. Hoch, *J. Magn. Reson.*, 2003, **161**, 43, DOI: 10.1016/S1090-7807(02)00189-1 (*Cited on page 142*).

[281] F. Marvasti, *Nonuniform sampling: theory and practice*, Springer Science & Business Media, 2012 (*Cited on page 142*).

[282] J. C. Hoch, M. W. Maciejewski, M. Mobli, A. D. Schuyler and A. S. Stern, *Acc. Chem. Res.*, 2014, **47**, 708, DOI: 10.1021/ar400244v (*Cited on page 142*).

[283] M. Pruski, J. W. Wiench and J.-P. Amoureux, *J. Magn. Reson.*, 2000, **147**, 286, DOI: 10.1006/jmre.2000.2190 (*Cited on page 145*).

[284] L. Marinelli and L. Frydman, *Chem. Phys. Lett.*, 1997, **275**, 188, DOI: 10.1016/S0009-2614(97)00746-X (*Cited on page 145*).

[285] U. Friedrich, I. Schnell, S. P. Brown, A. Lupulescu, D. E. Demco and H. W. Spiess, *Mol. Phys.*, 1998, **95**, 1209, DOI: 10.1080/00268979809483252 (*Cited on page 145*).

[286] M. Pernpointner, M. Seth and P. Schwerdtfeger, *J. Chem. Phys.*, 1998, **108**, 6722 (*Cited on page 146*).

[287] H. Koller, G. Engelhardt, A. P. M. Kentgens and J. Sauer, *J. Phys. Chem.*, 1994, **98**, 1544, DOI: 10.1021/j100057a004 (*Cited on page 146*).

[288] T. Vosegaard, F. H. Larsen, H. J. Jakobsen, P. D. Ellis and N. C. Nielsen, *J. Am. Chem. Soc.*, 1997, **119**, 9055, DOI: 10.1021/ja971355u (*Cited on page 147*).

[289] R. Lefort, J. Wiench, M. Pruski and J.-P. Amoureux, *J. Chem. Phys.*, 2002, **116**, 2493, DOI: 10.1063/1.1433000 (*Cited on page 147*).

[290] N. Ivchenko, C. E. Hughes and M. H. Levitt, *J. Magn. Reson.*, 2003, **160**, 52, DOI: 10.1016/S1090-7807(02)00108-8 (*Cited on page 148*).

[291] M. H. Levitt and R. Freeman, *J. Magn. Reson.*, 1979, **33**, 473, DOI: 10.1016/0022-2364(79)90265-8 (*Cited on pages 148, 261*).

[292] M. H. Levitt and R. R. Ernst, *J. Magn. Reson.*, 1983, **55**, 247, DOI: doi:10.1016/0022-2364(83)90236-6 (*Cited on pages 148, 261*).

[293] M. Baca, E. De La Rochefoucauld, E. Ambroise, J.-M. Krafft, R. Hajjar, P. P. Man, X. Carrier and J. Blanchard, *Microporous Mesoporous Mater.*, 2008, **110**, 232, DOI: 10.1016/j.micromeso.2007.06.010 (*Cited on page 150*).

[294] M. Bardy, C. Bonhomme, E. Fritsch, J. Maquet, R. Hajjar, T. Allard, S. Derenne and G. Calas, *Geochim. Cosmochim. Acta*, 2007, **71**, 3211, DOI: 10.1016/j.gca.2007.04.024 (*Cited on page 150*).

[295] J.-P. Amoureux, L. Delevoye, S. Steuernagel, Z. Gan, S. Ganapathy and L. Montagne, *J. Magn. Reson.*, 2005, **172**, 268, DOI: 10.1016/j.jmr.2004.11.001 (*Cited on page 150*).

[296] D. S. Middlemiss, F. Blanc and C. P. Grey, *ECS Trans.*, 2009, **25**, 1709, DOI: 10.1149/1.3205709 (*Cited on page 150*).

[297] T. Ball and S. Wimperis, *J. Magn. Reson.*, 2007, **187**, 343, DOI: 10.1016/j.jmr.2007.05.020 (*Cited on pages 150, 206*).

[298] H.-T. Kwak, S. Prasad, Z. Yao, P. J. Grandinetti, J. R. Sachleben and L. Emsley, *J. Magn. Reson.*, 2001, **150**, 71, DOI: 10.1006/jmre.2001.2313 (*Cited on pages 153, 253, 274*).

[299] K. Lim, T. Charpentier and A. Pines, *J. Magn. Reson.*, 2002, **154**, 196, DOI: 10.1006/jmre.2001.2471 (*Cited on pages 153, 253, 274*).

[300] P. K. Madhu and M. H. Levitt, *J. Magn. Reson.*, 2002, **155**, 150, DOI: 10.1006/jmre.2002.2508 (*Cited on pages 153, 253, 259, 274*).

[301] T. Mildner, M. E. Smith and R. Dupree, *Chem. Phys. Lett.*, 1999, **301**, 389, DOI: 10.1016/S0009-2614(99)00009-3 (*Cited on page 153*).

[302] K. H. Lim and C. P. Grey, *Solid State Nucl. Magn. Reson.*, 1998, **13**, 101, DOI: 10.1016/S0926-2040(98)00070-8á (*Cited on page 153*).

[303] R. Bhattacharyya and L. Frydman, *J. Chem. Phys.*, 2007, **127**, 194503, DOI: 10.1063/1.2793783 (*Cited on page 153*).

[304] B. Koczor and J. Rohonczy, *Solid State Nucl. Magn. Reson.*, 2016, **74-75**, 1, DOI: 10.1016/j.ssnmr.2016.02.001 (*Cited on pages 153, 316*).

[305] Z. Gan and P. J. Grandinetti, *Chem. Phys. Lett.*, 2002, **352**, 252, DOI: 10.1016/S0009-2614(01)01428-2 (*Cited on page 154*).

[306] J. D. Walls, K. H. Lim and A. Pines, *J. Chem. Phys.*, 2002, **116**, 79, DOI: 10.1063/1.1421613 (*Cited on page 154*).

[307] J. W. Logan, J. T. Urban, J. D. Walls, K. H. Lim, A. Jerschow and A. Pines, *Solid State Nucl. Magn. Reson.*, 2002, **22**, 97, DOI: 10.1006/snmr.2002.0084 (*Cited on page 154*).

[308] J. Haase, M. S. Conradi, C. P. Grey and A. J. Vega, *J. Magn. Reson. A*, 1994, **109**, 90, DOI: 10.1006/jmra.1994.1138 (*Cited on pages 158, 253*).

[309] E. Van Veenendaal, B. H. Meier and A. P. M. Kentgens, *Mol. Phys.*, 1998, **93**, 195, DOI: 10.1080/002689798169212 (*Cited on pages 158, 160, 163, 264*).

[310] R. Fu, V. L. Ermakov and G. Bodenhausen, *Solid State Nucl. Magn. Reson.*, 1996, **7**, 1, DOI: 10.1016/0926-2040(96)01231-3 (*Cited on pages 158, 389*).

[311] A. P. M. Kentgens and R. Verhagen, *Chem. Phys. Lett.*, 1999, **300**, 435, DOI: 10.1016/S0009-2614(98)01402-X (*Cited on pages 158, 162*).

[312] D. Iuga, H. Schäfer, R. Verhagen and A. P. M. Kentgens, *J. Magn. Reson.*, 2000, **147**, 192, DOI: 10.1006/jmre.2000.2192 (*Cited on pages 160, 161, 163, 164, 173, 230, 255*).

[313] D. Iuga and A. P. M. Kentgens, *J. Magn. Reson.*, 2002, **158**, 65, DOI: 10.1016/S1090-7807(02)00061-7á (*Cited on pages 162, 173, 256*).

[314] M. Goswami, P. J. M. van Bentum and A. P. M. Kentgens, *J. Magn. Reson.*, 2012, **219**, 25, DOI: 10.1016/j.jmr.2012.04.007 (*Cited on pages 163, 257*).

[315] M. Goswami, P. van Bentum and A. P. M. Kentgens, *Can. J. Chem.*, 2011, **89**, 1130, DOI: 10.1139/v11-053 (*Cited on pages 163, 257, 270*).

[316] H. Schäfer, D. Iuga, R. Verhagen and A. P. M. Kentgens, *J. Chem. Phys.*, 2001, **114**, 3073, DOI: 10.1063/1.1340576 (*Cited on pages 163, 173, 230, 259, 264*).

[317] J. Gu and W. P. Power, *Solid State Nucl. Magn. Reson.*, 2005, **27**, 192, DOI: 10.1016/j.ssnmr.2004.11.003 (*Cited on page 164*).

[318] A. Goldbourt, P. K. Madhu and S. Vega, *Chem. Phys. Lett.*, 2000, **320**, 448, DOI: 10.1016/S0009-2614(00)00298-0 (*Cited on pages 164, 166, 226, 234–236*).

[319] T. Bräuniger, *Solid State Nucl. Magn. Reson.*, 2012, **45-46**, 16, DOI: 10.1016/j.ssnmr.2012.04.002 (*Cited on page 165*).

[320] T. Bräuniger, G. Hempel and P. K. Madhu, *J. Magn. Reson.*, 2006, **181**, 68, DOI: 10.1016/j.jmr.2006.03.016á (*Cited on page 165*).

[321] S. A. Smith, T. O. Levante, B. H. Meier and R. R. Ernst, *J. Magn. Reson. A*, 1994, **106**, 75, DOI: 10.1006/jmra.1994.1008 (*Cited on page 166*).

[322] M. Veshtort and R. G. Griffin, *J. Magn. Reson.*, 2006, **178**, 248, DOI: 10.1016/j.jmr.2005.07.018 (*Cited on page 166*).

[323] J.-P. Amoureux, C. Fernandez and Y. Dumazy, *J. Chim. Phys.*, 1995, **2**, 1939, http://www-lcs.ensicaen.fr/pyPulsar/index.php/Home (*Cited on page 166*).

[324] P. Hodgkinson, *Durham University*, 2000, https://www.dur.ac.uk/paul.hodgkinson/pNMRsim (*Cited on page 166*).

[325] C. M. Morais, M. Lopes, C. Fernandez and J. Rocha, *Magn. Reson. Chem.*, 2003, **41**, 679, DOI: 10.1002/mrc.1238 (*Cited on pages 166, 226, 234–236, 315, 422*).

[326] I. The MathWorks, *MATLAB Release 2014b*, 2014, http://uk.mathworks.com/ (*Cited on pages 166, 413, 414*).

[327] V. G. Boltyanskiy, R. V. Gamkrelidze, Y. E. F. Mishchenko and L. S. Pontryagin, 1962 (*Cited on page 168*).

[328] A. E. Bryson, *Applied optimal control: optimization, estimation and control*, CRC Press, 1975 (*Cited on page 168*).

[329] Z. Tošner, T. Vosegaard, C. Kehlet, N. Khaneja, S. J. Glaser and N. C. Nielsen, *J. Magn. Reson.*, 2009, **197**, 120, DOI: 10.1016/j.jmr.2008.11.020 (*Cited on page 168*).

[330] T. Vosegaard, C. Kehlet, N. Khaneja, S. J. Glaser and N. C. Nielsen, *J. Am. Chem. Soc.*, 2005, **127**, 13768, DOI: 10.1021/ja054035g (*Cited on pages 168, 316*).

[331] K. Y. Leung and C. Calvo, *Can. J. Chem.*, 1972, **50**, 2519, DOI: 10.1139/v72-406 (*Cited on page 195*).

[332] E. Lippmaa, A. Samoson and M. Magi, *J. Am. Chem. Soc.*, 1986, **108**, 1730, DOI: 10.1021/ja00268a002 (*Cited on page 196*).

[333] M. E. Smith, C. Jaeger, R. Schoenhofer and S. Steuernagel, *Chem. Phys. Lett.*, 1994, **219**, 75, DOI: 10.1016/0009-2614(94)00061-1 (*Cited on page 196*).

[334] L. B. Alemany, S. Steuernagel, J.-P. Amoureux, R. L. Callender and A. R. Barron, *Solid State Nucl. Magn. Reson.*, 1999, **14**, 1, DOI: 10.1016/S0926-2040(99)00011-9 (*Cited on pages 196, 344*).

[335] J. H. Baltisberger, Z. Xu, J. F. Stebbins, S. H. Wang and A. Pines, *J. Am. Chem. Soc.*, 1996, **118**, 7209, DOI: 10.1021/ja9606586 (*Cited on page 196*).

[336] L. Alemany, D. Massiot, B. Sherriff, M. Smith and F. Taulelle, *Chem. Phys. Lett.*, 1991, **177**, 301, DOI: 10.1016/0009-2614(91)85035-u (*Cited on page 196*).

[337] S. Dahaoui, N. E. Ghermani, S. Ghose and J. A. K. Howard, *Am. Mineral.*, 2001, **86**, 159, DOI: 10.2138/am-2001-0117 (*Cited on page 196*).

[338] Z. Xu and B. L. Sherriff, *Appl. Magn. Reson.*, 1993, **4**, 203, DOI: 10.1007/BF03162564 (*Cited on page 196*).

[339] N. Kim, C.-H. Hsieh and J. F. Stebbins, *Chem. Mater.*, 2006, **18**, 3855, DOI: 10.1021/cm0605901 (*Cited on pages 199, 345*).

[340] S. Prasad, P. Zhao, J. Huang, J. Fitzgerald and J. Shore, *Solid State Nucl. Magn. Reson.*, 2001, **19**, 45, DOI: 10.1006/snmr.2000.0022 (*Cited on pages 199, 348*).

[341] O. B. Lapina, D. F. Khabibulin, A. A. Shubin and V. V. Terskikh, *Prog. Nucl. Magn. Reson. Spectrosc.*, 2008, **53**, 128, DOI: 10.1016/j.pnmrs.2007.12.001 (*Cited on pages 199, 348*).

[342] K. E. Johnston, J. M. Griffin, R. I. Walton, D. M. Dawson, P. Lightfoot and S. E. Ashbrook, *Phys. Chem. Chem. Phys.*, 2011, **13**, 7565, DOI: 10.1039/C1CP20258H (*Cited on pages 200, 349*).

[343] E. R. Parnham and R. E. Morris, *Chem. Mater.*, 2006, **18**, 4882, DOI: 10.1021/cm0615929 (*Cited on page 207*).

[344] M. Amri, S. E. Ashbrook, D. M. Dawson, J. M. Griffin, R. I. Walton and S. Wimperis, *J. Phys. Chem. C*, 2012, **116**, 15048, DOI: 10.1021/jp304868w (*Cited on pages 215, 346*).

[345] J. T. Ash and P. J. Grandinetti, *Magn. Reson. Chem.*, 2006, **44**, 823, DOI: 10.1002/mrc.1841 (*Cited on pages 216, 346*).

[346] S. S. Hafner, M. Raymond and S. Ghose, *J. Chem. Phys.*, 1970, **52**, 6037 (*Cited on pages 218, 344*).

[347] T. J. Bastow, *J. Chem. Soc., Faraday Trans.*, 1991, **87**, 2453, DOI: 10.1039/FT9918702453 (*Cited on pages 220, 221, 342, 345*).

[348] J. M. Griffin, A. J. Berry and S. E. Ashbrook, *Solid State Nucl. Magn. Reson.*, 2011, **40**, 91, DOI: 10.1016/j.ssnmr.2011.08.004 (*Cited on pages 221, 343*).

[349] K. J. D. MacKenzie and R. H. Meinhold, *Am. Mineral.*, 1994, **79**, 250, http://www.minsocam.org/ammin/AM79/AM79_250.pdf (*Cited on page 221*).

[350] K. J. D. MacKenzie and R. H. Meinhold, *Am. Mineral.*, 1994, **79**, 43, http://www.minsocam.org/ammin/AM79/AM79_43.pdf (*Cited on page 221*).

[351] K. J. D. MacKenzie and R. H. Meinhold, *Thermochim. Acta*, 1993, **230**, 339, DOI: 10.1016/0040-6031(93)80371-G (*Cited on page 221*).

[352] D. Nied, K. Enemark-Rasmussen, E. L'Hopital, J. Skibsted and B. Lothenbach, *Cem. Concr. Res.*, 2016, **79**, 323, DOI: 10.1016/j.cemconres.2015.10.003 (*Cited on page 221*).

[353] B. C. Chakoumakos, C.-K. Loong and A. J. Schultz, *J. Phys. Chem. B*, 1997, **101**, 9458, DOI: 10.1021/jp972225a (*Cited on page 221*).

[354] W. L. Bragg and G. B. Brown, *Z. Kristallogr.*, 1926, **63**, 538 (*Cited on page 222*).

[355] R. M. Hazen, *Am. Mineral.*, 1976, **61**, 1280, DOI: 10.1186/s13065-015-0086-3, http://www.minsocam.org/ammin/AM61/AM61_1280.pdf (*Cited on pages 222, 224*).

[356] B. Derighetti, S. Hafner, H. Marxer and H. Rager, *Phys. Lett. A*, 1978, **66**, 150, DOI: 10.1016/0375-9601(78)90023-3 (*Cited on pages 222, 224, 225, 343, 361*).

[357] K. Fujino, S. Sasaki, Y. Takeuchi and R. Sadanaga, *Acta Crystall. B-Stru.*, 1981, **37**, 513, DOI: doi:10.1107/S0567740881003506 (*Cited on pages 222, 224*).

[358] Y. Takeuchi, N. Haga and T. Yamanaka, *The Journal of the Japanese Association of Mineralogists, Petrologists and Economic Geologists*, 1982, **77**, 51, DOI: 10.2465/ganko1941.77.51 (*Cited on page 222*).

[359] S. Schramm and E. Oldfield, *J. Am. Chem. Soc.*, 1984, **106**, 2502, DOI: 10.1021/ja00321a002 (*Cited on pages 222, 224*).

[360] B. Winkler, P. Blaha and K. Schwarz, *Am. Mineral.*, 1996, **81**, 545 (*Cited on pages 222, 224*).

[361] S. E. Ashbrook, L. Le Pollès, C. J. Pickard, A. J. Berry, S. Wimperis and I. Farnan, *Phys. Chem. Chem. Phys.*, 2007, **9**, 1587, DOI: 10.1039/B618211A (*Cited on pages 222, 224*).

[362] C. P. Morrow, J. D. Kubicki, K. T. Mueller and D. R. Cole, *J. Phys. Chem. C*, 2009, **114**, 5417, DOI: 10.1021/jp9057719 (*Cited on page 222*).

[363] M. C. Davis, W. J. Brouwer, A. S. Lipton, Z. Gan and K. T. Mueller, *Am. Mineral.*, 2010, **95**, 1601, DOI: 10.2138/am.2010.3403 (*Cited on pages 222, 224*).

[364] J. M. Griffin and S. E. Ashbrook, *Solid-state NMR of high-pressure silicates in the earth's mantle*, 2013, vol. 79, pp. 241–332 (*Cited on pages 222, 224*).

[365] P. J. Pallister, I. L. Moudrakovski and J. A. Ripmeester, *Phys. Chem. Chem. Phys.*, 2009, **11**, 11487, DOI: 10.1039/B916076K (*Cited on pages 224, 342*).

[366] J. Rocha, Z. Lin, C. Fernandez and J.-P. Amoureux, *Chem. Commun.*, 1996, 2513, DOI: 10.1039/CC9960002513 (*Cited on page 226*).

[367] C. Fernandez, L. Delevoye, J.-P. Amoureux, D. P. Lang and M. Pruski, *J. Am. Chem. Soc.*, 1997, **119**, 6858, DOI: 10.1039/A701848G (*Cited on pages 226, 282*).

[368] T. Bräuniger, K. Pike, R. Harris and P. Madhu, *J. Magn. Reson.*, 2003, **163**, 64, DOI: 10.1016/S1090-7807(03)00124-1 (*Cited on page 226*).

[369] A. Goldbourt and S. Vega, *J. Magn. Reson.*, 2002, **154**, 280, DOI: 10.1006/jmre.2001.2475 (*Cited on page 226*).

[370] K. Saito, K. Kanehashi, Y. Saito and J. Godward, *Appl. Magn. Reson.*, 2002, **22**, 257, DOI: 10.1007/BF03166108 (*Cited on page 226*).

[371] T. Ohkubo, K. Kanehashi, K. Saito and Y. Ikeda, *Clays Clay Miner.*, 2003, **51**, 513, DOI: 10.1346/CCMN.2003.0510505 (*Cited on page 226*).

[372] R. Hajjar, Y. Millot and P. Man, *C. R. Chim.*, 2008, **11**, 380, DOI: 10.1016/j.crci.2007.07.003 (*Cited on page 226*).

[373] A. Pedone, T. Charpentier and M. C. Menziani, *Phys. Chem. Chem. Phys.*, 2010, **12**, 6054, DOI: 10.1039/B924489A (*Cited on page 226*).

[374] K. Shimoda, Y. Tobu, K. Kanehashi, T. Nemoto and K. Saito, *J. Non-Cryst. Solids*, 2008, **354**, 1036, DOI: 10.1016/j.jnoncrysol.2007.08.010 (*Cited on page 226*).

[375] K. Shimoda, K. Kanehashi, M. Hatakeyama, Y. Tobu, T. Shimizu and K. Saito, *Chem. Lett.*, 2007, **36**, 834, DOI: 10.1246/cl.2007.834 (*Cited on page 226*).

[376] S. Ganapathy, L. Delevoye, J. Amoureux and P. Madhu, *Magn. Reson. Chem.*, 2008, **46**, 948, DOI: 10.1002/mrc.2286 (*Cited on page 226*).

[377] J.-P. Amoureux and J. Trébosc, *J. Magn. Reson.*, 2006, **179**, 311, DOI: 10.1016/j.jmr.2006.01.008 (*Cited on page 226*).

[378] K. Shimoda, Y. Tobu, Y. Shimoikeda, T. Nemoto and K. Saito, *J. Magn. Reson.*, 2007, **186**, 156, DOI: 10.1016/j.jmr.2007.01.019 (*Cited on pages 226, 263*).

[379] S. Wang, Z. Xu, J. Baltisberger, L. Bull, J. Stebbins and A. Pines, *Solid State Nucl. Magn. Reson.*, 1997, **8**, 1, DOI: 10.1016/S0926-2040(96)01277-5 (*Cited on page 226*).

[380] A. Goldbourt, M. V. Landau and S. Vega, *J. Phys. Chem. B*, 2003, **107**, 724 (*Cited on page 226*).

[381] C. V. Chandran, J. Cuny, R. Gautier, L. Le Pollès, C. J. Pickard and T. Bräuniger, *J. Magn. Reson.*, 2010, **203**, 226, DOI: 10.1016/j.jmr.2009.12.021 (*Cited on page 226*).

[382] P. K. Madhu, O. Johannessen, K. Pike, R. Dupree, M. Smith and M. Levitt, *J. Magn. Reson.*, 2003, **163**, 310, DOI: 10.1016/S1090-7807(03)00159-9 (*Cited on pages 226, 259, 274*).

[383] P. S. Neuhoff, P. Zhao and J. F. Stebbins, *Microporous Mesoporous Mater.*, 2002, **55**, 239 (*Cited on page 226*).

[384] M. R. Hansen, M. Brorson, H. Bildsøe, J. Skibsted and H. J. Jakobsen, *J. Magn. Reson.*, 2008, **190**, 316, DOI: 10.1016/j.jmr.2007.11.014 (*Cited on pages 253, 259, 260*).

[385] P. K. Madhu, K. J. Pike, R. Dupree, M. H. Levitt and M. E. Smith, *Chem. Phys. Lett.*, 2003, **367**, 150, DOI: 10.1016/S0009-2614(02)01691-3 (*Cited on pages 253, 259*).

[386] H. J. Jakobsen, H. Bildsøe, J. Skibsted, M. Brorson, B. R. Srinivasan, C. Näther and W. Bensch, *Phys. Chem. Chem. Phys.*, 2009, **11**, 6981, DOI: 10.1039/B904841N (*Cited on pages 253, 259, 260*).

[387] S. Prasad, H.-T. Kwak, T. Clark and P. J. Grandinetti, *J. Am. Chem. Soc.*, 2002, **124**, 4964, DOI: 10.1021/ja025910q (*Cited on pages 253, 259*).

[388] H.-T. Kwak, S. Prasad, T. Clark and P. J. Grandinetti, *J. Magn. Reson.*, 2003, **160**, 107, DOI: 10.1016/S1090-7807(02)00139-8 (*Cited on pages 253, 259*).

[389] H.-T. Kwak, S. Prasad, T. Clark and P. J. Grandinetti, *Solid State Nucl. Magn. Reson.*, 2003, **24**, 71, DOI: 10.1016/S0926-2040(03)00051-1 (*Cited on pages 253, 259, 270, 274*).

[390] R. Siegel, T. Nakashima and R. Wasylishen, *Chem. Phys. Lett.*, 2004, **388**, 441, DOI: 10.1016/j.cplett.2004.03.047 (*Cited on pages 253, 259, 263*).

[391] R. Siegel, T. Nakashima and R. Wasylishen, *J. Magn. Reson.*, 2007, **184**, 85, DOI: 10.1016/j.jmr.2006.09.007 (*Cited on pages 253, 259, 260, 265*).

[392] R. Siegel, T. Nakashima and R. Wasylishen, *Chem. Phys. Lett.*, 2006, **421**, 529, DOI: 10.1016/j.cplett.2006.01.107 (*Cited on pages 253, 259, 261, 262*).

[393] R. Siegel, T. Nakashima and R. Wasylishen, *Concepts Magn. Reson. A*, 2005, **26**, 47, DOI: 10.1002/cmr.a.20037 (*Cited on pages 253, 259, 264*).

[394] W. Ling and A. Jerschow, *J. Magn. Reson.*, 2005, **176**, 234, DOI: 10.1016/j.jmr.2005.06.006 (*Cited on pages 253, 257*).

[395] G. M. Bowers and R. J. Kirkpatrick, *Cryst Growth Des.*, 2011, **11**, 5188, DOI: 10.1021/cg201227f (*Cited on pages 253, 257*).

[396] T. Nakashima, R. Teymoori and R. Wasylishen, *Magn. Reson. Chem.*, 2009, **47**, 465, DOI: 10.1002/mrc.2413 (*Cited on pages 253, 258, 259, 273*).

[397] L. A. O'Dell and R. W. Schurko, *J. Am. Chem. Soc.*, 2009, **131**, 6658, DOI: 10.1021/ja901278q (*Cited on page 253*).

[398] R. Schurko, I. Hung and C. Widdifield, *Chem. Phys. Lett.*, 2003, **379**, 1, DOI: 10.1016/S0009-2614(03)01345-9 (*Cited on pages 253, 257, 259*).

[399] G. M. Bowers, R. Ravella, S. Komarneni and K. T. Mueller, *J. Phys. Chem. B*, 2006, **110**, 7159, DOI: 10.1021/jp057205k (*Cited on pages 253, 257*).

[400] C. M. Widdifield and R. W. Schurko, *J. Phys. Chem. A*, 2005, **109**, 6865, DOI: 10.1021/jp058059l (*Cited on pages 253, 257*).

[401] J. C. C. Freitas, A. Wong and M. E. Smith, *Magn. Reson. Chem.*, 2009, **47**, 9, DOI: 10.1002/mrc.2328 (*Cited on pages 253, 257, 259*).

[402] R. Siegel, T. Nakashima and R. Wasylishen, *Concepts Magn. Reson. A*, 2005, **26**, 62, DOI: 10.1002/cmr.a.20038 (*Cited on page 253*).

[403] A. P. M. Kentgens, R. R. van Eck, Ernst, T. Ajithkumar, T. Anupold, J. Past, A. Reinhold and A. Samoson, *J. Magn. Reson.*, 2006, **178**, 212, DOI: 10.1016/j.jmr.2005.09.014 (*Cited on page 253*).

[404] S. Caldarelli, A. Buchholz and M. Hunger, *J. Am. Chem. Soc.*, 2001, **123**, 7118, DOI: 10.1021/ja0102538 (*Cited on pages 253, 274*).

[405] G. M. Bowers and R. J. Kirkpatrick, *J. Am. Ceram. Soc.*, 2009, **92**, 545, DOI: 10.1111/j.1551-2916.2008.02906.x (*Cited on page 257*).

[406] I. Hung and R. W. Schurko, *J. Phys. Chem. B*, 2004, **108**, 9060, DOI: 10.1021/jp040270u (*Cited on pages 257, 259*).

[407] T. Nakashima, R. Wasylishen, R. Siegel and K. Ooms, *Chem. Phys. Lett.*, 2008, **450**, 417, DOI: 10.1016/j.cplett.2007.11.032 (*Cited on pages 258, 261*).

[408] K. K. Dey, S. Prasad, J. T. Ash, M. Deschamps and P. J. Grandinetti, *J. Magn. Reson.*, 2007, **185**, 326, DOI: 10.1016/j.jmr.2006.12.013 (*Cited on page 259*).

[409] M. Edén, J. Grins, Z. Shen and Z. Weng, *J. Magn. Reson.*, 2004, **169**, 279, DOI: 10.1016/j.jmr.2004.05.009 (*Cited on page 259*).

[410] T. Vosegaard, D. Massiot and P. J. Grandinetti, *Chem. Phys. Lett.*, 2000, **326**, 454, DOI: 10.1016/S0009-2614(00)00779-X (*Cited on page 259*).

[411] L. Allen and J. H. Eberly, *Optical resonance and two-level atoms*, John Wiley, 1975 (*Cited on page 259*).

[412] J. Baum, R. Tycko and A. Pines, *Phys. Rev. A*, 1985, **32**, 3435, DOI: 10.1103/PhysRevA.32.3435 (*Cited on page 259*).

[413] E. Kupce and R. Freeman, *J. Magn. Reson. A*, 1995, **115**, 273, DOI: 10.1006/jmra.1995.1179 (*Cited on page 260*).

[414] M. Garwood and L. DelaBarre, *J. Magn. Reson.*, 2001, **153**, 155, DOI: 10.1006/jmre.2001.2340 (*Cited on pages 260, 264, 386*).

[415] L. A. O'Dell, K. J. Harris and R. W. Schurko, *J. Magn. Reson.*, 2010, **203**, 156, DOI: 10.1016/j.jmr.2009.12.016 (*Cited on pages 262, 273, 316*).

[416] J.-P. Amoureux, F. Bauer, R. R. Ernst, C. Fernandez, D. Freude, D. Michel and U.-T. Pingel, *Chem. Phys. Lett.*, 1998, **285**, 10, DOI: 10.1016/S0009-2614(97)01462-0 (*Cited on page 263*).

[417] D. R. Neuville, L. Cormier and D. Massiot, *Geochim. Cosmochim. Acta*, 2004, **68**, 5071, DOI: 10.1016/j.gca.2004.05.048 (*Cited on page 263*).

[418] K. Shimoda, T. Nemoto and K. Saito, *J. Phys. Chem. B*, 2008, **112**, 6747, DOI: 10.1021/jp711417t (*Cited on page 263*).

[419] Y. A. Tesiram and M. R. Bendall, *J. Magn. Reson.*, 2002, **156**, 26, DOI: 10.1006/jmre.2002.2531á (*Cited on pages 264, 386*).

[420] T. Mildner, M. E. Smith and R. Dupree, *Chem. Phys. Lett.*, 1999, **306**, 297, DOI: 10.1016/s0009-2614(99)00457-1 (*Cited on page 276*).

[421] M. Pruski, D. Lang, C. Fernandez and J.-P. Amoureux, *Solid State Nucl. Magn. Reson.*, 1997, **7**, 327, DOI: 10.1016/S0926-2040(96)01284-2 (*Cited on page 281*).

[422] H. Kampermann, A. D. Bain and R. Dumont, *J. Chem. Phys.*, 2002, **116**, 2464, DOI: 10.1063/1.1433003 (*Cited on page 281*).

[423] K. Gopalakrishnan and G. Bodenhausen, *J. Chem. Phys.*, 2006, **124**, 194311, DOI: 10.1063/1.2197827 (*Cited on page 281*).

[424] B. Hu, J.-P. Amoureux, J. Trébosc and S. Hafner, *J. Magn. Reson.*, 2008, **192**, 8, DOI: 10.1016/j.jmr.2008.01.008 (*Cited on page 281*).

[425] D. E. Woessner, *Z. Phys. Chem.*, 1987, **152**, 51, DOI: 10.1524/zpch.1987.152.Part_1_2.051 (*Cited on page 282*).

[426] G. Jeschke, W. Hoffbauer and M. Jansen, *Solid State Nucl. Magn. Reson.*, 1998, **12**, 1, DOI: 10.1016/S0926-2040(98)00045-9 (*Cited on page 282*).

[427] K. H. Lim and C. P. Grey, *Chem. Phys. Lett.*, 1999, **312**, 45, DOI: 10.1016/S0009-2614(99)00884-2 (*Cited on page 282*).

[428] S. Hayashi and K. Hayamizu, *Chem. Phys. Lett.*, 1993, **203**, 319, DOI: 10.1016/0009-2614(93)85575-9 (*Cited on page 282*).

[429] R. K. Harris and G. J. Nesbitt, *J. Magn. Reson.*, 1988, **78**, 245, DOI: 10.1016/0022-2364(88)90268-5 (*Cited on page 282*).

[430] S. M. De Paul, M. Ernst, J. S. Shore, J. F. Stebbins and A. Pines, *J. Phys. Chem. B*, 1997, **101**, 3240, DOI: 10.1021/jp9623711 (*Cited on page 282*).

[431] X. Ai, L. Chen, J. Dong, C. Ye and F. Deng, *J. Mater. Chem.*, 2003, **13**, 614, DOI: 10.1039/B209578E (*Cited on page 282*).

[432] S. Ding and C. A. McDowell, *Chem. Phys. Lett.*, 2000, **320**, 316, DOI: 10.1016/S0009-2614(00)00272-4 (*Cited on page 282*).

[433] M. G. Mortuza, R. Dupree and S. C. Kohn, *Appl. Magn. Reson.*, 1993, **4**, 89, DOI: 10.1007/BF03162557 (*Cited on page 282*).

[434] P. J. Barrie, *Chem. Phys. Lett.*, 1993, **208**, 486, DOI: 10.1016/0009-2614(93)87177-5á (*Cited on page 282*).

[435] H. D. Morris and P. D. Ellis, *J. Am. Chem. Soc.*, 1989, **111**, 6045, DOI: 10.1021/ja00198a012 (*Cited on page 282*).

[436] H. D. Morris, S. Bank and P. D. Ellis, *J. Phys. Chem.*, 1990, **94**, 3121, DOI: 10.1021/j100370a069 (*Cited on page 282*).

[437] L. Kellberg, M. Linsten and H. J. Jakobsen, *Chem. Phys. Lett.*, 1991, **182**, 120, DOI: 10.1016/0009-2614(91)80114-D (*Cited on page 282*).

[438] J. Rocha and J. Klinowski, *J. Chem. Soc., Chem. Commun.*, 1991, 1121, DOI: 10.1039/C39910001121 (*Cited on page 282*).

[439] C. A. Fyfe, K. T. Mueller, H. Grondey and K. C. Wong-Moon, *J. Phys. Chem.*, 1993, **97**, 13484, DOI: 10.1021/j100153a012 (*Cited on page 282*).

[440] G. Mali and V. Kaučič, *J. Chem. Phys.*, 2002, **117**, 3327, DOI: 10.1063/1.1493196 (*Cited on page 282*).

[441] D. M. Roberge, H. Hausmann and W. F. Hölderich, *Phys. Chem. Chem. Phys.*, 2002, **4**, 3128, DOI: 10.1039/B110679C (*Cited on page 282*).

[442] K. Kanehashi and K. Saito, *Fuel Process. Technol.*, 2004, **85**, 873, DOI: 10.1016/j.fuproc.2003.10.008 (*Cited on page 282*).

[443] T. H. Walter, G. L. Turner and E. Oldfield, *J. Magn. Reson.*, 1988, **76**, 106, DOI: 10.1016/0022-2364(88)90205-3 (*Cited on page 282*).

[444] T. H. Walter and E. Oldfield, *J. Phys. Chem.*, 1989, **93**, 6744, DOI: 10.1021/j100355a034 (*Cited on page 282*).

[445] J. Blanchard, C. Bonhomme, J. Maquet and C. Sanchez, *J. Mater. Chem.*, 1998, **8**, 985, DOI: 10.1039/A800118I (*Cited on page 282*).

[446] R. G. Bryant, S. Ganapathy and S. D. Kennedy, *J. Magn. Reson.*, 1987, **72**, 376, DOI: 10.1016/0022-2364(87)90303-9 (*Cited on page 282*).

[447] J. C. Edwards and P. D. Ellis, *Magn. Reson. Chem.*, 1990, **28**, S59, DOI: 10.1002/mrc.1260281312 (*Cited on page 282*).

[448] S. E. Ashbrook, S. P. Brown and S. Wimperis, *Chem. Phys. Lett.*, 1998, **288**, 509, DOI: 10.1016/S0009-2614(98)00308-X (*Cited on page 282*).

[449] S. E. M. Ashbrook, J. McManus, K. J. D. MacKenzie and S. Wimperis, *J. Phys. Chem. B*, 2000, **104**, 6408, DOI: 10.1021/jp000316t (*Cited on page 282*).

[450] S. E. Ashbrook and S. Wimperis, *Chem. Phys. Lett.*, 2001, **340**, 500, DOI: 10.1016/S0009-2614(01)00453-5 (*Cited on page 282*).

[451] T. Iijima, K. Kanehashi, K. Saito, M. Hatakeyama, T. Nemoto, T. Shimizu and S. Ohki, *Chem. Lett.*, 2005, **34**, 1380, DOI: 10.1246/cl.2005.1380 (*Cited on page 282*).

[452] S. E. Ashbrook and S. Wimperis, *Mol. Phys.*, 2000, **98**, 1, DOI: 10.1080/00268970009483265 (*Cited on pages 282, 287, 293, 295, 301, 309*).

[453] G. Bodenhausen, H. Kogler and R. R. Ernst, *J. Magn. Reson.*, 1984, **213**, 276, DOI: 10.1016/j.jmr.2011.08.033 (*Cited on pages 283, 373*).

[454] A. Wokaun and R. R. Ernst, *Chem. Phys. Lett.*, 1977, **52**, 407, DOI: 10.1016/0009-2614(77)80476-4 (*Cited on page 283*).

[455] R. Eckman, L. Muller and A. Pines, *Chem. Phys. Lett.*, 1980, **74**, 376, DOI: 10.1016/0009-2614(80)85182-7 (*Cited on page 288*).

[456] O. Rodrigues, *Des lois géométriques qui régissent les déplacements d'un système solide dans l'espace: et de la variation des cordonnées provenant de ces déplacements considérés indépendamment des causes qui peuvent les produire*, 1840 (*Cited on page 330*).

[457] E. W. Weisstein, 1999, http://mathworld.wolfram.com/SphericalCoordinates.html (*Cited on page 330*).

[458] M. Mehring, *Principles of high resolution NMR in solids*, Springer Science & Business Media, 2012 (*Cited on page 334*).

[459] A. Steigel, *NMR: basic principles and progress.* Springer, 1978, vol. 15 (*Cited on page 334*).

[460] J. W. Doane, F. Owens, C. Poole Jr and H. Farach, *Magnetic resonance of phase transitions*, ISBN: 9781483219059, 1979 (*Cited on page 334*).

[461] U. Haeberlen and M. Mehring, *High resolution NMR spectroscopy in solids*, 1976, vol. 1 (*Cited on page 334*).

[462] P. Pyykkö, *Mol. Phys.*, 2001, **99**, 1617, DOI: 10.1080/00268970110069010 (*Cited on page 341*).

[463] R. Dupree and M. E. Smith, *J. Chem. Soc., Chem. Commun.*, 1988, 1483, DOI: 10.1039/c39880001483 (*Cited on page 342*).

[464] R. W. Schurko, R. E. Wasylishen and H. Foerster, *J. Phys. Chem. A*, 1998, **102**, Al(acac)3, 9750, DOI: 10.1021/jp982367k (*Cited on page 344*).

[465] D. Lee and P. J. Bray, *J. Magn. Reson.*, 1991, **94**, 51, DOI: 10.1016/0022-2364(91)90293-3 (*Cited on page 344*).

[466] S. Hayashi and K. Hayamizu, *Bull. Chem. Soc. Jpn*, 1990, **63**, 913, DOI: 10.1246/bcsj.63.913 (*Cited on page 345*).

[467] K. E. Johnston, M. R. Mitchell, F. Blanc, P. Lightfoot and S. E. Ashbrook, *J. Phys. Chem. C*, 2013, **117**, 2252, DOI: 10.1021/jp310878b (*Cited on page 345*).

[468] J. Skibsted and H. J. Jakobsen, *J. Phys. Chem. A*, 1999, **103**, 7958, DOI: 10.1021/jp9912861 (*Cited on pages 347, 348*).

[469] O. B. Lapina, D. F. Khabibulin, K. V. Romanenko, Z. Gan, M. G. Zuev, V. N. Krasil'nikov and V. E. Fedorov, *Solid State Nucl. Magn. Reson.*, 2005, **28**, 204, DOI: 10.1016/j.ssnmr.2005.09.003 (*Cited on page 348*).

[470] J. Keeler, in *Multinuclear Magnetic Resonance in Liquids and Solids —Chemical Applications*, Springer, 1990, pp. 103–129, DOI: 10.1007/978-94-009-2149-8 (*Cited on page 370*).

[471] H. Kessler, M. Gehrke and C. Griesinger, *Angew. Chem. Int. Ed. Engl.*, 1988, **27**, 490, DOI: 10.1002/anie.198804901 (*Cited on page 370*).

[472] M. H. Levitt, P. Madhu and C. E. Hughes, *J. Magn. Reson.*, 2002, **155**, 300, DOI: doi:10.1006/jmre.2002.2520 (*Cited on page 371*).

[473] M. R. Bendall and D. T. Pegg, *J. Magn. Reson.*, 1986, **67**, 376, DOI: 10.1016/0022-2364(86)90447-6 (*Cited on page 385*).

[474] S. Conolly, D. Nishimura and A. Macovski, *J. Magn. Reson.*, 1989, **83**, 324, DOI: 10.1016/0022-2364(89)90194-7 (*Cited on page 385*).

[475] R. A. De Graaf and K. Nicolay, *Concepts Magn. Reson.*, 1997, **9**, 247, DOI: 10.1002/(SICI)1099-0534(1997)9:4<247::AID-CMR4>3.0.CO;2-Z (*Cited on page 385*).

[476] R. Freeman, 1987 (*Cited on page 387*).

[477] J.-M. Bohlen, M. Rey and G. Bodenhausen, *J. Magn. Reson.*, 1989, **84**, 191, DOI: 10.1016/0022-2364(89)90018-8 (*Cited on page 389*).

[478] J. Bohlen and G. Bodenhausen, *J. Magn. Reson. A*, 1993, **102**, 293, DOI: 10.1006/jmra.1993.1107 (*Cited on page 389*).

[479] E. Barbier, *Traitement du signal en RMN*, Université de Grenoble, INSERM U594, 2003, http://physique-eea.ujf-grenoble.fr/intra/Formations/M2/Physique/M2Recherche/UEs/PHY523r/cours_ebarbier_0304.pdf (*Cited on page 391*).

[480] L. Petrakis, *J. Chem. Educ.*, 1967, **44**, 432, DOI: 10.1021/ed044p432 (*Cited on page 396*).

[481] C. E. Shannon, *Proc. IRE*, 1949, **37**, 10 (*Cited on page 401*).

[482] J. W. Cooley and J. W. Tukey, *Math. Comput.*, 1965, **19**, 297, DOI: 10.2307/2003354 (*Cited on page 402*).

[483] P. Duhamel and M. Vetterli, *Signal Process.*, 1990, **19**, 259, DOI: 10.1016/0165-1684(90)90158-U (*Cited on page 402*).

[484] T. Vosegaard, A. Malmendal and N. C. Nielsen, *The flexibility of SIMPSON and SIMMOL for numerical simulations in solid-and liquid-state NMR spectroscopy*, Springer, 2003, DOI: 10.1007/978-3-7091-3715-4_5 (*Cited on page 414*).

[485] M. Bak, J. T. Rasmussen and N. C. Nielsen, *J. Magn. Reson.*, 2011, **213**, 366, DOI: 10.1016/j.jmr.2011.09.008 (*Cited on page 414*).

List of symbols and acronyms

This part lists and describes all symbols and acronyms used in this thesis, sorted by alphabetical order. In the case of Greek letters, symbols are sorted by the Greek alphabetical order, followed by other symbols. The page numbers where these symbols or abbreviations are first introduced in the main text (if applicable) are on the right-hand side of each entry.

Acronyms

Numbers

A

AFP - *Adiabatic Full Passage* 25, 254, 388
AHP - *Adiabatic Half Passage* 25, 388
AM - *Amplitude Modulation* 159
AMT - *Angular Momentum Theorem* 39

C

COMPACT - *COMposite Pulses Adapted for Central Transitions* 23, 30, 254
CP - *Cross Polarisation* 22, 24, 27, 106
CPMG - *Carr-Purcell-Meiboom-Gill* 22, 27, 104
CS - *Chemical Shift* 75, 378
CSA - *Chemical Shift Anisotropy* 75
CSCO - *Complete Set of Commuting Observables* 44
CT - *Central-Transition* 23, 88
CTP - *Coherence Transfer Pathway* 101, 369
CW - *Continuous-Wave* 142

D

DAS - *Dynamic Angle Spinning* 133
DFS - *Double Frequency Sweep* 23, 29, 159
DNP - *Dynamic Nuclear Polarisation* 27, 142
DOR - *DOuble Rotation* 133

E

EFG - *Electric Field Gradient* 84

F

FAM - *Fast-Amplitude Modulation* 23, 29, 162, 164
FAM-N - *Fast-Amplitude Modulation* with N pulses 22, 23, 25, 29, 139, 165, 166, 168
FASTER - *FAst Spinning gives Transfer Enhancement at Rotary resonance* 22, 29, 153
FFT - *Fast Fourier Transform* 402
FID - *Free Induction Decay* 62
FM - *Frequency Modulation* 159
FT - *Fourier Transform* 25, 62, 391
FTD - *Discrete Fourier Transform* 398

G

GPL - GNU *General Public License* 413

H

HS - *Hyperbolic Secant* 23, 24, 30, 253

I

IFT - *Inverse Fourier Transform* 393

SFAM - *Shifted Fast-Amplitude Modulation* . . . 315
SFS - *Single-Frequency Sweep* . . . 159
SIMPSON - *SIMulation Package for SOlid-state Nmr* . . . 25, 29, 165
SL - *Spin-Lock* . . . 22, 107
SNR - *Signal-to-Noise Ratio* . . . 104
SOLA - *SOlid Lineshape Analyser* . . . 132
SOQE - *Second-Order Quadrupolar Effects* . . . 95
SPAM - *Soft Pulse Adding Mixing.* . . . 22, 29, 148
ssDFS - *Sideband-Selective Double-Frequency Sweep* . . . 257
ST - *Satellite-Transition* . . . 22, 88
STMAS - *Satellite-Transition Magic-Angle Spinning* . . . 22, 25, 28, 134
sw-FAM - *frequency-SWept Fast-Amplitude Modulation* . . . 164

T

TDSE - *Time-Dependent Schrödinger Equation* . . . 51
TISE - *Time-Independent Schrödinger Equation* . . . 51
TPPI - *Time-Proportional Phase Increment* . . . 123

Symbols (Roman and numbers)

Numbers

$\hat{1}_3$ - Order-3 identity matrix . . . 53
$\hat{1}_N$ - Order-N identity matrix . . . 89

a A

a - Eigenvalue associated with $\hat{A}$ . . . 43
$\hat{A}$ - Generic operator . . . 43
A - First term of the dipolar alphabet . . . 79
A, B, C - The three orientation-dependent functions used $\nu_{CT}^{(2)}$ . . . 94
$\{A, B, C, D, E, F\}$ - Dipolar alphabet . . . 79
$A_{l,m}$ - Irreducible sperical tensor, spatial part of rank l and order m . . . 69
$A_{l,m}^{L}$ - $A_{l,m}$ written in Σ_{lab} . . . 70

b B

$\vec{b}$ - Unit magnetic field of the RF coil L . . . 61
$\vec{B}$ - Magnetic field . . . 37
$\hat{B}$ - Generic operator . . . 44
B - Second term of the dipolar alphabet . . . 79
$\vec{B}_0$ - Static magnetic field . . . 38
B_0 - (Scalar) Norm of $\vec{B}_0$ . . . 40

i I

q Q

r R

s S

t T

u U

v V

w W

Symbols (Greek and others)

Operations and others

α A

β B